NREL-CP-433-7748

Applications of Free-Jet, Molecular Beam, Mass Spectrometric Sampling

Proceedings

Estes Park, Colorado
October 11-14, 1994

Hosted by:
The National Renewable Energy Laboratory
and
Extrel Mass Spectrometry

Available to DOE and DOE contractors from:
Office of Scientific and Technical Information (OSTI)
P.O. Box 62
Oak Ridge, TN 37831
Prices available by calling (615) 576-8401

Available to the public from:
National Technical Information Service (NTIS)
U.S. Department of Commerce
5285 Port Royal Road
Springfield, VA 22161
(703) 487-4650

DISCLAIMER

Portions of this document may be illegible in electronic image products. Images are produced from the best available original document.

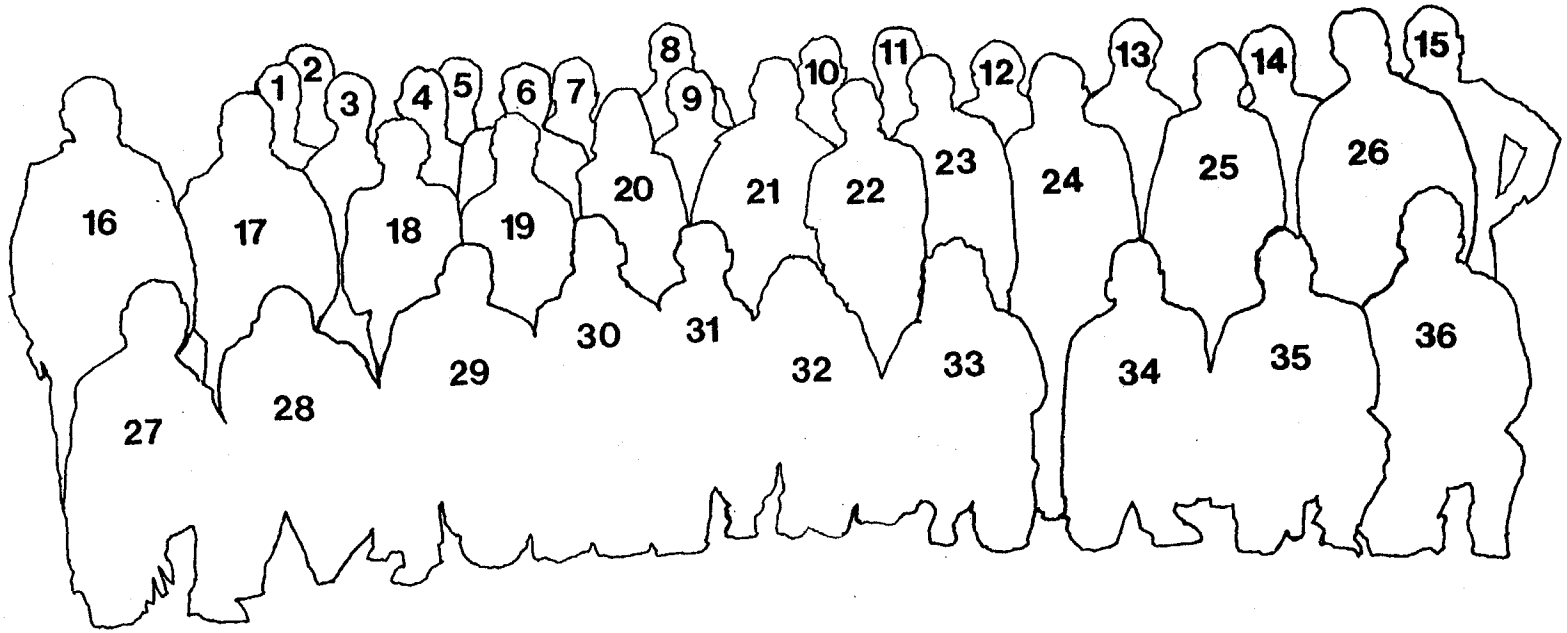

Front Row: T. Milne, O. Korobeinichev, K. Homann, M. Weisel, R. French, C. Amata-Wierda, M. Maniet, N.Jacobson, D. Dayton, D. Wang
Middle Row: R. Campargue, C. Vovelle, C. Doute, C. Fox, L. Yeh, D. Kern, J. Hastie, D. Miller, G. Pellett, J. Fenn, A. Amirav
Back Row: J. Vandooren, D. Anex, P. Westmorland, D. Rakestraw, R. Evans, E. Knuth, S. Gebhard, R. Behrens, J. Patrick, R. Pedder, R. Schaeffer, T. Litzinger, P. Ziemann, F. Greene, H. Meuzelaar

Organizing Committee

Thomas A. Milne
National Renewable Energy Laboratory
1617 Cole Boulevard
Golden, CO 80401
Phone: (303) 384-6245
Fax: (303) 384-6103

David C. Dayton
National Renewable Energy Laboratory
1617 Cole Boulevard
Golden, CO 80401
Phone: (303) 384-6216
Fax: (303) 384-6103

Richard J. French
National Renewable Energy Laboratory
1617 Cole Boulevard
Golden, CO 80401
Phone: (303) 384-6135
Fax: (303) 384-6103

Frank T. Greene
MRI
425 Volker Boulevard
Kansas City, MO 64110
Phone: (816) 753-7600
Fax: (816) 753-8420

Sponsored by the USDOE National Renewable Energy Laboratory, a Division of Midwest Research Institute

Preface

Over the past 35 years, the study of the behavior and uses of free-jet expansions for laboratory experiments has greatly expanded and matured. Not the least of these uses of free-jet expansions, is that of extractive sampling from high temperature, reactive systems. The conversion of the free-jet expanded gases to molecular flow for direct introduction into the ion source of a mass spectrometer offers several advantages, to be illustrated in these pages.

Two meetings on this subject were held in 1965 and 1972 in Missouri, sponsored by the Office of Naval Research and Midwest Research Institute. At these meetings rarefied gas dynamicists came together with scientists using free-jet sampling for analytical purposes. After much too long a time, this workshop was convened to bring together modern practitioners of FJMBS (Free-jet, Molecular-beam, mass spectrometry) and long time students of the free-jet process itself, to assess the current state of the art and to forge a community that can foster the development of this novel analytical approach.

The organizing committee thanks the then Director of the National Renewable Energy Laboratory, Dr. Duane Sunderman, for supporting this meeting with funds from the Director's Development Fund. We also express our appreciation to Extrel Mass Spectrometry and Rick Schaeffer for support of the meeting and for the equipment they have supplied many of us over the years.

Finally, thanks are due to Ms. Jeri Wagner (NREL Conferences), Ms. Gina Lindsey and Ms. Angela Goldie (Process Research Branch) for their assistance at the meeting, with arrangements, and in preparation of these proceedings.

Thomas A. Milne,
for the Organizing Committee

Applications of Free-Jet, Molecular Beam, Mass Spectrometric Sampling

FINAL PROGRAM

Tuesday, October 11, 1994

TIME	FUNCTION
5:00 - 6:00	Supper in Cafeteria (if desired)
6:00 - 9:00	Registration **Reception Hosted by Extrel Mass Spectrometry -** **Food and drinks will be served*

Wednesday, October 12, 1994

Morning - Session #1 Chair - Frank Greene	
TIME	**FUNCTION**
7:00 - 8:00	Breakfast served in cafeteria
8:00 - 8:10	Welcome
8:10 - 9:10	John Fenn - *The Free Jet Set of Sampling - A Motley Mix of Methods and Mortals* (Virginia Commonwealth University)
9:10 - 10:10	David Miller - *Principles of Free Jets* (University of California at San Diego)
10:10 - 10:40	Coffee Break
10:40 - 11:40	Eldon Knuth - *Composition Distortion in MBMS Sampling,* (UCLA)
11:40 - 12:30	Roger Campargue - *MBMS Sampling from Highly-Heated Gas Mixtures (1000-3000 K) and Weakly Ionized RF or Laser Plasmas (5,000 - 20,000 K)* (Laboratorie des Jets Moléculaires)
12:30 - 1:00	Lunch served in cafeteria
1:00	Afternoon - Free time, Set up Posters, Park Service Tour
1:15 - 3:15	Park Service Tour
5:00 - 7:00	Dinner served in cafeteria
Evening - Session #2 **Chair - Karl Homann** **(Refreshments served at 8:30pm)**	
7:00 - 7:30	Aviv Amirav - *Electron Impact, Hyperthermal Surface Ionization and Fast GC-MS in Supersonic Molecular Beams* - (Tel Aviv University)
7:30 - 8:00	Christian Vovelle - *MBMS and Gas Phase Chromatography Studies of n-heptane and Iso-Octane Flames (*Laboratoire de Combustion et Systemes Reactifs)
8:00 - 8:30	Henk Meuzelaar - *Comparison of On-Line MS Technique for Complex Reactive Systems* (Univ of Utah)
8:30 - 8:45	Break with refreshments
8:45 - 9:15	Frank Greene - *The Observation of Very Large Species in MBMS Experiments* (Midwest Research Institute)
9:15 - 9:45	Paul Ziemann - *Particle Beam Mass Spectrometry of Submicron Particles Sampled from Low-Pressure Environments* (U. of Minnesota)
9:45 - 10:15	David Miller - *Mass Spectrometer Sampling of Supercritical Water-Oxidation Reactions* (University of California at San Diego)
10:00	Adjourn

Thursday, October 13, 1994

MORNING - SESSION #3 **Chair - Mel Branch**	
TIME	**FUNCTION**
7:00 - 8:00	Breakfast served in cafeteria
8:30 - 9:00	Oleg Korobeinichev - *An MBMS Study of $H_2/O_2/Ar$ Flames Doped with Phosphorus Compounds* (Institute for Chem Kinetics and Combustion, Novosibirsk)
9:00 - 9:30	Richard Kern - *Time-of-Flight Mass Spectrometric Analysis of Reflected Shock Zone Gases and High Speed Data Analysis* (University of New Orleans)
9:30 - 10:00	Jacques Vandooren - *Mass Spectrometry as an Efficient Tool for Kinetic Studies in Flames* (U. Catholique de Louvain)
10:00 - 11:00	Poster Session with refreshments
11:00 - 11:30	Phillip Westmoreland - *Obtaining Kinetics from MBMS and Modeling of Propene Flame Structure* (U of Massachusetts)
11:30 - 12:00	Rosario Sausa - *Flame Structure Studies of Neat and NH_3 - Doped H_2/N_2O_2 Flames Employing Molecular Beam Mass Spectrometry and Modeling* (U.S. Army Research Laboratory)
12:00 - 12:30	William Anderson - *Molecular Beam/Mass Spectometry and Modeling Studies of CF_3Br Inhibited Flames* (U.S. Army Laboratory)
12:30 - 1:00	Lunch served in cafeteria
1:00 - 5:00	Afternoon - Free time
5:00 -7:00	Dinner served in cafeteria
	EVENING - SESSION #4 **Chair- Aviv Amirav**
7:00 - 7:30	Tom Litzinger - *A Study of Solid Propellant Combustion Using a Triple Quadrupole Mass Spectrometer with Microprobe Sampling* (Penn State)
7:30 - 8:00	Richard Behrens - *Application of the Simultaneous Thermogravimetric Modulated Beam Mass Spectrometry Technique (STMBMS) to the Study of Energetic Materials* (Sandia National Laboratory Livermore)
8:00 - 8:30	Karl Homann - *Analysis of Mass Distributions of Soot-Particles from Low Pressure Flames by Means of Free-Jet Sampling and a Wien Filter* (Institute for Physical Chemistry, Darmstadt)
8:30 - 9:00	Nathan Jacobsen - *Studies of Volatile High Temperature Corrosion Products via theFree-Jet MBMS Technique* (NASA Lewis Res. Center)
9:00 - 10:00	Poster Session with refreshments

FRIDAY, OCTOBER 14, 1994

MORNING - SESSION #5 **Chair - Nathan Jacobsen**	
Time	**Function**
7:00 - 8:00	Breakfast served in cafeteria
8:00 - 8:30	Ciaran Fox - *MBMS Studies of Gas-Phase Kinetics in CVD of Diamond* (Sandia National Laboratory, Livermore)
8:30 - 9:00	David Dayton - *Direct Sampling of Inorganic Vapors Released During Biomass Combustion* (NREL)
9:00 - 9:30	John Hastie - *Application of Free-Jet MBMS to Laser Ablation Plumes Particularly During Thin Film Deposition* - (NIST)
9:30 10:00	Break
10:00 - 10:30	Carmela Amato-Wierda - *Molecular Beam Mass Spectrometer Studies of the Decomposition of Tetraethoxysilane to SiO_2 Nanoparticles* (NIST)
10:30 - 11:00	Christian Vovell - *Mass Discrimination Effects in MBMS Study of Rich Pre-Mixed Flames* (Laboratoire de Combustion et Systemes Reactifs)
11:00 - 11:30	Oleg Korobeinichev - *A Study of Solid Propellant Flame Structure by Mass Spectrometric Sampling Including MBMS* (Institute for Chem Kinetics and Combustion)
11:30 - 12:30	Closing Discussion
12:30 - 1:00	Lunch served in cafeteria
2:00 - 4:00	**Shuttle or car pool to Denver and the Airport will be available**

POSTERS

Presenter	Affiliation	Title
Foster Agblevor	National Renewable Energy Laboratory	*Rapid Characterization of Lignocellulosic Feedstocks for Fuels and Chemicals: Molecular Beam Mass Spectrometric Approach*
Carolyn Elam	National Renewable Energy Laboratory	*The Application of MBMS to the Problem of Plastics Recycling Through Intelligent Chemical Processing*
Extrel	Extrel Mass Spectrometry	*Mass Spectrometers and Accessories for MBMS*
Rick French	National Renewable Energy Laboratory	*MBMS of Biomass Pyrolysis Vapors and Catalytic Upgrading*
Steve Gebhard	National Renewable Energy Laboratory	*Molecular Beam Mass Spectrometry Applied to Biomass Gasification Monitoring*
Frank Greene	Midwest Research Institute	*Chemistry and Kinetics of Chlorine Oxides Under Stratospheric Conditions*
Mark Nimlos	National Renewable Energy Laboratory	*Molecular Beam, Mass Spectrometric Sampling in Hazardous Waste Destruction*
Matthew Ratcliff	National Renewable Energy Laboratory	*The NREL Transportable MBMS and it's Applications*
Vasilii I. Smirnov	Ivanova State University	*A Study of Sampling Phenomena in a Probe Nozzle for High Temperature MBMS*
Dingneng Wang	National Renewable Energy Laboratory	*Quantitative Sampling Using Free-Jet, MBMS*
Mark Weisel	Exxon	*Quantitative Measurements of Radical Intermediates by Molecular Beam Sampling Mass Spectrometric*
Lisa Yeh	Exxon	*A New MBMS Flame Chamber for the Study of Molecular Weight Growth Reactions*

Table of Contents

Applications of Free-Jet, Molecular Beam Mass Spectrometric Sampling

Page

Preface iii

Program iv

Free Jet Set of Sampling - A Motley Mix of Methods and Applications
J. B. Fenn 1

Principles of Free Jets
D. R. Miller 7

Composition Distortion in MBMS Sampling
E. L. Knuth 18

MBMS Sampling from Highly-Heated Gas Mixtures (1,000 - 3,000K) and Weakly Ionized RF Plasmas (800-2800K) or Laser Plasmas (5,000 - 20,000K)
R. Campargue and A. Lebéhot 33

Electron Impact, Hyperthermal Surface Ionization and Fast GC-MS in Supersonic Molecular Beams- A. Amirav and S. Dagan 43

MBMS and Gas Phase Chromatography Studies of n-heptane and Iso-Octane Flames .....
C. Vovelle, C. Douté and J. L. Delfau 51

Comparison of On-Line Techniques for Complex Reactive Systems .....
H. L.C. Meuzelaar 57

The Observation of Very Large Species in MBMS Experiments
F. T. Greene 65

Particle Beam Mass Spectrometry of Submicron Particles Sampled from Low-Pressure Environments - P. J. Ziemann, P. Liu, D. B. Kittelson, P.H. McMurry, and S. A. Campbell 80

Mass Spectrometer Sampling of Supercritical Water-Oxidation Reactions
D.R. Miller and S. Maharrey 86

Molecular Beam Mass-Spectrometric Study of $H_2/O_2/Ar$ Flames Doped with Phosphorus Compounds - O. Korobeinichev, A. Chernov, V. Shvartsberg, S. Il'in 92

Time-of-Flight Mass Spectrometric Analysis of Reflected Shock Zone Gas Mixtures and High Speed Data Analysis
R.D. Kern, H. Chen, H.J. Singh, E.A. Branley and J. Yao 98

Mass Spectrometry as an Efficient Tool for Kinetic Studies in Flames
J. Vandooren and P.J. Van Tiggelen 104

Obtaining Kinetics from MBMS and Modeling of Propene Flame Structure
P. R. Westmoreland, S. D. Thomas and A. Bhargava 110

Flame Structure Studies of Neat and NH_3 - Doped H_2/N_2O Flames Employing Molecular Beam Mass Spectrometry and Modeling -
R. C. Sausa, G. Singh, G.W. Lemire and W.R. Anderson 116

Molecular Beam/Mass Spectrometric and Modeling Studies of CF_3Br Inhibited Flames
W.R. Anderson, R. C. Sausa, G. W. Lemire, G. Singh 122

A Study of Solid Propellant Combustion Using a Triple Quadrupole Mass Spectrometer with Microprobe Sampling - T.A. Litzinger, Y.J. Lee, C.J Tang 128

Application of Simultaneous Thermogravimetric Modulated Beam Mass Spectrometry to the Study of Energetic Materials - R. Behrens, Jr.. 136

Determination of Mass and Velocity Distributions of Soot Particles in a Nozzle Beam from a Flame by Means of a Wien Filter - K.-H Homann and W. Wiese 146

Studies of Volatile High Temperature Corrosion Products via the Free-Jet MBMS Technique
N. S. Jacobson 152

MBMS Studies of Gas-Phase Kinetics in Diamond Chemical Vapor Deposition
C. A. Fox, M. C. McMaster, D. M. Tung, W L. Hsu, M. E. Coltrin, D. S. Dandy 159

Direct Sampling of Inorganic Vapors Released During Biomass Combustion
D. C. Dayton and T. A. Milne 166

Free-Jet Mass Spectrometry of Laser Ablation Plumes in Thin Film Deposition
J. W. Hastie, A.J. Paul, D. W. Bonnell 175

Molecular Beam Mass Spectrometry Studies of the Thermal Decomposition of Tetraethoxy silane (TEOS)
C. A. Wierda, M. R. Zachariah and D. R.F. Burgess, Jr. 181

Mass Discrimination Effects in MBMS Study of Rich Premixed Flames
C. Vovelle, C. Douté and J.L. Delfau 187

Study of Solid Propellant Flame Structure by Mass Spectrometric Sampling, Including MBMS- O. P. Korobeinichev, L. V. Kuibida, A.A. Paletshii 193

Rapid Characterization of Lignocellulosic Feedstocks for Fuels and Chemicals: Molecular Beam Mass Spectrometric Approach-
F. A. Agblevor, M.F. Davis, and R. J. Evans 200

The Application of Molecular Beam Mass Spectrometry to the Problem of Plastics Recycling Through Intelligent Chemical Processing
C. Elam, R. Meglen, K. Tatsumoto, E. Evans, C. Chum 211

MBMS of Biomass Pyrolysis Vapors and Catalytic Upgrading
R. J. French and B. Rejai 216

Molecular Beam Mass Spectrometry Applied to Biomass Gasification Monitoring
S.C. Gebhard, D. A Gratson, R. J. French, and M.A. Ratcliff 227

Chemistry and Kinetics of Chlorine Oxides Under Stratospheric Conditions
F. T. Greene, D. A. Robaugh 239

Molecular Beam, Mass Spectrometric Sampling in Hazaradous Waste Destruction .....
M. R. Nimlos, T. A. Milne, K. T. McKinnon 243

Continuous Diesel Emissions Speciation with a Transportable MBMS System
M. A. Ratcliff, D. A. Gratson, and T. A. Milne 250

A Study of Sampling Phenomena in a Probe Nozzle for High Temperature MBMS .....
V. I. Smirnov 268

Quantitative Sampling Using Free-Jet, Molecular Beam Mass Spectrometry
D. Wang, R. Meglen, and R. J. Evans 275

Quantitative Measurements of Radical Intermediates by Molecular-Beam-Sampling-Mass-Spectrometry -A. Y. Chang, A. M. Dean, and M. D. Weisel 289

A New MBMS Flame Chamber for the Study of Molecular Weight Growth Reactions
L. I. Yeh, and K.M. Creegan 295

List of Attendees 300

FREE JET SAMPLING - A MOTLEY MIX OF METHODS AND APPLICATIONS

John B. Fenn, Department of Chemistry
Virginia Commonwealth University
Richmond, VA 23284-2006

Introduction. When flowing gas issues into a chamber from an orifice or nozzle whose diameter is much smaller than that of the chamber, the resulting flow field constitutes a "free jet" bounded by relatively quiesecent gas. If the pressure ratio across that nozzle or orifice exceeds a critical value (around 2.5 for most gases) the flow velocity will exceed the local speed of sound and the flow field is called a "supersonic free jet". Though somewhat exotic in name such supersonic jets are really quite common. They are formed from moderate leaks into vacuum systems and out of high pressure containers. They are produced by the venting of boilers or the cylinders of reciprocating heat engines. They are embodied in the flow from gas wells, jet engines and rockets, as well as in the discharge of fire arms and air guns. Even a vigorous sneeze will sometimes produce one. On Nature's larger canvas they appear when volcanoes erupt and when sun spots form. In spite of such ubiquity and except for ordnance ballistic studies, the behaviour of gas expanding through very high pressure ratios and without restraining walls did not receive much attention until after World War II. What might be regarded as the modern era for analysis and application of supersonic free jets began in 1948 with a calculation by Owen and Thornhill [1] who used the method of characteristics to solve Euler's equation for the flow field formed by the free expansion of gas from a sonic orifice into a region of zero pressure. Three years later in another now-classic paper Kantrowitz and Grey [2] proposed the use of a supersonic low density flow field as a source for molecular beams of high intensity. These two independent communications, motivated by entirely different interests and objectives, were destined to become related as the ancestors of a large progeny that form a flourishing family tree with many roots and branches.

Some of the fruits of that tree are being served at this conference. They come from a branch that sprouted from the early experiments of E.W. Becker and his colleagues [3] at the University of Marburg in 1954. These investigators were the first to achieve, by design, substantial success in reducing to practice the ideas set forth by Kantrowitz and Grey. However, in the interests of historical accuracy it should be noted 27 years earlier, T. H. Johnson at Yale [4] produced an intense molecular beam from a supersonic free jet of mercury vapor. Unfortunately, at that time his results were neither understood nor appreciated so he has not received the recognition and credit that he clearly deserves.

Free Jets and Mass Spectrometry. The now-available methods of detection and analysis by mass spectrometry must be carried out in vacuum, but many of the substances to be analyzed, i.e. "analytes", are in environments at substantial pressures. Therefore, the transfer of samples from their origin into a mass spectrometer frequently involves the formation, properties and behaviour of supersonic free jets, especially when the samples are gaseous or are dispersed in a gaseous medium. From the perspective of history it seems fair to say that much of what we know about these jets stems from their use as sources for molecular beams. Indeed, molecular beams are themselves "samples" that carry information about the composition and condition of the source material. Examination of such beam samples by a variety of techniques allows investigators to "read" that information and thus to know the source conditions as well as what happened to the molecules between the source and their interrogation. Such interrogation has revealed that the supersonic expansion of free jet sources embodies a remarkably variegated array of phenomena that can have a substantial effect on the nature of the beam sample. It is thus entirely appropriate that two of the papers in this conference will review what we know and understand about supersonic free jet expansions and the formation and properties of the molecular beams they produce. This report will describe some less familiar facets of free jet sampling that might be useful to know. It will also offer some anecdotal perspectives from one who has been both participant and bystander in the process of learning from these deliberate leaks.

Species Separation. The first paper from the Becker group [3] was on the production of an intense beam of hydrogen molecules. It reported apparent beam intensities that were ten times higher when the source hydrogen gas contained a few per cent of argon than when it was pure. The authors reasoned that this difference was due to a separation effect that somehow increased the argon content of the beam entering the detector. The second paper [4] reported that the separation was occurring in the supersonic free jet, upstream of the skimmer through which the core of that jet passed into the second stage of the vacuum system. The resulting enrichment was attributed to pressure diffusion by which the hydrogen molecules migrated away from the jet axis more rapidly than did the heavier argon molecules. The authors then concluded that to study this "trennduse" (separating nozzle) phenomenon it would be easier to sample the jet gas with a simple probe than with a molecular beam apparatus. Experiments with such a probe indeed seemed to showed substantial enrichment of heavy species in gas sampled on the jet centerline.

It has since emerged that the separation observed in the first experiment was due simply to so-called Mach number focusing aft of the skimmer by which the divergence of a beam of light molecules is greater than for a beam of heavy molecules. The enrichment in the probe samples turned out to be due to inertial slip effects during stagnation of jet gas at the probe entrance. When the probe was pumped hard enough so that the sample gas entered with no stagnation, the centerline gas samples showed the same compos-

ition as the source gas.[5] It now seems clear that radial diffusion played no role in the separations found by those early investigators. Even so, diffusion can bring about some separation, but only at much lower nozzle Reynolds numbers than those of the reported experiments. Moreover, when there are very large mass differences between heavy and light species, the inertial slip that produced stagnation separation in the first probe experiments can also bring about separation in the jet proper. However, diffusion is not the mechanism by which such separation occurs. Some further insight on inertial slip effects will emerge in the next section's account of experiments with aerosol particles.

Aerosol Flows. The idea that inertial slip during stagnation on a small probe could account for species separation at a molecular level was in retrospect a fairly straightforward extension of the well known size-dependent separation of particulate matter on impact probes in particle-gas flows. If the flow velocity is sufficiently high, the gas density sufficiently low, and the particles sufficiently massive, their inertia prevents them from following any sharp deflections of the gas stream lines in the flow around a body immersed in the flow. The extent of a particle's slip in an accelerating gas flow is characterized by its Stokes number, defined as the ratio of the time required for the particle to adjust to a change in gas velocity to the time available for adjustment. In small free jets the expansion takes place very rapidly, both radially and axially. Particles with large values of the Stokes number will lag behind the gas in both directions. Consequently, their concentration will be higher on the axis of the jet than at its boundary. In addition, their axial velocity will be less than that of the gas. During expansion the gas density, and therefore the aerodynamic drag on the particle, decrease rapidly. Thus, there is not enough time in the expansion for the particle to catch up with the gas so the consequences of the slip persist. In sum, the concentration of particles on the axis remains high relative to the gas and their terminal axial velocity remains lower. Clearly, in the free jet expansions of gas mixtures there can be combinations of gas density, jet scale, and molecular mass, that will result in analogous slip effects, and therefore relative axial enrichment, for heavy molecules in a light carrier gas. Such enrichment will always be accompanied by a "deficit" in axial velocity.

A less familiar variation on the separation-by-slip theme involves the "vena contracta" phenomenon. When a free jet of gas results from flow through an orifice in a flat plate the upstream gas is accelerated toward the axis of the orifice. Inertial persistence of the resulting radial velocity causes overshooting of the streamline convergence. Consequently, the flow diameter immediately downstream of the orifice becomes less than the diameter of the orifice. Israel and Friedlander recognized that in such a flow the trajectories of particles with large values of the Stokes number could converge more than the gas streamlines and thus increase the particle concentration on the jet axis. [6] In studies of this "focusing" de la Mora and his colleagues at Yale have been able

to increase the concentration of particles on the jet axis by factors of 600 or more.[7] They have also achieved similar focusing with molecules but the defocusing due to Brownian motion is much more severe for molecules than for particles.[8]

In addition to providing insight on what can happen to molecular species in free jet sampling the study of aerosol flow phenomena can provide insight on problems important in fields such as meteorology, the environment, medicine, and various branches of industrial technology. Because of relevance to the core theme of this conference it will be of interest to describe some recent work by Kimberly Prather and her colleagues at UC Riverside in which information from aerosol beam studies has led to an elegant solution of an important analytical problem. [9] From studies of aerosol particle beams formed by free jet expansions Dahneke and his collaborators developed a method for determining the size distribution of aerosol particles that is embodied in an instrument now on the market. [10,11] Particle laden gas at say atmospheric pressure is passed through a capillary into a low pressure region. During the flow through the capillary and in the free jet expansion at the capillary exit each particle is accelerated to a terminal velocity that depends upon its density, dimensions and shape, i.e. its "aerodynamic diameter". Upon passing through a low power laser beam the particle interrupts the flow of photons to a detector thus producing a signal pulse. The particle velocity is determined from the interval of time between the pulses from the interruption of two such laser beams a known distance apart. By means of calibration data the flight time can be translated into the terminal velocity of the particle and thus its size. The time at which the particle will arrive at the focal point of a high power third laser is determined from the velocity measurement. That third laser is fired as the particle arrives and the ions desorbed from the particle enter a drift tube and are mass analyzed by the Time-Of-Flight method. In this way Prather et al have been able to determine the composition of particles of particular size in an aerosol with a wide distribution of sizes. For example, in recent experiments they have measured the nicotine content of tobacco smoke particles of a size they select.

Surface Interference Problems. One frequently wants to carry out mass spectrometric analysis of gas samples from various points in a reacting system such as a burner or a flame. The usual approach is to withdraw the gas sample through a probe comprising a small tube with a tiny orifice at its inlet end. The probe is pumped so that the entering gas expands in a supersonic free jet. Clearly there are prospective problems with such sampling and there has been a lot of work done on the development of suitable probes. If the gas is reactive one can hope that the cooling during the expansion will arrest the reactions. Some investigators have provided for rapid mixing of the inhaled sample gas with a stream of cold inert diluent gas such as helium or argon to enhance quenching. A particularly nagging concern is the possible distortion of sample composition due to reaction induced by the probe surfaces, both external and internal. Because the dimensions of a

probe, and particularly its orifice, are usually very small the ratio of surface area to flow volume of the sampled gas is relatively high. Thus there would seem to be a strong likelihood that at least some of the sampled molecules will have contact with a surface. One handle on part of this problem comes from the measurements of Tang and Fenn on the discharge coefficients (DC's) of small orifices.[12] They obtained a formula for calculating the DC's of such orifices that was checked with a large number of very accurate measurements with orifice diameters down to 0.25 mm over Reynolds numbers from 100 to 10,000. As a result one can calculate DC's that are more reliable than measured values unless unusual care is taken with the measurements. It turns out that at nozzle Reynolds numbers down to 100 the DC is always above about 0.8. That figure translates into a boundary layer thickness of about 10 per cent of the nozzle diameter. Diffusion across a boundary layer is generally faster for momentum than for most species. Consequently, the composition of the core gas is not likely to be disturbed by wall effects during passage through the sampling orifice as long as the Reynolds number for flow through the inlet orifice remains above 50 or so, perhaps even less. Reassuring though this observation may be it leaves unanswered any questions about interaction between the sampled gas and the surface around the inlet aperture on the outside of the probe before the gas enters, or between that gas and the inside walls of the probe downstream from the inlet.

Combustion systems including flames and burners are popular sources of extracted samples for mass spectrometric analysis. Such systems are characterized by high temperatures and rapid reaction rates, both of which complicate the sampling problem. As an alternative approach to the study of combustion reactions Groeger and Fenn introduced a "microjet" burner. [13] It avoided some of the sampling problems by inverting the usual arrangement of apparatus. Combustion was carried out inside a refractory tube with a bore of 2 to 3 mm. The reaction zone, about 5 mm long and terminating at an exit nozzle 0.2 mm in diameter, was was stabilized by maintaining the tube walls at a sufficiently high temperature. The energy to maintain the temperature came in part from the reaction and in part from a resistance winding on the outside of the tube. The combustion intermediates and/or products exhausted through the nozzle and were rapidly cooled during the supersonic free jet expansion into a large vacuum system. Core gas of the free jet passed directly into the ionization source of a quadrupole mass spectrometer without further contact with any surface. By way of demonstrating the feasibility of this approach, mass spectra of exhaust gas were obtained for several fuel-oxidant combinations over a range of compositions, flow rates and temperatures. In addition, a Fourier Transform Infrared Spectrometer obtained emission spectra of the exhaust products. Work on this project ended before insight could be obtained on the combustion reactions by analyzing and interpreting the spectral data. Even so this "inside-out" approach seems worth pursuing. Also not tried but seemingly feasible with this burner is the mass analysis of ions produced by the combustion reactions.

Free Jets in Electron Microscopy. A final example of free jet versatility is its unusual role in the "Environmental Scannng Electron Microscope" (ESEM) introduced by G. D. Danilatos [14]. An electron beam is produced in vacuum and directed through the jet gas and source orifice to reach a specimen mounted in the stagnation chamber just upstream of the orifice. The very rapid axial decrease in gas density during free jet expansion from a small nozzle means that the integral product of gas density and path length is minimized and the beam can scan a specimen at pressures up to several tens of torr without undue scattering losses. Thus the free jet constitutes a window for SEM examination of processes and properties than cannot tolerate a vacuum. For example, the solvation of crystals by water vapor can be followed in great detail as can the interaction between polymers and solvent vapor. Indeed, an SEM picture of a live ant has been made. (At least it was alive at the beginning of the examination!)

References

1. P.O. Owen and C.K. Thornhill, Aeronaut. Res. Couuncil (UK) R & M No. 2616 (1948)

2. A. Kantrowitz and J. Grey, Rev. Sci. Instrum. 22, 328 (1951)

3. E.W. Becker and K.Bier, Z. Naturforsch. Teil A 9, 975 (2954)

4. E.W. Becker, K. Bier, H. Burghoff, Z. Naturforsch. Teil A 10, 565 (1955)

5. V.H. Reis and J.B. Fenn, J. Chem. Phys. 39, 3240 (1963)

6. G.W. Israel and S.K. Friedlander, J. Colloid Interface Sci. 24, 330 (1967)

7. J. Fernandez de la Mora, and P. Riesco-Chueca, J. Fluid Mech. 195, 1 (1988); S. Fuerstenau, A. Gomez, J. Fernandez de la Mora, J. Aerosol Sci. 25, 165 (1994)

8. J. F. de la Mora and J. Rosell, J. Chem. Phys. 91, 2602 (1989)

9. K.A. Prather, T. Nordmeyer, K. Salt, Anal. Chem. 66, 1403 (1994)

10. B. E. Dahneke and J. Hoover in Rarefied Gas Dynamics (S. S. Fisher, ed) AIAA, New York (1982)

11. B. E. Dahneke, U.S. Patent 4,358,302 (1982)

12. S.P. Tang and J.B. Fenn, AIAA Journal 16, 41 (1978)

13. W. Groeger and J.B. Fenn, Rev. Sci. Instrum. 59, 1971 (1988)

14. G. D. Danilatos, J. Microsc. 162, 391 (1991) [Information on availability, price and performance of commercial instruments can be obtained from Electroscan Corp., Wilmington, MA 01887]

PRINCIPLES OF FREE JETS

David R. Miller

Department of Applied Mechanics and Engineering Sciences
University of California, San Diego
La Jolla, California 92093-0310

The principles of the free jet expansion are well established and only a brief tutorial overview of selected concepts is presented below. Almost every important theoretical and/or experimental aspect of the free jet related to molecular beam sampling has appeared in one of the 19 International Symposium on Rarefied Gas Dynamics(1) and many detailed reviews exist(2,3). The first stage of pressure reduction in a mass spectrometer sampling system is often simply an aperture or short capillary tube across which a significant pressure ratio is maintained. When this pressure ratio between the system being sampled and the first vacuum stage exceeds about two then the gas flow reaches sonic conditions at the exit, Mach number $M = 1$, and the exiting flow is known as "choked" flow. It is called choked because for fixed source conditions the mass flux out of the aperture will not exceed this $M = 1$ condition regardless of how low the exit chamber pressure is taken, ie how much pumping is added. Beyond the exit the gas expands in a supersonic free jet expansion as it adjusts to the low pressure in the exit chamber. The expansion is called a free jet because there are no diverging nozzle walls to constrain the flow, which would lead to viscous boundary layers and a much smaller rate of expansion. Diverging nozzle walls are used in rockets to direct the exiting flows along the axis for better forward thrust, and researchers use them to slow the rate of expansion to, for example, grow clusters or study fast kinetics. Only the free jet is dealt with here. The free jet nozzle only consists of the subsonic nozzle geometry. The nozzle exit to be referred to here is then just the aperture or capillary exit, and the free jet expansion is the unconstrained subsequent supersonic flow downstream of this nozzle exit. A schematic of the idealized free jet expansion is shown in figure 1.

Supersonic flows have the important property that information about downstream boundary conditions, such as the presence of a solid surface, can not propagate upstream because the flow speed is higher than the speed of sound. This fundamental property of supersonic flows leads to the introduction of shock waves. In a sense the flows must be "shocked" into adjusting to downstream conditions. Shock waves are regions of high collision frequency which occur over distances of order of the local mean free path. Hence they are often treated as discontinuities, because in many flows the spatial scale of interest is much larger than the mean free path. Shock waves provide two mechanisms which permit a supersonic flow to adjust to downstream boundary conditions. Shocks which are at an oblique angle to the flow can turn the flow, and when that is not sufficient oblique and normal shocks can cause a transition to subsonic flows. Subsonic flows can then make the necessary adjustment to the downstream boundary condition. In figure 1 there are no solid boundaries and the shock structure is required to adjust to the background pressure in the exit chamber. Downstream of the normal mach disk shockwave on the axis the flow is subsonic, while downstream of the oblique barrel shocks the flow is turned but remains supersonic.

Another useful property of supersonic flows is that transport effects, viscosity, heat conduction, and species diffusion, are often negligible, making the isentropic approximation valid and rendering the differential equations much easier to solve. The reason for this approximation is

that the molecular transport diffusion time is much longer than the characteristic mean flow time. This ratio of times turns out to be approximately the Mach number over Knudsen number (M/Kn) which is also on the order of the Reynold's number Re. The following relations are useful to recall: $Kn = \lambda/L$; $Re = \rho vL/\mu$; $\mu \approx \rho\bar{c}\lambda/2$; $M = v/a = v/(\gamma RT)^{1/2} \approx v/\bar{c}$ where the variables λ, L, v, ρ, μ, γ, R, T, and $\bar{c}$, are respectively the mean free path, a characteristic length scale, mass average velocity, density, viscosity, specific heat ratio, gas constant per unit mass, temperature, and average molecular speed. Typically at the nozzle exit this ratio of times exceeds 100 and diffusion effects are too slow to be important in the core of the supersonic flow. Obviously near solid boundaries where the velocity and Mach number must go to zero transport effects become very important - referred to as boundary layers. In the subsonic nozzle these effects can be important and the viscous boundary layer is manifested in the discharge coefficient, discussed further below.

In the free jet the transition to the static chamber conditions at the jet boundary causes severe viscous shear dissipation and turbulent mixing. In the subsonic nozzle away from the walls and within the core of the free jet expansion the flow is essentially isentropic. The core of the free jet is termed the "zone of silence" because, as mentioned above, the supersonic flow is not aware of the external boundary conditions. It is from this isentropic core that one would like to extract a molecular beam to pass into a mass spectrometer. However, placing a sampling device in such a supersonic flow will create new shock structure.

The location of the normal Mach disk shock wave, X_m, measured from the nozzle exit is given in nozzle diameters as $(X_m/D) = 0.67\ (P_o/P_b)^{1/2}$ independent of the specific heat ratio, γ, of the gas. The ratio of the diameters of the barrel shock and the Mach disk to the Mach disk location X_m are approximately 0.75 and 0.5 ($\pm$ 25%) respectively, but the correct values depend substantially on γ.

All of the features in Figure 1 depend on a continuum mechanics description of the flow (sufficiently high density and collision frequency to allow for local equilibrium definitions of thermodynamic variables such as pressure and temperature), a condition which often is not valid for mass spectrometer sampling systems. As an example consider a 0.01cm aperture sampling a system at 1000 torr with a diffusion pump which is able to keep the background pressure near $5x10^{-4}$ torr (which would require about 2000l/s pumping speed). The Mach disk would be predicted to occur at about 950 diameters where the continuum Mach number would be predicted to be about 300 (for a monatomic gas). At the Mach disk the predicted continuum pressure would be about 10^{-8} torr and the mean free path would be of order 50cm ! Obviously the mean free path is much greater than the scale of the local apparatus and a continuum picture fails. There would be no shock structure at all and the free jet would be seen to accommodate by collisions with the background gas. In other words, rather than an isentropic core enclosed by non-isentropic shock structure, the free jet undergoes a smooth transition from continuum to free molecular flow, and a non-equilibrium kinetic theory is needed to predict the properties in the jet. With no shocks it is much easier to insert a sampling probe such as a skimmer.

On the other hand consider sampling the same 1000 torr monatomic gas source with a 0.01 cm aperture with a mechanical pump maintaining about 0.5 torr (requiring about 20 cfm). The Mach disk is near 30 diameters, where the Mach number, pressure, and mean free path would be about 30, 10^{-3} torr, and 0.05 cm respectively. The shock wave is spread over a finite region in which there will be strong collisional interactions. The jet boundary structure may be

somewhat porous (background gases can diffuse into the jet) and in a transition between the strong shocks depicted in Figure 1 and the limit of no shocks and free molecular flow for the diffusion pumped system example above. Placing a sampling probe upstream of this Mach disk will create a shock-like structure due to strong scattering from the skimmer surfaces and careful design procedures are advisable. Therefore there is a significant trade-off between the two experimental approaches; diffusion pumps are larger and more complicated to deal with but the subsequent sampling is easier. The use of different nozzles and pumps and the subsequent different regimes encountered by various investigators has led to a great deal of confusion and contradictory results over the years.

A useful model, the "quitting surface model", for discussion of the shock-free (diffusion pumped) configuration is shown in figure 2. Rather than a shock wave separating the isentropic core from the background, the isentropic continuum core is assumed to terminate and make a sudden transition to free-molecular flow. The quitting surface occurs approximately where the collision frequency becomes too low to adjust to the rate of expansion. Bird (4) has suggested that the transition occurs when the parameter $P = (1/\nu)D(\ln\rho)Dt = (v/\rho v)d\rho/dx$ exceeds about 0.02 ; P is simply a measure of the required continuum rate of change divided by the maximum rate which collisions can provide. Downstream of the quitting surface the free molecular expansion causes significant departures from local thermodynamic equilibrium, discussed further below.

Since all free jets of interest have some initial continuum isentropic core it is important to treat this regime first. The steady state equations of motion which describe the isentropic flow in either Figures 1 or 2, away from the viscous regions, are:

1. mass: $\nabla\cdot\rho\mathbf{v} = 0$

2. momentum: $\rho\mathbf{v}\cdot\nabla\mathbf{v} = -\nabla P$

3. energy: $\rho\mathbf{v}\cdot\nabla(h+v^2/2) = \rho\mathbf{v}\cdot\nabla(h_o) = 0$

4. a)equation of state: $P=P(\rho,T)$ b)ideal gas: $P=\rho RT$

5. a)caloric equation of state: $h=h(\rho,T)$ b)ideal gas: $dh=C_p dT$

Since all streamlines originate in the same reservoir Eqn. 3 really provides the result that h_o is the same constant everywhere, the flow is adiabatic and the total enthalpy is conserved; h_o is the stagnation source enthalpy. For the ideal gas, if it is further assumed that C_p is constant then eqns 3 and 4b can be rearranged to give:

6. $$T/T_o = 1/[1+((\gamma-1)/2)M^2]$$

which is the well known adiabatic relationship between temperature and Mach number; $M = v/a = v/(\gamma RT)^{1/2}$; T_o is the stagnation source temperature. Using the thermodynamic relations for an isentropic process in an ideal gas with constant specific heat we can use eqn 6 to derive the other useful and well known relations:

7. $$\rho/\rho_o = n/n_o = 1/[1+((\gamma-1)/2)M^2]^{(1/\gamma-1)}$$

8. $$P/P_o = 1/[1+((\gamma-1)/2)M^2]^{(\gamma/\gamma-1)}$$

Hence, if eqns 1-5 can be solved for Mach number at any position then eqns 6-8 give all the flow properties; they are restricted to steady state, isentropic flow (no viscosity, heat conduction, diffusion, or kinetic effects), ideal gases, and constant heat capacity. There are several methods available for solving the equations.

The method of characteristics is essentially an exact numerical solution which is possible in the supersonic portions of the flow field. It is a very fast numerical method, can be run on modern hand held calculators, and provided the first accurate solutions. In this method the spatial partial derivatives are combined to give ordinary derivatives (easy to integrate) along special directions, called characteristics. In subsonic flow the characteristics are imaginary and the method is not applicable. The method requires an initial supersonic Mach number distribution at the nozzle exit and then all of the supersonic structure of Figure 1 can be calculated. Many authors have produced correlations from characteristic calculations and two are summarized in Tables 1 and 2 for axi-symmetric and two dimensional free jets. (2,3,5)

A second general method rewrites eqns 1-3 to include the unsteady state terms, such as $\partial\rho/\partial t$ in eqn 1. These unsteady equations are parabolic and can be solved by one of several finite difference, time splitting techniques until a steady state is reached numerically.(6,7) Computation time is long even on the fastest computers to obtain stable solutions. The advantages of this method over the easier, more stable, and more accurate method of characteristics is that the method can deal with both subsonic and supersonic regions, can be extended to incorporate viscous, heat conduction, and diffusion effects, provides values at arbitrary grid points (convenient for obtaining gradients and better correlations off the axis of the flow), and it can be used to obtain the unsteady flow field for time dependent, pulsed sources.

The equations and two methods above are restricted to continuum flow. A third scheme which requires even more computational power than the time splitting finite difference method is the direct simulation monte carlo (DSMC) numerical solution of the more fundamental Boltzmann equation (4):

9. $$\bar{c}\cdot\nabla f(\bar{c},\bar{r}) = (\delta f/\delta t)_{coll} = \iint [f(c')f(\xi')-f(c)f(\xi)]g\sigma d\Omega d^3\xi$$

where $f(\bar{c},\bar{r})$ is the molecular velocity distribution function, c is the molecular velocity, and the right hand side is the rate of change of $f(\bar{c},\bar{r})$ due to binary collisions; the equation is written for steady state and no external forces. The equation is directly simulated by tracking a statistical Monte Carlo sample of molecules in time and space, and then after many collision times appropriate moments over the velocity distributions are taken to obtain the steady state mean properties, n, v, and T. Eqns 1-3 above are simply moments of the entire Boltzmann equation 9, integrated over molecular velocity space, but they are only valid when the velocity distribution function is given by the equilibrium Boltzmann distribution; which is the same limitation as the neglect of viscosity and heat conduction. The great advantage of the DSMC method is that it can treat the flow from nearly continuum to free molecular regimes, ie both

the limits of figures 1 and 2, is not limited to even an approximately equilibrium distribution of velocities, and is able to treat the gas-surface interaction at the molecular level. The advances in statistical sampling and averaging algorithms and approximate molecular models for the collision terms in the Boltzmann equations make it the most useful computational technique to investigate flow field properties in molecular beam sampling experiments. Only the necessity of approximating the intermolecular potentials in the collision integral keep the method from ab initio quantitative accuracy. Because the method is best in sampling a few molecules for many collision times it is not easily adapted to time dependent, near continuum flows. However, steady state sampling experiments will always involve non-equilibrium flows and transition to free molecular flow for which the continuum equations and concepts are no longer valid, while the DSMC method is.

While calculations of the isentropic supersonic free jet flow are straightforward, the subsonic nozzle flow is made difficult because of the viscous boundary layer along the nozzle walls. This flow is most simply, and usually sufficiently, dealt with by a superposition of two concepts, nozzle discharge coefficient and quasi-one dimensional flow. The discharge coefficient is used to adjust the actual nozzle exit area (or diameter) to the effective flow area to account for viscous boundary layer effects. Figure 3a shows the discharge coefficient from a boundary layer calculation and experiment for a particular subsonic nozzle shape (8), while Figure 3b shows the effective diameter for orifices (5); the discharge coefficient is proportional to D^2. Typical nozzles operate with discharge coefficients above 0.8, but as fig 3 suggests this requires the nozzle Reynold's number to be greater than 100, or Knudsen numbers less than 0.01 . Further, since the viscous boundary layer grows with length of the subsonic nozzle the geometry of the nozzle is important. As the flow speed increases, higher Re, and the nozzle length decreases, there is less time for viscosity effects to diffuse out from the nozzle walls, the thinner is the boundary layer, and the larger is the discharge coefficient, ie the larger is the exit core isentropic flow area.

Because the subsonic flow involves two dimensional, viscous, heat conducting, compressible flow the exact calculation is tedious, as mentioned above. The quasi-one dimensional equations are obtained by integrating the exact partial differential equations over the cross-section of the subsonic nozzle and, in their simplest form, assume constant average flow properties over the cross section.(9,10) The resulting steady state equations, including viscous and heat conduction effects, friction and heat transfer, which replace eqns 1-3 above are:

10. $d(\rho vA)/dx = 0$ or $\rho vA = \dot{m} = \text{constant}$

11. $\rho v dv + dP = -\frac{1}{2}\rho v^2 f d(x/D)$

12. $\dot{m} d(h+v^2/2)/dx = \dot{m} dh_o/dx = \dot{q}$

where f is the friction factor usually correlated with Re, eg $f = 64/Re$, and $\dot{q}$ is the heat transfer per unit length from the nozzle walls, which for a pipe is $\dot{q} = \pi Dh(T_w - T)$ and heat transfer coefficient h is given by a Nusselt number correlation, Nu=f(Re,Pr); f and h are often taken as some average constant for the integration of eqns 10-11.

Only the ordinary streamwise derivatives d/dx appear in eqns 10-11 because of the integration over the other dimensions. These three equations are easily integrated and indicate that the Mach number can be altered by changing the nozzle geometry, A(x), by friction in the nozzle, f, and/or by heat transfer from the nozzle walls, $\dot{q}$.

The Mach number variation is most typically caused by varying the area, decreasing A(x) from the source to the exit, with negligible friction (discharge coefficient close to 1) and heat transfer (adiabatic flow, $\dot{q}=0$); this is therefore an isentropic subsonic converging nozzle. Setting $f = \dot{q} = 0$ an exact algebraic solution to eqns 10-11 is obtained:

13. $(A/A^*) = (1/M)[(2/\gamma+1)(1+((\gamma-1)/2)M^2)]^{((\gamma+1)/2(\gamma-1))}$

where A^* is the subsonic nozzle exit area where M =1, $\pi D^2/4$. Knowing the actual geometry of the nozzle A(x) therefore gives M(x) and eqns 6-8 above give the properties just as for the supersonic free jet.

The second important case for mass spectrometer sampling is the case when there is no area change A(x) = constant, no heat transfer ($\dot{q}=0$), but there is friction, characterized by the friction factor f. This case would correspond to sampling by a capillary tube rather than through an aperture. Again the eqns 10-11 can be solved exactly for ideal gases and constant γ and again we find that M = 1 occurs at the nozzle (tube) exit. The flow is called a Fanno flow.(9,10) The acceleration of the flow to M =1 is opposed by friction which sets up a substantial pressure drop down the capillary tube. Tabulations are given in standard texts (9,10) for the parameter (fx/D) as a function of M(x) along the capillary tube, working back from the exit M = 1 state. The flow from the reservoir stagnation conditions to the tube entrance is assumed to be isentropic.

The most important effect of such subsonic frictional effects other than the discharge coefficient, is to lower the stagnation pressure, P_o , the effective reservoir pressure. Note that eqn 12 shows that for $\dot{q}=0$ the stagnation enthalpy, and hence temperature T_o , is a constant. A reasonable experimental approximation is to measure the mass flow from the capillary and calculate an effective stagnation pressure which would give the same mass flow from an ideal isentropic aperture of the same diameter. The effects are not great if the nozzle L/D is not large (<10).

The third case, A(x) = constant and f=0, but with heat transfer is termed Rayleigh flow. It also provides an M =1 exit flow by adding heat to the gas. However heat transfer is usually negligible in sampling systems and is not dealt with here.

Finally, the subsonic geometry is important because it effects the nozzle exit profiles of Mach number and streamline orientation, which are the initial conditions for the supersonic calculations. Figure 4 shows three types of nozzle geometries and the corresponding three different sonic (M=1) surfaces obtained by pitot tube measurements. Figure 5 shows method of characteristic calculations for these three nozzles; the ideal case corresponds to Table 1 solutions. The important result is that beyond five diameters the rates of expansion for the nozzles are essentially identical, but that there are substantially different rates near the nozzle exit. It would be difficult to observe the differences in the macroscopic jet properties (v,T,p) beyond five diameters, but molecular properties dependent on kinetics near the nozzle exit, such

as condensation, fast chemistry, vibrational relaxation, would be substantially effected by these different nozzle geometries.

Returning to the ideal case, figure 6 shows typical free jet properties as a function of distance. It is useful to note is that the mean velocity rapidly approaches the terminal maximum velocity, given by $V_\infty = (2C_pT_o)^{1/2}$, while the temperature, density , and collision frequency continue to fall with distance. Because the continuum flow is typically maintained for a few diameters the mean velocity can normally be approximated by V_∞ in a sampled beam. Further, it turns out that the density n falls as $1/x^2$ in both these continuum calculations and also for completely free molecular flow. Combining these two results makes a rapid estimate of number flux, nv, possible anywhere in the jet.

The rapid fall in collision frequency causes the transition from continuum flow, depicted in Fig 2. For example, for the 1000 torr, 0.01cm sampling discussed above (P_oD = 10 torr-cm) there would be less than one three-body collision beyond one diameter and less than 100 two body collisions beyond one diameter in the free jet expansion. Therefore kinetics requiring large numbers of collisions (vibrational relaxation, condensation, most chemistry) would not occur in the free jet, and are said to be frozen. It is for this reason that the vibrational temperature is usually taken as the source temperature. On the other hand kinetic processes that require only a few collisions (eg translation and rotational relaxation) must be considered by integrating the appropriate rate equations using the free jet properties calculated by the methods above.

The easiest method used to estimate kinetic rates is to integrate the appropriate rate equation along the center streamline using the M(x) results of Tables 1 or 2, together with the isentropic relations of eqns 6-8 . If there is concern that the phenomena is rate limited in the sub-sonic nozzle (eg condensation, vibrational relaxation) then one must use the A(x) and/or L(x) to get the subsonic M(x), as discussed above, and then start the integration of the appropriate rate equation in the reservoir. Once M(x) is known these integrations are very rapid and possible on hand held calculators. This method decouples the jet bath properties, M(x), from the kinetic processes being examined. The caveat in this procedure is that the M(x) results are for a given constant C_p or γ and for isentropic flow, while kinetic processes usually imply a variable γ and a non-isentropic process. However, one can usually estimate an average constant γ and assume the non-isentropic effects are small. It is also straightforward, yet tedious, to incorporate kinetic effects into all of the more rigorous computational methods discussed above.

Figure 2 is useful in understanding the effects of the transition to free molecular flow, ie running out of collisions. When there are insufficient collisions to maintain the equilibrium Boltzmann distribution of velocities (called translational relaxation because the velocity distribution can not relax to the equilibrium distribution) then the velocity distribution function rapidly becomes very anisotropic. The distribution along the streamline, characterized by a parallel temperature $T_\parallel$ becomes frozen, while the perpendicular temperature $T_\perp$, which characterizes the spread in molecular velocities perpendicular to the streamline, continues to drop approximately as the continuum theory temperature T_c would predicted to fall (but not quite). The insert to figure 2 shows a typical profile for these temperatures. The temperature follows the continuum calculation until the collision rate is insufficient and the $T_\parallel$ freezes. An integration for the rate of rotational relaxation, $dT_r/dt = (T_t-T_r)/\tau$, would show a similar freeze point but further upstream because of a slower relaxation time τ. The location of the quitting surface can be estimated by using Bird's "P" parameter above (4) and the continuum relations,

or by using experimental results for the terminal Mach number or speed ratio which has been well correlated by experimentalists.(2,3) For example, for argon one of the earliest terminal Mach number correlations is $M_\infty = 1.17Kn^{-0.4}$. For our case (P_oD = 10 torr-cm) argon at room temperature would have a terminal Mach number approximately M = 25. Using this and the correlations of Table 1 predicts the quitting surface to be at about 20 diameters. It is interesting to compare this with the Mach disk location for various background pressures as discussed above. The point is that either the Mach disk terminates the isentropic calculation or the quitting surface is utilized.

A more rigorous treatment of the actual transition from continuum to free molecular flow requires a solution to the kinetic eqn 9. This is accomplished either numerically by the DSMC method (4) or by a variety of analytically methods which introduced one of several approximate forms of the collision term and/or models for $f(\vec{c},\vec{r})$ and then either solve for $f(\vec{c},\vec{r})$ directly or the resultant moment equations (3,4,11).

Although not an inherent feature of the free jet expansion, the placement and effect of a skimmer is obviously important for mass spectrometry. Fortunately there exists reasonably good correlations for placement of the skimmer and for intensities downstream of the skimmer for both regimes, inside the Mach disk or beyond the quitting surface.(2,3,12-14) Especially important when placing the skimmer inside the Mach disk in near continuum conditions is to set the skimmer at the optimum intensity location. On the other hand, if the skimmer lies outside the quitting surface then the location is not as critical. As figure 2 suggests there are basically two reasons for loss of intensity due to the skimmer in the free molecular regime. Molecules which would have reached the detector are stopped by the skimmer walls and molecules from the jet can reflect from the outer skimmer surfaces and scatter the centerline beam. Background molecules also can scatter the beam molecules in this regime but they are not usually as important as reflected jet molecules. For the near continuum skimming substantial scattering can take place both outside and inside the skimmer. Bird (15) has provided a DSMC calculation of the role of these two interactions as a function of the local Knudsen number at the skimmer. In this regime there is a trade-off between the internal and external skimmer angles depending on the jet conditions at the skimmer location.

Finally, it is worth noting that good free jets typically operate at conditions between P_oD = 1 torr-cm and 10 torr-cm. Roughly, Kn = 0.005 P_oD (torr-cm) and Re = 200 P_oD (torr-cm) for 300K sources. Therefore below 1 torr-cm there will be boundary layer (discharge coefficient) and other diffusional effects (eg species separation), and the Knudsen number is sufficiently large that the continuum assumption will fail rapidly in the jet. For P_oD values greater than 10 one will need to be careful about collisional effects at low temperatures in the jet (using the correct cross-sections) which can lead to clustering, and condensation if the source temperature is low. If the source temperature is not 300K it is important to note that number density and not pressure is the fundamental correlating parameter for collisional effects, so that temperature must be scale into the parameters as P_o/T_o .

REFERENCES

1. A listing of the first 16 RGD Symposia is given in: "Proceedings of the 17th Int. Symp. on Rarefied Gas Dynamics", ed. by Alfred Baylich, VCH Publishers, Inc., New York, 1991.
2. Anderson, J.B., in "Molecular Beams and Low Density Gas Dynamics" ed by P.P. Wegener, Dekker,New York, pp1-91 (1974)
3. Miller, D.R., in "Atomic and Molecular Beam Methods", vol 1, ed by G. Scoles, Oxford Press, New York, pp 14-53 (1988)
4. Bird, G.A., "Molecular Gas Dynamics and The Direct Simulation of Gas Flows", Clarendon Press, Oxford, New York (1994)
5. Ashkenas,H.,and Sherman, F.S., in "Rarefied Gas Dynamics", Vol. 2, ed by J.H. de Leeuw, Academic Press, New York, pp 84-105 (1966)
6. Richtmyer, R.,and Morton,K., "Difference Methods for Initial-Value Problems", Interscience Publishers, New York 1967; see chap 13.
7. Saito,T., Nakatsuji,H., Teshima,K., "Numerical Simulation and Visualization of Freejet Flow-Fields", Department of Aeronautical Engineering, Kyoto University, Kyoto, Japan; private communication from K. Teshima.
8. Tang,S., and Fenn,J.B., AIAAJ, 16, 41 (1978)
9. John, J., "Gas Dynamcis", Allen and Bacon Pubs., Boston (1969)
10.Shapiro, A.H., "Compressible Fluid Flow", Ronald Press, New York (1953)
11. Vincenti, W., and Kruger, C., "Introduction to Physical Gas Dynamics", Wiley, New York (1965)
12. Beijerinck,H., and Verster,N., Physica,111C, 327 (1981)
13. Campargue, R., J.Phys.Chem., 88 , 4466 (1984)
14. Beijerinck,H., et.al., Chemical Physics,96, 153 (1985)
15. Bird, G.A., Physics of Fluids, 19 , 1486 (1976)

TABLES

Table 1 Centerline Mach Number and Off-Axis Density Correlations for Axisymmetric Flow

γ	x_0/d	A	ϕ	$(x/d)_{min}$
1.67	0.075	3.26	1.365	2.5
1.40	0.40	3.65	1.662	6
1.2857	0.85	3.96	1.888	4
1.20	1.00	4.29	—	—
1.10	1.60	5.25	—	—
1.05	1.80	6.44	—	—

$$M = A\left(\frac{x-x_0}{d}\right)^{\gamma-1} - \frac{\frac{1}{2}\left(\frac{\gamma+1}{\gamma-1}\right)}{A\left(\frac{x-x_0}{d}\right)^{\gamma-1}} \qquad \left(\frac{x}{d}\right) > \left(\frac{x}{d}\right)_{min}$$

$$\frac{\rho(y,x)}{\rho(0,x)} = \cos^2\theta\cos^2\left(\frac{\pi\theta}{2\phi}\right) \qquad \frac{\rho(R,\theta)}{\rho(R,0)} = \cos^2\left(\frac{\pi\theta}{2\phi}\right)$$

$$\tan\theta = \frac{y}{x} \qquad R^2 = x^2 + y^2$$

Table 2 Centerline Mach Number Correlations for Axisymmetric (3D) and Planar (2D) Expansions

Source	j	γ	C_1	C_2	C_3	C_4	A	B
3D	1	5/3	3.232	−0.7563	0.3937	−0.0729	3.337	−1.541
3D	1	7/5	3.606	−1.742	0.9226	−0.2069	3.190	−1.610
3D	1	9/7	3.971	−2.327	1.326	−0.311	3.609	−1.950
2D	2	5/3	3.038	−1.629	0.9587	−0.2229	2.339	−1.194
2D	2	7/5	3.185	−2.195	1.391	−0.3436	2.261	−1.224
2D	2	9/7	3.252	−2.473	1.616	−0.4068	2.219	−1.231

$$\frac{x}{d} > 0.5: \quad M = \left(\frac{x}{d}\right)^{(\gamma-1)/j}\left[C_1 + \frac{C_2}{\left(\frac{x}{d}\right)} + \frac{C_3}{\left(\frac{x}{d}\right)^2} + \frac{C_4}{\left(\frac{x}{d}\right)^3}\right]$$

$$0 < \frac{x}{d} < 1.0: \quad M = 1.0 + A\left(\frac{x}{d}\right)^2 + B\left(\frac{x}{d}\right)^3$$

FIGURES

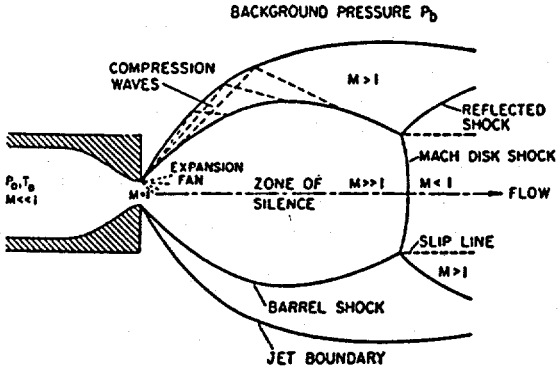

Figure 1 Continuum free-jet expansion. (ref 3)

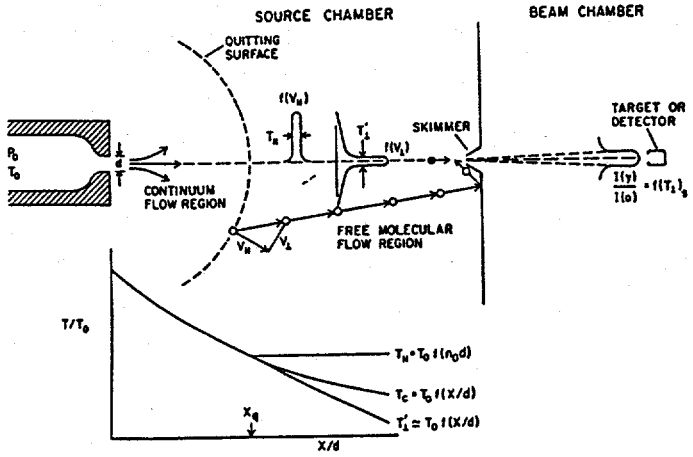

Figure 2 Free jet transition to free molecular flow; the "quitting surface" model separates the flow into continuum and free-molecular regimens. $T_\parallel$ characterizes the spread in parallel velocities $f(V_\parallel)$; $T'_\perp$, the spread in the narrow center gaussian of $f(V_\perp)$; T_c is the continuum temperature. (ref 3)

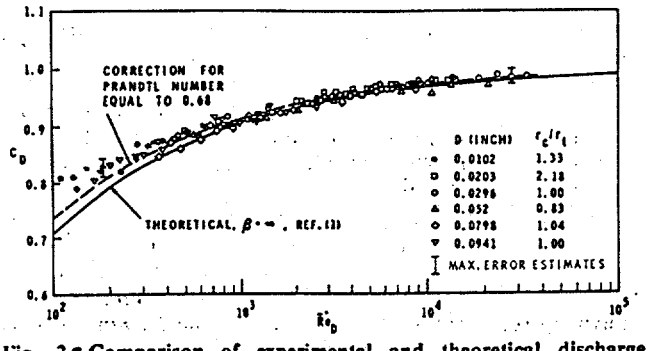

Fig. 3a Comparison of experimental and theoretical discharge coefficients for argon with $\gamma = 1.67$. (ref 8)

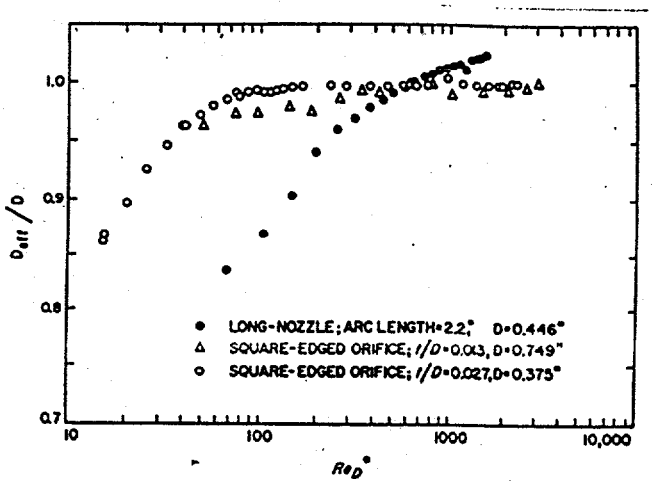

Fig. 3b Effective orifice diameter. (ref 5)

FIGURES (CON)

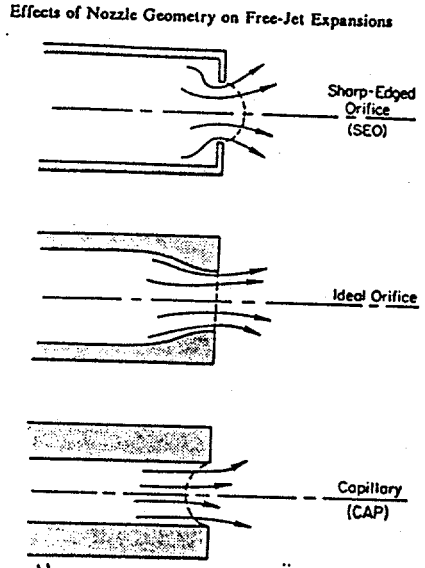

Figure 4 Schematic of three types of subsonic nozzles; dashed lines indicate the qualitative nature of the sonic surface.

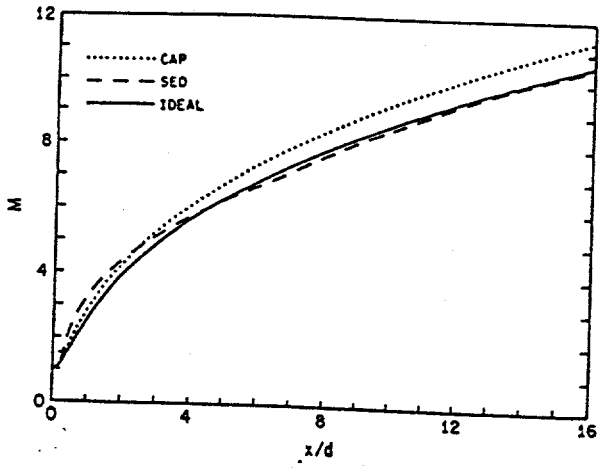

Figure 5 Effect of source geometry on centerline Mach number. CAP: capillary; SEO: sharp-edged orifice; IDEAL: ideal converging; differences are due to different initial sonic surfaces for MOC; $\gamma = 1.4$. (ref 3)

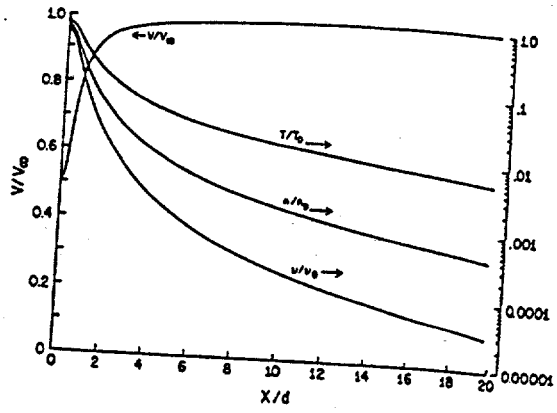

Figure 6 Free jet centerline properties versus distance in source diameters; $\gamma = 5/3$; temperature, T, density, n, and binary hard sphere collision frequency, ν, are normalized by source stagnation values T_o, n_o, ν_0. (ref 3)

COMPOSITION DISTORTION IN MBMS SAMPLING

Eldon L. Knuth
Chemical Engineering Department, UCLA
Los Angeles, CA 90024

Introduction

The focus in this review is on molecular-beam mass-spectrometer (MBMS) sampling systems, as opposed to microprobes. A typical MBMS sampling system consists of a sampling probe (usually conical), a skimmer (also usually conical), and a detection system (usually some form of mass spectrometer with signal averaging). Important advantages of MBMS sampling include (a) the characteristic time for the expansion in the free jet can be made very small in comparison with many chemical relaxation times and (b) the sample monitored by the detector comes essentially from near the centerline of the sampling probe, thereby minimizing interactions of the sample with the probe surface. Notwithstanding these advantages, experience has shown that care is required to either minimize or correct for composition distortions arising from the presence and operation of a MBMS sampling system.

Most of the known origins of such composition distortions were discussed already in the review of MBMS sampling prepared by the author in 1972 [1], the year of the first Molecular Beam Sampling Conference [2]. The present review is an update of that prior review. Hence, as appropriate, the present review will sometimes simply reference the earlier review, sometimes modify that review, and sometimes supplement it with results obtained during the past two decades. Hence the relevant literature appearing since 1972 is emphasized here; for additional references to the earlier literature, the reader is referred to [1].

The origins of distortions are reviewed here in approximately the order in which they are encountered by a sample as it is captured and processed. Hence, the main body of the review begins with the possibility of radical recombination at the external probe surface and ends with the possibility of species fragmentation during detection; a later section on miscellaneous origins begins with the possibility of condensation in the free jet and ends with the possibility of contaminating the time-averaged signal for a given sampling location by the stored time-averaged signal for the prior sampling location.

Radical Recombination at External Probe Surface

The presence of a MBMS sampling probe in a composition gradient associated with a flame has the potential for distorting the flame structure as a consequence of the heterogeneous recombination of radicals (e.g., O, H, OH and CN) at the probe surface. Such effects of radical recombinations have been observed experimentally for OH by Stepowski et al. [3] and for CN by Smith and Chandler [4]. Stepowski et al. used Laser-Induced Fluorescence (LIF) to observe OH concentrations upstream from the sampling

orifice when sampling from a low-pressure propane-oxygen flat flame. They found that the presence of the probe depleted the OH concentration when sampling from the preheat or reaction zone; the depletion decreased as the probe was moved downstream, and became negligible at the location where the net flux (convection plus diffusion) of OH reversed direction, from upstream to downstream. Smith and Chandler, also using LIF, observed CN concentrations in the vicinity of a sampling probe located in a weakly stabilized low-pressure hydrogen-oxygen-argon premixed flame doped with 1.3% HCN. The probe was made of quartz and had a 60^0 included angle. With the probe tip located upstream from the unperturbed peak, the measured CN concentration near the orifice entrance was up to 50% lower than in the unperturbed flame. Moving the probe downstream reduced the distortion. Particularly significant is that this distortion of the CN concentration was present even for the case of no flow through the probe orifice, indicating that the distortion is due to the presence of the probe rather than to the loss of gas mixture to the orifice. For sampling in flames with a net upstream flux of an important reactive species, these distortions appear to be unavoidable; they are more significant for weakly stabilized flames, and less significant for strongly stabilized flames. A need to reduce radical recombination at the external probe surface argues in favor of fabricating the probe from a material which is non-catalytic and reducing the angle of the probe exterior.

Recombination of radicals on the inner surface of the sampling orifice appears to affect negligibly the sample reaching the detector [5]. A generous estimate for the time for flow through the sampling orifice is provided by $10\ t_F = 10\ d^*/a^*$ where d^* is the orifice diameter and a^* is the sound speed at the orifice throat. A characteristic time for diffusion from the wall to the centerline is provided by $t_D = (d^*/2)^2/D$ where D is diffusivity (mass, momentum or energy, as the case may be). For sampling from atmospheric-pressure flames with $d^* = 0.025$ cm,

$$10\,t_F/t_D = 40D/a^*d^* \approx 0.03 \qquad (1)$$

Hence, for this case, wall effects are not diffused to the centerline, so that wall effects do not influence the sample reaching the detector.

Related closely to the possibility of flame distortion due to radical recombination at the external probe surface is the possibility of flame distortion due to heat transfer to the external probe surface. Some investigators have observed an "attachment" of the flame to the probe (downstream shift and narrowing of the reaction zone) which they interpret as cooling of the flame by the presence of the probe. E.g., Biordi et al. [6] probed methane-oxygen-argon flames at 0.04 atm and measured, with a thermocouple, temperatures upstream from the probe tip. For a quartz sampling cone with total angle of 40^0, they observed no attachment and no flame cooling. However, with a total angle of 78^0, they observed both flame attachment and significant cooling. Stepowski et al. [3] probed propane-oxygen flames at 0.033 atm using a quartz probe with a total angle of 40^0, also measuring temperatures upstream from the probe tip with a thermocouple. They also observed no attachment and no cooling. Smith and Chandler [4] probed hydrogen-oxygen-argon flames at 0.033 atm using a quartz probe with a total angle of 60^0,

measuring the rotational temperature of CN near the probe surface using laser-induced fluorescence. They observed no attachment and no cooling. No observable attachment of the flame to the probe appears to be a pragmatic criterion for negligible cooling of the flame by the probe.

Acceleration into Probe Orifice

Several investigators [6,3,7] have observed experimentally that sampling within a concentration gradient results in an apparent axial shift of the concentration profile. Biordi et al. [6] measured concentration profiles in methane-oxygen-argon flames at 0.04 atm; the methane concentration profile measured by MBMS sampling appeared to be shifted about 5 orifice diameters relative to that measured using a microprobe. Stepowski et al. [3] measured OH profiles in propane-oxygen flames at 0.033 atm; the profile measured by MBMS sampling appeared to be shifted about 2 orifice diameters relative to that measured using LIF. Cattolica et al. [7] measured OH profiles in methane-air flames at 1 atm; the OH profile measured by MBMS appeared to be shifted about 5 orifice diameters relative to that measured by LIF. These observations motivated a numerical study of velocity and concentration distributions realized when placing an infinitely long conical sampling probe at differing axial locations in an otherwise undistorted concentration profile [8]. Differing combinations of mass-diffusion coefficient D_{AB} and chemical-relaxation time t_C were investigated; compressibility and a nonzero sampling-orifice diameter were taken into account. If, at the sampling orifice, the chemical-relaxation time is much larger than the characteristic flow time t_F and $ReSc = a^*d^*/D_{AB} = t_D/t_F \gg 1$, then the apparent axial shift δ of the sampling location implied by the composition at the orifice centerline is found to be

$$\delta/d = 0.19(ReSc)^{1/2} \qquad (2)$$

Slightly larger values of δ/d are found for nonzero values of t_F/t_C.

Yoon and Knuth [5] find that an additional distortion occurs when sampling downstream from a flat-flame burner if the burner-to-cone distance is less than approximately one probe-tip diameter. This distortion is not surprising in view of the apparent axial shift described in the preceding paragraph.

For MBMS sampling of neutral species, the importance of modelling the composition at the orifice centerline (as opposed to the concentration averaged over the orifice area) is emphasized by a consideration of the fraction of the probe flow which passes through the skimmer. One finds [5]

$$\frac{\text{skimmer-orifice flow}}{\text{probe-orifice flow}} = f(\gamma)(d_1/x_1)^2 \qquad (3)$$

where γ is specific-heat ratio, d_1 is diameter of skimmer orifice and x_1 is distance from probe orifice to skimmer orifice. The function $f(\gamma)$ has values 0.48, 0.34 and 0.28 for γ = 5/3, 7/5 and 9/7 respectively. Hence for typical values of x_1/d_1, ranging from about 10

to about 10^2, only that portion of the sample in the immediate vicinity of the sampling-orifice centerline can reach the detector.

An exception to this emphasis on the centerline composition is the study by Hayhurst et al. [9] of ions in flames. Since they extracted the ions using electrostatic fields, the detected ions were drawn from the entire area of the sampling orifice so that, in modelling the sampling, one must include averaging over the entire orifice area.

Related closely to the apparent axial shift of the concentration profile is an apparent axial shift of the temperature profile. Cattolica et al. [7] determined the temperature profile from molecular-beam-sampling time-of-flight measurements; making both profile measurements for the same flame, they found that the apparent axial shift for the OH and the temperature profiles was the same. This result is to be expected since, for temperature sampling, the ReSc appearing in Eq. (2) for composition sampling would be replaced by RePr, where Pr is Prandtl number, and Pr ≈ Sc for gaseous mixtures. Hence a consistent set of concentration and temperature profiles would be given by MBMS concentration measurements and molecular-beam-sampling time-of-flight temperature measurements.

Chemical Relaxation in Free Jet

Chemical relaxation of the composition of the sample as it expands in the free jet appears to be less severe than investigators anticipated when MBMS sampling was first suggested. Among the most rapid chemical relaxations in flames are those involving radicals. Cattolica et al. [7] measured concentrations of the radical OH in atmospheric-pressure premixed methane-air flat flames using probes with two different orifice channel lengths, 0.3 mm and 1.4 mm, and hence with two different residence times for OH relaxation. The residence time for the longest channel was large in comparison with the characteristic time t_F for flow in the free jet. From these measurements, they were able to deduce the value of the OH relaxation time corresponding to the state in the orifice channel. This value, 2.9×10^{-6}sec, was found to be in excellent agreement with the value predicted using Eq. (33) of [1] and the reaction-rate coefficient for the fastest OH-consuming reaction, namely

$$OH + H_2 \rightleftharpoons H_2O + H \qquad (4)$$

and to be 4 times as large as the sum of the residence time for the shorter channel and the characteristic time for the flow in the free jet. Hence, since OH is one of the most reactive radicals, it is concluded that, in sampling from systems at pressures of one atmosphere or less, the use of an orifice-channel with length of 0.3 mm or less avoids concentration distortions due to chemical relaxations for reactions involving only stable species and for most reactions involving free radicals.

For those apparently infrequent cases in which chemical relaxations in the free jet are important, one might consider either (a) a detailed numerical calculation of the relaxation as a function of axial location or (b) use of a sudden-freeze model for the

determination of the location of the sudden-freeze surface and the composition at this location. The application of the sudden-freeze model to chemical relaxations is described in detail in [1] and [10]. The basis for the sudden-freeze model is the assertion that the freezing-point criterion

$$D\tau_{h,p}/Dt = C \tag{5}$$

is universally applicable to all relaxation processes (chemical, vibrational, rotational etc.). Here D( )/Dt is the hydrodynamic derivative, $\tau_{h,p}$ is the relaxation time at constant enthalpy and pressure and C is a constant. On the basis of information available in 1972, C was equated provisionally to 0.5. Twelve years later, the sudden-freeze model was revisited [11] with the result that the value of C was increased to 1.6, which value is recommended today.

Radial Diffusion in Free Jet

Separation of species due to radial diffusion occurs as a consequence of strong radial pressure gradients immediately downstream from the sampling orifice and is most severe for species with the greatest deviation from the major-species molecular weight. It is unavoidable but can be handled relatively easily using results based on the analysis by Sherman [12]. Neglecting second-order terms in $1/Re_0$, one may rearrange Sherman's result to obtain [1]

$$\alpha_p = \frac{n_H/n_L}{(n_H/n_L)_0} = 1 + \frac{C}{(ReSc)_0}\left(\frac{m_H - m_L}{m_0}\,\frac{\gamma}{\gamma-1} - \alpha_0\right) F(\gamma, x/d^*) \tag{6}$$

where α_p is enrichment factor for pressure diffusion, n is number density, C is the viscosity-temperature constant defined by

$$\frac{\mu}{\mu_0} = C\frac{T}{T_0} \tag{7}$$

m is molecular weight, γ is specific-heat ratio, α_0 is thermal diffusion factor evaluated at stagnation conditions, Re (= $\rho a d^*/\mu$) is Reynolds number, Sc (= $\mu/\rho D$) is Schmidt number, ρ is density, μ is viscosity, $F(\gamma, x/d^*)$ is (for given γ) a monotonically increasing function of the dimensionless axial distance x/d^*, and subscripts H, L and 0 refer respectively to heavy species, light species and stagnation conditions. The function F has reached its terminal value (for all practical purposes) already at $x/d^* = 3$. Terminal values of F have been calculated by Sharma et al. [13] for several values of γ. For γ = 5/3, 7/5 and 9/7 they obtain $F(\gamma,\infty)$ = 13, 16 and 18. For typical values of other factors appearing in the right-hand side of Eq. (5), mass separation due to pressure diffusion downstream from the probe orifice is negligible for Re_0 greater than about 10^3. Sherman's analytical results have been confirmed quantitatively by the measurements of McCay and Price [14].

Skimmer Interference

The term "skimmer interference" designates some form of beam distortion due to collisions of beam molecules with other molecules in the vicinity of the skimmer entrance. Typical consequences of skimmer interference are (a) decrease in beam density, (b) increase of velocity-distribution width, (c) decrease of mean velocity, and (d) distortion of beam composition, listed in order of decreasing sensitivity to the skimmer interference. Causes of skimmer interference include (a) location of the skimmer entrance too close to the Mach disk standing at the end of the free-jet barrel shock, (b) location of the skimmer entrance too close to a stand-off shock created by the impact of the free jet on the chamber wall to which the skimmer is mounted, (c) failure of the shock wave external to the skimmer to attach to the skimmer, (d) collisions of beam molecules with the inner surface of the skimmer, (e) a blunt skimmer lip, and (f) a large skimmer orifice. For sampling from a mixture with a uniform and steady state, skimmer interference usually can be avoided by careful system design; the reader is referred to design suggestions included in [1]. Problems arise frequently, however, when the system is required to sample from a wide range of states (a wide range of temperatures, pressures, etc.), as found, e.g., in sampling from a flame profile, from a cycling-pressure system, or from a transient-temperature system. Some quantitative information on composition distortions due to skimmer interference has appeared since the last review.

As a part of their study of species enrichment due to Mach-number focusing, Sharma et al. [15] measured overall enrichment factors for a premixed gas of 99% He and 1% Ar; source Reynolds number ranged from 90 to 900, nozzle-skimmer distance ranged from continuum to free-molecule flow at the skimmer. After validating a model for species enrichment due to Mach number focusing, they divided the overall enrichment factor by the enrichment factors for pressure diffusion and Mach-number focusing to extract the enrichment factor for skimmer interference, and did the same for overall enrichment factors reported in [16-18]. When plotted as a function of the skimmer-orifice Reynolds number, the resulting skimmer-interference enrichment factor was correlated by a single curve with a scatter of about 15%. This enrichment factor increased monotonically from about unity at very small Reynolds numbers to about 1.4 at a Reynolds number of 5. See Fig. 4 of [15].

Yoon and Knuth [19] extended the work of Sharma et al. [15], for a monatomic major species, to the important case of a diatomic major species. They found that the skimmer-interference enrichment factor for a diatomic major species is slightly higher than for a monatomic major species, and that the data for the two cases are correlated better if one plots the enrichment factor as a function of the diffusive separation parameter

$$\frac{\Delta m}{m}\,\frac{1}{Re_{01}Sc_1} = \frac{\Delta m}{m}\,\frac{D_{01}}{U_1 d_1} \qquad (8)$$

where Δm is difference in molecular masses, m is average molecular mass, D_{01} is the diffusion coefficient based on local temperature, local pressure and cross section evaluated

at stagnation temperature, U_1 is local hydrodynamic speed, and d_1 is the skimmer-orifice diameter. See Fig. 6 of [19].

Skimmer interference due to proximity of the Mach disk also was investigated by Yoon and Knuth [19]. They measured overall enrichment factor as a function of nozzle-skimmer distance for source conditions such that the skimmer interference described in the previous paragraph is negligible. The measured enrichment factor corrected for pressure diffusion and Mach-number focusing is shown in their Fig. 7 as a function of nozzle-skimmer distance x_1 divided by distance x_{MD} to the Mach disk. For the range of nozzle-skimmer distances investigated, the enrichment due to the proximity of the Mach disk increases as the nozzle-skimmer distance increases; an 80% enrichment is realized already at $x_1 = 0.5\ x_{MD}$.

Fisher [20] modelled species enrichment at the probe entrance for the case in which the species separation is due to pressure diffusion within a curved shock wave at the probe tip. His analysis quantifies the qualitative description given already in 1963 by Reis and Fenn [21]. Although Fisher's expression for the enrichment includes also contributions from the shock-wave pressure ratio and geometry, the most important contributions are from the $\Delta m/m$ and ReSc used also in Eq. (8) above.

Mach-Number Focusing

The discussion of Mach-number focusing in the earlier review [Ref. 1, pp. 344-347] was for the limiting case in which flow at the skimmer entrance is nearly parallel. Subsequent studies [15, 19] indicate that flow divergence upstream from the skimmer can influence dramatically the resulting heavy-species enrichment, so that a more general perspective is required. For a binary mixture of species A and B at the skimmer entrance, if the speed ratio is much larger than unity and $\cos^2\xi_{max} \approx 1$, then the Mach-number-focusing enrichment factor α_M may be written

$$\alpha_M = \frac{(n_A/n_B)_d}{(n_A/n_B)_1} \approx \frac{1-\exp(-S_{\perp 1A}^2 \xi_{max}^2)}{1-\exp(-S_{\perp 1B}^2 \xi_{max}^2)} \qquad (9)$$

where n is number density, $S_\perp$ is the hydrodynamic speed divided by the most-probable random speed perpendicular to the hydrodynamic velocity, ξ_{max} is the angle subtended by the orifice centerline and the line from the orifice to the skimmer lip, and the subscripts 1 and d refer respectively to the skimmer orifice and the detector. See Eq. (2) of [15], Eq. (3.15) of [19] or p. 13 of [22]. Comparisons with measured values are given for a monatomic major species in Fig. 2 of [15] and in the technically important case of a diatomic major species in Fig. 8 of [19]. It is seen that the enrichment factor for Mach-number focusing can range, as a function of $S_\perp \xi_{max}$, from approximately m_A/m_B to unity. Hence it is particularly important to make the appropriate correction for those species which differ significantly from the molecular weight of the major species.

Eq. (9) is applicable for arbitrary mixture ratios in the source, provided only that the relevant speed ratios can be assigned. Relatively detailed procedures for estimating the values of $S_\perp$ are given in [15,19] for the case of a binary mixture with $(n_A/n_B) \ll 1$. (Note that [15,19] supersede the last paragraph of p.346 and the first paragraph of p.347 of [1].) Measurements were made for 1% minor species in the source and good agreement between measurements and predictions was realized. Yamazaki et al. [23] measured an overall enrichment factor for Ar-He mixtures with 2, 5 and 10% Ar. For the region in which skimmer interference appears to be negligible, the values of $\alpha = \alpha_P\alpha_M$ predicted by Eqs. (6) and (9) were in good agreement with measured values for 2 and 5% Ar but were from 10 to 15% smaller than measured values for 10% Ar. The relative contributions of Eqs. (6) and (9) to this difference are not clear.

Analysis of the data is usually simplified if the system design and the operating conditions are such that transition to free-molecule flow occurs upstream from the skimmer and $(S_{\perp 1}\xi_{max})^2 \ll 1$ for all species. Then skimmer interference is easier to avoid and Mach-number focusing is independent of source conditions and system geometry.

Fragmentation During Detection

The most troublesome aspect of fragmentation during detection is the temperature dependence of the mass spectra. The several ion-formation probabilities are functions primarily of the vibrational energy of the parent ion immediately after electron impact. This energy is the sum of the initial vibrational energy possessed before electron impact and the excitation vibrational energy received during electron impact. Since the initial energy is a function of the gas temperature, the fragment pattern is temperature - dependent if the initial vibrational energy is a significant fraction of the total vibrational energy. It follows that the temperature dependence of the mass spectrum is weak for simple molecules (N_2, O_2, CO, NO, etc.) near room temperature and strong for complicated molecules (hydrocarbons, etc.) at higher temperatures. It is seen that meaningful interpretations of mass spectra require that the mean vibrational energy of the molecules prior to electron impact be known. Hence a criterion for predicting the extent of vibrational relaxation in the free jet is required.

A sudden-freeze model for estimating the terminal vibrational temperature of a given species in a free-jet expansion is given in [1,10]. The discussion found there is still relevant provided that one changes the value of the constant C in the freezing-point criterion to 1.6 [11]. Hopefully one can associate a fragment pattern with the value of the terminal vibrational temperature obtained from the sudden-freeze model.

Milne et al. [24] used an effusive beam to provide the temperature-dependent n-butane fragment pattern for MBMS studies of vibrational cooling in free-jets. This procedure was used subsequently by Sharma et al. in two MBMS studies of vibrational relaxations in free jets. In the first study, terminal vibrational temperatures were determined for CO_2 in free-jet flows of (a) pure CO_2 and (b) dilute binary mixtures of CO_2 in N_2 and CO_2 in H_2 [25]. In the second study, terminal vibrational temperatures

in free-jet flows were obtained for (a) pure propane (b) pure n-butane and (c) CO_2 in binary mixtures with He and H_2 [26].

Particularly valuable in the correlation of such relaxation data [25,26] is the dimensionless relaxation parameter $d^*/a_0\tau_{h,p0}$, where a_0 is sound speed, $\tau_{h,p0}$ is characteristic relaxation time and subscript 0 refers to stagnation conditions. This parameter may be thought of as the ratio of the flow characteristic time and the relaxation characteristic time.

Since freezing of vibrational degrees of freedom occurs sometimes near the orifice throat, a model for the velocity distribution near the throat is important. The best available profile for compressible flow of a diatomic gas immediately upstream from the orifice is perhaps that calculated numerically by Yi and Knuth [8] and shown in their Fig. 2. Immediately downstream from the orifice, results of method-of-characteristics calculations may be approximated by

$$d\ln T/d(x/d^*) \approx -4(\gamma-1)/(\gamma+1) \qquad (10)$$

In both [25] and [26], for x/d^* greater than about 2, the approximate algebraic expression given by Ashkenas and Sherman [27] for Mach number is used.

In general, but especially whenever axial distributions (Mach number, temperature, etc.) are given here as a function of the dimensionless distance x/d^*, it is to be understood that the effective value (as opposed to the geometrical value) of d^* is used. See S.P. Tang and J.B. Fenn [28] for measured values of discharge coefficients from which effective values of d^* may be calculated.

Miscellaneous Possible Origins of Distortions

The composition of the sample would be obviously disturbed if condensation were to occur in the free jet. Possible condensations during the free-jet expansion were discussed in the previous review [1]; the strong dependance of condensation initiation on temperature was emphasized. A convenient measure of condensation initiation is the appearance of dimers in the sample; for free-jet expansions of rare gases, the terminal mole fraction of dimers as a function of species properties and source conditions is given by Eq. (43) of [29]. The mole fraction is found to be proportional to $(p_0 d^{*0.4} T_0^{-2.4})^{5/3}$, emphasizing quantitatively the importance of temperature. A similar strong temperature dependance is observed also for diatomic gases. Hence, although it would be prudent to be alert for condensations when expanding from room temperature, experience has shown that species condensations are not significant in molecular-beam sampling studies of combustion processes.

Another possible origin of composition distortion is preferential scattering of beam molecules by background molecules. In principle, this scattering may occur in all vacuum stages; in practice, it is most likely in the collimation chamber, less likely in the source chamber (the chamber in which the free jet is located), and seldom in the detection

chamber. Expressions useful for either avoiding or handling effects of background scattering are summarized in [1]. By careful system design, one usually can avoid composition distortion due to background scattering.

A closely related possible origin of beam-composition distortion is known as "background invasion." Here the shock-wave system of the free jet is invaded by background molecules which then are carried through the skimmer by the supersonic flow. Campargue [30] measured the fluxes through the skimmer, and found that the fluxes of the background gases increased dramatically as the nozzle-skimmer distance was increased and the skimmer tip approached the upstream side of the Mach disk, with the flux of the lightest background gas increasing first. This difference in the species flux profiles in the immediate vicinity of the Mach disk is similar to the difference in the species density profiles observed by Gmurczyk et al. [31] for a shock wave in a binary mixture. Hence this phenomenon is apparently related closely to the shock-wave structure; the accompanying composition distortion can be avoided by reducing the background pressure and locating the skimmer tip suffficiently far upstream from the Mach disk. Young et al. [32] attempted to duplicate this phenomenon by systematically adding a low-molecular-weight species to the source chamber background. Although enrichment of the light species was observed in the collimating chamber, the only enrichment of this species observed at the detector located in the detection chamber was due to the effusive beam formed by the light species in the source chamber.

Yet another distortion is encountered if sampling from an unsteady source (e.g., a cycling-pressure source or a transient flame) such that faster molecules which are sampled later catch up with slower molecules which were sampled earlier. This phenomenon was observed and analyzed first apparently by Young et al. in 1971 [33]. A spike in the nitrogen signal observed near top dead center when sampling from an internal-combustion engine [33, Fig. 5] was interpreted as due to high-energy molecules from after combustion catching up with the slower molecules from before combustion. A relatively straightforward analysis [33] shows that this phenomenon, called "beam over-run," is avoided if

$$(DT_0/Dt) < 2T_0U/L \qquad (11)$$

where DT_0/Dt is rate of change of stagnation temperature, U is hydrodynamic speed (proportional to the square root of T_0) and L is the flight-path length. It is seen that beam over-run can be cured by reducing either DT_0/Dt or the flight-path length. The phenomenon was analyzed again by Smith in 1982 [34] and demonstrated experimentally again by Hurlbut et al. in 1984 [35]. Eq. (25) of [34] and Eq. (1) of [35] are equivalent to Eq. (11) above.

Finally, experience with sampling from a sequence of locations within a flame has demonstrated the possibility of contaminating the time-averaged signal for a given location by the stored time-averaged signal for the prior sampling location. If a lock-in amplifier is used, then one needs to use a sufficiently large amplifier time constant in order to reduce the noise level to an acceptable level. For a given amplifier time

constant, one needs to dwell at the new measurement location for a sufficiently long time period in order to achieve the required change from the prior signal level to the new signal level. If the dwell time is inadequate, an unacceptable distortion of the signal may result. If the dwell time is unnecessarily long, an unacceptable total time period for the entire sequence of measurements may result. A procedure for selecting, for a previously determined value of the time constant of the lock-in amplifier, the value of the dwell time for each new measurement location so as to reduce the total time required to complete the sequence of measurements, without distortions, has been presented by DiJulio and Knuth [36]. In a presented example, use of this procedure reduced the total sampling time by 70%.

Discussion

The most important possible sources of composition distortion in MBMS sampling are found to be:

Acceleration into the probe orifice
Radial diffusion in the free jet
Skimmer interference
Mach-number focusing

We find that the first two and the fourth can be handled satisfactorily using Eqs. (2), (6) and (9) of this review. Assistance in the handling of the species enrichment due to skimmer interference is provided by Fig. 4 of [15] and Figs. 6 and 7 of [19]. The overall enrichment factor α for a given species is given by the product of those for the several mechanisms. For example, if radial diffusion in the free jet, skimmer interference and Mach-number focusing exist simultaneously, then

$$\alpha = \alpha_p \alpha_S \alpha_M \tag{12}$$

where α_S is the enrichment factor for skimmer interference.

The various requirements for minimizing composition distortion place conflicting requirements on the design of the sampling probe, particularly regarding the cone angle. The need to minimize distortion in a reactive mixture, e.g., in a flame, argues in favor of an external probe surface with a small included angle. The need for a rapid expansion in the free jet, and the advantage of using a free jet with relatively well known expansion path, argue in favor of an internal probe surface with a relatively large included angle. Total angles used by the several investigators include 40^0 [3,6], 60^0 [4], 80^0 [5,7], 90^0 [16] and 110^0 [5,6,7]. Guidance in the evaluation of the flow inside the probe is provided by the analysis of Ashkenas and Sherman [27]. For a free jet expanding from an orifice in a flat plate, their analysis indicates that the fractional mass flow outside total angles of 40, 80 and 110^0 is 84%, 49% and 23%. The expansion within a cone with total angle less than about 80^0 is seen to be significantly constrained by the cone wall. For an included angle of 60^0, Smith et al. [37] approximated the axial Mach-number distribution within the probe by that for channel flow.

The dimensionless parameter

$$ReSc = Ud/D = (d^2/D)/(d/U) = t_D/t_F \quad (13)$$

where t_D is characteristic time for mass diffusion perpendicular to the free-jet axis and t_F is characteristic time for hydrodynamic flow parallel to the free-jet axis, appears here in Eqs. (1), (2), (6) and (8). The physical significance of ReSc is clarified if one notes that the larger the ratio t_D/t_F, the larger the role of hydrodynamic transport and the smaller the role of mass diffusion. Hence one might think of ReSc as the convection/diffusion parameter.

In summary, during the past two decades, since the publication of the earlier review [1] and since the first Molecular Beam Sampling Conference [2], significant progress has been made in our identification and quantification of composition distortions in MBMS sampling. At first glance, it might appear that our increased understanding has burdened us with an overwhelming number of possible pitfalls. The thorough investigator will find, however, that this increased understanding has provided also the means for either avoiding or handling these pitfalls sufficiently so that MBMS sampling has graduated from an object of research and development to a tool for quantitative studies of complicated reactive systems.

References

1. E.L. Knuth, "Direct-Sampling Studies of Combustion Processes," Engine Emissions: Pollutant Formation and Measurement (G.S. Springer and D.J. Patterson, eds.) 319-363. New York: Plenum Publishing Corp., 1973.

2. Molecular Beam Sampling Conference. Kansas City, MO: Midwest Research Institute, 1972.

3. D. Stepowski, D. Puechberty and M.J. Cottereau, "The Use of Laser-Induced Fluorescence of OH to Study the Perturbation of a Flame by a Probe," 18th Symposium (International) on Combustion 1567-1573. Pittsburgh: The Combustion Institute, 1981.

4. O.I. Smith and D.W. Chandler, "An Experimental Study of Probe Distortions to the Structure of One-Dimensional Flames," Combustion and Flame 63:19-29, 1986.

5. S. Yoon and E.L. Knuth, "Experimental Study of Probe-Induced Distortions in Molecular-Beam Mass-Spectrometer Sampling from Flames," Rarefied Gas Dynamics (S.S. Fisher, ed.) II:867-881. New York: AIAA, 1981.

6. J.C. Biordi, C.P. Lazzara and J.F. Papp, "Molecular Beam Mass Spectrometry Applied to Determining the Kinetics of Reactions in Flames. I. Empirical Characterization of Flame Perturbation by Molecular Beam Sampling Probes," Combustion and Flame 23:73-82, August 1974.

7. R.J. Cattolica, S. Yoon and E.L. Knuth, "OH Concentration in an Atmospheric-Pressure Methane-Air Flame from Molecular-Beam Mass-Spectrometry and Laser-Absorption Spectroscopy," Combustion Science and Technology 28:225-239, 1982.

8. A.C. Yi and E.L. Knuth, "Probe-Induced Concentration Distortions in Molecular-Beam Mass-Spectrometer Sampling," Combustion and Flame 63:369-379, 1986.

9a. A.N. Hayhurst and N.R. Telford, "Mass Spectrometric Sampling of Ions from Atmospheric Pressure Flames - I: Characteristics and Calibration of the Sampling System," Combustion and Flame 28:67-80, 1977.

9b. A.N. Hayhurst, D.B. Kittelson and N.R. Telford, " - II: Aerodynamic Disturbance of a Flame by the Sampling System," Combustion and Flame 28:123-135, 1977.

9c. A.N. Hayhurst and D.B. Kittelson, " - III: Boundary Layer and Other Cooling of the Sample," Combustion and Flame 28:137-143, 1977.

10. E.L. Knuth, "Relaxation Processes in Flow Systems," Proceedings of the 1972 Heat Transfer and Fluid Mechanics Institute (R.B. Landis and G.J. Hordemann, eds.) 89-107. Stanford: Stanford University Press, 1972.

11. L.-T. Dao-Gibner and E.L. Knuth, "The Sudden-Freeze Model Revisited," Rarefied Gas Dynamics (V. Boffi and C. Cercignani, eds.) 2:514-523. Stuttgart: B.G. Teubner, 1986.

12. F.S. Sherman, "Hydrodynamical Theory of Diffusive Separation of Mixtures in a Free Jet," Phys. Fluids 8:773-779, May 1965.

13. P.K. Sharma, W.S. Young and E.L. Knuth, "Pressure Diffusion in Free-Jet Flows of Binary Gas Mixtures," unpublished.

14. T.D. McCay and L.L. Price, "Diffusive Separation of Binary Mixtures of CO_2-H_2 in a Sonic-Orifice Expansion," Phys. Fluids 26:2115-2119, August 1983.

15. P.K. Sharma, E.L. Knuth and W.S. Young, "Species Enrichment due to Mach-Number Focusing in a Molecular-Beam Mass-Spectrometer Sampling System," J. Chem. Phys. 64:4345-4351, 1 June 1976.

16. F.T. Greene, J. Brewer and T.A. Milne, "Mass Spectrometric Studies of Reactions in Flames. I. Beam Formation and Mass Dependence in Sampling 1-Atm Gases," J. Chem. Phys. 40:1488-1495, 15 March 1964.

17. J.B. French and D.R. O'Keefe, "Omegatron Studies of a Skimmed Beam System," Rarefied Gas Dynamics (J.H. de Leeuw, ed.) II:299-310. New York: Academic Press, 1966.

18. J.H. Chang, "Supersonic Molecular Beam Sampling System for Mass Spectrometric Studies of High-Pressure Flow Systems," AIAA preprint 69-64. New York: AIAA, 1969.

19. S. Yoon and E.L. Knuth, "Species Enrichment due to Mach-Number Focusing. II. Diatomic Major Species," Rarefied Gas Dynamics (R. Campargue, ed.) I:639-654. Paris: Commissariat a l'Energie Atomique, 1979.

20. S.S. Fisher, "A Simple Model for Species Separation in Supersonic Impact Probes," Rarefied Gas Dynamics (R. Campargue, ed.) I:655-666. Paris: Commissariat a l'Energie Atomique, 1979.

21. V.H. Reis and J.B. Fenn, "Separation of Gas Mixtures in Supersonic Jets," J. Chem. Phys. 39:3240-3250, 15 Dec. 1963.

22. E.L. Knuth, "Lecture Notes on Supersonic Molecular Beam Sources," Bericht 20/1988. Göttingen: Max-Planck-Institut für Strömungsforschung, Nov. 1988.

23. S. Yamazaki, M. Taki and Y. Fujitani, "Mass Separation during Molecular Beam Sampling Process," Japanese Journal of Applied Physics 18:2191-2197, Dec. 1979.

24. T.A. Milne, J.E. Beachey and F.T. Greene, "Study of Relaxation in Free Jets Using Temperature Dependence of n-Butane Mass Spectra," J. Chem. Phys. 56:3007-3013, 15 March 1972.

25. P.K. Sharma, W.S. Young, W.E. Rodgers and E.L. Knuth, "Freezing of Vibrational Degrees of Freedom in Free-Jet Flows with Application to Jets Containing CO_2," J. Chem. Phys. 62:341-349, 15 Jan. 1975.

26. P.K. Sharma, E.L. Knuth and W.S. Young, "Vibrational Relaxations in Freejet Flows of C_3H_8, n-C_4H_{10}, and Binary Mixtures of CO_2," Rarefied Gas Dynamics (J.L. Potter, ed.) II:859-871. New York: AIAA, 1977.

27. H. Ashkenas and F.S. Sherman, "The Structure and Utilization of Supersonic Free Jets in Low Density Wind Tunnels," Rarefied Gas Dynamics (J.H. de Leeuw, ed.) II:84-105. New York: Academic Press, 1966.

28. S.P. Tang and J.B. Fenn, "Experimental Determination of the Discharge Coefficients for Critical Flow Through an Axisymmetric Nozzle," AIAA Journal 16:41-46, Jan. 1978.

29. E.L. Knuth, "Dimer-Formation Rate Coefficients from Measurements of Terminal Dimer Concentrations in Free-Jet Expansions," J. Chem. Phys. 69:5073-5076, 15 April 1977.

30. R. Campargue, "Aerodynamic Separation Effect of Gas and Isotope Mixtures Induced by Invasion of the Free Jet Shock Wave Structure," J. Chem. Phys. 52:1795-1802, 15 Feb. 1970.

31. A.S. Gmurczyk, M. Tarczyński and Z.A. Walenta, "Shock Wave Structure in the Binary Mixtures of Gases with Disparate Molecular Masses," Rarefied Gas Dynamics (R. Campargue, ed.) I.333-341. Paris: Commissariat a l'Energie Atomique, 1979.

32. W.S. Young, Y.G. Wang, P.K. Sharma, W.E. Rodgers and E.L. Knuth, "Molecular-Beam Sampling of Continuum Gas Mixtures," Rarefied Gas Dynamics (K. Karamcheti, ed.) 253-260. New York: Academic Press, 1974.

33. W.S. Young, W.E. Rodgers, C.A. Cullian, Y.G. Wang and E.L. Knuth, "A Method for Sampling the Instantaneous Chemical Compositions in an Internal Combustion Engine," Proceedings of the Second International Air Pollution Conference (H.M. Englund and W.T. Beery, eds.) 418-424. New York: Academic Press, 1971.

34. O.I. Smith, "Molecular Beam Sampling from Combustion Systems," WSS/CI 82-49. Presented at the Fall 1982 Technical Meeting of the Western States Section/The Combustion Institute, Livermore, CA, October 1982.

35. F.C. Hurlbut, A.K. Oppenheim, D. Lucas and R. Peterson, "Molecular Beam Mass Analysis of Transient Combustion Events," Rarefied Gas Dynamics (H. Oguchi, ed.) II:617-626. Tokyo: Univ. of Tokyo Press, 1984.

36. S.S. DiJulio and E.L. Knuth, "Selection of Dwell Time When Using a Lock-In Amplifier in a Sequence of Measurements," Rev. Sci. Instrum. 55:1154-1156, July 1984.

37. O.I. Smith, S.-N. Wang, S. Tseregounis and C.K. Westbrook, "The Sulfur Catalyzed Recombination of Atomic Oxygen in a CO/CO_2/Ar Flame," Combustion Science and Technology 30:241-271, 1983.

MBMS Sampling from Highly Heated Gas Mixtures (1000-3000 K) and Weakly Ionized RF Plasmas (800-2800 K) or Laser Plasmas (5000-20,000 K)

R. Campargue and A. Lebéhot
Laboratoire des Jets Moléculaires
CEA/DSM - DRECAM/SCM - CE de Saclay
91191 Gif-sur-Yvette - Cedex, France

I. Introduction

The properties of the free jet expansion and molecular beam skimming can be applied to the sampling of a wide variety of gaseous media, as those considered in this workshop: reactive systems, high temperature gases, flames, plasma flows, shock zone gases, laser ablation plumes, gas phase in CVD or in high temperature corrosion, etc.

In our laboratory, as well as in many molecular beam groups, the MBMS sampling is not generally made for analysing the gas stagnating in the nozzle, but for optimizing and using the beam source in research experiments. Nevertheless, this beam optimization has been of great interest to investigate and minimize the distortions through the interface used for MS sampling. They are due to the reality of the gas, the deviations from ideal free jet expansion, and the possible interactions along the MBMS sampling system, from the nozzle sampler to the quadrupole analyser.

The first part of this paper is an historical review on the various distortions observed at Saclay in skimming, or in MBMS sampling, from room temperature gases or gas mixtures. The second part deals with neutral energetic particles resulting either from the cluster generation in expansion or from the seeding and/or heating techniques. Finally the last part of the paper is devoted to recent developments in MBMS sampling of weakly ionized RF plasmas (800-2800 K) and laser sustained plasmas (5000-20000 K). The presentation is made with large reference to our previous papers, especially our later review on jets and beams[1] published in the special J. Phys. Chem. issue devoted to J.B. Fenn, after the memorable Fennfest organised at Yale in 1983.

II. Review on distortions in MBMS sampling as investigated and minimized at Saclay

This review is highly simplified just after the plenary lectures on the history of free jet sampling by J.B. Fenn, the principles of free jets and their deviations from ideal properties by D.R. Miller, and the composition distortions in MBMS sampling by E.L. Knuth. This latter author considers in details the distortions due to the presence and operation of the sampling probe (not treated by us) as well as those due to phenomena found downstream from the sampling orifice. Our paper is an attempt to describe, mainly from a complementary point of view, the procedures for minimizing the deviations from ideal free jet properties and composition distortions, as developed at Saclay during a period of about 30 years.

The possibilities of such deviations and distortions result from the reality of the gas (viscosity, condensation), background gas effects, separation phenomena, interactions of the jet and beam with the skimmer, background signals and interferences in the quadrupole analyser.

II.1 - Reduction or elimination of the distortions due to viscosity and condensation

The viscous effects appearing at the nozzle throat when operated at low pressure, become weak or negligible at the Reynolds number $Re^* > 10^3$. The distortions due to skimmer losses are not so easy to eliminate, as shown below.

The condensation in free jet expansions depends on the nozzle geometry as well as the stagnation pressure P_0 and temperature T_0.

In the various nozzle shapes shown in Fig. 1, *a* and *b* have a high collimating efficiency but they are not convenient in MBMS sampling because of enhancement of condensation and relatively long contact of the gas sample with the nozzle wall. The capillary nozzle *c*, with length to diameter ratio $L/D^* \cong 2$, is the most efficient one in our nozzle beam generation.[1] The nozzle *d* (with $L/D^* < 1$) and especially the nozzle *e* (with $L/D^* \ll 1$ obtained with a reversed skimmer), are mainly of interest for reducing the condensation effects. Finally, the conical nozzle *f* is the most appropriate and the most used in MBMS sampling for minimizing its interaction with the sampled gas media.

In any case, the condensation is not expected when probing high temperature gases even at high pressure P_0.

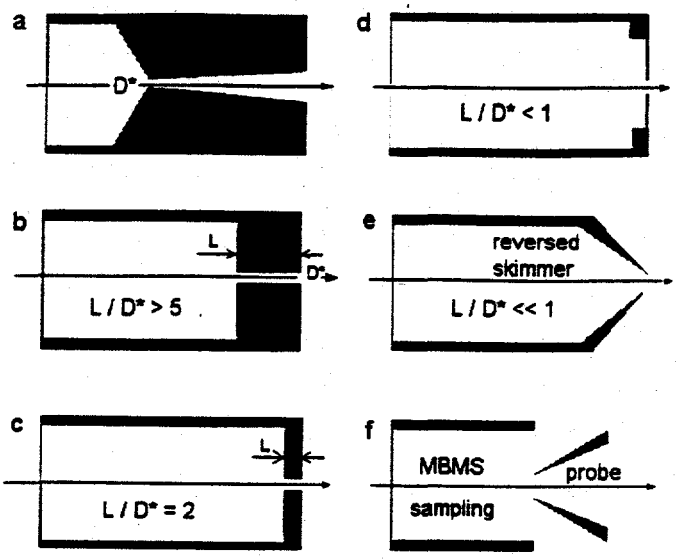

Fig 1. Different types of nozzles used at Saclay

II. 2 - Creation of a free jet zone of silence not affected by the background gas

The background gas in the expansion chamber can produce a strong disturbance in the nozzle beam generation especially when applied to MBMS sampling. Thus, the interest of producing the free jet in a low pressure environment ($P_{BG} \leq 10^{-4}$ Torr) has been obvious in the pioneering nozzle beam works due especially to J.B. Fenn and co-workers.[2,3] In these conditions, the main problem is the small mass throughput acceptable by diffusion pumps of reasonable size and, consequently, the limitation in jet and beam performance.

In the alternative approach developed at Saclay,[1,4] the free jet is produced at much higher background pressure ($P_{BG} = 10^{-1}$ to 1 Torr) using a Roots blower. Thus the gas is expanded in a free jet zone of silence, completely unaware of any external condition, because the shock wave structure shields the supersonic flow from the background gas. It should be emphasized that this shielding structure vanishes at the low background pressure used in the Fenn type sources.[2,3] The main advantage of our approach is the possibility of using, in the absence of background gas distortion, large nozzle mass flow rate for improving the free jet and beam properties.

The typical beam intensity I versus the nozzle skimmer distance X/D^* is shown in Fig. 2 for the two different approaches at the same stagnation conditions P_0 and T_0. Also the total skimmer flow rate $\dot{N}_s$ is presented as calculated for an ideal free jet expansion ($P_{BG} = 0$) and as measured in the conditions of a free jet zone of silence of length X_{ZS}, unaware of the background gas ($P_{BG} \geq 10^{-1}$ Torr).

In any case, for $X < X_{ZS}$, $\dot{N}_s$ and I are independent of the background pressure P_{BG}. Their variations in opposite directions are not expected in ideal conditions but can be explained by viscous effects and scattering within the conical skimmer (boundary layers, oblique shock waves, reflected molecules) as well as by self scattering in the skimmed streamtube. At the maximum beam intensity corresponding to a skimmer Knudsen number $Kn_s \sim 1$, all these disturbances seem to become negligible. Then it is possible to maintain the maximum beam intensity only at very low

background pressure ($P_{BG} \cong 0$). On the contrary, by using our alternative approach,[1] the background gas penetration at $X > X_{ZS}$ produces a sharp fall off in beam intensity. The skimmer flow rate for the background gas pumped by the free jet appears as the difference between experiment and theory in Fig. 2.

Certainly the ideal free jets and skimmed beams would be those obtained with an infinite pumping rate ($P_{BG} = 0$). From a practical point of view, the Roots blower used at $P_{BG} \geq 10^{-1}$ Torr makes it possible to operate the nozzle at very large mass flow rate and achieve very high molecular beam performance by skimming upstream and not far from the Mach disk. In the case of He beams,[1,6,7] skimmed speed ratios $S_{//}$ up to 400, i.e. translational temperatures $T_{//}$ in the range of 10^{-2} to 10^{-3} K, are obtained. Thus, the residual viscous losses and distortions seem to be weak in our He beam generation.

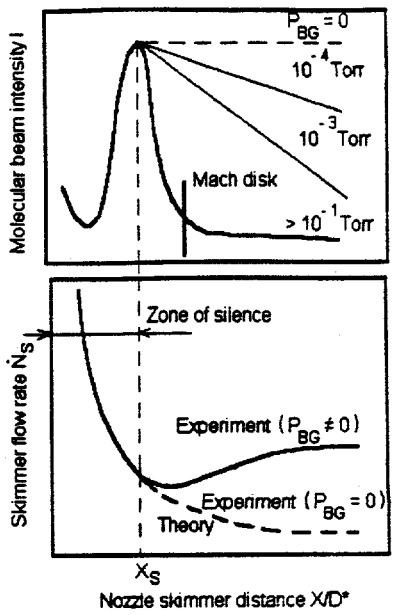

Fig. 2. Typical beam intensity and skimmer flow rate versus source - skimmer distance, at various nozzle chamber background pressures

II. 3 - Conditions for minimizing separation phenomena in free jets and molecular beams

The composition distortions, due to the presence and operation of the sampling probe in MBMS sampling, as well as those due to chemical relaxation in the free jet, are reviewed by E.L. Knuth in this volume. The other possibilities of distortions are due especially to separation phenomena in free jets and molecular beams. The separation can be induced by the jet, the background gas, the Mach disk, and the bow shock detached from a skimmer of poor quality. Furthermore, Mach number focusing[5] can increase the heavy species concentration on the beam centerline downstream of the skimmer (as discussed also by E.L. Knuth).

The jet induced separation results from pressure gradients and, consequently, a radial barodiffusion able to concentrate the heavy species on the jet axis (positive separation, Fig. 3). The theoretical results obtained by Sherman[8] for binary mixtures are well confirmed, at small distance from the nozzle, by flow visualization or by skimming with negligible probe effect.

The deviations from Sherman's predictions[8] and even the reversed or negative separation occuring relatively far from the nozzle throat, have been identified by Campargue[9] as an invasion separation, or differential penetration of the background gas into the free jet structure. This effect which appears in the absence of a real zone of silence, is favourable to light species and is the basic principle of the jet membrane process in the field of isotope separation.[10] Thus, the total separation measured on the free jet axis (Fig. 3) can be explained by the competition of two effects induced by the jet (+) and the differential background gas penetration (-). When the nozzle Reynolds number is high enough ($Re^* > 10^3$) the jet separation is negligible and the pure jet membrane effect can be observed as far as the presence of the Mach disk does not induce a positive separation.

The possibilities of observing either pure diffusive separation (at small distance from the nozzle throat) or pure invasion separation (at $Re^* > 10^3$) requires the absence of any probe influence. Reis and Fenn[11] have shown that, under certain circumstances, there is greater separation (+) induced by the sampling probe itself than by the jet diffusion. They have attributed this phenomenon to a detached bow shock in front of the probe (Fig. 4) where the separation is produced by inertial effects. Thus, a probe induced separation (positive) occuring in sampling supersonic free jets can be considerably higher than the classical effect due to the jet. Therefore, it

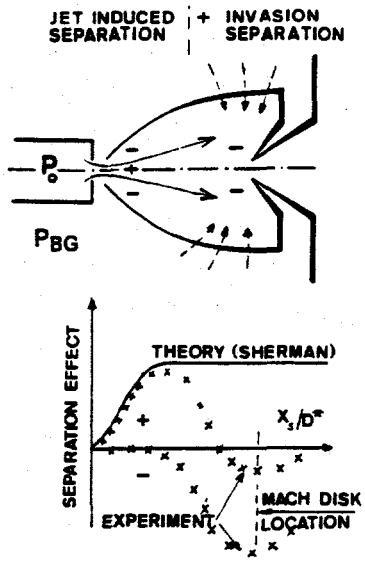

Fig. 3. Separation due to three competing effects induced by: free jet, background gas invasion, and Mach disk

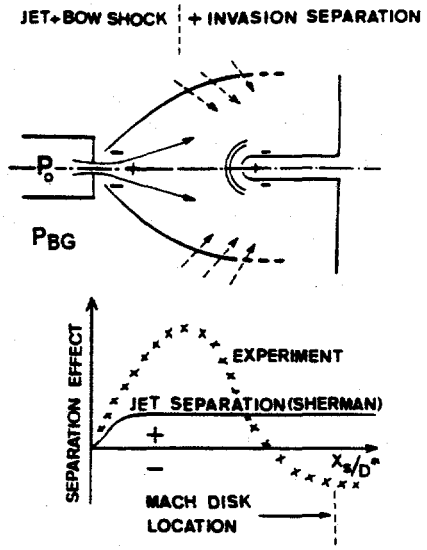

Fig. 4. Separation due to four competing effects induced by: free jet, bow shock, background gas invasion, and Mach disk

is easy to investigate the pure influence of the probe, with a negligible jet separation ($Re^* > 10^3$) as made by Campargue and Constant[12] (results published in Ref. 10) using binary gas mixtures and mainly the natural mixture of $^{36/40}Ar$ isotopes. Nevertheless, at relatively large distance from the nozzle throat, the invasion effect appears to be able to reduce the positive separation and even to reverse it (Fig. 4). Finally, the Mach disk interaction (+) is present. A review on these various separation phenomena, including also the velocity slip,[13] is available in Ref. 10.

In conclusion, in MBMS sampling, it is essential to generate the supersonic free jet in the conditions where the three separation effects briefly described above, are not observed. This is obtained by operating the nozzle at $Re^* > 10^3$ in order to have negligible jet separation (positive) and producing the expansion in a real free jet zone of silence in order to prevent any background gas penetration and, consequently, any negative separation. Finally the probe induced separation discerned by Reis and Fenn[11] and largely investigated at Saclay[10,12] can be avoided easily using a sharp edge skimmer able to swallow the shock as shown below.

Other composition distortions produced downstream of the skimmer orifice can be due to viscous effects, self-scattering, and Mach number focusing,[5] as described in the other reviews at this workshop. In the following part of our paper, the emphasis is on various skimmer interferences which can be reduced by optimizing the skimmer geometry and also by increasing the beam kinetic energy.

II. 4 - Optimization of the skimmer geometry

The various skimmer parameters are defined in Fig. 5. The bow shock, as induced by any blunt body placed in a supersonic flow, is also formed in front of the circular edge of a blunt skimmer. This can be avoided by using very sharp skimmers ($\delta \sim 1$ µm). When the length of the cone is not sufficient, the distortion can be due to an end wall effect[14,15] producing and placing a normal shock wave in the skimmer tip area. Furthermore, the bow shock is also produced, as in front of a blunt body, when the exterior angle is too large. If α_{ext} is small enough, the shock is then swallowed in front of the skimmer orifice and attached to the skimmer edge outside of the cone. The theoretical maximum value of α_{ext} for avoiding the shock detachment, is shown in Fig. 5 in terms of the skimmer Mach number. Finally, the viscous effects within the skimmer increase with decreasing α_{int}. By taking into account only the collisions with the wall due to the perpendicular

velocity component of the beam molecules, the minimum value of α_{int} has been also calculated and plotted in Fig. 5 versus Mach number. Only the blank area in the plot of α_{int} and α_{ext} can be used. Consequently, the skimming is not possible at low Mach number. Our best skimmers are operated in the blank area with the following characteristics: $\alpha_{int} = 40°$, $\alpha_{ext} = 50°$, $L_{ext} = 19$ mm, $D_S = 0.5$ mm and even $D_S = 0.25$ mm, with edge thickness $\delta \sim 1$ μm. These skimmers are made of polished stainless steel.

The effect of decreasing D_S for going nearly to quantum theory predictions,[4,16] in the case of supercooled He jets and beams, has been described in our previous review.[1] Nevertheless, the next part of this paper will show the possibility of using relatively large skimmer orifices when the beam kinetic energy is high enough.

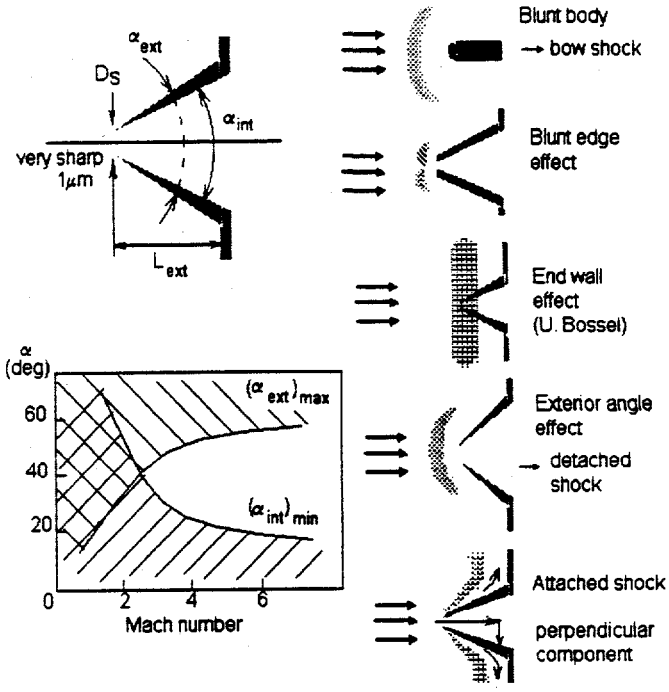

Fig. 5. Effects of skimmer parameters in skimming supersonic flows

III. Skimming and MBMS sampling of neutral energetic particles

III. 1 - Skimming in cluster beam generation

In our experiments, the simplification appearing in the skimming process, when the particle kinetic energy is increased, has been observed initially in the generation of hydrogen cluster beams.[15] These experiments have been performed using the cylindrical nozzle of type *b* in Fig. 1, operated at $P_0 = 50$ bar and $T_0 = 80$ K. From the results shown Fig. 6, the sharp fall off in beam intensity, usually obtained when the nozzle skimmer distance X/D* is reduced (as shown in Fig. 2), is not found for these cluster beams. On the contrary, their beam intensity increases slowly with decreasing X/D*. Thus, the distortions within the skimmer seem to be negligible (even at X = 2 mm) due to inertial effects of the heavy H_2 clusters.

The possibility of increasing the skimmer diameter D_S from 0.5 mm (normally) to 1 mm (here) has been well

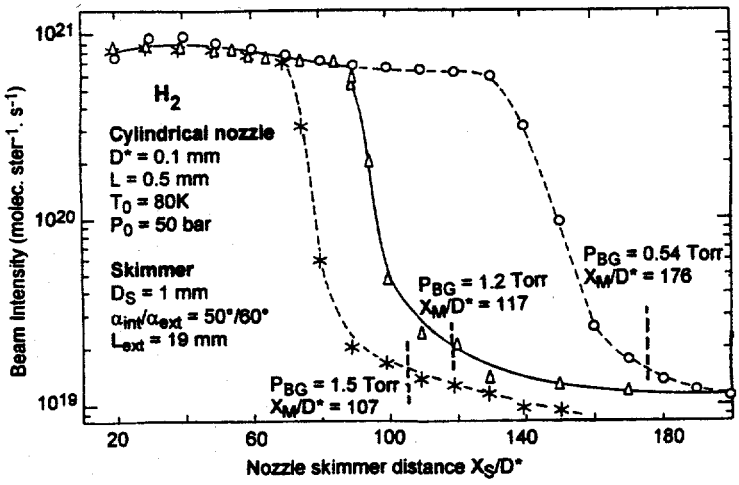

Fig. 6. H_2 cluster beam intensity not reduced by skimmer losses close to the source, due to inertial effects.

confirmed with D_S = 2 mm. This increase of D_S is possible without decreasing the value of the speed ratio $S_{//}$. Furthermore, it is accompanied by an enhancement of beam intensity instead of a reduction usually observed at low kinetic energy, in the absence of condensation.

III. 2 - MBMS sampling from highly heated gas mixtures (1000 - 3000 K)

Our high pressure, high temperature nozzle beam source ($P_0 \leq 100$ bar, $T_0 \leq 3000$ K) has been only patented and described briefly in our previous papers.[17] Heating is obtained by the Joule effect through small concentric tungsten tubings surrounded by concentric heat shields, and finally a water cooling jacket. As the entire enclosure is water cooled up to the nozzle throat, the source pressure can be very high even when the axial gas temperature is around 3000 K. Thus, an important temperature gradient is produced in the flow at the nozzle throat, but only its centerline part is used to generate the beam.

The MBMS sampling coupled with the time-of-flight (TOF) technique, as shown in Fig. 9, allows to measure the stagnation temperature T_0 in the case of pure gases.[6] The precision higher than 1% obtained in experiments performed at T_0 = 300 K, using a flight path of 4.2 m, reflects the high quality of the MBMS sampling system without any detectable temperature distortion due to viscosity or scattering effects. The results obtained from heated gases have been published[1,6,18] mainly for pure argon and helium and for gas mixtures as He-Ar, He-Xe, H_2-Xe (Fig. 7).

Heating and seeding, in helium or hydrogen, lead the kinetic energy for the heavy species in the eV range, up to about 40 eV for Xe in H_2 . Such a kinetic energy of neutral particles entering the ionization zone of the quadrupole is not negligible relative to the potential (30-40 volts) used to extract ions perpendicularly to the beam axis, from the ionizer to the quadrupole field (Fig. 9). This difficulty is circumverted by extracting ions in the beam direction, adjusting properly their energy,

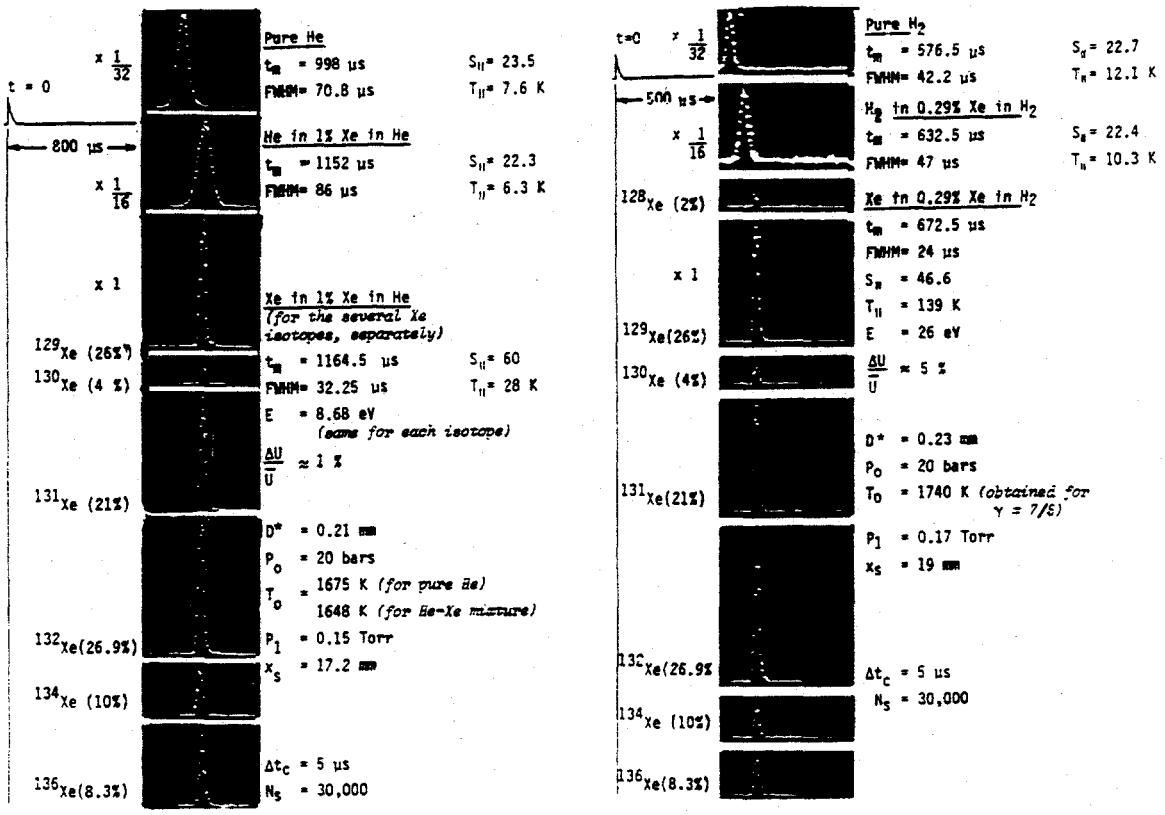

Fig. 7. Comparison between TOF distributions for pure He and 1% Xe seeded in He (left) and for pure H_2 and 0.29% Xe seeded in H_2 (right)

and using an electrostatic deflector. This deflector, adjusted for the extraction of ions in the eV range, totally discriminates against ions produced from the thermal energy background gas . Thus, very high signal-to-noise ratios are achieved as shown in Fig. 7. In this way, the MBMS sampling and TOF analysis make it possible to measure, at 4.5 m from the nozzle, the isotopic composition of Xe seeded in He or H_2 at total concentration of only 50 ppm. The absence of distortions is also reflected by the measured Maxwellian velocity distributions and TOF temperatures $T_{//}$ in excellent agreement with the theoretical predictions ($T_{light} < T_{heavy}$).[1,19]

Finally, it is worth mentioning that, in spite of the large mass ratios used, the separation due to the velocity slip[10,13] is nearly completely eliminated: only 1% for He/Xe and 5% for H_2/Xe mixtures. In any case, Mach number focusing[5] which is of great interest in the applications of seeded beams, cannot be avoided in MBMS sampling. The simplification of the skimming process at relatively high kinetic energy, as observed for cluster beams, is well confirmed in all these experiments performed with skimmers of relatively low quality and orifice larger than usually.

IV. MBMS sampling of weakly ionized RF and laser plasmas

IV. 1 - RF plasmas (800 - 2800 K)

Our RF plasma source described previously[20] has been used to generate energetic oxygen atom beams for investigating H_2 + O reactions in a crossed beam experiment. The dissociation of O_2 is produced by capacitive RF discharge maintained in a quartz tube supplied with 10% O_2 in He or Ar, for instance at total pressure of 180 Torr. The mixture thus obtained at the exit of the quartz tube used as a sonic nozzle (D* = 1.2 mm) can be analysed by MBMS sampling and TOF technique, as shown in Fig. 9. This makes it possible to measure:

- the stagnation temperature (800 - 2800 K) from the velocity distribution (Fig. 8) obtained by the time-of-flight technique
- the degree of dissociation in the plasma source achieving 50% with He and 90% with Ar, using a method described in Ref. 20.

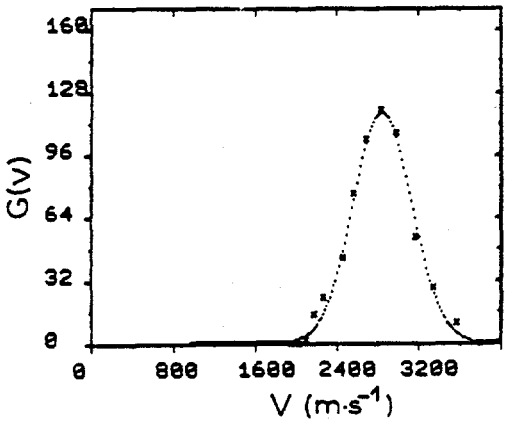

Fig. 8. Velocity distribution from TOF measurements (×) and best Maxwellian fit: V = 2800 m/s, $S_{//} \cong 8$, $T_0 \cong 1600$ K

The ground states O(^{3}P) are dominant. Nevertheless, the metastables O(^{1}D) have enough concentration for allowing to study the H_2 + O(^{1}D) reaction.[20]

In all these experiments, the increase of kinetic energy up to 0.65 eV, as obtained by seeding and heating, has improved largely the beam intensity. This is attributed in part to the decrease of the skimmer losses because of inertial effects. This simplification of the beam extraction process is also confirmed by the possibility of using skimmers of bad quality, especially after degradation by energetic atomic oxygen.

IV. 2 - MBMS sampling from weakly ionized laser sustained plasmas (5000 - 20000 K)

In our most recent developments at Saclay, we have constructed and investigated a new energetic atom source using a continuous optical discharge.[21] The advantages of the laser heating are as follows:

i) possibility of using a relatively high and wide pressure range (up to 200 bar) of interest for minimizing the distortions mentioned above and improving the beam performance

ii) absence of electrodes and, consequently, of gas pollution by material erosion as produced in electric arc sources

iii) plasma temperatures achieved up to 20000 K close to the nozzle throat and, consequently, absence of condensation effects

iv) maximum temperature obtained on the nozzle axis (as for heated neutral gases) in the core portion used to form the molecular beam, as shown in the calculated temperature map in Fig. 10.

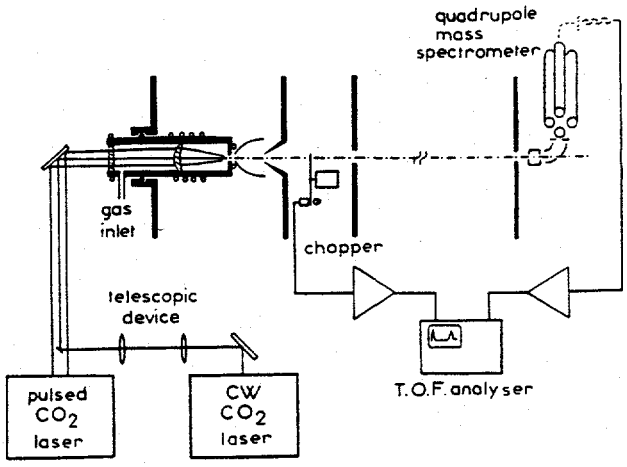

Fig. 9. Laser sustained plasma source coupled to MBMS sampling and TOF analyser

Our laser sustained plasma source has been developed mainly with the goal of producing energetic oxygen atom beams of interest in our crossed beam experiments.[20] Furthermore, this source could be used in aerospace research for studying re-entry problems as well as the material degradation produced by 5 eV atomic oxygen in low earth orbit at 8 km/s.

In our laser sustained plasma source (Fig. 9) already described,[21,22] the plasma is initiated by a pulsed CO_2 laser and maintained by a continuous CO_2 laser focused just ahead of a water-cooled sonic nozzle (D* = 0.5 mm). Typical experimental conditions are: laser power $P < 400$ W, focal length of 38.1 mm, and *laser waist - nozzle throat* distance of about 1.5 mm. The nozzle is supplied with pure argon, or Ar-He-O_2 mixtures, at the pressure $P_0 \leq 8$ bar. The plasma free jet is produced in a relatively high pressure environment ($P_{BG} < 0.3$ mbar) used to form a zone of silence.[1] For such conditions, the TOF stagnation temperature T_0 is found between 6000 and 13000 K (kinetic energy < 2.6 eV) as shown in Fig. 11.

The atom beam extracted from the plasma free jets exhibits velocity distributions reflecting isentropic expansions as in the case of neutral gases.[21] This indicates that the kinetic behaviour of the heavy particles is not affected by the interaction with the electron gas. Consequently, the MBMS sampling and TOF system can be used as a probe for analysing very accurately the properties of the plasma, just upstream of the nozzle throat.[21] This is possible, not only for the axial temperature, but also the temperature profile at the nozzle throat, when combining the time-of-flight analysis to the measurement of the gas flow rate through the nozzle, the heat flux, and the energy yield of the laser heating process (up to 75% of the laser energy is absorbed by the plasma free jet).[22]

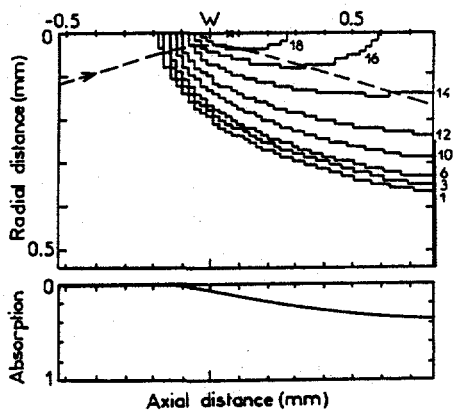

Fig. 10. Temperature map for $P = 2$ kW, $P_0 = 6$ bar. Axial distances are referred to the waist location (W). Isothermal lines are represented for 1 to 18×10^3 K. The laser beam profile is shown by the broken line and its absorption in the bottom part

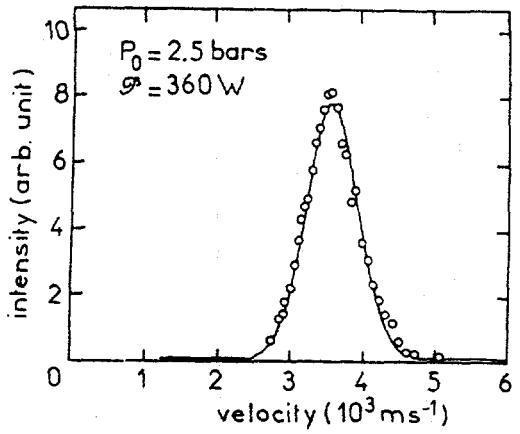

Fig. 11. Typical velocity distribution with speed ratio $S_{//} = 6.7$, obtained by TOF measurement (o) and best fit Maxwellian distribution (full line) corresponding to $T_0 = 12425$ K, $P_0 = 2.5$ bar, laser power $P = 360$ W

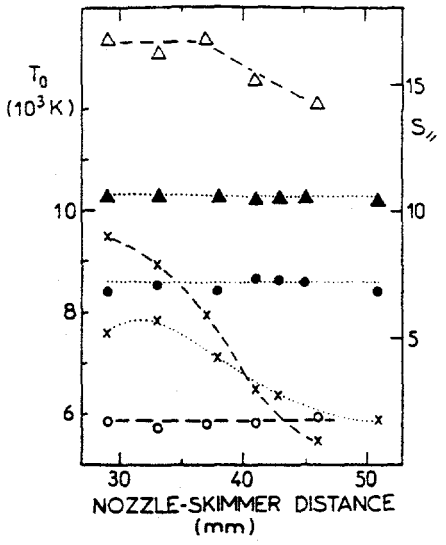

Fig. 12. TOF temperatures (o), speed ratios (Δ) and flux (×), versus nozzle-skimmer distance, for $P = 300$ W, $P_0 = 4$ bar (full symbols, dotted lines); $P = 300$ W, $P_0 = 7$ bar (open symbols, broken lines)

It is observed that the parallel temperature $T_{//}$ and speed ratio $S_{//}$, measured by the time-of-flight technique on the extracted atom beam, are nearly independent of the nozzle-skimmer distance, while the beam intensity drops drastically due to background gas penetration into the free jet (Fig. 12). In these conditions, the detector receives only the particles which undergo either no collision or forward elastic collisions with the background gas. This is rather due to the geometry of the apparatus (small solid angle of detection) than to the kinetic energy in the free jet. On the contrary, this latter effect explains why the quality of the skimmer edge is of low importance for the kinetic properties and intensity of the atom beam extracted from the plasma jet.

In contrast to the simple kinetic behaviour of the neutral particles, decoupled from the electron gas, electronic relaxation phenomena are expected to be mainly governed by the electron collisions, and rather complicated, due to electronic excitation with large number of states, ionization-recombination, dissociation, and radiative processes. Strongly non-equilibrium effects are found between the heavy particle translational temperature, the electron gas temperature, the excitation temperature, and between the different electronic states themselves.

IV. Conclusion

Our long experience at Saclay, on nozzle beam generation, has shown available procedures for avoiding or minimizing the distortions in MBMS sampling, especially those due to the reality of the gas (viscosity, condensation), background gas disturbances, and separation phenomena. The skimmer losses can become negligible upstream of the orifice but cannot be eliminated completely in the flow within the cone. Nevertheless, a high improvement in the reduction of these losses is obtained by increasing the particle kinetic energy either by clustering or by heating especially in combination with seeding.

The problems concerning the presence and operation of the sampling probe, the chemical relaxation in the free jet, the Mach number focusing[5] and the possible distortions in the mass spectrometer are treated by E.L. Knuth in this NREL workshop.

We have not considered the rotational and vibrational relaxation phenomena in the expansion process.The internal state populations in free jets and molecular beams are described in

our Rarefied Gas Dynamics review paper on this subject.[23] Also, results on electronic relaxation in laser plasma free jets have been published recently.[24]

Finally, it is worth mentioning that our nozzle beam technique using a free jet zone of silence has found industrial application with the inductively coupled plasma and mass spectrometer (ICP-MS) as developed by *SCIEX*,[25] Canada, and *FISONS INSTRUMENTS ELEMENTAL*,[26] GB.

References

1 R. Campargue, J. Phys. Chem. **88**, 4466 (1984)
2 J.B. Anderson, in "Molecular Beams and Low Density Gas Dynamics", P.P. Wegener ed. (Dekker, New York, 1974), pp. 1-91
3 J.B. Fenn, Applied Atomic Collision Physics **5**, 349 (1982)
4 D.R. Miller, in "Atomic and Molecular Beam Methods" Vol. 1, G. Scoles ed. (Oxford University Press, 1988), pp. 3-53
5 P.K. Sharma, E.L. Knuth, and W.S. Young, J. Chem. Phys. **64**, 4345 (1976)
6 R. Campargue and A. Lebéhot, in "Rarefied Gas Dynamics", M. Becker and M. Fiebig eds. (DFVLR Press, Porz-Wahn, FRG, 1974), p. C11-1
7 R. Campargue, A. Lebéhot, and J.C. Lemonnier, in "Rarefied Gas Dynamics", L. Potter ed. (AIAA, New York, 1977), Vol. II, p. 1033
8 F.S. Sherman, Phys. Fluids **8**, 773 (1965)
9 R. Campargue, J. Chem. Phys. **52**, 1795 (1970)
10 R. Campargue, J.B. Anderson, J.B. Fenn, B.B. Hamel, E.P. Muntz, and J.R. White, *On Aerodynamic Separation Methods*, in "Nuclear Energy Maturity", P. Zaleski ed. (Pergamon Press, Oxford and New York, 1975), Invited sessions, pp. 5-25
11 V.H. Reis and J.B. Fenn, J. Chem. Phys. **39**, 3240 (1963)
12 R. Campargue and M. Constant, 8th Int. Symp. on Rarefied Gas Dynamics, Stanford, USA, July 1972 (Results published in Ref. 10)
13 P. Davidovits and J.B. Anderson, Bull. Am. Phys. Soc. **20**, 46 (1975)
14 U. Bossel, F.C. Hurlbut, and F.S. Sherman, in "Rarefied Gas Dynamics", L. Trilling and H.Y. Wachman eds. (Academic Press, New York, 1969), Vol 2, p. 945
15 R. Campargue, Plenary Lecture, Discussion Meeting on "Experiments on Clusters", Deutsche Bunsengesellschaft für Physikalische Chemie, Königstein, FRG, 1983
16 J.P. Toennies and K. Winkelmann, J. Chem. Phys. **66**, 3965 (1977)
17 R. Campargue, A. Lebéhot, J.C. Lemonnier, D. Marette, and J. Marx, in "Mass Spectrometry and Chemical Kinetics", V.L. Talrose ed. (Nauka, Moscow, 1985), p. 94 (in Russian)
18 R. Campargue, A. Lebéhot, J.C. Lemonnier, and D. Marette, in "Rarefied Gas Dynamics", S.S. Fisher ed. (AIAA, New York, 1981) Vol. 74, p. 823
19 A. Chesneau and R. Campargue, in "Rarefied Gas Dynamics", O.M. Belotserkovskii, M.N. Kogan, S.S. Kutateladze, and A.K. Rebrov eds. (Plenum, New York and London, 1985) Vol. 2, p. 879
20 A. Lebéhot, S. Drawin, F. Aguillon, R. Campargue, and X. Chapuisat, J. Chem. Phys. **92**, 7340 (1990)
21 J.M. Girard, A. Lebéhot, and R. Campargue, J. Phys. D: Appl. Phys. **26**, 1382 (1993)
22 J.M. Girard, A. Lebéhot, and R. Campargue, J. Phys. D: Appl. Phys. **27**, 253 (1994)
23 R. Campargue, M.A. Gaveau, and A. Lebéhot, in "Rarefied Gas Dynamics", H. Oguchi ed. (University of Tokyo Press, 1984), Vol 2, p. 551 (Invited Review Paper)
24 J.M. Girard, A. Lebéhot, and R. Campargue, 19th Int. Symp. on "Rarefied Gas Dynamics", Oxford, GB, July 1994, to be published
25 D.J. Douglas and J.B. French, J. Anal. At. Spectrom. **3**, 743 (1988)
26 N.M. Reed, R.O. Cairns, R.C. Hutton, and Y. Takaku, J. Anal. At. Spectrom. **9**, 881 (1994)

Electron Impact, Hyperthermal Surface Ionization and Fast GC-MS in Supersonic Molecular Beams

AVIV AMIRAV and SHAI DAGAN
School of Chemistry, Tel-Aviv University, Tel Aviv 69978, Israel, Fax 972-3-6409293

Supersonic Molecular Beams (SMB) are characterized by undirectional motion with controlled hyperthermal kinetic energy (0.1-30 eV), intramolecular vibrational super-cooling, mass focusing as in an ideal high load jet separator, very high flow rate (on the gas chromatography flow rate scale) up to 240 ml/min and sample inlet at atmospheric pressure. These features make SMB an ideal sample introduction method, enable a unique fast GC inlet and result in important implications to molecular ionization processes including electron impact (EI) and hyperthermal surface ionization (HSI). Our research is aimed at exploring and exposing the benefits of SMB for analytical organic mass spectrometry. The experimental apparatus is shown in figure 1 and is described in refs. [1,2]. A 50 cm long megabore capillary column connects the atmospheric pressure open inlet to a supersonic nozzle, and serves as an ultra fast GC short column. In figure 2 we demonstrate ultrafast GC-MS achieved with this 50 cm transfer line capillary. One of the main features of this unique GC is the carrier gas relatively high flow rate of up to 240 ml/min which is possible due to the flow rates involved with the supersonic beam interface. This ultrafast GC is extensively described in reference [1]. Alternatively, a conventional GC with a short (4 meter) column serves as a fast GC inlet with intermediate GC resolution and unlimited choice of column length, ID and flow rate. Electron impact ionization in supersonic molecular beams is achieved using a Brink type open ion source operated with ~ 10-20 mA emission current. A background ion filtration method is applied, (described in figure 3) based on differences in the ion energy emerging from the hyperthermal molecular kinetic energy in the seeded SMB. Background ion filtration is achieved in our VG-SXP-600 quadrupole through biasing of its exit lens and the cancellation of its internal ion energy ramping with mass. About 1-2 eV retarding potential is required for effective filtration. The background ion filtration method, in addition to reduction of chemical noise contributes to a) ultra fast ion source response time as any molecule that scatters from surfaces thermalizes and thus does not interfere in the analysis. b). High emission current is obtained by the use of an open ion source with its filament close to the ion cage, as pyrolysis product and ion source temperature variation do not affect the obtained MS. c) The MS of vibrationally cold molecules is exposed as demonstrated in figure 4. The 70 eV EI-MS of alkanes was studied in SMB [2] and is characterized by a pronounced or dominant molecular

weight peak, together with all the fragment ions normally exhibited by thermal 70 eV EI-MS. In contrast, the NIST library spectra of most of these molecules did not show any molecular peak. The elimination of the intramolecular thermal vibrational energy also allowed the control over the degree of molecular ion fragmentation by the reduction of the electron energy. The GC-MS and fast GC-MS of C_8H_{18}-$C_{40}H_{82}$ alkanes was studied, and in contrast to conventional GC-MS, none of these molecules exhibited peak tailing. We have also studied the hyperthermal surface ionization (HSI) of polycyclic aromatic hydrocarbons, and explored the use of HSI for the selective ionization of aromatic molecules. A controlled selectivity of 10^4 anthracene/decane was achieved. HSI was studied by us from its discovery [3-5] through its mechanism and analytical applications and is briefly reviewed in reference [6]. HSI was found to be a very sensitive ionization method with minimum detected amount of 400 attograms of deuterated anthracene as demonstrated in figure 5. The use of short column high flow fast and ultrafast GC-MS allow the analysis of thermally labile compounds such as underivalized steroids and carbamate pesticides. In figure 6 we show the ultrafast GC-MS of carbamate pesticide combined with reconstructed single ion monitoring through their molecular weight peak. Note that some of these molecules such as aldicarb do not exhibit a molecular weight peak under thermal EI-MS, and in SMB their monitoring through their molecular weight peak improve their detection capability in complex mixtures [7].

References

1. S. Dagan and A. Amirav, "Fast, High Temperature and Thermolabile GC-MS in Supersonic Molecular Beams", Int. J. Mass Spectrom. & Ion. Proc., 133, 187-210 (1994).
2. S. Dagan and A. Amirav, "Electron Impact Mass Spectrometry of Alkanes in Supersonic Molecular Beams", J. Am. Soc. Mass Spectrom. (In press).
3. A. Amirav and A.Danon. "A Method and Apparatus for Producing Ions by Surface Ionization of Energy-Rich Molecules and Atoms". U.S. Patent No. 4845367, July 4, 1989, Israel Patent No. 81375 filed 23.1.87 and Great Britain Patent No. 8801195 filed 3.1.88.
4. A. Danon and A. Amirav. "Kinetic Energy Induced Surface Dissociative Ionization". J. Chem. Phys. 86, 4708-4709 (1987).
5. A. Danon and A. Amirav. "Molecular Ionization and Dissociative Ionization at Hyperthermal Surface Scattering". J. Phys. Chem. 93, 5549-5562 (1989).
6. A. Amirav. "Electron Impact and Hyperthermal Surface Ionization Mass Spectrometry in Supersonic Molecular Beams". Org. Mass. Spectrom. 26, 1-17, 1991.
7. S. Dagan and A. Amirav. "Fast and Ultrafast GC-MS of Thermally Labile Compounds in Supersonic Molecular Beams". In preparation.

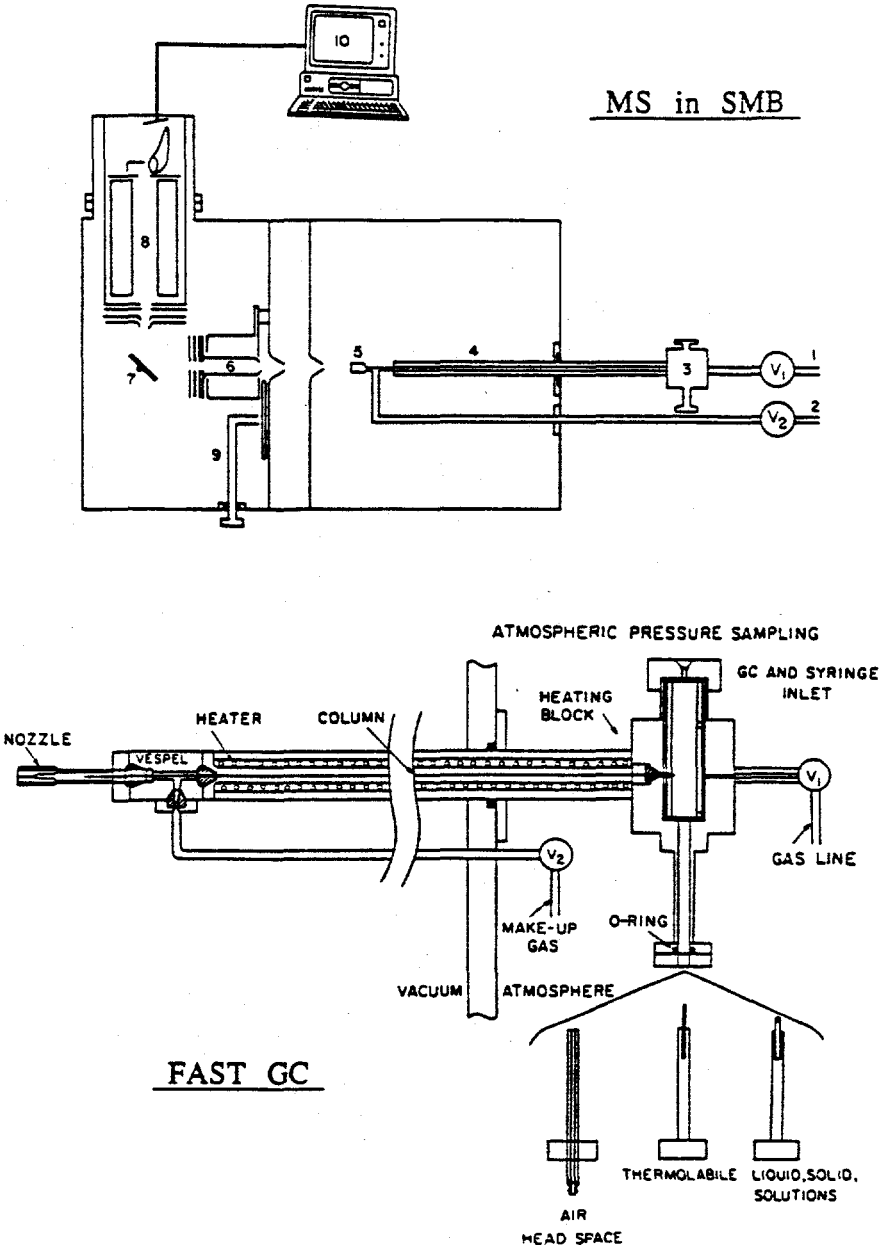

Fig.1. The Supersonic Molecular Beam - Mass Spectrometry Apparatus

The material is fed to the vaporizing inlet (3) in a conventional MS test tube or via an air sniffing device or from a syringe or from a conventional GC. The hydrogen or helium (V_1) mixed with the material is transferred through the capillary column (4) which serves as a transfer line or as a fast GC and expands through the supersonic nozzle (5) into a vacuum chamber. The carrier gas linear velocity is controlled by the make up gas valve V_2. The SMB is collimated and ionized by the fly through EI ion source (6). The ions are 90° deflected by the ion deflector (7) and mass analyzed by the QMS (8). The SMB can also be square wave modulated (9) for an additional lock in amplification signal processing. Alternatively a suitable surface is lowered to replace the ion deflector 7 for the hyperthermal surface ionization of the organic molecules in the SMB.

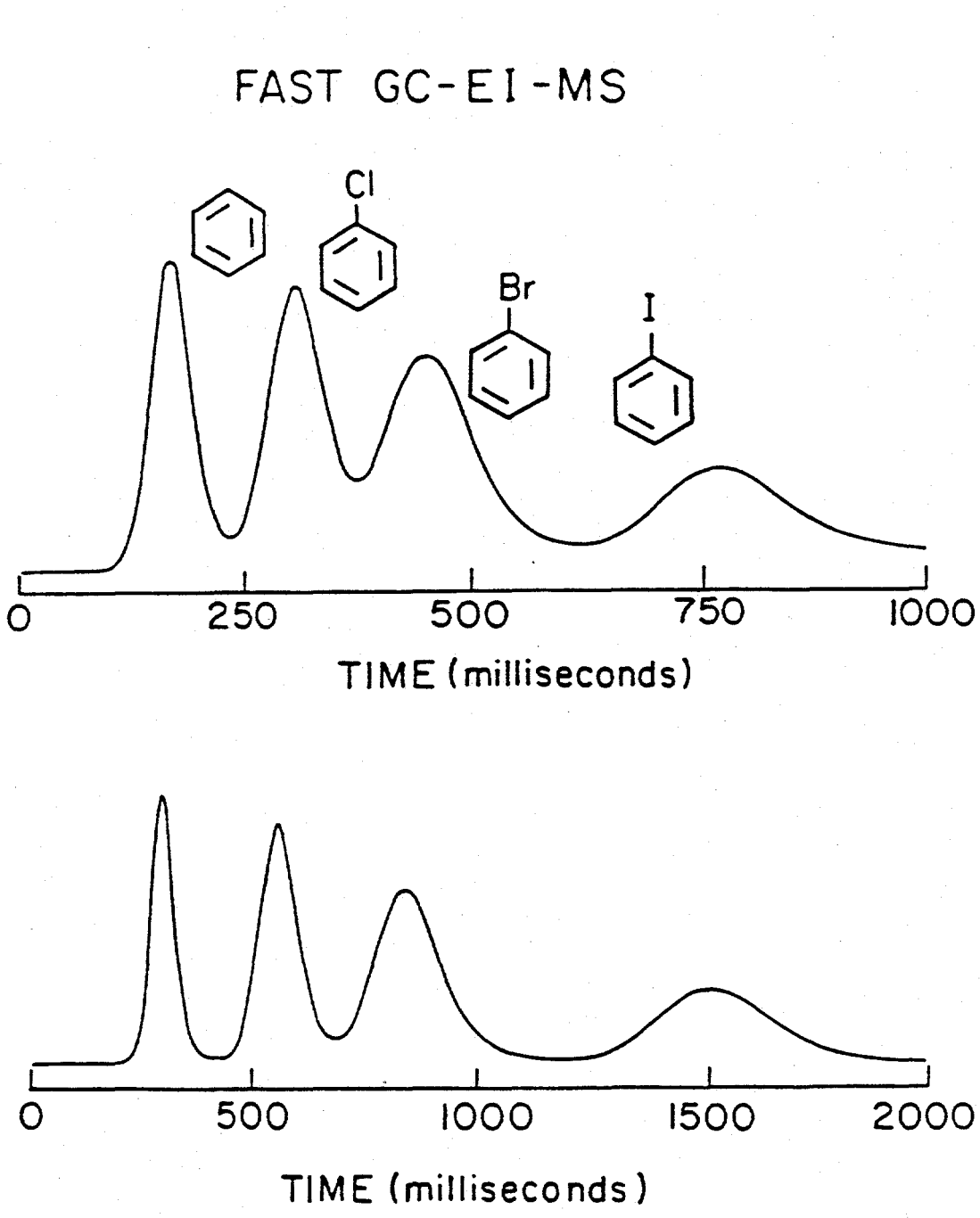

Fig. 2. The Ultra Fast GC-MS

A complete GC-MS is achieved in one second! At two seconds the resolution is improved. Methanol solution of benzene, chlorobenzene, bromobenzene and iodobenzene is used at 40°C with a 0.50 meter megabore column. A rapid consecutive injection is achieved due to the septum-free conventional injection. The high short column flow and ultra-fast MS response facilitate this fast GC-MS. Single ion monitoring was used at 77 amu.

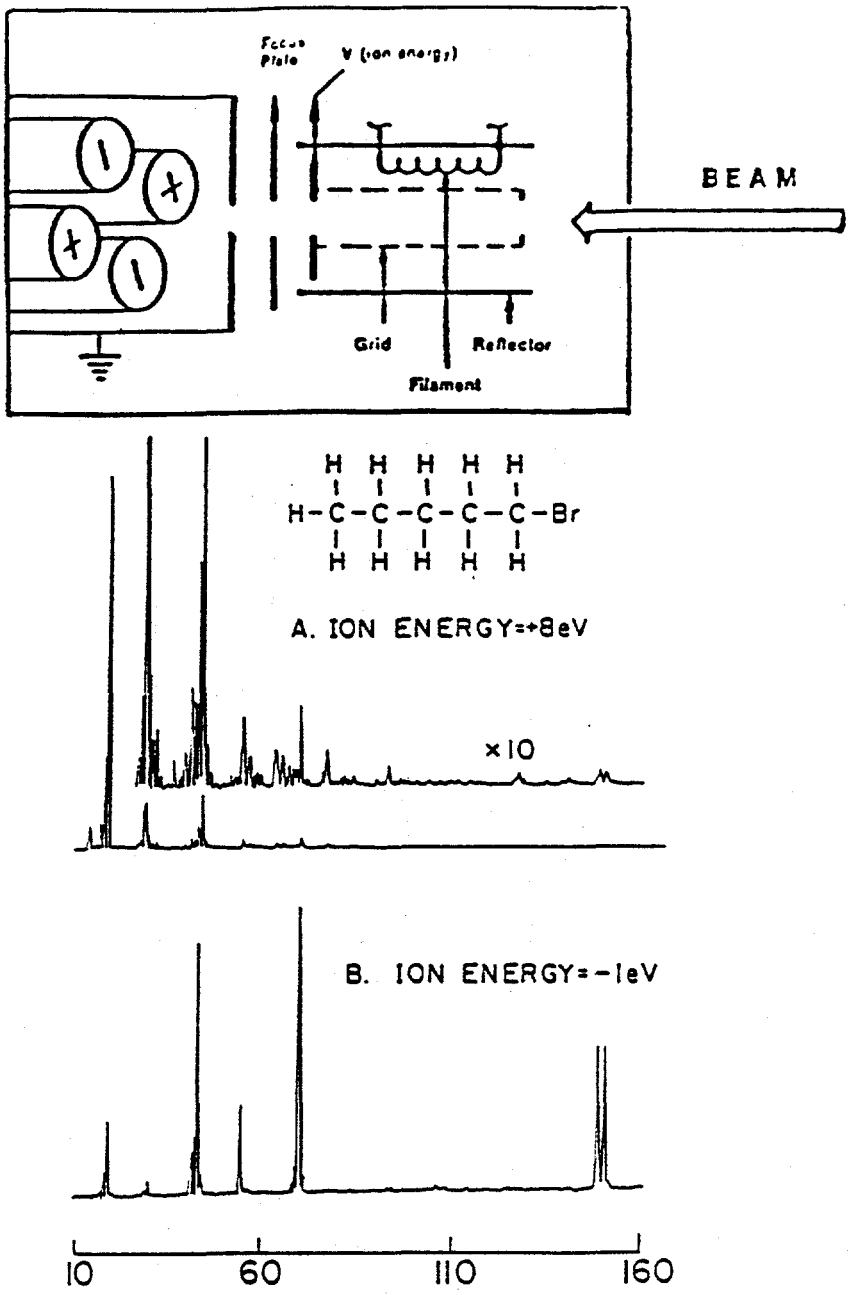

Fig. 3. Background Filtration in Electron Impact Mass Spectrometry

The upper schematic diagram describes the ion source and the SMB which enters axially to it. If the ion source grid is biased slightly negatively with respect to the ground, ions formed from the thermal background molecules are repelled from the mass analyzer and reneutralized. Hyperthermal beam species easily overcome this low retarding potential and are mass analyzed. The lower mass spectrum demonstrates this effect in the mass spectrum of 1-bromopentane.

Vacuum background ion filtration provides lower noise, ultrafast response time, tail free GC-MS traces, reveals the MS of cold molecules, allows the increase of emission current and eliminate memory effects.

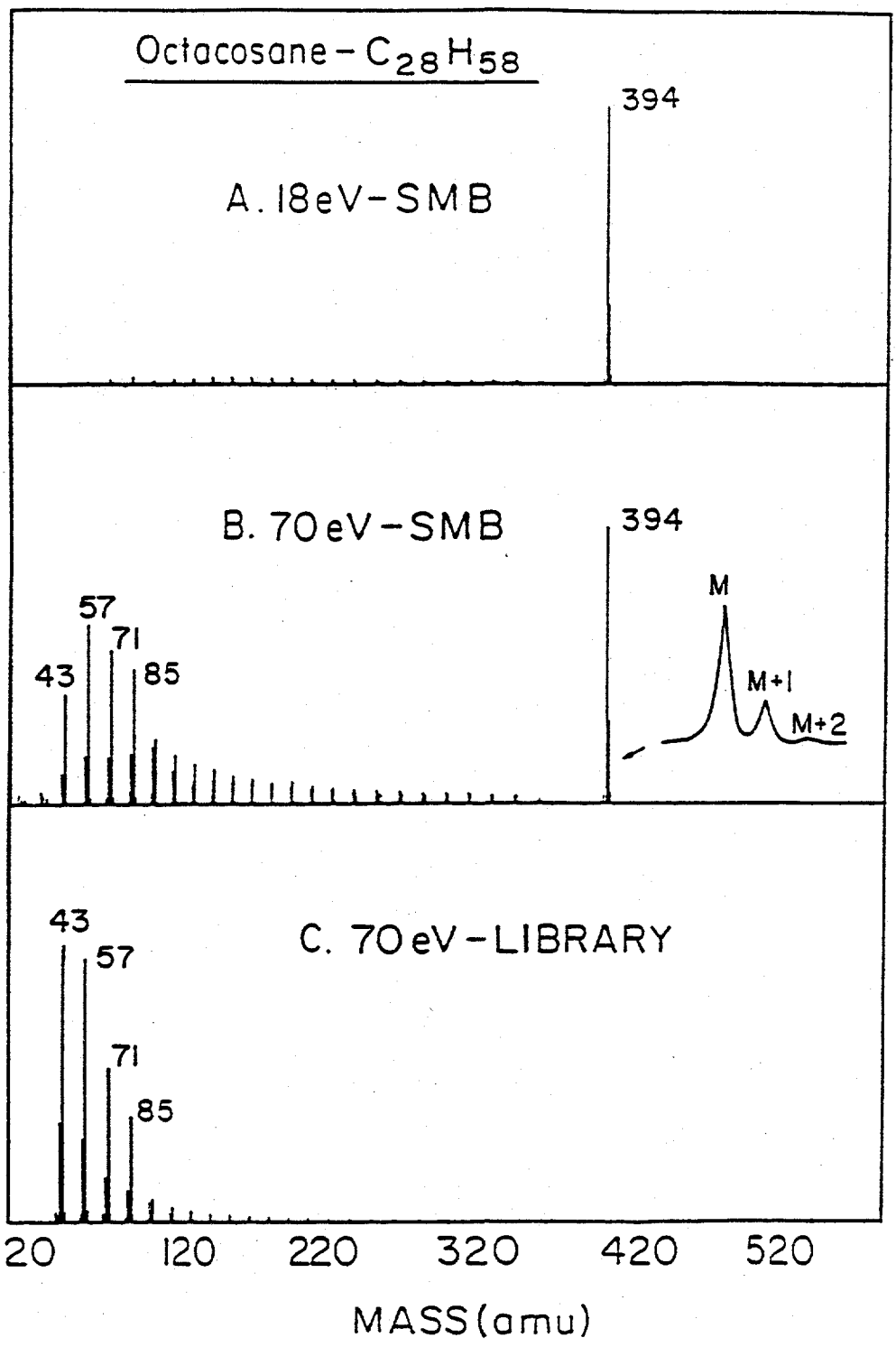

Fig.4. EI-MS in SMB of Octacosane - The Large Enhancement of M^+

EI-MS in SMB of octacosane ($C_{28}H_{56}$) is presented achieved at 18 eV electron energy (upper), 70 eV electron energy (middle) and the standard library (NIST) shown for comparison (lower). Note the over 10^3 enhanced M^+ combined with similar fragmentation pattern to that of the library. At 18 eV, the MS is dominated by M^+ with a marginal reduced M^+ peak height by a factor of 1.2 only.

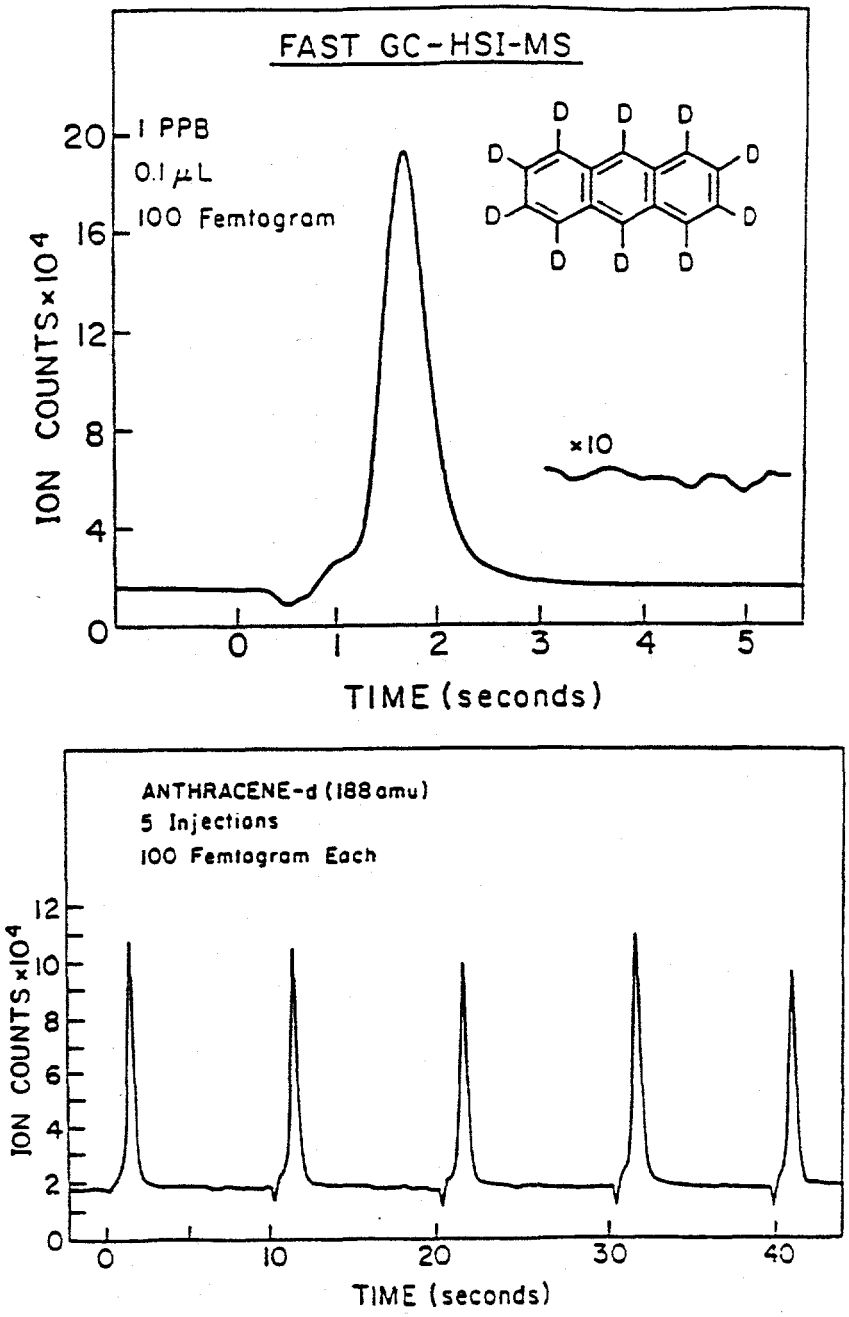

Fig. 5. The Very Fast GC-MS is also Ultra Sensitive - Attogram Range MDL

Subpicogram amounts at sub PPB concentration can be quantitatively integrated in a few seconds GC-MS with selected ion monitoring (SIM). The HSI-GC-MS of deuterated anthracene is demonstrated. 100 femtogram deuterated anthracene is detected with SIM at 188 amu (80 femtogram anthracene-D_{10}). The demonstrated signal to two RMS noise level is 220 (upper trace) and the linear extrapolated minimum detected amount is 400 attogram. The same amount can be quantitatively detected (lower trace) with less than two seconds elution time and manual injection rate of one per 10 seconds.

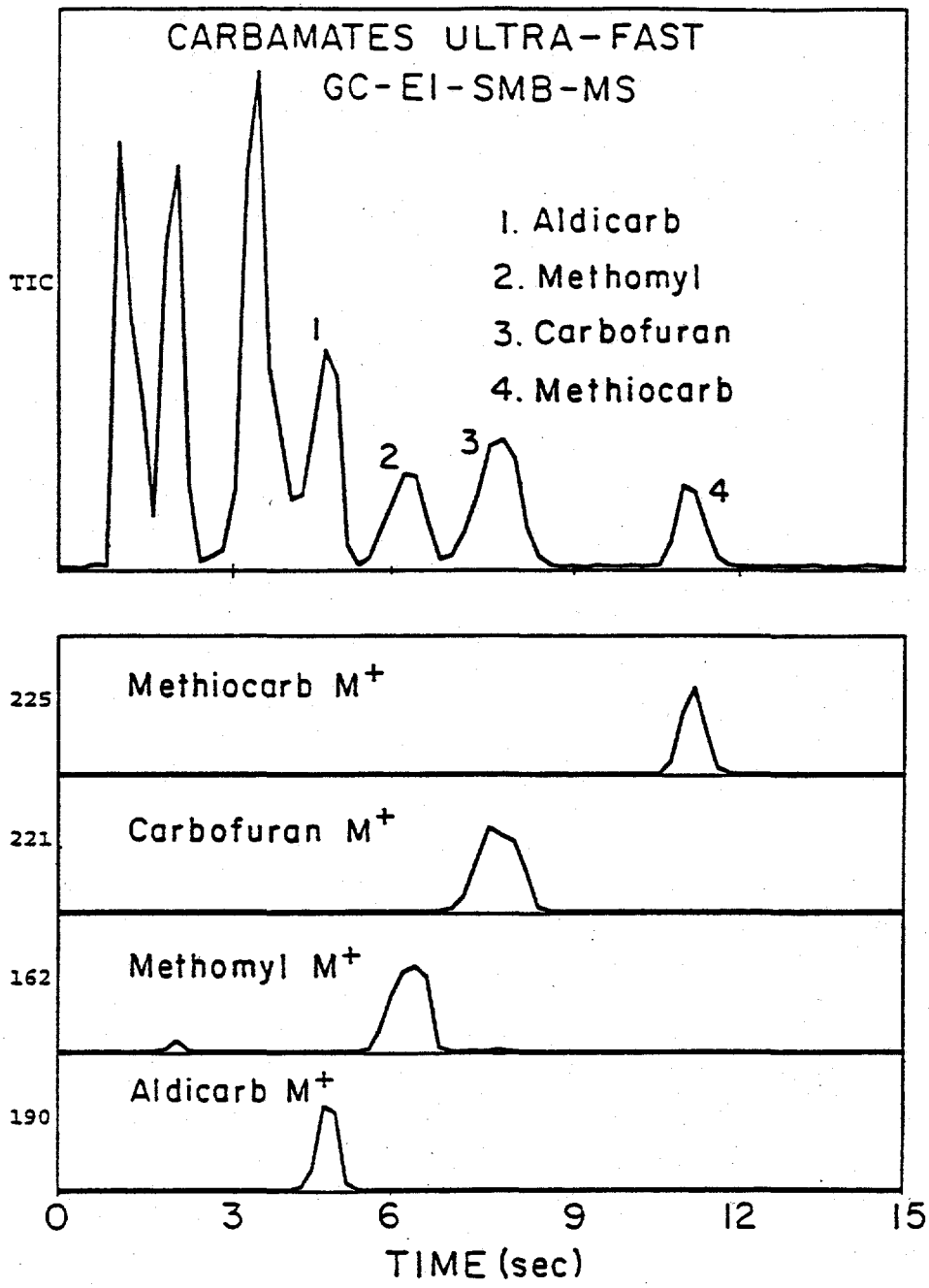

Fig. 6. Ultra-Fast GC-MS of Thermally Labile Carbamate Pesticides

The very fast injection, very short column, high carrier gas linear velocity and lack of ion source related molecular dissociation facilitate the GC-MS of thermally labile compounds and enhance the range of molecules amenable for GC-MS analysis. Methanol solution of aldicarb, methomyl, carbofuran, methiocarb and some of their solution dissociation products was injected at 170°C injector temperature and 130°C column temperature (50 ng each). The reconstructed SIM at the molecular weight demonstrate clean quantification of these compounds. Note that M^+ is exhibited for all these compounds.

MBMS and Gas Phase Chromatography Studies of n-heptane and iso-octane flames

Christian Vovelle, Christine Douté and Jean-Louis Delfau
Laboratoire de Combustion et Systemes Reactifs
1C Avenue de la Recherche Scientifique
45071 Orléans Cedex 2 - France.

Introduction

For many years, we measure the evolution of species concentration in premixed flames stabilized on a flat flame burner. Species identification and analyses are performed by using the Molecular Beam-Mass Spectrometric (MBMS) technique. The first studies carried out with this device were related to small fuel molecules : methane and acetylene [1, 2]. More recently, we started new experiments with more realistic fuel : decane and kerosene [3, 4]. Presently, these works are extended to n-heptane and isooctane flames. A large number of intermediate are formed in these flames, and the use of a mass spectrometer for the analysis of heavy hydrocarbon is frequently criticized because fragmentations of these species are likely to occur in the ionization source of the mass spectrometer. To check to which extent fragmentations can affect the accuracy of species concentration measurements we used both the MBMS technique and Gas Phase Chromatography (GPC) to derive mole fraction profiles in a premixed n-heptane-oxygen-argon flame stabilized under low pressure. Some preliminary measurements have been performed as well in the burned gases of isooctane-oxygen-argon flames and will be considered for the same purpose.

Experimental

Flames were stabilized on a flat flame burner (diameter 9 cm) enclosed in a low pressure chamber. The burner can be moved vertically and the flat flame was sampled along the symmetry axis with a quartz cone for mass spectrometry measurements and with a quartz microprobe for GPC. Volumetric flow rates were adjusted as follows : n-heptane : 7.3 cm3/s ; O_2 : 53.5 cm3/s Ar : 54.0 cm3/s. The corresponding equivalence ratio was 1.5 with 47% dilution. The total pressure was equal to 6 kPa. Mass discrimination effects in the molecular beam were taken into account with a procedure presented in a second paper [5]. These effects depends on the local temperature and the temperature profile was measured with a fine (wire diameter 0.08 mm) Pt-Pt 10% Rh thermocouple.

Figure 1 illustrates the three stage MBMS apparatus. The sampling cone had a 60° angle and a 0.1 mm diameter hole at the tip. Sudden expansion accross the orifice created a supersonic jet that preserves atoms and radicals. After selection of its central part by a skimmer and modulation by a chopper wheel, the jet entered the ionization source of the mass spectrometer. The skimmer was made of stainless steel. Its angle was equal to 45°C and the diameter of its tip orifice was 0.8 mm.. The skimmer was located 2 cm downstream from the tip of the sampling cone. A small tube (1.2 cm length, 0.3 cm diameter) was used to prevent the residual gas contained in the second stage to flow into the third stage. A liquid nitrogen trap located in the vincinity of the ionization source of the mass spectrometer contributed also to reduce the concentration of the residual gas. Each stage was evacuated with an oil diffusion pump. Flowrates were respectively 1500 l/s (first stage), 750 l/s (second stage) and 250 l/s (third stage).

GPC analyses were performed with samples withdrawn with a quartz microprobe (tube diameter : 0.3 cm) and collected in storage bottles. The pressure in the probe and the bottle was maintained at values lower than 0.8 kPa during sampling. Permanent gases (O_2+Ar, CO) were separated on a

Tamis 5A column with helium as carrier gas. H_2 was analyzed with the same column and nitrogen as carrier gas. A Poraplot column was used for the analysis of CO_2 and H_2O. All these species were detected with a TCD. Hydrocarbons were separated on an Al_2O_3/KCl column and detected with FID.

Results

Mixtures of known composition were analyzed to calibrate the Gas Chromatographs Three procedures were adopted to calibrate the mass spectrometer. (i) Analyses of mixtures of known composition were performed for the major species of the flame (C_7H_{16}, H_2, CH_4, CO, O_2, Ar, CO_2). (ii) Computation of the mole fraction of H, O, OH and H_2O in the post flame region by assuming partial equilibrium. (iii) Computation of ionization cross sections for minor molecular species and hydrocarbon radicals. Since the objective in this work was to compare GPC and MBMS results, only molecular species will be considered.

Figure 2 shows that both analytical techniques give very close results for the final concentration reached by the main products (H_2O, CO_2 and CO) in the post flame zone: A difference is observed for H_2 with the mole fraction measured by GPC (0.156) higher than the value obtained with MBMS (0.117). Computation of H atom balance indicates that the latter verifies more closely atom conservation. Examination of the results obtained in the burned gases of isooctane flames with equivalence ratios ranging between 0.7 and 2.0 confirms that both techniques lead to very close values for the major products (Table I).

	H_2O		CO_2		CO		H_2	
Eq. Ratio	GPC	MBMS	GPC	MBMS	GPC	MBMS	GPC	MBMS
0.7	0.212	0.208	0.182	0.186	0.000	0.003	0.049	$5\ 10^{-4}$
1.0	0.246	0.264	0.213	0.227	0.024	0.028	0.063	0.011
1.5	0.248	0.230	0.109	0.071	0.198	0.199	0.138	0.111
2.0	0.126	0.181	0.038	0.054	0.293	0.294	0.209	0.208

Table I

Comparison of the mole fraction measured by GPC and MBMS in the post flame zone of isooctane-O_2-Ar flames (P = 6 kPa).

It is apparent on Fig. 2 that sampling with the quartz cone moved the flame downstream while no displacement was noticeable with the microprobe. This shift appears more clearly when the mole fraction profile of an intermediate species such as ethylene is considered. (Fig. 3). A change in the temperature profile is likely to be associated with this shift. It was not taken into account in the discussion that follows.

High temperature combustion of heavy fuel molecules proceeds through β-scission of alkyl radicals with formation of a smaller alkyl radical and an olefin. GPC does not allow the analysis of radicals, but it is worth comparing the mole fractions measured for olefins by GPC and MBMS. Profiles measured for 1-butene have been plotted on Fig. 4. The maximum concentration measured by MBMS is slightly lower than the corresponding value obtained by GPC. The same result is observed with 1-pentene. Since MBMS measurements were performed at the parent pic, this underestimation can be due to fragmentations in the ionization source. It can be related also to the accuracy of the measurements, and the calibration procedure should be considered to check how significant are the differences observed between GPC and MBMS results.

As described by Mahnen [6], calibration factors for minor stable species and radicals are computed by reference to a species calibrated by direct analyses :

$$F_{c,i} = F_{c,ref} \cdot \frac{Q_{i,E_i}}{Q_{ref,E_{ref}}}$$

with $F_{c,i}$: calibration factor of species i ; $F_{c,ref}$: calibration factor of the reference ; Q_{i,E_i} : ionization cross section at the electron energy used to analyse the species i ; $Q_{ref,E_{ref}}$: ionization cross section at the electron energy used to analyze the reference.

The ionization cross sections are either the values measured by Rapp and Englander-Golden [7], or derived from the values computed at 70 eV with the additivity law proposed by Beran and Kevan [8] :

$$\frac{Q_{i,E_i}}{Q_{ref,E_{ref}}} = \frac{Q_{i,70}}{Q_{ref,70}} \cdot \frac{(E_i - PI_i)}{(E_{ref} - PI_{ref})}$$

with PI_i and PI_{ref} : ionization potentials of species i and reference.

For hydrocarbon radicals and intermediate olefins the difference $E_i - PI_i$ must be kept small to avoid a contribution to the signal from fragmentation of larger species. Table II compare the values of the electron energies and ionization potentials for the minor stable species :

	C_3H_4	C_3H_6	C_4H_6	C_4H_8	C_5H_{10}
E_i	11.4	10.4	11.4	9.8	9.6
PI	10.5	9.7	9.1	9.3	9.15

Table II

For each species analyzed with the mass spectrometer, the ionization potential was determined experimentally at the position in the flame corresponding to the maximum signal and by decreasing progressively the electron energy. Figures 6 and 7 illustrate the results obtained respectively with a minor stable species (C_4H_6) and a radical (C_4H_7). The dispersion of energies in the ionization source of the mass spectrometer produces a curvature of the signal at low energies, and this effect limit the accuracy of the determination of the ionization potential. A change in the ionization potentials from 9.3 to 9.43 eV for 1-butene and from 9.15 to 9.35 eV for 1-pentene, would lead to MBMS maximum mole fractions equal to the values obtained by GPC.

Figure 8 represents the evolution with the molar mass of the ratio of the mole fractions measured respectively by MBMS and GPC. The choice of the molar mass for the abscissa was aimed at studying the influence exerted by fragmentations that occurs more easily when the size and hence the molar mass of the species increases. No systematic variation in the ratio X_{MBMS}/X_{GPC} is observed when the molar mass increases.

The influence of temperature on fragmentations is frequently objected to heavy species analyses in flames by MBMS. In this work, mass spectrometric analyses of n-heptane were carried out at mass 100 (parent pic) with an electron energy (19.4 eV) that produces important fragmentations. Fig. 5 shows that MBMS and GPC led to very similar profiles from the burner exit (low T) up to the point were complete consumption occur (high T). At least for n-heptane, this result point out that the influence of temperature on fragmentations does not affect the accuracy of concentration measurements.

Conclusions

This work was aimed at checking the accuracy of species concentration measurements by MBMS in flames burning heavy fuel molecules. The main source of error is related to fragmentations, either of the species analyzed with a decrease in the parent pic contribution, or of heavier species with production of additional ions in the spectrometer source. The close agreement observed between MBMS and GPC concentration measurements in a n-heptane-O_2-Ar flame shows that when care is taken in the choice of electron energies, fragmentations can be avoided. However, the need to use very small excess energy above the ionization potential reduces the accuracy of MBMS measurements.

References

1. ROZKRES, V.J.M., BURGESS, A.R., VOVELLE, C. and DELFAU, J.L., *The Structure of Sooting Methane Flames*. I. Chem. E. Symposium Series N°94, pp. 84-4.92, (1985).
2. BASTIN, E., DELFAU, J.L., REUILLON, M. and VOVELLE, C., *Experimental and Computational Investigation of the Structure of a Sooting C_2H_2-O_2-Ar Flame* . Twenty-Second Symposium (International) on Combustion, The Combustion Institute, Pittsburgh, pp. 313-322, (1988).
3. DELFAU, J.L., AKRICH, R., BOUHRIA, M., REUILLON, M., SANOGO, O. and VOVELLE, C., *Experimental and Computational Investigation of the Structure of a Decane-O2-Ar Flame* . Twenty-Third Symposium (International) on Combustion, The Combustion Institute, Pittsburgh, pp. 1567, (1990).
4. VOVELLE, C., DELFAU, J.L., REUILLON, M, AKRICH, R., BOUHRIA, M., and SANOGO, O.,. *Comparison of Aromatics Formation in Decane and Kerocene Flames*, Fuel Chemistry Division, ACS, New York City, Vol. 36, N°4, pp. 1456-1463, (1991).
5. VOVELLE, C., DOUTE, C. and DELFAU, J.L., *Mass Discrimination Effects in MBMS Study of Rich Premixed Flames*, Specialists Workshop on Applications of Free-Jet. Molecular Beam Mass Spectrometric Sampling, Estes Park, (1994).
6. MAHNEN, G., *Contribution à l'Etude des Mécanismes des Déflagrations. Flammes Ethylène-Oxygène*. Thèse, Université Catholique de Louvain, Belgique, (1973).
7. RAPP, D. and ENGLANDER-GOLDEN, P., *Total Cross Sections for Ionization and Attachment in Gases by Electron Impact. I. Positive Ionization*, J. of Chem. Phys., Vol. 43, N°5, pp. 1464-1479, (1965).
8. BERAN, J.A., and KEVAN, L., J. *Molecular Electron Cross Section at 70 eV*, J. Phys. Chem., 73, p. 3866, (1969).

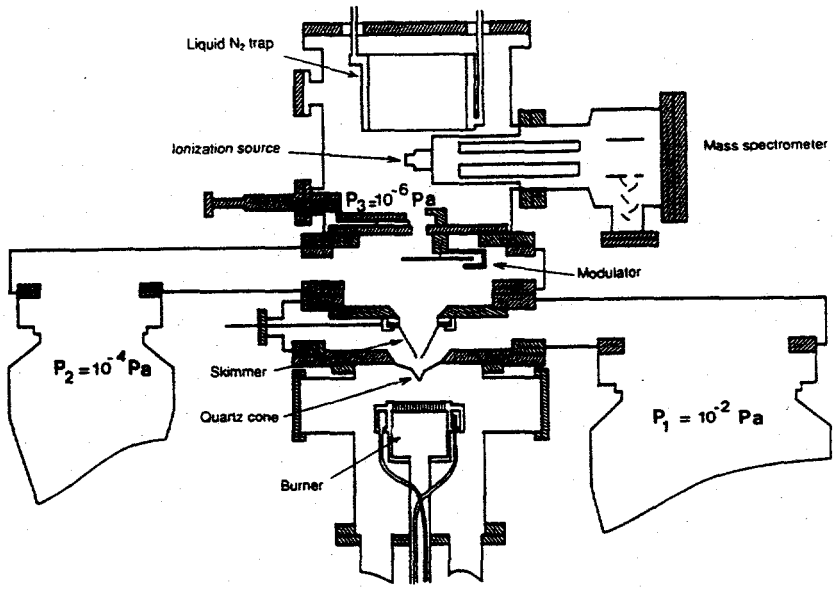

Figure I
Molecular Beam-Mass Spectrometer Apparatus

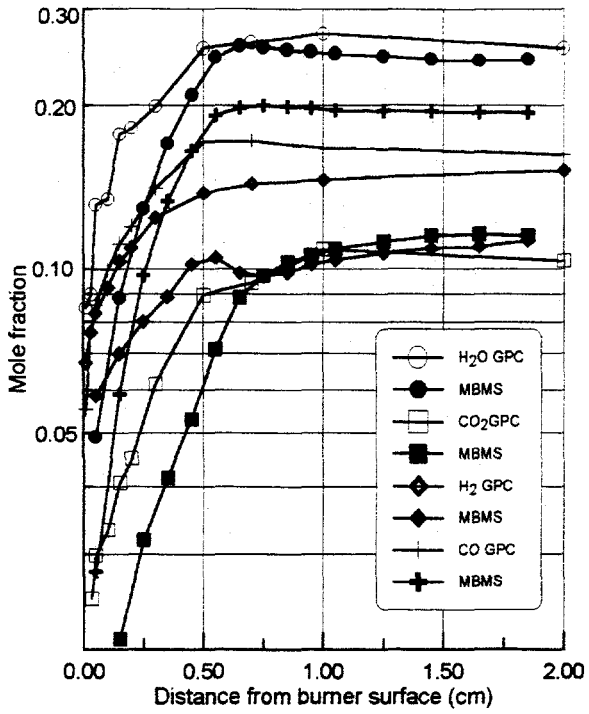

Figure 2
Comparison of mole fraction profiles
measured by GPC and MBMS
n-heptane O_2-Ar flame

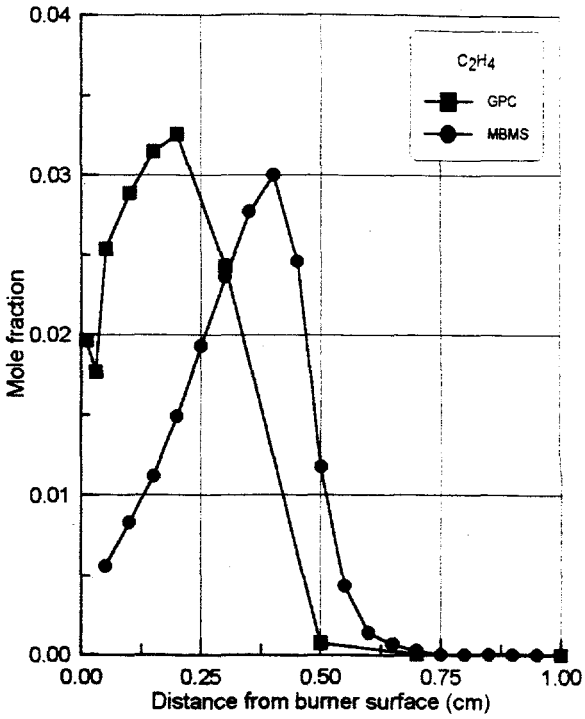

Figure 3
Comparison of mole fraction profiles
measured by GPC and MBMS
n-heptane O_2-Ar flame

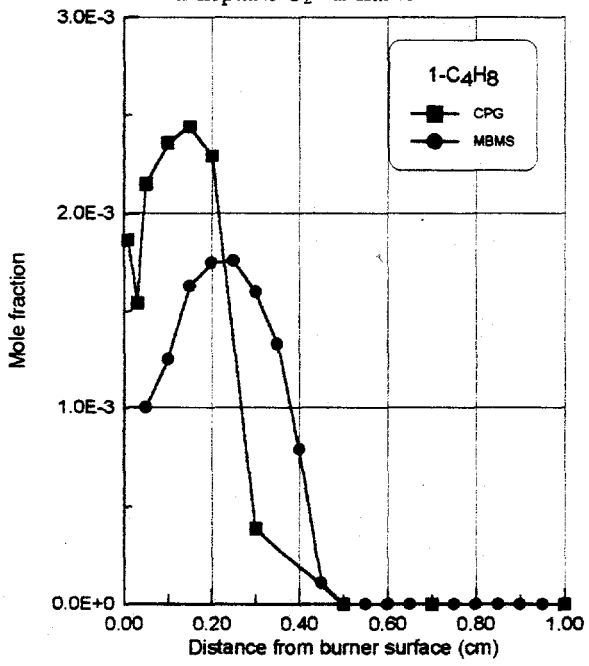

Figure 4
Comparison of mole fraction profiles
measured by GPC and MBMS
n-heptane O_2-Ar flame

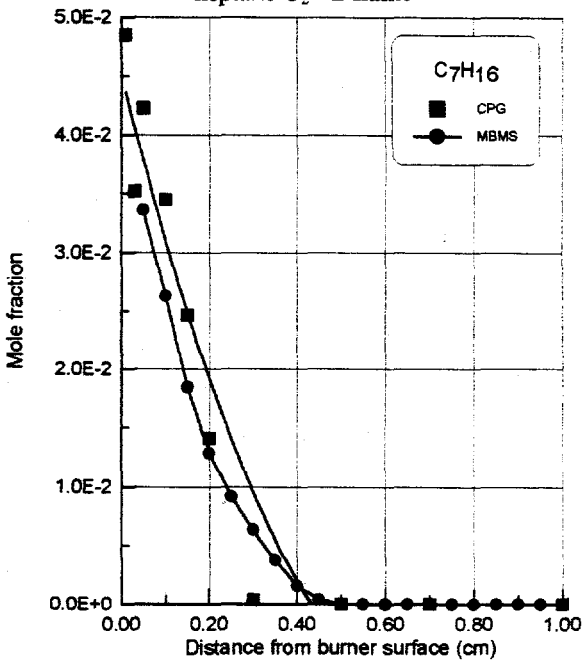

Figure 5
Comparison of mole fraction profiles
measured by GPC and MBMS
n-heptane O_2-Ar flame

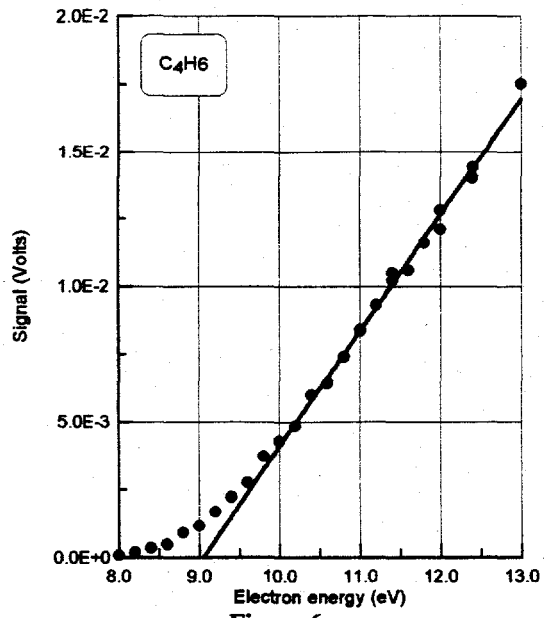

Figure 6
determination of the ionization potential
of a molecular species

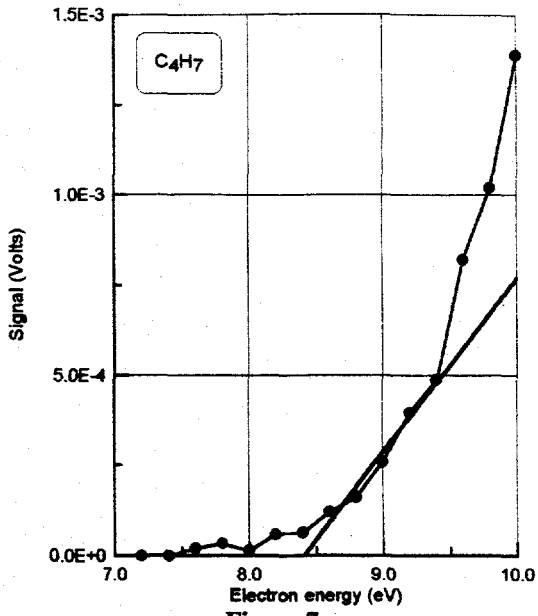

Figure 7
Determination of the ionization potential
of an alkyl radical

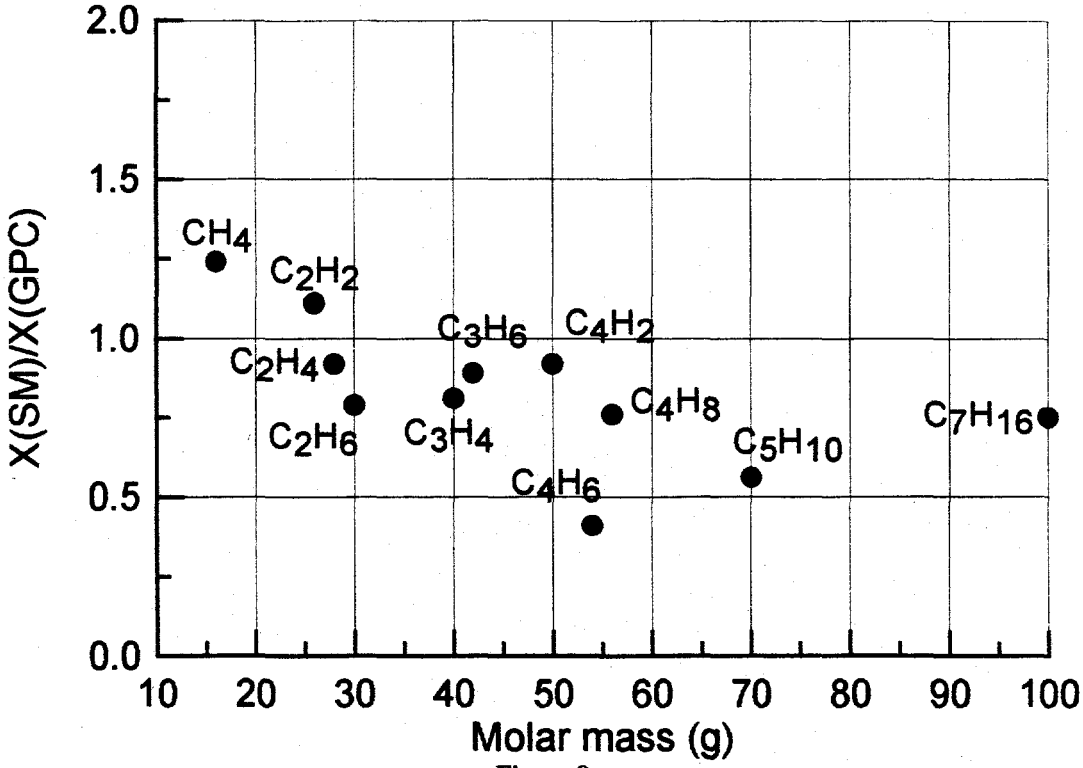

Figure 8
Evolution of the ratio of mole fractions
measures by MBMS and GPC
n-heptane-O_2-Ar flame

Comparison of On-Line MS Techniques for Complex Reactive Systems

Henk L.C. Meuzelaar
Center for Micro Analysis & Reaction Chemistry
University of Utah, 214 EMRL
Salt Lake City, UT 84112

ABSTRACT

Using mass spectrometry as an on-line analytical method for studying the mechanisms and kinetics of reaction processes requires detailed awareness of various reaction interaction transport zonesbetween the point of reaction and the point of ionization. The following zones (regimes, regions) can be more or less clearly recognized in most on-line MS studies of reactions in complex solids: (1) intramolecular; (2) intermolecular; (3) intraparticle; (4) interparticle (bed); (5) reactor (headspace); (6) pressure re-duction; and (7) ionization. In an ideal on-line system all products, intermediates and precursors of interest should reach the ionization region without selective losses, chemical degradation or unwanted background contributions. In practice, various secondary reactions occur well past zone 2, often resulting in chemical degradation of target analytes. Furthermore, marked losses of low volatile and/or highly polar compounds are likely to occur between reaction and ionization regions unless potential cold spots and/or active surfaces are carefully eliminated. Finally, unwanted background contributions from resi-dues of previous runs and/or ubiquitous contaminants may originate anywhere between zones 5 and 7.

EXPERIMENTAL CONFIGURATIONS

Figure 1 provides a schematic overview of some of the most frequently reported experimental configurations for interfacing reaction and ionization zones. The configurations shown are completely generic in that no attempt is made to define the process, the specific reaction conditions (other than pressure) the actual geometry of reactor and ion source, the method of ionization or the type of mass spectrometer. In configurations I-III the reaction zone is under vacuum whereas in IV and V reactions are performed at near-ambient pressures and in VI at high pressures. Configurations not shown here include Knudsen cell (more or less intermediate between II and III), pulsed supersonic beam [1] molecular beam (MB) with subsequent re-thermalization [2], short column GC/MB [3] or use of atmospheric pressure ionization in combination with ion beam expansion [4]. Examples of integral zones (I) can be found in pyrolysis field desorption MS (Py-FDMS) [5], laser pyrolysis/photolysis/desorption/ionization MS (e.g., LAMMA) [6], thermal ionization particle MS [7] and, to some extent, in-source pyrolysis chemical ionization MS [8]. In spite of its obvious advantages, configuration I suffers from inability to optimize reaction and ionization process conditions independently.

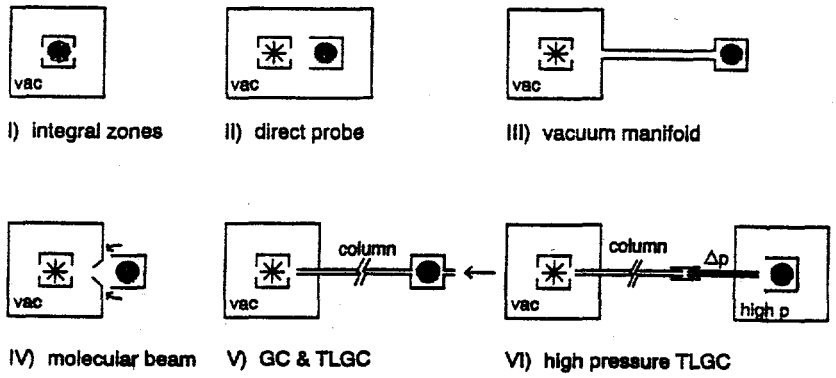

Figure 1. Six on-line MS configurations for complex reactive systems. *=ionization zone; ●=reaction zone.

In configuration II separation between the two zones is minimal. Typical examples of configurations include various dedicated pyrolysis MS designs, e.g., for Curie-point pyrolysis MS [9] or vacuum TG/MS [10] as well as standard MS systems with a special direct probe type pyrolysis accessory, e.g., pyrolysis field ionization MS [11], vacuum Pyroprobe devices [12], direct probe CI MS [8] and EIMS [13], as well as laser pyrolysis probes [14]. By closing off the exit of the direct probe crucible with a pinhole diaphragm or plug, even Knudsen cell conditions may be approximated. Configuration III includes a few specially designed pyrolysis MS systems, e.g., Curie-point pyrolysis MS with expansion chamber [9] but is usually the result of adapting an existing gas inlet manifold for on-line reaction studies [15].

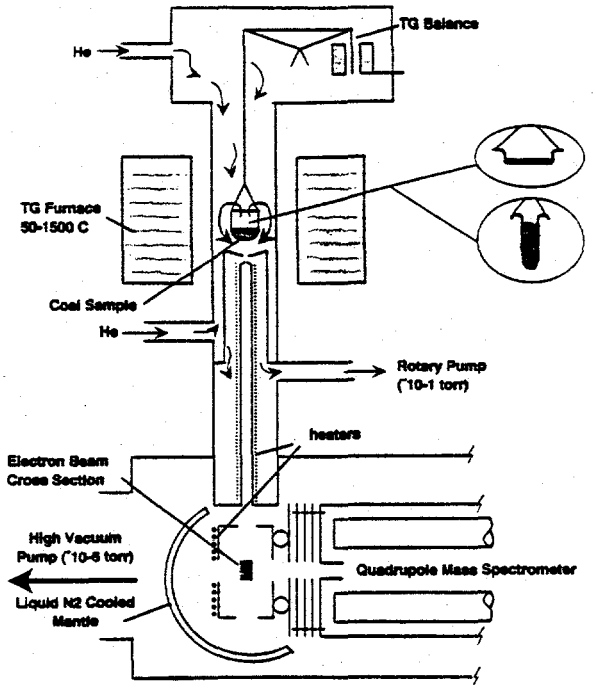

Figure 2. Home-built type IV TG/MS system (used to obtain data shown in Figures 3, 8 and 9). Note nozzle + skimmer combination and variations in crucible shapes/bed depths.

Molecular beam type inlets, schematically represented by configuration IV, are the main topic of this meeting and need not be discussed here in detail. Among the special MB versions mentioned in the previous paragraphs, our research group has chosen the rethermalized molecular beam (RMB) type inlet first proposed by Emminger, et al. [2] as a thermogravimetry/mass spectrometry (TG/MS) interface. Although this type of inlet is commercially available [16] we built our own version, shown in Figure 2 which uses a special reactor flow geometry designed to minimize wall contact. As a result, this is our only TG reactor (we also operate configuration V and VI TG/GC/MS systems) which shows no visible signs of tar deposition after running more than 100 coal and polymer samples over a period of 6 months or so. Apparently, all of the evolved tar exits the reactor through the funnel shaped quartz nozzle with 80-100 μm dia. opening.

Because of the overall similarity between the nozzle + skimmer geometry shown in Figure 2 and the well known jet separator (used in traditional GC/MS interfaces), use of low MW carrier gas such as H_2 or He should primarily result in the loss of carrier gas molecules or atoms. Once past the skimmer, the heated inner quartz tube enhances sensitivity while reducing loss of small molecules due to nonisokinetic effects. On the other hand, this negates one of the major potential advantages of molecular beam systems: reduced EI fragmentation and enhanced molecular, or quasimolecular, ion intensities. Also, the heated quartz tube may cause the loss of low volatile and/or highly polar compounds. In practice however, the results are highly encouraging as illustrated in Figure 3 comparing Py-FIMS and TG-LVEIMS (low voltage electron ionization MS) patterns of a Pittsburgh #8 (hvAb) coal sample. Most noteworthy is the close similarity between the two sum spectra which were obtained under widely different experimental conditions with regard to sample size, heating rate, pressure and interface configuration (type II vs. type IV) as well as MS techniques (ionization, dispersion and detection conditions). Here we should especially note the fact that two entirely different interface configurations (II and IV) are capable of producing very similar results for a highly complex, polar and reactive mixture of coal pyrolysis products.

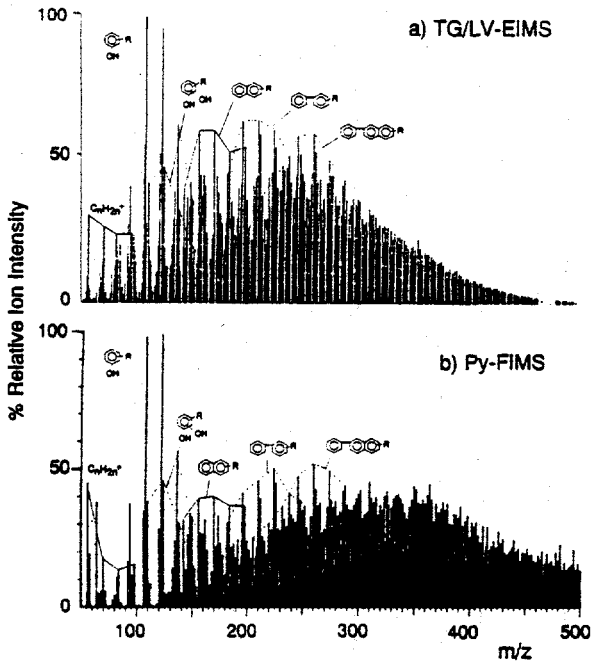

Figure 3. Comparison of TG/LV-EIMS and Py-FIMS profiles (summed spectra) of a Pittsburgh #8 coal obtained under near-ambient pressure and high vacuum conditions, respectively. Note highly similar homologous ion series up to m/z 300 in spite of widely different experimental conditions.

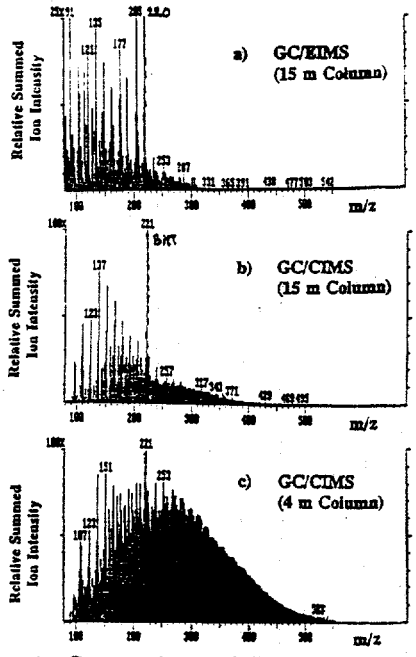

Figure 4. Comparison of Curie-point desorption GC/MS profiles (summed spectra over all GC peaks) of a coal liquid distillate fraction showing effect of column length and ionization methods (70 eV EI vs. isobutane CI).

This stands in sharp contrast to the effects of interface configurations possessing inherently lower molecular conductances, e.g., types V and VI, involving capillary transfer lines and/or GC columns. The dramatic effect of reducing column length (while increasing linear flow velocities) on the probability of larger molecules to elute and be detected is demonstrated in Figure 4. The profiles in Figure 4 represent the sum spectra for an entire GC/MS run using a Finnigan MAT ion trap. Since this prevents the use of LVEI, and thus the ability to reduce fragmentation of molecular ions, profiles b and c were obtained using isobutane CI. Although the coal products analyzed were obtained by a different process [17] and thus have a different composition than the pyrolyzate shown in Figure 3, short GC columns are obviously capable of eluting large, low volatile compounds, a conclusion also reached by Dagan et al. [3]. Examples of the type of data obtainable with the two-stage capillary interface used in configuration VI are shown in Figures 5 and 6. Since reactors processing complex materials at an industrial scale often operate at higher pressures (e.g., up to 3,000 psi) it is important to design on-line MS interfaces. The intermediate chamber serves as an ambient (or near ambient) pressure platform, can be used to dilute highly concentrated process streams, and provides a means of volatilizing liquid streams, as well as of separating out nonvolatile residues. Applications for studying thermal and catalytic hydroprocessing (H_2 atmosphere reactions on coals and polymers have been described elsewhere [10]. On-line monitoring of high pressure liquid environments is demonstrated in Figures 5 and 6, showing the ability to obtain fast repetitive chromatograms of polar building blocks of lignocellulosic materials (birch wood) and to investigate the effects of catalysts (Figure 6). This mode of analysis is capable of producing positive identification of reaction products and kinetic information from a single run.

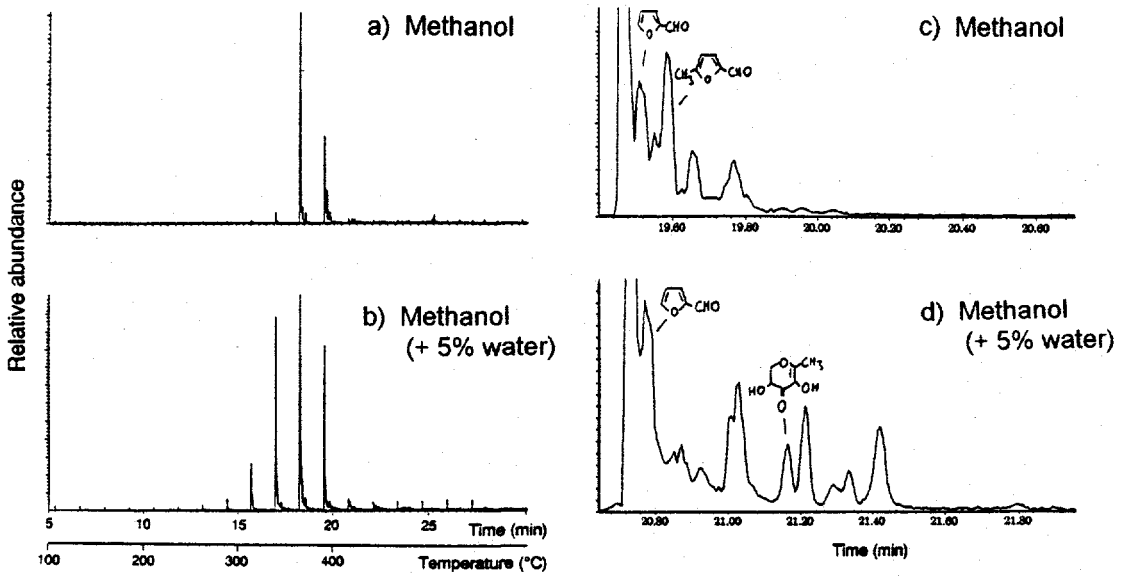

Figure 5. Fast, repetitive on-line GC/MS monitoring of the decomposition products from single birch wood toothpicks in methanol at 400 psi while heating the quartz tube reactor (1/8" i.d.) at 20 C/min. Note strong effect of adding 5% water on kinetic profiles (a and b) as well as on type and distribution of products (as shown by selected single GC intervals in c and d). GC column temp 120 C isothermal.

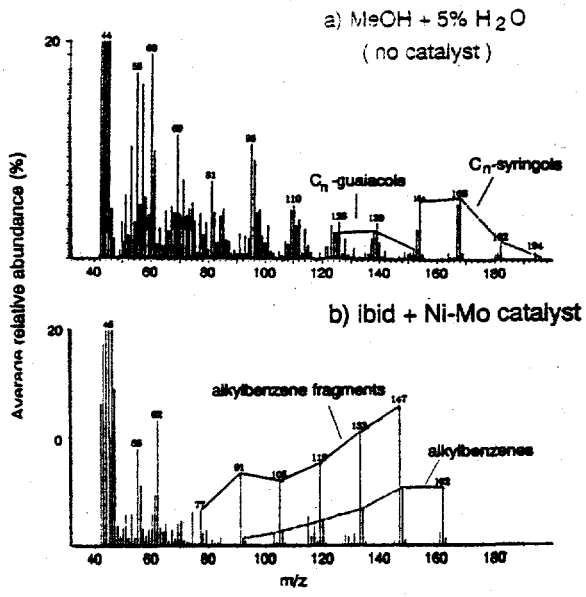

Figure 6. Effect of in-line Ni-Mo catalyst on birch wood degradation products (represented by summed spectra over all GC peaks). Notice complete disappearance of lignin type building blocks and formation of alkylbenzenes as also reported by Evans et al. [22].

HIDDEN BOTTLENECKS

Although the highly schematized overview in Figure 1 suggests that the reaction zone is usually interfaced to the ionization region in a single step, a more detailed analysis of the chemical and physical processes involved generally reveals the presence of less obvious zones or regimes with their corresponding interfaces, particularly when trying to study reactive processes in complex solids such as polymers, biomass or coal. Table I provides a generalized listing of the various zones and regimes encountered at the molecular (e.g., $\leq$ 0.1 μm), microscopic ($\leq$ 0.1 mm) and macroscopic levels. Since the latter have been discussed in the previous paragraphs, we will focus on the microscopic and submicroscopic (molecular) levels. Although Figure 3 demonstrates that, under favorable conditions, major differences in experimental parameters may have an almost negligible effect on the pyrolysis reaction, the opposite can also true: i.e., relatively minor changes (e.g., in noncovalent intermolecular bonding) may have a significant effect on yields and distributions of reaction products.

Table 1 - Potential Zones, Controlling Parameters and Effects on Analyte Distributions

#	Zone/Regime	Dominant Parameters	Effect on Analytes
1	intramolecular interaction	covalent bonding	primary reactions (chemically controlled)
2	intermolecular interaction	noncovalent bonding	
3	intraparticle transport	transport resistance	secondary reactions (physically controlled)
4	interparticle (bed) transport		
5	reactor headspace	z number surface activity	
6	pressure reduction	flow dynamics	losses (physically controlled)
7	ionization	cross section energy deposition	

Intramolecular and Intermolecular Interaction Regimes - The dramatic effect of modest percentages of certain fatty acids on the thermal degradation temperatures and yields of nylon is well known [19]. Similarly, as shown in Figure 5, solvents (whether added or produced during the reaction) can strongly influence the mechanisms and kinetics of the reaction. Naturally, compounds affecting covalent intramolecular bond strength, e.g., catalysts, have the greatest effect on reaction kinetics and pathways, as illustrated by Figure 6. Even relatively weak noncovalent bonds associated with degrees of crystallinity can have an effect on product type and yield. Figure 7a shows a Short Column GC profile of cholesterol injected by means of rapid Curie-point desorption. The minor anhydrocholesterol peak is thought to be due to an impurity. The two alkane peaks represent a few % of material added to disrupt the tendency of cholesterol to crystallize out of a suitable high purity solvent. The crystalline form of cholesterol desorbs at slightly higher temperatures during rapid (>1000 K/s) Curie-point heating, thereby promoting thermal decomposition to the anhydro form, as illustrated in Figure 7b.

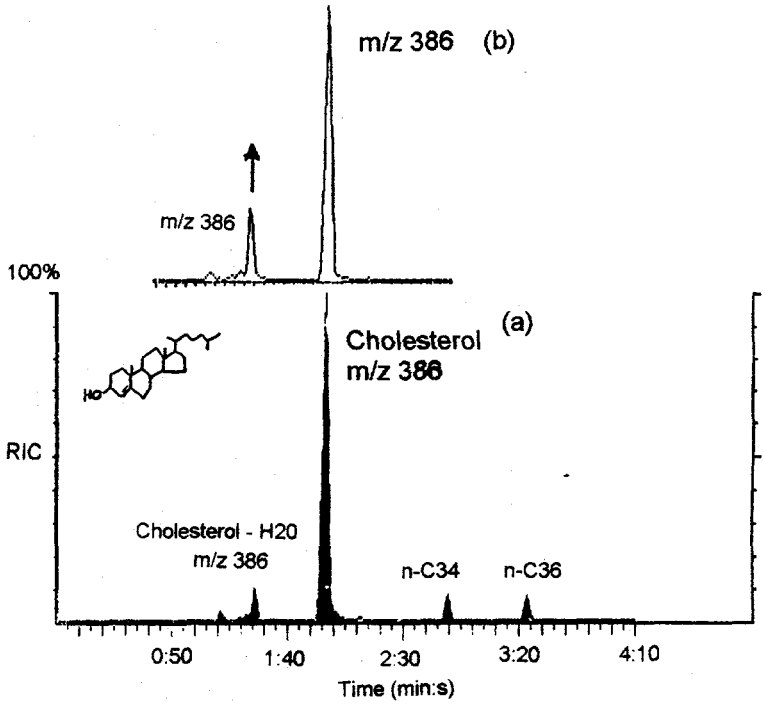

Figure 7. Effect of intermolecular (crystalline) forces on dehydration of cholesterol during Curie-point desorption. Note n-C_{34} and C_{36} alkane additive peaks in (a) preventing crystallization.

Intraparticle and Interparticle Transport Zones - Whereas the effects of solvents and catalysts are well recognized among process engineers an even more elusive set of parameters affecting the probability of reaction products reaching the ionization zone without marked losses or chemical modifications is often referred to as "transport resistance" and includes both mass and heat transport phenomena. The pronounced effects of mass and heat transport limitations on pyrolysis processes in polymers are illustrated in Figure 8. At the relatively high TG heating rate of approx. 90 K/min a single 3 mm block of an EPDM-Kevlar composite offers sufficient resistance to the escape of a semivolatile additive (dechlorane) that a substantial degree of dechlorination occurs which allows the nearly stoichiometric transformation of Sb_2O_3 (a second additive) into $SbCl_3$. When heating the same quantity of sample in a more finely divided form and at a more leisurely pace (10 K/min), no measurable quantities of $SbCl_3$ are formed!

Due to the strongly endothermic nature of cellulose pyrolysis, heat transport phenomena have been studied well in the field of biomass conversion [20]. Conversely, coal pyrolysis reactions are thermally nearly neutral and heat transport limitations are therefore generally ignored in the field of coal science for all but the highest heating rate (e.g., > 10 K/s) experiments. However, the widely different porosity and thermoplasticity characteristics of different coals have prompted extensive studies on mass transport limitations during "devolatilization" (moisture desorption + pyrolysis). Figure 9 shows that the intensity ratio of mass peaks at m/z 110 (mostly dihydroxybenzenes) and at m/z 108 (mostly cresols) is systematically affected by relatively minor changes in experimental parameters, including heating rate, particle size (mesh size) and bed depth in TG/MS runs using the system shown in Figure 2.

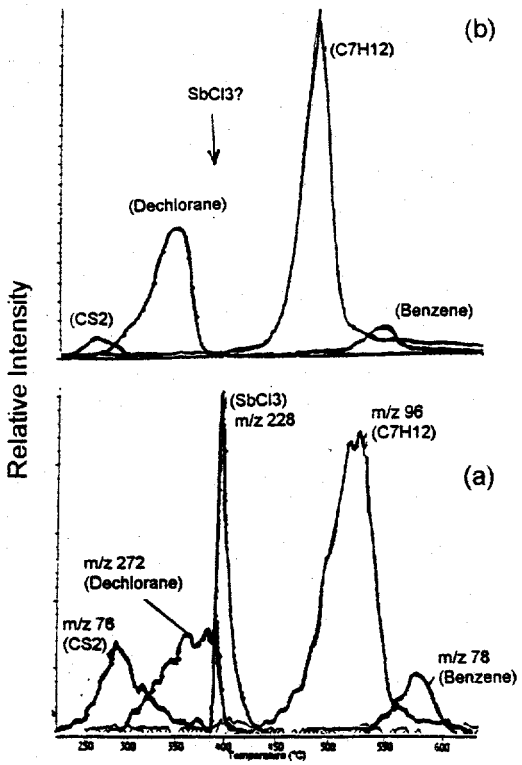

Figure 8. Combined effect of particle size and heating rate on $SbCl_3$ through dechlorination of dechlorane additive and subsequent chlorination of Sb_2O_3 additive in EPDM/Kevlar composite. (a) Single 3x3x3 mm cube at 90 K/min; (b) multiple smaller particles at 10 K/min.

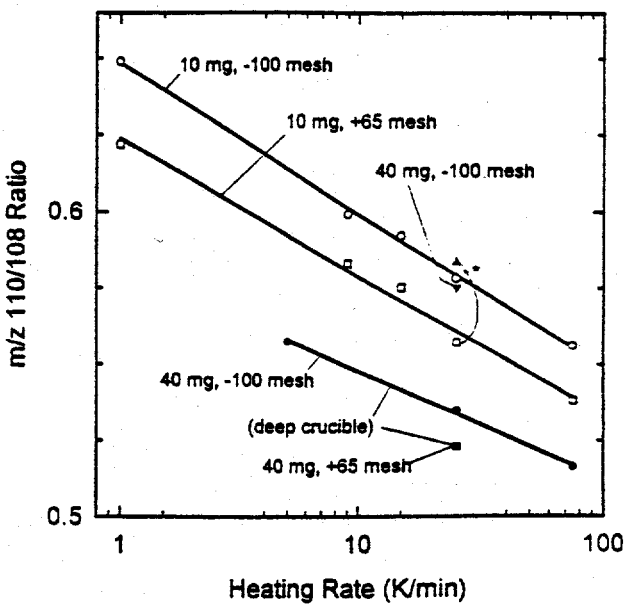

Figure 9. Effects of heating rate, mesh size and bed depth on m/z 110/108 (dihydroxybenzenes/cresols) ratios in TG/MS profiles of Illinois #6 coal.

Reactor Geometry; Z-Number - Reactor geometry in general, and average residence time plus wall collision probability (as expressed by the Z-number) in particular are often overlooked parameters in on-line MS analysis of pyrolysis reactions in complex solids. Whereas the importance of residence time is quite obvious to chemical engineers or kineticists, the Z-number tends to be completely ignored by everybody. Although its key role in pyrolysis of polymeric substances such as polystyrene was pointed out by Simon et al. as early as 1977 [21] most Pyroprobe users lump data obtained with platinum ribbon pyrolyzers together with the results of quartz capillary microfurnace experiments. Also, several manufacturers of Curie-point pyrolysis based systems promote the use of thin ferromagnetic foils, which may either be folded into an open boat or V-shape, or else completely wrapped around the sample. Figure 10 demonstrates the effect of increasing the Z-number of the reaction zone on the relative abundance of the labile styrene dimer products in polystyrene pyrolyzates as compared to the more stable trimers.

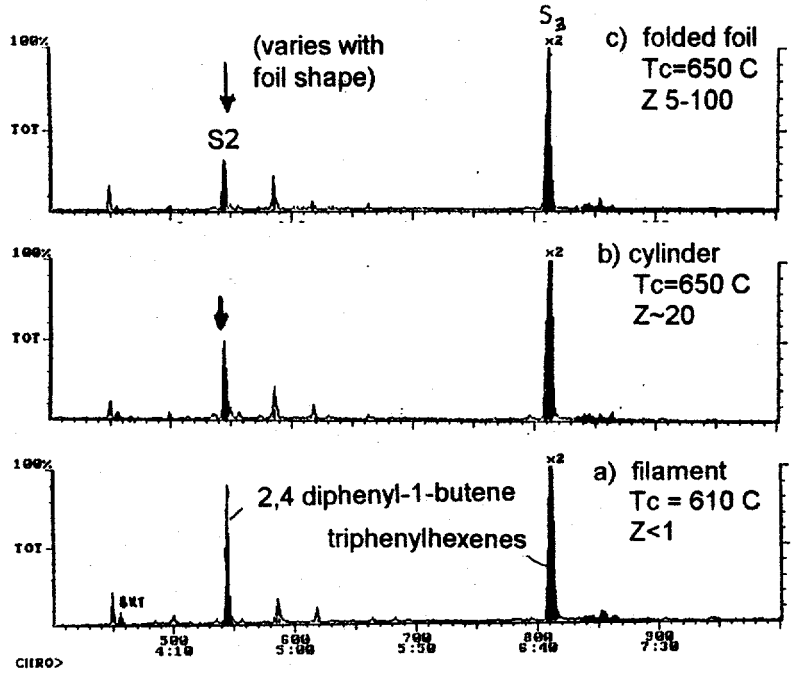

Figure 10. Effect of changing effective reactor geometry and Z number in Curie-point pyrolysis GC/MS analysis of polystyrene (only dimer and trimer region shown). Note loss of dimer (S_2) intensity with increasing Z number.

CONCLUSIONS

Among the many different configurations proposed and used to interface mass spectrometers with complex reactive systems, molecular beam inlets constitute powerful tools for transporting large labile molecules into the ion source intact. However, the GIGO ("garbage in garbage out") principle does apply here and the mixture of products arriving at the molecular beam inlet tends to be affected by less well studied secondary reaction and/or loss phenomena at the macroscopic, microscopic and submicroscopic levels. Considering the complexity, cost, size, nonisokinetic effects and relatively low sensitivity of typical molecular beam inlets, use of a less sophisticated interface may have some advantage in situations where the integrity of the target analyte(s) is likely to have been compromised prior to reaching the inlet.

ACKNOWLEDGMENTS

This work was supported by the Advanced Combustion Engineering Research Center (funded by NSF, State of Utah and 23 industrial participants) and the Consortium for Fossil Fuel Liquefaction Science

(funded by the Department of Energy). The expert technical assistance and advice of Drs. Kui Liu,William H. McClennen, Xiansheng Nie, Emma Jakab, Huaying Huai, and Jacek Dworzanski are gratefully acknowledged.

REFERENCES

1. Morse, M.D., *Chem. Rev.*, 1986, 86, 1049.
2. Emminger, W.D., Kaisersberger, E.J., *Thermal Anal.*, 1979, 17, 197.
3. Dagan, S.; Arnviav, A., *Int. J. Mass Spectrom. Ion Proc.*, 1994, 133, 187.
4. Sensar Corporation, Sandy UT.
5. Schulten, H.R.; Beckey, H.D.; Meuzelaar, H.L.C., *Analytical Chemistry*, 1973, 45, 2358-2362.
6. Unsold, E.; Renner, G.; Hillenkamp, F.; Nitsche, R., *Advances in Mass Spectrometry,* 1978, Heyden and Son, London, N.R. Daley (ed.), Vol. 7, 1425-1428.
7. Sinha, M.P., in: *Instrumental Methods for Rapid Microbiological Analysis*, 1985, VCH Publishers, W.H. Nelson (ed.), Chapter 6.
8. Boon, J.J., *Int. J. Mass Spectrom. Ion Phys.*, 1992, 118/119, 755.
9. Meuzelaar, H.L.C.; Haverkamp, J.; Hileman, F.D., *Curie-point Pyrolysis Mass Spectrometry of Recent and Fossil Biomaterials; Compendium and Atlas*, Elsevier, Amsterdam, 1982.
10. Yun, Y.; Meuzelaar, H.L.C., *Energy and Fuels*, 1991, 5, 22-29.
11. Simmleit, N.; Schulten, H.R.; Yun, Y.; Meuzelaar, H.L.C. , in: *Advances in Coal Spectroscopy,* H.L.C. Meuzelaar, Plenum Publishing Co., New York, New York, 1992.
12. Dworzanski, J.P.; Arnold, N.S.; Meuzelaar, H.L.C., *Proceedings of the 1992 U.S. Army ERDEC Scientific Conference of Chemical Defense*, November 17-20, 1992, Aberdeen Proving Grounds, MD, 1993, ERDEC-SP-007, 835-841.
13. Reiner, E.; Hicks, J.J.; Ball, M.M.; Martin, W.J., *Anal. Chem.*, 1972, 44, 1058-1061.
14. Posthumus, M.A.; Kistemaker, P.G.; Meuzelaar, H.L.C.; Ten Noever de Brauw, M.C., *Anal. Chem.*, 1978, 50, 985-991.
15. Winans, R.E, J. *Anal. Appl. Pyrol.*, 1991, 20, 1.
16. Netzch Instruments Inc., Stamford, CT.
17. Huai, H.;Meuzelaar, H.L.C., *ACS Preprints, Division of Fuel Chemistry,* April 5-10, 1992, San Francisco, CA, 1992, 37(1), 424-431.
18. Lui, K.; Jakab, E.; Meuzelaar, H.L.C. , *ACS Preprints, Division of Fuel Chemistry,* 1994, 39(2), 576-580.
19. Luederwald, J., personal communication.
20. Antal, M., *Adv. Solar Energy*, 1982, 1, 61.
21. Schmid, P.P.; Simon, W., *Anal. Chim. Acta*, 1977, 89, 1-8.
22. Evans, R.J.; Milne, T., in: *Pyrolysis Oils from Biomass*, 1988, ACS Symp. Series No. 376, 311.

THE OBSERVATION OF VERY LARGE SPECIES IN MBMS EXPERIMENTS

Frank T. Greene
Midwest Research Institute
Kansas City, MO 64110

INTRODUCTION

A molecular beam mass spectrometric system is arguably as close to a universal analytical device as has presently been achieved. However, various studies at MRI over the past 25 years suggest that some very large molecular entities may not be detected using typical MBMS techniques. Failure to account for these species may result in significant errors. These species may also be of importance in understanding nucleation and other molecular phenomena. It is the purpose of this paper to review the evidence for the presence of the very large species.

APPARATUS

The basic MBMS system used to all of the results discussed in this paper is shown in Figure 1. In this system the initial stage into which the sampled gas is expanded is pumped by a 10,000 L/sec diffusion pump, which typically maintains the pressure below a millitorr. The expanding gas is collimated into a molecular beam, which is pulsed by a rotating sector in order to permit phase sensitive detection and time-of-flight velocity analysis. The differentially pumped beam is passed sequentially through a large magnetic sector spectrometer, which provides resolution of up to 5000, and, for the current studies, a quadrupole mass spectrometer.

This system provides the capability for making convenient and accurate velocity analyses of the species in the molecular beam by the time-of-flight method. In this technique the molecular beam is pulsed on for a very short time interval and the distribution of arrival times of the neutral species at the ion source measured. This distribution can be used to calculate the velocity distribution, and computer codes for this purpose have been developed **[1]**. However, since the observed time-of-arrival (TOA) distributions are inversely related to the velocity distributions, it is often convenient to use them directly to identify the neutral precursors of observed ions, to determine molecular beam properties, and to make measurements of the temperatures of the sampled gas.

PREVIOUS STUDIES

The first indication of the presence of these very large species was obtained in a study of carbon vaporization by Milne, Beachey, Bennett and Greene**[1-3].** This study included velocity distribution measurements of species in beams formed from carbon vapor in order to determine the extent of fragmentation of carbon polymers. These time-of-flight velocity distribution measurements were made of the major carbon species generated over a wide range of temperatures but always under nearly effusive conditions. Some typical TOA curves for C_1, C_2, and C_3, which were made at an ionizing energy at 17 ev in order to reduce fragmentation, are shown in Figure 2. The mean flight times obtained in these measurements is in reasonable agreement with that calculated assuming effusive expansion and the measured cell temperature. However, there is a distinct, lower velocity shoulder on the TOA curve for C_3, but not for the C_1 or C_2 curves. TOA curves obtained under essentially identical conditions, but using an ionizing of 50 ev which would be expected to produce considerable fragmentation of the carbon clusters, are given in Figure 3. Under these ionization conditions, there was sufficient fragmentation that there are no significant differences in the TOA curves obtained for C_1, C_2, and the faster, "normal" TOA curve obtained for C_3. However, the intensity of the anomalous C_3^+signal is comparable to that of the "normal" C_3. These data suggested that one or more very large carbon species were present which fragmented to produce C_3+ but not the other low molecular weight carbon ions.

An instrumental artifact was suspected and so measurements were made of the velocity distributions of species in molecular beams formed by the expansion of small stable species in transition flow. For several of these beams the distributions indicated a very large species was present which fragmented principally to the parent ion, with little or no contribution to the other normal fragment ions. Typical TOA curves obtained for an n-heptane beam for the nominal parent ion peak (m/e = 100) and a typical fragment ion (m/e = 29) are shown in Figure 4. A variety of diagnostic measurements were made on the n-heptane peaks. These measurements included the use of either a pulsed electron ionizing beam or pulsed drawout from the ionization region. By varying the delay between the chopper function and the operation of the mass spectrometer, it was possible to obtain TOA curves which were largely independent of molecular reflections or the response time of the ion source. However, the TOA curves were identical to those obtained with continuous ionization and extraction. Ionizing energy and accessible ion source parameters were also varied. All were found to all have some effect on the TOA curves. A small mass dependence was also observed.

RESULTS

A series of experiments was undertaken to help characterize the phenomena involved in the observation of the anomalous, very large species and to determine the importance of this phenomena with respect to the interpretation of MBMS measurements. In addition, peripheral data from an unrelated current study in which anomalous very large species may have been present were reviewed.

DIAGNOSTIC STUDIES

MBMS measurements using the apparatus shown in Figure 1 were made of the species in convenient molecular beams which were generated by the expansion of various gases through a thin orifice with a diameter of 100 microns. Transition flow beam-forming expansions, which were used for most of the diagnostic measurements because differences in molecular weight can be detected, although not necessarily quantified, by making velocity distribution measurements. All of the transition beams were formed at room temperature at initial gas pressures which were manually adjusted to 30 to 100 torr. Measurements on beams formed by continuum flow expansions were also made using the same apparatus, but operated at pressures ranging from 1 to 5 atm.

High Resolution Measurements

Moderately high resolution (approximately 4000) spectra were obtained with the magnetic mass spectrometer for several organic species in molecular beams generated by transition flow expansions. The peak shapes for the parent ion (m/e = 100) and a typical fragment (m/e = 29) of n-heptane at approximately 60 torr and 300 °K is shown in Figure 5. TOF velocity analysis measurements were made on both the narrow higher mass peak and the diffuse lower mass satellite portion of the m/e = 100 peak. It was found that the narrow, higher mass peak produced a TOA curve which was almost identical to the higher velocity, shorter time peak in Figure 4 and which corresponded to a mean velocity within the expected range for a transition expansion at this temperature and pressure. TOF velocity distribution measurements on the diffuse portion of the peak produced a TOA curve which corresponded only to the lower velocity, longer time portion of the peak shown in Figure 4. Velocity distribution measurements on the fragment ions showed a distribution essentially identical to that obtained for the "normal" parent ion peak. Comparable results were obtained for methanol and acetone in molecular beams formed under comparable, transition flow conditions.

Measurements of the peaks shapes for parent and fragment ions were also made for several gases in molecular beams formed under continuum flow conditions. These beams were generated from N_2, O_2, Ar, CO_2, CH_4, He and H_2O in atmospheric pressure He. In all of these cases except He, a diffuse lower mass satellite peak was observed for the parent ion but not for the fragment ions.

Quadrupole Measurements

The axial quadrupole mass spectrometer shown in Figure 1 was also used to make velocity analysis measurements of heptane, acetone, methanol and water in the same transition flow molecular beams used for the velocity analyses with the magnetic mass spectrometer. The resulting TOA curves contained no indication of the slow component, but were in good agreement with the "normal" (fast) TOA curves obtained with the magnetic mass spectrometer when a correction was made for the additional flight distance. Variations in the quadrupole mass spectrometer ion source parameters, including ionizing energy, ion energy and focus voltage had no significant effect on the shapes of the TOA curves.

Discussion

All of the measurements, including those of carbon vaporization in the earlier work, are consistent with the presence of a very large species or cluster in the beam. One explanation for the observed mass spectrometric behavior is that the ion produced by electron impact undergoes a metastable ion decomposition to produce a daughter having a m/e equal to that of the principal constituent of the large species or cluster. Metastable ions observed in a magnetic mass spectrometer are those which decompose after leaving the ion source in the initial acceleration region, and which therefore appear at a lower apparent mass. The relationship between the masses of the ions which undergo a metastable ion transition in the acceleration region of a magnetic mass spectrometer is given by

$$m^* = m/m_o(V_1/V) + m(1-V_1/V)$$

where m^* is the apparent mass of the daughter ion, m is the actual mass of the daughter ion, and m_o is the mass of the parent ion. If $m_o = nm$ and n is very large, then this expression reduces to

$$m^* = m(1-V_1/V)$$

Consequently, if the metastable decomposition occurs very near the end of the acceleration

region, V_1 will be only slightly smaller than V, and m* will appear at an m/e only slightly smaller than m. These assumptions are consistent with the observation of very large species at a very slightly lower m/e than that of its nominal constituents. It is interesting that the daughter ions from the large species in the systems studied to date always appear at only slightly lower mass than that of the nominal parent ion. This could be the result of great consistency in the lifetimes of the metastable ions. Alternatively, it may be that only the most rapid decompositions are being observed in the various systems, and that most of the metastable transitions occur in the magnetic field. In this case, which is consistent with the observations at MRI of a mass spectrometric continuum related to the presence of clusters in molecular beams, only a fraction of the very large species may have been detected.

Quadrupole mass filters do not usually transmit metastable ions. Consequently, the failure of the quadupole to detect the very large, lower velocity species in the transition expansion beams is, at least superficially, consistent with the assumption of a metastable ion phenomenon. However, there were sufficient differences in ion source parameters, including possible trapping of ions in the electron beam and differences in extraction times, that this may not a reasonable inference.

OBSERVATIONS OF VERY LARGE SPECIES IN THE Cl-O SYSTEM

Very large vapor species may not always be detected even when using a high resolution MBMS system. In a study of the Cl-O system **[4]**, a low concentration of ClO_2 in O_2 was introduced into an atmospheric pressure photochemical flow reactor. The species present were measured using the MBMS system shown in Figure 1 in conjunction with a 100 micron sampling orifice. In the performance of these experiments it was found that, when ClO_2 was photolyzed in O_2 in order to generate ClO, the concentration of ClO_2 as measured using the magnetic mass spectrometer dropped as expected. However, the ClO_2 signal as measured with the axial quadrupole mass spectrometer approximately doubled. These data are shown in Figure 6. Time-of-flight velocity analysis measurements were therefore made of the neutral precursors of the species in the beam which yielded m/e = 67 and m/e = 51 using both the magnetic and the quadrupole mass spectrometers. The TOA curves obtained for the m/e =67 species are shown in Figures 7 and 8. The shape of the TOA curves obtained with the magnetic mass spectrometer were unchanged by the presence of the light. However, the TOA curves obtained using the quadrupole mass spectrometer show that, upon photolysis, most of the m/e = 67 signal was associated with a neutral precursor having a mean velocity which was much less than that of the O_2 matrix. Most of the m/e = 51 signal, which was obtained with the quadrupole, was also associated with a neutral precursor having the same.

The low mean velocity observed for the ClO-ClO_2 species, considering that the beam is formed by a continuum expansion from atmospheric pressure, indicates a very large mass which is more typical of small particles. The relatively narrow velocity distribution indicates a very limited range of sizes, or even a discrete structure. The association of ClO and ClO_2 ions with the large species suggest that it is produced from these components by a photoinitiated reaction, which could be of importance in
stratospheric chemistry. However, more work is needed to make any deductions regarding composition, structure, mechanism of formation and ionization behavior more than wild speculation.

SUMMARY AND CONCLUSIONS

The bimodal velocity distributions observed suggest that the very large species have a limited mass range. In at least some cases the species appeared under conditions in which there was relatively little adiabatic cooling of the gas, suggesting that their equilibrium concentration may be significant under static conditions. Could the large species could be the legendary critical nuclei of classical homogeneous nucleation theory? Regardless, they can be a significant source of error in MBMS measurements. They can also cause major errors in the calibration of mass spectrometers using total mass flux, such as the procedure of Lee and Fenn **[5]**.

ACKNOWLEDGEMENTS

The early, previously reported studies were performed in collaboration with Dr. Thomas Milne, Dr. Steve Bennett and Mr. Jacob Beachey. Dr. Owen Gan and Mr. Rick Robson participated in the diagnostic studies. The measurements of species in the Cl-O system part of a study undertaken in collaboration with Dr. David Robaugh. The measurements were made using equipment provided under NASA Contract No. NASW-4371.

REFERENCES

1. Milne, T.A., J. E. Beachey and F. T. Greene, **Vaporization Kinetics and Thermodynamics of Graphite Using The High Pressure Mass Spectrometer**, Final Technical Report AFML-TR-74-57, Midwest Research Institute, May 1974

2. Milne, T.A., J. E. Beachey and Frank T. Greene, paper presented at the Molecular Beam Sampling Conference, Lake of the Ozarks, MO (1972)

3. Milne, T. A., J. E. Beachey, S. L. Bennett, and F. T. Greene, paper presented at the 21st Annual Conference on Mass Spectrometry and Allied Subjects, San Francisco, CA (1973)

4. Greene, F.T., paper presented at A Specialists Workshop on Applications of Free-Jet Molecular Beam Mass Spectrometric Sampling, Estes Park, CO (1994)

5. Lee, N. and J. B. Fenn, Rev. Sci. Inst., 49,1269 (1978)

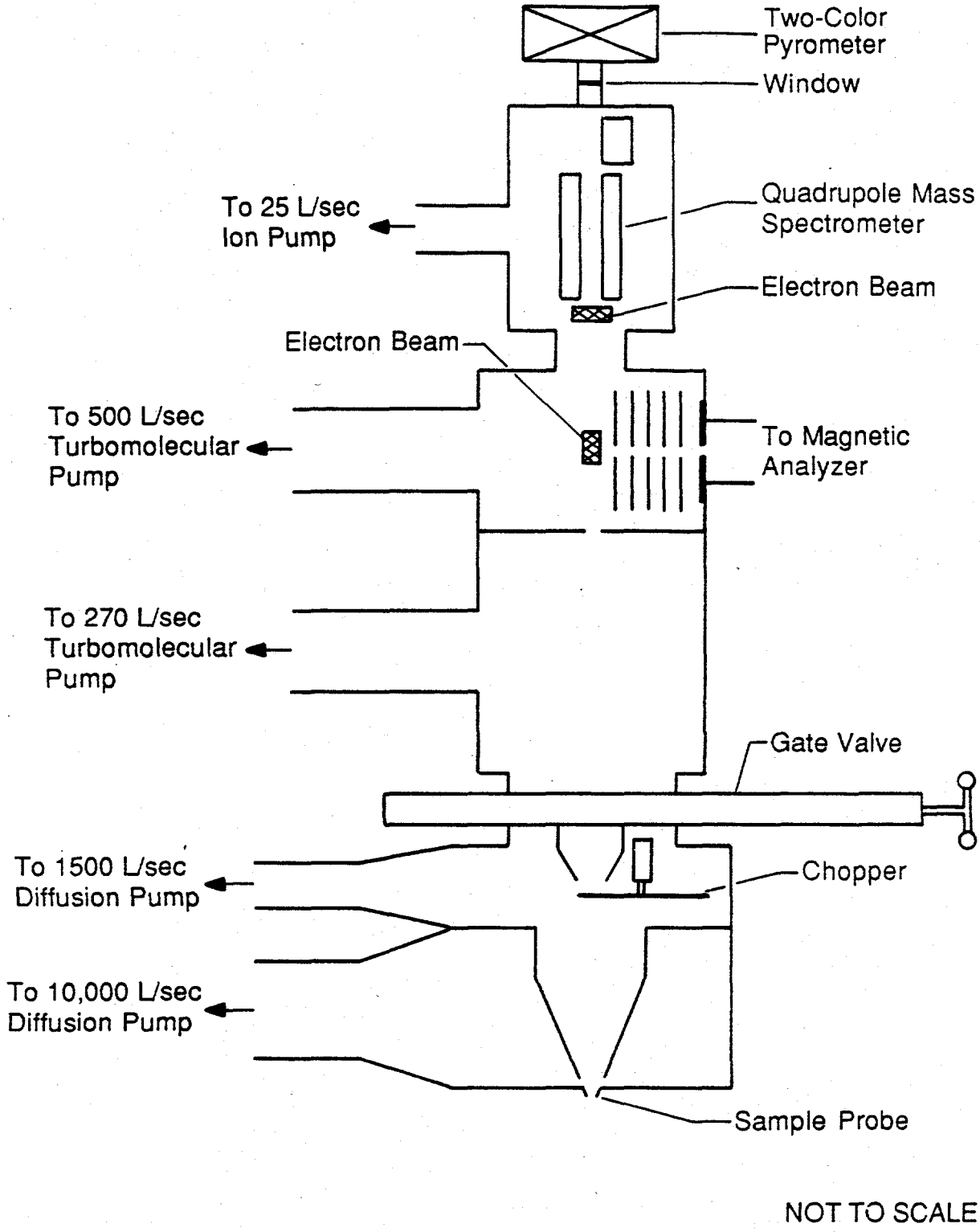

Figure 1. The high resolution MBMS system.

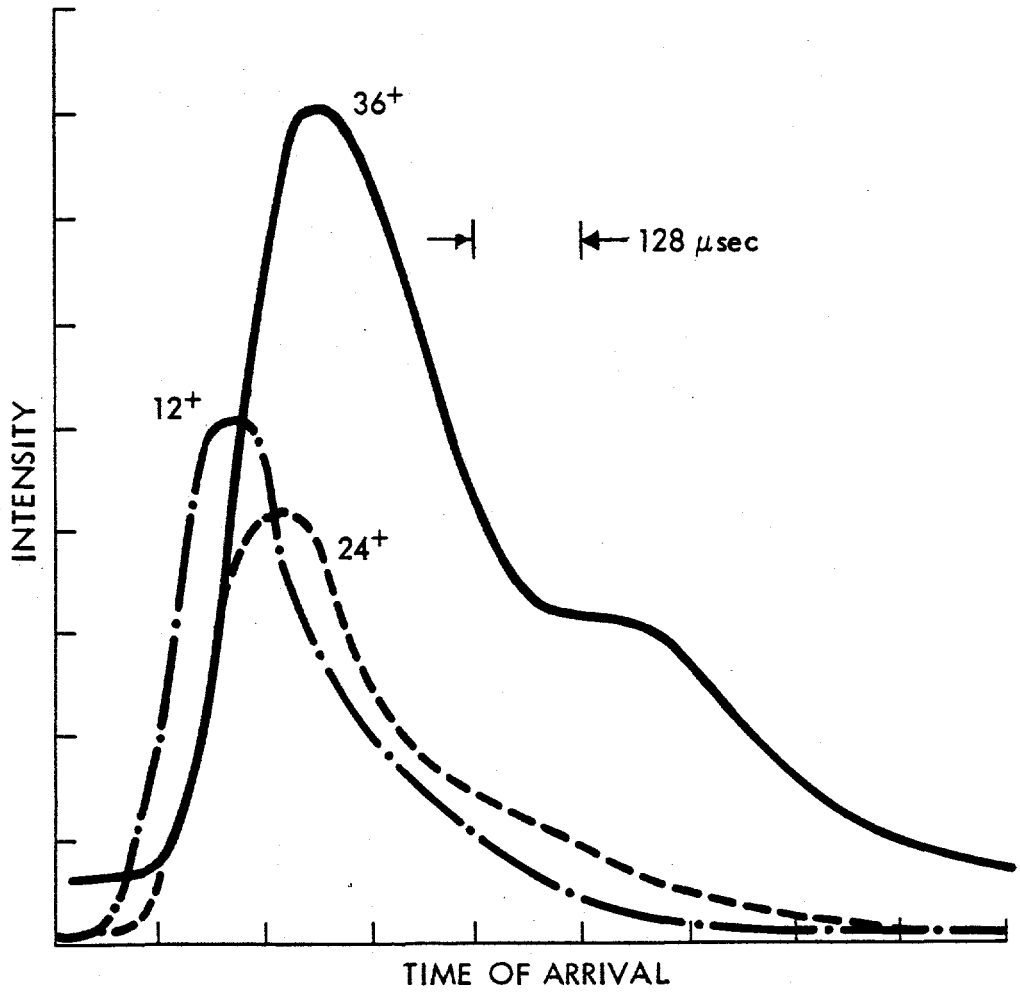

Figure 2. TOA curves for selected species in carbon vapor at 2780 °K obtained using 17 ev ionizing electrons.

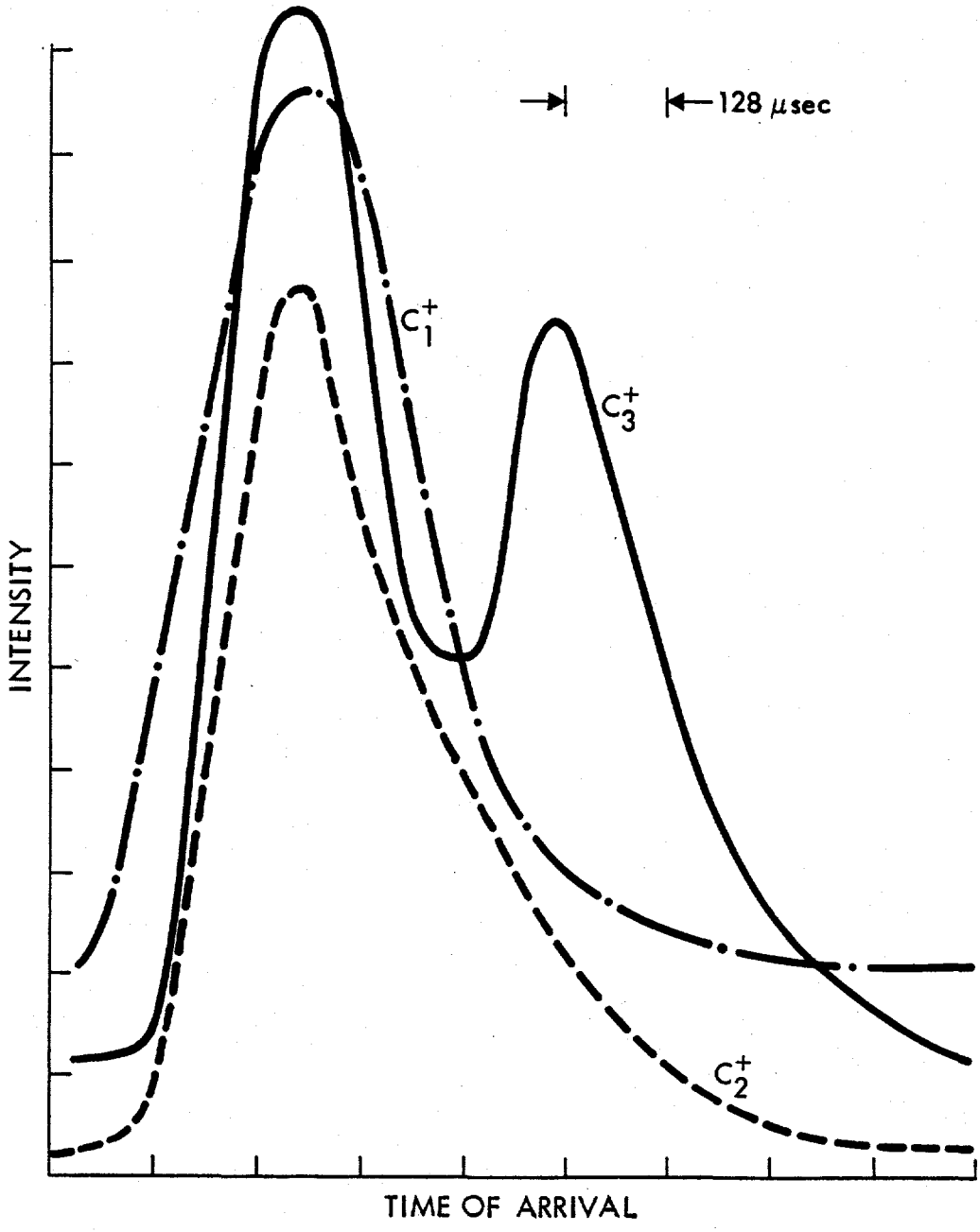

Figure 3. TOA curves for selected species in carbon vapor at 2800 °K obtained using 50 ev ionizing electrons.

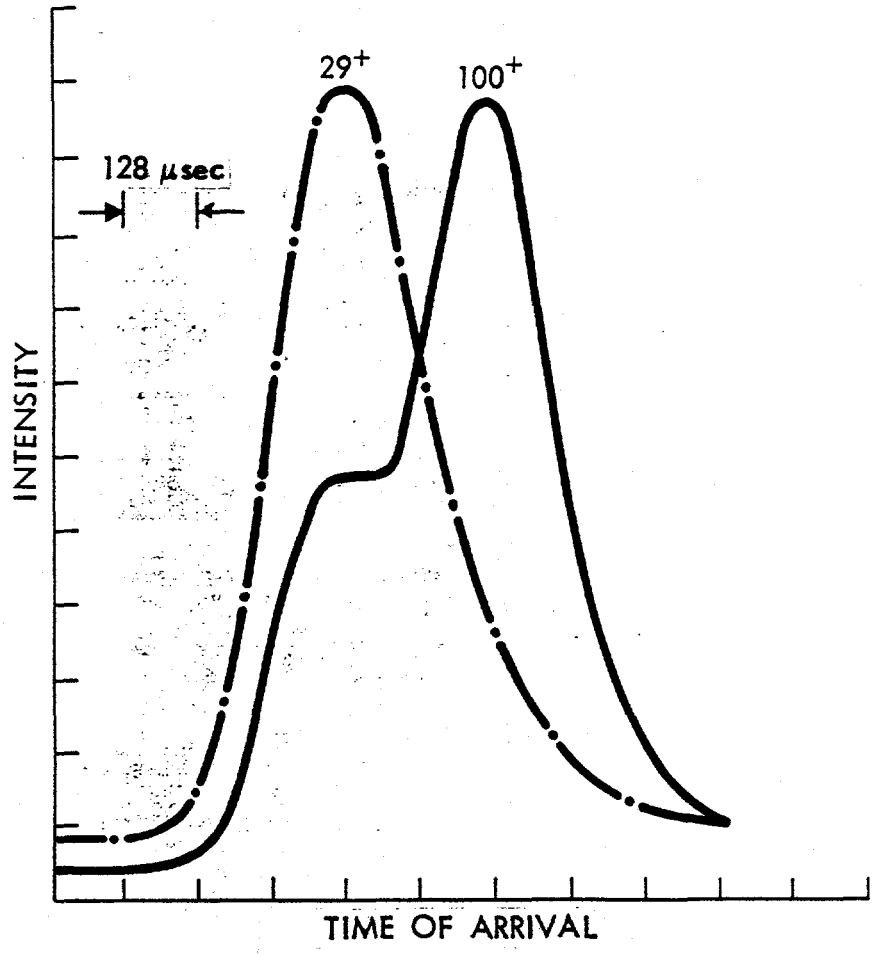

Figure 4. TOA curves observed for the parent and a fragment ion in a n-heptane beam

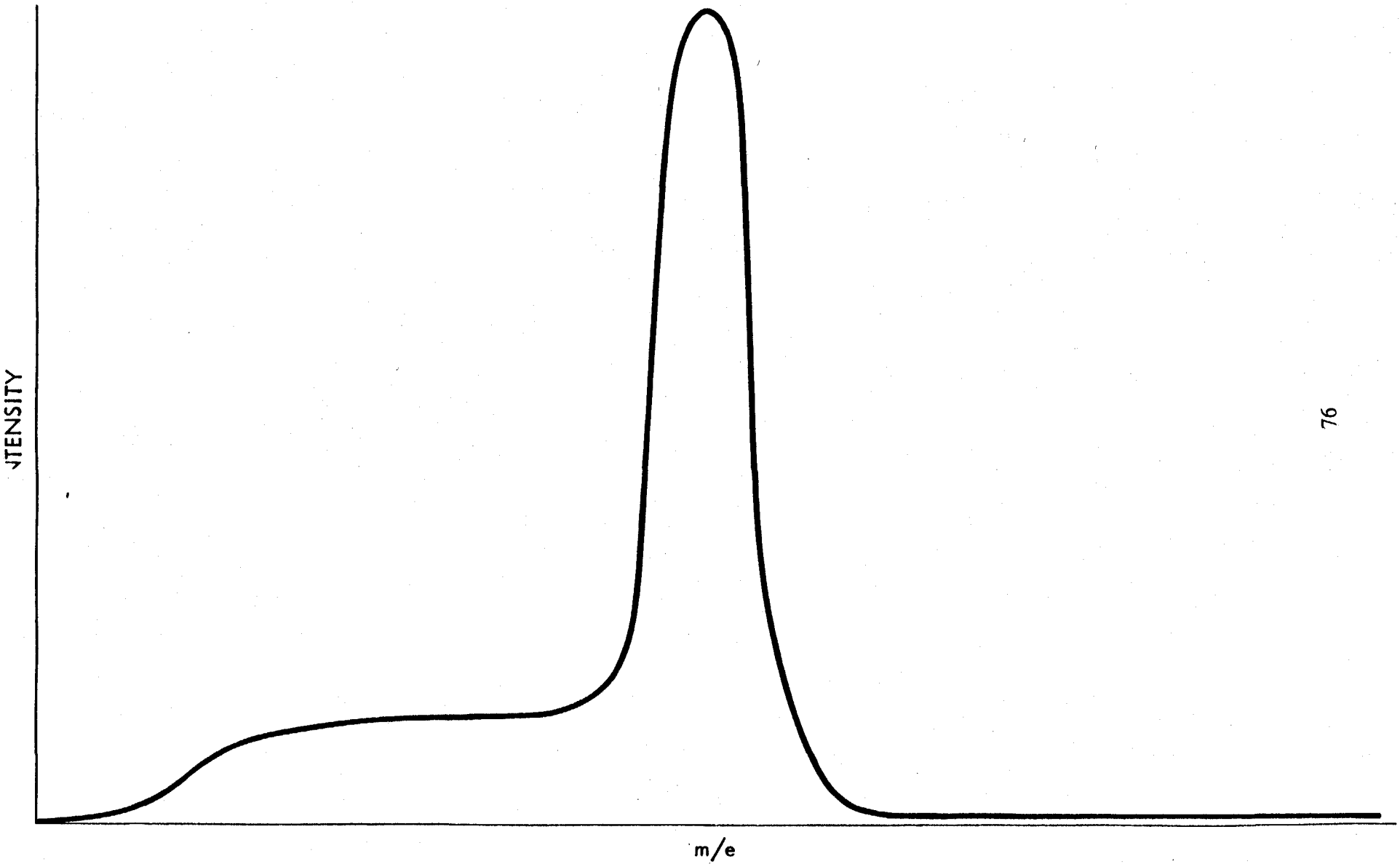

Figure 5. Peak profile obtained for the m/e = 100 ion observed in a transition flow n-heptane beam using 50 ev ionizing electrons.

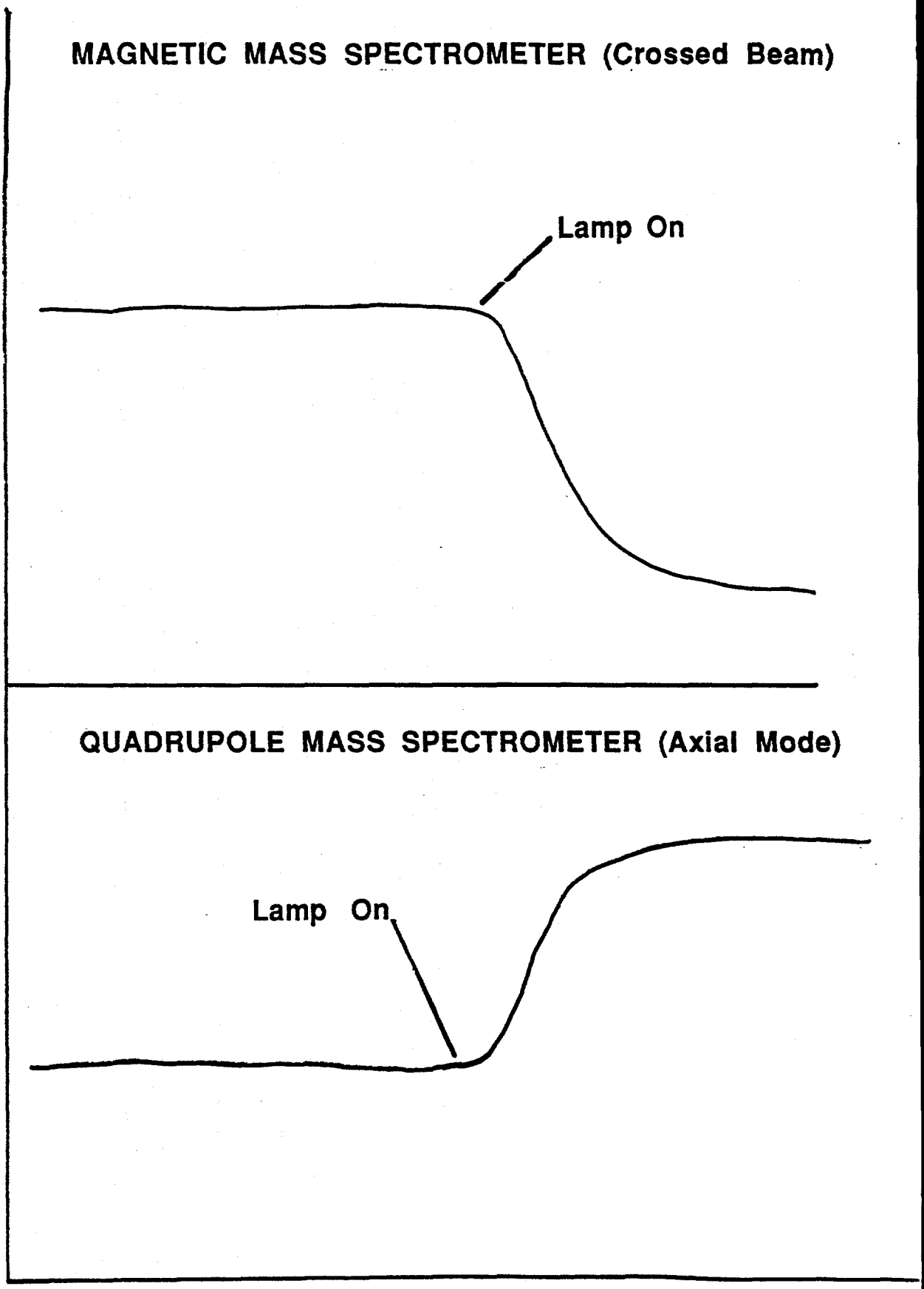

Figure 6. Variation in the mass spectrometric intensity at m/e = 67 upon introduction of uv radiation observed using the magnetic and quadrupole mass spectrometers.

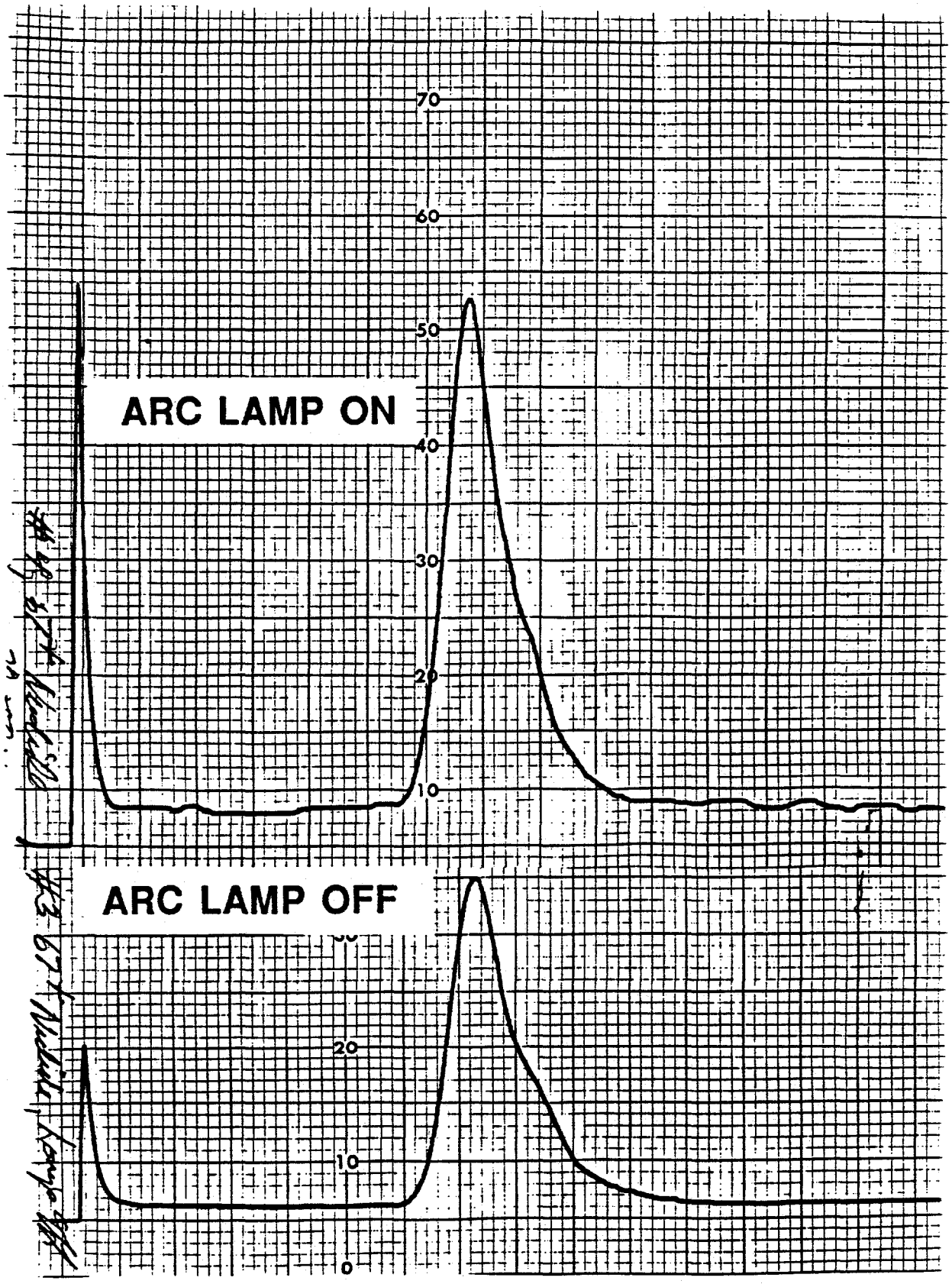

Figure 7. TOA curves obtained for the neutral precursor of m/e = 67 in the presence and absence of uv radiation obtained using the axial quadrupole mass spectrometer.

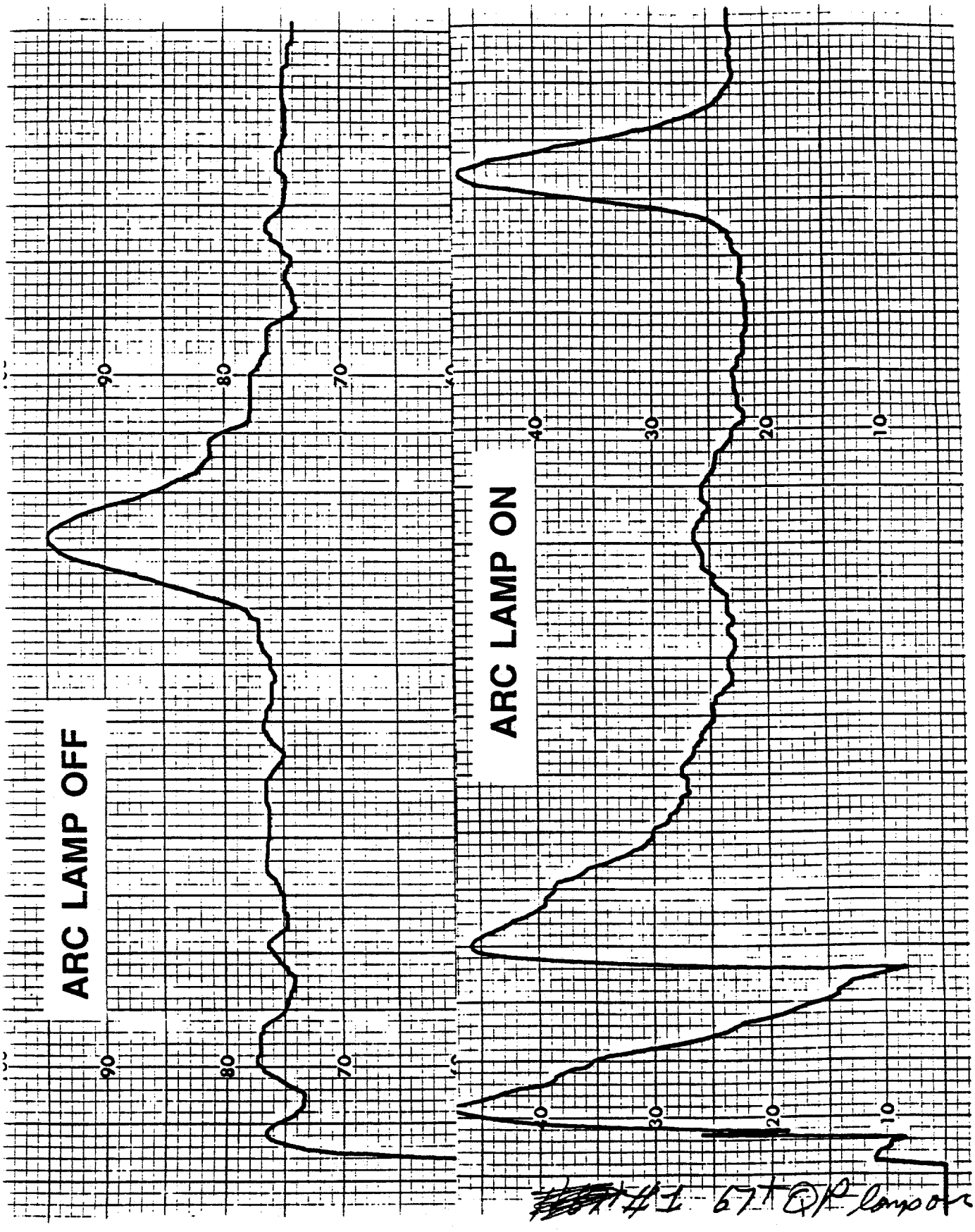

Figure 8. TOA curves obtained for the neutral precursor of m/e = 67 in the presence and absence of uv radiation using the magnetic mass spectrometer in a crossed beam mode.

Particle Beam Mass Spectrometry of Submicron Particles Sampled From Low-Pressure Environments

Paul J. Ziemann, Peng Liu, David B. Kittelson, and Peter H. McMurry
Particle Technology Laboratory
Department of Mechanical Engineering
and Stephen A. Campbell
Department of Electrical Engineering
University of Minnesota
Minneapolis, MN 55455

Introduction

The manufacture of semiconductor devices involves a variety of processes occurring over a wide range of operating pressures (from atmospheric to about 10^{-5} torr). During processing, particles can be produced by flaking from the walls of the equipment, or by homogeneous nucleation resulting from pump down or from reactions involving gas phase species that produce nonvolatile products. These particles can deposit on the surfaces of semiconductor devices, leading to defects which reduce product yield. It has been projected that by the year 2001 particles down to 15 nm, and perhaps as small as 5 nm, will be critical to the yield of 1 Gbit DRAMS. Semiconductor manufacturers will need to be able to detect aerosol particles down to these sizes at subatmospheric pressures, but there are currently no instruments available that can meet these requirements. Standard aerosol techniques for sizing and detecting particles are often limited to operation near atmospheric pressure (e.g. mobility analyzers, condensation nucleus counters), or cannot be used to detect low concentrations of ultrafine particles (e.g. light scattering). In an effort to alleviate this problem, we have recently developed a particle beam mass spectrometer that can be used to size and detect ultrafine particles in low-pressure environments. The instrument can be used as a particle detector in process control, and as a tool for investigating particle formation in semiconductor equipment or other low-pressure systems.

In this presentation we describe the operation of the instrument and the techniques used for calibration, data analysis, and measurements of particle size distributions. Size distributions measured using the particle beam mass spectrometer are compared with those obtained by differential mobility analysis, a standard technique for atmospheric pressure measurements. We also include some results from a recent investigation of particle formation during LPCVD of polysilicon films.

Experimental Apparatus and Technique

The particle beam apparatus is shown in Figure 1, beginning below the pressure reduction chamber. Aerosol at low pressure (~0.1-5 torr) is sampled into a tube containing a series of plate-orifice constrictions, which we call aerodynamic lenses. These constrictions generate gas flow patterns that cause the particles to move toward the center-line as they travel along the tube and into a 3 mm diameter plate-orifice nozzle. As a result of this focusing, the particles undergo very little radial acceleration as the aerosol expands through the nozzle into an intermediate-pressure (0.15 torr) chamber. The particles then travel unhindered through a 1 mm skimmer into a high vacuum chamber (2×10^{-5} torr), where they are charged using a home-built, strip-beam, electron gun. After passing through the electron beam the particles enter a housing containing a pair of parallel plates that can be used to

electrostatically deflect the particles. Further downstream is a three-grid deflector that can be used to deflect particles by 90°. Depending on the deflector being used, particles enter either a Faraday cup located on-axis with the beam, or strike a greased-plate Faraday detector located in a side-arm, for measurement of the particle current.

Solid KCl or liquid diffusion pump oil (dioctyl sebacate, DOS) particles were generated for laboratory experiments by nebulizing a solution of the material of interest in a Collison atomizer, and then drying the solution drops by passing the aerosol though a diffusion drier. Size-selected particles were obtained for calibration measurements by first passing the dried aerosol through a radioactive bipolar charger, which gives most of the particles zero or one charge. The aerosol then enters a Differential Mobility Analyzer (DMA), which separates particles according to their electrical mobility and allows those with mobilities in a narrow, selected range, to exit with the flow leading to the particle beam apparatus. The particle diameter D_p can be calculated from the measured mobility, thereby allowing us to obtain near-monodisperse distributions ($D_p/\Delta D_p \sim 10$) of size-selected particles for our experiments. The monodisperse aerosol is split upon leaving the DMA, with 90% of the flow going to a Faraday cage connected to an electrometer used to monitor the particle current. The other 10% of the flow expands through a 100 μm orifice into a pressure-reduction chamber (2 torr) and then into the particle beam generator.

Particle transport efficiencies were determined from the ratio of the particle currents measured inside the vacuum chamber and at the DMA exit. Particle beam widths were measured by observing the decrease in particle beam current at the on-axis Faraday cup as a knife-edge was moved across the beam. Particle velocities were determined from electrostatic deflection (parallel plates) measurements with singly charged particles of known shape, size, and density. All of these measurements were made with the electron gun turned off. The charges acquired by particles passing through the electron beam were determined from the ratio of the particle beam current measured with the gun on and off.

The particle size distribution of a polydisperse KCl aerosol was measured by scanning the DMA, and also by introducing dried particles directly into the pressure-reduction chamber for particle beam mass analysis using 90° deflection (the parallel plates were grounded). The size distributions of three DMA size-selected particles were also measured to check the calibration. The quantity measured is the integrated particle beam current $I_{PB}(V)$, determined as a function of deflection voltage V. The deflection voltage is proportional to the particle's kinetic energy-to-charge ratio, $V = MU^2/2AQe$, where M, U, and Q are the particle mass, velocity, and charge (in elementary units), respectively, A is a proportionality constant that depends on the configuration of the energy analyzer, and e is the magnitude of the electron charge. In order to express the particle beam current as a function of the particle diameter, it is necessary to know the relationship between particle mass and diameter $M(D_p)$, velocity and diameter $U(D_p)$, and charge and diameter $Q(D_p)$. These equations are substituted into the kinetic energy expression to obtain a calibration curve $D_p(V)$, which is used with a measured deflection curve and transport efficiencies to calculate the particle size distribution.

Results and Discussion

In Figures 2 and 3 we demonstrate the focusing properties of our particle beam lens. The DOS particle beam widths measured 43 cm downstream of the nozzle decrease from 3 to 0.3 mm as the particle size increases from 30 to 250 nm. These are the narrowest beams possible, the minimum width being determined by Brownian motion of particles in the nozzle. As a result of the focusing, the transport

efficiencies for these particles are close to 100%. The results for KCl particles are similar, although the beams broaden slightly due to the nonspherical shape. After 90° deflection, approximately 50% of the particles hit the detector.

The measured velocities of size-selected DOS particles is shown Figure 4, where the data have been fit to a power law. The equation is valid for this particle beam lens configuration and a 2 torr source pressure. The velocities of KCl particles can be calculated for the same conditions by substituting the density of KCl and a shape factor of 0.735, which is appropriate for cubic particles. This factor is equal to the ratio of the side length of a cube and its mobility diameter. The mass of a KCl particle is the product of density and $(0.735D_p)^3$.

The size-dependent charges on KCl particles after electron impact are shown in Figure 5. These measurements were made with electron currents high enough to cause charge saturation, which results when the potential barrier caused the particle's positive charge reduces the secondary electron yield to one. Under these conditions the charge on a particle is proportional to the saturation potential (which depends on the material) and the particle diameter. The result is a simple linear relationship between particle charge and diameter. The high particle charges significantly decrease the detection limit, compared to what it would be with singly charged particles.

Before using the mass spectrometer to measure the size distribution of a polydisperse KCl aerosol, the calibration obtained by combining the above relationships was checked on size-selected KCl particles with diameters of 64, 94 and 141 nm. The results are shown in Figure 6, where it can be seen that the particle diameters measured with the mass spectrometer are within a few percent of the DMA values. The full widths at half maximum of the distributions are approximately 20% of the particle diameters. Approximately half of the width is due to the DMA, which produces a size distribution having a width of about 10%. The true resolution ($D_p/\Delta D_p$) of the mass spectrometer measurements was therefore about 10, comparable to those made with a DMA .

The particle size distributions measured for the polydisperse KCl aerosol using the mass spectrometer (PBMS) and DMA are shown in Figure 7. The two distributions are quite similar. Both begin at about 20 nm, have maxima near 100 nm, and represent total particle concentrations of approximately 5×10^6 cm^{-3}. The major difference occurs at large particle diameters. Whereas particles as large as 700 nm were measured with the DMA, no particles larger than about 300 nm were observed with the mass spectrometer. The discrepancy is probably due to defocusing and loss of smaller particles at high voltages, caused by inhomogeneities in the fields near the energy analyzer entrance. The noise level for the measurement was about 10^{-13} Amps, which corresponds to a detection limit of about 10 particles cm^{-3} for sampling from 2 torr, and 4×10^3 particles cm^{-3} for atmospheric pressure sampling (for an average particle diameter of 100 nm (saturation charge ~200) and a volumetric flow rate through the beam lens of 625 cm^3/sec). The scan was performed in about 2-3 minutes.

We recently used our particle beam apparatus to investigate particle formation during low-pressure CVD of polysilicon films. The measurements were made on gas sampled directly into the particle beam generator from the outflow of a horizontal flow-tube reactor. The LPCVD process was carried out using pure silane flows of 10-90 sccm (no buffer gas), a reactor temperature of 620°C, and pressures ranging from 0.7 to 3 torr. The system was evacuated and temperature stabilized before adding silane.

When the process was operated at 0.7 torr, which is close to the pressure normally used for film production, no particles were observed with the mass

spectrometer and good films were formed on the wafers. We then carried out an experiment using higher silane flows in order to increase the reactor pressure. The results of one experiment, in which particles were sampled at the on-axis detector without deflection, are shown in Figure 8. When the silane was first introduced, the pressure quickly rose to about 3 torr, and high negative, and then positive bursts of particle current in the nanoamp range were immediately observed. These currents correspond to particle concentrations of about 10^5 cm^{-3} (assuming 50 nm particles with saturation charges of 50). The pressure then came back down, and at about 1.7 torr the current quickly dropped to zero, and for the remainder of the experiment (~1 torr), smaller negative particle currents were observed. We then performed a similar experiment using the 90° deflector, with the pressure kept at 2.0 torr throughout. For the first half of the experiment we deflected negatively charged particles, and then switched the deflector polarity in order to deflect positively charged particles. The results of those measurements are shown in Figure 9. The pressure rose slowly as silane was added and particles appeared when it reached 1.7 torr. Concentrations were on the order of 10^3 cm^{-3}, two orders of magnitude lower than the previous experiment. One size distribution measurement was made when the particle current was positive and steady for more than a minute, yielding an average size of approximately 45 nm. No particles we observed after about one hour. In experiments in which particles were detected with the mass spectrometer, wafers inside the reactor were found to be covered with powder.

There are a number of interesting results obtained from these experiments. The abrupt appearance of particles at 1.7 torr is indicative of homogeneous gas-phase nucleation of silane polymers, leading to particle formation. This critical pressure is close to the value predicted from a similar study that employed light scattering to detect particles. However, we continued to detect particles after the pressure dropped below 1.7 torr. The particle sizes we measure are also in accord with microscopic observations made by others of particles collected from a similar reactor. Our observation of positively and negatively charged particles indicates that a mixture of particle types is present, with different secondary electron yields. We think that the negatively charged particles are essentially pure silicon, and that the positively charged particles are hydrogenated silicon. Based on our observations that particle formation ceases after about one hour, even though reactor pressure and temperature are apparently unchanged, it appears that particle formation in the reactor may not be a purely homogeneous gas-phase process.

Conclusions

We have demonstrated that mass spectrometry can be used to measure the size distribution of submicron particles sampled from a low pressure region. The technique can be quite accurate, with a maximum resolution of about 10. A complete size distribution can be measured in about 2-3 minutes, and the detection limit is about 10 particles cm^{-3}, when sampling from a pressure of 2 torr. We have used the technique to detect particles in a low-pressure CVD reactor, and have observed a number of interesting phenomena regarding particle formation.

Acknowledgments-This research was supported by Contract No. SRC/MJ-225 from the Semiconductor Research Corporation.

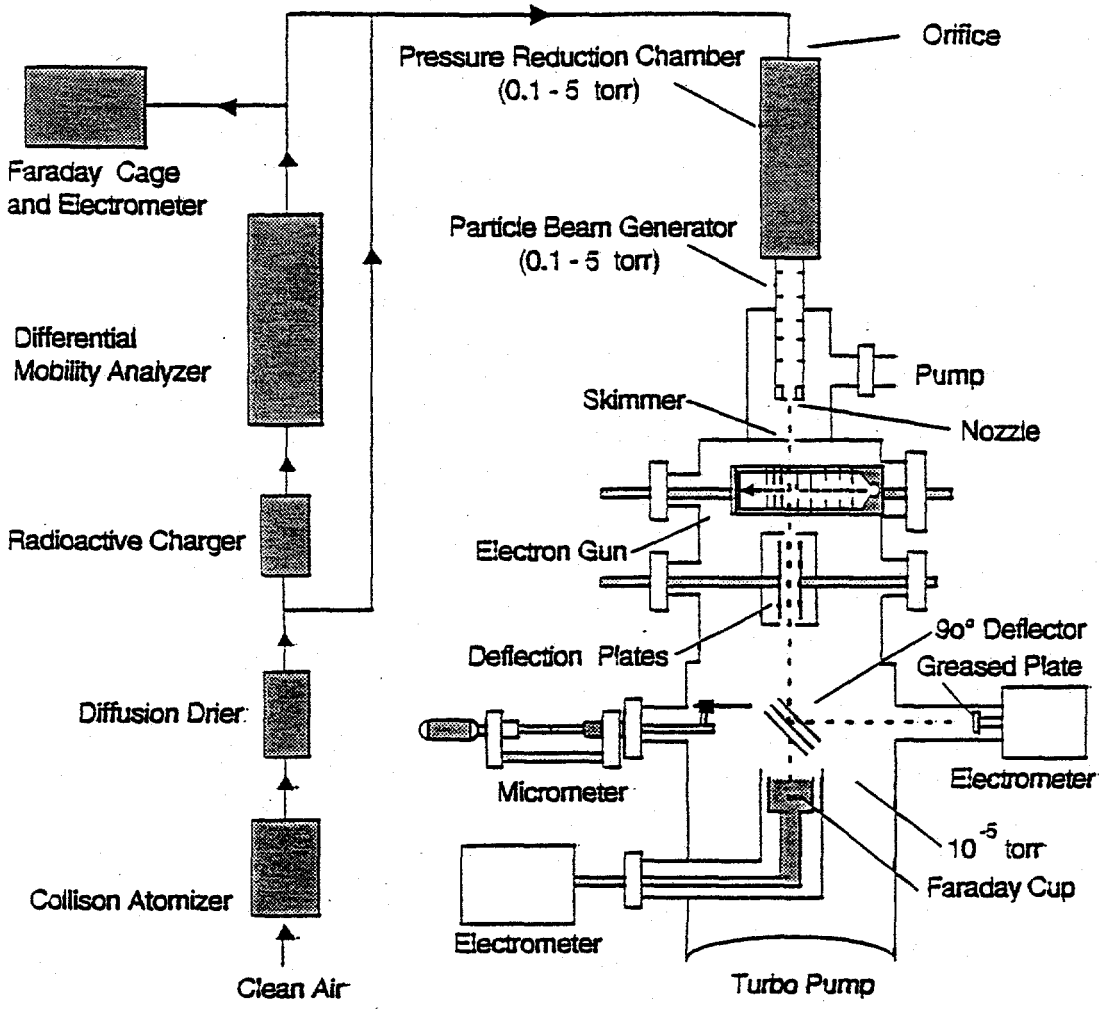

Figure 1. Particle Beam Apparatus

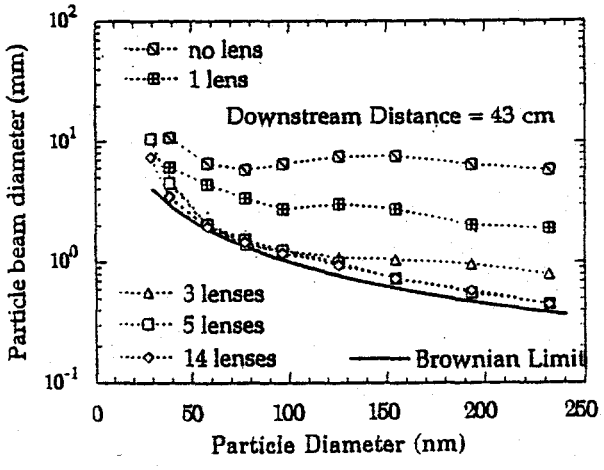

Figure 2. Measured DOS particle beam widths.

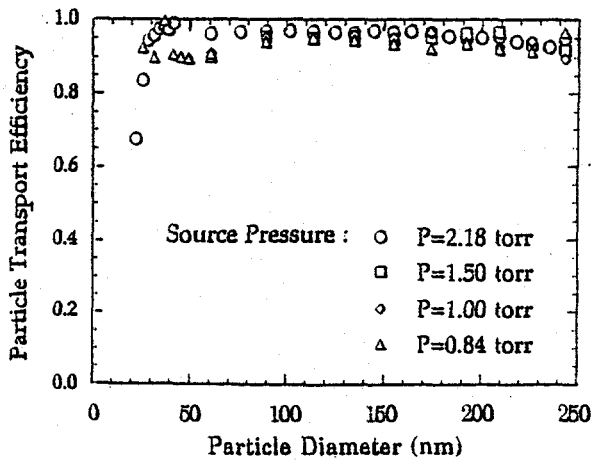

Figure 3. Measured DOS particle transport efficiencies.

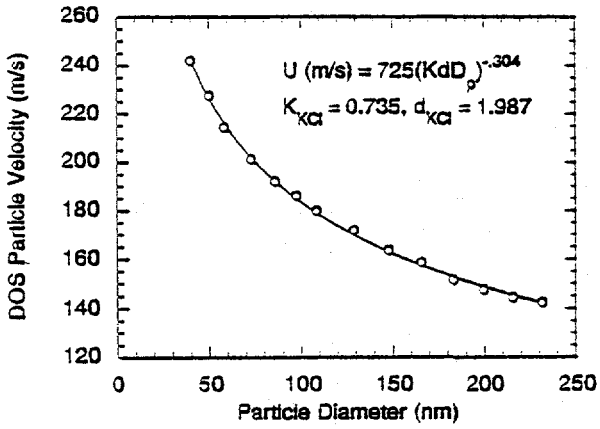

Figure 4. DOS and KCl Particle Velocities.

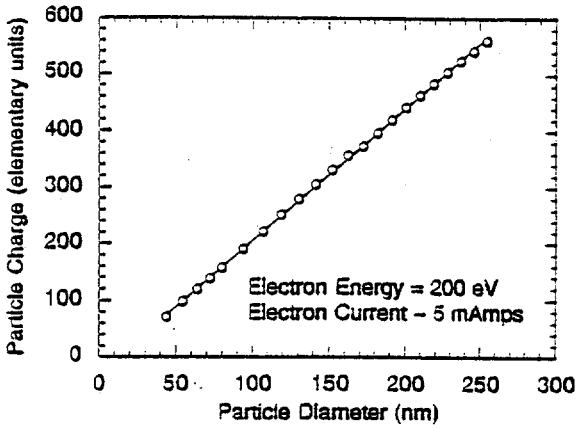

Figure 5. Saturation charging curve for KCl particles.

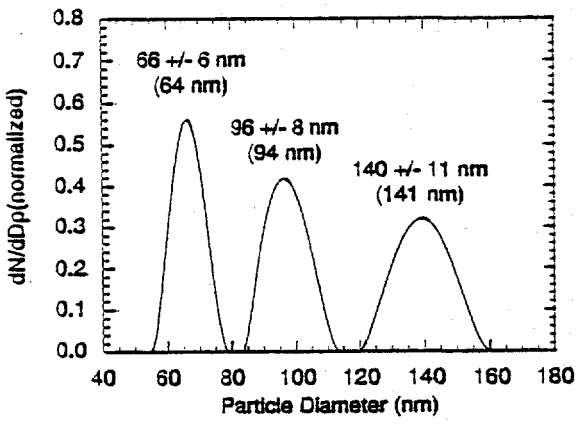

Figure 6. PBMS size distributions of size-selected particles.

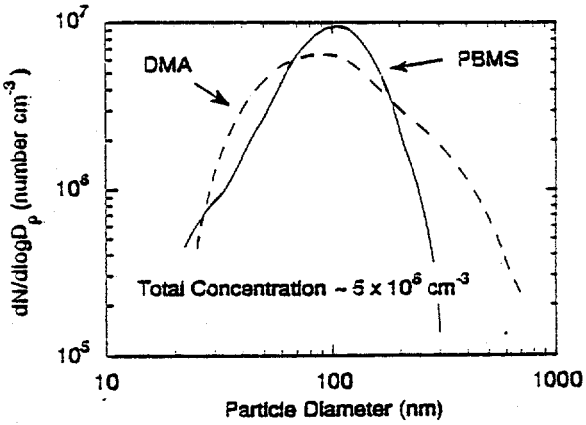

Figure 7. KCl size distributions measured with PBMS and DMA.

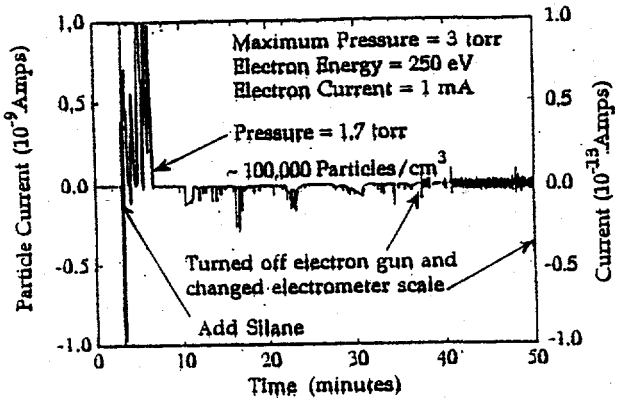

Figure 8. Undeflected particle currents measured in LPCVD.

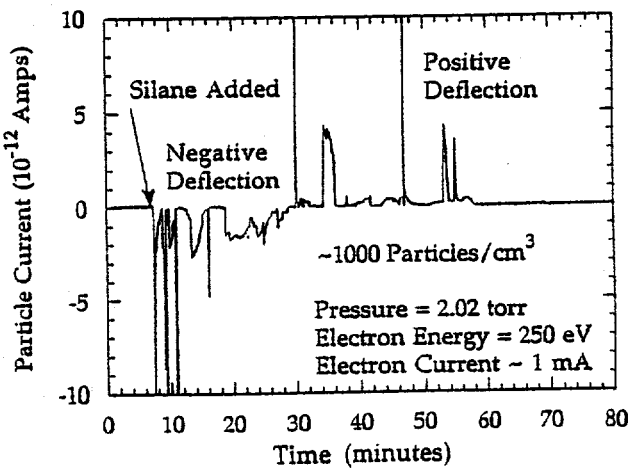

Figure 9. Deflected particle currents measured in LPCVD.

Mass Spectrometer Sampling
of Supercritical Water-Oxidation Reactions

David R. Miller and Sean Maharrey
Department of Applied Mechanics and Engineering Sciences
University of California, San Diego
La Jolla, California 92093-0310

Supercritical water is a useful medium for oxidation of toxic hydrocarbons because under such conditions hydrocarbons and oxidizers are dissolved into a single phase, diffusivities are high, the combustion is complete, and it occurs at relatively low temperatures. There is a large literature on the thermodynamics (1,2), kinetics (3,4), and applications (5,6) of supercritical water oxidation. Supercritical fluids have also been used as solvent carriers in chromatography and the interface of the column output to mass spectrometers has been investigated by many researchers (7-10). In the present investigation we seek to operate a micro-reactor in which supercritical water oxidation kinetics can be examined and for which the output flow can be injected directly into a mass spectrometer system. The motivation for this approach was the microjet burner utilized by Groeger and Fenn for combustion studies (11). Water is one of the more difficult supercritical solvents to interface with the mass spectrometer, compared with CO_2 for example, because the pressures and temperatures are of order 30MPa and 500°C , and because the large water throughput must be removed by the vacuum pumps. We discuss below our reactor design and analysis and the design of the vacuum sampling system.

We have fabricated supercritical nozzles from both stainless steel and from quartz capillary tubing. Despite the fact that supercritical water can dissolve quartz in the ppm range we have been able to operate quartz capillary reactors and nozzles in excess of 20hrs without any measurable degradation in performance. Because these nozzles are much easier to fabricate, especially to diameters below 0.004cm, we have been recently using them exclusively. The major drawback has been the fragile nature of the quartz capillary compared to the stainless steel. The free jet nozzle is formed at the end of the quartz reactor by drawing down the end in a methane flame to any desired nozzle diameter. This variable nozzle diameter is important because it permits us to vary the range of residence times in the reactor. The converging nozzle length is less than two capillary diameters, so the flow time through the nozzle is very short compared with the residence time in the reactor.

Figure 1 shows the reactor assembly. It is designed for high energy density at small scale. An approximately 0.006cm inside diameter quartz tube is used with a nozzle exit diameter in the range of 0.002cm to 0.003cm. This quartz capillary reactor is then inserted inside 0.25cm thin walled tantalum tube (wall thickness 0.012cm) and held away from the tantalum wall by ceramic inserts. Current is passed down the tantalum tube and the net effect is a micro oven which can heat the quartz to 1000°C. In order to maintain the exit end at the required high temperature the current is taken out with small nichrome wire loops selected to run slightly hotter than the tantalum tube; therefore this connection does not serve as a heat sink. Thermocouples are placed inside the tantalum tube and cemented onto the quartz tubing near the exit. The remainder of the reactor is filled with insulating materials. Heat input is measured and calculated by conduction through the reactor walls and convection into the flowing water. Typical performance for an input electrical power of 95 watts to the tantalum is an input power to the water of 78 watts to achieve a water temperature at supercritical conditions of 500°C. The reactor/heater assembly is enclosed within a shell with a nitrogen purge to eliminate any degradation of the heater due to oxygen. A small coaxial flow of nitrogen can therefore be swept out with the free jet; when installed into the mass spectrometer sampling system the tip of the quartz nozzle is pressed against a stainless steel aperture to reduce this flow so that it is insignificant with the mass flow of water.

Figure 2 shows the delivery system. A Varian 8500 high pressure liquid chromatography piston syringe pump is the primary water pump. The reservoir holds 250cc and, depending on the nozzle diameter, steady state run times of about three hours can be achieved. The hydrocarbon and oxidizer are currently premixed and injected with the 12 port injection loop after steady state is achieved. A second nitrogen purge is also introduced inside the quartz reactor before and after each run. This nitrogen system is also used to maintain calibration of the nozzle exit by measuring the decay time of the nitrogen pressure upstream of the nozzle when the nitrogen source is valved off. Any degradation in the quartz exit diameter due to water corrosion can be monitored in this way.

Figure 3 shows the reactor assembly inserted into a small three chamber vacuum system. The water free jet evacuates directly into the first chamber which is pumped by a 330 cfm roots pump backed by a 25 cfm oil mechanical pump. A liquid nitrogen trap is inserted between the

two pumps to trap water upstream of the oil mechanical pump. The remainder of the pumping is standard as is the entire system. The nozzle exit is placed at the optimum nozzle-to-skimmer distance (~1.2cm) as estimated from the literature correlations (12) and the skimmers have been varied from external angles of 30° to 50° with openings between 0.025 cm and 0.125 cm. The aperture between the chopper and quadrupole mass spectrometer chambers can be varied from 0.025cm to 0.1cm. The initial alignment is made with a He/Ne laser and then tuned up with the beam signal. While we have been able to detect inert gas beams with this system we have not yet extracted a good supercritical water beam.

Figure 4 shows results for pure supercritical water mass flow rate through the reactor. These experiments are run to verify the gas dynamic calculations and effective nozzle diameter. The figure compares the measured and theoretical mass flow rates and nozzle diameters over a range of source temperatures and pressures. The theoretical calculation is an integration of the quasi-one dimensional gas dynamic equations. The calculation includes compressible effects, heat transfer and friction along the capillary, and the non-ideal gas effects. The thermodynamics for the non-ideal gas effects are taken into account using the full 78 parameter free energy formulation used to establish the steam tables (13). Several approximate equations of states were examined for $P(\rho,T)$ and $h(\rho,T)$ but none were sufficiently accurate for the complete range of conditions throughout the reactor and into the free jet. There are no adjustable parameters in the figure 4 theory and we feel the calculation is accurate. The error can be accounted for by a 0.001 cm error in the nozzle diameter or errors of order 50°C in the stagnation source temperature at the end of the reactor and just prior to the rapid expansion, or a combination of both. These error values are currently possible. We are most concerned about the temperature measurement and we intend to use time-of-flight measurements on the supercritical water free jet to cross-check the source temperature.

We have calculated and measured reactor conversion rates for the oxidation of acetic acid with H_2O_2 ($CH_3COOH + 4H_2O_2 \rightarrow 2CO_2 + 6H_2O$) in supercritical water in this reactor system. The reaction rate heat release was inserted into the energy equation and, together with the conversion rate, was integrated with the rest of the equations down the reactor. Most of the reaction occurs near the end of the reactor, within the last 50 capillary tube diameters; inclusion of the heat release is necessary for conversions above 10%. Reactor residence times are varied between

approximately 0.1-2 sec by varying the nozzle diameter and source pressure and temperature. The absolute data was made by collecting all of the exiting flow and titrating the acetic acid against 1 N NaOH. Figure 5 shows the experimental results compared with a simple Arrhenius rate law for the loss of acetic acid, $r = -Ae^{-E/RT}C_A$, 1st order in acetic acid and zeroth order in peroxide. Our best fit gives $A = 2.7x10^{10}$ sec^{-1} and E = 167 kJ/gmole. This result is in excellent agreement with the data of Lee (14) who reported values of $2.63x10^{10}$ sec^{-1} and 167 kJ/gmole over the same range. These calibrated conversions will be used to calibrate the mass spectrometer signal.

We have one unusual phenomena periodically occurring with the reactor source in the sampling system. When a metal surface approaches too close to the nozzle we can observe discharges back to the quartz nozzle exit. We believe this may be related to electrokinetic charging of the supercritical water as it flows through the capillary. Such effects have been studied by Faubel and Steiner (15). We are setting up the appropriate probes to measure charges coming out of the nozzle.

REFERENCES

1. Franck, E.U., J. Chem. Thermo., 19, 225 (1987)
2. Brennecke, J.F., and Eckert, C.A., AIChE Journal, 35 (9), 1409 (Sept. 1989)
3. Webley, P.A., and Tester, J.W., SAE Technical Paper Ser., 881039, (1988)
4. Lee, D.S., Li, L., Gloyna, E.F., AIChE Meeting, Orlando, FL. (Mar. 18-22, 1990)
5. Thomason, T.B., and Modell, M., Hazardous Waste, 1 (4), 453 (1984)
6. Shaw, R.W., Brill, T.B., Clifford, A.A., Eckert, C.A., Franck, E.U., Special Report Chemical & Engineering News, Dec. 23, 26 (1991)
7. Randall, L.G., and Wahrhaftig, A.L., Anal. Chem., 50 (12), 1703 (Oct. 1978)
8. Smith, R.D., Udseth, H.R., Kalinoski, H.T., Anal. Chem., 56 (14), 2971 (1984)
9. Hsu, S.H., Lee, E.D., Henion, J.D., Presented at the 35th ASMS Conference on Mass Spectrometry and Allied Topics, Denver, CO., (May 24-29, 1987)
10. Huang, E.C., Jackson, B.J., Markides, K.E., Lee, M.L., Anal. Chem., 60 (24), 2715 (Dec. 1988)
11. Groeger, W., and Fenn, J.B., Rev. Sci. Instrum., 59 (9), 1971 (Sept. 1988)
12. Miller, D.R., in "Atomic and Molecular Beam Methods", Vol. 1, ed by G. Scoles, Oxford Press, New York, pp 14-53 (1988)
13. Keenan, J.H., Keyes, F., Hill, P., and Moore, J., "Steam Tables", Wiley, New York (1969)
14. Lee, D.S., PhD Diss., "Supercritical Water Oxidation of Acetamide and Acetic Acid", Civil Eng. Dept., Univ. of Texas, Austin (1990)
15. Faubel, M., and Steiner, B., Ber. Bunsenges. Phys. Chem., 96 (9), 1167 (1992)

FIGURES

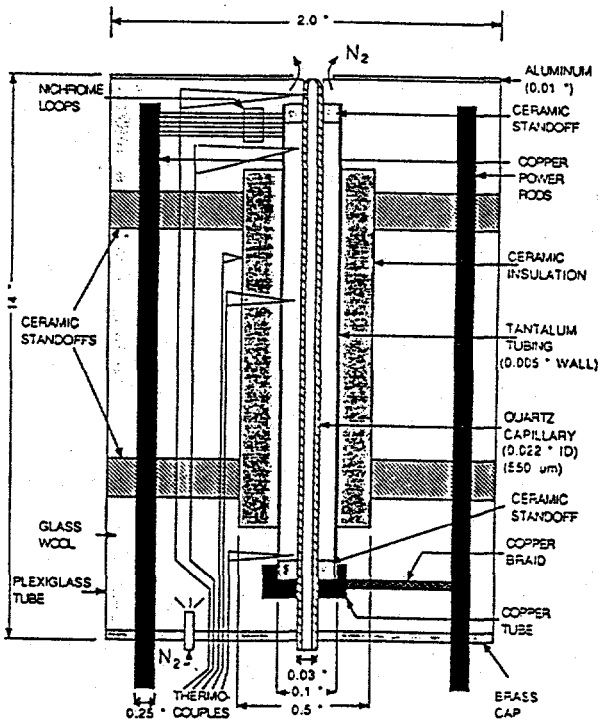

Figure 1. The Reactor

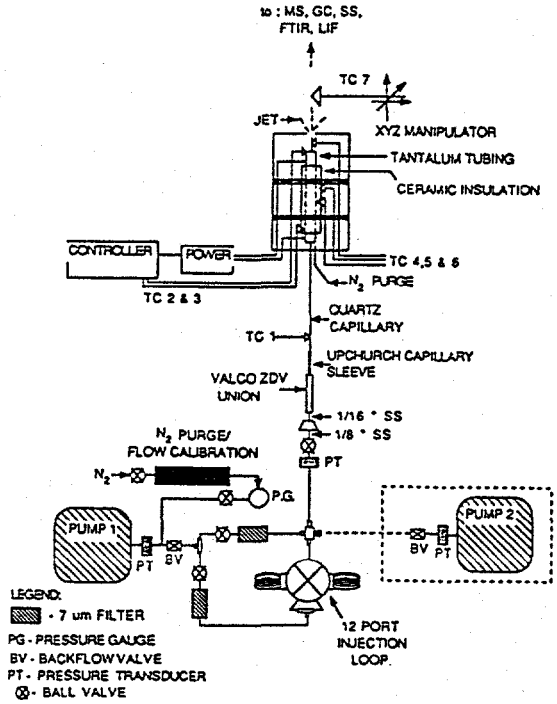

Figure 2. The Delivery System

FIGURES (CON)

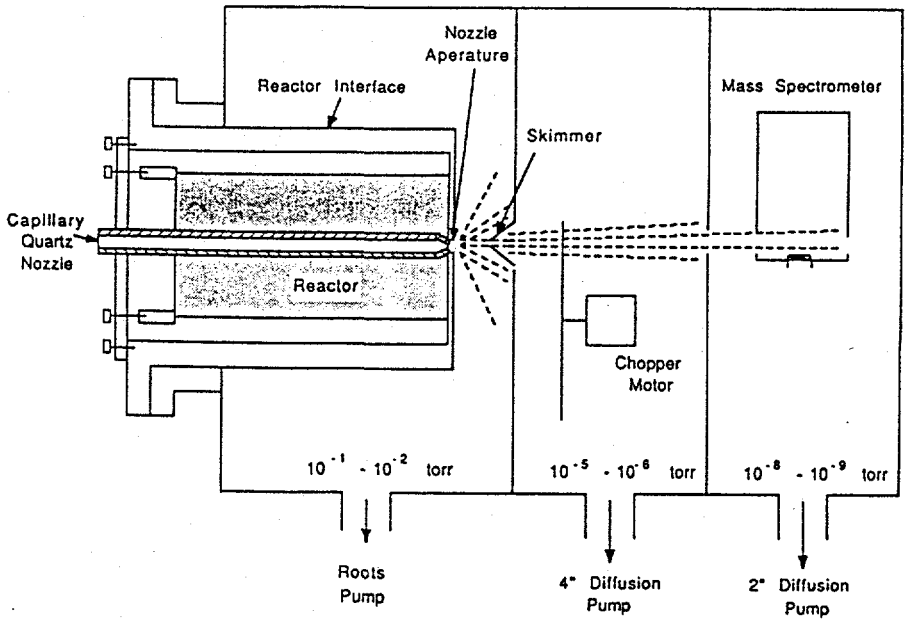

Figure 3. The Mass Spectrometer System

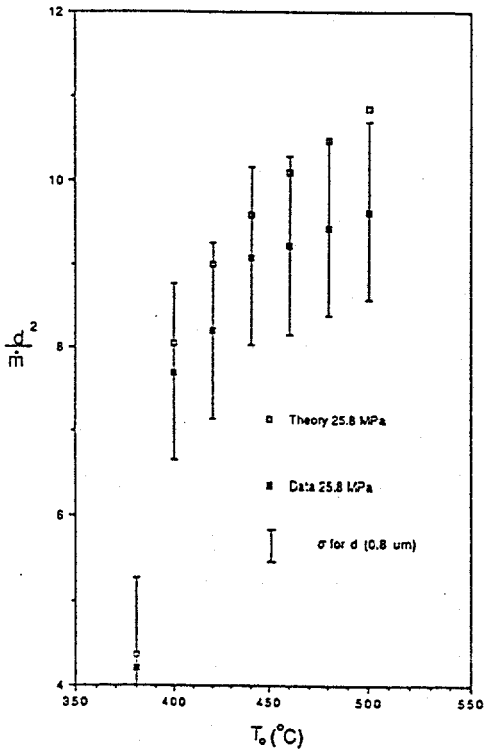

Figure 4 SCW Flow Rate Data at 25.8 MPa versus Temperature. The coordinate is the square of the nozzle diameter divided by the mass flow rate in um²-hr/gm ; nozzle diameters varied from 15 - 25 μm .

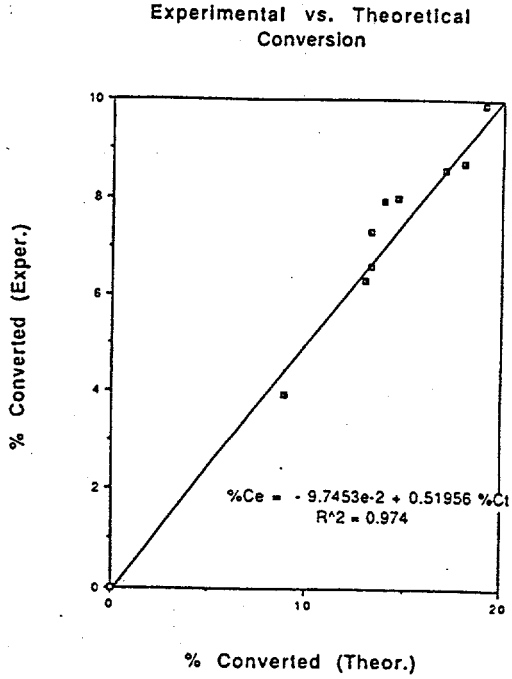

Figure 5. Oxidation of Acetic Acid

Molecular Beam Mass-Spectrometric Study of $H_2/O_2/Ar$ Flame Doped with Phosphorus Compounds

Oleg Korobeinichev, Anatoliy Chernov, Vladimir Shvartsberg, Sergey Il'in
Institute of Chemical Kinetics and Combustion
Siberian Branch Russian Academy of Sciences
630090 Novosibirsk, Russia

The combustion of phosphorus compounds (PC) is of a great interest in connection with the disposal of toxic and hazardous chemical wastes and other undesirable substances containing these compounds. One of the most promising technologies for the disposal of wastes is their incineration. This can totally destroy these toxic and hazardous substances. However, for better reliability and control over these processes one needs to know the mechanism of their combustion and especially its chemical details. An alkylphosphate and an alkylphosphonate are typical organophosphorus compounds (OPC). On the one hand, some of them are industrial wastes. Fro example, tri-n-butylphosphate - TBP - is the product of uranium ore treatment [1]. Phosphorus compounds are applied as additives in polymers for improving their properties. DMMP - dimethyl methylphosphonate - can be used as retardant to polymers [2]. On the other hand, they can be model species for studying the problems of the incinerating pesticides and some of the components of chemical weapons. DMMP is a model simulant of warfare agent sarin. The chemistry of OPC combustion is not understood. Interest in the behavior of phosphorus-containing substances in flames is not limited to the problem of their destruction. These substances (e.g. TMP-trimethylphosphate, phosphine) can act as inhibitors or promoters of the combustion. There are only a few data on chemistry of OPC transformations in flame. In 1980 J.Hastie and D. Bonnell [3,4] studied inhibition of atmospheric $CH_4/O_2/N_2$ and $H_2/O_2/N_2$ bunsen flames doped by TMP using molecular beam mass-spectrometry - MBMS. They detected PO, PO_2 and measured profiles of their concentrations in flame. A.Twarowski [5] studied promotion effect of phosphorus oxides on recombination reaction of H and OH. There are only a few data on mass spectra of OPC [6,7]. The aim of the present paper is to investigate the behavior of TMP and DMMP as typical OPC in a well-studied stoichiometric flame of $H_2 + O_2 + Ar$, stabilized at low pressure on a flat burner. Also this paper deals with the chemistry of these reactions destroying TMP and DMMP in flame. This is achieved by identifying intermediate and end products (including atoms and radicals) by their mass-spectra, and also by measuring the concentration profiles of initial, intermediate and end products. This could well provide a basis for developing a model of OPC combustion.

EXPERIMENTAL

The premixed $H_2 + O_2 + Ar$ (mole fractions: 0.254/0.127/0.619) flame has stoichiometric composition without additives. It was stabilized at 80 Torr on a flat Spalding-Botha burner [8] 24-mm in diameter. The total volumetric flow rate of the unburned gas mixture was 65 cm^3/s (NTP). A uniform distribution of flow velocity was reached with the help of a brass disc with about 250 holes with diameter 0.8-mm each. With such a burner, a flame at 80 Torr is in effect one-dimensional. The burner was moved along its axis to perform sampling using a fixed probe at different distances from the burner. A quartz cone (15-mm high, with an apex angle of 40°, an orifice diameter of 0.2-mm, the width of walls at the top 0.150-mm) was used. The probe was fixed to stainless steel flange cooled with water (Fig 1). Calibrated regulators controlled the flows of each gas of the mixture. A cathetometer provided an exact measurement of the burner's

position inside the combustion chamber. TMP and DMMP (0.03-0.5 vol.%) were supplied by a peristaltic pump or chromatographic syringe via an evaporator into the gas mixture. The combustible mixture was heated to 95° C and then passed to the burner. The temperatures of the evaporator and burner were kept equal to 95° C with a help of thermostat. The combustion chamber and flat burner together with system of combustible gases and liquid OPC supplement and OPC evaporator are shown in Fig.2. Flame temperature was measured using a microthermocouple of platinum - platinum + 10% rhodium, made of wires diameter 50 μm. This was welded together and covered with a layer of SiO_2 (10μm thick). Corrections were made for radiative losses. Molecular beam sampling of the flame enable a quadrupole mass-spectrometer to be used for analysis of the flame gases and measurement of the concentrations of different species in the flame. The mass-spectrometric setup with molecular-beam sampling system shown in Fig.3. is partially described before [9]. Distance probe - skimmer was 20- mm, probe - collimator - 450-mm, probe - ion source - 550-mm. Stage 1 was pumped by oil diffusional pump 1100 l/s, which maintained pressure of the order 5×10^{-4} Torr when a 0.2-mm orifice was used to sample flame. Stage 2 and 3 were pumped by turbomolecular pump 500 l/s, which maintained pressure of the order 10^{-5} Torr (stage 2) and 7×10^{-8} Torr (stage 3) during experiments. Molecular beam was modulated using disc with slits. Modulation of molecular beam with chopper was registered by photocell. Signal of photocell was used at measurement of modulated component of the molecular beam under ion-counting conditions by CAMAC apparatus and computer. The modulation frequency was 49 Hz. The time of measurement was not more than 12 sec. The MS7302 quadrupole mass-spectrometer had a modernized ion source with a small spread of electron energies (±0.1 eV); this permitted operation at low ionization energies close to the ionization potentials of the atoms, radicals and molecules. The concentrations of stable species were determined by direct calibration at ambient temperature by a procedure reported in [10]. The uncertainty in the measured concentration of a stable species is estimated as ±10%.

RESULTS

The probe is known to perturb the flame. In this case the lines of equal concentration near the probe's tip are shifted relative to the unperturbed flame. The magnitude of this shift, Z, can be estimated from [11]: $Z = 0.4D_0(A_0)^{½}$, where D_0 is the diameter of the probe's orifice, A_0 is the sampling degree and equals $4Q/V_\infty\pi D_0^2$. Here Q is the volumetric rate of sampling, V_∞ is the velocity of the unperturbed flow. For the flame described and the probe used Z = 0.6-mm. Although this value is small compared to the width of the flame front (2-3 mm), in the represented data this shift was taken into account. In the profiles of measured concentrations the origin was put at a distance of 0.6-mm from the burner surface. Fig. 4 shows the profile of peak intensities for m/e = 32 (O_2) and 18 (H_2O) in flame without additives and with additive 0.2% TMP. It is seen that small additions of TMP promote combustion by causing an appreciable decrease in the width of combustion zone. The chemistry of TMP reactions in the flame was studied by measurements of the profiles of peak intensities of masses related to the possible intermediate and end products. For these low ionization energies, close to the ionization potentials of these products, were used. Several such products have been found. Figure 5 shows the profiles of peak intensities for m/e=110 in the flame for ionization energies of U = 13.1 eV (curve 1) and 11.6 eV (curve 2). This peak is presented in the TMP mass-spectrum as a fragmentary ion $C_2H_7O_3P^+$ with the appearance potential 11.9±0.2eV. With U = 11.6 eV there is practically no contribution to the peak at m/e = 110 from TMP ion. Curve 2 thus characterizes the concentration profile of the intermediate product resulting from TMP reacting. Now there is not enough data for definitive identification this intermediate. The peak with m/e=100 can be

molecular ion of $PO(OCH_3)_2H$ or for example fragmentary ion of $PO(CH_3O)(OH)_2$. Figure 6 gives the profiles of the peaks with m/e=32 (CH_3OH^+), 31 (CH_3O^+), 30 (CH_2O^+) and140 (TMP^+) in the flame. These were measured for different U: the peaks with m/e=32 and 140 had U=13.1 eV, but with m/e=30 U=16.5 eV was used. Finally at m/e=31 U=11.6 eV was employed. The ions CH_3OH^+ and O_2^+ both contribute to the peak at m/e=32. The contribution of O_2^+ was taken into account by measuring the peak at m/e=34 (oxygen isotope). This profile with m/e=32 in Fig. 6 has had the contribution of O_2^+ subtracted. This profile thus characterizes the concentration profile of CH_3OH.

Figure 7 presents the profiles of mass peak intensities with m/e=80 ($CH_5O_2P^+$, HPO_3^+), 64 (HPO_2^+), 63 (PO_2^+), 48 (HPO^+) and 47 (PO^+) with U=13.1 eV in the flame. Analysing the behavior of these peaks in the flame, it is assumed that the contributions to the peak with m/e=47 of the PO^+ fragmentary ion, being formed from the ionization of PO_2, HPO_2 or HPO, are rather little. Therefore, the profiles of the intensities of peaks at m/e=47 and 64 characterize the concentration profiles of PO and HPO_2, the behavior of the profiles for m/e=64, 63, 48, and 47 points to the following sequence of $H_xP_yO_z$ compound transformations in the flame:

$$HPO_2, PO_2 \rightarrow PO$$

Additive DMMP (0.2%) promotes flame similar to TMP. Relative species concentration profiles have been measured at 124 (DMMP), 64 (HPO_2), 63 (PO_2), 48 (HPO), 47 (PO) and 31 (CH_3O+CH_3OH) amu. We have also obtained relative concentration profile of a mass 110, 94, and 80 intermediates. The peaks for m/e=110, 94, 80 can be molecular and fragmentary ions of $PO(CH_3)(CH_3O)(OH)$. The peak for m/e=94 can be also fragmentory ion of $PO(CH_3)(OH)_2$. The formation of above-mentioned intermediates is most likely to be result of the following reactions:

$PO(CH_3)(CH_3O)_2 + H \rightarrow PO(CH_3)(CH_3O)(OH) + CH_3$
$PO(CH_3)(CH_3O)(OH) + H \rightarrow PO(CH_3)(OH)_2 + CH_3$

Table shows the peak intensities (I_i^0) in mass-spectra DMMP at different ionization energies (IE).

I_i^0	Ion	IE, eV				
m/e		11.5	12	13	13.5	14
124	$C_3H_9O_3P^+$	1	1	1	1	1
94	$C_2H_7O_2P^+$	0.81	1.8	2.5	3.3	4
80	$CH_5O_2P^+$	<0.015	---	---	0.64	---
31	CH_3O^+	---	---	0.04	---	0.16

There is no peak for m/e=110 in mass-spectra DMMP. Following formula was used for calculation peak intensities I_i^* for m/e=94, 31with regard of fragmentation DMMP (I_i - measured peak intensities,without correction):

$$I_i^* = I_i - I_{124}I_i^0/I_{124}^0$$

Fig. 8 shows profile of peak intensities for DMMP and intermediate products of DMMP reacting. Fig. 9 shows profiles of peak intensities for 124, 94 and 80 amu. The profile of the

peak for m/e=110 is not shown on Fig. 9. This peak is about two times higher than the peak for m/e=80 and two times lower than the peak for m/e=94. The possible explanation of promotion: the promoting effect of DMMP and TMP on H_2/O_2 combustion can be explained by the influence of phosphorus oxides on the reaction of H and OH recombination. This termolecular reaction is source of heat release in flame and goes slowly at low pressure. Phosphorus oxides can catalyze this reaction by following way:

$H + PO_2 \rightarrow HOPO$, $OH + H_2 \rightarrow H_2O + H$, $H + HOPO \rightarrow H_2 + PO_2$.

This work was supported by the European Research Office of the U.S.Army under contract N681719C9056.

REFERENCES

1. Bruneau C., Soyer N., Brault A., Kerfanto M., Jornal of Analytical and Applied Pyrolysis, 3. (1981), 71-81.

2. Kettrup A., Ohrbach K-H, Matuschek G., Joachim A. Thermochimica Acta, 166 (1990), 41-52.

3. Hastie J.W., Bonnell D.W., Molecular Chemistry of Inhibited Combustion Systems, National Bureau of Standards Report No., NBSIR, 1980, 80-2169.

4. Hastie J.W.,J.Res.N.B.S.Sect.A., 1973, 77, 733.

5. Twarowski A.,Combust.Flame, 1993, 94, 91-107.

6. Bafus D.A., Gallegas E.J., Kisser R.W. Journal of Phys. Chemistry., v.70, N8, (1966), 2614-2619.

7. Sass S., Fisher T.L. Organic Mass-Spectrometry, vol.14, N5 (1979), 257-264.

8. Botha J.P. and Spalding D.B. Proc. R. Soc. Lond. A225, 1954, 71-96.

9. Amosov K.A., Kuibida L.V., Korobeinichev O.P. and Bol'shova, T.A., in Flame structure. (Ed. Korobeinichev O.P.) Novosibirsk, Nauka S.B., 1991, vol.1, p.93.

10. Peeters J., and Mahnen G., Fourteenth Symposium (International) on Combustion,The Combustion Institute,Pittsburgh,1973,pp.133-146.

11. Korobeinichev O.P., Tereschenko A.G., Emel'yanov, I.D., Rudnitskii A.L., Fedorov S.Yn., Kuibida L.V., Lotov V.V., Fiz.Goreniya Vzryva, 1985, 21, 5, 22-28.

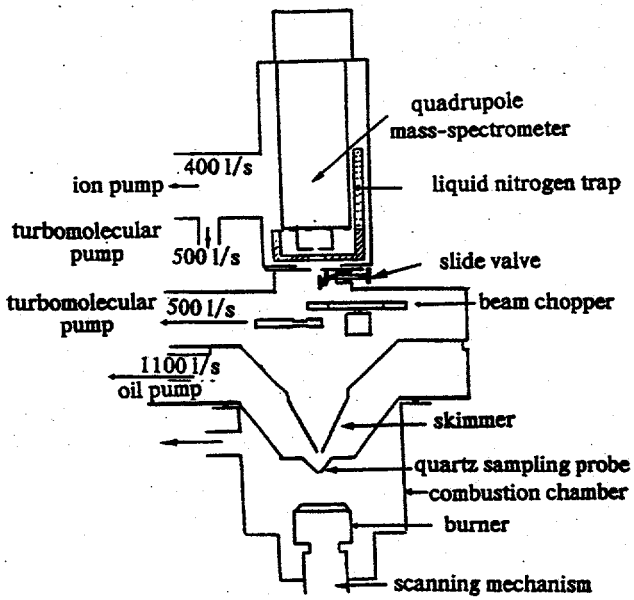

Fig.3. Molecular beam setup for mass-spectrometric studies of flames doped by organophosphorus compounds

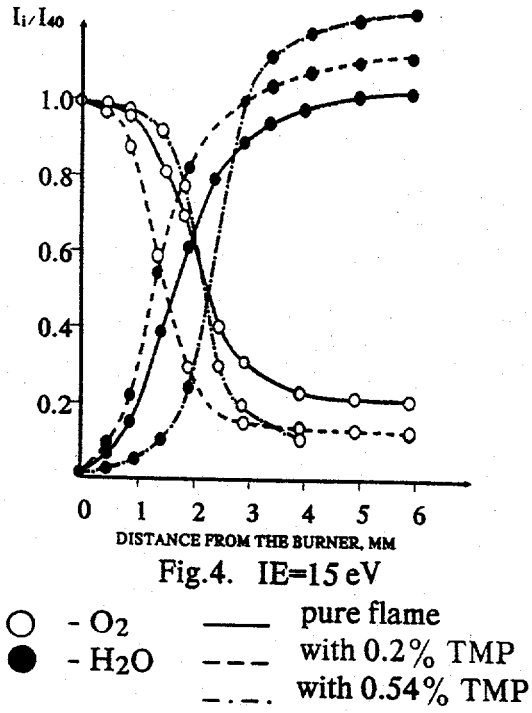

Fig.4. IE=15 eV

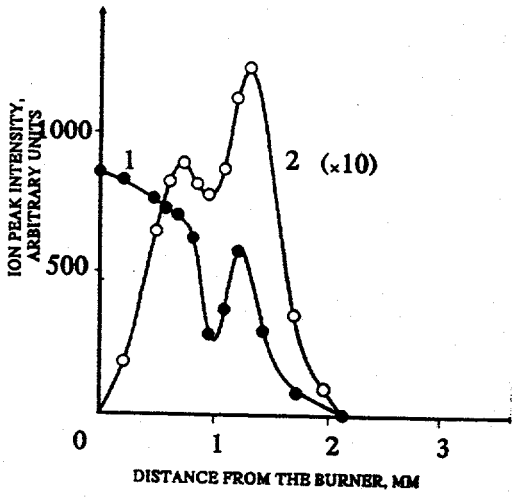

Fig. 5. THE PROFILES OF THE INTENSITIES OF MASS PEAKS WITH M/E = 110 FOR U = 13.1 eV (CURVE 1) AND U = 11.6 eV (CURVE 2) IN THE FLAME OF $H_2/O_2/Ar$ WITH ADDITIVE

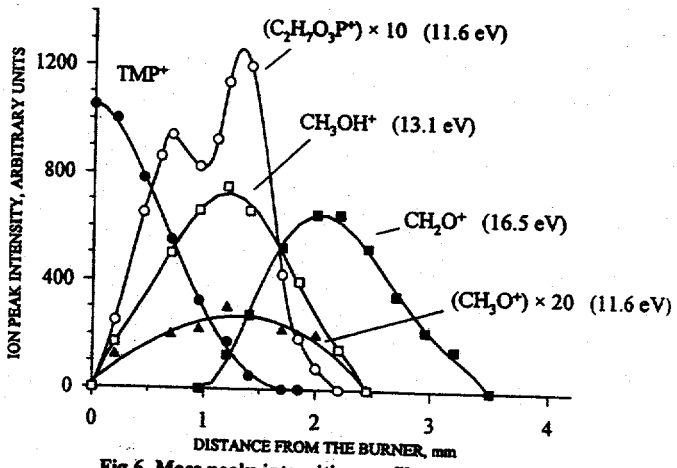

Fig 6. Mass peaks intensities profiles of TMP and some products of its transformation in flame obtained at different ionization energies.

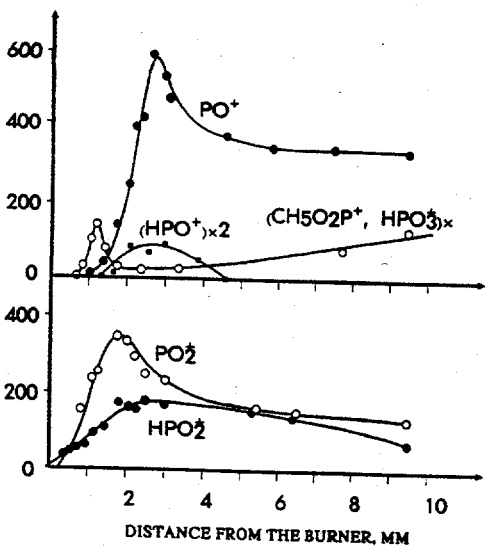

Fig. 7 THE PROFILES OF THE INTENSITIES OF MASS PEAKS IN THE H_2/O_2/Ar FLAME WITH TMP ADDITIVE WITH: M/E = 47(PO^+), 48(HPO^+), 63(PO_2^+), 64(HPO_2^+), 80(HPO_3^+, $CH_5O_2P^+$). U = 13.1 eV.

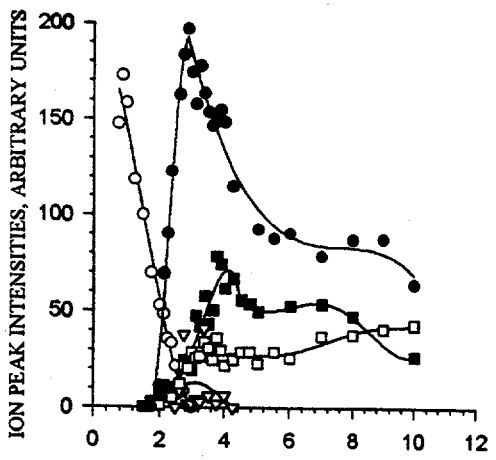

Fig.8 (without the shift) **0.2% DMMP, IE=13 eV**

○ - 124 amu $PO(CH_3O)_2CH_3$ ● - 64 amu HPO_2

■ - 63 amu PO_2 ▽ - 48 amu HPO □ - 47 amu PO

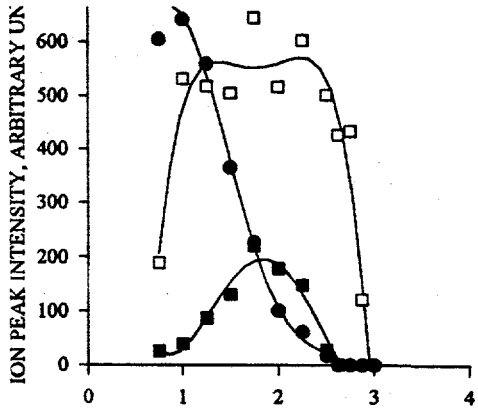

Fig.9 (without the shift) **0.2% DMMP, IE=11.5 eV**

● - 124 amu - $PO(CH_3O)_2(CH_3)$ □ - 94 amu - $PO(CH_3O)(CH_3)H$

■ - 80 amu - $PO(CH_3O)H_2$

Time-of-Flight Mass Spectrometric Analysis of Reflected Shock Zone Gas Mixtures and High Speed Data Analysis

R. D. Kern, H. Chen, H. J. Singh, E. A. Branley and J. Yao
Department of Chemistry
University of New Orleans
New Orleans, LA 70148

The shock tube technique has been applied to the study of high temperature gas reactions employing a variety of analytical devices to monitor selected key species. The reader is referred to a recent review of the shock tube literature for examples and as a guide to previous work.[1]

The focus herein is on a particular technique; the dynamic sampling of the reflected shock zone by time-of-flight mass spectrometry over typical temperature and total pressure ranges of 1200 - 2500 K and 0.15 to 0.5 atm. Recent examples involve the thermal decompositions of propargyl chloride[2] and propargyl bromide.[3] A review of previous work devoted to the reactions pertaining to the pre-particle soot formation process is also available.[4]

Although the coupling of a shock tube to a time-of-flight mass spectrometer offers the kineticist a well controlled environment to investigate the time histories of major and minor species, it must be acknowledged that there are several deficiencies and problems associated with the technique. The deficiencies are identified as an inability to perform trace analysis, detection of H atoms, differentiation of structural isomers, and limitations on the variability of the total pressure in the reaction zone. Many of these deficiencies are resolved with the reliance on complementary techniques such as laser schlieren densitometry, atomic resonance absorption spectrometry, UV and visible absorption, and single pulse shock tube analysis.

One of the challenges associated with shock tubes is the fact that they are single shot experiments occurring over the time scales of 1 μs to 4 ms. A schematic of the apparatus is shown in Figure 1. The reacting gas is ionized at pre-selected fixed intervals; e.g., every 30 μs during typical observation times of 700 μs to 1.5 ms. Each ionizing event produces a mass spectrum which typically covers the range of 1 - 400 amu. 25 - 30 mass spectra are recorded for each experiment at the temperature and pressure of the reflected shock zone. The various reactant, intermediate, and

TOF SHOCK TUBE

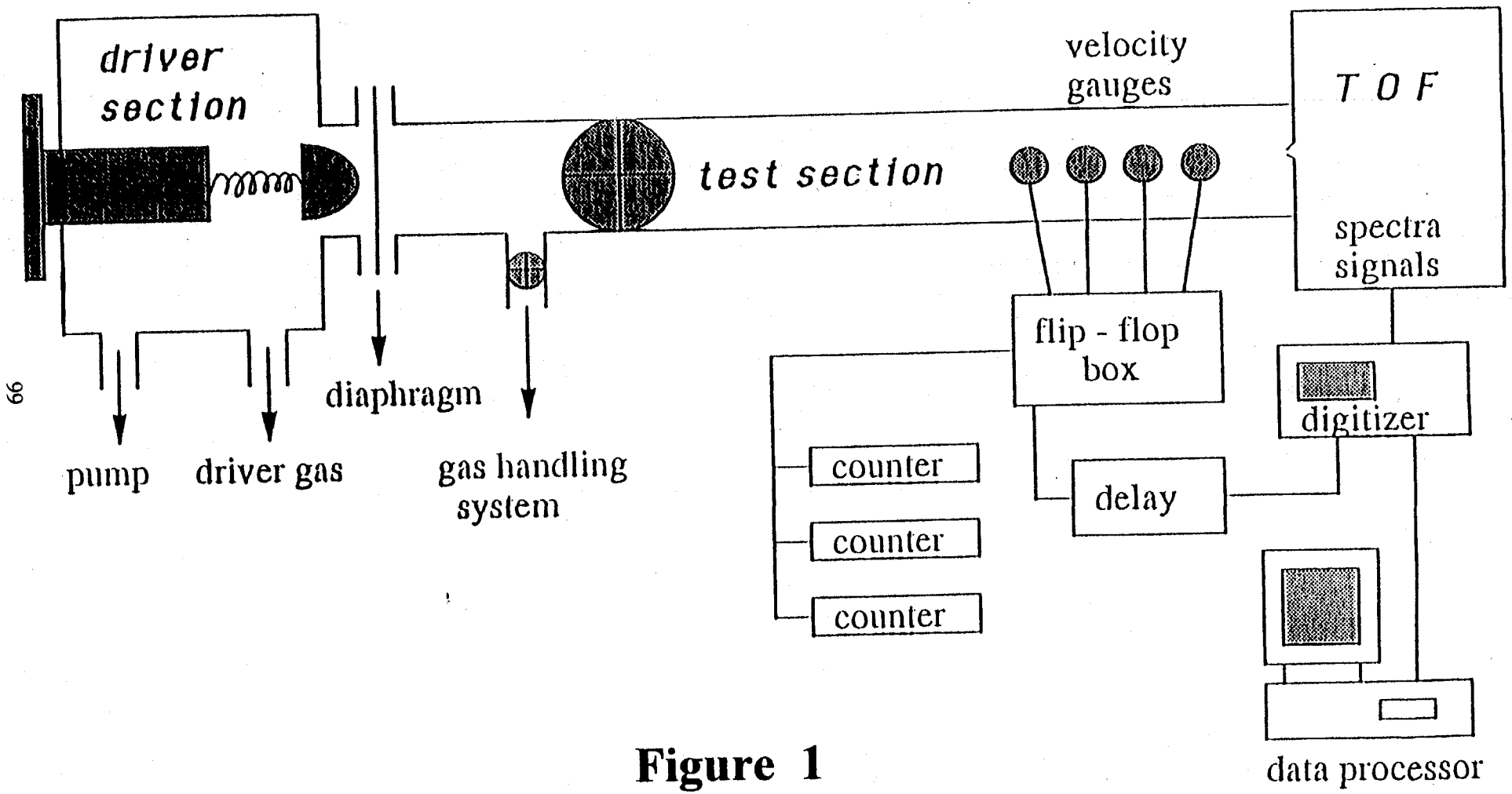

Figure 1

product peak heights are identified and measured as a function of reaction time. Neon is routinely employed as the inert diluent gas. In order to ensure hydrodynamic flow conditions and to minimize the influx of boundary layer into the ion source region, a re-entrant nozzle with a conical height of 1 mm and a 0.1 mm diameter opening at the apex is located at the end plate of the shock tube; the cone height faces the reflected shock zone.[5] The distance from the end plate to the pulsed ionizing beam is critical and is less than 6 mm. Several independent checks on the integrity of the sample have been performed by comparing kinetic and thermodynamic data obtained in other experiments employing different methods of analysis and/or theoretical computations.

The arrival of the shock wave at the end wall produces a sudden increase in the room temperature pre-shock pressure, ~ 5 Torr, to reflected shock pressures in the range 150 - 350 Torr. The particular pressure depends upon the driver pressure chosen for the experiment. One of the serious problems is caused by the sudden influx of gas into the TOF ion source. In order to maintain the TOF operating conditions and to prevent arcing of the high voltage elements in the TOF, two ballast volumes of approximately 5 L capacity each are attached above and below the ion source cross. The TOF vacuum system is composed of two diffusion pumps, 4" and 6", backed by two mechanical pumps with speeds of 500 and 160 L/min, respectively. The driver tank is connected to a 500 L/min pump and the test section to a 160 L/min pump. Measurement of the shock velocity and a knowledge of the thermodynamic properties of the gas mixture allow the calculation of the reflected shock zone gas density (ρ_5), total gas pressure (P_5), and temperature (T_5). A plot of ρ_5 vs T_5 for a mixture of 99 % Ne - 1% Ar is shown in Figure 2. Pressure fluctuations in the gas flow from the reflected shock zone to the ion source are smoothed by taking the ratios of the respective peak heights of reactive species to the peak height of a chemically inert species present in the gas mixture (usually neon or argon) at the same reaction time. Although the individual peak heights for non-reacting species vary during the observation times for a particular experiment, their ratio is reasonably constant as shown in Figure 3. The ratios of individual reactive species to a chemically inert species constitute the basis for the construction of the concentration vs. reaction time profiles. The conversion of peak heights to concentrations is accomplished by shocking the various components of the reacting mixture individually in a series of calibration runs at non-reacting temperatures to determine the respective mass spectral sensitivities. The mass spectral data for these single-shot experiments are collected and stored in a Tektronix RTD 720A digitizer. The digitizer

Figure 2

99% Ne - 1% Ar

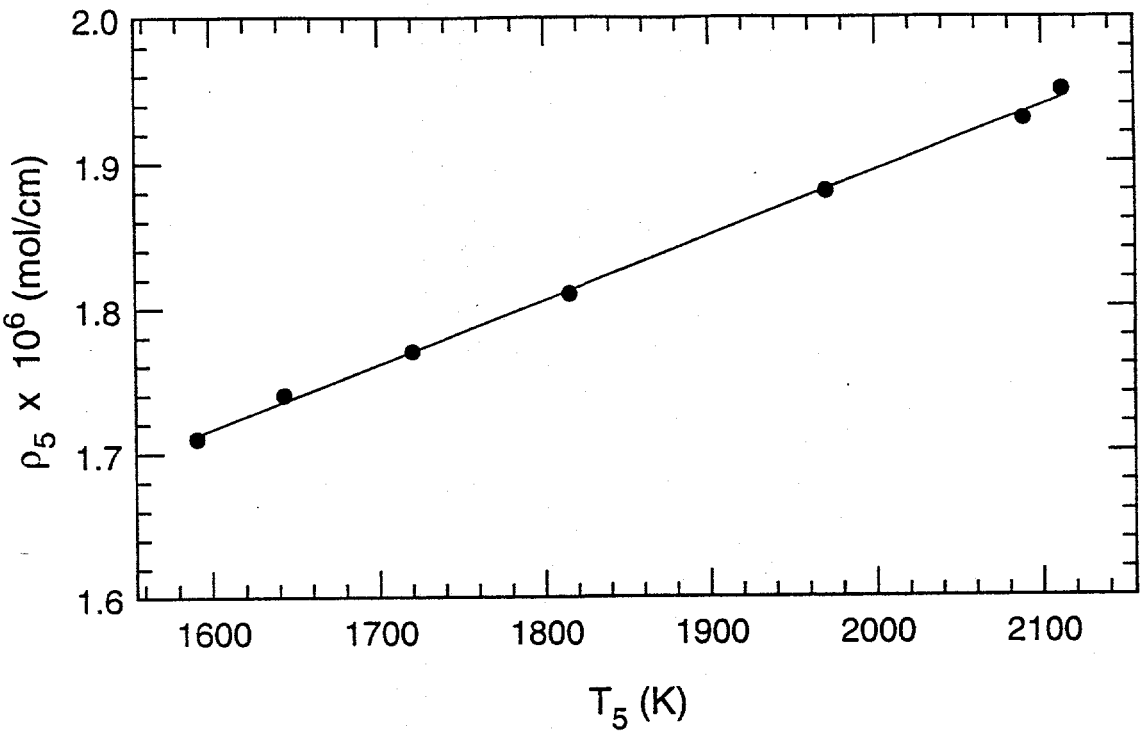

Figure 3

99% Ne - 1% Ar, 1800 K

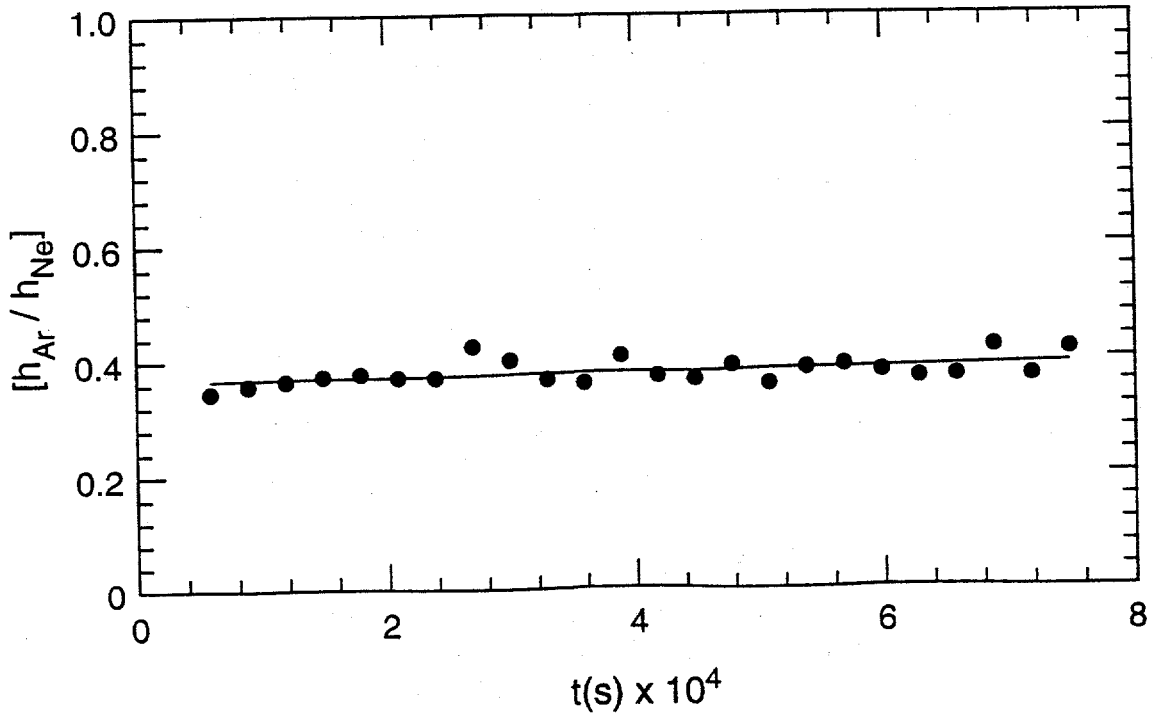

has the capability of storing one million points at various sampling rates: 1 ms observation time (typical) with 1 ns sampling intervals; 2 ms with 2 ns intervals; 4 ms with 4 ns intervals. Since a typical mass peak half-width is 40 ns, at least 10 points at the slowest sampling rate of 4 ns are available to define the peak shape. The data for a given run are transferred to a 486 microcomputer and processed for input into programs used to model the chemical kinetics of a particular reaction.

Two Microsoft QuickBASIC programs are used to transfer the data from the digitizer to the PC and to display the data on the PC monitor. The transfer program uses the NI-488.2 software supplied by National Instrumental Corp. in conjunction with the Microsoft QuickBASIC software. The RTD 720A commands supplied by Tektronix are transmitted to the digitizer over the General Purpose Interface Bus (GPIB). The data stored in the RTD 720A memory are transferred over the GPIB bus to a binary data file on the RAMDISK in the PC. The information concerning the digitizer switch settings is transferred to an ASCII data file on RAMDISK; both files are copied to a floppy for future use. A program written in Turbo-Pascal is used to analyze and process the mass spectral data. The program provides several options for displaying interesting parts of mass spectra, selecting the peak heights of particular m/e values to be measured automatically, and creating files for input into the modeling programs.The reaction profiles for the thermal decomposition of propyne are displayed in Figure 4. The solid lines represent the results of modeling calculations.[6]

Support of this work is provided by the Division of Chemical Sciences, Office of Basic Energy Sciences, Office Of Energy Research, U.S. Department of Energy.

References

1. J. V. Michael and K. P. Lim, Annu. Rev. Phys. Chem. 44, 429 (1993).
2. R. D. Kern, H. Chen, Z. Qin and K. Xie, 19th International Symposium on Shock Waves, 1994, in press.
3. R. D. Kern, H. Chen, J. H. Kiefer and P. S. Mudipalli, 25th Symposium (International) on Combustion, in press, Combustion and Flame.
4. R. D. Kern and K. Xie, Prog. in Energy and Combust. Sci. 17, 191 (1991).
5. J. E. Dove and D. Moulton, Proc. Roy. Soc. London A283, 254 (1961).
6. R. J. Kee, F. M. Rupley and J. A. Miller, Chemkin-II: A Fortran Chemical Kinetics Package, Sandia National Laboratories Report No. SAND 89-8009, 1989.

Figure 4

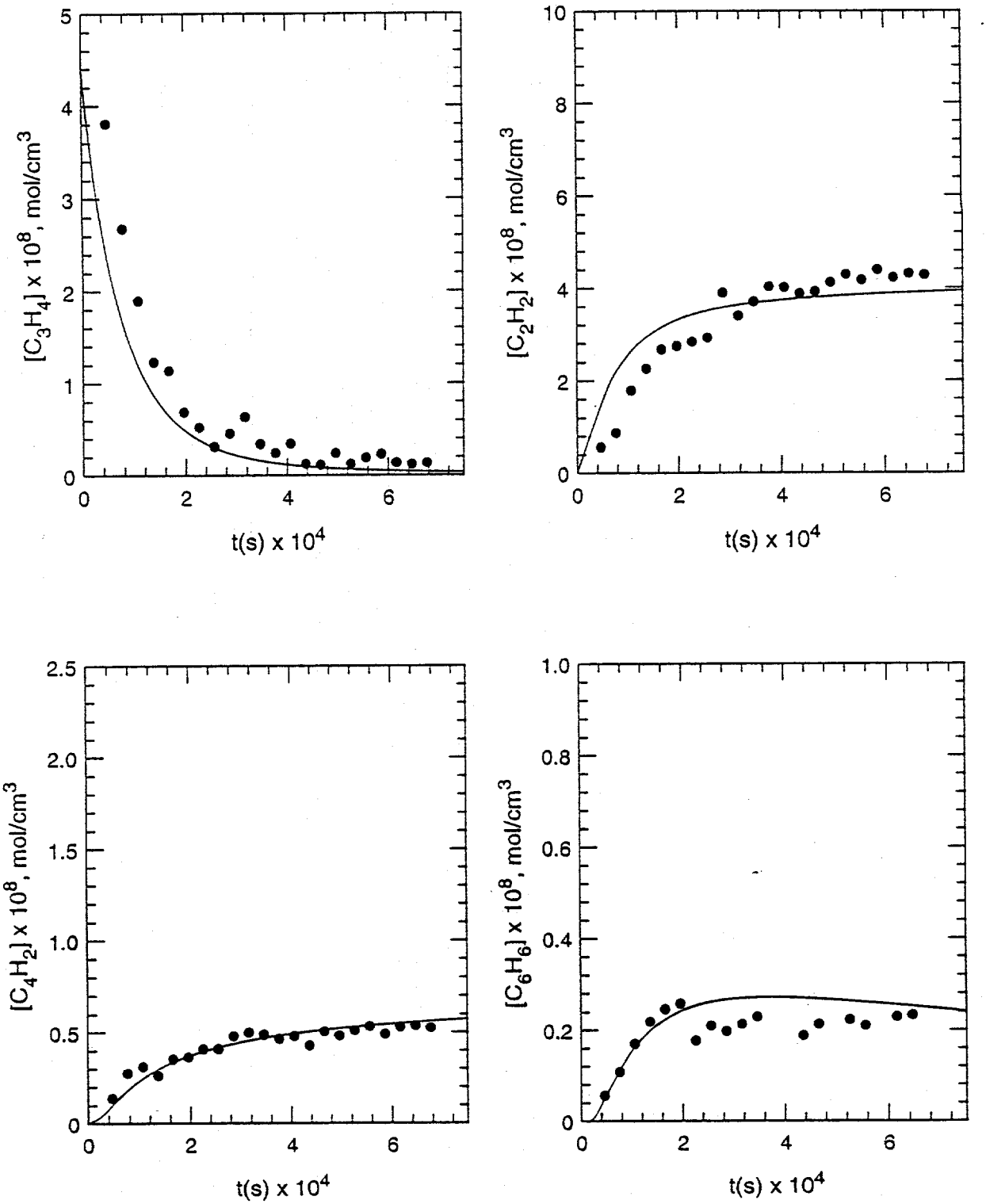
2% C_3H_4P T = 1884 K, P = 0.34 atm
$[C_3H_4] \times 10^8$, mol/cm^3
$[C_2H_2] \times 10^8$, mol/cm^3
$[C_4H_2] \times 10^8$, mol/cm^3
$[C_6H_6] \times 10^8$, mol/cm^3
t(s) x 10^4

MASS SPECTROMETRY AS AN EFFICIENT TOOL FOR KINETIC STUDIES IN FLAMES

J. Vandooren and P. J. Van Tiggelen
Laboratoire de Physico-chimie de la Combustion
Université Catholique de Louvain
B-1348 Louvain-la-Neuve
Belgium

INTRODUCTION

Among the analytical techniques regarding flame structure investigations, mass spectrometry has brought numerous data in several burning systems. Spectroscopic analysis using light absorption or emission and laser techniques like CARS or LIF being more and more sophisticated allow now to determine, at least in relative quantities, the evolution of some species throughout the flame (OH, CN, NO, NH, N_2, H_2O, CO_2,...). However, this non-intrusive techniques can measure only one or two species at a time and the number of different equipments needed to cover the entire set of compounds occurring in a flame will be large. Another technique, but intrusive, the gas chromatography has the advantage to measure all stable species and the sampling can be done with microprobes without strongly perturbing the flame. Unfortunately, the extraction has to be made fast enough to avoid further reactions inside the probe and of course very reactive species like atoms and radicals cannot be recorded. The mass spectrometry coupled with molecular beam sampling allows to monitored by only one technique as well stable species as unstable ones. This technique has been applied to flame studies in the early 70's by Peeters and Mahnen[1] and Biordi et al[2] and since then some similar equipments have been used mainly in Belgium, England, France, Russia and USA. However, this technique using a large conical sampling probe can induce non negligible perturbations of the flame. In addition, the formation of the molecular beam depends on the pressure behind the probe and the pressure depletion through the orifice must be strong enough to keep unstable species alive. It means that the working pressure at which the flame burns, is generally below one atmosphere. Moreover, the reaction zone of the flame which is generally very thin at atmospheric pressure,~ 0.1 - 0.3 mm, needs to be enlarged to ensure a good spatial resolution and to diminish at the same time the perturbing effect of the large probe. This is accomplished by decreasing the working pressure to 10 - 80 Torr. This paper will present the equipment in some details, the data acquisition conditions, the calibration and data reduction, the comparison of the flame structure with some calculated by using the PREMIX code with different reaction mechanisms, the determination of a rate constant of a reaction like CO + OH.

DESCRIPTION OF THE EQUIPMENT

A schematic of the apparatus is shown in figure 1. The combustion chamber, 22 cm in diameter and 40 cm in length contains the Spalding-Botha type burner, 11.5 cm in diameter, upon it a flat flame can be stabilized. Facing the burner is located a quartz cone 3.5 cm high with an angle of 45° at the apex but at a distance of 2 cm from the tip the angle becomes larger, 90-100°. The base of the cone is glued on a stainless steel truncated cone having an angle of about 120° splaying toward the base. This kind of design allows to minimalize the flow perturbation and heat losses. In addition, heat losses on the cooled stainless steel plate supporting the quartz cone have been reduced by covering the plate with a thin foil of ceramic fabric. At the apex of the cone an orifice of about 0.01 cm has been drawn to sample through the flame front. The dimension of the orifice is critical to generate a good molecular beam. Moreover, the cone

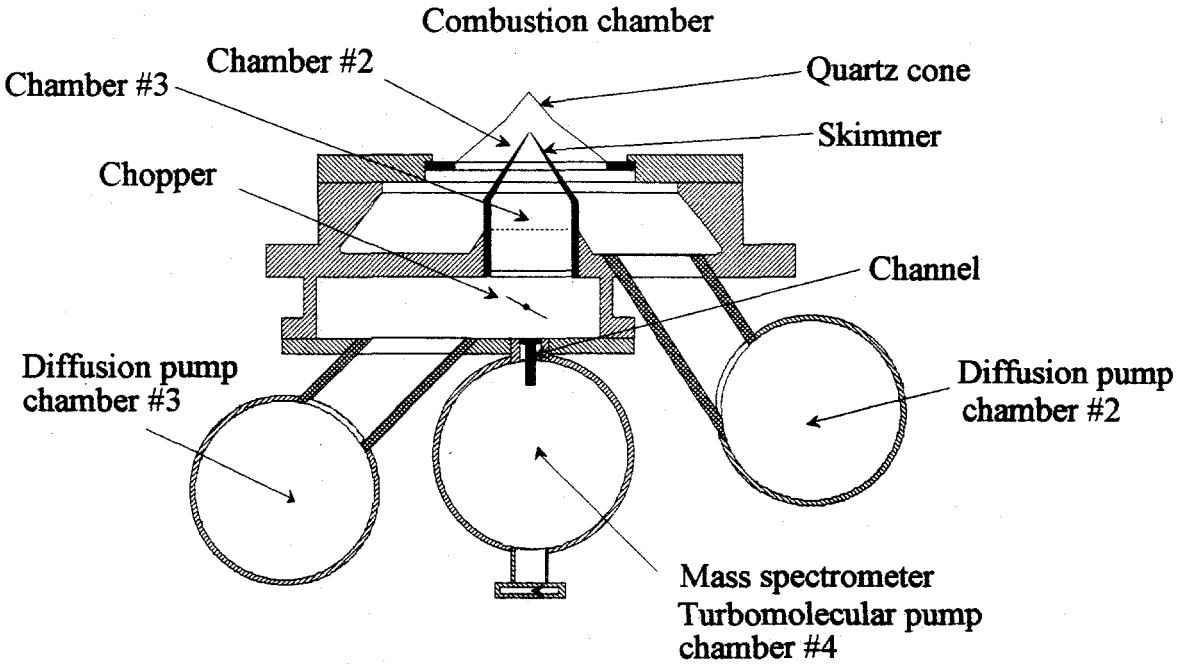

Figure 1. Schematic of the apparatus

surface is treated with fluorhydric acid to lower catalytic radical recombinations. The burner being movable, the sampling can be performed at various heights in the flame up to 10 cm downstream the burner surface. Behind the extraction nozzle, the equipment is made up three successive compartments, differentially pumped, to achieve ultimately high vacuum.

- The extraction chamber immediately behind the quartz cone is evacuated by an oil diffusion pump (300 l/s). The attained pressure is about $5\ 10^{-4}$ to $1\ 10^{-3}$ Torr for working conditions of about 40-50 Torr in the combustion chamber. This arrangement generates a rapid isentropic expansion of the sampled gas at the orifice of the nozzle and therefore the formation of the molecular beam is ensured. The molecular beam composition can be considered identical to that prevailing in the flame at about 0.2 - 0.3 mm upstream the cone tip[3].

- The extraction chamber communicates with the next chamber (modulation chamber) through a conical skimmer having a hole of 0.1 cm in diameter at the top. The pressure in this compartment is about $1\text{-}2\ 10^{-6}$ Torr in operating conditions and it is obtained by a oil diffusion pump (300l/s). The apex of the skimmer is located at 2.5 cm behind the tip of the quartz sampler. This layout allows to select the central part of the molecular jet and impedes the formation of recompression waves and therefore effusive interferences are reduced to a large extent. Inside this chamber, a mechanical device (asynchronous motor with a paddle) allows to modulate the beam for a better signal/noise ratio detection achieved by a Lock-in-Amplifier. The modulation frequency is 32 Hz.

- The modulation chamber connects with the mass spectrometer chamber by a small opening. The shape and the dimension of this opening have been varied in order to enhance the signal. Tests have been achieved with orifices of different diameters (0.7 - 3 mm) and with slits with variable widths. The best signal/noise ratio for OH radicals has been obtained by employing a slit of 1 mm wide (Fig. 2). This chamber pumped by a turbomolecular pump (330 l/s) contains

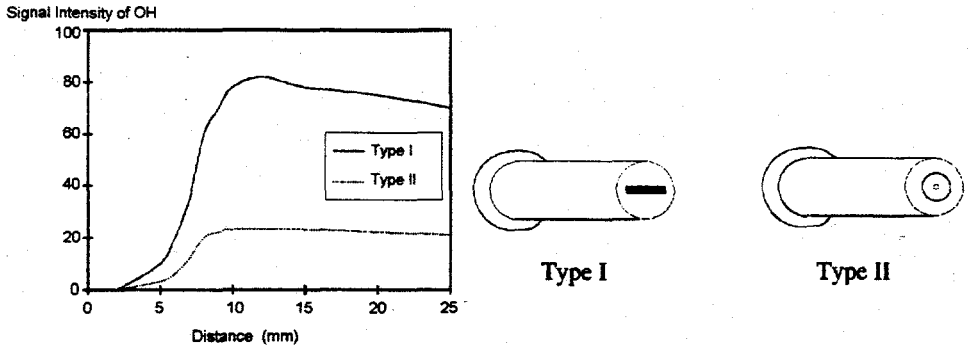

Figure 2. Influence of the size and the shape of the opening between the modulation and the analyzer chambers

a quadrupole mass spectrometer (Balzers QMG-511) operating at a mass range between 1 and 127 a.m.u.. The pressure in this chamber is 1-2 10^{-7} Torr. The axis of the mass spectrometer is perpendicular to that of the molecular beam entering through the opening. The ions produced by electron impact in the ionization source are extracted and collimated in a perpendicular direction with respect to both molecular and electron beams. These ions are separated according to their mass in the quadrupole mass filter. The electron multiplier is located off-axis and amplifies the signal by a factor of 10^5 -10^6 which is further processed by the Lock-in-Amplifier device. The output signals are treated by a data acquisition instrument and collected by a P.C.

EXPERIMENTAL

Mass spectrometer adjustments must be carefully selected in order to measure signal intensities of a well-defined species exclusively. This requirement can be fulfilled in most cases by adjusting the acceleration potential of the electron beam or by selecting an appropiate mass resolution. A compromise between mass discrimination and sensitivity must be chosen for each individual species in connection with the fragmentation pattern.

Mass	$I_{isobutane}/I_{Ar}$x100 673K	$I_{isobutane}/I_{Ar}$x100 408K	$I_{673\ K}/I_{408\ K}$
58	0.079	0.135	0.59
43	50.000	48.400	1.03
42	1.560	1.970	0.79
41	2.870	2.580	1.11
29	0.730	0.720	1.01
27	0.270	0.290	0.94
Mass	$I_{n\text{-}butane}/I_{Ar}$x100 673 K	$I_{n\text{-}butane}/I_{Ar}$x100 408 K	$I_{673\ K}/I_{408\ K}$
58	2.620	5.100	0.51
43	44.500	43.100	1.03
42	0.400	0.456	0.88
41	0.482	0.434	1.11
29	0.651	0.620	1.05
27	0.136	0.170	0.80

Table. Fragmentation pattern of isobutane and n-butane with temperature

So, it has been noticed[4,5] that the fragmentation pattern of some hydrocarbons in the ionization source can vary with the temperature of the sample. As for instance, for n-butane or

isobutane the signal intensities for some fragments varies with the temperature. In such a case, the signal at mass 43 is non sensitive to the temperature while at mass 58 is strongly dependent (Table).

The energy of the electron impact has also to be carefully selected in order to avoid large interferences from fragmentation contribution. So, as an example, to detect OH radicals free of any interference in an H_2/O_2 flame, it is necessary to work at an acceleration potential of the ionizing electrons of 18 eV.

$OH + e \rightarrow OH^+ + 2e$ 13.2eV

$H_2O + e \rightarrow OH^+ + H + 2e$ 18.3 eV

Sometimes it is practically impossible to avoid contribution from fragments. However, very often the contribution proceeds from stable species occurring in large quantities in flames and assuming that the fragmental contribution is independent from the temperature it is possible to substract the contribution from the overall signal. In such cases, the ionizing potential has to be selected low enough in order to minimize this contribution with respect to the global signal. For species having a similar mass like CH_3OH and O_2, 32.043 and 31.999 a.m.u. respectively and very close ionization potentials, the mass resolution of the mass spectrometer must be at least 745, which is too high for our equipment. However, in such a case, both signals can be discriminated by taking into consideration the wings of the recorded signal. Adjusting the mass properly out of the maximum of the signal, on both sides, the separation can be made and easily tested by an appropiate mixture of the two gases.
When the difference in mass is to low, like for N_2O and CO_2, it is necessary to use the isotopic pattern abundance of C and N. This procedure has been used in CH_4/N_2O flames with a certain success by measuring profiles at masses 44 and 45 u.m.a.[6].

CALIBRATION

The measured intensity I_i is directly related to the molar fraction by the sensitivity factor S_i which depends on the ionization cross sections, the sampling conditions and the sensitivity of the mass spectrometer: $I_i = S_i X_i$. The factor S_i depends also on the temperature and on the mean molecular weight, but varies on a similar way for all species as it has been demonstrated by Peeters and Mahnen[1] who used a mixture of He and Ar to check their constant ratio throughout the flame. This means that the ratio S_i/S_j remains constant wherever in the flame. Therefore for stable species, ratios S_i/S_j can be deduced using calibrated mixtures of i and j species. So $S_i/S_j = (I_i X_j / I_j X_i)_{cal.}$. However, for such a calibration, the signal intensities of a given species recorded in the calibrated mixture and in the flame itself must be measured keeping the settings of the mass spectrometer totally identical. Thus $(I_i X_j / I_j X_i)_{cal} = (I_i X_j / I_j X_i)_{fl.}$
In the burnt gases region, signal intensities of species related to the H_2/O_2 system are related one to each other by a certain ratio corresponding to the so-called partial equilibrium. It means that some reactions reach their own equilibrium from a given distance downstream in the post-combustion zone. The reactions are

$O_2 + H \rightarrow OH + O$ (1)

$H_2 + O \rightarrow OH + H$ (2)

$H_2 + OH \rightarrow H_2O + H$ (3)

and therefore some combinations of the above processes

$OH + OH \rightarrow H_2O + O$ (4)

$OH + OH \rightarrow H_2 + O_2$ (5)

In systems containing CO and CO_2 as products, the equilibrium of the reaction $CO + OH \rightarrow CO_2 + H$ is attained further downstream in the burnt gases.

The occurrence of this partial equilibrium allows to determine the absolute concentrations of H, O, and OH radicals in the burnt gases region providing that, the temperature is known. Therefore, according to processes (1) to (3) and with the equilibrium constant K of the corresponding reaction, the mole fractions of H, O and OH are deduced. However in rich hydrocarbon flames this procedure is not applicable by the fact that some reactions producing higher hydrocarbons continue to proceed in the burnt gases. In general the calibration of H, O, and OH in any system can be made by comparing the signal intensities with those measured in an hydrogen oxygen flame where the calibration has been made carefully. Moreover, in the burnt gases region, the equation of the conservation law of the total number of atoms is applicable and therefore can be used for the calibration purpose too.
For intermediates, stable or unstable, like CH_3 in methane flames, it is assumed the simple additivity of ionization probability of the atoms which constitute the molecule (Q_H=0.65, Q_C=1.8). The calibration is made by comparison with CH_4 by using the expression $X_{CH_3} = \frac{Q_{CH_4} I_{CH_3}}{Q_{CH_3} I_{CH_4}} X_{CH_4}$. Signal intensities ($I_i$) are recorded at ionizing potentials corresponding to the same energy increment with respect to the ionisation potential for CH_3 and CH_4, respectively. Q_i are calculated along the additivity approximation of Q for the elements.
The individual mole fractions profiles are determined by comparison with the calibrated value somewhere in the flame and the signal intensities profiles. Finally, the mole fractions at every distance in the flame are normalized in order to obey to the equation $\Sigma X_i = 1$.

VALIDATION OF REACTION MECHANISMS

The validation of a reaction mechanism can be performed by comparing the experimental structure with the calculated one. The temperature profile measured by means a Pt/PtRh thermocouple, 0.1 mm in diameter and with the junction located at 0.2-0.3 mm upstream the tip of the sampling cone has been used as an input parameter. This procedure allows to consider that the temperature is measured in the same perturbed conditions as the individual mole fraction profiles. As an example, the experimental mole fractions profiles of rich H_2/O_2/Ar flame [7], burning at 35.5 Torr, has been used to validate several reaction mechanisms of the H_2/O_2 system. The experimental mole fraction profiles of stable species, atoms and radicals have been compared with those calculated by using the PREMIX code. The comparison has been made with four different mechanisms: Miller et al's[8], Dixon-Lewis's[9], Westbrook's [10] and Warnatz's [11].The best agreement is observed for Miller's and Westbrook's mechanisms. For radicals some mechanisms can lead to calculated values diverging by a factor of 2. It means that even for a very simple system, the rate coefficients used for "well known" reactions can differ by a substantial amount.

DATA REDUCTION AND DETERMINATION OF RATE CONSTANTS

The experimental data can be used to determine rate coefficients at high temperature. This implies to calculate mole flux profiles of some species in order to discriminate chemical processes from physical ones. It has been observed that the binary approximation instead of considering multicomponent diffusion processes gives the same results when a species is in large concentration like argon or oxygen or nitrogen. The mole flux can be then expressed as $F_i = N_o T_o \left[\frac{V_o M_o}{T_o M} X_i - \frac{D_{ij}}{T} \left(\frac{dX_i}{dz} - X_i \frac{d \ln M}{dz} + k_T \frac{d \ln T}{dz} \right) \right]$ where N_o, T_o, M_o and V_o are the initial total concentration, temperature, mean molecular weight and velocity respectively. D_{ij}, the binary diffusion coefficient, k_T the binary thermal diffusion parameter, z the distance. The gradient of the mole flux of a given species at a given distance from the burner corresponds to the net molar reaction rate of the species at that distance. From these data and by assuming a

simplified mechanism or by introducing some known rate coefficients in the kinetic scheme, it is possible to deduce some rate coefficients in a specific temperature range. So, the rate coefficient of the reaction CO + OH has been deduced in a large temperature range in a $CO/H_2/O_2$ flame[12]. The figure 3 exhibits two sets of data. One corresponds to the values obtained by using the temperature profile measured in the absence of sampling probe (T_{far}), the second with the temperature measured close to cone tip (T_{close}). It is noticeable that a better agreement is obtained with the literature data when the temperature is measured close to the nozzle.

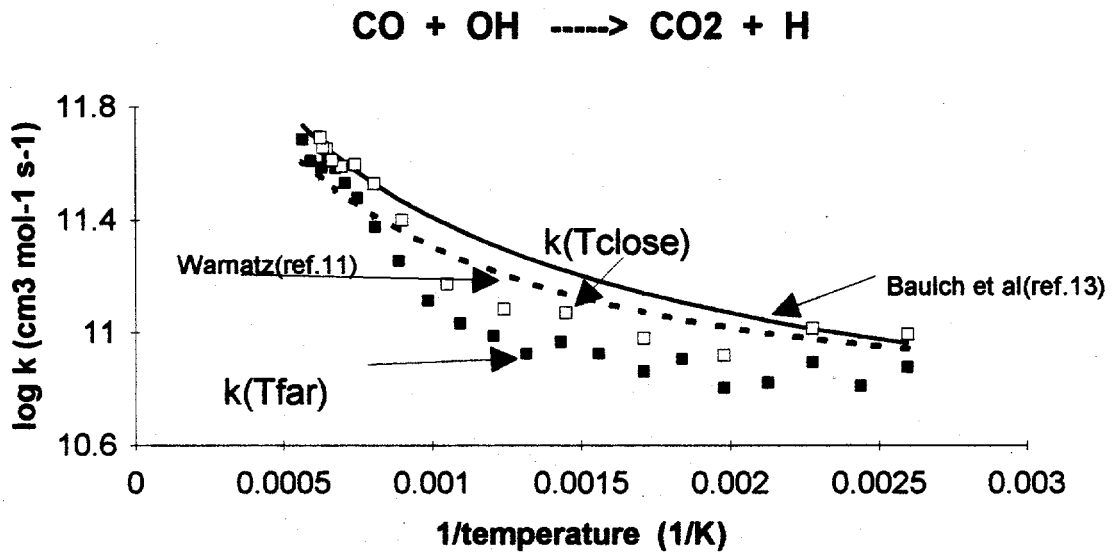

Figure 3. Rate constant deduced using the temperature profile far or close to the tip of the nozzle

CONCLUSIONS

The ability of the mass spectrometry coupled with molecular beam sampling to establish flame structures is unquestionable. However data acquisition must be made carefully and by taking into account possible interferences. The technique provides useful data for validation and even for rate coefficient determinations.

References

1. J. Peeters and G. Mahnen. Fourteenth Symposium (International) on Combustion. p. 133, 1973
2. J. C. Biordi, C. P. Lazzara and J. F. Papp. Fourteenth Symposium (International) on Combustion. p.367, 1973
3. T. A. Milne and F. T. Green. Tenth Symposium (International) on Combustion. p. 153, 1965
4. B. Smets and J. Peeters. Second European Symposium on Combustion. Orléans, p. 38, 1975
5. B. Walravens, J. Vandooren and P. J. Van Tiggelen. Bull. Soc. Chim. Belges 99, 461, 1990
6. J. Vandooren, M. C. Branch and P. J. Van Tiggelen. Comb. and Flame, 90, 247, 1992
7. J. Vandooren and J. Bian. Twenty third Symposium (International) on Combustion. p.341, 1990
8. J. A. Miller, M. D. Smooke, R. M. Green and R. J. Kee. Comb. Sc. Techn. 34, 149, 1983
9. G. Dixon-Lewis. Archivum Combustionis 4, 279, 1984
10. C. K. Westbrook. Comb. Sc. Techn. 34, 201, 1983
11. J. Warnatz. Combustion Chemistry (Gardiner W.C. Jr. Editor) p.197. Springer-Verlag NY1984
12. J. Vandooren, J. Peeters and P. J. Van Tiggelen. Fifteenth Symposium (International) on Combustion. p.745, 1975.
13. D.L. Baulch, C. J. Cobos, R. A. Cox, C. Esser, P. Frank, Th. Just, J. A. Kerr, M. J. Pilling, J. Troe, R. W. Walker and J. Warnatz. J. Phys. Chem Ref. data, Vol. 21, 1992

Obtaining Kinetics from MBMS and Modeling of Propene Flame Structure

Phillip R. Westmoreland, Scott D. Thomas, and Anuj Bhargava
Department of Chemical Engineering, University of Massachusetts Amherst
159 Goessmann Lab, Box 33110; Amherst, MA 01003-3110
413-545-1750; FAX 413-545-1647; westm@ecs.umass.edu

Abstract

Molecular-beam mass spectrometry is being used to map hydrocarbon flat flames for subsequent modeling. The paper focuses on describing our apparatus and its use. Difficulties and solutions for modeling MBMS flame data are discussed using the particular case of a fuel-lean flat flame of propene, oxygen, and argon (ϕ = 0.229, 30 Torr, v_o = 57.5 cm/s at 298 K). Here, the MBMS technique has led to the identification of new kinetics for allyl + O_2 at high temperatures.

Introduction

Molecular-beam mass spectrometry (MBMS), when combined with reaction theory and modeling, has been especially useful for unraveling details of combustion chemistry. Ideally, it yields concentration profiles of many different radical and stable species with only modest perturbation by the sampling cone. Other necessary data are temperatures and area expansion ratios.

The technique was exploited effectively by Lazzara, Biordi, and Papp at the Bureau of Mines, Pittsburgh, to study CH_4 flames and flame retardants.[1] That flame MBMS apparatus is now at the University of Massachusetts Amherst, where it has been modernized and used in studies of hydrocarbon oxidation and molecular-weight growth.

Apparatus and Procedures

The original apparatus has been described in detail by Biordi[1] although it has been extensively modified and updated (Fig. 1).

Flame system. Fuel, O_2, and Ar flows are set (MKS Baratron mass flowmeters and controllers), mixed thoroughly, and fed into the flame chamber through a 13-cm-diam., sintered-metal, water-cooled burner. The mixture is ignited by a Tesla-coil-generated spark from a wire positioned near the burner. Because the flat flame is stabilized by heat loss to the burner, the position of the MBMS sampling nozzle along the flame axis is set by moving the burner, leaving the sampling nozzle fixed. Pressure is set approximately at 20 to 40 Torr using a 6-inch vacuum gate valve in the exhaust line,

operated as a critical-flow "orifice" to isolate the burner chamber from any downstream pressure variations. Precise control of flame-chamber pressure is then maintained by a capacitance manometer, pressure controller, and flow-control valve (MKS), which leaks a controlled ballast flow of air into the exhaust line just upstream of the gate valve. From the flame chamber, burned gases are pumped away through the gate valve to a Roots blower and 300-cfm mechanical vacuum pump (Stokes Microvac 412H-10).

Molecular-beam mass spectrometry. The molecular beam is formed and analyzed in a two-stage vacuum system mounted above the burner chamber. Background pressures in the stages are approximately 10^{-2} Pa (10^{-4} Torr) and 0.1 mPa (10^{-6} Torr) or less, respectively. With a quartz sampling nozzle of the 40°/90° hybrid type described by Biordi *et al.*,[2] flame molecules are supersonically expanded, cooling them to nonreacting temperatures and bringing them into free molecular flow. Molecules in this first stage are collimated by a 2.1-mm-diameter skimmer nozzle 18 mm behind the first nozzle, creating the beam that enters the second stage; the beam is chopped (e.g., at 340 Hz) within the second stage using a toothed-wheel chopper. Each stage is pumped by a 300 liter/sec, 6-inch diffusion pump (Vacuum Enterprises X-610) aided by an liquid-N_2-cooled cryotrap and roughed by a mechanical vacuum pump. The second, mass-spectrometry stage also contains a liquid-N_2-cooled cold trap beside the mass spectrometer which acts as a supplementary cryopump. Pressure-gauge interlocks and pneumatic valves are used to control the vacuum system during start-up, routine shutdown, and emergency shutdown. Pressures are measured with thermocouple and ionization gauges.

Beam species are measured in the second stage using a quadrupole mass spectrometer (Extranuclear Laboratories (now Extrel)) with electron-impact ionization. Molecules and radicals are ionized at electron energies slightly above ionization potentials of the species to avert fragmentation. The resulting ions are formed into an ion beam and are focused by electrostatic lenses into the quadrupole. Mass number is dialed into the quadrupole power controller or set by a digital mass programmer (both by Extranuclear). Signal then is collected with am off-axis, channeltron-type electron multiplier (Galileo Electro-optics 4816), which can be operated to give analog or pulse (single-ion) electron multiplication. For the analog signal, background is subtracted from the beam using a lock-in amplifier (Princeton Applied Research Model HR-8) tuned to the resonant circuit of the chopper. For high-sensitivity pulse counting, photon-counting electronics (PARC/SSR Instruments Model 1110) are used. Foreground and background counting windows are established by mapping them directly, using narrow time intervals and a strong signal.

An AT-class personal computer (AST Premium 286) and a data acquisition board (Scientific Solutions Labmaster) are used to collect, plot, and store the data. Analog data

from the lock-in amplifier are measured in a scaled range of -10 to +10 V with 12-bit precision, while the pulse-counting data are logged as BCD integer counts with a parallel I/O port. Signal vs. position, calibration data, or signal vs. electron energy (an ionization efficiency curve) are recorded, corrected for isotopic interferences (successive subtraction from M-1 and M-2 peaks), and plotted using software which we have developed.

Calibration for mole fractions are by direct measurement with prepared gas mixtures for all major stable species except H_2O, by oxygen balance for H_2O at a point late in the flame, by overall mass balance throughout the flame for Ar, and by the method of relative ionization cross-sections for radical species. Mass discrimination within the beam is not measured separately in this apparatus. This potential complication is controlled by sampling complete mixtures of calibration gases from the burner chamber at process velocities and densities, set by flow controllers and chamber pressure control.

Standard procedures compensate for any drift in system electronics. Signals are measured in the pattern Ar, gas(es) of interest, Ar. Also, the flame is sampled beginning in the post-flame zone, moving to the burner, and moving back out to the post-flame zone. In fuel-rich flames, deposits on the nozzle are burned away periodically with a lean flame.

Temperatures and area expansion ratios. Temperatures are measured with 0.076-mm Pt/PtRh thermocouples, constructed with beadless welds for good spatial resolution and to allow use of heat-transfer coefficients for flow normal to a cylinder. These thermocouples are coated with a noncatalytic Y_2O_3/BeO glass, applied in the manner of Kent.[3] Temperatures are then obtained using a heat-loss compensation method.[4] The thermocouple is resistively heated with an AC current, filtered from the DC thermocouple voltage. The temperature/heating-current curve in the flame (convective and radiative heat transfer) is compared to that in a vacuum (only radiative heat transfer). When the flame and calibration measurements match, the thermocouple is measuring flame temperature because the temperature difference (and thus the convective heat transfer) between the thermocouple and flame is zero; the only heat transfer is then by radiation, just as in the calibration.

Area expansion ratio $A(z)$ is calculated from velocity measurements obtained with hot-wire anemometry in room-temperature gas. $A(z)$ is the flow cross-section at position z ratioed to the initial cross-section, but it is also the density-velocity product rv ratioed to the initial value $(rv)_o$. By measuring velocity vs. z using cold gas at a constant, flame-like density, $A(z)$ is found as the velocity ratio.

Data analysis. With mole fractions x_i of the i species, T, $A(z)$, and calculated diffusivities $D_{i,mix}$, we calculate the total concentration $c = P/RT$, the species fluxes F_i:

$$F_i = x_i\, cv{\cdot}A(z) - D_{i,mix} c \frac{dx_i}{dz} A(z) \quad ,$$

and the net reaction rates K_i for each species

$$K_i = \frac{1}{A(z)} \frac{d(F_i A(z))}{dz} .$$

The fluxes are used to calculate elemental flux balances through the flame (there should be no change), and reaction rates can sometimes be used to calculate rate constants.

MBMS measurements and flame modeling

Data from a fuel-lean propene flame are used here to show the interplay between MBMS measurements[5] and mechanistic modeling.[6] In this work, profiles were mapped for 22 radical and stable species, and point measurements or upper bounds were measured for eight species. Uncertainties of the absolute mole fractions were <5% for species calibrated directly, approximately <15% for H_2O and Ar, and within a factor of two for other species.

To illustrate the radical data, the allyl profile is shown in Figure 2. Other radicals which were mapped were H, CH_2 (upper bound), CH_3, O, OH, C_2H_3 (upper bound), HCO, HO_2 (upper bound), C_3H_3 (upper bound), C_3H_3O, and C_3H_5O.

Modeling issues. The flame was modeled with the PREMIX/Chemkin codes of Sandia[7] using the measured temperature profile, the measured area-expansion profile, and a set of elementary reactions and thermodynamics which we developed from various databases and the mechanisms of Wilk *et al.*[8] and Dagaut *et al.*[9]

Even if a reaction set is perfectly accurate, representing the temperature profile is of major concern. Whether measured with thermocouples or optical means, the temperature profile of an unperturbed flame is not the proper temperature to use in interpreting or modeling the data. Conventional modifications were used here: the temperature profile was lowered 100 K to account for local cooling, and the positions of the mole-fraction data were shifted toward the burner by two orifice diameters (0.2 mm).

Nevertheless, the probe perturbation is mostly local. When sampling is very close to the burner, concentrations and temperatures are perturbed too much to be used because both the burner and the probe combine to cool the gases. When post-flame gases are sampled, the perturbation is only to the local radical pool because the fuel destruction pathways are proceeding unaffected, far from the probe. Such problems are often not taken into account by modelers unfamiliar with these data realities, and an accurate resolution of the problem is not available. Perhaps most accurately, a different temperature profile and flame-structure prediction could be made for each probe position in the flame. Even with the simpler assumptions, though, the model predictions can be quite useful for testing proposed mechanisms.

Insights from modeling combined with MBMS data. Agreement with the data was quite good for many species. The biggest problem with earlier mechanisms was that allyl was seriously overpredicted – by factors of 20 to 30. Analysis showed that the rate constants of allyl formation were reasonable, indicating that the problem was under-prediction of allyl destruction.

Allyl destruction kinetics was then determined from the measurements, interpreted with theory and mechanistic modeling. A revised mechanism introduced new, theoretically predicted reactions including $H+C_3H_5 \rightarrow C_2H_3+CH_3$, $O+C_3H_5 \rightarrow$ acrolein+H, and $HO_2+C_3H_5 \rightarrow CH_2=CHCH_2O+OH$, but allyl predictions were still excessive.

The net reaction rate of allyl was then analyzed from the data in the region of allyl destruction. The only co-reactant in high enough concentration to give the measured rates, even with high rate constants $\leq 10^{14}$ $cm^3mol^{-1}s^{-1}$, was O_2. The reaction $O_2+C_3H_5 \rightarrow C_3H_5OO$ is recognized to fall off with increasing temperature. Chemically activated decompositions of the adduct at high reactant temperatures opens new possibilities, though.

Using rate constants inferred from the data, allyl was subsequently predicted remarkably well. The rate constant is approximately $(3\pm1)x10^{12}$ at 1000-1700 K, and the reaction possibly forms propenal+OH.

ACKNOWLEDGMENTS

We gratefully acknowledge sponsorship of this research by the United States Government under Department of Energy Contract DE-FG02-91ER14192.

REFERENCES

1. Biordi, J. C. *Prog. Energy Comb. Sci.* **1977**, *3*, 151.
2. Biordi, J. C., Lazzara, C. P., Papp, J. F. *Comb. Flame* **1974**, *23*, 73.
3. Kent, J. H. *Comb. Flame* **1970**, *14*, 279.
4. Wagner, H. Gg., Bonne, U., and Grewer, T. *Z. Phys. Chem.* **1960**, *26*, 93.
5. Thomas, S. D. Ph.D. dissertation, University of Massachusetts Amherst, 1992.
6. Thomas, S. D., and Westmoreland, P. R. (submitted).
7. Kee, R. J., Grcar, J. F., Smooke, M. D., Miller, J. A. *A Fortran Program for Modeling Steady Laminar One-Dimensional Premixed Flames*, Sandia National Laboratories Report No. SAND85-8240, 1985; PREMIX Version 2.5, CHEMKIN II version 3.2, and TRANFIT version 1.6.
8. Wilk, W.J., Cernansky, N.P., Pitz, W.J., Westbrook, C.K. *Comb. Flame* **1989**, *77*, 145.
9. Dagaut, P., Cathonnet, M., Boettner, J.C., Gaillard, F. *Comb. Flame* **1988**, *71*, 295.

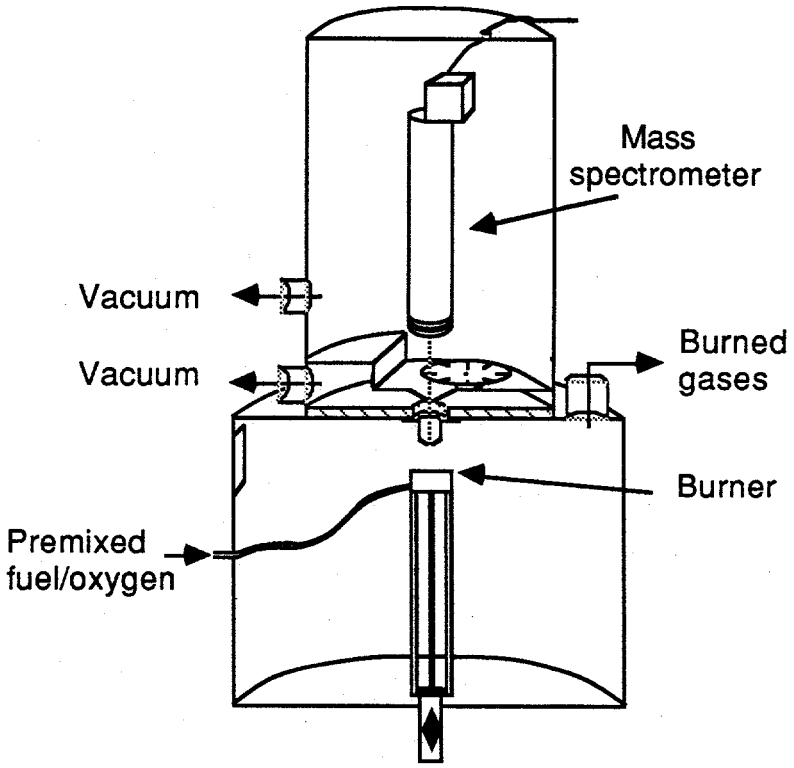

Figure 1. Flat-flame/MBMS apparatus at the University of Massachusetts.

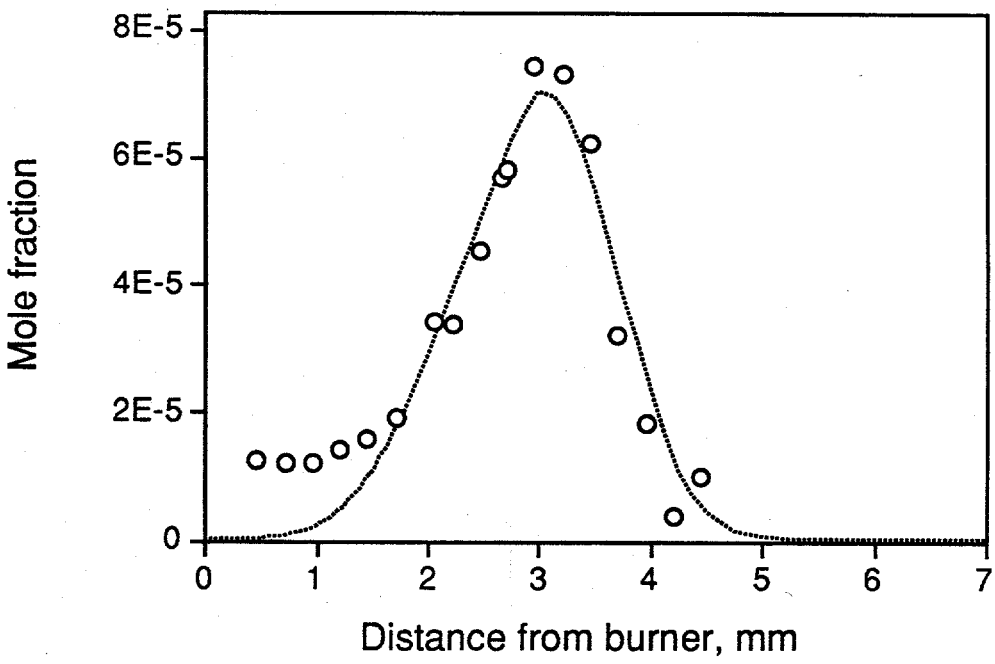

Figure 2. Allyl profile with model prediction.

FLAME STRUCTURE STUDIES OF NEAT AND NH_3 DOPED H_2/N_2O FLAMES EMPLOYING MOLECULAR BEAM MASS SPECTROMETRY AND MODELING

R.C. Sausa, G. Singh[a], G.W. Lemire[b], and W.R. Anderson
U.S. Army Research Laboratory
AMSRL-WT-PC
Aberdeen Proving Ground, MD 21005

INTRODUCTION: The H_2/N_2O chemical system has received much interest in recent years. For representative studies see references 1-10, and references therein. Much of this interest stems from the fact that this system is fairly simple and that it has important implications in understanding NO_x pollutant formation, and nitramine propellant combustion and decomposition. The elementary reactions of this system are form a subset of a larger mechanism needed to understand the nitrogen chemistry of more complex combustion systems.

An understanding of the way additives alter the chemical pathways in combustion systems is a prerequisite for controlling and enhancing system performance. In a recent comprehensive experimental and modeling study of a 20 Torr, burner stabilized flame, we reported that the burned gases of the flame contain concentrations of NO and H_2 that are ten times more than that computed from equilibrium calculations.[1] NO, a product of incomplete combustion (PIC), acts as an inhibiter and prevents full energy release of the system within or near the flame zone. For propellant systems, the production of NO frequently causes the formation of a dark zone which is believed to be associated with recent observations of nonreproducible gun ignition delays.[12] NO is an environmental pollutant and its formation also poses problems during demilitarization operations. Thus, it behooves us to investigate the incorporation of various additives in nitrogen combustion systems for NO reduction or elimination.

This paper reports experimental and modeling studies of $H_2/N_2O/NH_3$ flames in order to explore the conversion of NO to final products by adding trace concentrations of NH_3. NH_3 was used as the additive because of its proven use in the thermal deNO_x process to remove NO from effluent streams of industrial furnaces.[12] Temperature and species concentration profiles are obtained in both a neat and on a NH_3-doped $H_2/N_2O/Ar$ flame at 30 Torr employing a Pt/Pt-Rh(10%) thermocouple and molecular beam mass spectrometry, respectively. The low pressure environment enables the profiles to be examined at higher spatial resolution than can be obtained at atmospheric pressure. Species profiled include H_2, N_2O, NH_3, H_2O, N_2, O_2, and NO. These profiles are compared to calculated profiles generated using PREMIX, a one dimensional premixed laminar flame code.[13] The detailed chemical mechanism employed in the code consists of 88 reactions and 20 species, and was derived from preliminary calculations using a more comprehensive set of reactions (>200) obtained from a critical literature review. Rate and sensitivity analyses were performed on the PREMIX results using an interactive postprocessing code we have written so that the details of the chemistry may be understood. The efficacy of the NH_3 additive on the conversion of NO to N_2 as well as the mechanisms of NO formation from both neat NH_3-doped flames are presented and discussed.

EXPERIMENTAL: The experimental apparatus used in this study is a low pressure burner constructed for molecular beam mass spectrometry (MB/MS), laser spectroscopy, and thermocouple temperature measurements. A schematic of the experimental apparatus is presented in Figure 1. The neat and NH_3 doped $H_2/N_2O/Ar$ flames were supported on a McKenna flat-flame burner housed in a cylindrical stainless

[a] *Visiting Summer Research Faculty, Department of Natural Sciences, University of Maryland Eastern Shore, Princess Anne, MD 21853-1299.*
[b] *NRC/ARL Postdoctoral Research Associate, Present Address: Joint Contact Point Directorate, Dugway Proving Ground, UT 84022-5000.*

steel vacuum chamber maintained at 30 Torr. The burner was scanned vertically using a motorized high vacuum feedthrough translator interfaced with a PC-AT computer. The software was written in-house. Commercial high-purity grade gases were metered with MKS mass flow controllers, which were cross checked with a GCA Precision Scientific wet test meter. Volumetric flow rates for H_2, N_2O, and Ar were 1.78, 1.64 and 1.23 standard liters per minute, respectively. This slightly fuel rich flame was then doped with up to 7% NH_3.

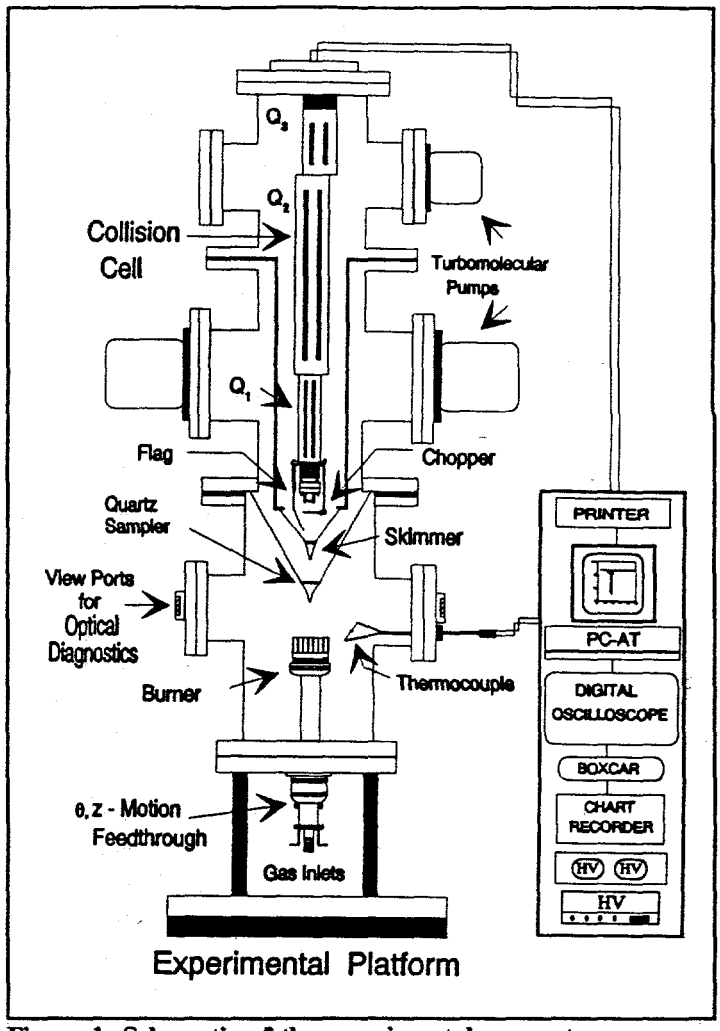

Figure 1: Schematic of the experimental apparatus.

Flame temperatures were measured with a coated Pt/Pt-Rh(10%) fine wire thermocouple coated with a beryllium oxide(15%)/yttrium oxide mixture, and corrected for temperature radiation losses. The coating was performed according to the procedure described by Kent[14] in order to avoid surface catalytic effects. The overall uncertainty of temperature measurements ia ± 50K in the region of the peak temperature and ± 20K in the preheat region. The measured temperature profiles for both neat and NH_3 doped $H_2/N_2O/Ar$ flames are very similar. The temperature increases away from the burner surface, reaches a peak temperature of approximately 2000K near 10 mm, and then levels off. Doping the neat flame with 3% of NH_3 results in approximately a 2 mm displacement of the temperature profile away from the burner surface, and approximately a 12K drop in the peak temperature. The drop in peak temperature is consistent with NASA-Lewis equilibrium calculations[15] which yield a temperature difference of 9K.

The species concentrations were measured using molecular beam mass spectrometry. The flame gases are sampled through a 200 μm diameter orifice in a conical quartz sampler and supersonically expanded into the first differential vacuum chamber of the triple quadrupole mass spectrometer system. Collimating the expanding gases with a second 2 mm diameter skimmer forms a molecular beam. The molecular beam is modulated by a tuning fork chopper and directed into the ionization region of an Extrel C-50 triple quadrupole mass analyzer. Only a single quadrupole was utilized in the present study. The modulated electron multiplier current intensity at each ion mass-to-charge ratio is phase sensitively detected with a lock-in amplifier to discriminate against background gases and accommodate signal averaging to increase sensitivity. The ionization energies were varied from 15.0-32.0 ± 0.3 eV depending on the species of interest to avoid or minimize interference from other species. An electron current of 0.14 ± 0.01 mA was maintained for all of the species profiles measured in this study.

The concentration of H_2, N_2O, NH_3, Ar, N_2, O_2, and NO was determined by direct calibration at ambient temperature by a procedure reported in our previous publication[1]. For H_2O, the signals measured

in the flame were quantified by equating the ratio of N/O in the premixed gases to the ratio of N/O in the burnt gases and assuming that the mole fractions of the radical species are comparatively small.[16] The errors associated with the absolute species concentrations are ± 10%.

The computations were performed on a SGI workstation and/or CRAY Y/MP computer using the Sandia National Laboratories flame code PREMIX (Ver. 2.5B) with the CHEMKIN-II (Ver.3.0) library.[13] The PREMIX program provides a one-dimensional calculation of species profiles for a laminar premixed flame. The calculations were performed with the temperature profiles used as input into the flame code, the inclusion of thermal diffusion and multicomponent transport package option, and with normal boundary conditions. The boundary conditions exclude recombination of H atoms at the burner surface. This effect causes little change in the computed concentrations except for the H-atoms very near the burner surface for flames under the present conditions.

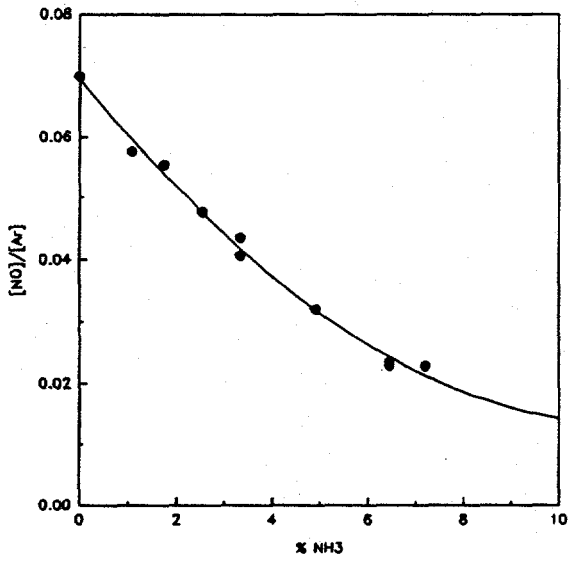

Figure 2: NO Concentration as a function of % NH_3 added to flame.

<u>RESULTS/DISCUSSION</u>: Presented in Figure 2 is a plot of NO concentration as a function of %NH_3 added to a H_2/N_2O flame. The addition of 4% of NH_3 significantly reduces the NO concentration by half. A leveling off effect of the NO concentration is also observed for NH_3 concentrations greater than 6%. The cause of this effect is revealed and discussed in the latter part of this paper.

The calculated and experimental concentration profiles of NO for both a neat and NH_3-doped H_2/N_2O flame are shown in Figure 3. Qualitatively, excellent agreement between model and experiment is obtained in the post flame region. The addition of 3% NH_3 reduces the NO concentration by approximately 37%. Qualitatively, the model and experimental shapes of the NO profiles are similar, however, both modeled NO profiles are shifted by approximately 2 mm toward the burner surface versus the experimentally measured ones. Part of the shift may be accounted by the introduction of the quartz sampler in the flame. A shift of 5 times the sampling orifice diameter was observed by Cattolica and coworkers for the OH radical measured in a stoichiometric CH_4/air flame with both laser absorption spectroscopy and molecular beam mass spectrometry.[17] Figure 3 also reveals that the modeled NO profile for the NH_3 doped flame peaks at 9 mm and gradually decreases thereafter. This is in contrast to the experimental profiles which plateau at 9-10 mm. At present this discrepancy is not well understood and is under investigation. A comparison of the experimental and predicted mole fractions of the major stable species, H_2, N_2O, N_2, H_2O, and Ar,

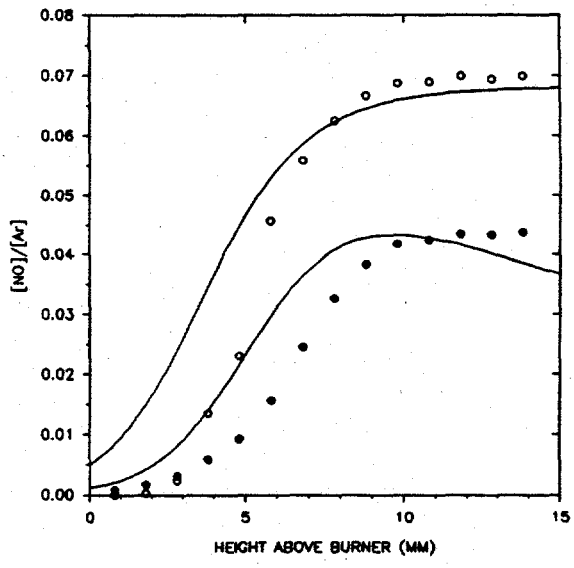

Figure 3: Experimental and calculated NO profiles in a neat and NH_3-doped flame.

reveals that the computed profiles accurately model the experimental results throughout the entire flame.

Analysis of the postprocessor results yields reaction pathway diagrams depicting the nitrogen chemistry occurring in the neat and NH_3 doped H_2/N_2O/Ar flames. These diagrams which are presented in Figures 4 and 5 are constructed using a mechanism consisting of 88 reactions and 20 species. The reduced mechanism is derived from preliminary calculations using a more comprehensive set of reactions, greater than 200, obtained from a critical literature review. Figure 4 depicts a reaction pathway for the neat flame. The numbers in parenthesis are the relative rates of the various reactions normalized to 100 for the reaction $NH_3+OH=NH_2+H_2O$ in the doped flame. As can be seen from Figure 4, the reaction $N_2O+H=N_2+OH$ represents the fastest step consuming N_2O to generate N_2. The initiation step, $N_2O+M=N_2+O+M$, and the reaction $N_2O+OH=HO_2+N_2$ are also important reactions in the conversion of N_2O to N_2. According to the diagram, NO is formed predominantly from the reaction $N_2O+H=NO+NH$, R29. The formation of NO from NH, via the HNO intermediate, and reaction $N+OH=NO+H$ is also significant. The partial conversion of NO to N_2 occurs exclusively by reactions involving N and NH. Not surprisingly, the species NH_3, NH_2, NNH, and N_2H_2 do not play major roles in the neat flame.

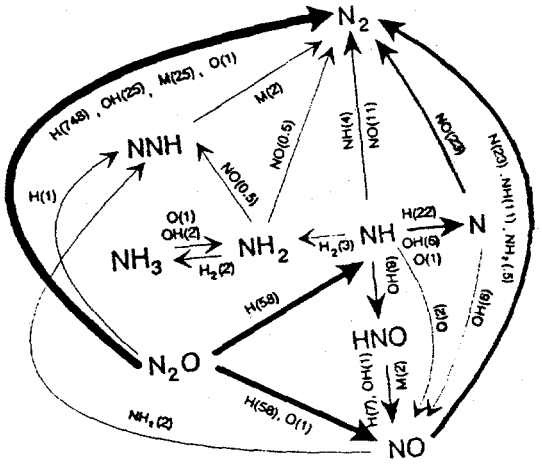

Figure 4: Pathway diagram of nitrogen chemistry for H_2/N_2O flame.

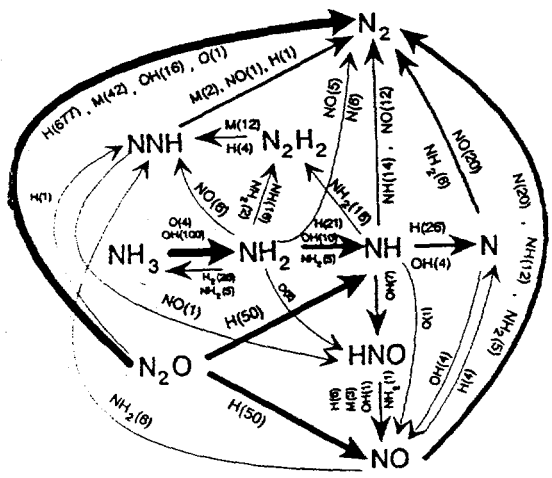

Figure 5: Pathway diagram of nitrogen chemistry for NH_3-doped H_2/N_2O flame.

Figure 5 shows the reaction pathway diagram for the NH_3-doped flame. The addition of 3% NH_3 increases the number of reactions and species having major effects on the flame. Nevertheless, detailed chemical structure of the flame can be understood by examining the pathway diagram. As expected, with the addition of the dopant only a small perturbation in the reactions involving the major species is observed as compared to those in the neat flame. However, the addition of 3% NH_3 does reduce the NO concentration by approximately 37%. This can be explained by (1) a slight decrease in NO formation from reactions $N_2O+H=NO+NH$ and $N+OH=NO+H$, and (2) an increase in NO consumption by the NH_2 radical. NH_2 can convert NO to N_2 directly, or indirectly via the NNH intermediate. It should be specifically noted that the lowering of NO concentration in the doped flame is primarily chemical in origin, rather than due to the slight change in temperature profiles. This was proven by switching the input temperature profiles in the calculations. Switching the temperature profile used causes only a slight change in the predicted NO profile, particularly in the burnt gases, for either the neat or doped flame.

The sensitivity analysis singles out reactions whose rate coefficients are extremely important in the model for further attention by the scientific community and is an important result of this work. Presented in Table I is a comparison of logarithmically normalized sensitivities of NO to various reaction rate coefficients for both neat and NH_3-doped H_2/N_2O/Ar flames. The sensitivity coefficients were calculated at 13.75 mm for both flames. They are scaled to 100 for reaction R22, $N_2O+H=OH+N_2$. A positive sensitivity coefficient means that an increase in the rate coefficient of the indicated reaction would yield an increase in predicted NO concentration. Conversely, a negative coefficient means that a similar change in the rate coefficient would result in a reduced NO concentration. Table I reveals that for the neat flame the NO concentration has a strong negative sensitivity to R22 and strong positive sensitivity to the reaction N2O+H=NH+NO, -[R28+R29] as shown in Table I. (In this case a negative sign means the reaction is reversed under our conditions). This result is clearly due to the competition between the two channels for the N_2O+H reaction, one forming NO, the other N_2. NO exhibits a lesser but still important sensitivities to reactions R33, R2, R74, R29, R78, R24, and R30. For most of these reactions the trends are similar for the doped flame. However, one notes that in comparison, the doped flame shows much stronger sensitivities than the neat flame to several additional reactions. This trend is indicative of the more complex nature of the chemistry when NH_3 is added. In particular, note that most of these additional reactions involve NH_2, NH, or N. This is not surprising since the pathway diagrams indicate these species play key roles in the consumption of NO. The sign of some of the sensitivity coefficients may be understood in terms of the competition between NH_x + NO reactions, which result in the destruction of NO, and NH_x + NH_y reactions, which ultimately result in conversion of the NH_3 to N_2 without removal of NO. For example, the two NH_2 + NO reactions, R45 and R46, have negative coefficients because they convert NO to N_2. In contrast the NH_2 + NH reaction, R47, merely converts two NH_x molecules ultimately to N_2 without destroying NO, thus exhibiting a positive NO sensitivity coefficient. Another apparent tendency is for reactions which abstract an H atom from NH_x, -R36, R44, R43, and R53, to exhibit negative coefficients. This result is likely due to the fact that at least under the present conditions, as more H atoms are stripped from the NH_x, the product NH_{x-1} will have a greater tendency than NH_x to react with NO, resulting in higher conversion of NO to N_2; see the pathway diagram depicted in Figure 5.

Table I: Sensitivity coefficients for NO in a neat and NH_3-dope flame

	REACTION	SENSITIVITY COEFF.(Rel.) SIGN	NEAT	DOPED
22	N2O+H=OH+N2	(-)	100.0	100.0
28+29	NH+NO=N2O+H	(+)	58.1	60.0
33	NH+OH=HNO+H	(+)	26.8	23.7
2	H2+OH=H2O+H	(-)	26.2	20.8
74	NO+N=N2+O	(-)	21.7	27.5
78	NO+H=N+OH	(+)	19.8	15.1
24	N2O+M=N2+O+M	(+)	14.0	<3
30	NH+NO=N2+OH	(-)	12.2	20.4
37	NH+O=NO+H	(+)	6.3	4.6
39	NH+NH=N2+2H	(+)	4.6	10.7
3a	H2+O=H+OH	(-)	3.7	6.3
26	N2O+O=NO+NO	(+)	2.9	<3
36	N+H2=NH+H	(-)	2.5	5.4
15	HO2+H=OH+OH	(-)	1.5	<3
27	N2O+OH=N2+HO2	(-)	1.3	<3
77	NO+H+M=HNO+M	(+)	1.2	<3
47	NH2+NH=N2H2+H	(+)	1.1	20.2
41	HNO+H=NH2+O	(+)	1.1	6.3
34	NH+OH=N+H2O	(-)	0.9	<3
45	NH2+NO=NNH+OH	(-)	<1	11.7
46	NH2+NO=N2+H2O	(-)	<1	10.6
48	NH2+N=N2+H+H	(+)	<1	9.9
44	NH+H=NH+H	(-)	<1	9.4
3b	H2+O=H+OH	(-)	<1	6.3
41	HNO+H=NH2+O	(+)	<1	6.3
36	N+H2=NH+H	(-)	<1	5.4
37	NH+O=NO+H	(-)	<1	4.6
53	NH3+H=NH2+H2	(-)	<1	3.8
43	NH2+OH=NH+H2O	(-)	<1	3.3

CONCLUSIONS: A combined experimental and detailed chemical modeling study of a neat and NH_3 doped H_2/N_2O/Ar flame has been performed. The experiments were performed in a low pressure burner apparatus equipped for molecular beam mass spectrometry and thermocouple temperature measurements. A chemical mechanism for the system was developed from a critical literature review, and was employed to model the experimental results. We have shown that the addition of small amounts of NH_3 to a premixed

flame of propellant intermediates, which forms large amounts of NO, will convert the NO to final product N_2. To that end, a detailed mechanism for the case of NH_3 addition to H_2/N_2O flames has been developed and tested. The agreement between the model and experiment is excellent, both showing approximately a 37% decrease in NO concentration when 3% of NH_3 is added to the H_2/N_2O flame. Rate and sensitivity analysis reveal that dopant decreases slightly the amount of NO formed by the reactions $N_2O+H=NO+NH$ and $N+OH=NO+H$, and increases its consumption via reaction with NH_2, which ultimately lead to conversion of NO to N_2.

ACKNOWLEDGEMENTS: This work was supported by the ARL Combustion Research mission program. Support from the NRC/NAS Postdoctoral Research Associateship Program (GWL), ARL Visiting Faculty Program GS), and Productivity Capital Investment Program (RCS and WRA) is gratefully acknowledged.

REFERENCES

1. R.C. Sausa, W.R. Anderson, D.C. Dayton, C.M. Faust and S.L. Howard, *Combustion and Flame* **94**, 407 (1993).
2. H. Henrici and S.H. Bauer, *J. Chem. Phys.*, **50**, 1333 (1969).
3. A.M. Dean, D.C. Steiner, and E.E. Wang, *Combust. Flame*, **32**, 73 (1978).
4. K.M. Pamidimukkla and G.B. Skinner, *J. Chem. Phys* , **89**, 4903 (1985).
5. Y. Hidaka, H. Takuma, and M. Suga, *J. Chem. Phys.*, **89**, 4903 (1985).
6. R.R. Baldwin, A. Gethin, J. Plaistowe, and R.W. Walker, *J. Chem. Soc. Faraday Trans.*I, 71, **1265** (1975).
7. R. Cattolica, M. Smooke, and A.M. Dean, Western States Section Meeting of the Combustion Institute, Western States Section/Combustion Institute, 82 (1982).
8. J.A. Vanderhoff, S.W. Bunte, A.J. Kotlar, and R.A. Beyer, *Combust. Flame*, 28, 165 (1977).
9. V.P. Balakhnine, J. Vandooren, and P.J. Van Tiggelen, *Combust. Flame*, **28**, 165 (1977).
10. K. Kohse-Hoinghaus, J. Jefferies, R.A. Copeland, G.P. Smith, and D.R. Crosley, *22nd Symp. (Int.) Combust.*, p. 1867, The Combustion Institute (1988).
11. D.E. Kooker, L.M. Chang, and S.L. Howard, Army Research Laboratory Report, ARL-MR, June 1993.
12. J.A. Miller and C.T. Bowman, *Prog. Energy Combustion Sci.*, **15**, 287 (1989).
13 R.J. Kee, F.M. Rupley, and J.A. Miller, Sandia Report SAND-89-8009, Sept. 1989.
14 J.H. Kent, *Combust. Flame*, 14, p. 279 (1970).
15. R.A. Svehla and B.J. McBride, NASA-TN-D-7057, Jan. 1973.
16 J. Vandooren, M.C. Branch, and P.J. Van Tiggelen, *Combust. Flame*, **90**, 247 (1992).
17. R.J. Cattolica, S. Yoon, and E.L. Knuth, Paper 88, Western States Section/Combustion Institute, (1980).

Molecular Beam/Mass Spectrometric and Modeling Studies of CF_3Br Inhibited Flames

William R. Anderson, Rosario C. Sausa, George W. Lemire[a], Gurbax Singh[b]
U.S. Army Research Laboratory
Aberdeen Proving Ground, MD 21005-5066

and

Joseph W. Bozzelli
New Jersey Institute of Technology
Newark, NJ 07102

Introduction

The halogenated compound CF_3Br, halon 1301, has been widely used as a flame inhibitor and fire suppression agent. It has been implemented into many fire protection systems dating back as far as the early 1940's. Despite the favorable - experimentally observed flame suppression properties, the detailed chemistry and physics effecting the inhibition in flames by this and similar compounds is not well understood. Notable research efforts in this regard were MB/MS experiments by Biordi, Lazzara and Papp[1] in the 1970's, by Safieh, Vandooren and Van Tiggelen[2] in 1982, and the benchmark modeling efforts of Westbrook[3] in the early 1980's. That there has been very limited research on the chemistry of brominated fire retardants in the past decade is probably due to their known effectiveness and ease of availability. The recent discovery that these bromides promote degradation of the earth's ozone layer and their subsequent use restrictions has, however, led to a resurgence of research on these and other fluorinated hydrocarbons. The purpose of the current studies is to more fully understand the fundamental physical and chemical processes of flame inhibition and to help guide the search for safe and effective replacements.

This paper reports new experimental data and results on modeling this data and data from the literature on flames inhibited by CF_3Br. The new experiments were performed on a 20 torr, stoichiometric, premixed, laminar $CH_4/O_2/Ar$ flame with and without 1.6% CF_3Br. Profiles of the detailed structure of the flame were obtained by using MB/MS and thermocouple techniques to measure species concentration and temperature, respectively. These are compared with predicted profiles generated by a premixed laminar flame code using a large detailed mechanism. In addition to modeling of the low pressure detailed structure studies, the model has been used to compute flame speeds for atmospheric pressure conditions at several stoichiometries ranging from rich to lean and for a wide range of CF_3Br concentrations. Due to space limitations and the nature of the meeting, the flame speeds will not be discussed further here.

---

[a]NRC/ARL Postdoctoral Research Associate, Present Address: Joint Contact Point Directorate, Dugway Proving Ground, UT 84022-5000.

[b] Visiting Professor, Department of Natural Sciences, University of Maryland Eastern Shore, Princess Anne, MD 21853-1299

Experimental

Experimental data were taken for a 20 torr, stoichiometric flame of $CH_4/O_2/Ar$ with and without ~ 1.6% of CF_3Br. The apparatus is discussed in detail in the preceding paper[4]. Briefly, the flames are stabilized on a water cooled, porous plug burner (McKenna). High purity gases were metered with MKS flow controllers and mixed at the burner. An MB/MS system employing a triple quadrupole mass spectrometer (Extrel) is used to measure profiles of both majority and trace species in the flames. The temperature profiles are measured using Pt/Pt-Rh thermocouples coated to avoid surface catalysis of flame radicals. The concentration of majority species is determined by direct calibration with known concentrations of the unburned species, while radical and some trace halogen species are determined using estimated ionization cross sections.

Computational Details

The calculations were performed using the PREMIX code[5] developed at Sandia National Laboratories and an interactive postprocessor written at Army Research Laboratory. Given input conditions, a detailed chemical mechanism, and detailed transport properties of the gases, the PREMIX code calculates species concentration and temperature as function of height above the burner. For most of the present burner stabilized studies, the code was used in the mode in which the user inputs the measured temperature profile as a fixed input parameter and species profiles are then calculated. A starting mechanism was compiled of three major reaction sets: the hydrocarbon/oxygen network developed by a consortium of workers supported by the Gas Research Institute[6] (~175 reactions), the chemistry set for fluorinated species, excluding CF_3Br, recently developed at the National Institute of Standards and Technology[7] (NIST; ~630 reactions), and the brominated species chemistry, including CF_3Br, also developed at NIST[8] (~75 reactions). The resulting mechanism contains about 100 species. We have further developed and modified this reaction set as needed to achieve better agreement between experiment and theory, including adjustments of pressure dependent rate coefficients to 20 torr as needed. In the course of mechanism development, only a modest level of theory has been used because the higher level theory is prohibitively expensive for preliminary calculations. The simplifying assumptions made were: using only about 75 - 150 grid points, ignoring thermal diffusion and using the mixture averaged diffusion model. However, even at this level of theory our experience shows results to be fairly accurate. The calculations have been performed on a CRAY Y/MP supercomputer.

Results and Discussion

There are three pairs of burner stabilized $CH_4/O_2/Ar$ flames, neat and with added CF_3Br, studied by Biordi and coworkers, and one such pair of $CO/O_2/H_2/Ar$ flames, studied by Safieh et al, in the literature. Modeling results have been obtained for all of these studies. A brief discussion will be presented here.

The studies of Biordi and coworkers illustrate, we believe, a problem which can sometimes be encountered in low pressure MB/MS flame studies. The species profiles from their first paper[1a] exhibit flames with an induction region of about 3 mm length above the burner where there is clearly little reaction taking place (that is, the reactant concentrations do not decay over this region). The given temperature profiles (both uninhibited and inhibited flames) were, however, measured without the MB/MS probe present. These profiles show T rises rapidly near the burner indicating significant reaction there. The temperature and species profiles are therefore not consistent. This was borne out by modeling calculations using those temperature profiles as input parameters. (The resulting reactant concentrations drop rapidly.) We have encountered this type

of experimental situation in the past (unpublished). We believe what is happening in such cases is due to the usually slight effect of the MB/MS probe, cooling the flame. In such cases, the flame is close to the blowoff limit, resulting in a flame very susceptible to perturbation and stretch of profiles when the MB/MS probe extracts heat. This situation is generally to be avoided as it leads to complication both in experiment and modeling. It appears that quantitative modeling studies of Biordi and coworkers first pair of flames cannot be performed, although there is useful qualitative information regarding relative positions of species profiles. It is unfortunate that this perturbing effect cannot be quantified. The second[1b] and third[1c] pairs of flames of Biordi et al utilized more strongly stabilized conditions; thus the flames were not as easily perturbed. Our modeling studies yield predictions in excellent agreement with their experiments for most of the H/C/O related species in the second pair of flames. The largest disagreement is that the predicted CO to CO_2 conversion is slightly too slow vs experiment. Agreement for the inhibitor related species (halogen-containing) using the base mechanism is good to fair. Most of our modeling to date is on the second pair of flames as neat flame profiles were not reported for the third pair. Comparison between experiment and theory of the very important relative flame zone thicknesses of neat and inhibited flames is not possible without this data. We hope to further study the third data set in the near future.

We also have had difficulty obtaining a quantitative match to major species in the flames of Safieh et al, surprisingly even for their neat flame. We intend to pursue this problem further. We therefore have performed most of our flame structure comparisons using our data and data from the second study of Biordi and coworkers.

Relative concentration profiles from our experiment (we have not yet performed the necessary calibrations to put the results on an absolute scale) will be shown and compared to predictions for selected species. The most striking feature of these (and all) the profiles is that the model predicts a strong inhibiting effect, while the experiment exhibits only a modest effect. This can be seen in figures 1 and 2 which contain the CH_4 and CO profiles. The model predicts approximately a 2 mm increase in flame zone thickness (which corresponds to a decrease in flame velocity) when inhibitor is added, while the experiment exhibits a much less pronounced effect. The relative profiles for the neat flame agree quite well. A significant increase in flame zone thickness with inhibitor added is not predicted for Biordi's second pair of flames, presumably because a small concentration of CF_3Br was used resulting in a less pronounced effect. Our experimental data indicate the inhibition predicted by the model is too strong. This difference in experiment and model for our new data is currently under study.

The CF_2O profiles have received particular attention. This species is a trace, relatively stable product. Because of its high toxicity, its concentration is a subject of concern. Measured and predicted profiles for our flame are given in Fig. 3. The experimental profile peaks at about 6 mm, whereas the modeling profile for the base mechanism exhibits virtually no consumption of the CF_2O formed in the flame zone. We believe that reactions of this species with O and OH, which were omitted in the base mechanism, are important and that the rate constant for its reaction with H atoms may be too small. We have examined[9] the reactions with O and OH using the CHEMDIS program (which utilizes a QRRK type approach) and estimated thermodynamics and barrier heights for formation of the various products from group additivity, comparisons to similar reactions, and semi-empirical theory (MNDO/PM3). The dashed profile exhibiting a peak at about 9-10 mm results from including our estimated rate coefficients for the O and OH reactions. The agreement is better, but the decay is still too slow. Preliminary results upon revision of the H atom reaction suggest it will easily explain the remaining discrepancy in decay rates and some of the peak position difficulty. Very similar results are obtained for the Biordi flame, except

that agreement for the peak position is better than for our low pressure flame. It is likely the remaining larger discrepancy for our flame is due to the use of about 5 times the amount of inhibitor, coupled with the model's prediction of too strong inhibition. We intend to continue refining and developing the mechanism.

References

1. a. J.C. Biordi, C.P. Lazzara and J.F. Papp, Fourteenth Symp. (Int.) Combust. (The Combustion Institute, Pittsburgh, 1973) p. 367. b. J.C. Biordi, C.P. Lazzara and J.F. Papp, Fifteenth Symp. (Int.) Combust. (The Combustion Institute, Pittsburgh, 1975) p. 917. c. J.C. Biordi, C.P. Lazzara and J.F. Papp, J. Phys. Chem., Vol. 81, p. 1139 (1977).

2. H.Y. Safieh, J. Vandooren and P.J. Van Tiggelen, Nineteenth Symp. (Int.) Combust. (The Combustion Institute, Pittsburgh, 1982) p. 117.

3. C.K. Westbrook, Combust. Sci. Tech., Vol. 34, p. 201 (1983).

4. R.C. Sausa, G.W. Lemire, G. Singh and W.R. Anderson, proceedings of this meeting (preceding paper).

5. R.J. Kee, J.F. Grcar, M.D. Smooke and J.A. Miller, Sandia National Laboratories Report SAND85-8240 (1991).

6. M. Frenklach, H. Wang, C.T. Bowman, G.P. Smith, D.M. Golden, W.C. Gardiner, Jr. and V. Lissianski, to be published.

7. D.R.F. Burgess, Jr., M.R. Zachiariah, W. Tsang and P.R. Westmoreland, NIST Technical Note, submitted for publication.

8. D.R.F. Burgess, Jr. and W. Tsang, private communication.

9. J.W. Bozzelli, T.H. Lay, W.R. Anderson and R.C. Sausa, to be presented at the Eastern States Section Fall Technical Meeting of the Combustion Institute, Clearwater, Florida, Dec. 5-7 (1994).

Figure Captions

1. CH_4 profiles. a. Experimental; dotted line without inhibitor, dashed line with inhibitor. b. Model; dotted line without inhibitor, solid line with inhibitor.

2. CO profiles. a. Experimental. b. Model; dotted line without inhibitor, solid line with inhibitor.

3. CF_2O profiles. Points: Experimental (relative, normalized to model). Dashed line: model with base mechanism. Solid line: model with added reactions $O+CF_2O$ and $OH+CF_2O$.

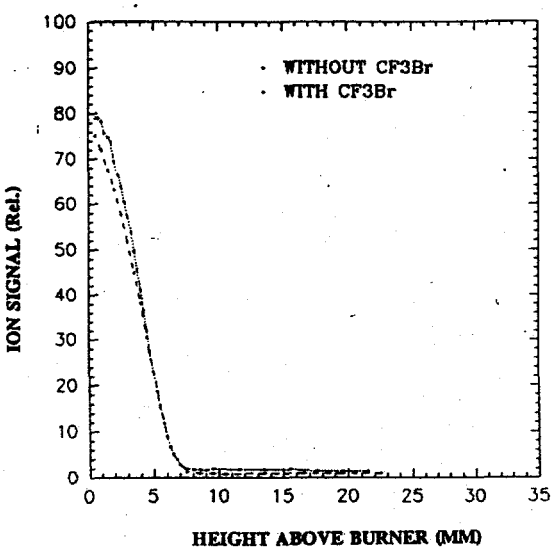

Fig. 1a.

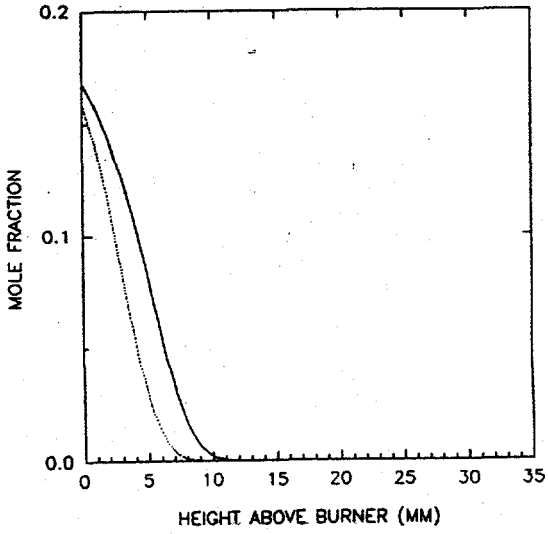

Fig. 1b.

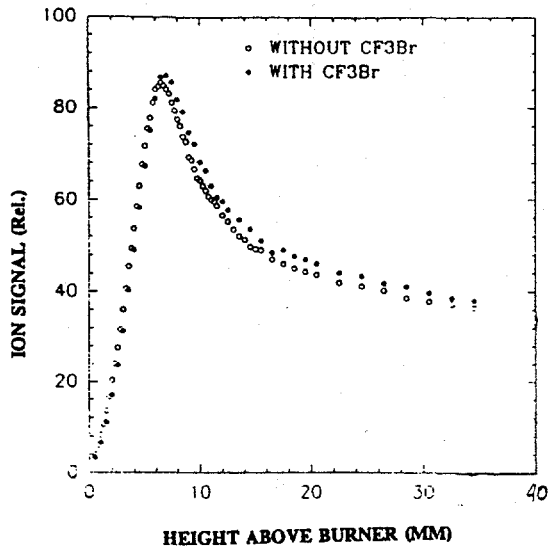

Fig. 2a.

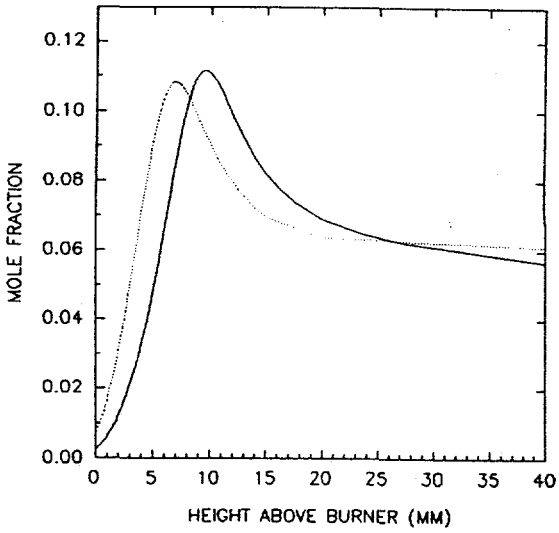

Fig. 2b.

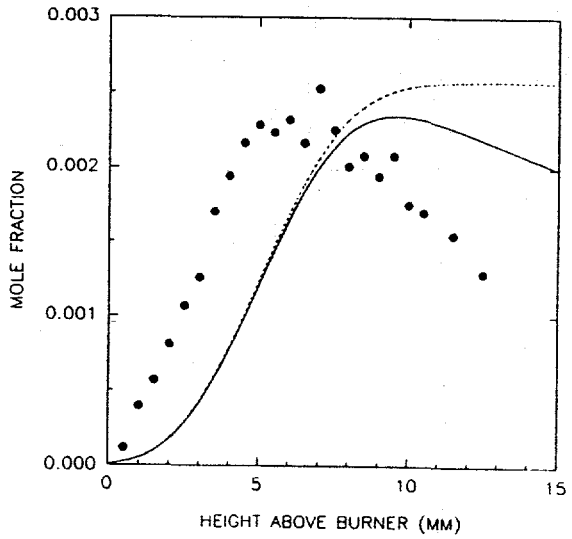

Fig. 3.

A Study of Solid Propellant Combustion using a Triple Quadrupole Mass Spectrometer with Microprobe Sampling

Thomas A. Litzinger, YoungJoo Lee and Ching-Jen Tang
Penn State University
Dept. of Mechanical Engineering
201D Reber Mechanical Engineering Building
University Park, PA 16802

Introduction

RDX (1,3,5-trinitrohexahydro-s-triazine) is a highly energetic material which is used in solid propellants in rocket motors and artillery guns. While a substantial amount of literature has been published on RDX, its complicated combustion behavior, which involves chemical reactions in the solid, liquid and gas-phases, is not yet fully understood. In order to better understand the gas-phase chemical reactions of RDX and propellants with RDX as the primary ingredient, a study of the gas-phase chemistry of these materials has been undertaken using a triple quadrupole mass spectrometer and quartz microprobe sampling. In this abstract, after a summary of the experimental apparatus, results are presented for the analysis of masses 28, 29 and 30 as well as complete results for a typical test with RDX mono-propellant.

Experimental Apparatus

Over the past few years this laboratory has developed a microprobe/mass spectrometer (MPMS) technique with high spatial resolution. Results for the gas phase species profiles have been obtained for double base and nitramine propellants using the technique. The schematic diagram of the experimental setup is given in Figure 1. In addition to the mass spectrometer, major components of the system include a CO_2 laser which is used to heat and ignite the propellant samples, the test chamber which houses the sample in an argon bath gas, and a linear positioner which moves the sample towards the stationary probe to provide spatial resolution.

To resolve species with the same molecular weights, the single quadrupole mass spectrometer previously used was replaced with a triple quadrupole mass spectrometer (TQMS). The TQMS unit was an EX500 system from Extrel capable of measuring gaseous species in the mass range of 1-500 amu with a variable scan speed between 0.2 and 1000 amu/sec. A resolution of 4864 is obtainable at a mass of 414 amu, and the sensitivity is 4 ma/torr at mass 28 amu before electronic amplification. The ionization energy was set at 22ev to minimize fragmentation of molecules but still produce a significant number of ions to generate a strong signal.

A two-stage pumping system was employed to obtain the pressures required for the TQMS system. A mechanical rotary vane pump evacuated the primary chamber from the one atmosphere pressure in the test chamber to about 0.2 torr. The probe chamber containing the MS unit was pumped down to a pressure of 2×10^{-6} torr by two turbomolecular pumps.

The real time experimental control, data acquisition, and data reduction were all performed through an 80486-based IBM PC compatible computer with a Data Translation 2823 D/A-A/D board. The board had a maximum sampling rate of 100 KHz that could be divided among a maximum of four A/D inputs. For most tests, the TQMS control program was set to investigate ten different amu values at a sampling speed 1.5 ms/amu for parent mode and 8 ms/amu for daughter mode. A second Hewlett Packard programmable universal source board, model HP 3245A, was added to the MPMS control electronics for precise and simultaneous control of the two mass filters in the first and third quads. Thus, specific ions could be sampled by selecting designated molecular masses or ranges of molecular masses in the first and third quads during the test event.

A Pulnix camera with a Nikon macro lens normally provided a magnification of 30 to 40 times and high resolution so that the distance between the propellant surface and the probe tip could be determined precisely. A video cassette recorder was employed for recording images from the camera.

The MPMS system was calibrated for each test so that quantitative species profiles for the stable gas species products could be determined. Water vapor and formaldehyde were calibrated by heating a small cup of liquid water or paraformaldehyde powder under the probe with the CO_2 laser in an argon or nitrogen environment. The calibrations of species for which standards were not readily available (e.g.,HCN) were estimated by correlating the signal intensity of that species with that of a calibrated species with a similar appearance potential through the ratio of their ionization cross-sections. The gas composition as a function of height above the surface was reported as a normalized mole fraction by adding the concentrations of the measured species together and dividing each concentration by this total.

Results and Discussion

Mass 28

Possible sources of mass 28 are N_2, CO and C_2H_4. Using the TQMS, these three species could be differentiated and identified in the daughter mode. Q1 was fixed at mass 28 and Q3 was scanned over possible masses of daughters in each species. By this method, N_2 was identified by mass 14 (N), CO was by 12 (C), and C_2H_4 by 15 (CH_3). In case of C_2H_4, the signal intensities of mass 27 (C_2H_3), 26 (C_2H_2), 25 (C_2H) and 14 (CH_2) should be higher

than that of mass 15 (CH_3) because they are easier to create by fragmentation than mass 15 . However, mass 25 to 27 were too near to the parent mass 28 to identify because of high noise level in signal, and mass 14 overlapped with the daughter mass from N_2. In the actual experiment, the signal of mass 15 was just above the noise range, thus C_2H_4 appears not to be a major product of RDX. Without C_2H_4 present, N_2, CO were easily distinguished in the daughter mode.

Unfortunately C_2H_4 is present in composite propellants that have been studied and leads to significant complications in the detection of N_2, since N_2 was very sensitive to the weak signals of daughter mass 13 and 15 at mass 28. Although C_2H_4 is only present at approximately 0.02 mole fraction, its ease of ionization and fragmentation relative to N_2 caused the concentration of N_2 to be very low in comparison with the expected results. The lack of N_2 was in contrast to the results for pure RDX where N_2 was found to be responsible for about 0.5 of the signal at mass 28. A recalculation of the 28 amu signals under the assumption that the signal at mass 28 for the composite propellants was only from N_2 and CO resulted in much better agreement with the RDX results.

Masses 29 and 30

At mass 30, NO and CH_2O are possible; however, fragments formed during the ionization of N_2O and NO_2 also contribute to mass 30. In past experiments with the single quadrupole MS, mass 29 was selected to identify CH_2O. From calibration data, the absolute intensities of the masses from CH_2O were measured, and the equivalent intensity for mass 30 from CH_2O was deducted from the total intensity of signal at mass 30. Also the contributions from N_2O and NO_2 were deducted from mass 30, to get only the NO concentration.

Some questions have been raised regarding the mole fraction of CH_2O near the surface of deflagrating RDX obtained from mass 29. The mole fraction of CH_2O has been reported to be almost zero near the surface in two other studies [1,2]. In these studies, the ranges of experimental conditions were not too different from those of the present study and therefore experimental conditions cannot explain the differences. This discrepancy demanded careful consideration of other possible sources of the 29 amu signal, as well as a reexamination of the 30 amu signal in an effort to determine CH_2O from its daughters.

The results of calibration in daughter mode for NO, CHO and CH_2O at 1 atmosphere are shown in Figure. 2. Mass 14 (N) and 16 (O) were detected with the ratio of ~1.65 to 1 for NO. For CHO, mass 13 (CH) and 12 (C) were identified with the ratio of ~2.4 to 1, and for CH_2O mass 14 (CH_2), 13 (CH) and 12 (C) with the ratio of ~20 : 2.5 :1. In experiments with RDX at 1 atm and 100 W/cm^2, several interesting results were acquired in terms of mass 29 and 30. In Figure 3a, daughter masses 14 and 16 were measured for the parent mass 30,

and the ratio of mass 14 and 16 was calculated. In the region where mass 30 signal is large, the ratio was within the bounds of 1.6 and 1.73. Comparing this ratio to the calibration of Figure 2 suggests that the amount of CH_2O is small or the ratio would deviate from the NO calibration data due to the presence of a strong 14 signal from CH_2O. Based upon these results, the maximum possible mole fraction of CH_2O near the surface was about 3 %. Considering the inevitable fluctuation of signals in calibration and actual experiments in daughter mode of TQMS, it is possible that CH_2O does not exist near the surface at this test condition.

Results from RDX experiments at mass 29 and 30 are given in Figure 3b. From the calibration of CHO, mass 13 and 12 were identified as the only possible daughters if only CHO existed at mass 29. In the test results presented in Figure 3b, however, a large signal at mass 14 was detected near the surface. Possible chemical species should be just CH_2 or N for mass 14, and possible other parent masses could be H_2CNH or C_2H_5, a radical which would have to come from fragmentation of a larger species in the ionizer. C_2H_5 was eliminated as a possible species because mass 15 (CH_3) is formed in its fragmentation, and mass 15 was not detected in daughter mode. Therefore, the most likely species appears to be something containing N, such as H_2CNH. However, any firm conclusion about mass 29 must be delayed until more decisive evidence can be found for the existence of H_2CNH.

RDX Chemical Species Profiles

Measurements of major species at the condition of 1 atm and 100 W/cm^2 are shown in Figure 4. Several experiments were actually conducted at this condition to increase the resolution of sampling. Increasing resolution was achieved by changing the starting height of sampling probe, because the quartz microprobes were found not to withstand more than 400 msec outside flame zones without melting. Figure 4 is a combination of two results with different starting heights; the results were cross-checked with other results at same condition to validate measured mole fractions.

One of difficulties in the analysis of data was identification of the exact position of propellant surface. Other researchers determined that the sampling distances for microprobes were a function of free stream velocity (burning rate), orifice diameter and flow rate at the orifice of the microprobe, and that the real sampling distance should be shifted based on this analysis [3]. However, in tests of the microprobes used in the current study in an argon jet directed toward the longitudinal axis of microprobe, the discrepancy between actual and apparent sampling height was small, on the order of one micron. Therefore, no correction of sampling height was applied in this study.

Decomposition chemistry in the gas-phase starts by the disappearance of mass of 29 and NO_2 in the primary flame zone very near the surface. Primary products by this consumption were H_2O, NO, CO and CO_2. The following global reaction has been suggested by other researchers as the major heat release reaction in the primary flame zone

$$5CH_2O + 7NO_2 ==> 7NO + 3CO + 2CO_2 + 5H_2O.$$

H_2 was relatively inert in this zone. While it is not included in above reaction, the existence of N_2 from the surface should not be overlooked. N_2 has been reported to be produced directly from the condensed/liquid phase in RDX experiments. The amount of N_2 at the surface was unaffected by the change of pressure and heat flux. This species was relatively inert in the primary flame zone and became one of primary products in the secondary flame zone.

The secondary flame zone has been characterized by the consumption of NO and HCN, and by the production of CO_2, N_2, CO, H_2O and H_2. The consumption of N_2O produces N_2 in this zone. At approximately 3mm from the surface, the reaction zone was nearly complete at this condition. In the post-flame region, major products were identified as CO_2, N_2, CO, H_2O, H_2 and a small amount of NO (~ 2 %). Small signal intensities of N_2O, NO_2, HCN were noticed in this region, but they are in the range of noise fluctuation.

References

1. Hanson-Parr D., and Parr, T., "RDX Flame Structure", to appear in The Proceedings of the 25th International Symposium of Combustion (the Combustion Institute), 1994.
2. Ermolin, N. E., Korobeinichev, O. P., Kuibida, and Fomin V. M., "Study of the Kinetics and Mechanism of in Hexagen Flames", *Fizika Goreniya I Vzryva*, 1986, Vol 22, No. 5, pp. 54-64.
3. Korobeinichev, O. P., Kuibida, L. V., Orlov, V. N., Tereshchenko, A. G., Kutsenogii, K. P., Mavliev, R. V., Ermolin, N. E., Fomin V. M., and Emel'yanov I. D., "Mass Spectrometric Probe Study of the Flame Structure and Kinetics of Chemical Reactions in Flames", *Mass-Spektrom. Khim. Kinet.*, 1985, pp. 73-93.

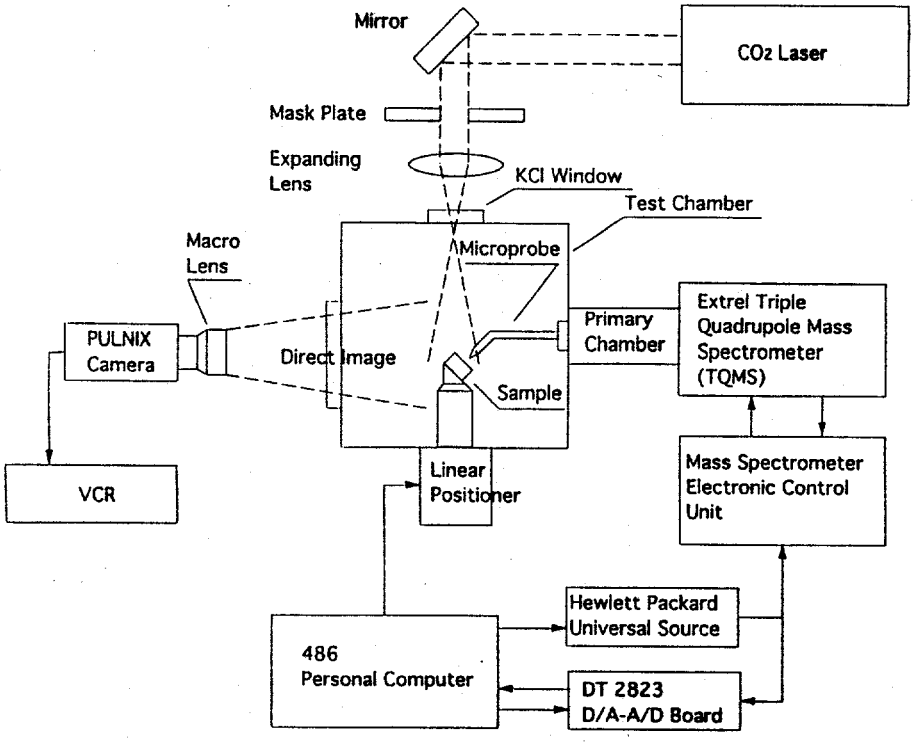

Figure 1. Experimental apparatus

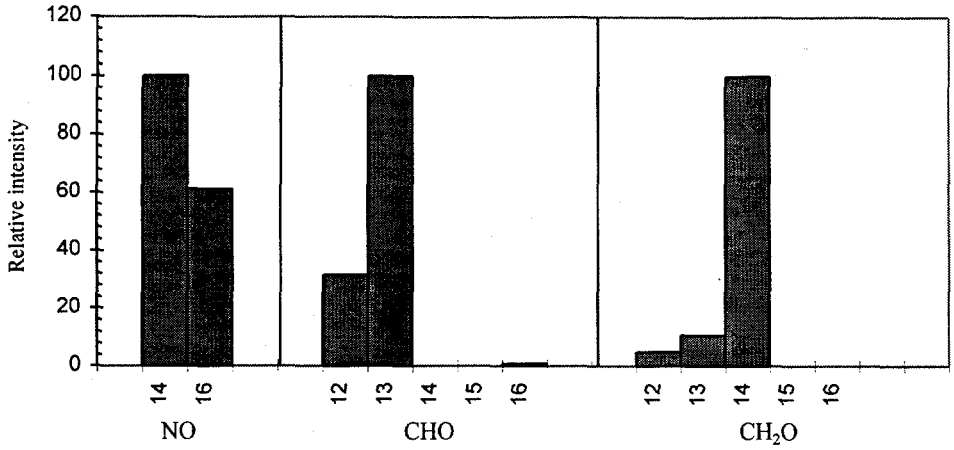

Figure 2 Intensities of daughter ion signals for the calibration of parent NO, CHO, and CH_2O. All tests were performed at 1atm and in N_2 environment.

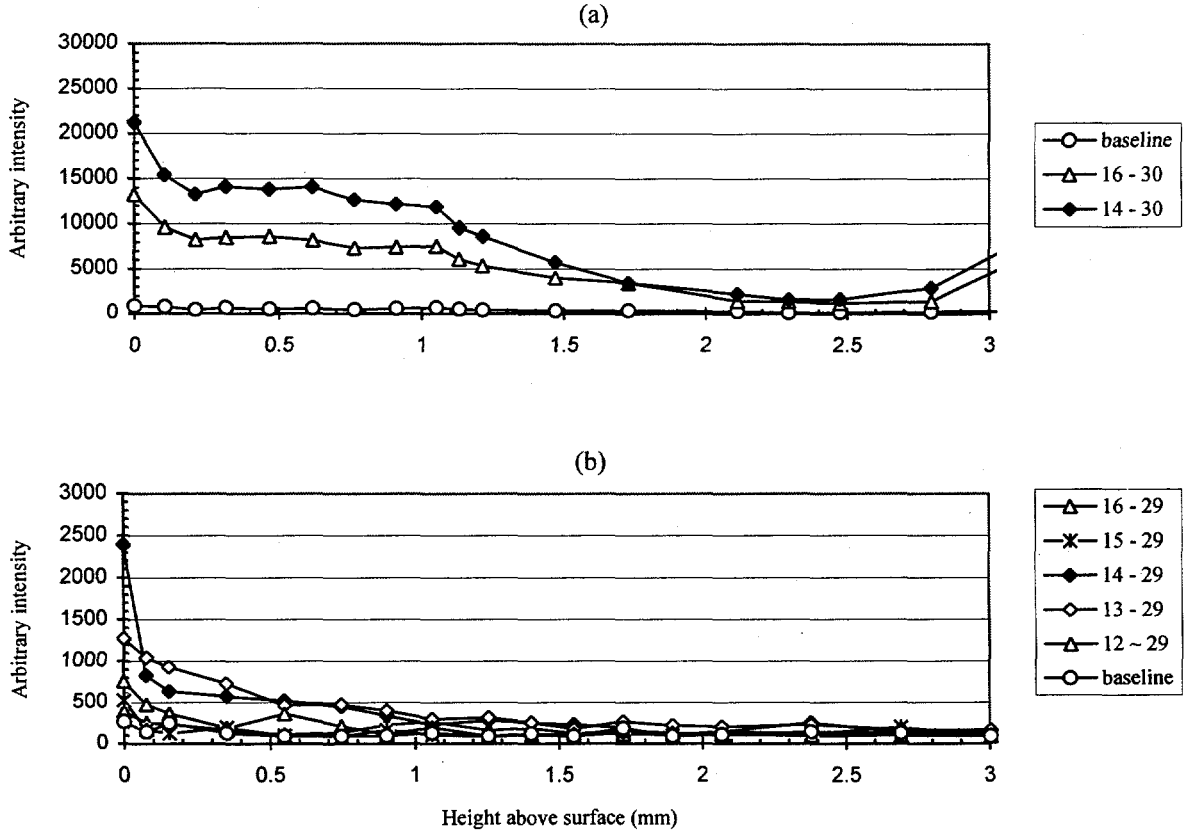

Figure 3 Intensities of daughter ion signals in the conditions of 1atm and 100 W/cm^2 for (a) mass 30 and (b) mass 29.

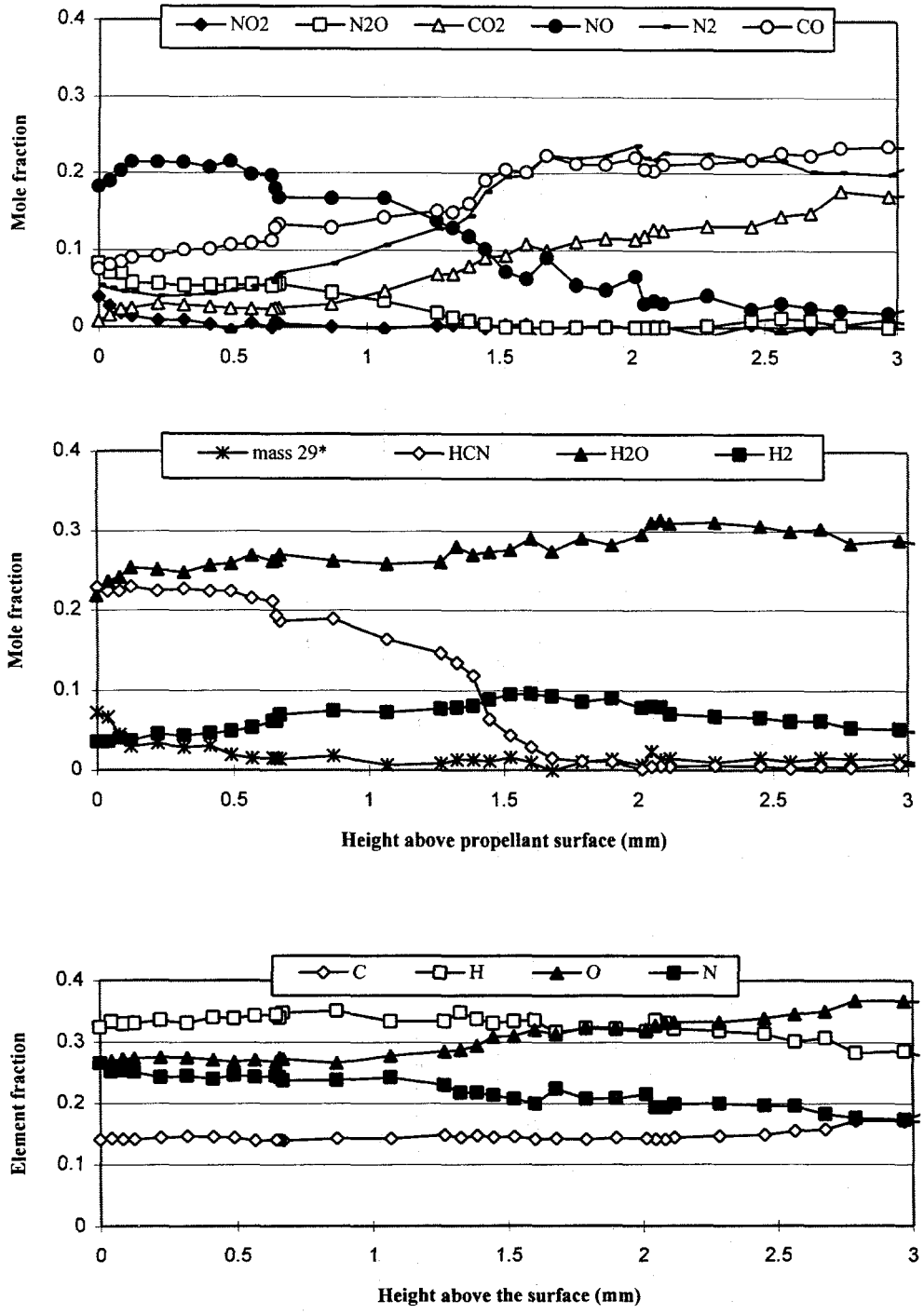

Figure 4 Species profiles and element fraction profiles for deflagration of RDX at heat flux of 100 W/cm^2 in argon at one atmosphere. * Mole fraction for mass 29 was estimated by the assumption that mass 29 was totally composed of CH_2O.

Presented at the Workshop on Free-jet, Molecular Beam, and Mass Spectrometry Sampling, Estes Park, Colorado, October 12 to 14, 1994.

Application of Simultaneous Thermogravimetric Modulated Beam Mass Spectrometry to the Study of Energetic Materials

Richard Behrens, Jr.
Combustion Research Facility
Sandia National Laboratories
Livermore, CA 94551

Abstract

Simultaneous thermogravimetric modulated beam mass spectrometry (STMBMS) and time-of-flight velocity (TOF) spectra have been developed to study reactions that occur during the thermal decomposition of liquids and solids. The data obtained with these techniques are the identity of the reaction products and their rates of gas formation as a function of time. Over the past several years, these techniques have been applied to the study of energetic materials that are used in propellants and explosives. In this presentation, the details of the STMBMS and TOF velocity spectra techniques will be reviewed, the advantages of the techniques over more conventional thermal analysis and mass spectrometry measurements will be discussed, and the use of the techniques will be illustrated with results on the thermal decomposition of hexahydro-1,3,5-s-triazine (RDX).

Introduction

Energetic ingredients such as RDX and HMX are used in formulating materials for use as propellants and explosives. The use of these materials requires being able to characterize their performance when used in propulsion or explosive devices and also knowing how these materials will respond to heat, impact, shock and electrostatic discharge when the systems are subjected to abnormal conditions that are found in various accident scenarios.

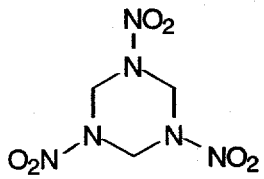

RDX

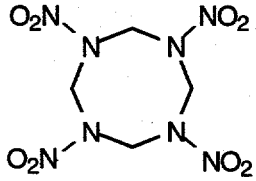

HMX

The development of new formulations for explosives has relied heavily on a "formulate, test and evaluate" cycle with little use, or development, of fundamental knowledge of the physical and chemical processes that underlie the behavior of these materials. In part, this is due to the chemical complexity of the reacting materials and the harsh environments (high temperature and high pressure deflagrations associated with rocket motors and guns or detonations associated with the use of high explosives). However, over the past 10 years a number of groups throughout the world have been conducting experiments to understand the chemical and physical processes that control the behaviors of energetic materials under conditions ranging from the fast reactions associated with detonations to the slow reactions associated with the response of these materials to slow "cookoff" situations associated with fires.

In our work using STMBMS and TOF velocity spectra methods, we have concentrated on understanding the reaction mechanisms that control the initial transformation of an energetic material, such as RDX or HMX, to its intermediate products. These intermediate products undergo further reactions toward final products (i.e., N_2, H_2O, CO_2 ...), releasing heat in various steps of the process. Understanding these processes is important for developing reliable models that can predict the behavior of these materials under various conditions. For example, during the combustion of a propellant, the partition of heat release between the liquid layer on the burning surface and the gas phase region of the secondary flame zone will determine the burn rate characteristics of the propellant. In another example, the response of an energetic material in a slow 'cookoff" situation may either lead to a mild accident associated with the deflagration of the material or a more serious accident associated with the detonation of the material. Thus, one would like to utilize a better understanding of energetic materials to characterize the safety associated with energetic material formulations presently in use and to develop new formulations that will be safer and provide better performance.

The paper for this workshop concentrates on the molecular beam techniques and how they have been used to provide details on the chemical reaction mechanisms that control the behavior of energetic materials at low heating rates.

Experimental: The STMBMS and TOF Velocity Spectra Methods

The goal of our experimental measurements on energetic materials is to determine the identity of the thermal decomposition products and their rates of formation as a function of time. From these measurements, we then strive to develop reaction mechanisms and the associated reaction kinetics parameters that control the thermal decomposition process. Ultimately, we will include these pathways and the associated kinetics in three-dimensional chemical/thermal/mechanical codes that can be used to predict the response various energetic material formulations.

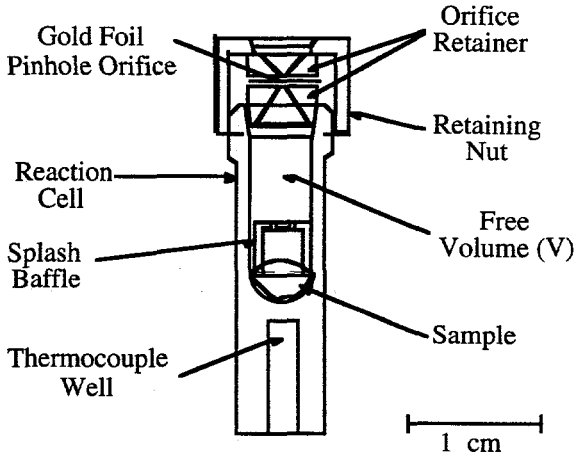

Figure 1. Cross section of the alumina reaction cell.

The thermal decomposition experiment is carried out on a 10mg sample of material that is contained in an alumina reaction cell shown in Fig. 1. The reaction cell is located in the STMBMS apparatus shown in Fig. 2. The STMBMS apparatus, the data collection system and the STMBMS and TOF velocity spectra data analysis methods have been described in detail elsewhere.[1-3] Briefly, this instrument allows the concentration and rate of formation of each gas-phase species in a reaction cell to be measured as a function of time by correlating the ion signals at different m/z values measured with a mass spectrometer with the force measured by a microbalance at any instant. In the experimental procedure, a small sample (~10 mg) is placed in an alumina reaction cell that is then mounted on a thermocouple probe that is seated in a microbalance. The reaction cell is enclosed in a high vacuum environment ($< 10^{-6}$ torr) and is radiatively heated by a bifilar-wound tungsten wire on an alumina tube. The molecules from the gaseous mixture in the reaction cell exit through a small diameter

(~2.5 μm to 1000μm) orifice in the cap of the reaction cell, traverse two beam-defining orifices before entering the electron-bombardment ionizer of the mass spectrometer where the ions are created by collisions of electrons with the different molecules in the gas flow. The background pressures in the vacuum chambers are sufficiently low to eliminate significant scattering between molecules from the reaction cell and background molecules in the vacuum chambers. The different m/z-value ions are scanned with a quadrupole mass filter and counted with an ion counter. The gas flow is modulated with a chopping wheel and only the modulated ion signal is recorded. The containment time of gas in the reaction cell is a function of the area of the orifice, the free volume within the reaction cell, and the characteristics of the flow of gas through the orifice. For the reaction cell used in the experiments with RDX, the time constant for exhausting gas from the cell (i.e., the time it takes after its formation, for a gaseous product to exit from the reaction cell) is short (~3.2 sec) compared to the duration of the experiments (>~1000 sec). Since the evaporation rate of the reactant is controlled by the size of the reaction cell orifice, the relative rates of reactant evaporation and reactant decomposition are controlled by adjusting the size of the reaction cell orifice.

Identification of decomposition products. The decomposition products are identified by: 1) using isotopically labeled analogues to determine the formulas of the ion signals at the different m/z values measured with the mass spectrometer, 2) performing an autocorrelation analysis on all of the ion signals measured during one thermal decomposition experiment and separating the different m/z values into temporally correlated groups that represent the major ion signals in the mass spectra of each product, and 3) measuring time-of-flight (TOF) velocity spectra of ion signals at m/z values representing each decomposition product to determine the molecular weight of the respective thermal decomposition product. Explicit details of this procedure have been described previously for the case of HMX decomposition.[3]

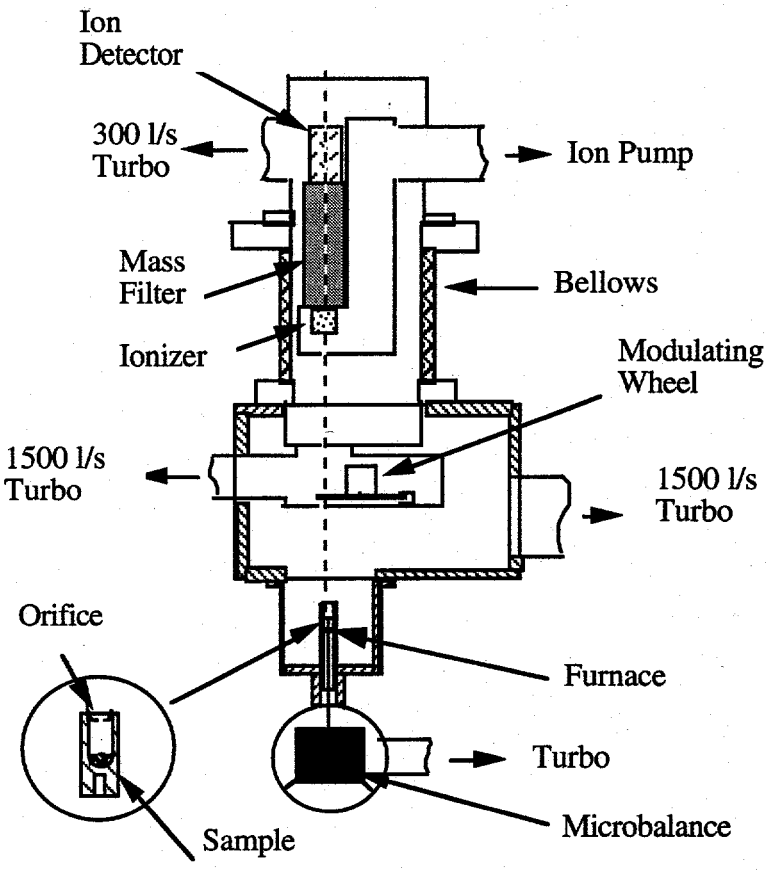

Figure 2. Schematic diagram of the simultaneous thermogravimetric modulated beam mass spectrometer (STMBMS) apparatus.

Quantification procedure. The procedures used to convert the ion signals measured with the mass spectrometer to rates of gaseous decomposition product formation have also been described previously.[1,2] Basically, the rate of force change measured by the microbalance (due to gas exiting the cell and the thrust due to gas in the cell) and the ion signals measured with the mass spectrometer are related to each other by the number density of the gases within the reaction cell, the gas flow characteristics of the cell, and the geometry of the apparatus. From this relationship the sensitivity factors that relate the number densities of the different gaseous species within the cell to

the ion signals measured with the mass spectrometer can be determined. After the mass spectrometer sensitivity factors are determined, the results are expressed as either the number density, partial pressure or the rate of molar gaseous product formation of each species as a function of time. For decomposition products that are present only in the gas phase and have low solubilities in the condensed phase, the rates of release from the reaction cell are equal to the rates of formation of these decomposition products. For products that are present in both the gas and condensed phases, the rate of release from the reaction cell is determined by the equilibrium vapor pressure of the species in the reaction cell.

Thermal Decomposition of RDX: Illustration of the Experimental Methods

The thermal decomposition of RDX is used to illustrate the various aspects of the STMBMS and TOF velocity spectra measurements. Details of the RDX experiments have been published elsewhere.[4,5]

Raw Data from STMBMS. The raw data from one experiment with RDX is shown in Fig. 3. The temperature and force (mass and thrust from gas exiting the reaction cell) are shown on the "billboard". The ion signal is illustrated on the surface plot as a function of m/z value and time. One can see a clear correlation between the increase in signal measured with the mass spectrometer and the decrease in force measured by the microbalance. A more careful examination of the ion signals shows differences in their temporal behavior. For example, the ion signals at m/z values of 75, 120, 128 and 148 show an earlier appearance and more gradual increase compared to the ion signals at m/z values of 70 and 97. The ion signals at m/z values of 75, 120, 128 and 148 originate from the electron bombardment induced ion dissociation of evaporating RDX in the mass spectrometer and the ion signals at m/z values of 70 and 97 originate from a thermal decomposition product of RDX that only forms upon melting of the RDX sample. Careful examination of the temporal behaviors of the ion signals at the other m/z values allows one to group the signals into groups of temporally correlated m/z values. This is the first step in the identification of the thermal decomposition products.

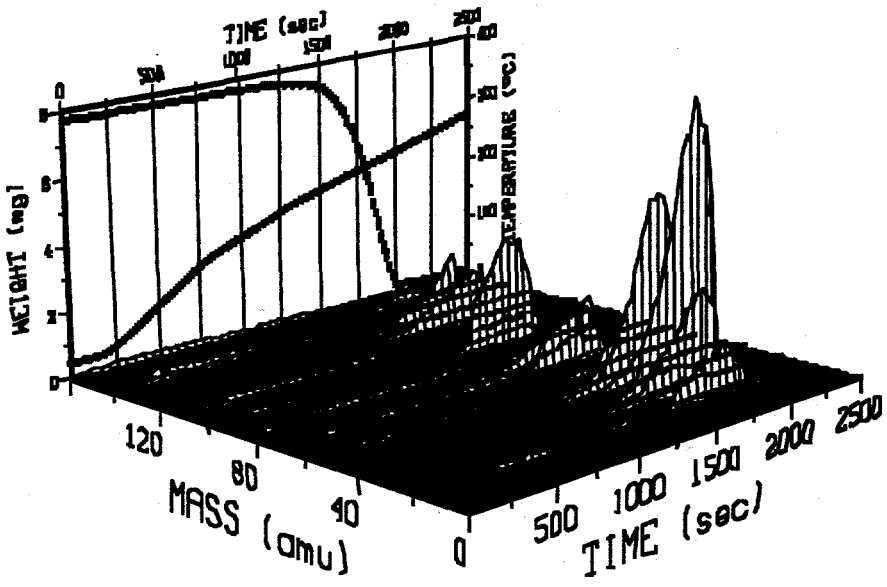

Figure 3. STMBMS data from the decomposition of RDX.

TOF Velocity Spectra. The TOF velocity spectra of the ion signals at various m/z values associated with the decomposition of RDX are shown in Fig. 4. The TOF spectra are used to determine the molecular weight of the thermal decomposition product that leads to the various ions formed in the mass spectrometer. TOF spectra in Fig. 4 show that ion signals at some of the m/z values arise solely from the thermal decomposition products. These products include HCN(m/z=27), N_2O(m/z=44), methylformamide H_2NCHO(m/z=45), HONO(m/z=47), and $C_3H_3N_3O$(m/z=97). On the other hand, TOF velocity spectra of ion signals at several other m/z values show that the ion signals at these m/z values arise from a decomposition product in addition to RDX that evaporates from the reaction cell without undergoing decomposition. Contributions from both RDX and its decomposition products are found at m/z values associated with CO(m/z=28), CH_2O(m/z=29,30),

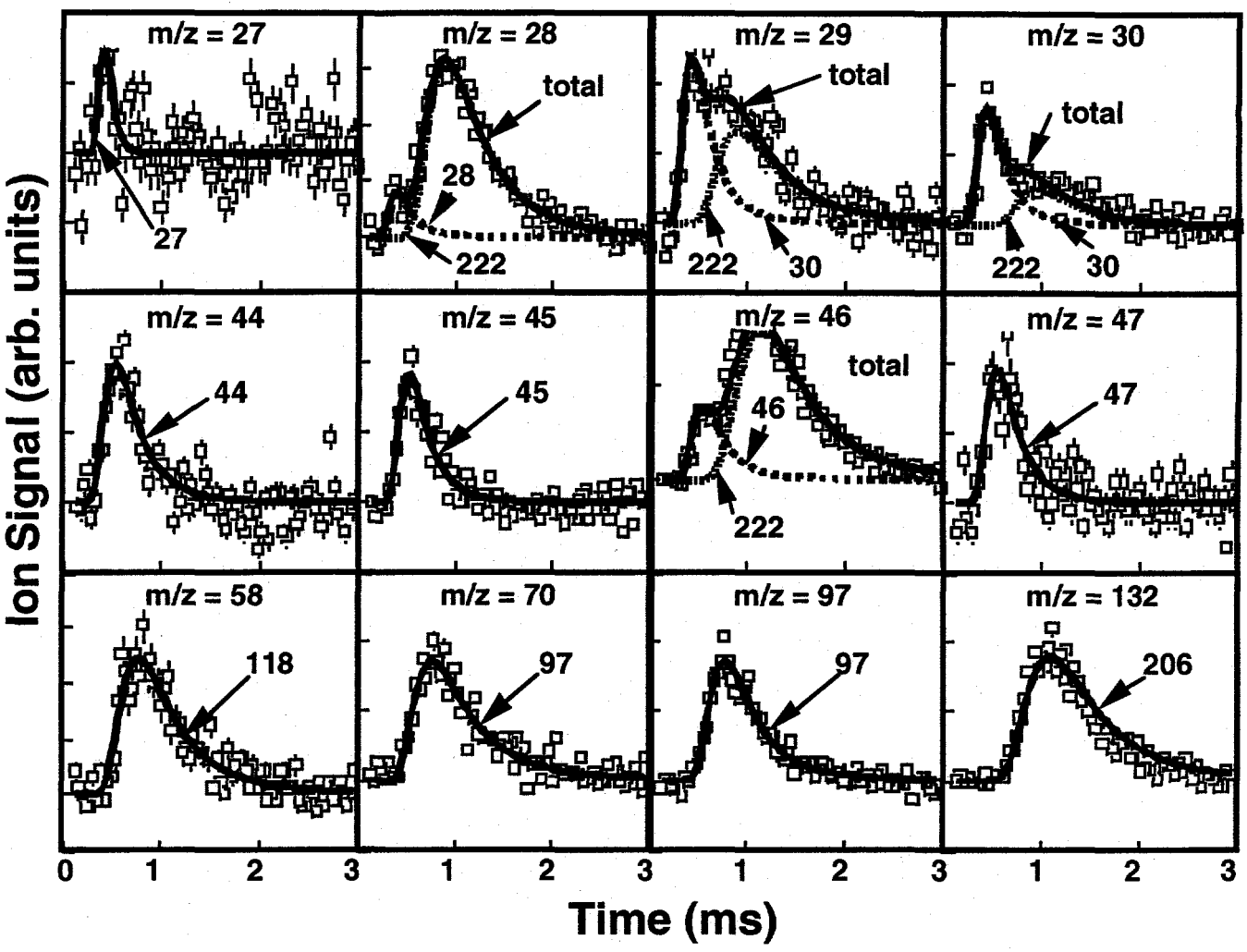

Figure 4. Time-of-flight velocity spectra of ion signals at various m/z values measured with the mass spectrometer. The signals are formed from the mixture of products evolving from the reaction cell during the decomposition of RDX. The symbols represent the measured data, the error bars denote the one-sigma standard deviation, and the solid and dashed curves represent the contribution to the ion signals from the various species (denoted by their molecular weights) that are contained in the mixture of products flowing out of the reaction cell during the decomposition. The details of the deconvolution procedure to fit the data are described in Reference 2. Details on the conditions under which the data was collected may be found in Ref. 4.

NO(m/z=30), and NO_2(m/z=46). Finally, the TOF velocity spectra show that ion signals at several m/z values are daughter ions formed in the mass spectrometer from thermal decomposition products (e.g. 132). These include the ion signal at m/z=58 that probably originates from the N-methylformamide dimer (MW = 118), the ion signal at m/z=70 that originates from the $C_3H_3N_3O$ product, and the ion signal at m/z=132 that originates from 1-nitroso-3,5-dinitro-hexahydro-s-triazine (ONDNTA) (MW = 206).

Several of the TOF velocity spectra displayed in Figure 5 show that major ion signals recorded at several m/z values are formed solely from evaporating RDX. These spectra were collected during the isothermal decomposition of RDX under the conditions listed for Experiment VI in Table I. The TOF velocity spectra at m/z values of 74, 75, 120, 128, and 148 clearly show that these ion signals originate from the electron bombardment ionization of RDX followed by the fragmentation of the RDX molecular ion into its daughters. If thermal decomposition products are present at any of these m/z values, they are masked by the large signals originating from evaporating RDX. In light of the low electron energies (18.4 eV) used in these experiments and the significant fragmentation of HMX found in experiments with HMX,[3] this limitation is likely to be present in any thermal decomposition experiment that utilizes electron bombardment ionization mass spectrometry to measure the mixture of decomposition products directly from a sample of RDX.

Isotopic analogues for formulas of m/z values. Using isotopic analogues of RDX allows one to determine the formulas of the various ion signals measured with the mass spectrometer. The results have been published elsewhere.[4]

Identification of the RDX thermal decomposition products. Through the use of simultaneous thermogravimetric modulated beam mass spectrometry (STMBMS) measurements, TOF velocity spectra analysis, and ^{2}H, ^{13}C, ^{15}N, and ^{18}O labeled analogues of RDX, the thermal decomposition products of RDX have been identified as H_2O, HCN, CO, CH_2O, NO, N_2O, NH_2CHO, NO_2, HONO, $(CH_3)NHCHO$, oxy-s-triazine (OST, III to V), and hexahydro-1-nitroso-3,5-dinitro-s-triazine (ONDNTA, VI).

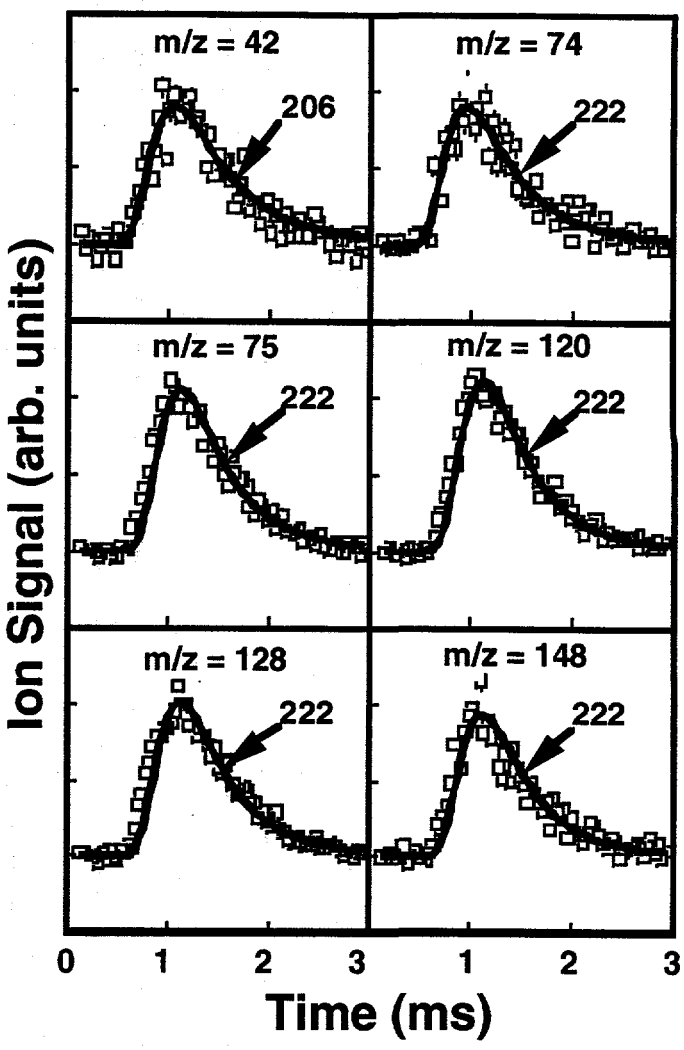

Figure 5. Time-of-flight velocity spectra of ion signals at various m/z values measured with the mass spectrometer. The signals are formed from the mixture of products evolving from the reaction cell during the decomposition of RDX. The symbols represent the measured data, the error bars denote the one-sigma standard deviation, and the solid and dashed curves represent the contribution to the ion signals from the various species (denoted by their molecular weights) that are contained in the mixture of products flowing out of the reaction cell during the decomposition. Details on the conditions under which the data was collected may be found in Ref. 4.

Quantification of the data. After identifying each of the decomposition products formed during the process and extracting an ion signal at one m/z value that is associated with each product, the data can be quantified according to the process described in Ref. 3. The rates of gas formation for each of the products formed in the decomposition of RDX are shown in Fig. 6. Careful examination of the data in Fig. 6 shows different temporal behaviors for each of the decomposition products. For example, the gas formation rate of OST is zero until the sample melts at ~201°C, at which time, it rises to it greatest rate of formation and then decays as the amount of RDX in the cell decreases. In contrast, the gas formation rate of ONDNTA is smallest when the sample melts and rises to its maximum value just before the RDX is depleted. Analysis of this behavior allows reaction pathways for the decomposition process to be determined as outlined below.

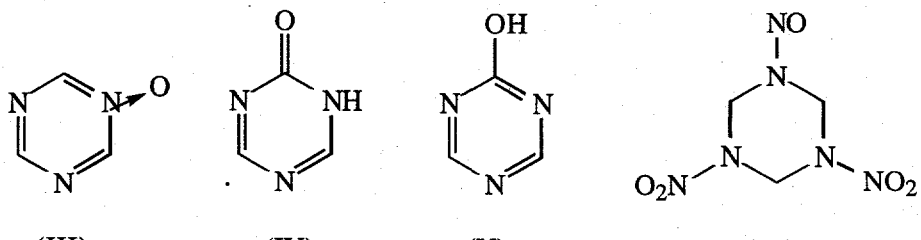

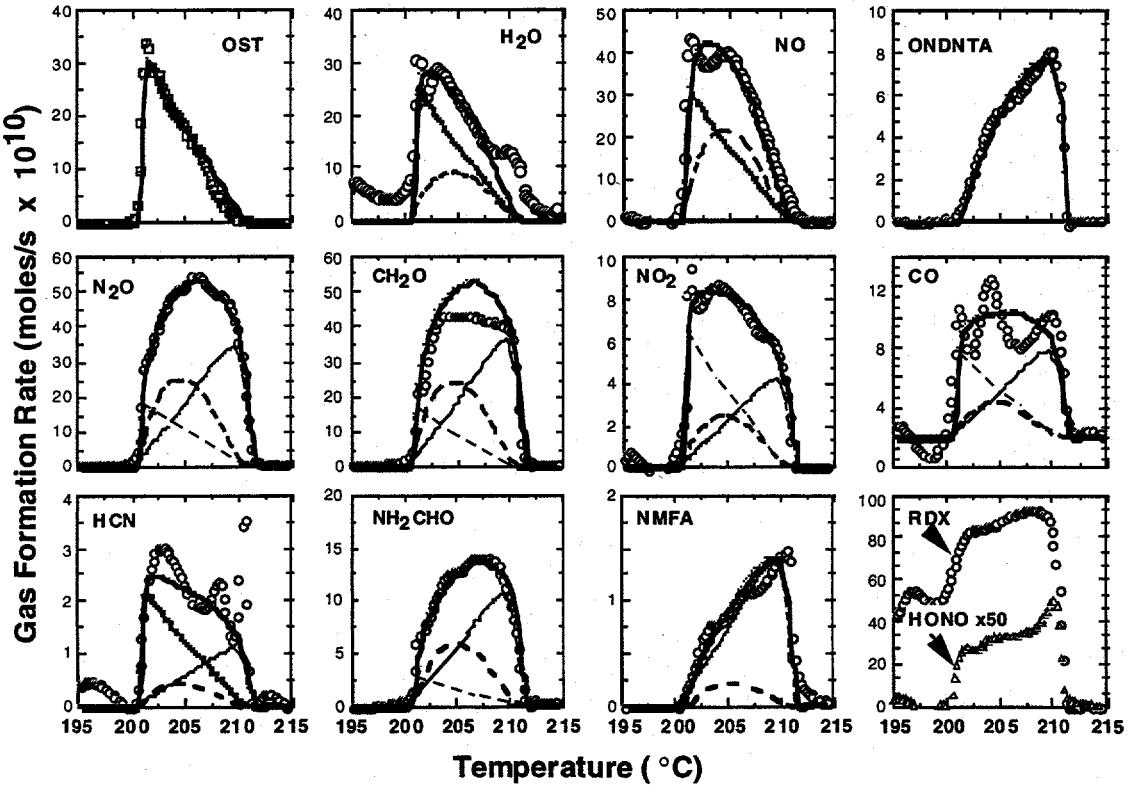

Figure 6. Contributions of the four primary decomposition pathways to the various products formed during the thermal decomposition of pure RDX. The bold line (——) in all of the graphs represents the total contribution from all of the reaction channels. The bold line (——) in OST represents the contribution by reaction pathway P1. The thin dashed (— —) lines shown in N_2O, CH_2O, NO_2, and NH_2CHO represent the contributions from reaction pathway P2. The bold dashed lines (— —) represent the contribution from the ONDNTA decomposition pathway P3. The thin solid lines (——) that peak near the highest temperature correspond to the contribution from the catalytic decomposition pathway P4. The calculated rate of formation of CH_2O is equivalent to the rate of formation of N_2O. The difference between the calculated and measured rates of formation of CH_2O is due to its reaction within the sample cell.

Deuterium kinetic isotope effect (DKIE) and isotope crossover experiments. The use of deuterium labeled analogues allows one to determine whether hydrogen transfer is involved in the rate limiting step of a particular pathway. The use of ^{2}H, ^{13}C, ^{15}N and ^{18}O can be used in isotope crossover experiments to determine whether particular bonds in the parent compound remain intact or are broken during the reaction process. This is illustrated for the decomposition of RDX by examining the behavior of the OST product as shown in Fig. 7. The results for a 50/50 mixture of $^{14}N/^{15}N$ labeled RDX is shown in Fig. 7a. Ion signals are observed at m/z values of 97($^{14}N_3$) and 100($^{15}N_3$) but no signals are observed for the cross over products at m/z values of 98 and 99. Thus, all of the nitrogen in the ring of the OST products comes from one parent RDX molecule. The results for a 50/50 mixture of $^{1}H/^{2}H$ labeled RDX is shown in Fig. 7b. Here again there are ion signals at m/z values of 97($^{1}H_3$) and 100($^{2}H_3$) but no signals are observed for the cross over products at m/z values of 98 and 99. Thus, the three hydrogen atoms in OST originate from the one parent RDX molecule. In addition, the ratio of the ion signals at m/z values of 97($^{1}H_3$) and 100($^{2}H_3$) is approximately 2 to 1, indicating that the rate limiting step in the formation of OST involves the transfer of a hydrogen atom. Finally, the results for a 50/50 mixture of $^{13}C/^{18}O$ labeled RDX is shown in Fig. 7c. The lack of a temporally correlated ion signal at m/z=102 shows that there are no OST is completely formed by an intramolecular process. The ion signals at m/z= 97 and 99 originate from the RDX-^{18}O sample that is enriched to 4% ^{18}O.

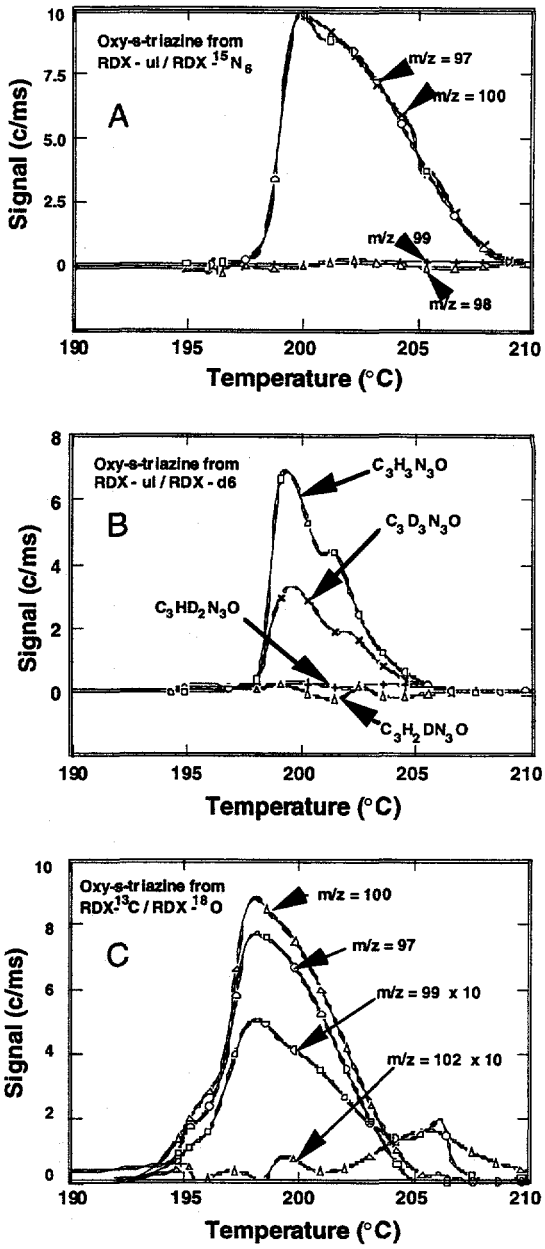

Figure 7. Ion signals, formed in the mass spectrometer, from oxy-s-triazine and its isotopic analogues: a) RDX-unlabeled and RDX-$^{15}N_6$; b) RDX-unlabeled and RDX-$^{2}H_6$; c) RDX-^{13}C and RDX-^{18}O.

Determination of a reaction mechanism. From the identification of the products, analysis of the DKIE and isotope crossover experiments and the temporal behaviors of the gas formation rates of the various products the following four reaction pathways were developed.

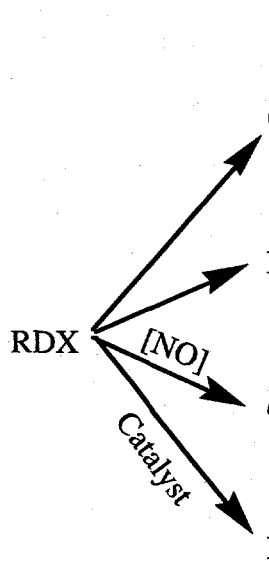

Products	Path	Fraction	DKIE	$^{14}N/^{15}N$ Exchange
$OST + H_2O + NO + NO_2$	1	30%	Yes	No
$NO_2 + H_2CN + 2\,N_2O + 2\,CH_2O$	2	10%	No	No
$ONDNTA \longrightarrow N_2O + CH_2O + other$	3	35%	No/Yes	Yes
$N_2O + CH_2O + NO_2 + NH_2CHO$	4	25%	No	No

The first reaction pathway is first order in OST and is based on the temporal behavior of the OST, H_2O and NO signals in addition to the lack of isotopic scrambling in the OST product. The second pathway is based on the rapid rise in the CH_2O and N_2O signals. This behavior appears to be first order in RDX, similar to OST. Clearly, the CH_2O and N_2O products cannot form by pathway 1 and therefore a second first order pathway was invoked to explain their temporal behavior. The third pathway involves the formation of ONDNTA and its decomposition predominantly to N_2O and CH_2O. This pathway is consistent with the formation of ONDNTA in the liquid RDX. As the mole fraction of ONDNTA in RDX increases its vapor pressure will increase and thus its rate of release from the reaction cell. This is consistent with the observed data for ONDNTA. If one assumes that the observed rate of release of ONDNTA is proportional to its mole fraction within the sample, then one can calculate its rate of thermal decomposition and its contribution to the formation of the other products as shown in Fig. 6 for pathway 3. The fourth pathway is attributed to an autocatalytic reaction. The pathway was invoked to account for the very high rates of formation of CH_2O and N_2O as the RDX sample was nearing depletion. Few details are known about the pathway.

Conclusion

The use of STMBMS and TOF velocity spectra methods have allowed the determination of many details of the thermal decomposition mechanism of RDX. Although normal mass spectrometry measurements of thermal decomposition processes provide large amounts of data, the data can be ambiguous and difficult or impossible to interpret. We have shown that by using isotopically labeled analogues and TOF velocity spectra measurements, much of the ambiguity can be eliminated and the identity of the thermal decomposition products determined. In addition, we have shown that by simultaneously measuring the force change due to gas evolution from the reaction cell and the mass spectra of the evolving gas, the sensitivity factors needed to relate the ion signals to the gas formation rates of the thermal decomposition products can be determined, thus reducing the need to measure sensitivity factors for each decomposition product. Finally, we have shown that by employing these techniques with isotopically labeled samples insight into the bond breaking and bond forming steps in the reaction mechanism can be obtained.

Acknowledgment

The studies on the thermal decomposition of RDX were carried out in collaboration with Dr. Suryanarayana Bulusu, Dept. of Army, ARDEC. The design of the apparatus was done by Mr. Norman Toly, the initial assembly and testing was done by Mr. Jan Collins. The coding for the TOF analysis was done by Mr. Cliff Schaeffer. The experiments on RDX were carried out in part by Mr. Yancy Lutz, Mr. Joe Damino and Mr. Mark Mitchell. Work supported by the U.S. Department of Energy under contract DE-AC04-94AL85000, the U.S. Dept. of Army, and the Army Research Office.

---

[1] a) Behrens, Jr., R., *Rev. Sci. Instrum.*, **1986**, 58, 451; b) Behrens, Jr., R., "The Application of Simultaneous Thermogravimetric Modulated Beam Mass Spectrometry and Time-of-Flight Velocity Spectra Measurements to the Study of the Pyrolysis of Energetic Materials," in "Chemistry and Physics of Energetic Materials," Bulusu, S. N., Ed.; Proceedings of the NATO Advanced Study Institute, Vol. 309, Kluwer Academic Publishers, Netherlands, 1990, p. 327.

[2] Behrens, Jr., R., *Int. J. Chem. Kinetics*, **1990**, 22, 135.

[3] Behrens, Jr., R., *Int. J. Chem. Kinetics*, **1990**, 22, 159.

[4] R. Behrens, Jr. and S. Bulusu, J. Phys. Chem., **96**, 8877, 1992.

[5] R. Behrens, Jr. and S. Bulusu, J. Phys. Chem., **96**, 8891, 1992.

Determination of Mass and Velocity Distributions of Soot Particles in a Nozzle Beam from a Flame by Means of a Wien Filter

K.-H. Homann and W. Wiese
Institut für Physikalische Chemie, Technische Hochschule Darmstadt
Petersenstr. 20, D-64287 Darmstadt

1. Introduction

Size distributions of soot particles in flames have mainly been determined from electron micrographs of particles. However, there is a limit of about 3 nm below which the uncertainty in particle diameter determined in this way becomes too large for a sufficiently accurate mass determination [1]. For an understanding of the soot formation mechanism it is of particular interest to study the mass growth of the first soot particles after their inception from large hydrocarbon molecules. This concerns a mass range of some 10^3 to some 10^4 u. High-resolution mass spectrometry (MS) has the shortcoming that ionization of soot particles in an ion source does not seem to be very effective. Furthermore, the sensitivity of the usually applied electron multiplier detectors decreases with ion mass in a uncontrollable way.

We therefore developed a new method for the mass analysis of very small particles. Charged soot particles can be sampled from low-pressure flames via a nozzle beam which generates a current large enough to be measured with a Faraday detector and a sensitive electrometer. Their mass distribution is quasi-continuous so that high mass resolution is not necessary.

2. Experimental (Fig.1)

A sooting pre-mixed hydrocarbon/oxygen flame burning on a flat flame burner at a pressure of p_0 = 26.6 mbar (20.0 Torr), directed downwards for technical reasons (not shown in Fig. 1), was sampled through a conical quartz nozzle probe with an orifice, the diameter of which was varied in different experiments (0.45 to 1.0 mm). The probe delivered a nozzle beam with a radially Gaussian flow distribution of the charged particles [2]. For the sampling of charged species, the tip and the inside of the cone were coated with a platinum paint to keep it on ground potential, as was the burner. A skimmer with a rectangular cross section (0.95×5.0 mm) in the first vacuum chamber (p_1 < 0.05 Pa) collimated the molecular beam onto the entrance slit of the Wien filter in the second vacuum chamber ($p_2 \approx 10^{-4}$ Pa).

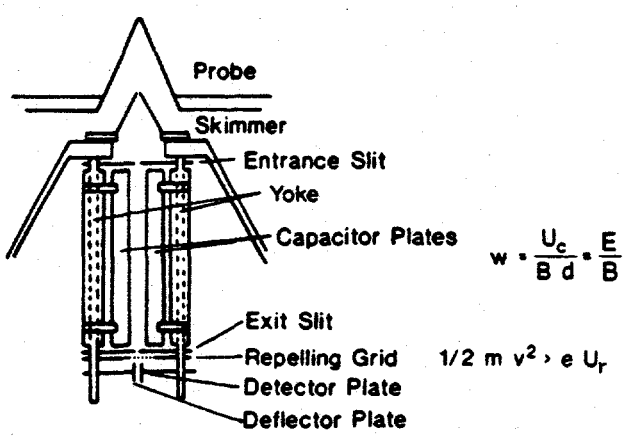

Fig. 1. Wien Filter Mass Spectrometer

The Wien filter consisted of a magnetic (B = 0.59 T) and a variable electric field (E = 0 to 10 V/cm) which stand perpendicularly to each other. Depending on the strength of the E-field, only

particles with a certain velocity, $w = E/B$, independent of their mass, could pass the Wien filter undeflected [3]. The variable dc field was applied in such a way as to keep the plane through the rectangular entrance and exit slits along the long axis of the Wien filter at ground potential, in order to avoid any acceleration or deceleration of the particles in this direction. The length of the Wien filter was 100 mm. By these measures a sufficient resolution of velocity w of the undeflected particles could be achieved up to masses of $3 \cdot 10^4$ u. Due to cycloidal trajectories of light particles crossing the long axis of the filter, the low-mass limit was at about $2 \cdot 10^3$ u. The trajectories of the particles in the Wien filter, which are used for evaluation of the measurements, have been described elsewhere [4].

Behind the Wien filter the particles passed a repelling grid, the bias voltage, U_r, of which was varied so that only particles with kinetic energies above eU_r, could reach a Faraday detector placed behind the grid. From the detector current as a function of the repelling voltage for particles within a certain range of velocities, which then is varied, the mass and velocity distribution of the soot particles is calculated. The method may be applied to charged particles of either sign. More details of the experimental set-up are given in references [4] and [5].

3. Measuring and Evaluation Procedure

The detector current, $I_w(U_r)$, as function of the repelling voltage, U_r, is related to the quantities of interest, the particle mass, m, and velocity, v, by the equation

$$I_w(U_r) = e \int_0^\infty \int_0^\infty K_w(m, v)\, K_U(m, v)\, F(m, v)\, \mathrm{d}m\, \mathrm{d}v \qquad (1)$$

where K_w is the transmission function of the Wien filter at constant w, and K_U that of the repelling grid. $F(m, v)$ is the combined distribution function of flow of charged particles entering the Wien filter. Under most flame conditions these small particles carried only one elementary charge e. The total mass distribution function, $G(m)$, which is of interest for the process of soot formation, is given by

$$G(m) = \int_0^\infty F(m, v)\, \mathrm{d}v \qquad (2)$$

while the velocity distribution, $H(v)$, is obtained from

$$H(v) = \int_0^\infty F(m, v)\, \mathrm{d}m \qquad (3).$$

The method of evaluation has been described in detail in reference [5]. Briefly, since the repelling voltage, U_r, is proportional to the kinetic energy, E_k, the right-hand side of Eq. (1) is transformed to the variable E_k. An approximation is that the (unknown) m and v are replaced by their 'nominal' values, m_n and w, which are given by

$$m_n = 2\, e\, U_r / w^2 \qquad (4)$$

U_r and w could be set in the experiments (see above) and are no unknown values. Eq. (1) is differentiated with respect to E_k at constant w. The transmission function, $K_w(m, v)$ was obtained from the trajectories of the charged particles in the Wien filter and from the areas of the entrance and exit slits and was integrated over $\mathrm{d}v/v^2$. Since the transmission function with respect to v becomes broader with m, the resolving power of the Wien filter as a velocity selector becomes poorer with increasing mass of the particles. However, up to masses of about $3 \cdot 10^4$ u the resolving power for $B = 0.59$ T is fully satisfactory. The integrals (2) and (3) were replaced by sums obtained from different but equally spaced settings for w and m_n [5].

4. Computer Experiments

This approximate evaluation method was tested using a computer experiment in which the detector currents, $I_w(U_r)$, from particles with a given pre-set mass and velocity distribution were simulated [6]. These values were then treated with the same evaluation procedure as described for the experimental values. In Fig. 2 the obtained distributions are compared with the pre-set distributions, both being normalized to their maxima. The most probable mass is exactly reproduced and the half width is wider by only 7 % than that of the original distribution. It shows that this simple Wien filter 'mass spectrometer' is very well suited to measure continuous mass distributions, although its resolving power is very poor, if discrete masses are regarded which has also been confirmed through computer experiments [6].

The width of the total velocity distribution is very well reproduced. However, the recovered function of nominal velocities is shifted to somewhat lower values, so that the most probable velocity ist 575 instead of 600 m/s, a deviation of about 4 %. The reason for this is the asymmetry of $K_w(m, v)$ in v with respect to w, cf. ref [5].

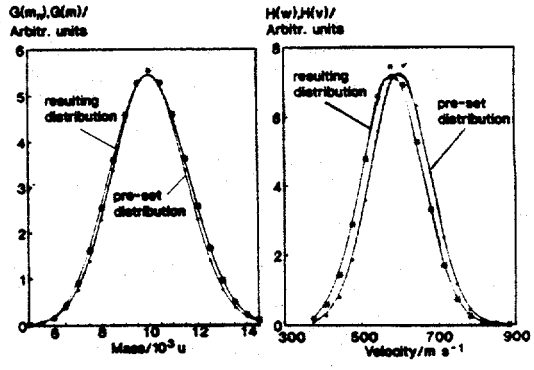

Fig. 2. Comparison of pre-set mass and velocity distributions with recovered distributions from the computer experiment

5. Velocity Distributions

If this slight asymmetry in filtering the velocity is taken into account, this device is a simple means of measuring very exactly the velocity distribution of charged particles of larger mass in a seeded beam. It is also possible to evaluate the measurements to give the velocity distribution of particles in a certain range of masses.

Several experiments showing the influence on the velocity distribution by varying parameters of the beam system have been performed. The average velocity of the particles increases with the nozzle diameter

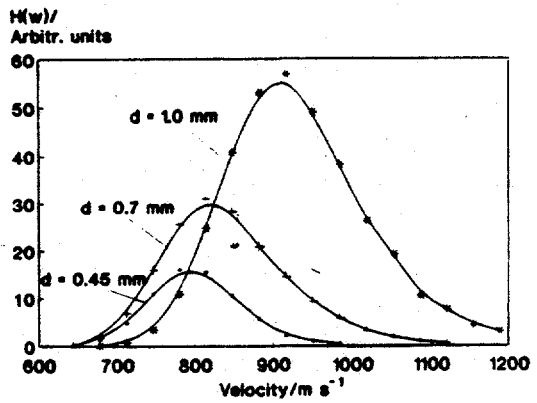

Fig. 3. Particle velocity distributions obtained with different nozzle diameters; C_2H_2/O_2 flame, $p_0 = 27$ mbar, $v_u = 42$ cm/s, C/O = 1.06

of the probe. Fig. 3 shows the influence on the velocity distribution, $H(v)$, of charged soot particles for three different nozzle diameters. The distributions are not quite symmetric about their maximum value. This increases from 780 m/s for 0.45 mm to 910 m/s for 1.0 mm diameter. The increase in intensity is approximately proportional to the cross section of the nozzle.

The final average gas velocities were estimated according to the theory of expanded supersonic nozzle flow for the diameters 0.45, 0.70 and 1.0 mm to be 1.80, 1.94 and $2.01 \cdot 10^3$ m/s, respectively [7]. The ratio of the mean velocity of the particles to that of the gas are 0.43 and 0.45 for the nozzle diameters 0.45 and 1.0 mm, respectively, showing the slip in velocity of the soot particles. These numbers may be compared with the velocity slip calculated by Schwartz and Andres for seeded beams [8]. Fig. 4 shows three theoretical curves of this velocity ratio for heavy atoms (Xe) and large particles (latex) as a function of the so-called slip number. The soot particles lie between these extremes. The influence of the charge on the effective collision cross-section of the particles is insignificant, as can be estimated from ion-dipole and ion-induced dipole interaction.

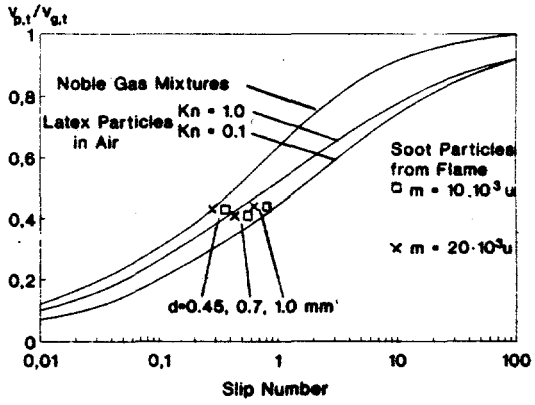

Fig. 4 Comparison of calculated with experimental values of the particle-to-gas final velocity ratios in the seeded beam.

Figure 5 shows the change in velocity distribution, if the background pressure, p_1, is increased. With an increase from 1 to 4×10^{-4} Torr the most probable velocity decreases from about 700 to 560 m/s and the absolute half width of the distribution increases slightly. The distribution becomes more asymmetric. By dilution of the flame with helium, thereby increasing the ratio $\gamma = C_p/C_V$ and decreasing the mean molecular mass of the gas, the velocity of the particles is increased (not shown in a figure).

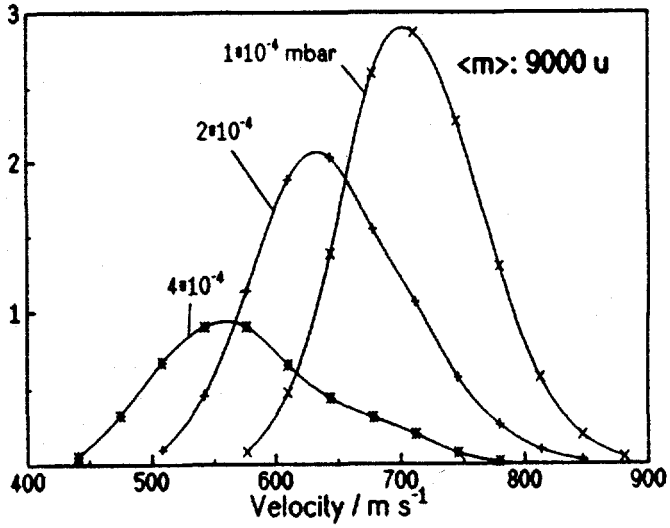

Fig. 5 Dependence of the velocity distribution on the background pressure, p_1, behind the nozzle for an average particle mass of 9×10^3 u.

6. Mass Distributions

Mass distributions of soot particles are dependent on the fuel and the burning conditions and their measurement should not be influenced by parameters of the measuring method, such as the nozzle diameter. Fig. 6 shows mass distributions of soot particles from an acetylene/oxygen flame sampled with nozzle probes of different diameters under the same conditions as in Fig. 3. Independent of the nozzle diameter, the most probable mass is found to be $(13 \pm 0.5)\times10^3$ u. However, the width of the distribution changes by 20 % when changing the diameter from 1.0 to 0.45 mm. This minor discrepancy may be due to various small effects which are intrinsic with sampling by cone-shaped nozzle probes: With a larger nozzle diameter, gas is entrained on the average from a point somewhat more distant from the probe tip; a different inflow into the nozzle might influence the temperature profile in the vicinity of the nozzle, and furthermore small differences in the shape and wall thickness of the tips of different probes may also influence the flame temperature.

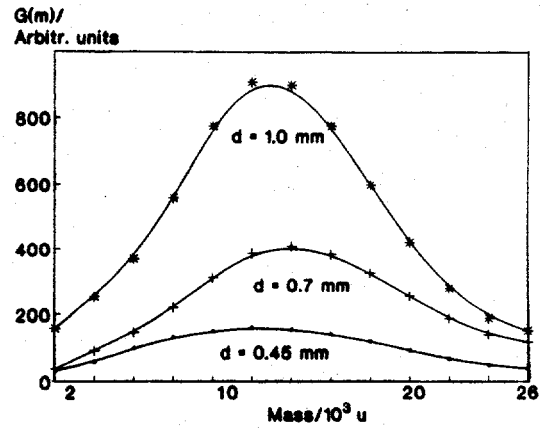

Fig. 6. Mass distributions obtained with different nozzle diameters. Same flame conditions as in Fig. 3

Care must also be taken that the mass distribution is not changed by a high background pressure in the vacuum chamber. Two effects may be disturbing: Scattering will decrease the intensity of the light particles more than that of the heavier ones. If the velocity is decreased too much, the flight time of the particles through the Wien filter will increase, and the more pronounced cycloidal motion will influence the resolution or will cause these particles to hit the wall [4].

When increasing the distance to the burner in the flame from where the sample was taken, the change in the mass distribution, that is the mass growth process of very small soot particles, can be followed with an accurateness that has not been reached before. Fig. 7 shows mass distributions from different heights in a 1,3-butadiene/oxygen flame with a C/O ratio of 0.90, the soot threshold being at 0.85. These sites lie in the burned gas of the flame. In contrast to the log-normal distributions, which have been found for larger particles [9], they are more nearly Gaussian, although not completely so. With increasing distance the maximum shifts to larger values, by about 5×10^3u per 5 mm. The half width of the distribution increases more than linearly with the most probable

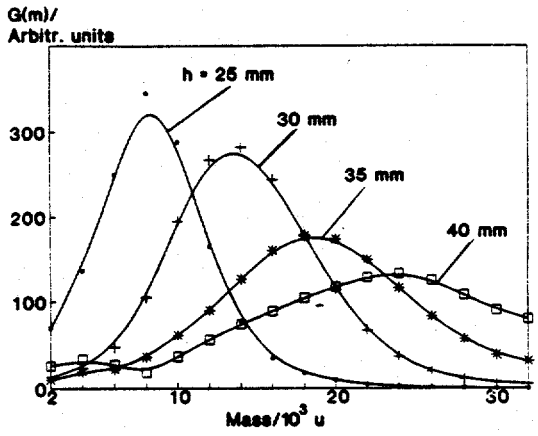

Fig. 7. Mass distributions at different heights, h, from the burner in a 1,3- butadiene/O_2 flame; C/O = 0.90; p_0= 27 mbar; v_u= 42 cm/s

mass. The small maximum at 3 to 4×10^3u in the distribution at 40 mm is not due to soot particles but to large fullerene ions, as has been confirmed by time-of-flight mass spectrometry [10]. The change in the mass distribution can be simulated with a modell which assumes heterogeneous decomposition of acetylene at the surface of the particles with a negligible contribution of coagulation of particles at the low pressure. More details of this modell, on the influence of burning pressure and unburned gas velocity, v_u, on the particle mass distribution and of the results for negatively charged particles are given in reference [5].

Acknowledgment

This work was supported by the Fonds der Chemischen Industrie which is gratefully acknowledged.

References

[1] Wersborg,. B. L., Howard, J. B., and Williams, G. C., Fourteenth Symp. (Internat.) on Combustion, The Combustion Institute, Pittsburgh, 1973, p. 929

[2] Gerhardt, Ph. and Homann, K. H., Combust. Flame *81*, 289 (1990)

[3] Glaser, W., *Handbuch der Physik, Korpuskularoptik*, Band XXXIII, Flügge, S., Hrsg., Springer, 1956, p. 141

[4] Homann, K. H. and Traube, J., Ber. Bunsenges. Phys. Chem. *91*, 828 (1987)

[5] Wegert, R., Wiese, W., and Homann, K. H., Combust. Flame *95*, 61 (1993)

[6] Wiese, W., Diplomarbeit, Technische Hochschule Darmstadt, 1991

[7] Scott, J. E. and Phipps, J. A., *Rarefied Gasdynamics, Advances in Applied Mechanics*, Suppl. 4, Vol. II, 1967, p. 1337, Academic Press, New York,

[8] Schwartz, M. H. and Andres, R. P., Progr. Astronaut. Aeronaut. *51*, 135 (1976)

[9] Bockhorn, H., Fetting, F., Meyer, U., Reck, R., and Wannemacher, G., Eighteenth Symp. (Internat.) on Combustion, The Combustion Institute, Pittsburgh, 1981, p. 1137

[10] Baum, Th., Löffler, S., Löffler, Ph., Weilmünster, P., and Homann, K. H., Ber. Bunsenges. Phys. Chem. *96*, 841 (1992)

STUDIES OF VOLATILE HIGH TEMPERATURE CORROSION PRODUCTS VIA THE FREE-JET MBMS TECHNIQUE

N. S. Jacobson
NASA Lewis Research Center
Cleveland, Ohio

In high temperature applications such as heat engines, heat exchangers, and chemical process plants, metal and ceramic structural materials are exposed to harsh chemical environments. It is important to understand the mechanism of corrosion of these materials under such conditions. Most laboratory studies of corrosion involve a sensitive microbalance with the sample suspended in a furnace and particular gas atmosphere (thermogravimetric apparatus--TGA). This system allows one to follow the kinetics of reaction and then characterize the corrosion products.

Corrosion products are often condensed phase oxides, sulfides, carbides, etc. However, they may often be volatile products such as volatile oxides, hydroxides, chlorides, and oxychlorides. In a TGA, these form as down-stream deposits, which must be chemically analyzed after an experiment. In such a "pseudo-transpiration" experiment, speculations can then be made regarding the composition of these vapor species. Clearly, an in-situ mass spectrometric sampling method is far superior for such analysis.

The free-jet expansion, molecular beam mass spectrometric technique allows direct identification of these species. The features of this technique--a rapid transition to collisionless flow, beam cooling, and a high velocity molecular beam--preserve the chemical and dynamic integrity of the beam. A schematic of our instrument is shown in Figure 1. The main chamber was built at Midwest Research Institute in 1975. The instrument was constructed at NASA by Stearns, Kohl, and Fryburg (1). It has been operational for almost twenty years and used to study not only volatile corrosion products, but also species in flames (2) and pack diffusion processes (3). It consists of four differentially pumped chambers and includes a chopper to separate the signal from the background. Recent modifications to the instrument include updating the mass spectrometer with an Extrel C-50 unit and the addition of a turbo-molecular pump to Stage IV.

In this paper, several studies on volatile corrosion products will be summarized. It will be shown how the mass spectrometric results are combined with other data to elucidate the reaction mechanism. These studies fall into two categories: volatile chlorides and oxychlorides, and volatile hydroxides. Corrosion by chlorine occurs in waste incineration and chemical process plants; formation of volatile hydroxides occurs in combustion environments since water is always a product of combustion.

Consider first the reaction of a pure metal, cobalt, and 1% Cl_2/1, 10, 50% O_2/Ar at 650°C (4). Table 1 shows the mass spectrometric data for this reaction.

Gas Mixture	I($CoCl^+$)	I($CoCl_2^+$)	I($CoCl_3^+$)
1%Cl_2--1%O_2--Ar	1.1 x 10^{-3}	1.2 x 10^{-3}	1.2 x 10^{-4}
1%Cl_2--10%O_2--Ar	1.5 x 10^{-3}	1.7 x 10^{-3}	1.9 x 10^{-4}
1%Cl_2--50%O_2--Ar	1.3 x 10^{-3}	1.4 x 10^{-3}	1.2 x 10^{-4}

Table I. Mass spectrometric results for Co + Cl_2/O_2 at 650 C. Ion intensities are normalized to Cl_2^+.

This indicates the major products are $CoCl_2$(g) and $CoCl_3$(g) and there is no dependence on oxygen pressure. The lack of oxygen pressure dependence eliminates direct reaction with the oxide:

$$3Cl_2\ (g) + Co_3O_4\ (s) = 3\ CoCl_2\ (g) + 2\ O_2\ (g) \qquad (1)$$

Instead it suggests reaction with the metal:

$$Cl_2 + Co = CoCl_2(s) \qquad (2)$$
$$CoCl_2(s) = CoCl_2(g)$$
$$CoCl_2(s) + 1/2\ Cl_2(g) = CoCl_3(g)$$

Examination of a cracked portion of the scale with the electron microscope shows that condensed phase chlorides have indeed formed in the region of low oxygen potential below the oxide scale. Thus the mechanism of cobalt corrosion in this environment involves oxide scale formation followed by chlorine penetration to form condensed phase chlorides at the oxide/metal interface. These chlorides vaporize to form the observed volatiles.

Next consider some binary Ni-Cr alloys and 1% Cl_2/50% O_2/Ar at 1200 K (5). These alloys were studied with the TGA, mass spectrometer, and the condensed phase products were characterized with x-ray diffraction and the electron microscopy. Table II shows the mass spectrometric results.

Ion	Parent	Ni-5Cr	Ni-15Cr	Ni-30Cr
$NiCl^+$	$NiCl_2$	1.5 x 10^{-2}	2.9 x 10^{-2}	6.4 x 10^{-3}
$CrOCl^+$	CrO_2Cl_2	--	5.6 x 10^{-4}	4.4 x 10^{-4}
CrO_2Cl^+	CrO_2Cl_2	1.6 x 10^{-4}	6.9 x 10^{-4}	3.8 x 10^{-4}
$NiCl_2^+$	$NiCl_2$	1 x 10^{-4}	2.5 x 10^{-2}	4.2 x 10^{-3}
$CrO_2Cl_2^+$	$CrO_2Cl_2^+$	1.1 x 10^{-4}	5.6 x 10^{-4}	3.9 x 10^{-4}

Table II. Mass spectrometric results for three Ni-Cr alloys + 1% Cl_2/50% O_2/Ar at 1200 K. Intensities normalized to Cl_2^+.

These results show that the principle vapor species at low Cr contents is $NiCl_2$ and at higher Cr contents it is a mixture of $NiCl_2$ and CrO_2Cl_2. X-ray diffraction showed the Ni-30Cr scale formed the largest quantity of Cr_2O_3 as an outer protective oxide scale. The larger amount of CrO_2Cl_2 from this alloy is consistent with a larger amount of Cr_2O_3 as the outer protective oxide. TGA measurements showed that each of the three alloys exhibited a linear weight loss. Calculations of $NiCl_2$ transport through a boundary layer gave results close to those measured, indicating gas phase diffusion of $NiCl_2$ was rate-controlling. The measured weight loss rate of the Ni-30Cr alloy was lower than Ni-5Cr and Ni-15Cr. The microstructure of the Ni-30Cr indicates a layer of NiO covered by a layer of Cr_2O_3. It is likely the outer layer of Cr_2O_3 partially blocked the escape of $NiCl_2$.

Two commercial alloys--Alloy 600 and Hastelloy S--were also examined in this 1% Cl_2/50% O_2/Ar environment at 900 C after a two hour oxidation in pure oxygen (6). Both alloys formed Cr_2O_3 and $NiCr_2O_4$ as protective oxides. Their compositions (in weight percent) are listed below:

Alloy 600: Ni bal, Cr 16, Fe 8
Hastelloy S: Ni bal, Cr 15.5, Mo 14.5, Fe 3, Co 2

TGA measurements showed that Hastelloy S lost weight about an order of magnitude faster than Alloy 600. Table III shows the mass spectrometric data for these alloys:

Ion	Parent	Ion intensities (x 10^4) for Alloy 600	Ion intensities (x 10^4) for Hastelloy S
$NiCl^+$	$NiCl_2$	2	14.7
$CrOCl^+$	CrO_2Cl_2	1.4	1.2
CrO_2Cl^+	CrO_2Cl_2	1.6	1
$NiCl_2^+$	$NiCl_2$	2.4	27.9
$CrO_2Cl_2^+$	CrO_2Cl_2	4.2	1.9
MoO_2Cl^+	MoO_2Cl_2	---	5.9
$MoO_2Cl_2^+$	MoO_2Cl_2	---	8.4

Table III. Mass spectrometric data for two commercial alloys in 1% Cl_2/50% O_2/Ar at 900°C. Ion intensities are normalized to Cl_2^+.

An explanation for the different behavior can be made based on this mass spectrometer data. Both alloys formed $NiCl_2$ and CrO_2Cl_2. Hastelloy S also formed MoO_2Cl_2, due to the large amount of Mo in this alloy. The larger amount of $NiCl_2$ formed from the Hastelloy S suggests scale penetration. It is likely that the Cr_2O_3 scale on Hastelloy S has more defects (cracks, micropores) than that on Alloy 600, which may be due to the formation and escape of MoO_2Cl_2 vapor from below the Cr_2O_3 scale.

Chlorination studies were also done on Si and SiC (7,8). These compounds were reacted with 2% Cl_2/Ar and 1% Cl_2/1-20% O_2/Ar at 950°C. A number of important phenomena were observed in this case. In general, the higher oxygen gas streams led to limited reaction due to the formation of an impervious silica scale. At lower oxygen contents, the observed products were $SiCl_x(g)$, where x=1-4, and smaller amounts of Si_2OCl_6 and Si_3OCl_8. To our knowledge, the silicon oxychloride compounds had not been observed before under these conditions.

Identification of the complex chlorine species in mass spectrometry is simplified by the two stable isotopes of chlorine. This leads to a clear "fingerprint" of the unknown species, with peaks separated by two amu. The relative intensities were calculated via an isotopic distribution computer program (8) and compared to the measured intensities. In such a way, Si_2OCl_6 and Si_3OCl_8 were identified. These compounds appear to form under conditions where large amount of $SiCl_4$ are present. It is likely that they form via gas phase or near surface reactions:

$$4SiCl_4(g) + O_2(g) = 2Si_2OCl_6(g) + Cl_2(g) \quad (3)$$

$$Si_2OCl_6(g) + SiCl_4(g) = Si_3OCl_8(g) + Cl_2(g) \quad (4)$$

In order to check this possibility, a stream of 50% O_2/Ar was passed over a flask containing $SiCl_4$ liquid at room temperature. A similar set of silicon oxychloride species were observed as those found in the high temperature reaction of Si and Cl_2/O_2.

Another type of volatile corrosion products is volatile hydroxy species. It well known that most high temperature oxides (e.g. Cr_2O_3, Al_2O_3, and SiO_2) produce these species in high temperature water vapor containing environments. Combustion processes always generate water vapor and future high pressure combustors will generate water vapor at pressures near 1 atm. Previous work in our laboratory has identified $CrO_2(OH)$, $CrO_2(OH)_2$, and $MoO_2(OH)_2$ with the free-jet MBMS technique (9). The chromium hydroxides contrast with Kim and Belton, who only postulated the existence of $CrO_2(OH)$ on basis of their transpiration experiments with Cr (10). The $MoO_2(OH)_2$ molecule is consistent with the transpiration results on Mo of Belton and Jordan (11). Tungsten also shows similar behavior (12). Note that for these compounds, (OH) behaves as a "pseudo-halogen", leading to hydroxy species with similar compositions to the oxychlorides discussed previously. In addition to Cr, Mo and W, hydroxy species have been reported for alumina (AlOH, AlO_2H) (13).

Currently there is a good deal of interest in ceramic matrix composites (CMCs) for combustion applications. These consist of a SiC or Si_3N_4 matrix with continuous SiC fibers. The fibers are coated with carbon or boron nitride for optimum mechanical properties. The major limitation of these composites is their susceptibility to high temperature oxidation and corrosion. This is due both to problems with a protective SiO_2 scale and internal oxidation of the fiber coating. It has recently been shown that combustion atmospheres may lead to the volatilization of SiO_2 (14). Studies of SiO_2 behavior in steam suggest the vapor species may be $Si(OH)_4$, $SiO(OH)_2$, and $Si_2O(OH)_6$ (15,16). Again, note the "pseudo-halogen" behavior of OH. Recently, the molecules SiO(OH)(g) and $SiO(OH)_2$(g) have been observed with effusion cell mass spectrometry (17). These formed from

the reaction of SiO_2 and water vapor at pressures up to 5×10^{-5} atm at temperatures near 2000 K. Further information is needed on the species formed at higher pressures and lower temperatures.

The second mode of degradation is internal oxidation, which may lead to attack of the BN fiber coating. It has been shown that BN readily oxidizes and then reacts with residual water vapor to form B-O-H species (18-20). This is currently under study in our laboratory.

Several experimental issues have complicate these studies of Si-O-H and B-O-H species. The first is the limited sensitivity of our instrument. We have found that our instrument can detect about a minimum vapor pressure of NaCl(g) of about 5×10^{-6} atm. The estimated vapor pressure of $Si(OH)_4$ is slightly less then this and to date we have been unable to observe it. The second problem is peak overlap--many of Si and B oxides and hydroxides may overlap with common background gases such as CO, N_2, and CO_2. The use of a chopper minimizes this, but does not eliminate it.

In summary, the NASA Lewis free-jet MBMS instrument has been described. It has played a critical role in our understanding of many high temperature corrosion problems involving volatile corrosion products. Chlorination/oxidation reactions of Co, Ni-Cr alloys, and SiC ceramics have been discussed. Studies of volatile hydroxides have also been summarized. Current interests focus on volatile hydroxides of boron and silicon.

References

1. C. A. Stearns, F. J. Kohl, G. C. Fryburg, and R. A. Miller, "High Pressure Molecular Beam Mass Spectrometric Sampling of High Temperature Molecules," NBS Special Publication 561, Proceedings of the 10th Materials Research Symposium on Characterization of High Temperature Vapors and Gases, NBS, Gaithersburg, MD, 1979.

2. C. A. Stearns, R. A. Miller, F. J. Kohl, and G. C. Fryburg, "Gaseous Sodium Sulfate Formation in Flames and Flowing Gas Environments," NASA TM X-73600, 1977.

3. R. Bianco, R. A. Rapp, and N. S. Jacobson, "Volatile Species in Halide-Activated Diffusion Coating Packs," Oxid. Met. 38 [1/2], 33-43 (1992).

4. N. S. Jacobson, M. J. McNallan, and Y. Y. Lee, "The Formation of Volatile Corrosion Products during the Mixed Oxidation-Chlorination of Cobalt at 650°C," Met. Trans. 17A [7], 1223-1228 (1986).

5. M. J. McNallan, Y.Y. Lee, Y. W. Chang, N. S. Jacobson, and J. Doychak, "Oxidation-Chlorination of Binary Ni-Cr Alloys in Flowing Ar-O_2-Cl_2," J. Electrochem. Soc. 138 [12], 3692-3696 (1991).

6. N. S. Jacobson, M. J. McNallan, and Y. Y. Lee, "Mass Spectrometric Observations of Metal Oxychlorides Produced by Oxidation-Chlorination Reactions," Met. Trans. 20A [8], 1566-1568 (1989).

7. J. E. Marra, E. R. Kreidler, N. S. Jacobson, and D. S. Fox, "Direct Mass Spectrometric Identification of Silicon Oxychloride Compounds," J. Electrochem. Soc. 135 [6], 1571-1574 (1988).

8. J. E. Marra, E. R. Kreidler, N. S. Jacobson, and D. S. Fox, "Reactions of Silicon-Based Ceramics in Mixed Oxidation Chlorination Environments," J. Am. Ceram. Soc. 71 [12], 1067-1073 (1988).

9. G. C. Fryburg, R. A. Miller, F. J. Kohl, and C. A. Stearns, "Volatile Products in the Corrosion of Cr, Mo, Ti, and Four Superalloys Exposed to O_2 Containing H_2O and Gaseous NaCl," J. Electrochem. Soc. 124 [11], 1738-1743 (1977).

10. Y.-W. Kim and G. R. Belton, "The Thermodynamics of Volatilization of Chromic Oxide: Part I. The Species CrO_3 and CrO_2OH," Met. Trans. 5 [8], 1811-1816 (1974).

11. G. R. Belton and A. S. Jordan, "The Volatilization of Molybdenum in the Presence of Water Vapor," J. Phys. Chem. 69 [6], 2065-2071 (1965).

12. G. R. Belton and R. L. McCarron, "The Volatilization of Tungsten in the Presence of Water Vapor," J. Phys. Chem. 68 [7], 1852-1856 (1964).

13. M. W. Chase, Jr., C. A. Davies, J. R. Downey, Jr., D. J. Frurip, R. A. McDonald, and A. N. Syverud, JANAF Thermochemical Tables, Third Edition, American Chemical Society and American Physical Society, New York, 1985.

14. E. Opila, in preparation for J. Am. Ceram. Soc.

15. E. L. Brady, "Chemical Nature of Silica Carried by Steam," J. Phys. Chem. 57 [10], 706-710 (1953).

16. A. Hashimato, "The effect of H_2O gas on volatilities of planet-forming major elements: I. Experimental determination of thermodynamic properties of Ca-, Al-, Si-hyroxide gas molecules and its application to the solar nebula," Geochimica et Cosmochimica Acta, 56, 511-532 (1992).

17. D. L. Hildenbrand and K. H. Lau, "Thermochemistry of gaseous $SiO(OH)$, $SiO(OH)_2$, SiO_2," J. Chem. Phys. 101 [7], 6076-6079 (1994).

18. N. S. Jacobson, "Thermochemical Considerations in SiC/SiC Composites with BN Fiber Coatings," presented at Aeromat '94, Anaheim, CA.

19. O. Glemser and H. G. Wendlandt, "Gaseous Hydroxides," Adv. in Inorganic Chemistry and Radiochemistry, Vol 5, 1963.

20. D. J. Meschi, W. A. Chupka, and J. Berkowitz, "Heterogeneous Reactions Studied by Mass Spectrometry. I. Reactions of $B_2O_3(s)$ with $H_2O(g)$," J. Chem. Phys. 33, 530-33 (1960).

MBMS STUDIES OF GAS-PHASE KINETICS IN DIAMOND CHEMICAL VAPOR DEPOSITION

Ciaran A. Fox
Stanford University
Stanford, CA 94305

Mark C. McMaster
IBM San Jose
San Jose, CA

Dave M. Tung and Wen L. Hsu
Sandia National Laboratories
Livermore, Ca 94551

Michael E. Coltrin
Sandia National Laboratories
Albuquerque, NM 87185

David S. Dandy
Department of Chemical Engineering
Colorado State University
Fort Collins, CO 80523

Abstract

A molecular beam mass spectrometer system (MBMS) has been used to determine the near-surface gaseous composition involved in the low pressure chemical vapor deposition of diamond. With this system, radical and stable species can be detected with a sensitivity better than 10 ppm. Threshold ionization techniques have been employed to distinguish between radical species in the deposition environment from radical species generated by parent molecule cracking. An extensive calibration procedure was used to enable the quantitative determination of H-atom and CH_3 radical mole fractions. Using the MBMS system, the gaseous composition involved in LPCVD of diamond has been measured for a wide variety of deposition conditions, including hot-filament gas activation, microwave-plasma gas activation, and a variety of precursor feed mixtures (ex: CH_4/H_2, C_2H_2/H_2). For microwave-plasma activation (MPCVD), the radical concentrations (H-atom and CH_3 radicals) are independent of the identity of the precursor feed gas provided the input carbon mole fraction is constant. However, in hot-filament diamond deposition (HFCVD), the atomic hydrogen concentration decreased by an order of magnitude as the mole fraction of carbon in the precursor mixture is increased to .07; this sharp reduction has been attributed to filament poisoning of the catalytic tungsten surface via hydrocarbon deposition. Additionally, we find that the H-atom concentration is independent of the substrate temperature for both hot-filament and microwave plasma deposition; radial H-atom diffusion is invoked to explain this observation.

Introduction

The chemical vapor deposition of diamond from gaseous mixtures of hydrocarbons and hydrogen has been an area of active interest because of diamond's unique material's properties. Typically, small amounts of hydrocarbons (CH_4, C_2H_2) mixed with molecular hydrogen are chemically excited by hot-filaments, plasma discharges, or combustion flames. The excitation results in the production of radical species, principally atomic hydrogen and CH_3, which are then directed towards a heated substrate (typically 500-1000°C). The importance of atomic hydrogen and methyl radicals to diamond synthesis has been addressed by various researchers. It is well documented that a super-equilibrium concentration of atomic hydrogen is vital to growing high quality diamond films via chemical vapor deposition. Recently, Kelly and coworkers demonstrated that diamond film quality and growth rate increase as the atomic hydrogen concentration is increased during sequential deposition of diamond. In addition to determining the fraction of sp^2 carbon incorporated into the diamond film (i.e. graphite impurities), residual atomic hydrogen has been shown to affect such properties as the residual stress, the thermal conductivity, and electrical resistivity of diamond films. Researchers have hypothesized that methyl radicals are the primary growth species for diamond growth in a typical hot filament CVD diamond reactor with a precursor mixture of excited hydrogen and methane[1]. These conclusions are a consequence of both theoretical thermodynamic and kinetic gas phase calculations and experimental in-situ growth diagnostics. Various techniques have been utilized to probe the gas composition in CVD diamond growth including Fourier Transform Infrared Reflection (FTIR)[2,3], optical emission spectroscopy (OES)[4-7], laser induced fluorescence (LIF)[8-10], and Resonance-enhanced Multi-Photon Ionization (REMPI)[11]. Although several of these techniques can be applied with high sensitivity and are capable of detecting radical species, they are unable to detect all the species involved in diamond growth simultaneously. Additionally, in the case of OES, typically qualitative information rather than quantitative mole fractions can be determined.

One of the most useful techniques for characterizing the complex diamond CVD gas environment, which overcomes many of the aforementioned problems associated with other analysis techniques, is molecular beam mass spectroscopy. When this method is utilized in conjunction with threshold ionization techniques, absolute mole fractions of stable and radical species can be directly ascertained. Recently, Hsu and coworkers have applied this technique near the growth surface in a CVD diamond reactor[12-19]. In this study, we review previous studies involving the effect of surface temperature, hydrocarbon identity, and excitation sources on the gas composition in CVD diamond growth; for more complete descriptions of these effects, the reader is referred to the original study.

Experimental

The molecular beam mass spectrometer system used in this study has been described elsewhere[16] and is shown schematially in Figure 1. The apparatus consists of a deposition chamber connected to a three stage molecular beam line via a 300μm extraction orifice in the diamond-coated molybdenum substrate. Precursor gases (C_2H_2/H_2, CH_4/H_2, etc.) are introduced into the deposition chamber and dissociated thermally via a hot tungsten filament or by a microwave plasma which rests on the growth surface. In the case of HFCVD, the tungsten filament is .25mm and is located 1.25 cm from the extraction orifice in the substrate. Gas effusing through the orifice is collimated to form a molecular beam that enters the ionization region of an electron-impact mass spectrometer located in the third stage of differential pumping ($\approx 10^{-7}$ Torr). The calibration procedures used to quantify the gas composition in the deposition chamber have been previously reported.[16] It should be noted that argon was introduced as a calibration reference and to eliminate mass discrimination effects that occur during the supersonic expansion process. The overall error in the mole fraction analysis is estimated to be ±30%.

Results and Discussion

In figure 2 a and b, we plot the gas composition as a function of carbon mole fraction in the precursor mixture (X_c) for hot-filament and microwave plasma deposition from CH_4/H_2 mixtures, respectively. In both experiments, the substrate temperature was 825°C and the reactor pressure was maintained at 20 Torr. In HFCVD, a sharp reduction in the atomic hydrogen concentration occurs as the methane mole fraction is increased above .02, while in the case of microwave plasma deposition, the atomic hydrogen mole fraction is relatively independent of methane additions. Celii and Butler observed such a reduction in atomic hydrogen concentration when either C_2H_2/H_2 or CH_4/H_2 gas mixtures were utilized in a HFCVD reactor.[20,21] Sommer and Smith attributed the atomic hydrogen reduction to the catalytic poisoning of atomic hydrogen production due to hydrocarbon deposition on the hot-filament surface.[22] Presumably, the sharp decrease observed in this study can also be attributed to filament poisoning. In the case of MPCVD, where atomic hydrogen is generated both by thermal dissociation and by gas phase reactions between H_2 molecules and electrons[15], the atomic hydrogen concentration is independent of the carbon mole fraction in the precursor feed. For a more complete description of these effects and filament poisoning, the reader is referred to recent studies by McMaster et al[18,19] and Sommer et al.[22]

In figure 3, the species composition as a function of carbon mole fraction in the feed (X_c) for an acetylene reactant feed in HFCVD is presented. In HFCVD, for both acetylene and methane (Figure 2a) reactant feeds, the extent of hydrocarbon disassociation is reduced as the hydrocarbon mole fraction in the feed is increased. Atomic hydrogen is

reduced by an order of magnitude for both reactant feeds. However, for Xc below .02, the gas compositions are approximately identical for both inlet carbon species. In the case of diamond deposition using a microwave plasma, where the atomic hydrogen concentration is independent of Xc, the gas composition is the same for acetylene and methane feeds provided the carbon mole fraction is constant.[19] As a result, at a given carbon mole fraction in the feed, the films properties are independent of the carbon identity in MPCVD. Recently, this has been demonstrated by McMaster et al[19] and Toyoda.[23]

In figure 4, the gas composition as a function of surface temperature is plotted for hot-filament chemical vapor deposition. During these experiments, the inlet carbon mole fraction in the feed was constant (.0044) and the reactor pressure was 20 Torr. From an Arrhenius plot, an activation energy of 3 ± 1 kcal/mole was determined for CH_3 and C_2H_2 production. Recent numerical simulations of diamond growth suggest that the lateral transport of atomic hydrogen is a major loss mechanism and can be invoked to explain the experimentally observed constant atomic hydrogen concentration.[18] The experimentally observed effect of surface temperature on gas composition suggests that changes in the kinetics of surfaces processes are responsible for the observed reduction in film growth rate.[19]

Conclusion

In this study, a molecular beam mass spectroscopy system was used to determine the various deposition parameters which control the gas composition near the substrate surface in the chemical vapor deposition of diamond. The atomic hydrogen mole fraction was seen to be independent of the inlet methane concentration for MPCVD. However, when hot filaments are employed as the gas activation source, the atomic hydrogen mole fraction drops by an order of magnitude as the hydrocarbon content is increased from .002 to .075 mole percent. This significant reduction was attributed to a reduction in the catalytic activity of the tungsten filament due to hydrocarbon deposition. Finally, the gas composition in hot filament-assisted diamond deposition was seen to be independent of surface temperature.

Acknowledgments

This work was supported by the U.S. Department of Energy under contract #DE-AC0476DP00789 and the ARPA/DSO Material Science Program.

References

1. S. J. Harris and A. M. Weiner, *J. Appl. Phys.* **67** (1990) 6520.

2. A. Campargue, M. Chenevier, L. Fayette, B. Marcus, M. Mermoux and A. J. Ross, *Appl. Phys. Lett.* **62** (1993) 134.

3. T. Mitomo, T. Ohta, E. Kondoh, K. Ohtsuka and Y. Habu, in *Proceedings of the Second International Conference on New Diamond Science and Technology*, edited by R. Messier, J. T. Glass, J. E. Butler and R. Roy, (Materials Research Society, Washington, D.C., 1990), p. 213.

4. F. Zhang, Y. Zhang, Y. Yang and G. Chen, *Appl. Phys. Lett.* **57** (1990) 1467.

5. W. Zhu, A. Inspektor, A. R. Badzian, T. McKenna and R. Messier, *J. Appl. Phys.* **68** (1990) 1489.

6. L. S. Plano, D. A. Stevenson and J. R. Carruthers, in *Second International Conference on New Diamond Science and Technology*, edited by R. Messier, J. T. Glass, J. E. Butler and R. Roy, (Materials Research Society, Washington, D.C., 1991), p. 257.

7. Y. Mitsuda, K.-I. Tanaka and T. Yoshida, *J. Appl. Phys.* **67** (1990) 3604.

8. A. D. Tserepi, J. R. Dunlop, B. L. Preppernau and T. A. Miller, *J. Vac. Sci. Technol.* **A 10** (1992) 1188.

9. H. R. Thorsheim and J. E. Butler, *Unknown* (1993) .

10. U. Meier, K. Kohse-Hoinghaus, L. Schafer and C.-P. Klages, *Appl. Opt.* **29** (1990) 4993.

11. J. E. Butler, F. G. Celii, D. B. Oakes, L. M. Hanssen, W. A. Carrington and K. A. Snail, *High Temp. Sci.* **27** (1990) 183.

12. W. L. Hsu and D. M. Tung, in *Proceedings of the Second International Conference on New Diamond Science and Technology*, edited by R. Messier, J. T. Glass, J. E. Butler and R. Roy, (Materials Research Society, Washington, D.C., 1990), p. 239.

13. W. L. Hsu, *Appl. Phys. Lett.* **59** (1991) 1427.

14. W. L. Hsu, in *Proceedings of the 2nd International Symposium on Diamond Materials*, edited by A. J. Purdes, J. C. Angus, R. F. Davis, B. M. Meyerson, K. E. Spear and M. Yoder, (The Electrochemical Society, Washington, D.C., 1991), vol. 91-8, p. 217.

15. W. L. Hsu, *J. Appl. Phys.* **72** (1992) 3102.

16. W. L. Hsu and D. M. Tung, *Rev. Sci. Instrum.* **63** (1992) 4138.

17. W. L. Hsu, M. C. McMaster, M. L. Coltrin and D. S. Dandy, *Jpn. J. Appl. Phys.* **33** (1993) .

18. M. C. McMaster, W. L. Hsu, M. E. Coltrin and D. S. Dandy, *J. Appl. Phys.* **submitted** (1994) .

19. M. C. McMaster, W. L. Hsu, M. E. Coltrin and D. S. Dandy, *J. Appl. Phys.* **submitted** (1994) .

20. F. G. Celii and J. E. Butler, in *Proceedings of the Second International Conference on New Diamond Science and Technology*, edited by R. Messier, J. T. Glass, J. E. Butler and R. Roy, (Materials Research Society, Washington, D.C., 1990), p. 201.

21. F. G. Celii and J. E. Butler, *Appl. Phys. Lett.* **54** (1989) 1031.

22. M. Sommer and F. W. Smith, *J. Mater. Res.* **5** (1990) 2433.

23. H. Toyoda, M. A. Childs, K. L. Menningen, L. W. Anderson and J. E. Lawler, *J. Appl. Phys.* (1993) .

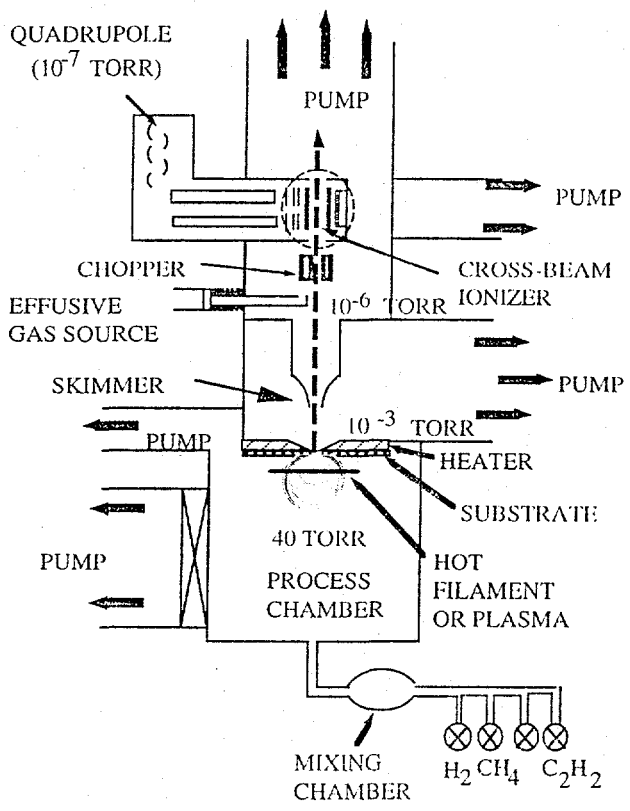

Figure 1. Diagram of Molecular Beam Mass Spectroscopy Apparatus

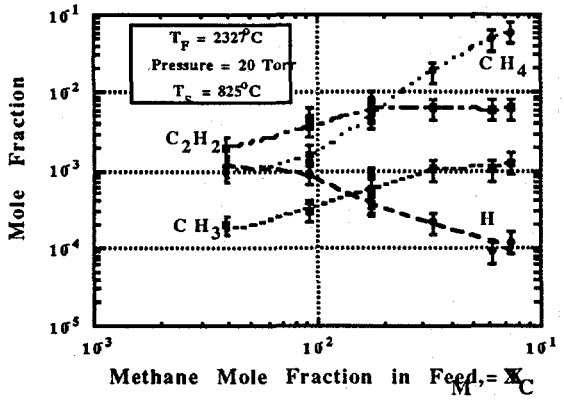

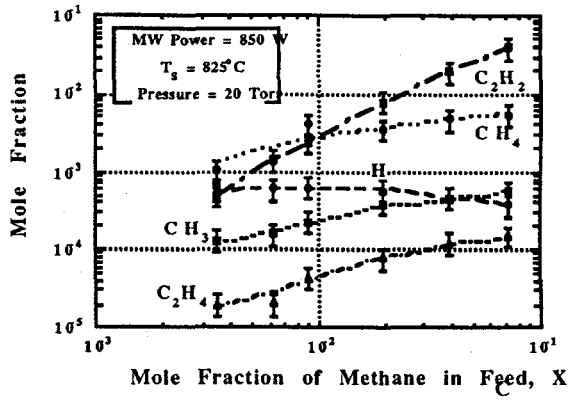

Figures 2a. and b. Species mole fractions are plotted as a function of inlet methane concentration for the case of hot-filament assisted diamond deposition (a) and microwave plasma-assisted diamond deposition (b). Note the sharp reduction observed in the hydrogen atom concentration in HFCVD.

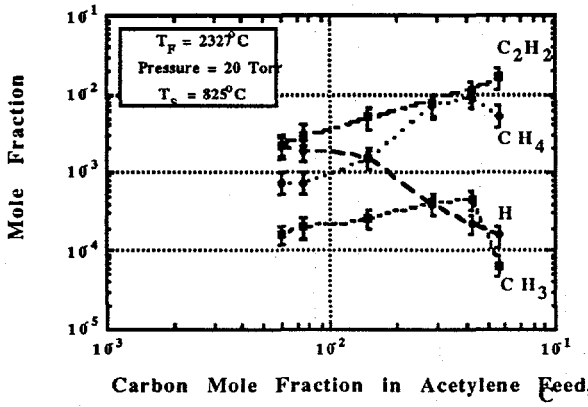

Figure 3. Species mole fractions are plotted as a function of the carbon mole fraction in the acetylene feed. Note that for $X_C \leq .02$, the gas composition is identical to the case where methane is the inlet hydrocarbon (see Figure 1a).

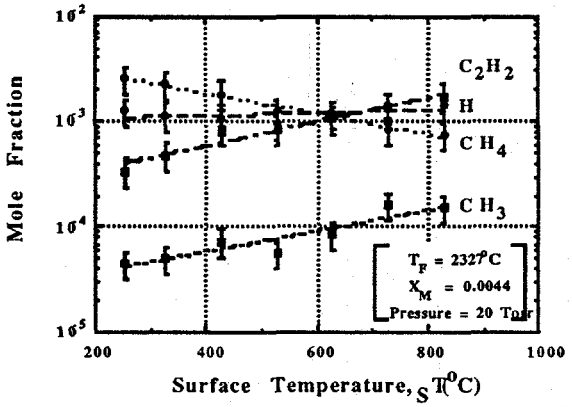

Figure 4. Species mole fractions are plotted as a function of surface temperature in HFCVD using methane as the inlet hydrocarbon species. Note that the hydrogen atom concentration is approximately independent of substrate temperature.

DIRECT SAMPLING OF INORGANIC VAPORS RELEASED DURING BIOMASS COMBUSTION

David C. Dayton and Thomas A. Milne
National Renewable Energy Laboratory
1617 Cole Boulevard
Golden, CO 80401-3393

INTRODUCTION

Alkali metal vapors released during biomass combustion cause significant problems in power generating facilities that convert biomass to electricity. Gas phase transport of alkali vapors increases the potential for fouling and slagging heat transfer surfaces in boilers and will cause accelerated erosion and corrosion of turbine blades in future direct biomass-fired facilities. Biomass power is an attractive renewable energy resource; however, alkali deposits that form on surfaces in power generating facilities reduce the efficiency of electricity production. As a result, there is a need to develop methods or define combustion conditions for reducing the transport of alkali metal containing vapors during biomass combustion. One solution to fouling and slagging problems is to develop methods of hot gas cleanup that reduce the amount of alkali vapor to acceptable levels. This requires a detailed understanding of the mechanisms of alkali metal release during biomass combustion and identification of these alkali metal vapors, how these vapors lead to fouling and slagging, and how they may be sequestered.

Our approach is to sample directly the hot gases liberated from the combustion of small biomass samples in a variable temperature quartz tube reactor employing a molecular beam mass spectrometer (MBMS) system to monitor the combustion event. We have successfully used this experimental technique to identify alkali metal containing species released during the combustion of selected biomass feedstocks at four different conditions: 1100° C in He/O_2(20%), 800° C in He/O_2(20%), 1100° C in He/O_2(5%), and 1100° C in He/O_2(10%)/Steam(20%). These conditions were chosen to study the effect of temperature, oxygen concentration, and excess steam on alkali metal release and speciation.

EXPERIMENTAL APPARATUS

The release of alkali metal vapors during biomass combustion was monitored and studied using a direct sampling, molecular beam mass spectrometer (MBMS) system. The MBMS system is ideally suited for studying the high temperature, ambient pressure environments encountered during the present alkali screening studies. The integrity of the sampled, high temperature combustion gases is preserved by the free-jet expansion because chemical reactions are effectively quenched, and condensation is inhibited. The nonequilibrium nature of the free jet expansion and the subsequent formation of a molecular beam allows reactive and condensable species, such as alkalis, to remain in the gas phase at temperatures far below their condensation point for long periods of time compared to reaction rates. Comprehensive detection of gas phase species of interest is possible using the mass spectrometer, and facilities for pattern matching and tandem MS are available to aid in deciphering complex mass spectra. This apparatus has been described in the literature [1-3], so only the salient points will be discussed in relation to the present study.

Submitted for inclusion in the proceedings of the Specialists Workshop on Applications of Free-Jet, Molecular Beam, Mass Spectrometric Sampling, Estes Park, CO October 12-14, 1994.

A total of 23 different biomass feedstocks have been screened for alkali metal vapor release. The list of feedstocks is as follows: planer shavings of lodgepole pine (*Pinus contarta*), eucalyptus (*Eucalyptus saligna Sm.*), poplar (*Populus deltoides x nigra var. Caudina*), corn stover (*Zea mays L.*), switchgrass (*Panicum virgatum L.*), wheat straw (*Triticum aestivum*), rice straw, (Sandia) switchgrass (*Panicum virgatum L.*), pistachio shells (*Pistacia vera*), almond shells (*Prunnus amygdalus*), almond hulls (*Prunnus amygdalus*), wood waste #1, wood waste #2, waste paper, Danish wheat straws (*Triticum aestivum*) from Slagelse and Haslev (SLAG001, SLAG002, and HAS001), alfalfa stems (*medicago sativa L.*) (IGT001 and IGT002), summer switchgrass (*Panicum virgatum L.*), Dakota switchgrass (*Panicum virgatum L.*), and two willows (*Salix veminalus*, *Salix alba*, tops only). This set of feedstocks can be divided into various classes of biomass identified as woody feedstocks, herbaceous feedstocks, grasses, agricultural residues, and waste feedstocks. It will become apparent that the varying nature of the feedstocks results in unique differences in terms of alkali metal release during combustion.

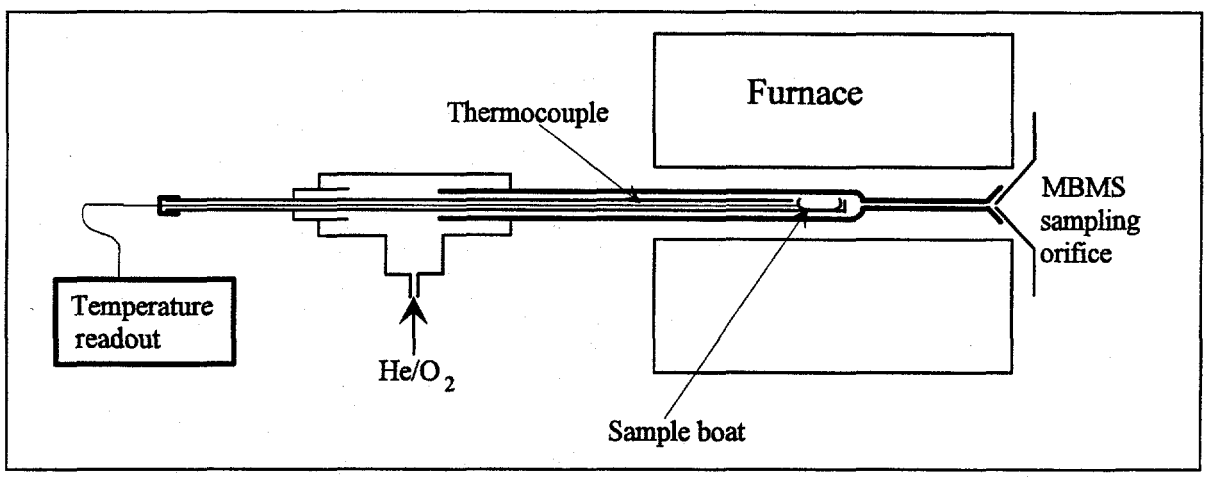

Figure 1. A schematic of the quartz tube reactor used to study biomass combustion

The biomass samples used in the present study were ground in a mill to +20/-80 mesh. Small (20-60 mg) samples were combusted in a tubular quartz reactor (O.D.=18 mm and I.D.=16 mm) which was placed into a standard two-zone, electric clam-shell furnace as depicted in Figure 1. The heated zone in the furnace was 30 cm long. For the experiments discussed below, the furnace temperature was set at either 1100° C or 800° C.

Biomass samples were loaded into hemi-capsular quartz boats of such a size that approximately 40 mg of ground, loosely packed, material filled the boat, depending on the feedstock. The boats were then placed on the end of a 6-mm-diameter (0.25"-diameter) piece of stainless steel (or quartz) tubing that was inserted into the furnace through an 18-mm (0.75") brass Swagelock tee. A type-K thermocouple surrounded by a 0.5-mm-diameter (0.020"-diameter) inconel sheath was inserted through the tubing such that the junction was close to the edge of the sample boat. The actual boat temperature and flame temperature were not measured; however, the hot gas temperature in the vicinity of the sample boat could be monitored.

A mixture of oxygen (5%, 10%, or 20%) in helium was flowed through the reactor from back to front at a total gas flow rate of 4.4 standard liters per minute. Under these conditions, the combustion gases have a residence time of about 0.1 second in the reactor before reaching the sampling orifice. When appropriate, steam was added to the reactor atmosphere by injecting water into the rear of the furnace through a needle fed by a syringe pump. Stainless steel shot was packed around the tip of the needle to increase the surface area for water evaporation. This provided a steady flow of 20% steam by volume.

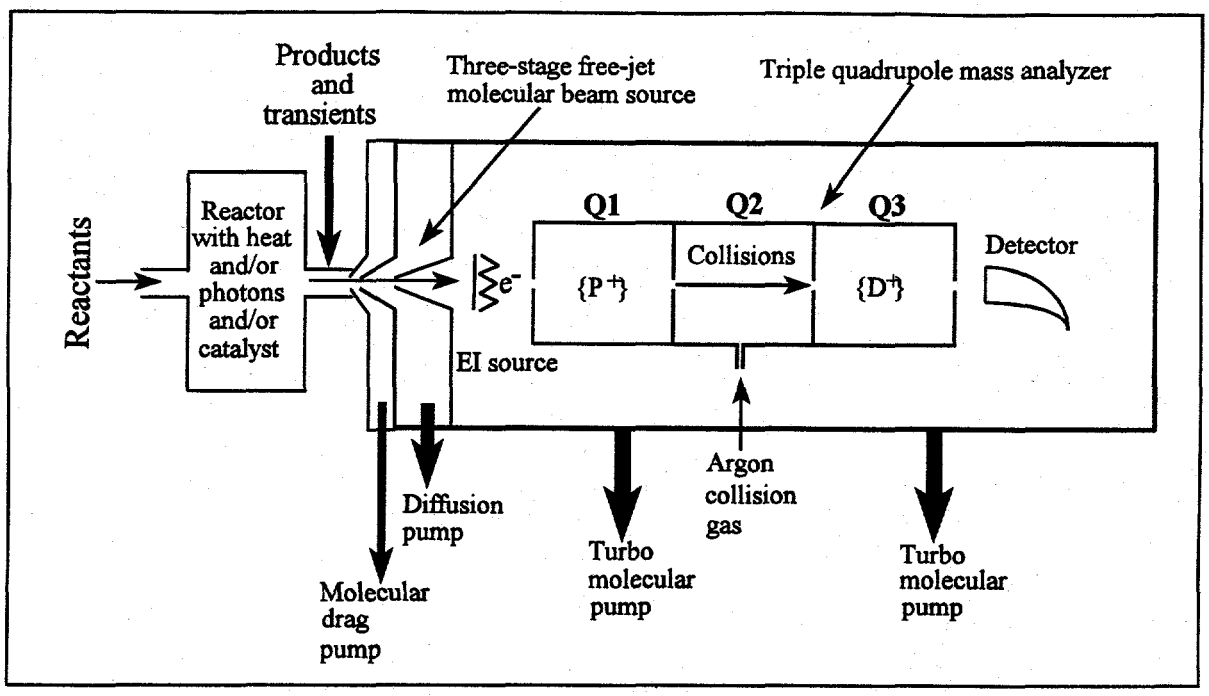

Figure 2. A schematic of the NREL molecular beam/mass spectrometer system

A stainless steel cone, 25-mm high with a 90° interior angle and an orifice diameter of 200 μm was used for molecular beam sampling. The end of the reactor was fitted around the tip of the sampling orifice positioned at the downstream end of the quartz tube reactor to sample the high temperature, ambient pressure biomass combustion gases. The orifice protruded into the furnace to keep it at an elevated temperature and thus prevent condensation on the sampling cone. The actual temperature of the orifice was not routinely measured; however, when the furnace temperature was set at 1100° C, the tip of the orifice was observed to glow orange.

Sampled gases underwent a free jet expansion into the first stage of the differentially pumped vacuum system illustrated in Figure 2. Stage #1 is pumped on by an Osaka TS440 helical grooved, molecular drag pump with a pumping speed of 440 l/sec at 1 mtorr. The molecular drag pump is backed by a Galileo D045 modular rotary pump with a pumping speed of 730 l/min. The molecular drag pump has a high pumping performance from several torr to high vacuum and also has the capacity needed to evacuate the high gas loads in Stage #1 following the free jet expansion with the advantage of being smaller and quieter than a booster pump/backing pump combination. Nominal pressure in Stage #1 under normal experimental conditions is 20 mtorr. The expanded gases were skimmed by a second conical skimmer (1 mm orifice diameter) at the entrance to the second stage forming a molecular beam that was directed into the ionization region of the mass spectrometer in the third stage of the vacuum system. Stage #2 is evacuated by a Varian VHS-6 six-in. oil diffusion pump with a liquid nitrogen baffle to minimize backstreaming. In this configuration, the diffusion pump has a pumping speed of 1200 l/sec at 10^{-5} torr. The diffusion pump is backed by an Edwards E2M8 2-stage mechanical pump with a pumping speed of 190 l/min. The mass spectrometer chamber (Stage #3) is pumped on by two Balzers (TPU270 and TPU330) turbomolecular pumps with pumping speeds of 270 l/sec and 330 l/sec, respectively. The turbomolecular pumps are backed by a Leybold D8A mechanical pump with a pumping speed of 127 l/min. Pressures in Stages 2 and 3 are nominally 5×10^{-5} torr and 1×10^{-7} torr, respectively.

Ions were formed by electron impact ionization of the sampled gases with a nominal electron energy of 25 eV. The ions were filtered by an Extrel C-50 triple quadrupole mass analyzer and detected with an off-axis

electron multiplier. In the present experiments, only the first quadrupole was scanned while a constant voltage offset was applied to the third quadrupole. The second quadrupole is a collision cell that can be used for collision induced dissociation experiments. For the present experiments, the collision cell remained evacuated.

A Teknivent Vector Two computer and software package were used to control the scanning parameters of the mass spectrometer and to collect the pre-amplified electron multiplier signal as a function of time and mass-to-charge ratio. The mass spectrometer was scanned continuously at a rate of approximately 100 amu/sec. In this configuration, a complete mass spectrum was recorded once every 1.0 to 1.5 seconds. Background subtraction from the total ion signal yielded corresponding mass spectra at a given time during the combustion event or averaged over a given phase of the combustion event.

Selected biomass samples were screened for alkali metal vapor release and speciation at four different combustion conditions: 1100° C in He/O_2(20%); 800° C in He/O_2(20%); 1100° C in He/O_2(5%) and; 1100° C in He/O_2(10%)/Steam(20%). These conditions were chosen to study the effect of temperature, oxygen concentration, and excess steam on alkali metal release and speciation.

EXPERIMENTAL RESULTS

Continuous combustion of biomass from initial heating to ignition to complete char burnout and ash "cooking" is simulated in a laboratory reactor. A typical experimental run consisted of loading a quartz boat containing the sample into the cooler end of the reactor and waiting for a short time to pass for air to be flushed from the system. Data collection was then initiated, and a background was recorded for 18-30 s. The sample was then inserted into the furnace as quickly as possible (typically 3 to 6 s). After insertion, the sample underwent rapid heating (3700 °C/min-see Figure 3), and combustion occurred almost immediately. Data were collected for at least an additional minute to encompass the three separate phases of combustion that have been observed. These phases are distinguished in Figure 3, which shows the total ion intensity and hot gas temperature as a function of time for combustion of a switchgrass sample in 20% O_2 in helium at 1100° C. The data points in the ion intensity plot represent complete mass spectra scanned over the interval from m/z = 15 through m/z = 130. Masses 32 and 44 were skipped to avoid overloading the detector.

The first phase, called the combustion or devolatilization phase, is completed in approximately 0.1 min (6 s) and is dominated by the production of CO, CO_2, and H_2O while O_2 is consumed. SO_2 and NO are also detected during the combustion phase.

After the volatile species have been liberated, the char combustion phase begins. The duration of this phase is approximately 0.2 min (12 s) and is a function of feedstock and furnace temperature. Most of the alkali metal containing species are liberated during the char combustion phase. Consequently, the char phase contains the most valuable information for studying alkali metal release during biomass combustion. For example, the mass spectrum averaged over the char phase of switchgrass combustion at 1100° C in 20% O_2 in helium is shown in Figure 4.

The ion intensities in Figure 4 were normalized to the background $^{34}O_2^+$ signal intensity. It is possible to identify the combustion products CO_2, H_2O, and CO. NO, SO_2, and HCl are still observed during this phase of combustion; however, the majority of these species were liberated during the combustion phase. The parent potassium chloride ions are easily identified in the char phase spectrum in Figure 4 and are assigned to the peaks at m/z = 74 and m/z = 76. Potassium chloride also fragments [4,5] in the ionizer, producing substantial intensity at m/z = 39, assigned to K^+. The potassium isotope at m/z = 41 (6.7% natural

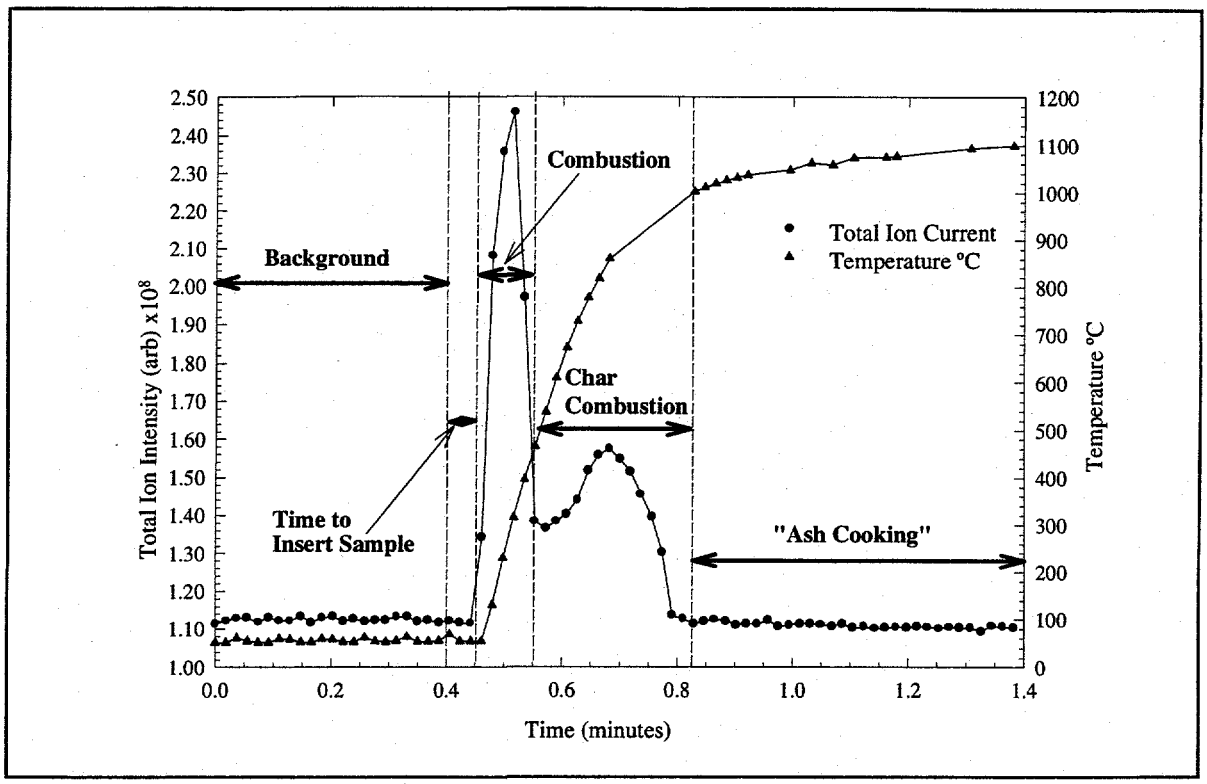

Figure 3. Temporal profile of the total ion current (•) and hot gas temperature (▲) measured during switchgrass combustion at 1100° C in 20% O_2 in helium

abundance [6]) is also observed. Fragmentation of other potassium containing species may also contribute to the m/ z= 39 signal intensity; however, potassium released as the free metal is not likely to contribute to the m/z = 39 signal. In a previous study [3], the m/z = 74 signal intensity was used to quantify the amount of potassium from KCl released into the gas phase during switchgrass combustion. The m/z = 74 signals in Figure 4 correspond to 532±62 ppm of K from KCl [3] in the dilute postcombustion gases. The estimated detection limit for KCl is 9 ppm.

The two peaks at m/z = 113 and m/z = 115 in Figure 4 also exhibit the characteristic intensity ratio of a single chlorine containing species. These peaks are assigned to K_2Cl^+, a fragment ion of the KCl dimer. The ratio of the KCl dimer to monomer intensity is consistent with the expected KCl vapor concentrations at these temperatures [4,5]. Sodium chloride is also released as indicated by the peaks at m/z = 58 and m/z = 60, corresponding to $NaCl^+$. Fragmentation of NaCl produces the Na^+ signal at m/z=23.

The final phase of the combustion process is termed the "ash cooking" phase. Most of the volatile matter has been liberated by the beginning of this phase, however, the remaining ash is left in the high temperature reactor for an additional 0.5 min to insure that all of the volatile material has been released.

Similar data were collected during combustion of the 23 feedstocks listed above. Alkali metal containing species were identified in the mass spectra averaged over the char phase during combustion of the selected biomass feedstocks. Four different combustion conditions have been studied to investigate the effect of temperature, oxygen concentration, and excess steam on alkali release. The baseline condition chosen for studying alkali release during biomass combustion was 1100° C in He/O_2(20%). Under these conditions, the large excess of oxygen assured complete combustion and the furnace temperature was high enough to insure the volatilization of alkali metal containing species.

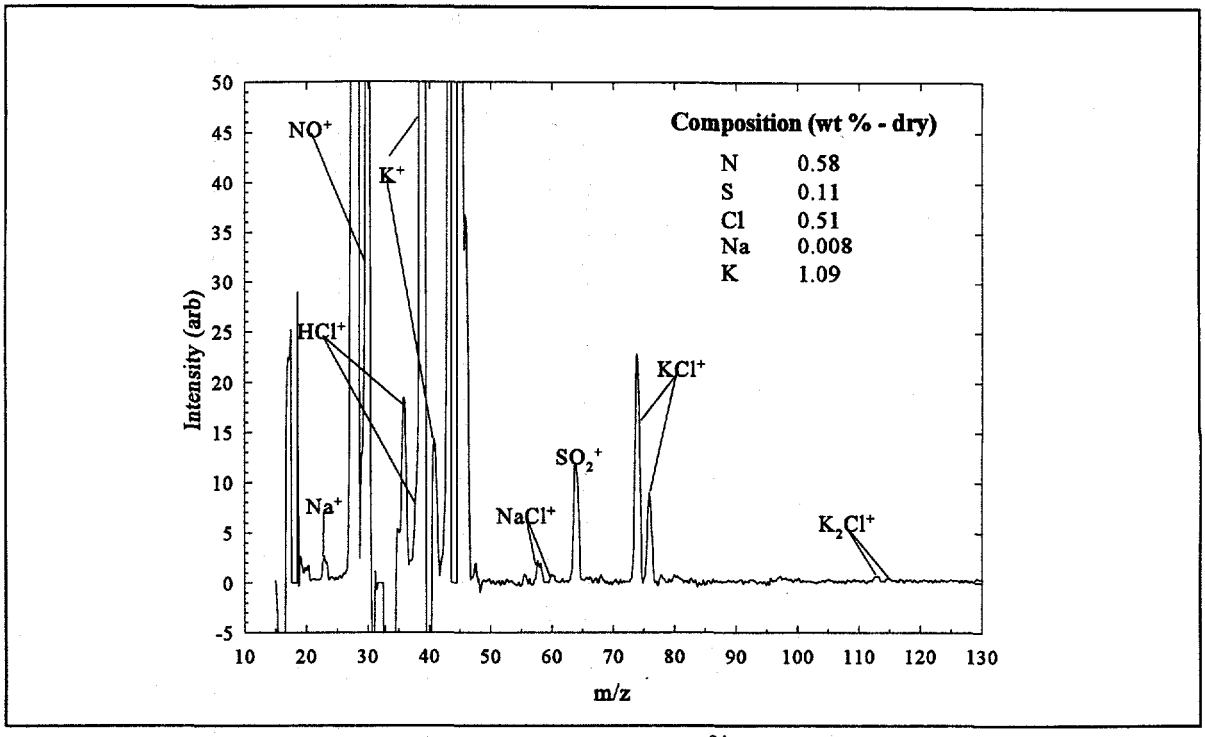

Figure 4. Mass spectrum (normalized to the background $^{34}O_2$ signal intensity) averaged over the char phase of switchgrass combustion at 1100° C in 20% O_2 in helium. The composition in the inset is from the ultimate analysis of the feedstock on a moisture-free basis

Several general conclusions have been drawn from screening the set of 23 feedstocks for alkali metal release during biomass combustion. The amount of alkali metal released during biomass combustion is strongly a function of the feedstock combusted. The trend observed in these screening studies is that the gas phase species identified in the char phase mass spectra recorded during biomass combustion qualitatively reflects the feedstock composition as determined in the ultimate (moisture, C, H, N, S, O, Cl, and ash) and ash (Si, Al, Ti, Fe, Ca, Mg, Na, K, and P) analyses.

Woody feedstocks such as lodgepole pine, poplar, eucalyptus and willow tend to have very low levels of alkali metal (<0.5% by weight on a dry basis) and chlorine (<0.1% by weight on a dry basis) as determined in the ultimate and ash analyses of the feedstocks. As a result, very little alkali metal is released during combustion, and individual alkali metal containing species were not identified in the char phase mass spectra recorded during the combustion of woody feedstocks.

Herbaceous feedstocks, grasses, and some agricultural residues such as alfalfa stems, switchgrass, corn stover, rice straw, and wheat straw can have very high levels of potassium (up to 1.4% by weight on a dry basis in the case of rice straw) and chlorine (up to 0.7% by weight on a dry basis in the case of rice straw). The high potassium and chlorine levels in these feedstocks result in significant alkali metal release in the form of potassium chloride during combustion. Potassium chloride is easily identified in the char phase spectra recorded during combustion of these feedstocks.

The agricultural residues pistachio shells, almond shells, and almond hulls tend to have high potassium levels (up to 2.6% by weight on a dry basis in the case of almond hulls) but low chlorine levels (<0.1% by weight on a dry basis). Potassium hydroxide is the dominant form of alkali metal released during combustion of these feedstocks.

The composition of the waste feedstocks tends to vary depending on the waste stream sampled. In terms of alkali metal release, the waste feedstocks are quite "clean." Individual alkali metal containing species are not observed in the char phase spectra recorded during combustion of the waste feedstocks.

THE EFFECT OF COMBUSTION CONDITIONS ON ALKALI METAL RELEASE

Combustion of the 23 feedstocks was investigated at 800° C in $He/O_2(20\%)$ and at 1100° C in $He/O_2(5\%)$ and compared to the baseline condition to determine what effect, if any, temperature and oxygen concentration, respectively, has on the release of alkali metal during biomass combustion. Independent of the feedstock, organic hydrocarbon fragment ions dominate the mass spectrum averaged over the first phase of combustion at these two conditions. This implies that the released hydrocarbons are not completely converted to products in the time it takes the combustion gases to reach the sampling orifice at the lower furnace temperature and in a reduced oxygen atmosphere, respectively. Similar combustion products are observed in the char phase spectra compared with the results for the baseline combustion condition. CO_2 and CO are still the dominant combustion products observed during the char combustion phase, and similar alkali species are observed in the char phase spectra for the individual feedstocks. Alkali metal is still primarily released during the char combustion phase. The amount of alkali metal released into the gas phase appears to be unaffected by the reduced furnace temperature or the reduced oxygen concentration.

Excess steam was added to the reactor atmosphere to simulate an environment in which water vapor is continuously being supplied by the random combustion of multiple biomass particles. Such an environment is one that would occur in an industrial boiler or combustor in which biomass is constantly fed. The combustion conditions established for the purpose of studying the effect of added steam were 10% O_2 and 20% steam in helium at a furnace temperature of 1100° C. The added steam has little effect on the combustion phase of biomass combustion. Similar to previous "dry" combustion conditions, CO_2, CO, SO_2, and NO are the most abundant products observed in the mass spectra averaged over the combustion phase during biomass combustion. Excess steam has no observable affect on the char combustion phase of the woody feedstocks or the waste feedstocks.

During the combustion of those feedstocks with high potassium and chlorine contents, there are noticeable differences in the char phase mass spectra. As an example, the char phase mass spectrum recorded during switchgrass combustion at 1100 ° C in 10% O_2 and 20% steam in helium is shown in Figure 5. In addition to the alkali metal containing species previously observed during "dry" combustion, two new features are observed in the switchgrass char phase spectrum with added steam. The feature at m/z = 56 is assigned to KOH^+ and indicates that some of the alkali metal is being released in the form of the hydroxide in the presence of water vapor. Even though there is a considerable amount of chlorine in the feedstock, alkali metal release is partially shifted from the chloride to the hydroxide during switchgrass combustion in excess steam. This release is not completely shifted because potassium chloride is thermodynamically more stable than potassium hydroxide [7].

The char phase spectrum of switchgrass with steam added (Figure 5) also shows a peak at m/z = 57 that is larger than the KOH^+ signal. This peak has been assigned to KH_2O^+; however, the mechanism of formation of this species is still not known. Given the high potassium content of this switchgrass and the high concentration of water vapor in the reactor atmosphere, it is possible that this species is an artifact of the free jet expansion during which a K-species/H_2O cluster is formed and subsequently fragments on ionization.

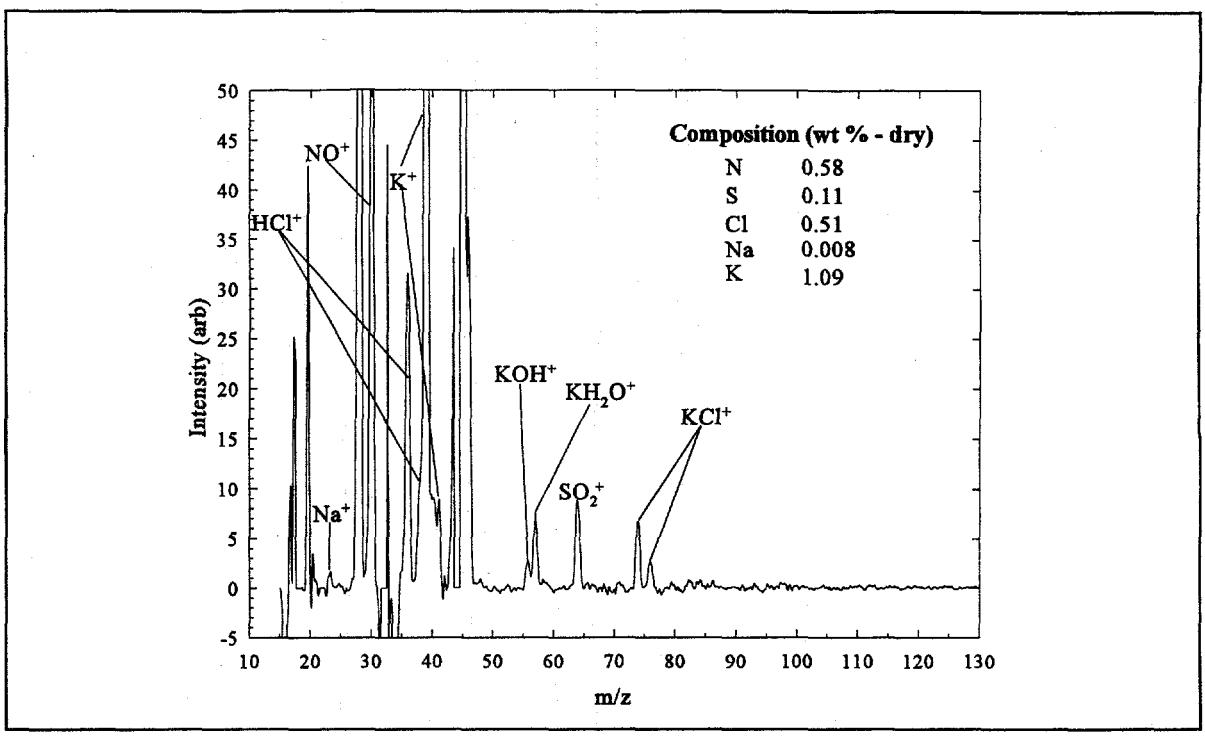

Figure 5. Mass spectrum (normalized to the background $^{34}O_2$ signal intensity) averaged over the char phase of switchgrass combustion at 1100° C in 10% O_2 and 20% steam in helium. The composition in the inset is from the ultimate analysis of the feedstock on a moisture-free basis

SUMMARY AND CONCLUSIONS

Molecular beam sampling/mass spectrometry has proven invaluable in the study of biomass combustion. This is reflected in the results from the screening studies presented above; these results provide important insights into alkali metal speciation and release during biomass combustion. Biomass combustion occurs in three phases; however, the most valuable information concerning alkali metal release and speciation is contained in the char combustion phase. In fact, the gas phase species measured in the char phase mass spectra qualitatively agree with the feedstock compositions as determined in the ultimate and ash analyses.

The mass spectral results confirm that KCl is the dominant form of the alkali metal released during combustion of high potassium and chlorine containing herbaceous feedstocks, grasses, and agricultural residues. Although the ultimate analysis can accurately be used to determine the total amount of a given element, the mass spectral results complement this information by yielding the species released into the gas phase during combustion. Identification of the gas phase alkali metal containing species can be important for determining the method of hot gas cleanup needed to reduce the alkali vapors and for understanding the types of deposits that form in commercial-scale biomass power facilities.

Alkali metal release is strongly a function of the feedstock composition. Only minor changes in alkali metal release during biomass combustion are observed for the different combustion conditions studied. At a lower furnace temperature, changes in alkali release are too subtle to be noticed in the char phase mass spectral results. Reducing the oxygen concentration in the combustion atmosphere has no observable effect on alkali metal release. Adding steam to the combustion environment, however, suggests that potassium release is shifted slightly from KCl to KOH during combustion of high potassium and chlorine containing feedstocks. For the remaining feedstocks studied, excess steam in the reactor atmosphere does not produce noticeable changes in the char phase mass spectra recorded during biomass combustion.

ACKNOWLEDGEMENTS

The authors are grateful for the support of the Solar Thermal and Biomass Power Division of the Department of Energy Office of Energy Efficiency and Renewable Energy. Special thanks go to Richard L. Bain and Ralph P. Overend for both programmatic and technical support and guidance. Richard J. French is acknowledged for developing some of the extractive sampling techniques.

REFERENCES

1. R.J. Evans and T.A. Milne (1987). "Molecular Characterization of the Pyrolysis of Biomass: I. Fundamentals," *Energy and Fuels* 1, pp. 123-127.

2. R.J. Evans and T.A. Milne (1987). "Molecular Characterization of the Pyrolysis of Biomass: II. Applications," *Energy and Fuels* 1, pp. 311-319.

3. R.J. French, D.C. Dayton, and T.A. Milne (1994). *The Direct Observation of Alkali Vapor Species in Biomass Combustion and Gasification*, NREL Technical Report (NREL/TP-430-5597). January 1994.

4. T.A. Milne and H.M. Klein (1960). "Mass Spectrometric Study of Heats of Formation of Alkali Chlorides," *J. Chem. Phys.* 33, pp.1628-1637.

5. J.W. Hastie, K.F. Zmbov, and D.W. Bonnell (1984). "Transpiration Mass Spectrometric Analysis of Liquid KCl and KOH Vaporization," *High Temperature Science* 17, pp. 333-364.

6. R.C. Weast, Ed. (1985). *66th Edition of the CRC Handbook of Chemistry and Physics*, CRC Press, Inc., Boca Raton, FL.

7. L.A. Scandrett (1984). "The Thermodynamics of Alkali Removal from Coal-Derived Gases," *Journal of the Institute of Energy*, December 1984, pp. 391-397.

Free-Jet Mass Spectrometry of Laser Ablation Plumes in Thin Film Deposition*

John W. Hastie, Albert J. Paul, and David W. Bonnell

Materials Science and Engineering Laboratory, NIST
Gaithersburg, MD 20899

INTRODUCTION

Plumes generated by high-power pulsed (10 — 30 ns) laser vaporization or ablation of refractory materials can attain ultra-high temperatures (5,000 — 30,000 K) and relatively high pressures (> 1 bar ≡ 10^5 Pa). However, plume expansion into a vacuum is sufficiently rapid that the initial species information can be retained and representative sampling with molecular beam mass spectrometry (MBMS) can be achieved. In order to verify and supplement the MBMS results, complementary investigations using emission spectroscopy and real-time imaging, coupled with gasdynamic, thermodynamic, and gaskinetic models are also carried out. In addition to plume species identities and abundances, MBMS analysis also provides beam time-of-flight information, yielding velocity distributions and gas temperatures. MBMS applications are considered here for systems important in thin film processing, such as Al_2O_3 and C. Attention is also given to the essential features required of a free-jet MBMS system for representative sampling of laser ablation plumes.

Significant progress in defining the general nature of laser vaporization/ablation plumes, used for thin film deposition, has been made in recent years (1). Our current understanding of the main plume features are summarized by the idealized schematic of Fig. 1. As shown, the plume initiates at the laser focus spot on the target surface and moves away along an axis normal to the target (*i.e.* to the right in Fig. 1). After a few ns time delay from the onset of the laser pulse, sufficient vapor density develops for collisional local equilibrium ("loc. eq." in Fig. 1) to become established, followed by a supersonic adiabatic expansion process. This expansion process is isentropic and rapidly leads to a free-flight, collision-free condition. In the present work, species are sampled from this free-flight region for MBMS analysis (note orifice shown at the extreme right in Fig. 1).

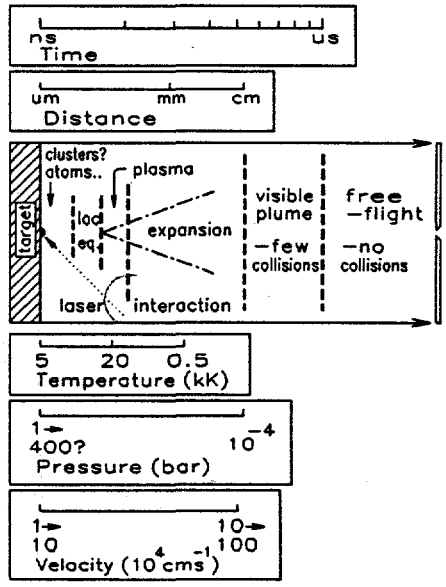

Figure 1 — Laser vaporization/ablation schema

APPARATUS

Laser vapor plumes are particularly complex, and their detailed characterization is not amenable to a single measurement technique. Hence, a variety of *in situ*, real-time monitoring devices are used, as discussed elsewhere (2). These techniques involve rapid (ns-time scale) video imaging and spectroscopic analysis, using photodiode linear arrays and two-dimensional CCD (charge-coupled-device) array detection, in addition to MBMS analysis.

Here, we consider application of the MBMS technique. Fig. 2 shows, schematically, the main features of the apparatus developed for this purpose. This system has high speed differential

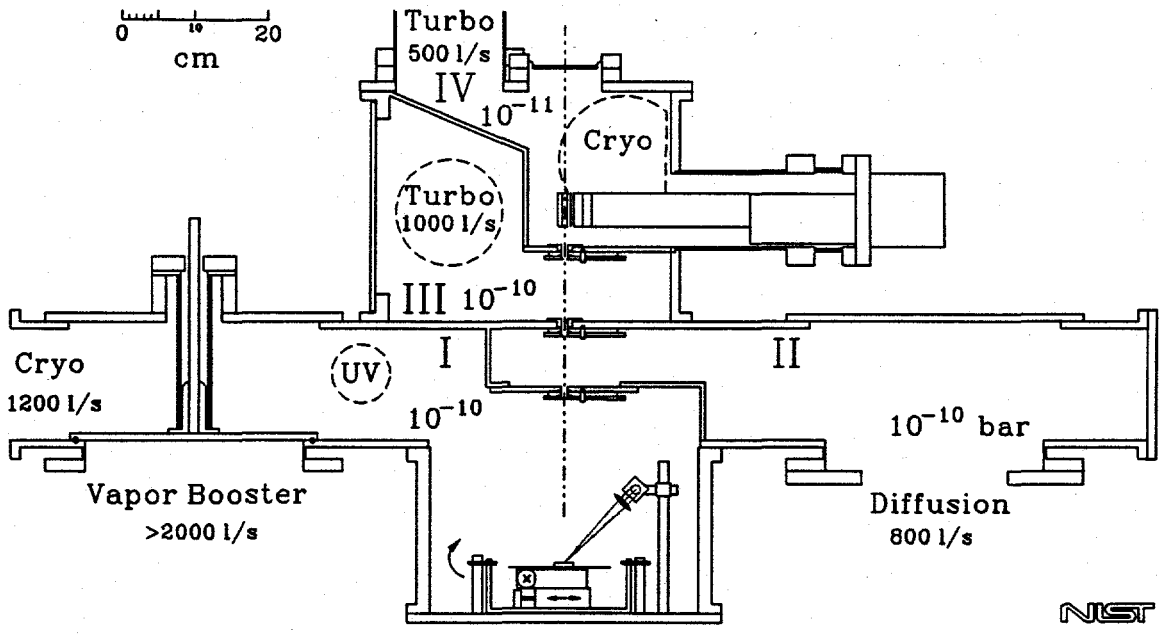

Figure 2 — Laser vaporization/ablation molecular beam mass spectrometer

pumping to allow for rapid free-jet expansion and representative sampling of the expanded vapor. Because of the high temperatures and velocities accompanying laser plumes, coupled with the differential pumping requirement, the distance between the plume and the mass spectrometer ion source has been made relatively long (47.9 cm). As will be shown, this distance allows for sufficiently long flight times to permit observation of velocity distributions over the range of 10^4 to $> 10^6$ cm s^{-1}, which is characteristic for expanded plumes.

RESULTS AND DISCUSSION

Results from a few representative investigations are presented here to demonstrate application of the MBMS technique to laser plumes. Table 1 indicates the variety of materials studied by us and lists the identities of the dominant plume species. It is noteworthy that no evidence of cluster species, present in the plume or formed in the expansion cooling process, was found in these studies. For the most part, the species observed are those we predict from their thermochemical stabilities for conditions near the atmospheric boiling points of the target materials (3-5).

Velocity Distributions In a typical experiment, the mass spectral intensity (I) of each species is monitored as a function of time-of-arrival (TOA) at the detector, relative to the termination of the laser pulse. Fig. 3 shows an example for Al produced by 1064 nm Nd/YAG laser interaction (~ 10 ns pulse) with an Al_2O_3 target at a moderate fluence. The intensity scale (I') has been corrected for the velocity (v) discrimination associated with the density detection nature of the electron impact ion source. As we have shown elsewhere (2), an appropriate velocity distribution [P(v)] model in this case is that of a full-range Maxwellian distribution referenced to a center-of-mass net flow or drift velocity (u):

$$P(v_z) \propto v_z^3 \exp[-(m/2kT_c)(v_z-u)^2]. \qquad [1]$$

The z axis is the molecular beam axis (see Fig. 2); T_c is the local terminal gas temperature at the onset of collisionless flow; m is molecular mass and k is the Boltzmann constant. In practice,

Table I. Species identified in laser ablation plumes

Material	Application	Atoms	Ions (M^+)	Molecules
Nd/YAG Laser:				
C	Thermo at 4000 K	C	C_{1-3}	C_2 - C_9
BN	Thermo at 2800 K	B, N	-	B_2, B_3, BN, N_2
SiC	Thermo at 3500 K	Si, C	-	SiC, Si_2C, SiC_2, Si_2, Si_3, C_2, C_3
HfO_2	Thermo at 4900 K	Hf, O	Hf, HfO, HfO_2	HfO, HfO_2
MgO	Thermo at ~3300 K	Mg, O	-	MgO
$BaYCuO_x$	High T_c films	Ba, Cu, O	Ba, Cu	CuO, O_2, BaY
Ag/Fe_3O_4	Plasma study	Ag, Fe, O	Ag, Fe, O	-
$BiPbCaCuSrO_x$	Plasma Study	O, Cu, Pb, Ca, Sr	Cu, Ca, Sr	CuO, SrO, CaO
Al_2O_3	Thermo at 4000 K	Al, O	-	AlO, Al_2O
Pb_2ZrTiO_6	Ferroelectric Films	Pb, Zr, Ti, O	Pb, Zr, Ti	PbO, ZrO, TiO, ZrO_2, TiO_2
Eximer Laser:				
Ag/Fe_3O_4	Nanostr. mag. films	Ag, Fe, O	Ag, Fe	-
Pb_2ZrTiO_6	Ferroelectric films	Pb, Zr, Ti	Pb, Zr, Ti	ZrO, TiO
$BaTiO_3$	Dielectric films	Ba, Ti, O	Ba, Ti	BaO, TiO, TiO_2
$BaYCuO_x$	High T_c films	Ba, Y, Cu	Ba, Y, Cu	YO
$BiPbCaCuSrO_x$	High T_c films	Pb, Bi, Ca, Cu, Sr	(to be analyzed)	(to be analyzed)
AlN	thermal	Al, N	AlN, N	AlN
Al_2O_3	thermal	Al, O	-	AlO, Al_2O

as the experimental data are obtained (initially) in time rather than velocity space, an analogous time-dependent expression $P(t_z)$ may also be used to fit the TOA profiles (as in Fig. 3). These nonlinear fits provide values of T_c and u. Similar results are obtained from plotting the observed mass-dependence of the peak TOA values for various species (see Fig. 4). As shown in Figs. 3

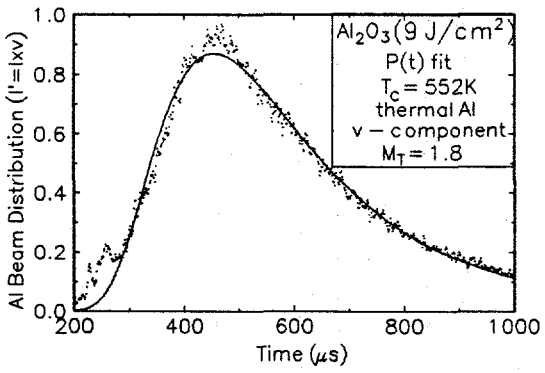

Figure 3 — Time-of-arrival for Al (Al_2O_3); λ = 1064 nm, fluence = 9 J cm^{-2}

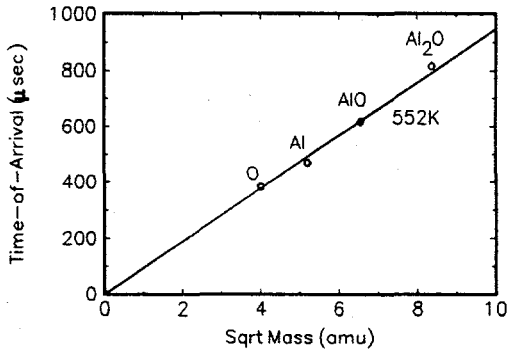

Figure 4 — Peak TOA dependence on $(mass)^{1/2}$ for species from Al_2O_3; λ = 1064 nm.

and 4, the value of T_c = 552 K is evidence of considerable expansion cooling. From the magnitude of the mass spectral intensities, we have determined that the initial pre-expansion pressure is typically of the order of one bar (4). For Al_2O_3, a surface temperature of 4500 K would be needed to generate a pressure of this magnitude.

Conversion of the TOA profiles to a velocity scale shows that the data of Fig. 3 correspond to relatively low velocities ($\sim 10^4$ cm s^{-1} range), characteristic of moderate terminal Mach numbers ($M_T \sim 1.8$). As the laser fluence is increased, an additional discrete faster velocity distribution(s) is found (see Fig. 5). This faster velocity distribution becomes relatively more significant with increasing fluence and has a very high T_c ($\sim$31,000 K). These effects can be attributed to laser-plasma interactions (2,6). The plasma gasdynamic model fit, shown in Fig. 5. and discussed in detail elsewhere (2,6), agrees well with the observed high-energy distribution,

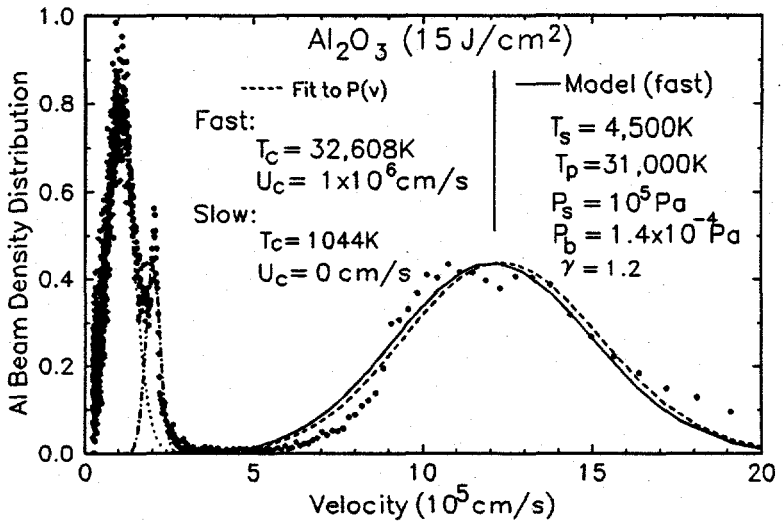

Figure 5 — Velocity distribution for Al (Al_2O_3) at 15 J cm^{-2}; λ=1064 nm

Sampling Fidelity A key question concerning any free-jet MBMS measurement approach is the reliability of the sampling process. In contrast with our earlier sampling of atmospheric pressure flames (7) and transpiration vapors (8,9), a sampling probe was not inserted into the active high pressure core of the plume. Instead, the sampling orifice was located (usually) well downstream of the shock front (Mach disc) location and in a region of collisionless flow. The target-to-orifice distance was 22 cm, compared with the calculated (from measured Mach numbers) distance to collisionless flow in the range of 0.05 — 5 cm. Also, the pumping speed and conductance was high enough that the calculated Mach disc location was always downstream of the transition to collisionless flow. Agreement between experimental and calculated expansion temperatures indicates that the sampling process was indeed located at a fully expanded jet location, and no gasdynamic or other thermal perturbation was occurring.

There is strong evidence that local thermal equilibration of neutral species occurs in these laser plumes. It can be shown (*e.g.* from Eq. [1]) that the peak time-of-arrival times should vary inversely with species mass provided the local thermal equilibration condition is maintained. In general we have found such a dependence (Fig. 4). Data analysis using this type of relationship also provides an additional benefit in assuring the reliability of the mass spectral species assignments. If electron impact fragmentation interference occurs, it would be evident as a displacement from the line in Fig. 4, since the peak times refer to the preionized condition of each species. As we have indicated elsewhere, free-jet MBMS can lead to very different fragmentation patterns than those found conventionally (4,10). With a few notable exceptions (10), the expansion cooling process can be very beneficial in reducing electron impact fragmentation (4).

A more stringent, and more difficult to establish, test of sampling fidelity is provided by examination of possible shifts in chemical equilibria or kinetics. That is, are the relative concentrations of the sampled species modified by the sampling and analysis process? We have shown elsewhere that, for systems that are demonstrably in thermodynamic equilibrium, sampling perturbations are negligible (8,9). In laser-generated plumes, however, there is no *a priori* assurance that the pre-expansion plume is chemically equilibrated. We have shown elsewhere that

for moderate laser fluences, sufficient to attain a near-atmospheric boiling condition at the target surface, the pre-expansion species are frequently present in local thermodynamic equilibrium (4,6). The MBMS species distributions are also found to agree well with thermodynamic equilibrium calculations, *e.g.* for C (4), BN (11), HfO_2 (5), $BaTiO_3$ (2,6) and Al_2O_3 (6). For the Al_2O_3 case, we have also carried out detailed gaskinetic calculations, showing that relatively small changes in species concentrations are possible and particularly during the first 20 ns of plume expansion (6).

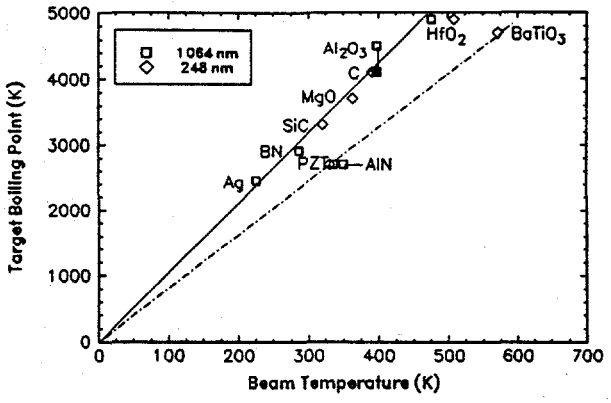

Figure 6 — Beam-surface temperature correlation

<u>Conversion of Final (Expansion) to Initial State Properties</u> The MBMS measurements yield information on terminal velocities (v_T) and temperatures ($T_T \equiv T_b \equiv T_c$). If we assume that the formation of an expanding vapor plume from a focused hot spot is gasdynamically similar to expansion through an orifice, then various standard gasdynamic relationships apply. The initial pre-expansion temperature of the gas, T_o, may then be obtained from:

$$T_T/T_o = [1 + \frac{\gamma-1}{2} M_T^2]^{-1} \qquad [2]$$

Typical values fall in the range 2500 — 8000 K (for gas heat capacity ratio γ = 1.4 — 1.2 range). Pressure ratios may be obtained from:

$$T_T/T_o = [P_T/P_o]^{\frac{\gamma-1}{\gamma}} \qquad [3]$$

Typical values of P_T/P_o in our system fall in the range 10^{-4} — 10^{-5}, or lower. When combined with P_T values determined from calibration of the mass spectral intensities, values of P_o in the range of 1 — 10 bar are obtained. Direct and indirect measurement of surface temperatures also indicate target temperature and pressure conditions near the boiling point at moderate fluence conditions ($\lesssim$ 1 — 10 J cm^{-2}). Based on eq. [3], we should then expect to find a linear correlation between the thermodynamically derived target boiling temperature ($T_{bpt} \sim T_o$) and the final, or beam, temperature (T_b) if T_o is strongly correlated with the surface temperature. The solid curve in Fig. 6 shows such a correlation for a variety of materials. The second dashed curve was obtained with significantly high laser fluence, where laser-plume interactions raised the effective values of T_o to values much greater than T_{bpt} (*i.e.* > 10,000 K).

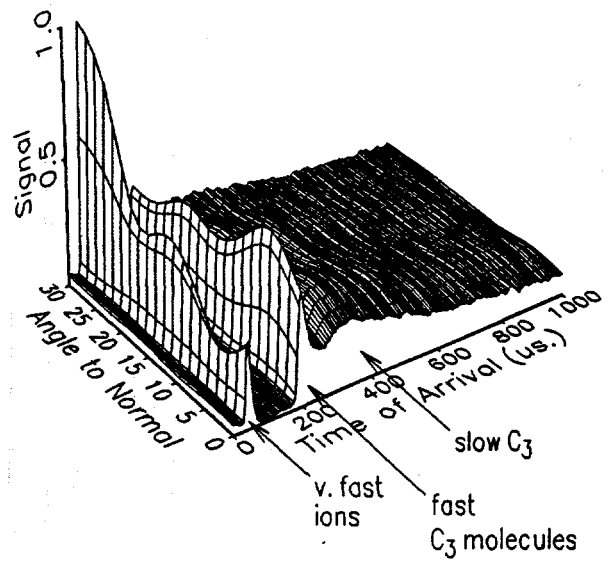

Figure 7 — Angular distribution TOA behavior for C_3 from graphite.

Plume Angular Distribution Effects The target kinematic stage can be tilted, *in situ*, relative to the fixed MBMS sampling axis. Measurement of species intensity changes, as a function of angle from the normal, have allowed us to observe high order cos θ^n distributions with $n \sim 5 - 20$. These values of n are consistent with other arguments made here concerning the supersonic nature of expanding laser plumes. Other intriguing observations, such as are shown in Fig. 7, have also been made (work in progress). The unusual angle dependencies shown for the fast neutral and charged species are attributed to laser-plume interactions, which are more significant for ions and can lead to non-symmetrical geometry effects in the plume.

CONCLUSIONS

In summary, the application of free-jet MBMS to laser plumes is of considerable value. Identities and concentrations of all significant species can be obtained. Velocity distributions and temperatures, combined with gasdynamic and plasma models, yield information on the pre-expansion plume properties. These results also complement those obtained by optical probes [not discussed here, see (2)].

The species identity, flux and kinetic energy information obtainable is directly applicable to growth models of thin film formation. Information on spatial and temporal plume evolution can indicate optimal target, laser, and substrate positioning. Determination of species relationships with process variables (fluence, wavelength, pulse time, pressure, ...) also allows for selection of optimum process conditions. Finally, MBMS results complement and enhance the development of more non-intrusive optical probes for *in situ*, real-time process monitoring and control.

REFERENCES

1. Chrisey, D. B. and Hubler, G. H.,(eds.) *Pulsed Laser Deposition of Thin Films* (John Wiley and Sons, Inc., 1994).
2. Hastie, J. W., Bonnell, D. W., Paul, A. J., and Schenck, P. K., "Gasdynamics and Chemistry in the Pulsed Laser Deposition of Oxide Dielectric Thin Films," *MRS Proc.* 334, (MRS, Pittsburgh, PA, 1994), p. 305.
3. Hastie, J. W., Bonnell, D. W., and Schenck, P. K., "Molecular Basis for Laser-Induced Vaporization of Refractory Materials," *NBSIR 84-2983* (National Technical Information Service, Washington, DC., 1984).
4. Hastie, J. W., Bonnell, D. W., and Schenck, P. K., *High Temp. High Press.*, 20, 73, (1988).
5. Bonnell, D. W., Schenck, P. K., Hastie, J. W., and Joseph, M."Ultra-High Temperature Laser Vaporization Mass Spectrometry of SiC and HfO_2," *5th Intl. Symposium on High Temperature Materials Chemistry*, PV90-18, (Electrochemical Society, Pennington, NJ, 1990).
6. Hastie, J. W., Paul, A. J., Yeheskel, J. Bonnell, D. W., and Schenck, P. K., *High Temp. Sci.*, in press (1994).
7. Hastie, J. W., *Combust. and Flame*, 21, 187 (1973).
8. Hastie, J. W., Bonnell, D. W., "Transpiration Mass Spectrometry: A New Thermochemical Tool," in *Thermochemistry and Its Applications to Chemical and Biochemical Systems*, (ed.), M. A. V. Ribeiro da Silva, (Reidel Publishing, Boston, MA, (1984), p. 183.
9. Hastie, J. W. and Hager, J. P., "Vapor Transport in Materials and Process Chemistry," *Proc. The Elliott Symposium on Chemical Process Metallurgy*, (Iron and Steel Soc., 1990), p. 301.
10. Bonnell, D. W., Hastie, J. W., and Zmbov, K. F., *High Temp. High Press.* 20, 251 (1988).
11. Hastie, J.W., Bonnell, D. W., and Schenck, P. K., *High Temp. Sci.*, 25, 117 (1988).

* Presented at *Specialists Workshop on Applications of Free-Jet Molecular Beam Sampling*, Estes Park, CO. (US DOE National Renewable Energy Laboratory, October 12-14, 1994,)

Molecular Beam Mass Spectrometry Studies of the Thermal Decomposition of Tetraethoxysilane (TEOS)

Carmela Amato Wierda, Michael R. Zachariah and Donald R.F. Burgess, Jr.
National Institute of Standards and Technology, Process Measurements Division
Gaithersburg, MD 20899

Abstract

Molecular beam mass spectrometry and time-of-flight techniques have been used to reveal the gas phase chemistry that occurs during the thermal decomposition of TEOS. Evidence in our laboratory was consistent with the presence of the following species during decomposition at 600°C: ethylene, ethanol, acetaldehyde, possibly diethoxysilanone, triethoxysilanol, hexaethoxysiloxane. A grayish white powder, which presumably consists of silicon oxides containing residual carbon and hydrogen, was also produced. Under the following reaction conditions: reactor pressure=266 Pa (2 torr), residence time=6 ms, and TEOS partial pressure=26 Pa (0.2 torr), the onset of decomposition occurs at 400°C. The amount of TEOS decreases at residence times greater than 6 ms with concurrent increase in ethanol and ethylene. Hexaethoxysiloxane also increases at residence times between 6 and 20 ms, but then decreases at longer times probably because it reacts to form larger siloxanes and silicon oxides.

Introduction

The thermal decomposition of tetraethoxysilane (TEOS) is used for the production of SiO_2 in the form of both thin films and particles. For the case of thin films, TEOS is used extensively by the microelectronics industry to deposit SiO_2 films[1]. The main advantages of using TEOS are: low deposition temperature, absence of corrosive reaction products, and excellent insulating properties and conformality of the resultant film. To a lesser extent, TEOS has also been used for the gas phase condensation of ultrafine SiO_2 particles[2].

A detailed understanding of the gas phase decomposition chemistry is necessary in order to modify the conditions in either the chemical vapor deposition or particle formation process to favorably affect the final product. Previous investigations on the thermal decomposition of TEOS have mostly been carried out by GC or FTIR analysis on the trapped effluent from a reactor.[3-7] Recently Takeuchi[8] reported studies with an experimental CVD apparatus connected to a mass spectrometer. Most of these investigations found ethylene, ethanol and acetaldehyde as products of TEOS decomposition. Both Ivanov[3] and Takeuchi[8] reported the presence of a siloxane dimer of TEOS–hexaethoxysiloxane, $((CH_3CH_2))_3Si–O–Si(OCH_2CH_3)_3)$. Lin,[4] Desu[6] and Heunisch[5] proposed diethoxysilanone, $(O=Si(OCH_2CH_3)_3)$, as a vapor phase intermediate. Takeuchi suggested that triethosysilanol, $(HO–Si(OCH_2CH_3)_3)$, is present during the deposition process.[8] These investigations also proposed several TEOS decomposition mechanisms, including: free radical mechanisms[3,4,6], unimolecular rearrangement and elimination reactions[4,5], as well as condensation reactions[4,8].

In this study, a molecular beam mass spectrometer has been directly coupled to a high temperature flow reactor in order to study the details of the thermal decomposition of TEOS. This apparatus provides an *in situ* and real time analytical tool for determining the vapor phase species that occur during TEOS decomposition as a function of process variables, such as reactor temperature, total pressure, TEOS concentration, and residence time of the gas flow in the reactor.

Apparatus and Experimental Procedure

Reactor Figure 1 schematically shows the apparatus used for this study. It consists of two separate parts: (1) the high temperature reactor chamber, and (2) the molecular beam mass spectrometer. The reactor assembly was custom built to operate at temperatures up to a 1000°C in

an inert atmosphere or vacuum. The reactor consists of Hoskins 875 heater wire wound around a 99.8% alumina tube measuring 3.75 cm i.d. by 90 cm long. The heating elements are divided into three 20 cm long zones to minimize temperature gradients along the tube. Two Pt/Pt-10%Rh thermocouples are cemented to each zone. Power is supplied to the heaters by variable transformers and PID microprocessor temperature controllers. Each zone has a power capability of 530W at 40V.

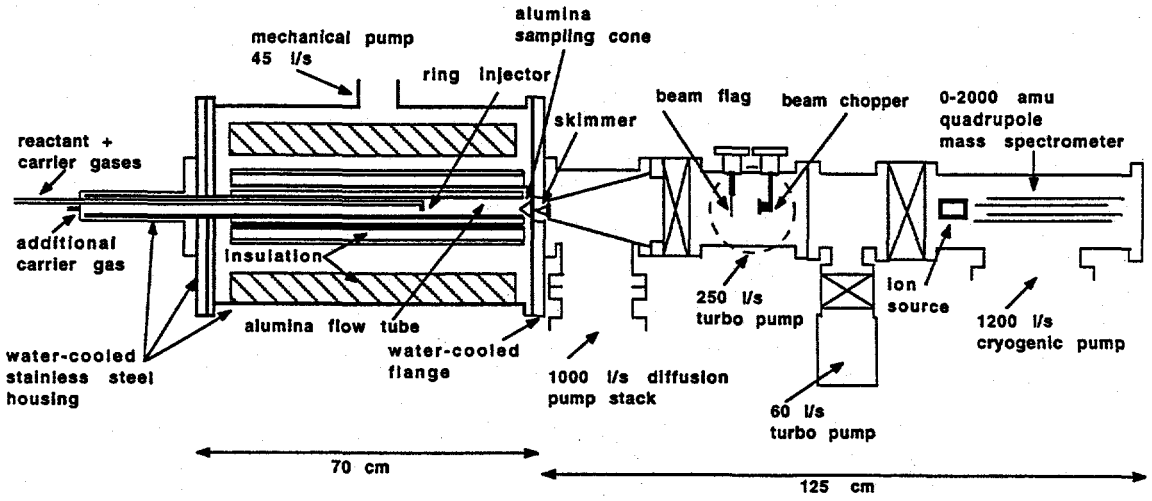

Figure 1. Schematic of high temperature furnace-molecular beam mass spectrometer system.

The reactor assembly was placed inside the inner tube of two concentric 60 cm long mullite tubes. The inner tube measures 8.75 cm o.d. and the outer tube is 15 cm o.d. The space between these concentric tubes is filled with ceramic fiber blanket for insulation. The fiber blanket is contained in this manner to minimize contamination of the chamber with particulate matter generated upon thermal cycling. This entire assembly is supported inside the reactor chamber by a heavy-duty linear motion feedthrough at one end, and by a stainless steel mounting plate at the other end. The motion feedthrough also serves to align the reactor tube in the vertical direction. The remaining space between the reactor chamber wall and the outer mullite tube is filled with zirconia fiber blanket. This blanket is wrapped with 0.005 cm thick inconel foil in order to contain particulate matter coming from it.

The reactor chamber is a stainless steel 42.5 cm o.d. tube by 67.5 cm long with two clamp flanges at each end. The upstream end flange holds the power and thermocouple feedthroughs, as well as a stainless steel tube which covers the part of the alumina tube not contained within the reactor chamber. This stainless steel tube connects to the gas inlet system, which controls the composition and flow of gases into the reactor. The wall of the reactor chamber, the upstream end flange and the tube connecting to the gas inlet system are all wrapped with copper tubing to provide water cooling. The downstream end flange serves two purposes: (1) it connects to the molecular beam mass spectrometer and (2) it holds and cools the sampling aperture which forms the molecular beam. The entire reactor chamber is pumped by a mechanical pump with a pumping speed of 45 l/s.

Gas Inlet System The gas inlet system is made from 0.64 cm (0.25 in) o.d. stainless steel tubing and bellows valves. The TEOS is contained inside a home-made stainless steel bubbler at room temperature. The TEOS and argon carrier gas flow is introduced into the reactor via a moveable quartz ring injector. It is constructed from 0.635 cm o.d quartz tubing by 125 cm long, attached to a 3 cm o.d loop of tubing having sixteen 0.4-0.5 mm diameter holes to promote mixing. Moving the ring injector along the axis of the reactor allows the gas residence time to be varied at a constant flow rate. The residence time of the gas is defined as the amount of time the gas spends inside the

reactor tube at temperature before being pumped away. The term "residence time" can also be equated with reaction time.

Molecular Beam Mass Spectrometer The reactor chamber is connected to the molecular beam mass spectrometer by the sampling aperture. This aperture is a 99.9% alumina cone measuring 3.75 cm high. The wall thickness near the tip of the cone is approximately 0.125 cm. The aperture at the tip is 0.0125 cm in diameter with a channel length of approximately 0.15 cm. The alumina cone is sealed to the downstream reactor flange with a Kalrez o-ring.

The molecular beam mass spectrometer consists of four differentially pumped stages. The first chamber behind the alumina cone is pumped by a 20 cm (6 in) diffusion pump stack with an effective pumping speed of 1000 l/s. This chamber also holds a stainless steel skimmer assembly which allows the skimmer to be moved in directions perpendicular to the beam axis for alignment. The skimmer is rhodium-plated nickel with a 0.150 cm aperture. The sampling aperture-to-skimmer separation is 1.6 cm.

The next chamber is pumped by a 200 l/s turbo pump and houses a beam flag and DC motor-driven, variable frequency controlled chopper. The 31 mm diameter chopping wheel has 8 – 22.5° apertures to provide a 50% duty cycle for normal beam modulation. For time-of-flight experiments, this wheel was removed and replaced by one with only a single 2° aperture to provide delta function modulation of the beam. The chopping frequencies of the 8 aperture wheel range from 50 to 2200 Hz, while those of the single aperture wheel are from 10 to 290 Hz. The chopper controller provides a sync output signal that is generated from a LED-phototransistor pair measuring the rotation of the chopper blade directly.

An ante-chamber is located in front of the mass spectrometer chamber in order to minimize background molecules that might scatter the beam directly in front of the mass spectrometer. This chamber is pumped by a 50 l/s turbo pump. A 0.3475 cm collimating aperture separates the chopper chamber from the ante-chamber, and another 0.42 cm collimating aperture separates the ante-chamber from the mass spectrometer chamber.

The mass spectrometer chamber is pumped by a 1500 l/s cryopump. The pressure in this chamber is typically in the 10^{-8} Pa (10^{-10} torr) range. This chamber houses a quadrupole mass spectrometer with a mass range from 0-2000 amu. The ionizer aperture has a diameter of 0.45 cm (0.1875 in). The time-of-flight path length between the chopper wheel and the ionizer is 37.39 cm.

Data Acquisition System The signal from the electron multiplier of the quadrupole is first amplified by a counting preamplifier/discriminator. The output is sent to a data acquisition system which consists of a computer controlled multi-channel scaler.

Experimental Procedure For all experiments except the time-of-flight measurements, the ion signal intensities were determined by collecting, at a given mass, the modulated signal generated by the square wave chopping wheel at a frequency of 200 Hz. The intensity of the signal is taken as the amplitude of the waveform ignoring any background. In all experiments, the electron energy was 70 ev. Operating at electron energies lower than 50 ev resulted in almost complete loss of the signal. In the case of the time-of-flight experiments, the same procedure was used with the delta function wheel at a frequency of 80 Hz.

Results and Discussion

Figures 2a and 2b show the signal intensity at several m/z values as a function of reactor temperature. The remaining reactor parameters were held constant at the following values: total reactor pressure= 266 Pa (2 torr), TEOS partial pressure=26 Pa (0.2 torr), residence time=6 ms. All signal intensities are reported relative to the argon signal intensity at m/z=40. These intensities have been plotted relative to the intensities at the starting temperature of 25°C. The m/z=193 and m/z=149 signals in Figure 2a are thought to originate from undecomposed TEOS. TEOS has a molecular weight of 208 g/mol; loss of a methyl group in the ion source generates a fragment at m/z=193 while loss of two methyl group and one ethyl groups generates a fragment at m/z=149.

The m/z=193 signal is constant until 400°C, and then it decreases as the temperature is raised until completely disappearing at 700°C. The m/z=149 signal by comparison increases initially, then decreases approximately at the same rate as the m/z=149 signal and disappears at 700°C. The different behavior in these two signals may result from either scatter, or more likely, species are produced during the decomposition that generate fragments at the same m/z values as TEOS. This would account for the increase in the signal at m/z=149. Several other observed signals at the following m/z values: 180, 179, 165, 164, 163, 152, 151, 150, 148, 135, 134, 124, 123, 121, 119, 107, 106, 105, 103, 93, 91, 90, 89, and 79 also followed the behavior of the m/z=149 signal; but these will not be discussed here for reasons of space limitation.

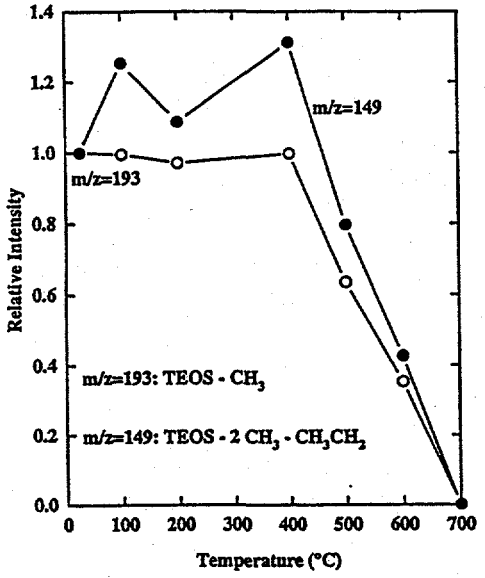

Figure 2a. Intensity of signals at m/z=193 and 149 versus reactor temperature.

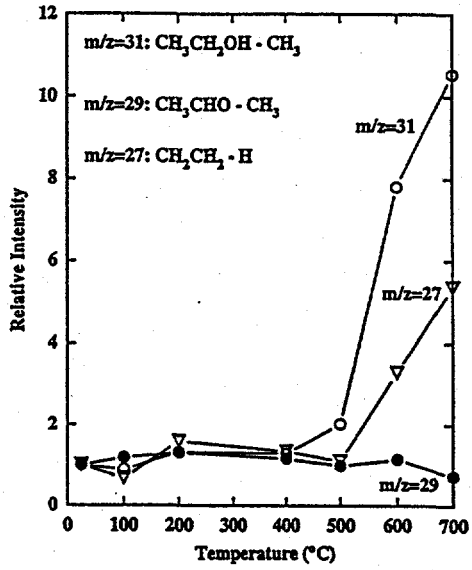

Figure 2b. Intensity of signals at m/z=27, 29, and 31 versus reactor temperature.

The m/z=31 and m/z=27 signals in Figure 2b are assigned predominantly to ethanol and ethylene, respectively, at high temperatures. The molecular weight of ethanol, (CH_3CH_2OH), is 46 g/mol and that of ethylene, (CH_2CH_2), is 28 g/mol. The m/z=31 fragment results from ethanol losing a methyl group in the ion source, and the m/z=27 signal results from ethylene losing a hydrogen. Both signals remain essentially constant until 400°C and then steadily increase at higher temperatures. The increase in these hydrocarbon products with the simultaneous decrease in TEOS indicates that TEOS is thermally decomposing. The m/z=31 from ethanol is observed at low temperatures due to some residual ethanol in the TEOS reagent bottle. The m/z=27 signal can also result from fragmentation of undecomposed TEOS, explaining its non-zero intensity at low temperatures. The m/z=29 signal is tentatively assigned to an ethyl fragment from undecomposed TEOS, as well as possibly acetaldehyde. Acetaldehyde, ($O{=}CHCH_3$), has a molecular weight of 44 g/mol and loss of a methyl group generates a fragment at m/z=29. This signal remains constant at all temperatures. If the signal originated only from TEOS, it should decrease at 400°C. The constant signal level suggests that acetaldehyde is also a product of TEOS decomposition.

Figure 3 shows the relative intensities of several signals as a function of residence time in the reactor. It can be seen that as the m/z=193 signal from TEOS decreases, the ethanol and ethylene signals at m/z=31 and m/z=27, respectively, increase. A low intensity signal at m/z=297, previously unobserved, is tentatively assigned to a fragment of the TEOS dimer, hexaethoxysiloxane. The molecular weight of hexaethoxysiloxane , ($(CH_3CH_2O)_3Si{-}O{-}Si(OCH_2CH_3)_3$), is 342 g/mol, and loss of an ethoxy group in the ion source generates the m/z=297 signal. This signal increases at residence times up to 10 ms and then decreases, probably due to subsequent reaction to form larger siloxanes and silicon oxides.

The species assignments made from the above preliminary data were further supported by qualitative information from time-of-flight waveforms of the signals, shown in Figures 4a-c. These peaks are shifted to the right on the time axis by 180° due to a synchronization offset caused by the relative positions of the beam and the LED/phototransistor pair. Figure 4a compares the

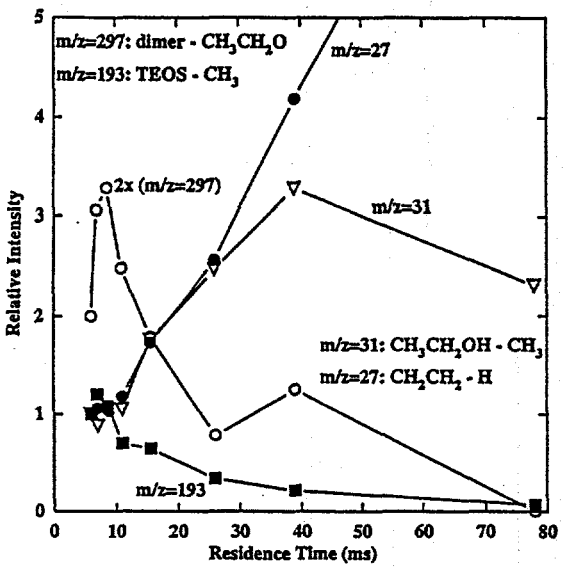

Figure 3. Intensity of signals at m/z=297, 193, 31, and 27 versus residence time.

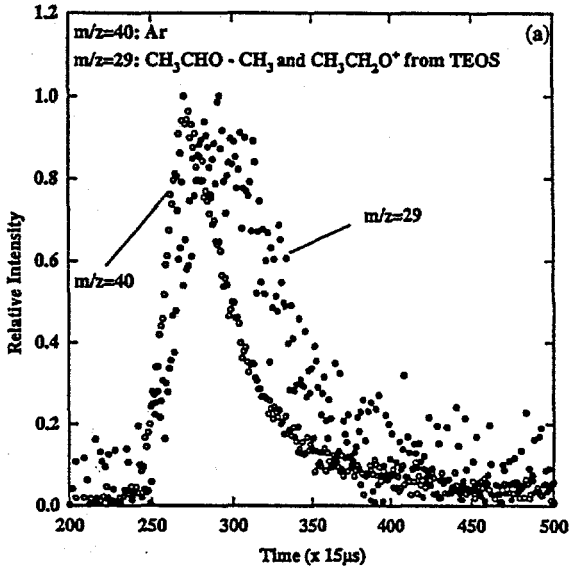

Figure 4a. Time-of-flight waveform at m/z=29 and 40 (argon).

signals at m/z=40 from argon (hollow circles) and m/z=29 (solid circles). The m/z=29 peak lies close to the argon peak at short flight times, but also has significant intensity at longer times most probably resulting from undecomposed TEOS. It is the proximity of the rising edge of this waveform to that of argon, and the fact that m/z=29 is the most intense fragment in the mass spectrum of acetaldehyde, that support our assertion of the presence of acetaldehyde during TEOS decomposition. Although not shown in the figure, the waveforms of the signals at m/z=27 and m/z=31 were visually indistinguishable from the argon waveform. This observation is consistent with the assignment of these signals to ethylene and ethanol, respectively.

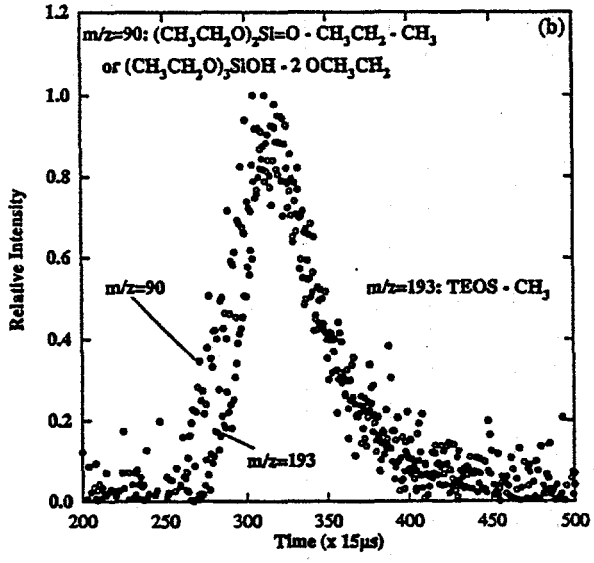

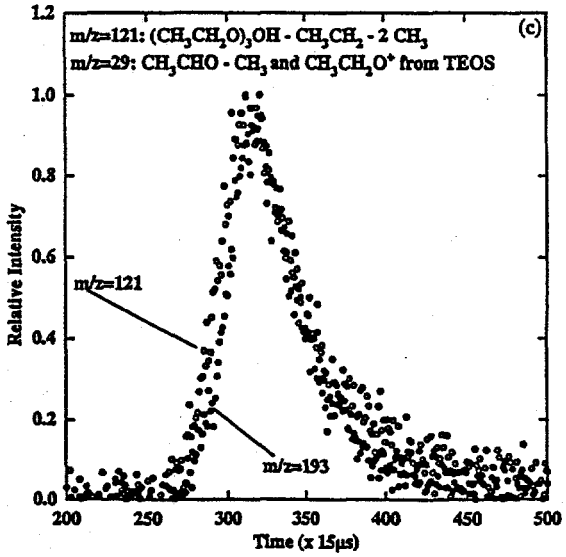

Figure 4b-c. Time-of-flight waveforms at: (b) m/z=90 and 193 (TEOS) and (c) m/z=121 and 193 (TEOS).

Figures 4b and 4c compare the waveforms of the m/z=193 TEOS fragment with the m/z=90 and m/z=121 waveforms, respectively. Both of these signals have time-of-flight peaks that are shifted to shorter times than that of TEOS, indicating that one or more lower molecular weight species are contributing to these signals. For the case of the m/z=90 signal, this species may be diethoxysilanone, ($O=Si(OCH_2CH_3)_2$), with a molecular weight of 134, which generates an m/z=90 fragment upon loss of ethyl and methyl groups in the ion source. Triethoxysilanol, ($HO–Si(OCH_2CH_3)_3$), with a molecular weight of 180 g/mol, would generate an m/z=121 fragment upon loss of two methyl and one ethyl groups; and therefore may contribute to the m/z=121 signal.

It is also possible for triethoxysilanol to form an m/z=90 fragment upon loss of two ethoxy groups in the ion source. Thus this species can also contribute to the m/z=90 waveform. The m/z=90 peak is shifted to shorter flight times than the m/z=121 peak. Either a lower molecular weight species contributes to the m/z=90 signal, or the contributions from the lower molecular weight components are different for the two signals. More quantitative curve fittings to the time-of-flight data are currently underway to address these issues.

The other decomposition product found during this study is a grayish powder and film coating the inside of the reactor and the sampling cone. This solid product probably consists of silicon oxides with residual carbon and hydrogen. We plan to perform elemental analysis, TEM and SEM of this solid product as a function of reactor conditions.

Conclusion

Molecular beam mass spectrometry is proving to be a very powerful real time and *in situ* analytical tool for elucidating the gas phase chemistry of TEOS decomposition. Evidence has been found consistent with the presence of the following species during decomposition at 600°C: ethylene, ethanol, acetaldehyde, diethoxysilanone, triethoxysilanol, hexaethoxysiloxane, and a grayish white powder and film–probably silica with residual carbon and hydrogen. Using the following reaction conditions: total reactor pressure=266 Pa (2 torr), residence time-6 ms, and TEOS partial pressure=26 Pa (0.2 torr), the onset of decomposition occurs at 400°C. Under these conditions, the amount of TEOS decreases at residence times greater than 6 ms with concurrent increase in ethanol and ethylene. Hexaethoxysiloxane also increases at residence times between 6 and 10 ms, but then decreases at longer residence times as it reacts further to form larger siloxanes and silicon oxides. More quantitative studies on the identification of these species and their behavior as a function of the various reaction parameters are underway.

Acknowledgements

The National Research Council (NRC) is gratefully acknowledged for supporting Carmela Amato Wierda as an NRC/NIST Postdoctoral Research Fellow. We thank Raymond R. Fink for many technical discussions and for the assembly of the apparatus.

References

(1) Kern, W. and Ban, V.S. in *Thin Film Processes*; Vossen, J.L. and Kern, W., Ed.s; Academic Press, CA, 1978, p 290.
(2) Okuyama, K., Kousaka, Y., Tohge, N., Yamamoto, S., Wu, J.J., Flagan, R.C. and Seinfeld, J.H. *AIChE J* **1986**, *32*, 2010-2019.
(3) Ivanov, M.Ya., Kupryashkina, T.N., Kompaniets, V.Z., Kopteva, M.A. and Konoplev, A.A. *J. Appl. Chem. USSR* **1985**, *58*, 1691-5.
(4) Chu, J., Breslin, J., Wang, N.S. and Lin, M.C. *Materials Letters* **1991**, *12*, 179-184.
(5) Heunisch, G. W. *Anal. Chim. Acta* **1969**, *48*, 405-9.
(6) Desu, S. B. *J. Am. Ceram. Soc.* **1989**, *72*, 1615-21.
(7) Delperier, B.,Vinante, C. and Morancho, R. *J. Anal. Appl. Pyrolysis* **1988**, *13*, 141-149.
(8) Takeuchi, Hideki, Izumi, H. and Kawasaki, A. *Mat. Res. Soc. Symp. Proc.* **1991**, *334*, 45-50.

Mass Discrimination Effects in MBMS Study of Rich Premixed Flames.

Christian Vovelle, Christine Douté and Jean-Louis Delfau
Laboratoire de Combustion et Systemes Reactifs
1C Avenue de la Recherche Scientifique
45071 Orléans Cedex 2 - France.

I. INTRODUCTION

Sampling by formation of a molecular beam in mixtures containing both light and heavy species can be affected by mass discrimination effects. This situation is faced in rich premixed flames where H_2 and H atoms are present in high concentration in mixture with heavier combustion products. This paper describes the results of a specific study carried out to derive a procedure that take into account these effects and improve the accuracy of H_2 and H measurements in flames.

A three stage Molecular Beam Mass Spectrometer (MBMS) apparatus especially designed for the experimental determination of the structure of low pressure premixed flames has been used to study the effect of temperature (T) and mean molar mass ($\overline{M}$) on the signals measured for species in mixtures of known composition. Variations of T and $\overline{M}$ where aimed at reproducing the evolution observed in flames when the sampling probe is moved from unburned (low T, high $\overline{M}$) to burned gases (high T, low $\overline{M}$). However, as temperature variations were limited to the range 300-800K, the pressure was also varied from 13 down to 0.8 kPa to create sample density conditions equivalent to those prevailing in post flame gases. Most measurements have been performed with $H_2/CH_4/N_2/O_2/Ar/CO_2$ mixtures while variations of the mean molar mass were achieved with binary H_2/Ar mixtures

II. EXPERIMENTAL

The MBMS apparatus has been described in another paper presented in this Workshop [1] and only the main characteristic will be mentionned here. Table I groups the main informations on the shape, dimensions; positions of the sampling cone, skimmer and collimator. These elements were fixed to three separated chambers pumped by oil diffusion pumps.

Chambers	Characteristic dimensions	Position (cm)	Pumping Speed (L/s)	Pressure (Pa)
Burner housing	Diameter 20 cm			800 - 13000.
	Sampling quartz cone ϕ = 0.13 mm ; Angle = 40°	0		
First			1500	$1.3\ 10^{-2}$
	Stailess Steel Skimmer ϕ = 0.8 mm ; Angle = 45°	2		
Second			750	$6.6\ 10^{-5}$
	Collimator (SS tube) L = 1.2 cm ϕ = 3 mm	22		
Third	ionization source	32	250 (+ Liquid N_2 trap)	$2.6\ 10^{-6}$

Table I

The only change brought to the system was the replacement of the burner by a tubular furnace heated electrically. Gas flow rates in this furnace were measured with the same devices than during flame structure studies : Sonic orifices, mass flowmeters or rothameters.

III. RESULTS

The theory of free jets expansion predicts a linear increase of the density in the jet with the pressure at the sampling point [2]. Figure 1 shows that in the case of a mixture ($H_2/CH_4/O_2/N_2/Ar/CO_2$, 4.9%/10.3%/9.4%/6.4%/49.6%/19.3%) with light and heavy components, a marked deviation from linear variation is observed for the lighter species. Two phenomena contribute to this deviation :

- For pressure higher than 2.6 kPa, collisions of the jet molecules with the residual gas downstream the sampling cone deviates the lighter species
- At very low pressures (less than 2.6 kPa), the Knudsen number increases and a transition from a supersonic jet towards an effusive jet occurs. Since velocities in an effusive jet are inversely proportional on the molar mass, this transition favors light species and is responsible for the high value of the signal measured for H_2.

Both effects were taken into account to predict the variation with pressure of the signal (considered as proportional to the density of each species in the mass spectrometer detector) measured with mixtures of known composition and temperature.

III.1. Intensity of the effusive jet

Since the solid angle limited by the collimator is smaller than those limited by the ionization source, the intensity of the effusive jet was computed at the collimator by using the expression proposed by Campargue for a pure gas [2].

$$I_{eff} = n_i c_i A_{or} \frac{A_{co}}{4\pi X_{co}^2} \qquad (1) \qquad \text{with} \quad c_i = \left(\frac{8\,RT_0}{\pi M_i}\right)^{1/2} \qquad (2)$$

with
- n_i : density of species i in the source (mole.cm^{-3})
- c_i : mean velocity of species i (cm.s^{-1})
- M_i : molecular mass (g)
- A_{or} : Area of the sampling cone orifice (cm^2)
- A_{co} : Area of the collimator (cm^2)
- X_{co} : Distance between sampling cone and collimator (cm)
- R : Perfect gas constant (g.cm^2.K^{-1})
- T_o : temperature at the sampling point (K)

The molar flow rate (mole.s^{-1}) across the sampling orifice is : $\phi_{eff} = \frac{1}{4} n_i c_i A_{or}$ (3)

III.2. Intensity of the supersonic jet

Intensity of the supersonic jet is given by the molar flux in the mass spectrometer detector :

$$I_{sup} = n_d V_s X_i \qquad (4)$$

with n_d : density at the detector (mole.cm^{-3}) ; V_s : velocity of the jet at the skimmer ; X_i : mole fraction of species i.

V_S is related to the Mach number at the skimmer Ms by :

$$V_S = M_S \sqrt{\frac{\gamma R T_0}{\bar{M}}} \left[1 + \frac{\gamma - 1}{2} M_S^2\right]^{-1} \quad (5)$$

with $\bar{M}$: mean molar mass of the mixture (g) and γ : ratio of specific heats.

The centerline Mach number of the jet increases with the the distance X from the sampling orifice. From the empirical law established by Ashkenas and Sherman [3], Campargue [2] derived a simple expression:

$$M = A \left(\frac{X}{D_0}\right)^{\gamma - 1} + B \left(\frac{X}{D_0}\right)^{1-\gamma} \quad (6)$$

A and B are constants for a given γ value. D_o is the diameter of the sampling orifice.

This evolution is observed only in the continuum part of the jet. There is a transition region in the flow field beyond which further cooling and acceleration are precluded by the rarefied nature of the flow. Anderson and Fenn [4] derived an expression for the terminal Mach number, by considering the point in the expansion beyond which the temperature cannot change as rapidly as required for isentropic continuum behavior:

$$M_T = \left(\frac{\gamma}{\gamma - 1}\right) \left(\frac{2}{A}\right)^{\frac{1}{\gamma}} \left(\frac{8}{\gamma \pi}\right)^{\frac{\gamma - 1}{2\gamma}} \left(\frac{Kn_0}{\varepsilon}\right)^{\frac{1-\gamma}{\gamma}} \quad (7)$$

with Kn_o : Knudsen number at the sampling orifice and ε : collision effeciency

M_s is related to this terminal Mach number by : $M_S = M_T \left(\frac{X_S}{X_T}\right)$ (8)

Xs : position of the skimmer (cm) and X_t : distance (cm) where the Mach number reaches its terminal value. Xt is computed by Eq. 7 and 6.

Stearns et al. [5] expressed the density at the detector : n_d to the density at the skimmer n_s :

$$n_d = n_S \left(\frac{X_S}{X_{CO}}\right)^2 \left[1 - \exp\left(-M_S^2 \frac{\gamma}{2} \left(\frac{R_S}{X_S}\right)^2\right)\right] \quad (9)$$

with Rs : radius of the skimmer orifice (cm)

n_s is related to the density at terminal Mach number position (n_T) [5] : $n_S = n_T \left(\frac{X_T}{X_S}\right)^2$ (10)

Upstream X_T, the flow is continuum and the decrease in the density can be predicted by the properties of an isentropic expansion :

$$\frac{n}{n_0} = \left[1 + \frac{\gamma - 1}{2} M^2\right]^{\frac{1}{1-\gamma}} \quad (11)$$

with n_o : density of the gas mixture at the sampling point, and n : density in the free jet. n_T is computed by using this expression with $M = M_T$.

Since M = 1 at the sampling orifice, the molar flow rate of the free jet entering the sampling cone is expressed as :

$$\phi_{sup} = n_0 \left(1 + \frac{\gamma - 1}{2}\right)^{\frac{1}{1-\gamma}} \sqrt{\frac{\gamma R T_0}{\bar{M}\left(1 + \frac{\gamma - 1}{2}\right)}} A_{OR} \qquad (12)$$

III.3. Attenuation of the jets

Campargue [2] reported that collision between the jet and the residual gas downstream the sampling orifice decreases exponentially the density in the jet : $I' = I \exp(-n_r Q_f x_r)$. With n_r : density of residual gas ; x_r : distance from the orifice and Q_f : collision cross section. The density of the residual gas depends linearly on the flow across the sampling orifice, so that we introduced for each jet, an attenuation factor expressed as : $\exp(-\beta \phi_{tot})$ with $\phi_{tot} = \phi_{eff} + \phi_{sup}$

III.4. Simulation of the mass spectrometer signal

Simulation of the evolution with the total pressure was performed by considering contributions from effusive and supersonic jets :

$$I_i = k_{1,i} I_{eff,i} \exp(-\beta_{1,i} \phi_{tot}) + k_{2,i} I_{sup,i} \exp(-\beta_{2,i} \phi_{tot}) \qquad (13)$$

For each species , the four parameters : $k_{1,i}$, $\beta_{1,i}$, $k_{2,i}$, $\beta_{2,i}$ have been determined by fitting the curves Ii = f(P) with the values obtained experimentally. The main part of this work has consisted to relate these four parameters to variables such as the molar mass (Mi), the mean molar mass ($\bar{M}$) and the temperature (T). Analyses of the 6 components mixtures at ambiant temperature led to relationships with M_i. Analyses of H_2/Ar mixtures were carried out to obtain the variation with $\bar{M}$. A third serie of experiments was performed with a 4 components mixture, with temperature varying in the range 300-800 K. The final expressions derived are as follows :

$$k_{1_i} = A_1 . Q_i . F \sqrt{\bar{M}} \frac{M_i}{(M_i + \bar{M})} \left(B_1 \sqrt{\frac{M_i}{\bar{M}}} (T - 273) + 1\right)^{-1} \qquad (14)$$

$$k_{2_i} = A_2 . Q_i . F \sqrt{\frac{M_i}{\bar{M}}} \left(1 + \frac{M_i}{\bar{M}}\right) \left(\frac{T}{273}\right)^{1 - \left(\frac{M_i}{\bar{M}}\right)^{0,3}} \qquad (15)$$

$$\beta_{1_i} = C_1 \frac{\bar{M}}{M_i^{0,1}} \qquad (16) \qquad \beta_{2_i} = B_2 \left(C_2 M_i + \frac{D_2}{M_i} + E_2\right) \bar{M} \qquad (17)$$

Values of the constant factors are : $A_1 = 3.4\ 10^{-13}$; $B_1 = 2\ 10^{-3}$; $A_2 = 6.4\ 10^{-15}$; $C_1 = 1.6\ 10^{-20}$; $B_2 = 1\ 10^{-21}$; $C_2 := -0.03$; $D_2 = 0.99$; $E_2 = 1.38$. Q_i is the ionization cross section of species i and F a factor that account for day to day variations of the mass spectrometer signal.

Figures 1 and 2 illustrate the accuracy of the prediction of the evolution with the total pressure of the signal measured for 2 species with molar mass respectively equal to 4 and 44. These figures show that influence of the temperature is also well predicted.

III.4. Species concentration measurements in flames.

To measure species concentration in flames, a calibration factor is needed for each species. These factors are obtained by analyses of mixtures of known composition for the main stable species. For minor and labile species they are derived by reference to a stable species with similar structure. These procedures lead to values of the calibration factors at fixed temperature, pressure and mean molar mass of the misture. Expressions 14 to 17 and 13 have been used to correct the calibration factors for effects of both discrimination effects (important for H_2 and H) and of transition from supersonic to effusive jet (important at high temperature). Verification of the conservation of C, H and O atoms in flames is a good test to check the accuracy of species concentration. The initial and final values of the ratio H/C, O/C and Ar/C in n-heptane-O_2-Ar flames with equivalence ratio ranging from 0.7 to 2.0 have been compared in Table II. A very good agreement is observed for the four flames, corresponding to marked variations in H_2 concentrations.

Eq. ratio	unburned gases (Flowmeters values)			Burned Gases (MBMS measurements)		
	H/C	O/C	Ar/C	H/C	O/C	Ar/C
0.7	2.29	4.49	2.49	2.31	4.74	2.52
1.0	2.29	3.14	1.79	2.20	3.15	1.74
1.5	2.29	2.09	1.06	2.36	2.16	1.06
2.0	2.29	1.57	0.82	2.21	1.57	0.77

Table II

IV. CONCLUSIONS

The objective in this work was to study the influence of mass discrimination effects when MBMS analyses are performed in mixtures with light and heavy species. Analyses in mixtures of known composition pointed out that a transition from supersonic jet to effusive jet must be also taken into account for the light species at high temperature. Empirical factors derived from experiments with variations of the mean molar mass of the mixture and of temperature can be used to correct the calibration factors and improve the accuracy of MBMS analyses in flames with high hydrogene concentrations.

V. REFERENCES

1. VOVELLE, C., DOUTE, C. and DELFAU, J.L., *MBMS and Gas Phase Chromatography Studies of n-heptane and iso-octane flames*, Specialists Workshop on Applications of Free-Jet. Molecular Beam Mass Spectrometric Sampling, Estes Park, Colorado, (1994).

2. CAMPARGUE, R., *Etude, par simple et double extraction de jets supersoniques purs ou dopés, des effets intervenant dans la formation d'un faisceau moléculaire de haute intensité et d'énergie comprise entre 0 et 25 eV*, Thèse, Commissariat à l'Energie Atomique, (1972).

3. ASHKENAS, H. and SHERMAN, F.S., rarefied Gas Dynamics, Proc. of the Fourth (International) Symposium, Vol. 2, De Leeuw J.H. Ed. p. 84, (1966).

4. ANDERSON, J. B. and FENN, J. B., Phys. Fluids, 8, pp. 780, (1965).

5. STEARNS, C. A., KOHL, F. J., FRYBURG, G. C. and MILLER, R. A., *High Pressure Molecular Beam Spectrometric Sampling of High Temperature Molecules*, Proceedings of the 10th Materials Research Symposium on Characterization of High Temperature Vapors and Gases held at NBS, pp.303, (1979).

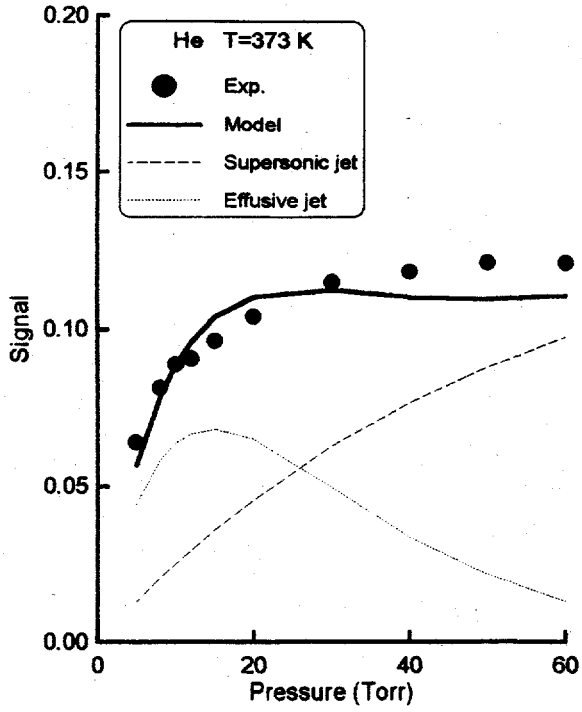

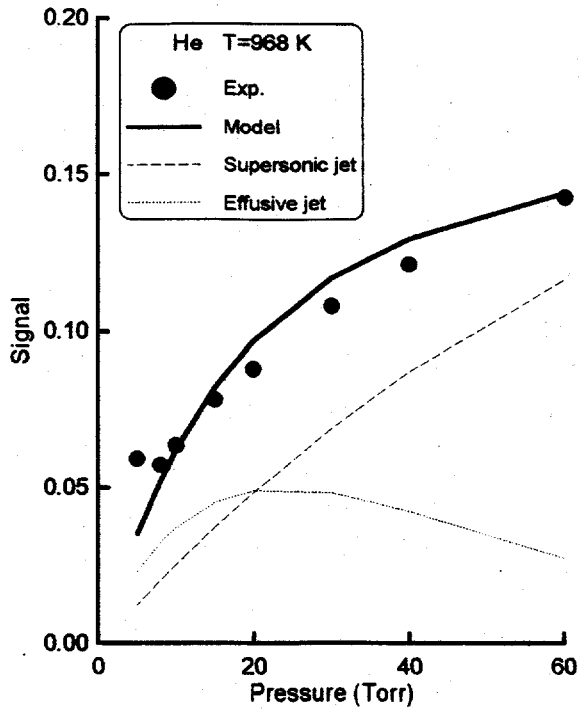

Figure 1
Prediction of the evolution with pressure of the mass spectrometer signal

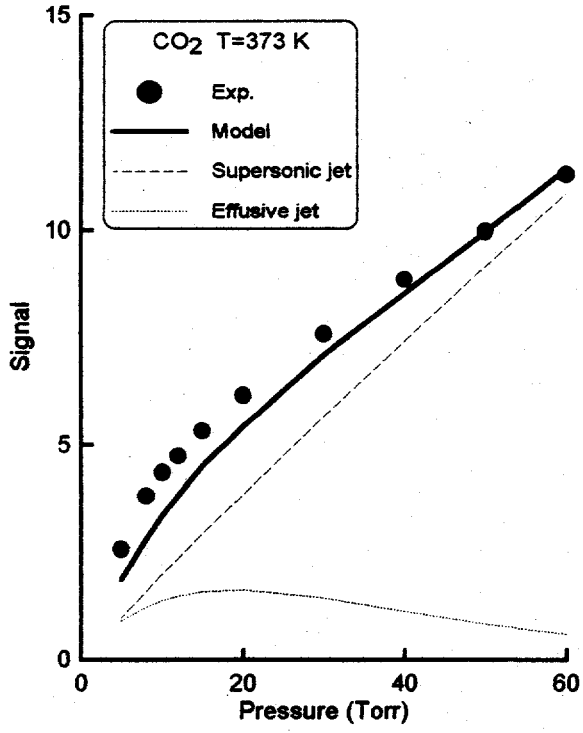

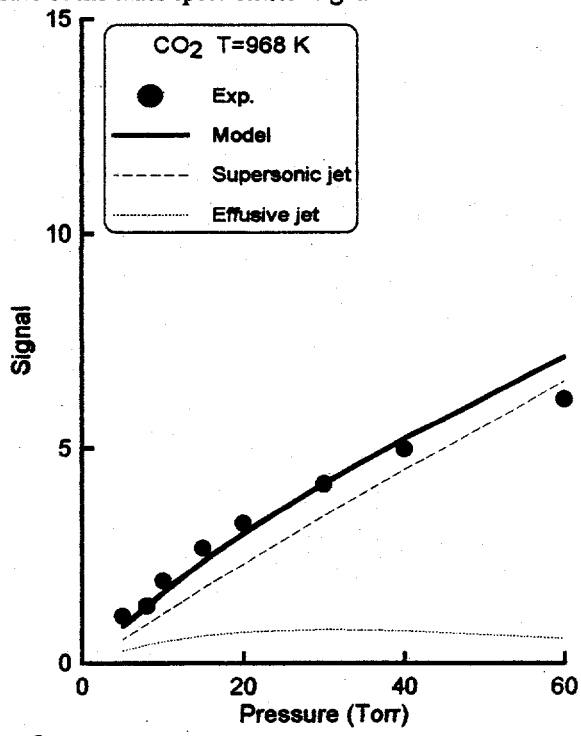

Figure 2
Prediction of the evolution with pressure of the mass spectrometer signal

Study of Solid Propellant Flame Structure By Mass-Spectrometric Sampling, Including MBMS

Oleg P. Korobeinichev. Leonid V.Kuibida, Alexander A.Paletskii.
Institute of Chemical Kinetics and Combustion - Siberian Branch
Russian Academy of Sciences,
630090 Novosibirsk, Russia.

At present the most effective and universal experimental technique for studying the condensed systems (including solid propellants) flame structure is the method of mass-spectrometric probing of condensed system (CS) flames (MSPCSF) which was improved in our laboratory in 1975 [1-3]. It allows to record all stable species present in the flame as well as the structure of CS flame with the resolution sufficient to study CS combustion at low pressures. The use of spectroscopic methods requires certain parameters which are not available.The MSPCSF method consists in the following: a burning stand of solid propellant moves with a speed exceeding the burning rate towards the probe so that the probe is sampling continuously the gaseous species from all the zones including those adjacent to the burning surface. The sample is transported to the ion source of a time-of-flight (TOF) or quadrupole (QMS) mass-spectrometer. The mass spectra of samples are recorded with simultaneous filming of the probe and burning surface. The data allow one to identify stable components, to determine their concentrations and spatial distributions, i.e. to study the flame microstructure.

EXPERIMENTAL.

The apparatuses of two types have been developed for studying the flame structure. The sample is transported to the ion source as a molecular flow using a microprobe with an inlet orifice of 10-20 Fm in the first type of setup and as a molecular beam using a sonic probe with the inlet orifice 50-200 ym in the second type. The former setup has a high spatial resolution and negligible disturbs the flame that allows one to study the flame with a narrow combustion zone up to 0.1 mm. However, in this case, radicals recombine and quenching can become a problem. The latter setup allows detecting the radicals, but more strongly disturbs the flame and therefore has a smaller spatial resolution. Figure 1 shows the system [4], which has been used to examine flame structures for nitramines (hexogen and octogen), which give combustion zones of about 1 mm at about 0.1 MPa. The suite includes: an apparatus for probing the flame containing a molecular-beam sampling system, a time-of-flight mass-spectrometer (TOFMS) type MSKh-4 as detector, the combustion chamber, and a scanning system; a data-acquisition system and experiment controller based on CAMAC equipment and a computer. The fiame-probe apparatus includes the combustion chamber, which is linked on one side to the scanner, which scans the zones with respect to the sampler, which is a quartz or metal cone. The sample gives a molecular beam that passes to the ion source. The beam is modulated by a chopper (slotted disk driven by a motor) to correct for the scattered background. The apparatus for sampling CS flames is shown schematically in Fig. 2. It consists of combustion chamber (1) connected to the scanning device (2). The ion source (4) of the MSKh-4 TOFMS serves as a detector of the molecular beam sampled from the CS flame.

The flame is sampled by a probe (3), a 25 mm high cone with a 50-deg external angle, a 40-deg internal angle, and a 0.1 mm diam orifice at the apex. Gas expansion in the cone results in a supersonic jet directed into the skimmer chamber (5), which is evacuated by a oil diffusion pump BN-3 (500 Vs). Behind the sampling cone is a stainless steel skimmer (8), a 50-mm-high cone with a 40-deg external angle, a 30-deg internal angle, and a 2 mm diameter orifice at the apex. The skimmer is designed so that only the supersonic jet core enters the collimator chamber (6), which is evacuated by an oil diffusion pump NO5 (500 I/s). The pressure in the skimmer chamber is $2\text{-}10^{-3}$ Torr. The molecular beam from the skimmer passes through a 4 mm diam collimator orifice (9) to the detector chamber with the TOFMS ion source. The background gas pressure in the collimator chamber is 10-5 Torr. In the collimator chamber are: an electromagnetic chopper modulator which can cut offthe molecular beam, and a beam modulator which is a slotted disk (11) rotated by a DG-2TA engine with

an adjustable frequency from 1 to 100 Hz. The ion source of the MSKh-4 TOFMS is evacuated by a heteroion pump NORD-250 (250 l/s), and the drift tube of MSKh-4 by a turbomolecular pump TMN-200. The pressure in the ion source is less than 104 Torr. The distance between the orifices varies: the skimmer-collimator is 310 mm; the collimator-detector is 50 mm; and the skimmer-sampling cone is varied from 5 to 25 mm by changing the flange to which the probe is attached. In the combustion the ignition spiral (12), after ignition, is automatically removed from the combustion zone. To scan a CS flame a control system and step-by-step motor (13) are required. With the motor (13) the burning strand (14) is moved. Thermocouple (15) senes to measure temperature profile in flame. The strand is moved at speed less than 10mm/sec and is driven by a step-by-step motor, step 1.25 1lm. The data acquisition and control system consists of a Elektronika-60 microcomputer, a CAMAC apparatus, a double-beam oscilloscope, a scanner control, and an XY plotter.

The data acquisition and control system [5] provides automatic spectrum recording, i.e., the peak intensities and mass numbers, as well as temperature as a function of time. In a single spectrum sweep, a strobe system measures the intensities of 6 peaks, the results being stored. The setup of last generatoin with a molecular oeam inlet system for sampling of flame is shown on Fig.3. Fig.4 shows the setup of the first type, which was used for investigation of double-base propellant flame at high pressure about 10-20 atm [6].

Quantitative aspects of the results of MS sampling investigations of the CS flame structure are essentially defined by the accuracy of detemmination of errors of the sampling technique. In the case of flame with narrow zones of combustion (0.1 mm) the zone width is comparable with the extemal diameter of the probe tip. This case was studied in our laboratory [7]. In order to analyze this problem, model flat methane-air flame (flame zone width 0.5 mm) has been studied at atmospheric pressure using several methods: I) microprobing mass-spectrometry (with two probes with the outer diameter of probes tip: I) 0.5 mm so called "macroprobe" and 2) 0.07 mm so called "microprobe"); 2) spontaneous Raman scattering (SRS) using spectrometer with intracavity Raman scattering; 3) microthermocouple. Figure 5 show the mole fractions aj as referred to the maximum values *a,m,,,Js* in the methane flame. The points (0) on curve 1 are from *a/a, =,~ T/Tma,<*, which was derived on the assumption that the temperature and methane-concentration profiles are similar. On the curve 1 points (x) are SRS data, on the curve 2 points Δ - for "microprobe", - "macroprobe". The model experiments showed that the error in concentration determination at the burner surface was less than 10%. When the tip diameter was reduced by a factor 7 in the "macroprobe", the change in concentration was about 15%. Curve 2 in Fig.5 coincides within 15% with the unperturbed profiles (curve 1) if curve 2 from the probe measurements is shifted towards the burner by an amount close to the calculated displacement of the sampling point z0 with respect to the unperturbed flow. Calculations [7] have been made from assumptions on the flame and the perturbations "perturbations (Rosen's model [8]) and gave $z=0.4D_0\sqrt{\alpha_0}$; $\Delta=0.3D_0\sqrt{\alpha_0}$, where Δ is the sampling zone width, which represents the spatial resolution. Here α_0 is sampling degree [7], d_0 - probe's orifice. Mass spectrometry sampling applied to ammonimum perchlorate (APC) was with d=0.012 mm, aO = 75. When appropriate correction is made for the sampling point on the concentration profiles (z_0 shift), the error in determining the concentrations by the probe method is less than 15% of the maximal value. This error and the sampling zone width constitutes ±15% of the APC burning zone width, and it is reasonably small for quantitative treatment of the APC flame structure.

RESULTS

The results of flame structure investigation of high temperature zone RDX at different pressures using MBMS technique (profiles of intensities of the mass-spectral peaks) are shown on Fig.6 (P=0.5 atm), 7 (P=1 atm), 8 (P=2 atm). L - is a distance of the probe from the burning surface. Subscript at I is amu. Below the set of peaks of fragmentary and molecular ions are presented: I_{14} (N_2, NO_2, NO, N_2O, HCN), I_{28} (CO, N_2, N_2O, CO_2, CH_2O), I_{30} (NO, NO_2, N_2O, CH_2O), I_{29} (CH_2O), I_{27} (HCN), I_{44} (N_2O, CO_2) I_{46} (NO_2), I_{43} (HNCO), I_{42} (NCO), I_{18} (H_2O), I_2 (H_2). These ions have to be taken into account at analysis of mass-spectral data of samples taken from RDX and HMX flames. Fig.9 shows the profiles of mole fraction for RDX flame at 0.5 atm. (results of analysis data presented on Fig.6), which are in a good enough agreement with results of

modelling by C. Melius [9] and N. Ermolin et.al. [10].

The burning surface was identified with allowance for the z_0 calculated from the abovementioned formula ($\alpha_0 = 70$, $d_0 = 0.1$ mm). These results show that the main reaction in high temperature zone of RDX flame is reaction HCN + NO. With increasing of the pressure from 0.5 to 2 atm the width of reaction zone is decreasing from about 2 to 0.5 mm. Similar results have been obtained for HMX flame structure at 1 atm. (Fig.10).

Mass-spectrometric probing technique can be used for investigation of unstable combustion of solid propellants. Fig. 11 shows results of flame probing of HMX unstable flame at 0.5 atm: time dependencies of mass peak intensities when the strand have been moved to the probe.

Fig.12 shows the dependencies of mass peak intensities (with different m/e) in the mass spectra of the sample taken from the double-base propellant "N" flame (using MBMS technique at 1 atm and initial temperature of 120°C) versus the distance to the burning surface L (determined from the corresponding time-dependences). The propellant "N" composition is the following: nitrocellulose- 57%; nitroglycerin - 28%; dinitrotoluene - 11%; stabilizer, plasticizer - 4%. The strand was placed in the combustion chamber N1 on the distance 5 mm from the probe. The moments of a strong decrease and increase of the peak with m/e=13.3 (Ar^{+3}) correspond to the ignition and extinction of the sample. The propellant combustion products contained: CO+N_2 (m/e=28), NO (30), CO_2 (44), H_2O (18), CH_2O (29), HCN (27), CH_4 (16), dinitrotoluene (63, 91), nitroglycerin (76).

The methods of probing mass-spectrometry and modeling were used to study double-base propellant flame structure (powder "N") at 10 atm using setup, shown on Fig.4. Sampling was performed with the help of a ceramic probe (300 μm diameter of orifice). The structure of the dark and flame zones was studied at the distances more than 2 mm from the burning surface. In the first zone, situated 2-6 mm from the burning surface, the concentrations of compounds CO_2, N_2+CO, NO and H_2 were almost constant. In the second, beginning from 6 mm to 12 mm, the NO concentration decreased to zero (Fig.13). The concentrations of CO_2, N_2+CO and H_2 varied less drastically. The equations of material balance were used to calculate the concentrations of CO,CO_2, N_2, NO and H2Oin the first and at the end of the second zones. In this case, it was taken into account that the fraction of carbon (up to 5% of its total quantity) was in the form of soot. The temperature profile was measured with a W/Re-thermocouple (50 μm). The composition of products and the temperature in the first zone were used as the boundary conditions to compute the structure of the flame second zone by a multi-stage mechanism (81 reactions, 22 components). A satisfactory agreement was achieved between the experimental and calculated data of themperature profiles and species concentrations (Fig. 14).

Similar studies have been performed at P=20 atm for the double-base propellant N2 of a higher (than "N" propellant) energetics and the following composition: nitrocellulose- 58%; nitroglycerin - 40%; centralite - 2%. A fair agreement is observed between the mole fractions of the combustion products of the propellant N2 - the experimental (the product combustion temperature was 2700K) and the calculated equilibrium at 2700K (Table). The data obtained allow this method to be reccommended for the study of flames at high pressures.

α_i	α_{CO}	α_{CO2}	α_{N2}	α_{H2}	α_{H2O}
experiment	0.348	0.164	0.135	0.0745	0.279
calculation	0.35	0.161	0.135	0.073	0.28

REFERENCES

1. O.P.Korobeinichev, Combustion, Explosion and Shock Waves, 23, 565 (1988).
2. T.Edwards, "Survey of recent US research in solid propellant flame structure. Experiments and modeling." Paper presented at International workshop on transient combustion and stability of solid propellant, Milan,Italy, November 12-14 (1990).
3. O.P.Korobeinichev and A.G.Tereshchenko, Dokl. Akad. Nauk USSR, 231, 1159 (1976).
4. O.P.Korobeinichev and L.V.Kuibida, in: Prog. Astron. and Aeron., Vol. 88, New York (1982).
5. A.G.Vorob'eva, O.P.Korobeinichev, L.V.Kuibida, et al., Avtometriya, No. 6, 40 (1982).
6. O.P.Korobeinichev, A.A.Paletsky, G.A.Machov et al., "Method of probing mass-spectrometry and laser spectroscopy and their application for study of gaseous and condensed systems flame structure" Joint meeting of the Soviet and Italian sections of the Combustion Institute, Book of Abstracts, Pisa, Italy, 8.2 (1990).
7. O.P.Korobeinichev, A.G.Tereshchenko et al., Fiz. Goreniya Vzryva, 21, 5, 22 (1985).
8. P.Rosen, Potential Flow of a Fluid into a Sampling Probe, Johns Hopkins Univ., Report CF-2248, Silver Spring, Md. (1954).
9. C.F.Melius Proc. 25th JANNAF Combust. Mtg., CPIA Publication 498, 2, 155 (1988).
10. N.E.Ermolin, O.P.Korobeinichev et al., Fiz. Goreniya Vzryva, 21, 5, 22 (1985).

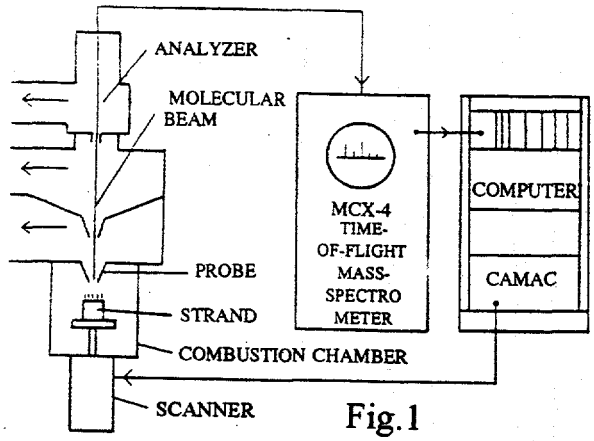
ANALYZER
MOLECULAR BEAM
PROBE
STRAND
COMBUSTION CHAMBER
SCANNER
MCX-4 TIME-OF-FLIGHT MASS-SPECTRO METER
COMPUTER
CAMAC

Fig.1

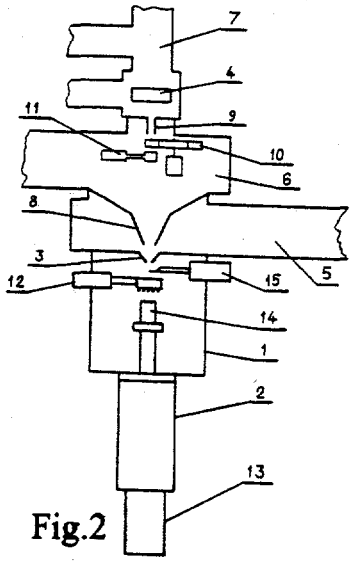
7
4
11
9
10
6
8
3
12
15
5
14
1
2
13

Fig.2

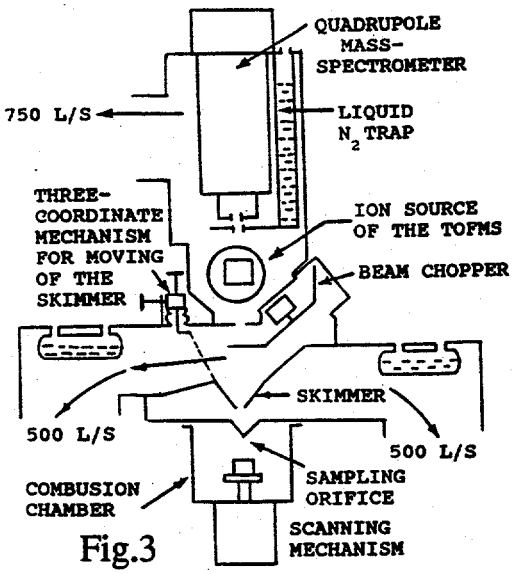

Fig.3

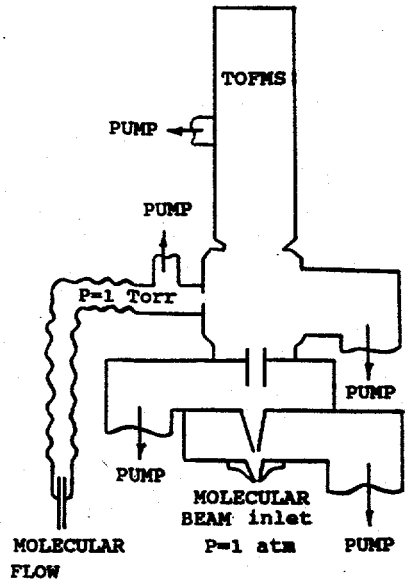

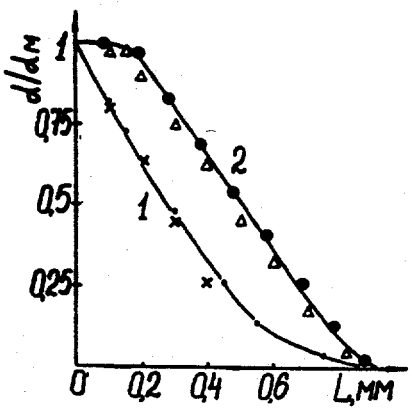

Fig.5

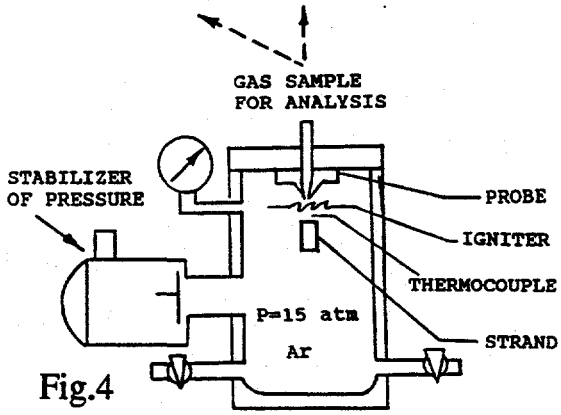

Fig.4

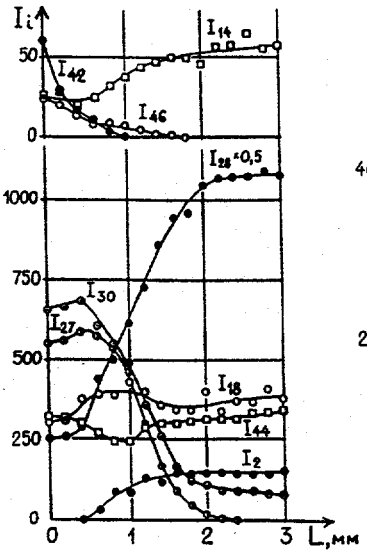

Fig.6

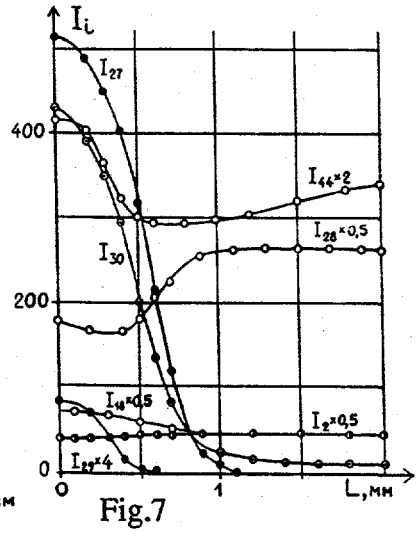

Fig.7

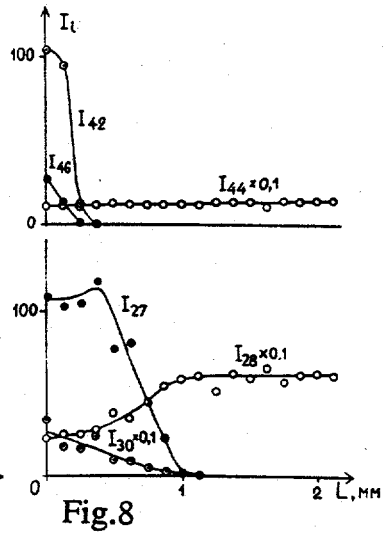

Fig.8

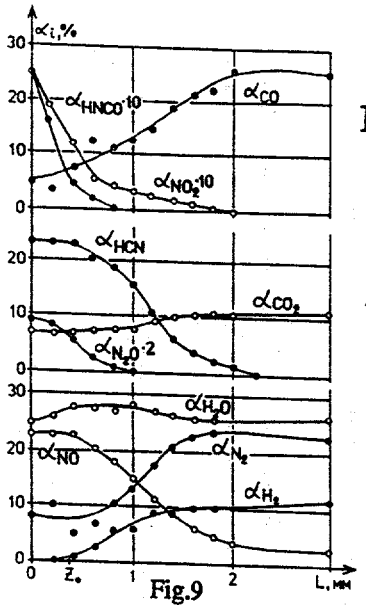

Fig.9

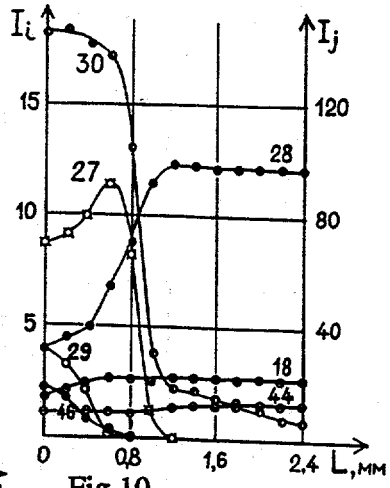

Fig.10

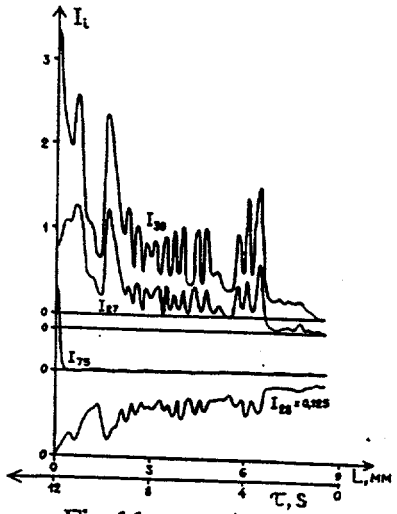

Fig.11

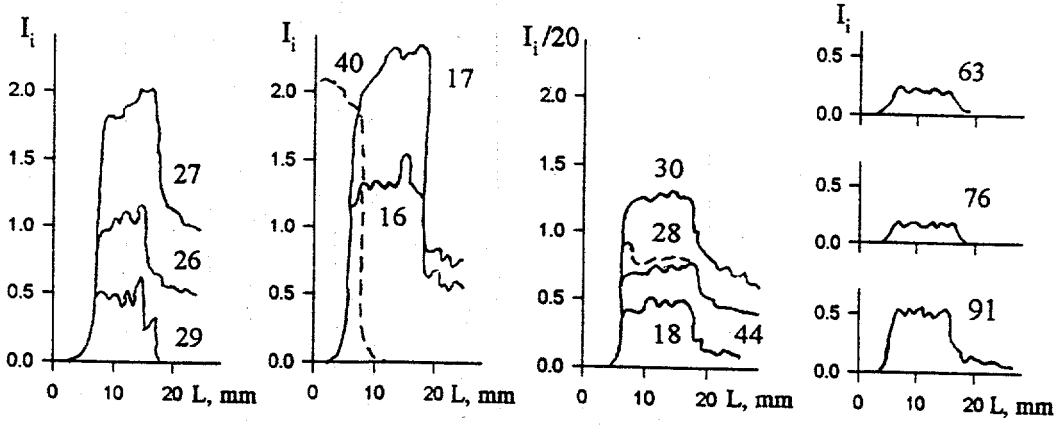

Fig.12

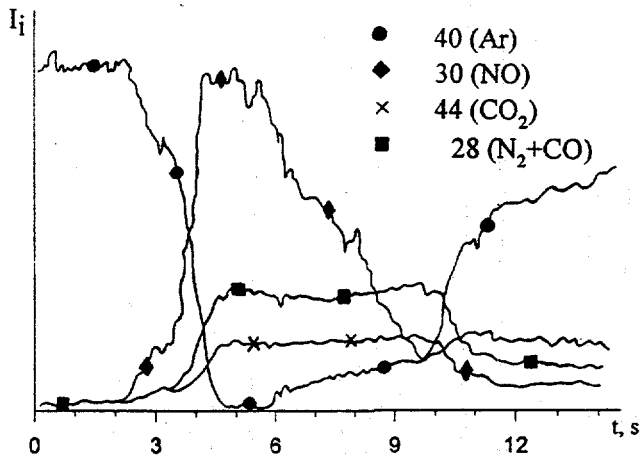

distance from the probe, mm

Fig.13

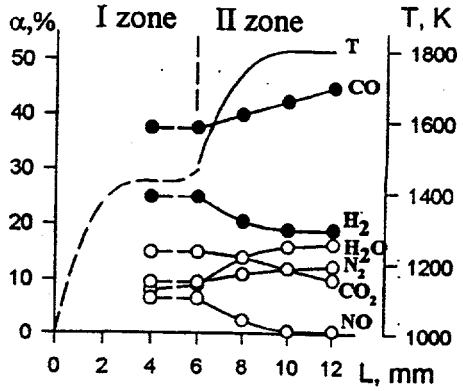

Fig.14

RAPID CHARACTERIZATION OF LIGNOCELLULOSIC FEEDSTOCKS FOR FUELS AND CHEMICALS: MOLECULAR BEAM MASS SPECTROMETRIC APPROACH

F.A. Agblevor, M.F. Davis, and R.J. Evans
National Renewable Energy Laboratory
1617 Cole Boulevard, Golden, CO 80401

Abstract

Rapid characterization of biomass feedstocks has a pivotal role in the development of biomass energy because of the large number of samples that must be analyzed due to the diversity of biomass feedstocks and the significant differences in the chemical and physical properties of these feedstocks. Conventional chemical analysis of biomass feedstocks, although very useful, is time-consuming and not very practical for large scale screening experiments, hence the need for rapid characterization techniques. The molecular beam mass spectrometer and pyrolysis gas chromatography, which can analyze biomass pyrolysis vapors in real time, are unique tools for rapid qualitative and quantitative analyses of biomass feedstocks.

Several biomass feedstocks (herbaceous, woody, and agricultural residues) were screened for the effects of storage, season of harvest, geographic location, clonal, and species variation on the pyrolysis products of the feedstocks. For herbaceous species such as sericea lespedeza, the season of harvest had a significant effect on the pyrolysis products.

Effects of clonal variation on the composition of hybrid poplar feedstocks was easily discerned with the molecular beam mass spectrometric analysis. The effect of geographic location on the poplar clones pyrolysis products was minimal. However, in the case of switchgrass, varietal influence on the pyrolysis products was minimal, but where the plant was grown had a strong influence on the pyrolysis products of the feedstock. Significant differences because of species variation could also be shown from the pyrolysis products of various biomass feedstocks. The influence of storage time on biomass samples stored outside in the open could also be discerned from the pyrolysis products of the feedstocks. The differences noted in the pyrolysis products of the feedstocks were noted for samples which were significantly degraded during storage either through the action of microflora or weathering.

Quantitative analysis of some biomass feedstocks were also effectively carried out by a combination of multivariate statistical analysis and molecular beam mass spectrometric analysis. There was agreement between the multivariate analysis data and conventional chemical analysis of the same samples.

Introduction

Although the long-term effect of global warming on the earth's climate is not definitively known, air pollution and smog problems in large urban areas are spurring interest in

developing and using oxygenated fuels for transportation and power generation. Biomass is a potential source of oxygenated fuels and has several advantages over other resources because it is renewable, globally dispersed, and above all, it will not contribute net carbon dioxide to the atmosphere if production and use are managed in a sustainable manner. However, biomass resources are diverse there is no single matured technology for converting this resource into a portable convenient energy resource. To make maximum use of this resource, both physical and chemical characterization must be carried out on the raw materials as well as the primary fuels produced from them (e.g., biofuel oils). The quality of the raw biomass feedstocks is affected by several factors including biological degradation, weathering during storage, geographic location of the plants, environmental stresses, and species and clonal variations.

To assess the quality of diverse feedstocks and to tailor them to specific process needs, a rapid characterization technique is required. Pyrolysis molecular beam mass spectrometry (Py-MBMS) and other pyrolytic techniques offer such unique and rapid capabilities for the analysis of these resources. Py-MBMS, pyrolysis-gas chromatography-mass spectrometry, and insource Curie-point pyrolysis provide real time analysis of pyrolysis products without the intermediate steps of condensation and revaporization which often introduce errors.

The strength of Py-MBMS is in its rapid screening technique. However, coupled with multivariate statistical analysis and a good calibration set, quantitative/semiquantitative data on the pyrolytic products could be obtained. In this paper, we present some rapid screening results as well as semiquantitative and quantitative analysis of biomass pyrolysis products.

Experimental

Several biomass feedstocks were used in these studies including: switchgrass (*Panicum virgatum L.*), tall fescue (*Festuca arundinacea L*), alfalfa/orchardgrass (*Medicago sativa L./Dactylis glomerata L*), hybrid poplar (*Populus deltoides x nigra var. Caudina*), and sericea lespedeza (*Lespedeza cuneta L.*). Both stored and unstored feedstocks were used in these studies. The details of the storage studies are described elsewhere [1]. Materials were stored unprotected in the open from 6 to 9 months. Samples for analysis were taken from both the weathered outer layers as well as unweathered layers. The samples were ground in a Wiley mill to pass a 2-mm screen.

Biomass samples (20-30 mg) were weighed in quartz boats in triplicates and pyrolyzed in a quench pyrolysis reactor. The reactor consisted of a quartz tube (2.5 cm inside diameter) with helium flowing through at 5 L/min (at STP). The reactor tube was interfaced with the orifice of the molecular beam mass spectrometer (MBMS), Extrel™ Model TQMS C50, for pyrolysis vapor analysis (see detailed description of the MBMS in [2]). The reactor was electrically heated and its temperature maintained at 550±5 °C. The temperature profile of the biomass samples once introduced into the reactor, is unknown, although the pyrolysis reaction was completed in 50 s. Total pyrolysis time was 90 s (including the time the quartz boat heats up to 550°C), but the residence time

of the pyrolysis vapors in the reactor pyrolysis zone was ~75 ms and this prevented secondary cracking reactions. The pyrolysis vapors were sampled through the MBMS orifice in real time. During the sampling process, the pyrolysis vapors underwent free-jet expansion during their passage through the orifice and this sufficiently cooled the pyrolysis vapors to prevent secondary reactions or condensations. The cooled pyrolysis vapors passed through a skimmer to form a molecular beam that was fed to a 22.5 eV electron impact ionization triple quadrupole mass spectrometer for real time analysis. Mass spectral data for 15-300 Da were acquired on a Teknivent Vector 2™ data acquisition system.

Results and Discussion

Effect of Time of Harvest on Biomass Pyrolysis Products

Switchgrass, hybrid poplar, and sericea lespedeza that were harvested at different times during plant growth were pyrolyzed to determine the effect of harvest time on the pyrolysis products. Molecular beam mass spectrometry coupled with multivariate statistical techniques were used to assess the effect of harvest time on the pyrolysis products. The mathematical details of the statistical technique are published elsewhere [3].

The Py-MBMS of the switchgrass and hybrid poplar feedstocks did not appear to be affected by the time of harvest; the spectra of the two harvest times appeared very similar and multivariate statistical analysis of the spectra did not reveal any significant differences in the pyrolysis products of the feedstocks. The samples from the two harvest times clustered together in the factor space as shown in Figure 1.

In the case of the sericea lespedeza feedstocks, the time of harvest appeared to have a significant effect on the feedstocks as shown by both the mass spectral and the factor analysis data. The major difference between the pyrolysis products of the two harvests was the carbohydrate component of the feedstocks. The resolution of the pyrolysis spectra showed a relatively high carbohydrate component in the December harvest of the sericea lespedeza compared to the October sericea lespedeza harvest. This observation is similar to the seasonal carbohydrate cycles noted in deciduous trees in the temperate climate. Carbohydrate contents of stems and branches of deciduous trees are maximized near the time of leaf fall and start to decrease in late winter [4]. Although sericea lespedeza is technically not a tree, it is a woody shrub that defoliates in the fall like the deciduous trees. It is probable that the total reserve carbohydrate accumulation in this shrubby species follows a similar cycle to those observed for the trees.

In addition to the high carbohydrate content of the December sericea lespedeza harvest, the char produced during the pyrolysis was lower (16.2±1.0%) than that for the October sericea lespedeza harvest (21.4±1.0%). The difference in char yields was attributed to the significant differences between the nitrogen and ash contents of the two harvests. The October sericea lespedeza harvest had a high leaf to stem ratio (0.26) and consequently a high nitrogen content (1.14±0.10%) compared to the December sericea lespedeza

harvest that was defoliated and had a nitrogen content of 0.75±0.10%. The ash contents of the October and December sericea lespedeza harvests were 2.1±0.3 and 1.3±0.4% respectively. Both the nitrogen and ash components of the biomass are known to promote char formation. Nitrogen compounds are known to react with carbohydrate decomposition products during the pyrolysis process which results in char [5].

Influence of Storage on Biomass Pyrolysis Products

The effect of storage on the pyrolysis products of switchgrass, tall fescue and alfalfa/orchardgrass are shown in Figure 2. The major influence of the storage affected only the surface areas of bales of feedstock exposed to the elements (i.e. the weathered fraction of the feedstock). Samples taken from the interior of the bales were not weathered and therefore had similar composition as the fresh unstored feedstock. These difference are clearly shown in Figure 2. The weathered samples had lost some carbohydrate components and consequently, the lignin components of these samples had increased significantly. These difference were responsible for the separation of the samples in the factor space shown in Figure 2. The resolution of the pyrolysis spectra into various components (pentosans, hexosans, lignin, and nitrogen-compounds) showed that factor extracted components correlated well with wet chemical analysis data generated from these feedstocks.

The major difference between the wet chemical data and the pyrolysis data was observed only for the lignin pyrolysis products. The linear correlation between the two methods was very poor. The poor correlation between the two methods was attributed to the weathered samples. Basically, two trends were observed corresponding to the weathered and unweathered fractions of the feedstocks. With weathering of the feedstocks, humic compounds are produced and these condensed as insoluble material during the Klason lignin determination of the feedstocks. Further, some fraction of the nitrogen compounds in the feedstock also condense on the lignin and hence the wet chemical method overestimated the lignin content of the feedstock. On the other hand, the pyrolysis methodology is based on only the lignin pyrolysis products of the feedstocks and hence there is little interference from the humic and nitrogen compounds.

Effect Plant Location and Variety on Pyrolysis Products

The effect of plant location and clonal variation were studied in the case of hybrid poplar and switchgrass feedstocks. For hybrid poplar, four clones were grown at two different sites (Ashland and Mondovi). The major climatic difference between the two sites was one site had a higher average annual rainfall than the other. The pyrolysis mass spectral data did not reveal any significant differences in the pyrolysis products of hybrid poplar clones grown at the different sites. The carbohydrate and lignin contents of the feedstocks were similar and this was further confirmed by wet chemical analysis of the feedstocks. However, significant differences were observed between the pyrolysis products of various hybrid poplar clones. Hybrid poplar clone NC5260 had higher concentration carbohydrate pyrolysis products compared with the other clones. The lignin contents showed the reverse trend. The pyrolysis mass spectral results were corroborated

harvest that was defoliated and had a nitrogen content of 0.75±0.10%. The ash contents of the October and December sericea lespedeza harvests were 2.1±0.3 and 1.3±0.4% respectively. Both the nitrogen and ash components of the biomass are known to promote char formation. Nitrogen compounds are known to react with carbohydrate decomposition products during the pyrolysis process which results in char [5].

Influence of Storage on Biomass Pyrolysis Products

The effect of storage on the pyrolysis products of switchgrass, tall fescue and alfalfa/orchardgrass are shown in Figure 2. The major influence of the storage affected only the surface areas of bales of feedstock exposed to the elements (i.e. the weathered fraction of the feedstock). Samples taken from the interior of the bales were not weathered and therefore had similar composition as the fresh unstored feedstock. These difference are clearly shown in Figure 2. The weathered samples had lost some carbohydrate components and consequently, the lignin components of these samples had increased significantly. These difference were responsible for the separation of the samples in the factor space shown in Figure 2. The resolution of the pyrolysis spectra into various components (pentosans, hexosans, lignin, and nitrogen-compounds) showed that factor extracted components correlated well with wet chemical analysis data generated from these feedstocks.

The major difference between the wet chemical data and the pyrolysis data was observed only for the lignin pyrolysis products. The linear correlation between the two methods was very poor. The poor correlation between the two methods was attributed to the weathered samples. Basically, two trends were observed corresponding to the weathered and unweathered fractions of the feedstocks. With weathering of the feedstocks, humic compounds are produced and these condensed as insoluble material during the Klason lignin determination of the feedstocks. Further, some fraction of the nitrogen compounds in the feedstock also condense on the lignin and hence the wet chemical method overestimated the lignin content of the feedstock. On the other hand, the pyrolysis methodology is based on only the lignin pyrolysis products of the feedstocks and hence there is little interference from the humic and nitrogen compounds.

Effect Plant Location and Variety on Pyrolysis Products

The effect of plant location and clonal variation were studied in the case of hybrid poplar and switchgrass feedstocks. For hybrid poplar, four clones were grown at two different sites (Ashland and Mondovi). The major climatic difference between the two sites was one site had a higher average annual rainfall than the other. The pyrolysis mass spectral data did not reveal any significant differences in the pyrolysis products of hybrid poplar clones grown at the different sites. The carbohydrate and lignin contents of the feedstocks were similar and this was further confirmed by wet chemical analysis of the feedstocks. However, significant differences were observed between the pyrolysis products of various hybrid poplar clones. Hybrid poplar clone NC5260 had higher concentration carbohydrate pyrolysis products compared with the other clones. The lignin contents showed the reverse trend. The pyrolysis mass spectral results were corroborated

by wet chemical analysis data.

In contrast to the hybrid poplar samples where location of the plant had very little influence on the pyrolysis products but clonal differences had significant influence on the pyrolysis products, the switchgrass samples showed differences because of plant location and no influence due to plant variety. The switchgrass samples used in these studies were planted at three sites: Mead, OK; West Lafayette, IN; and Ames, IA. At each of these sites, three varieties of switchgrass were planted and harvested at approximately the same time at efflorescence. Factor analysis of the pyrolysis products did not reveal any differences due to varieties because the varieties from one site clustered together. However, significant differences were observed for samples from different sites. The major effect of the influence on plant location on the pyrolysis products was because of differences in the pentosan contents of the various feedstocks. For samples from the Mead site, the feedstock was high in nitrogen content and vice versa for all the other sites. On the other hand, the Ames site was relatively high in pentosan content and low in lignin. Thus, the samples were widely separated in the factor space as shown by Figure 3.

Conclusions

The application of molecular beam mass spectrometry to various biomass feedstocks has clearly demonstrated the versatility of this method as a rapid analytical tool. Small changes in biomass feedstocks due to storage, harvest time, plant location and clonal differences can be easily detected and their subsequent influence on the biomass pyrolysis products can be ascertained. It is also a very useful as a semiquantitative analytical tool for summative analysis of biomass feedstocks.

References

1. A. Wiselogel, F.A. Agblevor, D.K. Johnson, S. Deutch, J.A. Fennell and M.A. Sanderson, "Compositional Changes During the Storage of Large Round Switchgrass Bales." In: Proceedings of *An Alternative Energy Conference:Liquid Fuels, Lubricants and Additives from Biomass*, B.E. Dale (ed), American Society of Agricultural Engineers, St. Joseph, MI. (1994), pp 29-38.

2. Evans, R.J., and Milne, T.A., "Molecular Characterization of the Pyrolysis of Biomass I, Fundamentals," *Energy and Fuels* (1987), 1 (2), 123-137.

3. Windig, W.; Haverkamp, J.; and Kistemaker, P.G., "Interpretation of Sets of Pyrolysis Mass Spectra by Discriminant Analysis and Graphical Rotation," *Anal. Chem.* (1983), 55, 81-88 .

4. Kramer, P.J. and Kozlowski, T.T. *Physiology of Woody Plants;* Academic: New York, 1979; Chapters 7, 9, and 10.

5. Agblevor, F.A., B. Rejai, R.J. Evans, and K.D. Johnson. 1993. Pyrolytic Analysis and Catalytic Upgrading of lignocellulosic Materials by Molecular Beam Mass Spectrometry. In: *Energy from Biomass and Wastes XVI*, (D.L. Klass,ed.), Institute of Gas Technology (IGT), Chicago, IL. pp. 767-795.

Figure Captions

Figure 1. Factor score plot of Factor 2 versus Factor 3 of the different harvests of sericea, black locust, hybrid poplar and switchgrass showing the clusters of similar biomass samples in the factor space. The triangles show the repeatability of the pyrolysis runs.

Figure 2. Factor score plot of Factor 2 versus Factor 3 showing the clustering of the samples because of species variation and weathering effects. The triangles indicate the repeatability of the pyrolysis mass spectra. A0 = all switchgrass samples; A1 = weathered switchgrass samples; A2 = unweathered switchgrass samples; B0 = all alfalfa/orchardgrass and tall fescue samples; B1 = weathered alfalfa/orchardgrass and tall fescue sample; B2 = unweathered alfalfa/orchardgrass and tall fescue samples.

Figure 3. Factor score plot of Factor 2 versus Factor 3 of the pyrolysis products of the different hybrid poplar clones. The triangles indicate repeatability of the pyrolysis mass spectral run. 1,2,3,4,5,6,7,8,9,10 = DN poplar clones and 11, 12 = NC5260 poplar clone.

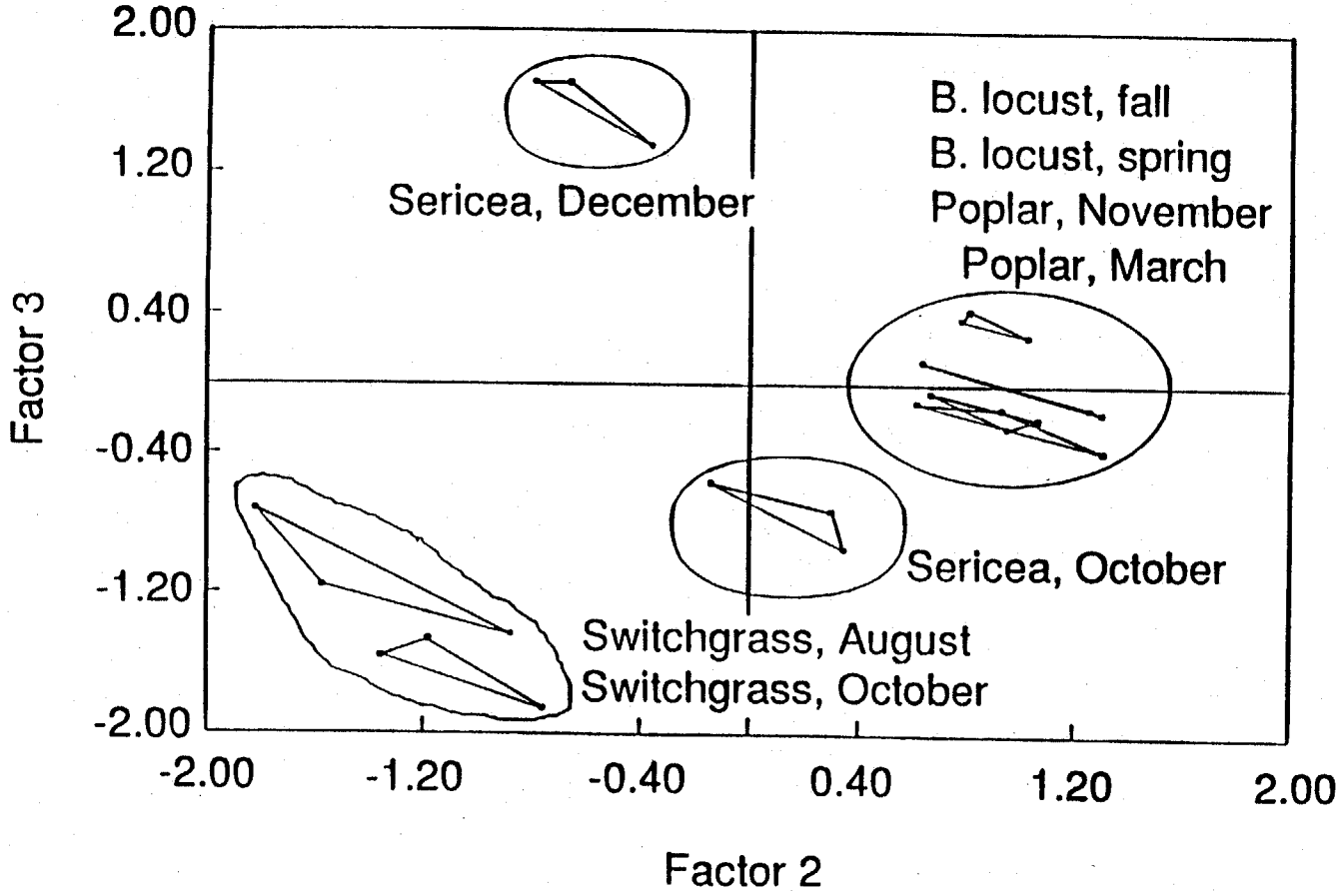
2.00
1.20
0.40
-0.40
-1.20
-2.00
Factor 3
-2.00
-1.20
-0.40
0.40
1.20
2.00
Factor 2
Sericea, December
B. locust, fall
B. locust, spring
Poplar, November
Poplar, March
Sericea, October
Switchgrass, August
Switchgrass, October

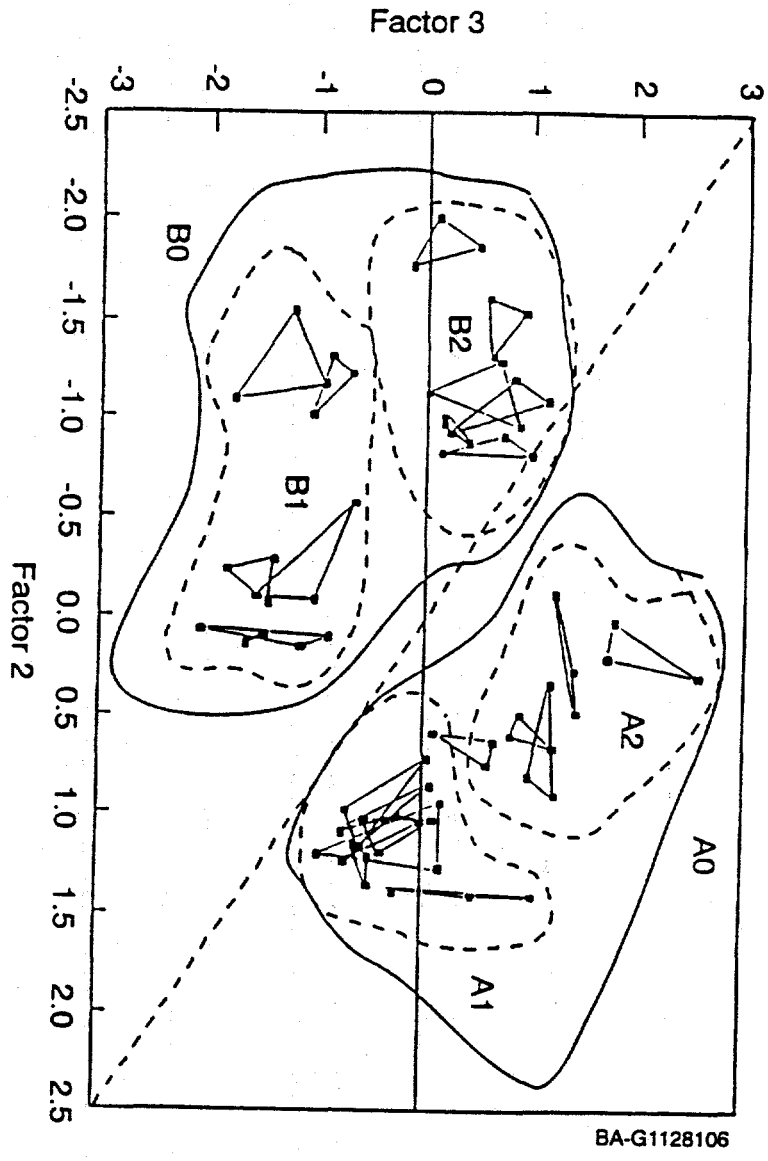
Factor 3
-3
-2
-1
0
1
2
3
-2.5
-2.0
-1.5
-1.0
-0.5
0.0
0.5
1.0
1.5
2.0
2.5
Factor 2
B0
B1
B2
A0
A1
A2
BA-G1128106

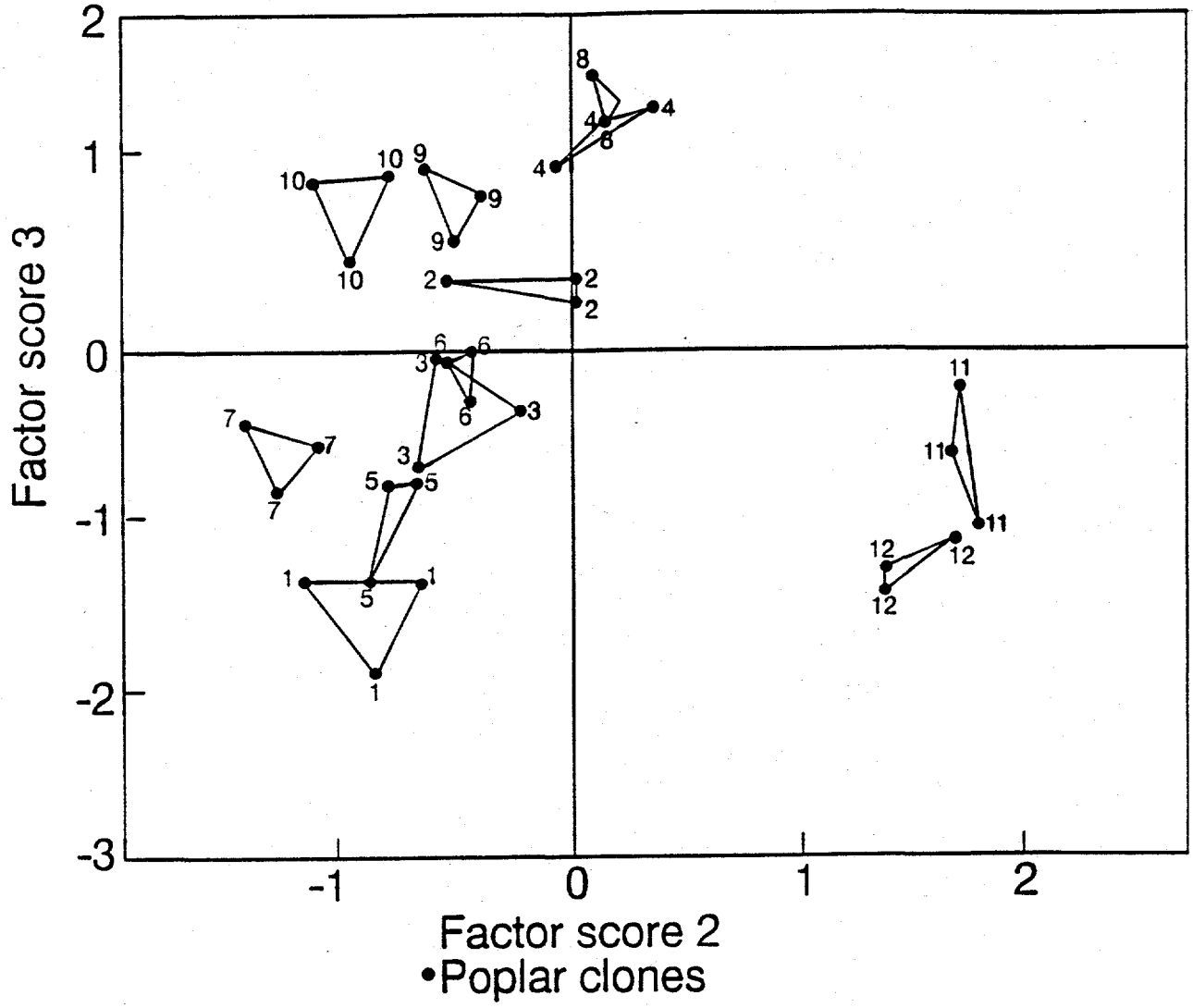
Factor score 3
Factor score 2
•Poplar clones
2
1
0
-1
-2
-3
-1
0
1
2

The Application of Molecular Beam Mass Spectrometry to the Problem of Plastics Recycling Through Intelligent Chemical Processing

Carolyn C. Elam, Robert R. Meglen, Kuni Tatsumoto
Robert J. Evans and Helena L. Chum
National Renewable Energy Laboratory
1617 Cole Boulevard
Golden, CO 80401

INTRODUCTION

The increased use of mixed plastics and composites has presented a difficult problem for recycling. Selective pyrolysis can be used to thermally and catalytically recover the starting material(s) or other high-value chemicals from mixed plastic waste streams. This technique is currently being applied to the development and scale-up of chemical recycling techniques for a variety of mixed polymer waste streams such as nylon-6 carpet, polyurethane foam, polyester/cotton blends, and mixed waste bottles.[1] Numerous small scale screening experiments are necessary prior to scale-up to identify the appropriate catalyst(s) and conditions to optimize the separation and recovery for each of the waste streams. Milligram scale experiments can be studied using pyrolysis molecular beam mass spectrometer (py-MBMS). The effective quenching of species in their sampled state through free-jet expansion[2-3] makes py-MBMS a valuable tool for identifying pyrolysis products.

Characterization, property prediction, product identification, catalyst selection and parameter optimization are all aided by applying multivariate statistical techniques to py-MBMS data. The large database generated in these studies makes it possible to extract information to gain insight into optimal process conditions for larger scale processes. Py-MBMS spectra for new waste streams can also be collected and projected into the database for qualitative and quantitative identification. Nearest neighbor(s) identification narrows the array of possible recycling pathways. As the database grows, the time for evaluation of recycling processes for new waste streams can be dramatically reduced. Intelligent chemical processing (ICP) is the application of the information gained at the laboratory scale to the definition and development of new recycling technologies.

EXPERIMENTAL

INSTRUMENTAL: The MBMS used in this study is equipped with an Extrel C-50 triple quadrupole mass analyzer. For a schematic and further description of this instrument, see Wang's paper[4] from these same proceedings.

DATABASE DEVELOPMENT: Py-MBMS spectra of over 20 different plastics from multiple sources recorded under different conditions were compiled into a database. In addition to the plastics, pyrolysis spectra from caprolactam, the monomer of nylon-6, and terephthalic acid, dimethyl terephthalate and monomethyl terephthalate, the monomers of poly(ethylene terephthalate) were collected. The spectra used were averaged over the entire evolution of the pyrolysis vapors from 10mg samples pyrolyzed in flowing helium at 550°C with sampling and

analysis of the vapors by MBMS. The spectral range consisted of species and fragments with molecular weights of up to 300 atomic mass units. A total of 137 spectra were used for the study.

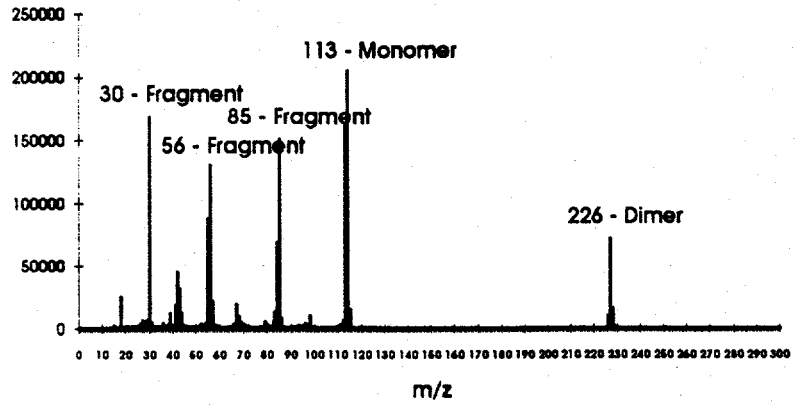

Figure 1 - Example of a nylon-6 spectra used for database development. The parent ion of caprolactam, the monomer of nylon-6, is shown at m/z 113. Other peaks show fragment and byproduct ions. A typical plastics pyrolysis spectrum can contain between 20 and 100 mass spectral peaks.

QUALITATIVE AND QUANTITATIVE ESTIMATES OF COMPLEX MIXTURES: Calibration mixtures of nylon-6, nylon-6/6, styrene, and polypropylene were prepared as simulations for possible mixtures in carpet waste. Prediction mixtures of these same components were also prepared. Replicates of py-MBMS spectra were collected over a period of several weeks for all of the mixtures, including 100% samples for each of the components. Jute and poly(ethylene terephthalate) were used to create six component calibration/prediction mixtures to examine the generalizability of the method.

CATALYST IDENTIFICATION AND PARAMETER OPTIMIZATION: MBMS spectra of nylon-6 in the presence of numerous catalysts and supports were collected. The half-life for the pyrolysis evolution of caprolactam was calculated and added to the database as a measure of the kinetics. Multivariate analysis, primarily principal component analysis, was performed to aid in catalyst selection for scale-up.

RESULTS

DATABASE DEVELOPMENT: Principal component analysis was applied to the 137 spectra in the database. This analysis clearly showed the ability to distinguish between the different plastics in multidimensional space. Figure 1 shows that in two dimensions the different plastics are easily distinguishable. Each type of plastic is represented by a single cluster. The spread in the clusters can be attributed to different sampling conditions and/or different sources for the plastics. As more dimensions are plotted, each type of plastic can be represented by a single principal component axis as shown by the five dimensional plot in Figure 2. There is a single axis for nylon-6 and poly(ethylene terephthalate) as well as axes that distinguish between the two types of polyurethane. Both polypropylene and polyethylene are shown to lie along the same axis. These too, along with the cluster of samples in the center of the plot, can be distinguished as more dimensions are explored. Each of the principal component axes can be represented by a single spectrum, which is the portion of the original spectrum that is unique to a particular plastic.

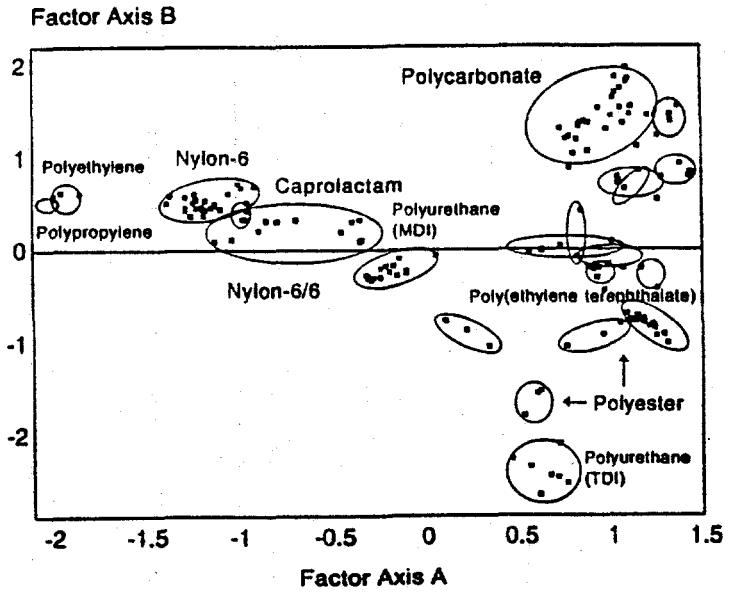

Figure 2 - Two dimensional plot of 137 plastic samples projected from the 300 dimensions of their pyrolysis spectra.

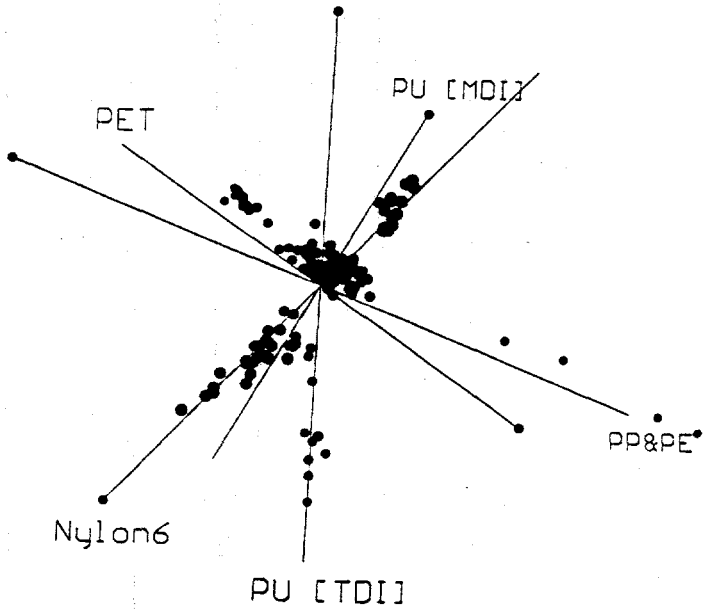

Figure 3 - Separation of plastics in five dimensions. The first five principal components represent Nylon-6, Polyethylene terephthalate (PET), Polypropylene (PP) and Polyethylene (PE) combined, Methylenediisocyanate (MDI) based Polyurethane (PU), and Toluenediisocyanate (TDI) base PU.

QUALITATIVE AND QUANTITATIVE ESTIMATES OF COMPLEX MIXTURES: By applying multivariate statistical analysis to py-MBMS data of complex mixtures, it is possible to accurately identify individual mixture components both qualitatively and quantitatively as shown by the calibration/prediction experiments of the four component mixtures. For these experiments, the root-mean-square prediction errors were less than 10%. The triangular placement of points at the base of the three dimensional tetrahedron shown in Figure 3 is defined by the pure components

(polypropylene, styrene and nylon). Other points represent several ternary mixtures of plastics. The robustness of the qualitative identification was shown when the mixture complexity was expanded to six components. The root-mean-square prediction errors increased slightly, however, indicating that more work needs to be done to tighten up the quantitation.

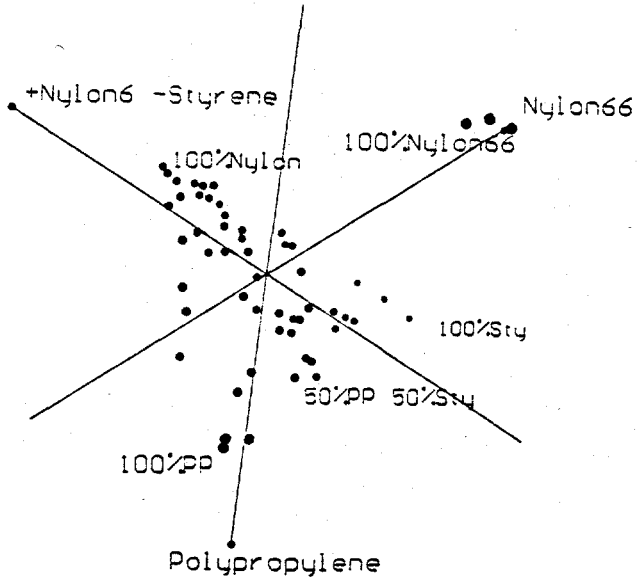

Figure 4 - Quantitative Analysis of Quaternary Mixtures - 100% Samples form the apexes of the tetrahedron. [Sty=Styrene, PP=Polypropylene]

CATALYST IDENTIFICATION AND PARAMETER OPTIMIZATION: The ability to use principal component analysis to aid in parameter optimization was demonstrated when a number of products in addition to the desired caprolactam were identified. The catalyst range could be narrowed down significantly based on product purity. Furthermore, the kinetic calculations identified large differences between catalyst experiments yielding the same product purity. A catalyst was selected for scale-up based on the combination of product purity and speed of pyrolysis.

CONCLUSION

Coupling of multivariate statistical techniques with py-MBMS by ICP aids in developing selective pyrolysis techniques for plastics recycling. Parameter optimization at the laboratory scale is essential for successful scale-up and commercialization. Additionally, ICP techniques can be used to qualitatively and quantitatively identify new plastics, identify possible recycling techniques, and decrease the number of screening experiments necessary for the scale-up of laboratory processes.

Database development is essential. New plastics must be identified and added to the database. As more catalyst screening and parameter optimization experiments are performed on the various waste streams currently being studied, this data will also be added. The qualitative aspects of ICP appear to be fairly straight forward, but further work is needed to refine the quantitative identification of multicomponent mixtures.

REFERENCES

1. Evans, R.J.; Tatsumoto, K.; Czernik, S.; and Chum, H.L., "Innovative Pyrolytic Approaches to the Recycling of Plastics to Monomers", Proceedings of the RecyclingPlas VII Conference: Plastics Recycling as a Business Opportunity, 175 (1992).

2. Atomic and Molecular Beams, Vol. 1, G. Scoles, ed., Oxford University Press, New York, 14-53 (1988).

3. Evans, R.J. and Milne, T.A., Energy & Fuels, 1(2), 123 (1987); 1(4), 311 (1987).

4. Wang, D.; Meglen, R.; Milne, T.; and Evans, R., "Quantitative Sampling with Free-Jet, Molecular Beam Mass Spectrometry," Proceedings of the MBMS Workshop (1994).

MBMS of Biomass Pyrolysis Vapors and Catalytic Upgrading

Richard J. French and Bahman Rejai
Process Research Branch
National Renewable Energy Laboratory
1617 Cole Boulevard
Golden, Colorado 80401

Abstract

Studies of the production of transportation fuels from woody plants and other biomass sources at NREL have included the catalytic upgrading of vapors produced by the pyrolysis of wood and other materials. Molecular beam mass spectrometry is uniquely suited to the screening of this chemistry because of its ability to fingerprint the complete slate of pyrolysis or catalysis products in real time. It can also follow transient behavior at the rate of several spectra per second, which is useful in modeling the behavior of a riser-cracker or similar industrial system.

Laboratory work was done on a dual-bed vertical reactor in which the sample (3-80mg of solid sample) is pyrolyzed in the lower section of the reactor and then passed over 0.2-1.0g of various catalysts. It is then diluted and introduced into the molecular beam. This system can be used to compare various catalysts and feedstocks. In other experiments, a pilot-scale (15kg/hr) pyrolysis plant with catalytic riser cracker was monitored with the NREL transportable MBMS. Continuous sampling was done via an atmospheric pressure, heated line. Nitrogen dilution was used to suppress condensation and water clusters.

Results will be shown comparing products from wood, sunflower seeds, and mixtures of paper and plastics. Over MFI zeolite catalyst, a product slate similar to the methanol-to-gasoline process is observed--a mixture of alkane, alkene and aromatic compounds--with additional CO and CO_2. Higher yields of alkenes are produced by the oily and plastic-containing samples. The pilot plant gives spectra similar to the laboratory data. The TMBMS correctly identified improved operating conditions.

Introduction

The NREL free-jet molecular beam mass spectrometer(MBMS) provides a unique opportunity to study catalytic upgrading of pyrolysis oils. The complete product slate can be viewed at any level of catalytic conversion and raw, intermediate, and final products can be identified in spite of their very diverse chemistry ranging from very non-polar alkanes through aromatics to highly polar organic acids. Many of the raw and intermediate products are not thermally stable. These abilities have been exploited in the past to demonstrate the formation of hydrocarbon products from biomass and waste streams.[1-6] Recently this project has focused on hydrocarbon rich streams and the comparison of on-line monitoring to laboratory results to guide pilot-scale development. For this purpose, the ability of the MBMS to see changes in the product slate in a fraction of a second may be helpful in modeling the behavior of transitory processes such as a catalytic riser cracker system. Some recent results are discussed below.

Experimental

The laboratory micro-reactor shown in Figure 1 was used for all the small-scale tests. It is discussed in detail elsewhere.[5] The most salient feature is the use of dual 8mm I.D. inner tubes which allow for the comparison of two 0.1-1g samples of catalyst or one catalyst to raw pyrolysis. Residence times over such beds are typically 0.02-0.4s and 1-60 mg solid samples can be inserted through the side ports. Liquid samples are usually injected through needles into the bottom of the reactor. Gaseous samples or standards are mixed into the helium carrier gas flows which are typically 5-100 standard cm^3 in the inner tubes and 3 standard liters in the outer tube.

The pilot scale riser-cracker system currently in operation at NREL is shown schematically in Figure 2. Note that the biomass vapors and catalyst are fed together continuously but are only in contact for 1-5 s in which they are mixed in the riser. The steam in the stripper section is believed to remove coke precursors from the catalyst before being recycled with more feed. In a complete system, part of the catalyst would be regenerated with air or oxygen each cycle so that a steady-state level of coke would be achieved eventually.

The sample transfer line used to connect the pilot-scale reactor to the transportable MBMS[7] is shown in Fig. 3. The 1/2 inch line and preheated nitrogen dilution were chosen as a compromise between wall contact, residence time at temperature, condensation, and water clustering, similar to the monitoring at Battelle Columbus laboratories.[8] The differences here are that argon injected into the system was used for concentration comparisons instead of an orifice metering plate, and the pyrolysis oil has a more severe tendency to condense and polymerize than does the synthesis gas. There were some problems with plugging of the sample lines and valves. In some cases the pressure drop through the riser was high enough to severely limit the flow that could be obtained from this atmospheric-pressure system. At these times, a lower dilution ratio and longer residence times had to be tolerated, with the associated larger water clusters and occatsional plugging of the MBMS orifice.

All spectra shown were obtained with a quadrupole mass filter by electron impact ionization at nominally 25eV electron energy.

Results

The results of upgrading wood vapors in the laboratory and pilot-scale systems is shown in Figure 4. A commercial ZSM-5 (MFI) catalyst from Mobil Corporation was used in both cases. The product slates are similar, as listed in Table 1. The differences are largely due to lower conversion in the case of the pilot plant. This results in more oxygenates such as phenol, cresol, acetone and perhaps some furan. The 58 can be assigned to acetone instead of propane because acetone was found in the product of the pilot plant and it was indicated by time-resolved laboratory data (below). The high 43 and 41 suggest some fragments in the propene region. Over half of the 43 can be assigned to acetone, and the rest of the excess 41 and 43 can be attributed to fragments from higher alkenes and changes in mass spectrometer between the two mass spectrometers (laboratory and transportable) and over time. The relative amounts of oxygenated compounds decreased with catalst/wood feed rates in

a fashion similar to that seen in the laboratory. This was useful for guiding the selection of operating parameters in the pilot plant.

Table 1

Assignment	m/z
H_2O	18,17
CO, N_2	28
CO_2	44
ethene	28,27
propene	41,42
butene	56,41,55
pentene	70,55,42
benzene	78
toluene	92,91
xylene or ethylbenzene	106,91
C_3 alkyl benzenes	120
naphthalene	128
methylnaphthalene	142
dimethylnaphthalene or ethylnaphthalene	156
acetone	43,58
furan	68
phenol	94
cresol	108,107

The pyrolysis of an NIST standard Teledyne National RDF (refuse derived fuel) in the laboratory microreactor is shown in Figure 5. This physically processed municipal solid waste is another low-cost material that could be used as an alternative source of fuels and chemicals. The paper content is revealed by the typical ligno-cellulosic peaks at m/z 180, 126, 98, 85 and 60. In addition, 104 is present indicating styrene from decomposition of polystyrene. When this material is passed over ZSM-5, the spectrum simplifies somewhat to aromatics and alkenes as the major species along with styrene. The large fraction of alkenes in the vapors is attributed to the depolymerization of polypropylene and polyethylene wastes in the RDF.

Vegetable oils are another possible source of hydrocarbons. The pyrolysis of sunflower seeds in the laboraroty microreactor is shown in Figure 6a. This contains a hydrocarbon-like fragmentation pattern with what appear to be fatty acid monomer parents (256,280) from the sunflower seed oil. When these vapors are passed over ZSM-5, the result is suggestive of aromatics with a fairly high yield of olefins. Though the assignments are somewhat uncertain in this more complex spectrum it seems likely that vegetable oils are another source of alkenes.

The behavior of the mass spectrum in time helps assign the mass spectrum and may be of use in an industrial process. The changes in mass 91, 94, and 58 with time are shown in Figure 7. This is the result of passing a very short pulse of wood pyrolysis vapors over a bed of ZSM-5. The pulse was produced by pressing a wood dowel against the hot quartz interior wall of the reactor. The difference in the time response of the different species may be due to the strength of the absorption on the catalyst or a difference in reaction rates. In either case, the difference may be sufficient in a riser-cracker that the residual oxygen containing compounds could be removed in the stripper while the bulk of the hydrocarbons was removed directly from the top of the riser. This could reduce the cost of purifying the products.

Conclusions

The data above show that the pilot scale and laboratory scale reactors give similar results. However, a

more thorough comparison is needed to derive a predictive relationship between the laboratory results and the pilot plant. Since the production of alkenes from the RDF and sunflower seeds seems better than that for wood, other oily or hydrocarbon rich plant materials will be tested for hydrocarbon production with pyrolysis and zeolite catalysis. Different kinds of catalysts and different pyrolysis environments, perhaps with co-fed solvents will also be examined for their effect on the production of useful pyrolysis products.

References

1 Evans, R. J. and Milne, T. A., "Molecular-Beam Mass-Spectrometric Studies of Wood Vapor and Model Compounds over HZSM-5 Catalyst," in Pyrolysis Oils from Biomass, ACS Symposium Series 376, ed. E. J. Soltes and T. A. Milne. Washington: ACS, 1988, pp. 311-327.

2 Milne, T. A., Evans, R. J., and Filley, J., "MBMS Studies of HZSM-5 Activity During Wood Pyrolysis Product Conversion," Research in Thermochemical Biomass Conversion, ed. A. V. Bridgewater and J. L. Kuester. New York: Elsevier Applied Science Publishers, 1988, pp. 910-926.

3 Milne, T. A., Evans, R. J., and Nagle, N., "Catalytic Conversion of Microalgae and Vegetable Oils to Premium Gasoline, with Shape-Selective Zeolites", Biomass 21, 1990, pp. 219-232.

4 Rejai, B., Evans, R. J., Milne, T. A., Diebold, J. P., and Scahill, J. W. "The Conversion of Biobased Feedstocks to Liquid Fuels Through Pyrolysis," Proc. Conference on Energy from Biomass & Wastes XV, Washington D.C., March 1991.

5 Rejai, B., Agblevor, F.A., Evans, R.J., and Wang, D., "Catalyst and Feedstock Effects in the Thermochemical Conversion of Biomass to Liquid Fuels" Proceedings of the Annual Conference of American Solar Energy Society, Cocoa Beach, FL, June 1992. pp. 259-263.

6 Wang, D. and Rejai, B., "Ion-Molecule Reactions of Ionized Butenes in a Triple Quadrupole Mass Spectrometer" Proceedings of the 40th Conference on Mass Spectrometry and Applied Topics, Washington, D.C., May 31-June 5, 1992. pp. 1058-1059.

7 Rattcliff, Matthew A., "The NREL Transportable MBMS and It's Applications" proceedings of this conference.

8 Gebhard, Steven C., Gratson, David A., French, Richard J. Ratcliff, Matthew A., and Patrick, Joseph A., "Characterization and Catalytic Conditioning of Synthesis Gas Produced by Biomass Gasification" ACS Division of Fuel Chemistry Preprints 39(4)(1994)1048-1052.

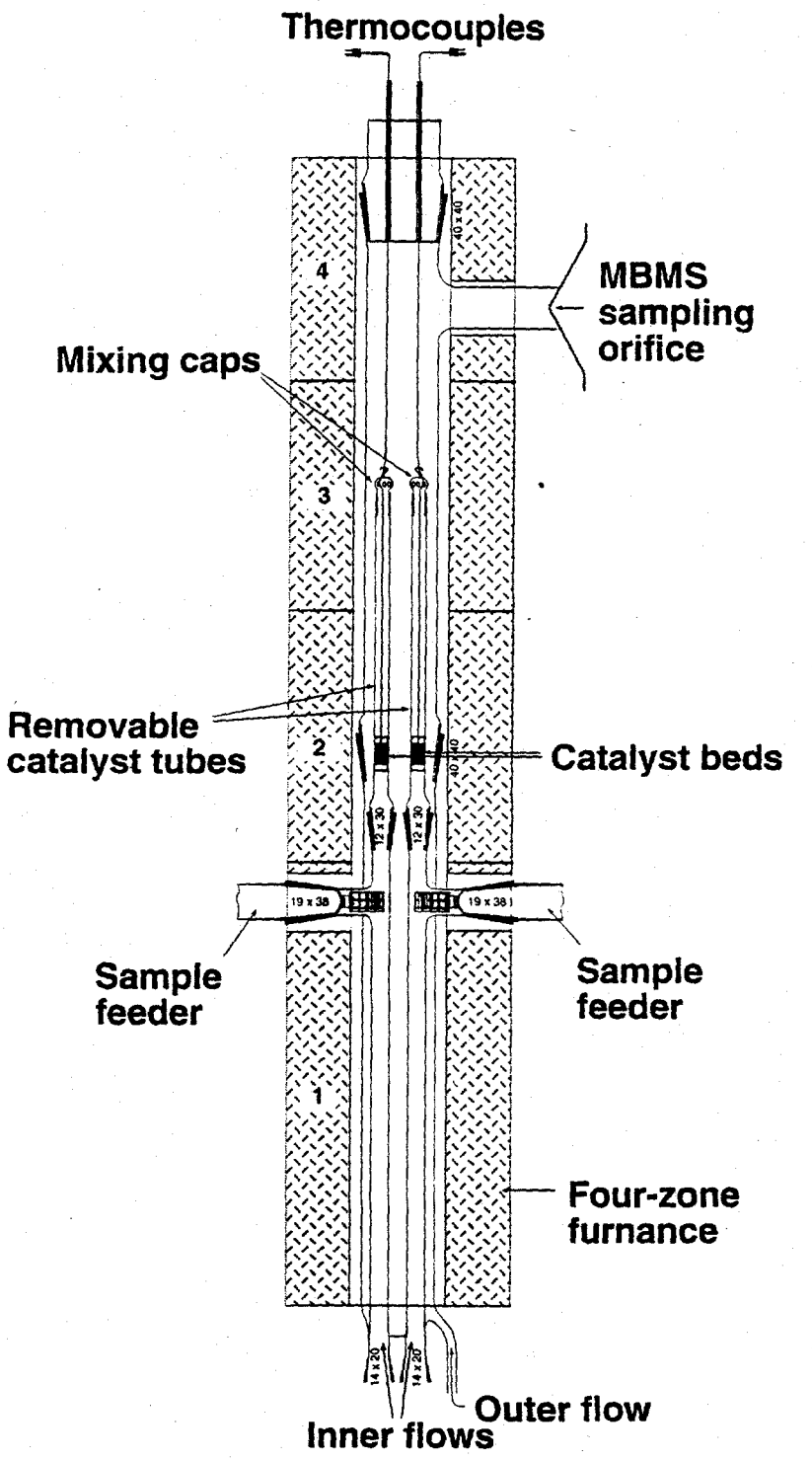

Figure 1. Laboratory Catalytic Microreactor

Pilot Scale Riser Cracker System Showing MBMS Sampling Points

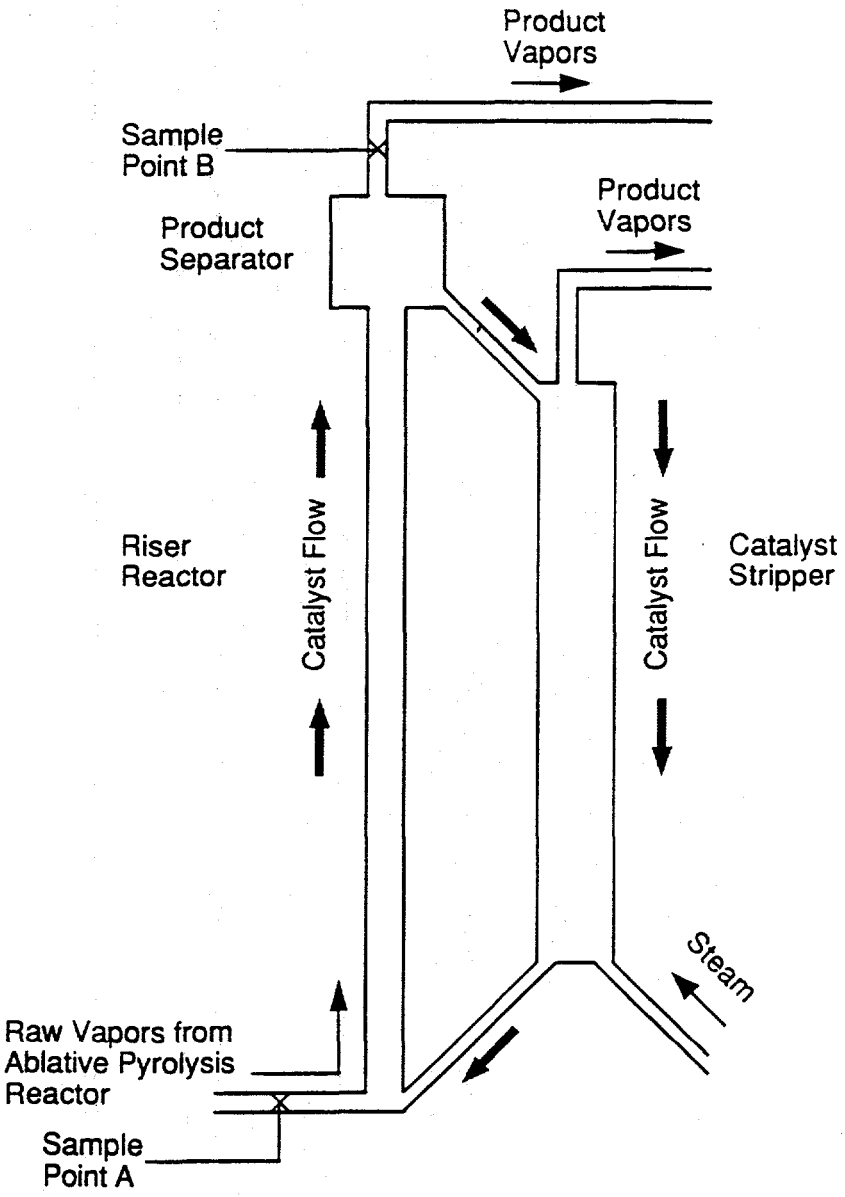

Figure 2. Schematic of NREL Pilot Scale Biomass Riser Cracker System

Schematic of MBMS Sample Transfer Line on Pilot Scale Riser Cracker

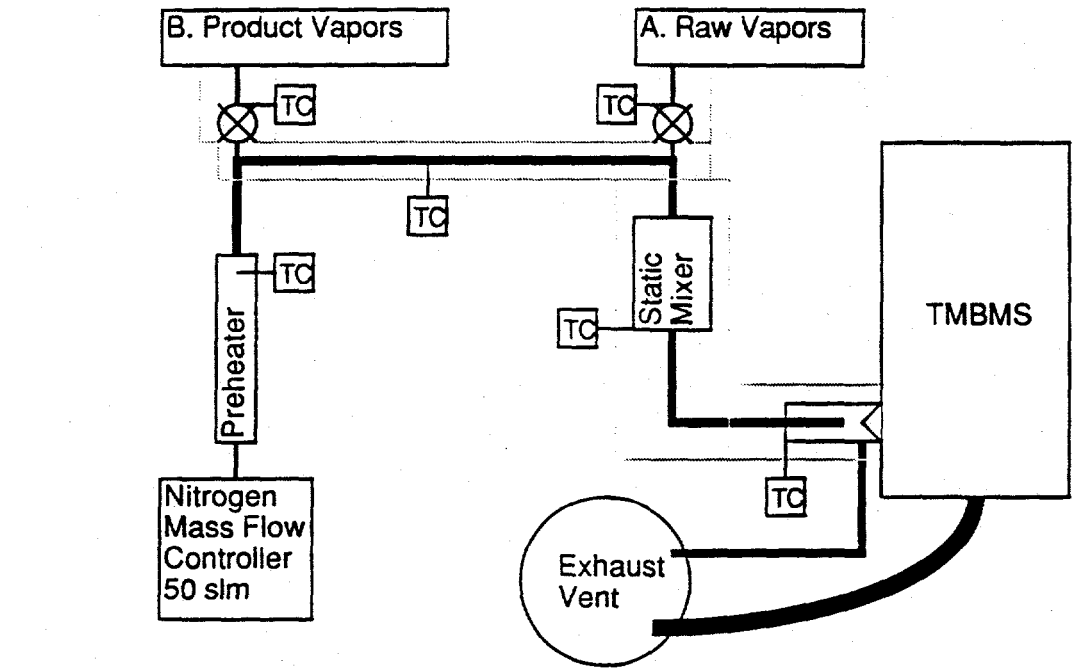

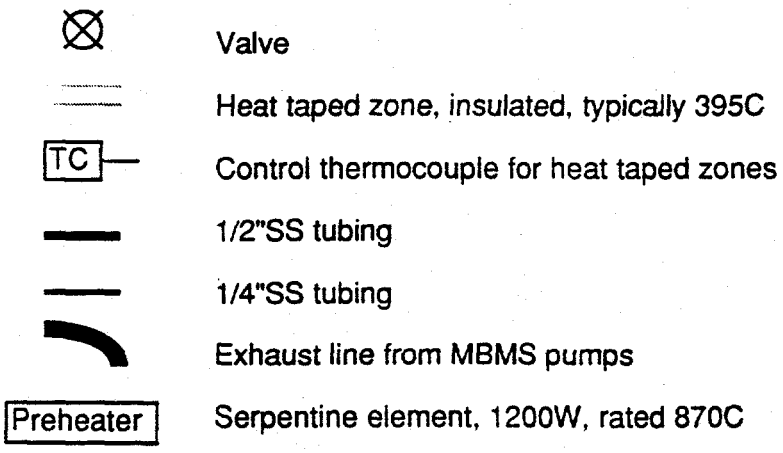

Figure 3. Schematic of MBMS Sample Transfer Line of Pilot Scale Biomass Riser Cracker System

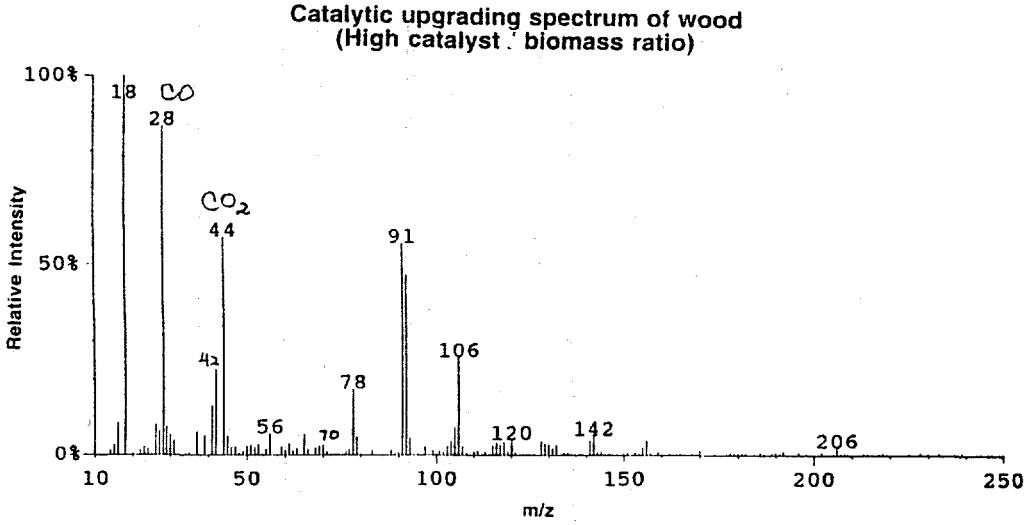

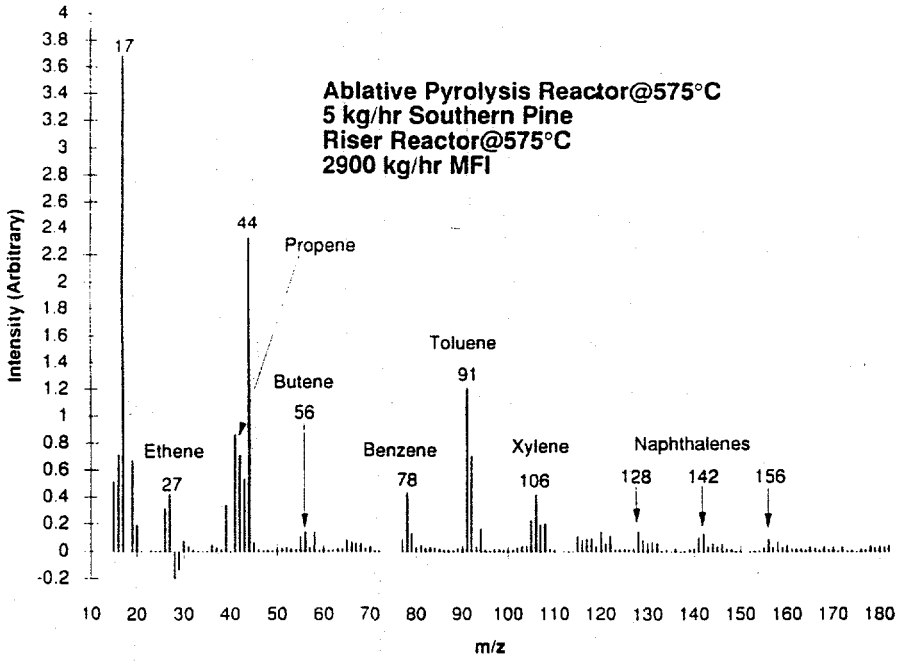

Figure 4. a.) Catalytic Upgrading Spectrum of Wood. In laboratory catalytic microreactor. b.) Catalytic Upgrading Spectrum of Wood. By TMBMS on pilot scale biomass riser cracker system.

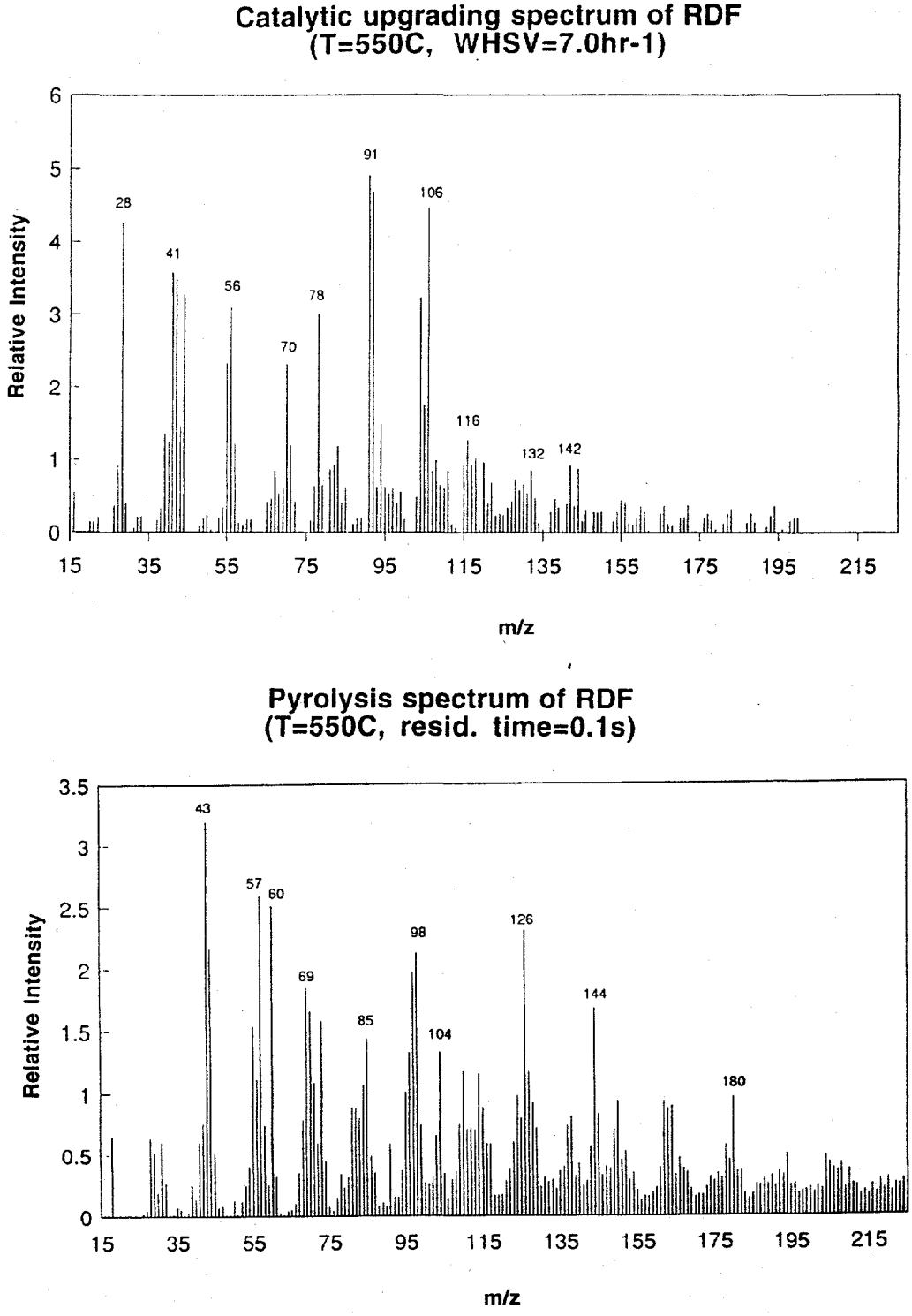

Figure 5. a.) Pyrolysis Spectrum of Teledyne National RDF. In laboratory microreactor. b.) Catalytic Upgrading of Pyrolysis Vapors from Teledyne National RDF. In laboratory microreactor with Mobil ZSM-5.

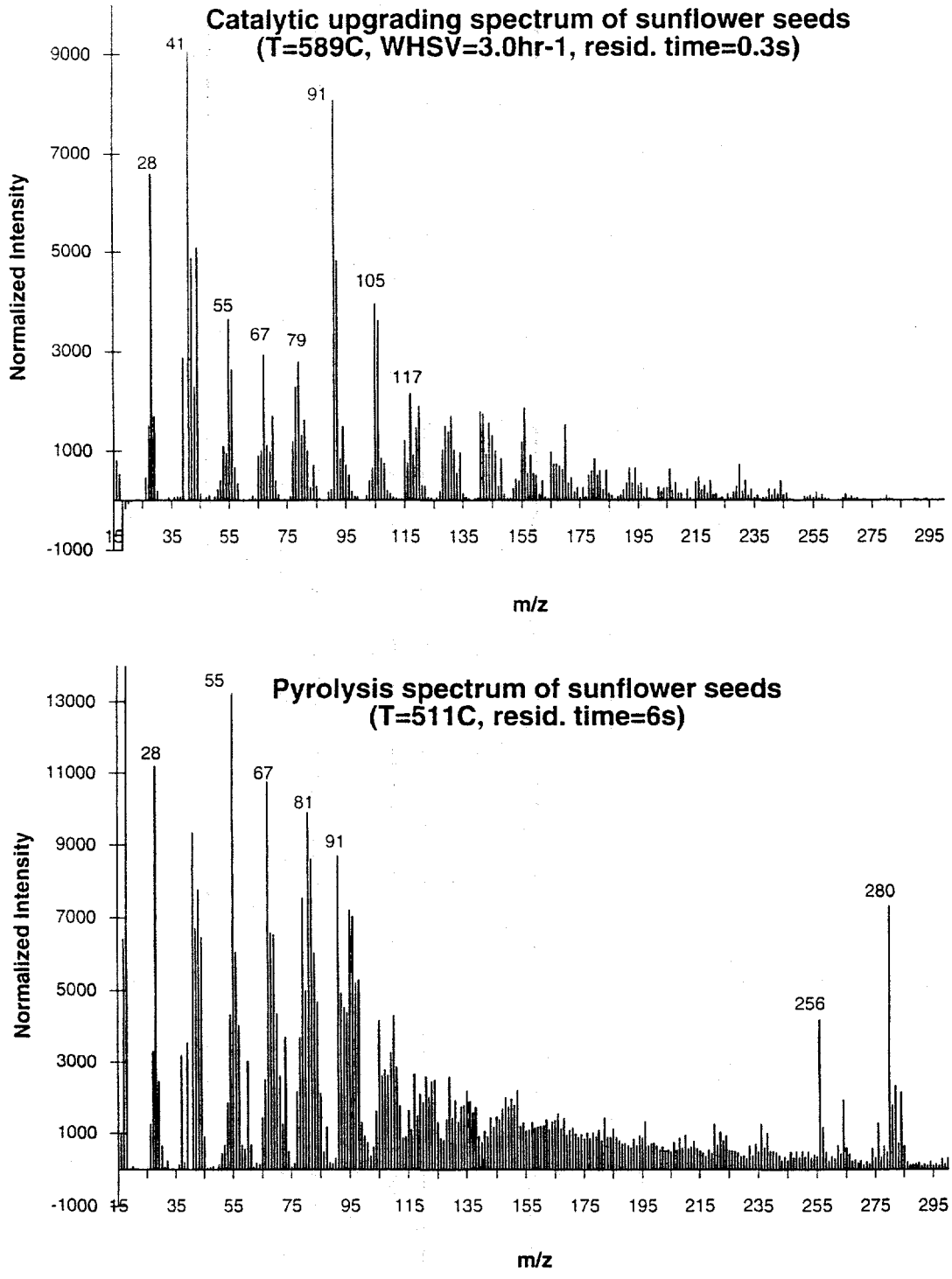

Figure 6. a.) Pyrolysis Spectrum of Sunflower Seeds. In laboratory catalytic microreactor. b.) Catalytic Upgrading of Pyrolysis Vapors from Sunflower Seeds. In laboratory microreactor with Mobil ZSM-5.

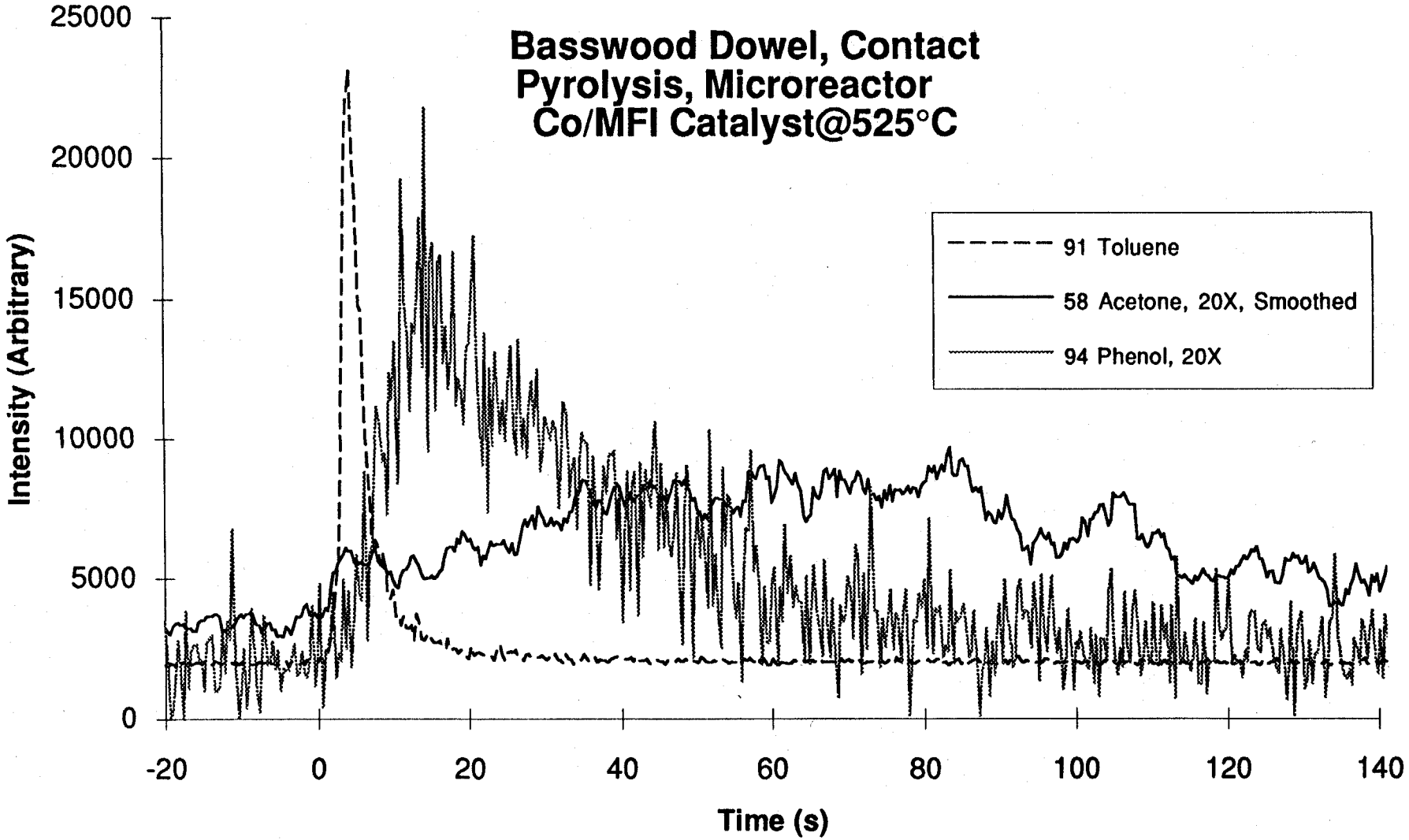

Figure 7. Time Evolution of Catalysis Products.

MOLECULAR BEAM MASS SPECTROMETRY APPLIED TO BIOMASS GASIFICATION MONITORING

Steven C. Gebhard, David A. Gratson, Richard J. French, and Matthew A. Ratcliff
Industrial Technologies Division
National Renewable Energy Laboratory
1617 Cole Blvd
Golden, CO 80401.

1. BACKGROUND

1.1 Syngas Fuels via Biomass Gasification

Synthesis gas (syngas) is a physical mixture of carbon monoxide and hydrogen used as a feedstock in methanol, higher alcohols, and Fischer Tropsch hydrocarbon synthesis. Syngas generated by thermal biomass gasification (biosyngas) represents a renewable fuel feedstock because alcohol/hydrocarbon combustion returns the carbon and hydrogen to the atmosphere as CO_2 and H_2O. These are subsequently converted back into plant material during photosynthesis when replacement biomass is cultivated. Biomass gasification in this respect is a form of solar energy conversion.

There are two biomass gasification technologies being investigated by the National Renewable Energy Laboratory, 1) *indirect gasification* which uses an external heat transfer agent, and 2) *direct gasification* which uses air or oxygen to generate the required heat by partial biomass combustion. Syngas from either gasifier cannot be used directly for fuel synthesis because it contains particulate matter, methane, C_2 hydrocarbons, and tar. These impurities cannot be tolerated by downstream catalytic fuel synthesis processes.

The economics of biomass to syngas fuels is improved if the raw syngas is purified near the gasification temperature (700-800° C). This high temperature process is referred to as syngas conditioning. Syngas conditioning avoids scrubbing the raw syngas with water to remove tar because the syngas must then be reheated to 800° C to steam reform methane and other low molecular weight hydrocarbons in a separate step. Table 1, shows a typical analysis of raw syngas produced by the Battelle Columbus Laboratory (BCL) indirectly heated 9 tonne/day biomass gasifier. The H_2/CO ratio from Table 1 is 0.7. This represents too much CO for most syngas fuels chemistry; for example methanol synthesis stoichiometry requires that $H_2/CO = 2$. Lower H_2/CO ratios can be tolerated by some Fischer Tropsch hydrocarbon processes however.

Battelle Columbus Laboratory and NREL are jointly developing a catalytic syngas conditioning process that operates at 800° C and uses a proprietary catalyst designated DN34. In addition to steam reforming tar compounds, the catalyst exhibits water-gas shift activity and can adjust the H_2/CO from 0,7 in raw syngas to between 2 - 3 depending on the specific process conditions thus eliminating the need for a separate water-gas shift step. In addition, DN34 is resistant to deactivation in this application. DN34 has been operated on-stream with the BCL gasifier for more than 100 hours without measurable deactivation (Paisley *et al.*, 1994; Paisley and Litt 1993). This is in contrast to the behavior observed when conventional steam reforming catalysts are used for syngas conditioning, Most nickel based steam reforming catalysts deactivate rapidly when directly exposed to the full tar load in the raw syngas. An interesting exception is a nickel-molybdenum-copper catalyst developed at Pacific Northwest Laboratory (Mudge *et al.*, 1987; Mudge *et al.* 1988). Unfortunately, DN34 exhibits unacceptably poor activity for steam reforming methane and other low molecular weight hydrocarbons. The PNL catalyst is a potential candidate for a two reactor syngas conditioning process that is anticipated to address the methane problem.

1.2 Gasifier Streams Characterization

Detailed knowledge about the composition of biomass gasification derived syngas is essential for successful syngas conditioning process development. A large number of tar compounds are formed during biomass gasification and tar composition is a strong function of gasifier operating conditions (Evans and Milne 1987a; Evans and Milne 1987b; Elliot 1986). Typical gasification temperatures are near 800° C yielding a tar that is mostly aromatic hydrocarbons. In addition to the total amount of tar, the relative concentrations of specific compounds present in the syngas before and after catalytic gas cleanup needs to be known because different compounds have different reactivities (Gebhard *et al.* 1994; Mudge *et al* 1987; Mudge *et al.* 1988).

A transportable molecular beam mass spectrometer (TMBMS) has been developed at NREL for monitoring processes where gas phase compositions need to be known. Direct monitoring of syngas conditioning catalyst performance at the engineering scale with the TMBMS permits catalytic clean-up to be evaluated under realistic conditions (i.e. real tar laden syngas). The TMBMS detects all gases and vapors simultaneously including high molecular weight aromatic hydrocarbons such as those found in biomass gasifier tar.

Real-time TMBMS data are discussed in this report for unprocessed and catalytically conditioned biosyngas obtained from the 9 tonne/day indirectly heated biomass gasifier at BCL. These data show that biomass gasification can be monitored to give information about flow transient behavior of gasifier stability with simultaneous acquisition of a qualitative syngas analysis as a function of time.

1.3 Battelle Gasifier

Battelle Columbus Laboratory's indirect gasification process is steam gasification using hot sand as the heat transfer agent. Process details can be found elsewhere (Paisley and Litt, 1993; Paisley *et al.* 1994). The gasifier is a vertical type 310 alloy stainless steel pipe approximately 25 feet (7.5 m) high and about 10 inches (25 cm) in diameter. It is heated by external electric clamshell heaters because of heat loss at this scale. In a larger commercial scale unit, external heating would not be needed. Biomass is mixed with steam and hot sand and injected into the bottom of the gasifier. The hot sand pyrolyses the biomass and thermally cracks the resulting pyrolysis vapors at 700° C to 800° C. The steam acts as both a physical transport agent for the solids and as a reactant in the water-gas shift reaction ($CO + H_2O \rightleftharpoons CO_2 + H_2$). Char and sand from the gasifier are separated from the medium-BTU product gas using a cyclone. These solids drop into a fluidized bed combustor vessel (which acts as the sand reservoir) and the char is burned to reheat the sand. The hot sand is then injected back into the gasifier along with fresh feed. An L-valve at the bottom of a vertical leg from the combustor controls the hot sand flow into the bottom of the gasifier. The gasifier and combustor are pressure isolated from each other by the dip leg on the bottom of the char/sand cyclone that separates the solids from the product gas. The dip leg penetrates the sand bed in the combustor and prevents air from entering the gasifier. The sand continuously circulates between the gasifier and combustor during gasification.

2. EXPERIMENTAL METHODS

2.1 Transportable Molecular Beam Mass Spectrometer (TMBMS)

The TMBMS is based on molecular beam mass spectrometry (MBMS) and takes advantage of extractive sampling coupled with mass spectrometric analysis to identify the chemical compounds found in complex reactive gas systems. Examples relevant to the work discussed here include biomass pyrolysis (Evans and Milne 1987a; Evans and Milne 1987b) and catalytic upgrading of biomass pyrolysis vapors (Agblevor *et al.* 1992). The ability to study particle laden streams is especially advantageous for gasifier studies since char and other fines are always present in these systems.

The TMBMS uses an Extrel model EXM750 quadrupole mass analyzer equipped with all necessary control

electronics. The instrument is described in detail elsewhere (Ratcliff, 1994). The TMBMS has a mass range of m/z = 1 - 720 with unit mass resolution and a selectable time resolution down to one millisecond. Data are collected with a Teknivent Vector II computer interface/software system. The TMBMS has a demonstrated dynamic range greater than 10^6 and a 0.5 parts per million by volume (ppmv) detection limit. The detection limit varies with the specific chemical compound and depends somewhat on the system being analyzed.

2.2 Sample Transfer Line

Successful process monitoring requires that the syngas sample be transferred to the TMBMS without vapors condensing or chemical reactions occurring such as thermal decomposition. This is especially important when sampling gasifier streams which may contain reactive compounds such as those generated during the initial pyrolysis stages of biomass gasification. Figure 1 shows details of the sample transfer line system as it was assembled on the BCL gasifier. The combined length was about 36 ft (11 m) when complete.

The sample transfer line was maintained at 300° C during sampling by the commercial tubing section's built in heaters, and heating tapes. All heaters were controlled by commercial (Love Controls) microprocessor units equipped with proportional-integral-differential (PID) programming capability. From previous work at NREL, we determined that 300° C does not cause thermal decomposition of the tar compounds expected from the BCL gasifier but is hot enough to prevent the condensation of aromatic hydrocarbons with molecular weights below about 300 daltons. The residence time in the sample transfer line was also kept to less than one second to further minimize chances for transfer line artifacts (discussed later). The tubing sections were 1/2 inch O.D. with the lengths chosen according to a Fibonacci sequence (i.e. 1, 2, 3, 5 and 8 ft sections) so that we could assemble any length we needed in one foot increments. The 3, 5 and 8 ft sections were purchased from Technical Heaters Inc; the 1 and 2 foot sections were homemade. A Fibonacci sequence was used because the transfer line had to be custom fit and assembled at the BCL gasifier site. Each tubing section is equipped with a permanent insulated heating jacket and is rated for continuous operation at 500° C.

3. RESULTS

3.1 Transfer Line Artifacts Test

To test for possible condensation/reaction problems when designing the sample transfer line, we examined how reproducible the transfer of basswood pyrolysis vapors would be through a heated section of the commercial (Technical Heaters Inc.) stainless steel tubing. Basswood dowel pieces were cut, weighed, and pyrolyzed in a 2.5 cm diameter stainless steel tubular pyrolysis reactor. The dowels were 1/16 inch (1.6 mm) in diameter and each piece weighed about 7 mg. The dowel pieces were pyrolyzed at 547° C and mass spectra were compared with and without an 8 ft section between the TMBMS and the pyrolysis reactor. The tubing was maintained at 308° C during the experiments. The temperature was maintained by a dedicated microprocessor controller. The stainless steel microscale pyrolysis reactor was heated in a microprocessor controlled tube furnace and attached to the tubing section with stainless steel fittings. The end of the tube was attached to the TMBMS with gas-tight stainless steel fittings. Helium was used as an inert carrier gas to sweep the pyrolysis vapors from the reactor through the tubing to the TMBMS at a flow rate of approximately 4 standard liters/min

Figures 2 and 3 are typical mass spectra from the basswood pyrolysis experiments with and without the heated tubing in place. The data displayed in the figures have been normalized to the largest intensity peak in each spectrum. There are numerical differences in individual peak intensities and there was an overall baseline shift with the same general intensity versus m/z profile, but importantly, the ratios between the various peaks are similar between the two figures. A few low molecular weight peaks changed considerably

in intensity. The 5 second residence time in the tubing during these tests was apparently sufficient for some thermal cracking of the primary pyrolysis products to occur before they reached the TMBMS. The complete sample transfer line system installed on the Battelle gasifier operated with a residence time of less than one second to minimize these effects. Figures 2 and 3 also indicate that the peak intensity ratios of the higher molecular weight tar compounds were relatively unchanged with and without the tube in place. This indicates that qualitative tar analysis is possible because the transfer line tubing does not introduce significant artifacts into the tar composition, and with proper calibration, semiquantitative analysis should be possible. Time limitations constrained us to make only qualitative measurements in the work reported here.

3.2 Carrier Gas Experiments

Experiments were performed with the stationary MBMS at NREL to determine if N_2 could be used instead of He as a carrier gas. This was mostly motivated by cost and availability considerations. Diluting the syngas to between 1:5 and 1:10 was observed to minimize interfering water cluster peaks in the mass spectrum. This also decreases the chance for tar condensation by reducing the dew point of these compounds by lowering their partial pressures. Water clustering was more pronounced with helium than nitrogen, for example the intensity of the water trimer cluster peak at *m/z* 55 was decreased by a factor of four when N_2 was used in place of He. The disadvantages of using N_2 included a slight decrease in overall sensitivity and the inability to directly monitor carbon monoxide (both *m/z* 28). The intensity decrease was about 66% with N_2 and was most pronounced below *m/z* 50. Fortunately this reduction was not as pronounced for compounds having $m/z > 50$, the region of interest in tar analysis. The diminished water clustering with N_2 was a distinct advantage in this work because of the high steam content of the sampled gas (40-60 vol% in undiluted syngas).

To keep the residence time in the 11 meter long transfer line less than one second, 40 standard liters/min of N_2 was mixed with the syngas prior to being introduced into the transfer line. The N_2 was heated to 300° C in a separate preheater before being mixed with the syngas to minimize potential condensation problems. As mentioned earlier, undiluted raw biomass syngas is 40-60 vol % water and directly sampling this steam laden gas can lead to severe water cluster formation in the free jet of the molecular beam. Water cluster peaks appear in a regular sequence as H_2O^+ coordinates with successive neutral water molecules (*m/z* 19, 37, 55, 73, 91 etc.). Even more troublesome is that we observed evidence for water coordinating with other molecules during basswood pyrolysis experiments done with varying amounts of steam and dilution gas; for example *m/z* 136 could be naphthalene coordinated with water. Thus, the mass spectrum for a steam rich sample cannot be corrected by simply subtracting out the water cluster mass spectrum. There was less water cluster formation when N_2 was used instead of He as the diluent which helps further. The results of the steam plus basswood pyrolysis experiments were the basis for choosing 5:1 to 10:1 as the dilution ratios for N_2:syngas.

3.3 Raw Synthesis Gas Analysis

Real time TMBMS data were obtained for unprocessed syngas and syngas processed over a proprietary catalyst designated DN34. The gasifier was run for system shakedown and were therefore done without the use of a continuous dryer that was to be installed on the biomass feeding system at a later date. Hog fuel was the feedstock and is waste material (bark, roots etc.) normally used as boiler fuel. The feed was supplied by Weyerhaeuser. Unfortunately the wet hog fuel feed was very difficult to feed because it is very fibrous, and since not thoroughly dry, it periodically jammed in the feeding system interrupting gasification. We were able to collect TMBMS data for only 2-3 hours because of these difficulties.

Two unprocessed syngas samples were taken. Figure 4 is a time trace for the benzene peak (*m/z* 78) for the first sample and shows how the raw syngas flow rate, as measured by this trace syngas component, fluctuated

over 10 minutes of gasification. The large pulse-like fluctuations were due to the feed jamming problems. It is important to point out that this behavior is not typical for the BCL gasifier. With properly dried feed (e.g. poplar chips and switchgrass) the gasifier operates very smoothly in steady state (Paisley and Litt 1993). The difficulties in feeding, however, did demonstrate that the TMBMS response time was sufficient to measure flow rate transients in the gasification system on the order of a few seconds.
The two arrows in Figure 4 indicate the time interval used to obtain an averaged mass spectrum that is shown in Figure 5, the *m/z* 15-350 window for the first sample of unprocessed biosyngas. Peaks for methane (*m/z* 16), water (*m/z* 18), CO_2 (*m/z* 44), benzene (*m/z* 78), and naphthalene (*m/z* 128) were among the largest peaks in the spectrum. The peak for carbon monoxide (and N_2) at *m/z* 28 was not scanned because N_2 was the carrier gas making this peak off scale.

The aromatic hydrocarbon peak intensities over represent the amount of these compounds in the syngas relative to the permanent gases (e.g. CO_2) because the sensitivity factors for aromatic hydrocarbons are typically 10-100 times larger than those of the low molecular weight gases. The greater sensitivity for aromatic hydrocarbons aids in analysis and identification of trace tar components. Figure 6 shows data from Figure 5 in the *m/z* 50-350 region enlarged to show the tar species present. Figure 6 indicates that benzene (*m/z* 78), toluene (*m/z* 92), phenol (*m/z* 94), styrene (*m/z* 104), cresol (*m/z* 108), indene (*m/z* 116), naphthalene (*m/z* 128) methylnaphthalene (*m/z* 142 isomer unknown) and phenanthrene/anthracene (*m/z* 178) are among the more abundant tar compounds. Figure 6 also shows that TMBMS detects the large number of species identified in previous studies of gasifier tar (Mudge *et al.* 1987; Mudge *et al.* 1988).

3.4 Catalytically Conditioned Syngas

The performance of a previously developed, proprietary syngas conditioning catalyst (DN34) was examined. The catalyst was tested in slip-stream fluidized bed reactor attached to the BCL gasifier. The total slip-stream flow to each reactor was about 2.8 N-m^3/h (100 SCFH) and the catalyst was operated using a gas hourly space velocity (GHSV) of about 2000 $cm^3_{syngas}cm^{-3}_{catalyst}h^{-1}$ at approximately 800° C. Details of the reactor configuration and test procedures are reported elsewhere (Paisley and Litt 1993).

The mass spectral peak intensities for the condensed ring aromatic hydrocarbons were reduced, and the secondary pyrolysis product peaks were below detection in syngas that had be conditioned with DN34 (Figure 7). Benzene, naphthalene and smaller amounts of higher molecular weight aromatic hydrocarbons remained in the reactor outlet gas. Therefore, DN34 is more effective at steam reforming secondary pyrolysis products (i.e. phenol, cresol, styrene, etc.) but is less effective for destroying the more stable aromatic hydrocarbons under these experimental conditions. This is consistent with previous microscale tests of DN34 (Gebhard *et al.*, 1994; Zhao and Cowley, 1994) using synthetic syngas and a model compound gasifier tar in a fixed bed reactor. In that work, cresol, indene, 1-methylnaphthalene and 2-methylnaphthalene destruction at 815° C, with 50 vol % steam at a GHSV of 1500 $cm^3_{syngas}cm^{-3}_{catalyst}h^{-1}$ was more than 99% complete. This is in contrast to the levels observed for benzene and naphthalene destruction, where 30 to 50 mol % was typical (Gebhard *et al.* 1994). In the microscale experiments the initial concentration of benzene and naphthalene were 1200 and 400 ppmv respectively out of a total 4000 ppmv synthetic tar concentration. For 30 and 50 mol % conversions, the benzene and naphthalene concentrations exiting the microreactor were 840 and 200 ppmv respectively.

We were not able to make semiquantitative tar concentration measurements with the TMBMS because of the time constraints. Experiments where standards were injected into the sample line with only N_2 flowing (no syngas from the gasifier) enabled us to estimate some of the tar compound concentrations however. Table 2 shows the detection limits calculated for compounds injected into the sample transfer line with a syringe pump at a known flow rate. The compounds were dissolved in toluene and the concentrations were known. From the detection limits in Table 2 and the microscale work, we estimate that the concentrations

of unreacted aromatic hydrocarbons exiting the DN34 slip-stream reactor were in the few hundred ppmv range. Kinetic data are not available for DN34, however, lower space velocity operation may improve benzene and naphthalene destruction with DN34. Complete syngas conditioning to remove methane and these remaining traces of aromatic hydrocarbons could be done by adding a small reactor containing a n alkali/alkaline earth promoted nickel steam reforming catalyst after the DN34 reactor (Gebhard *et al.* 1994) similar to a similar concept published in the literature (Aznar *et al.*, 1993). A two-reactor process is currently being studied.

5. SUMMARY

The NREL transportable molecular beam mass spectrometer (TMBMS) was successfully used to monitor the composition of unprocessed and catalytically conditioned synthesis gas produced during hog fuel gasification with the Battelle Columbus Laboratory 9 tonne/day indirectly heated biomass gasifier. Variations in biomass feed rate were observed with simultaneous qualitative chemical analysis of the entire gasification product slate. A large number of tar compounds were observed in the unprocessed syngas in addition to the known low molecular weight permanent gases. Tar compounds include a variety of oxygenated and substituted aromatic hydrocarbons, and condensed ring aromatic hydrocarbons. Catalytic conditioning with DN34 effectively destroyed the more reactive oxygenates and stripped off alkyl groups from aromatic rings, but some benzene, naphthalene, phenanthrene/anthracene and pyrene (plus other aromatic hydrocarbons) remained. The concentration of these compounds was estimated to be in the few hundred ppmv range.

ACKNOWLEDGEMENTS

The authors wish to acknowledge the Battelle gasification project manager Mark Paisley P.E, the Battelle operational staff Don Hupp, Harry Leonard, Don Taylor, Ted Tewksbury, and Ron Wood; and NREL staff Dr. Robert Meglen for valuable suggestions on experimental planning, and Dr. Tom Milne for advice on making the TMBMS measurements.

REFERENCES

Agblevor, F. A.; Rejai, B.; Evans, R. J.; Johnson D. K. "Pyrolytic Analysis and Catalytic Upgrading of Lignocellulosic Materials by Molecular Beam Mass Spectrometry," *Proceedings of the 16th Conference on Energy from Biomass and Wastes*, Orlando, FL (1992) Chicago, IL: Institute of Gas Technology.

Aznar, M.P.; Corella, J.; Delgado, J. and Lahoz, J. "Improved Steam Gasification of Lignocellulosic Residues in a Fluidized Bed with Commercial Steam Reforming Catalysts," *Ind. Eng. Chem. Res.*, 32, (1993) 1.

Elliott, D.C., "Analysis and Comparison of Biomass Pyrolysis/Gasification Condensates," *Report PNL-5943* (1986) Pacific Northwest Laboratory, Richland, WA.

Evans, R.J. and Milne, T.A., "Molecular Characterization of the Pyrolysis of Biomass, 1 Fundamentals," *Energy and Fuels* 1 (1987a) 123.

Evans, R.J. and Milne, T.A., "Molecular Characterization of the Pyrolysis of Biomass, 2 Applications," *Energy and Fuels* 1 (1987b) 311.

Gebhard, S.C.; Wang, D.; Overend, R.P. and Paisley, M.A., "Catalytic Conditioning of Synthesis Gas Produced by Biomass Gasification," *Biomass and Bioenergy* (1994), in press.

Mudge, L.K.; Baker, E.G.; Brown, M.D. and Wilcox, W.A., "Bench-Scale Studies on Gasification of Biomass

in the Presence of Catalysts," Report PNL-5699 (1987) Pacific Northwest Laboratory, Richland, WA.

Mudge, L.K., Baker, E.G., Brown, M.D. and Wilcox, W.A., "Catalytic Destruction of Tars in Biomass-Derived Gases," *Research in Thermochemical Biomass Conversion*, A.V. Bridgwater and J.L. Kuester (eds), (1988) 1141, Elsevier, London.

Paisley, M.A. and Litt, R.D., "Hot-Gas Conditioning of Biomass Derived Synthesis Gas," *Proc. 1st Biomass Conf. of the Americas*, Burlington, Vermont (1993) 1133.

Paisley, M.A.; Litt, R.D.; Taylor, D.R.; Tewksbury, T.L.; Hupp, D.E. and Wood, R.D., "Operation and Evaluation of an Indirectly Heated Biomass Gasifier," *Phase Completion Report, Battelle Columbus Laboratory, NREL Subcontract No. YM-2-1110-1,* (1994).

Ratcliff, M.A., M.S. Thesis (Chemistry), Colorado School of Mines (1994).

Zhao, X and Cowley, S.W., "Catalyst Lifetime Testing for Methanol Syngas Conditioning," *Subcontractor Report, NREL subcontract number RAE-3-133442*, February (1994).

Component	Mole Percent
H_2	15.8
CO	23.0
CO_2	9.2
CH_4	9.1
C_2H_2	0.4
C_2H_4	3.0
C_2H_6	0.3
Tar (for M.A. = 100)	0.2
H_2O	39.0

Table 1. Typical composition of unprocessed syngas from the BCL gasifier.

Compound	**Detection Limit (ppmv)**	**Measurable Quantity Limit (ppmv)**
Phenol	3.1	11
Naphthalene	0.6	2.6
Phenanthrene	1.3	4.5
Pyrene	0.6	2.8

Table 2. Estimated detection limits for standard compounds

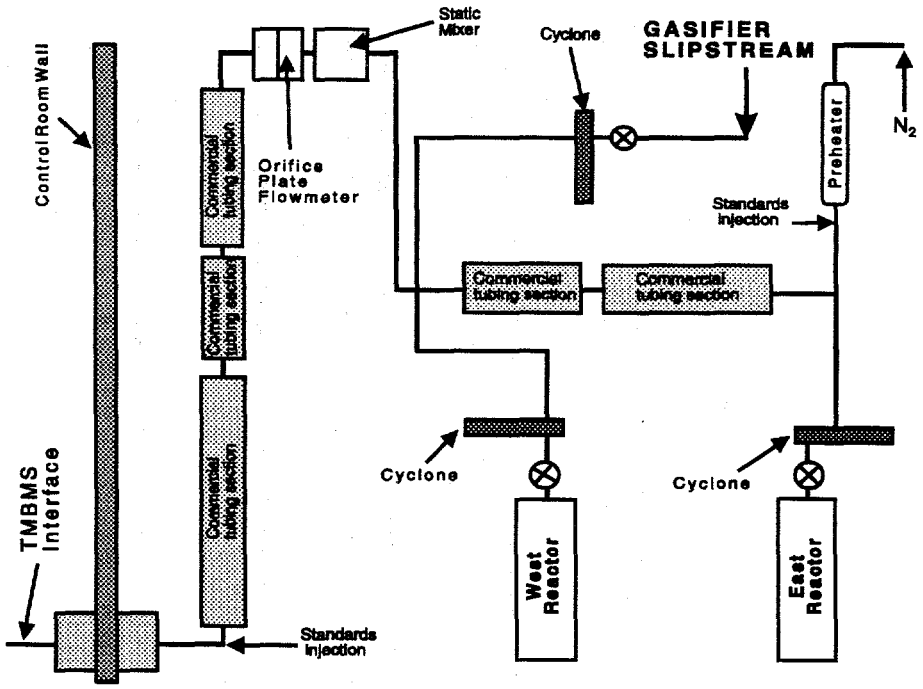

Figure 1. Sample to TMBMS transfer line

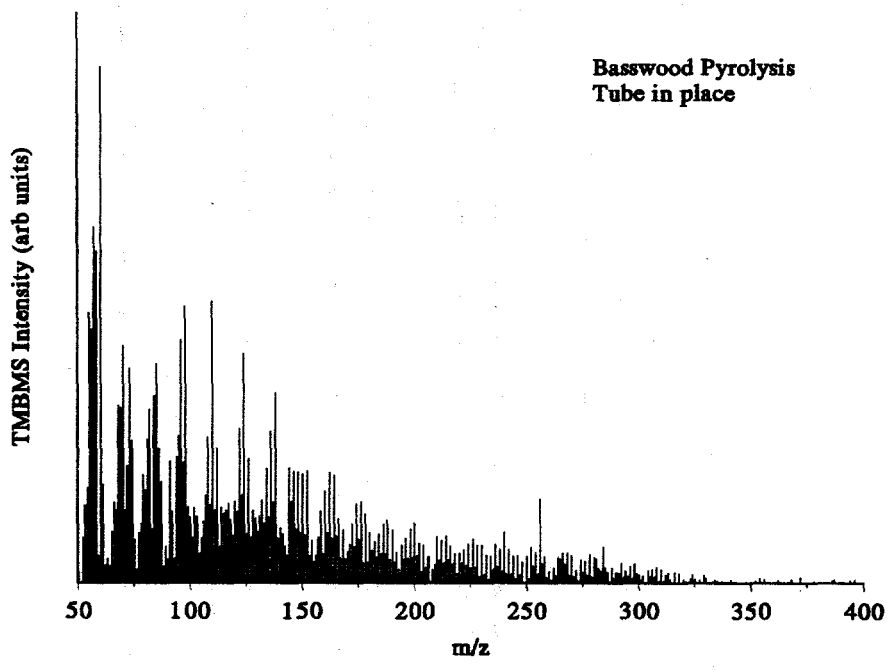

Figure 2. Basswood pyrolysis through 1/2"O.D. x 8' stainless steel tube

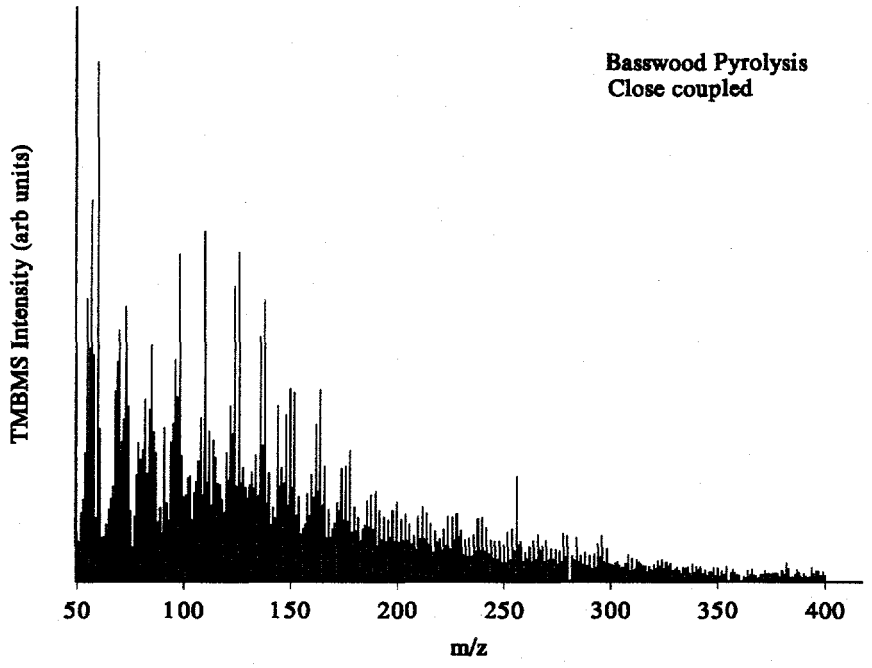

Figure 3. Basswood pyrolysis - close coupled to TMBMS

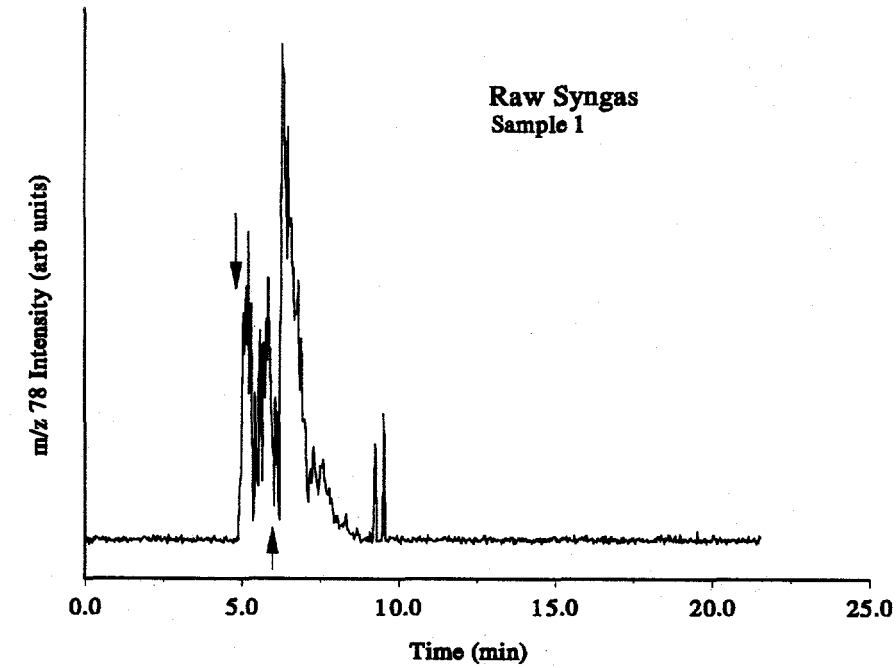

Figure 4. Benzene (m/z 78) intensity vs. time for raw biosyngas

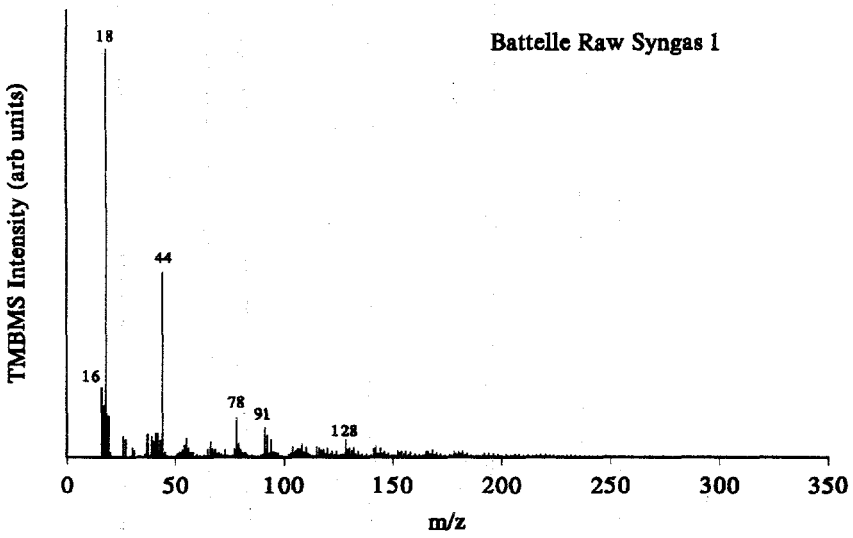

Figure 5. Overall mass spectrum of raw biosyngas

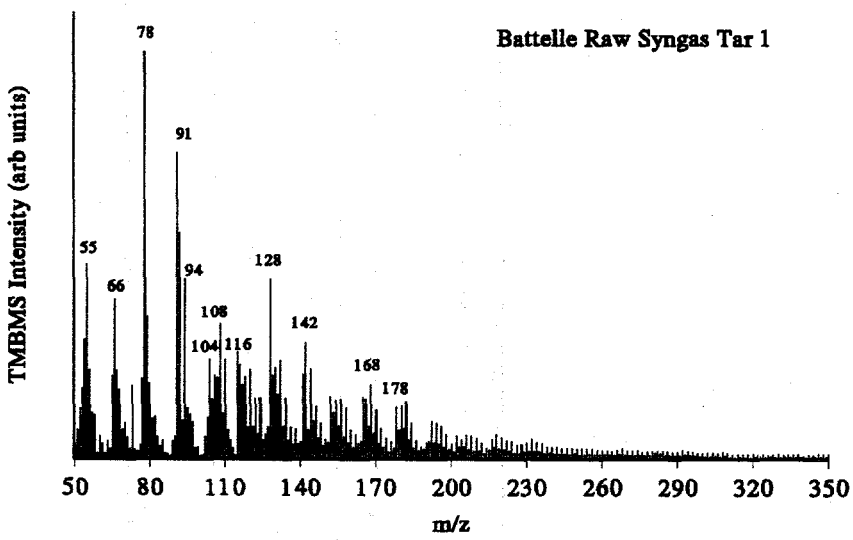

Figure 6. Tar mass spectral region for Fig. 5

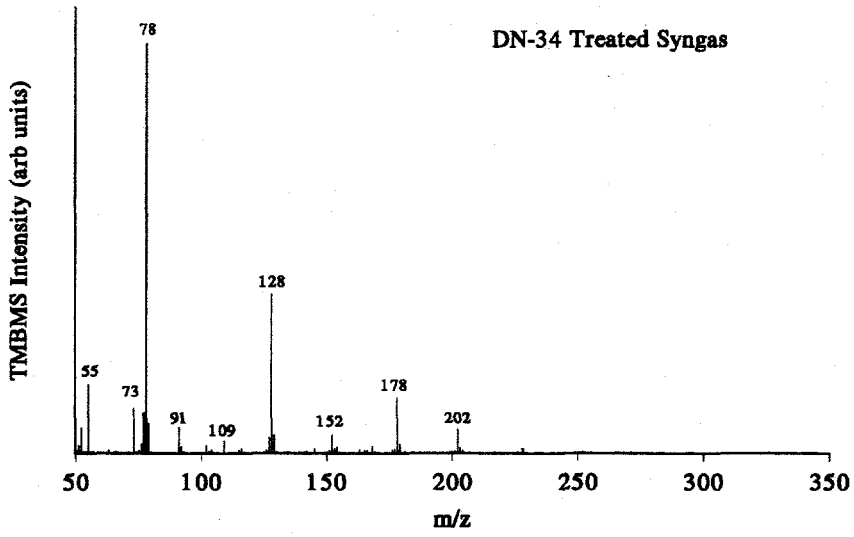

Figure 7. Syngas conditioned with DN34 catalyst

CHEMISTRY AND KINETICS OF CHLORINE OXIDES UNDER STRATOSPHERIC CONDITIONS*

Frank T. Greene and David A. Robaugh
Midwest Research Institute
Kansas City, MO 64110

Introduction

The accepted mechanism for the destruction of O_3 by chlorinated species in the stratosphere at equatorial latitudes does not apply under Antarctic winter conditions because of the low intensity of solar uv radiation. Consequently, a number of novel chemical mechanisms were proposed for ozone destruction, including one which invoked ClO dimer. This study was therefore undertaken to determine whether ClO dimer, which had not been positively identified, was a significant species under Antarctic stratospheric conditions and to determine its rate of formation.

Apparatus

The MBMS system used for this study is shown in Figure 1. In this system the initial stage into which the sampled gas is expanded is pumped by a 10,000 L/sec diffusion pump, which typically maintains the pressure below a millitorr. The expanding gas is collimated into a molecular beam, which is chopped by a rotating sector in order to provide phase sensitive detection and time-of-flight velocity analysis. The differentially pumped beam is passed sequentially through a large magnetic sector spectrometer, which provides resolution of up to 5000, and, for most experiments, one or more quadrupole mass spectrometers.

The Cl-O species were generated in low temperature photochemical flow reactors, which were integrated with the MBMS system. A typical reactor is shown in Figure 2. This reactor was capable of operation at temperatures from ambient to -80 $^{\circ}$C and pressures from 0 to 10 atm. The photochemical sources used were a 1000 W filtered Xe-Hg lamp and a tripled Nd-YAG laser.

Results

It was found that the gas phase chlorine-oxygen system was quite complex at low temperatures; characterization of this system was required before the major

tasks could be undertaken. ClO dimer was unambiguously identified using MBMS and velocity analysis and found to be thermodynamically very stable under stratospheric conditions. It was also found that any chemical system which contained ClO_2 and ClO also contained a larger oxide. This oxide was identified by mass spectrometric and velocity analysis techniques as Cl_2O_3. A survey of possible higher oxides, which have been postulated as possible chlorine sinks in the stratosphere, was also carried out. Only low concentrations chlorine-oxygen species having molecular weights between those of Cl_2O_3 and Cl_2O_8 were detected in several chemical systems.

The rate of formation of ClO dimer was measured as a function of temperature and pressure. Measurements were made of both the decay of ClO and the formation of the dimer. By comparing these rates it was determined that virtually all of the ClO was converted to the dimer under stratospheric conditions, and that the other ClO reactions were not important under these conditions. The rate constants for formation of the dimer from ClO were measured at temperatures from -20 to -70 $^{\circ}C$ and pressures from 30 to 120 torr.

---

*This work was supported by NASA under Contract No. NASW-4371

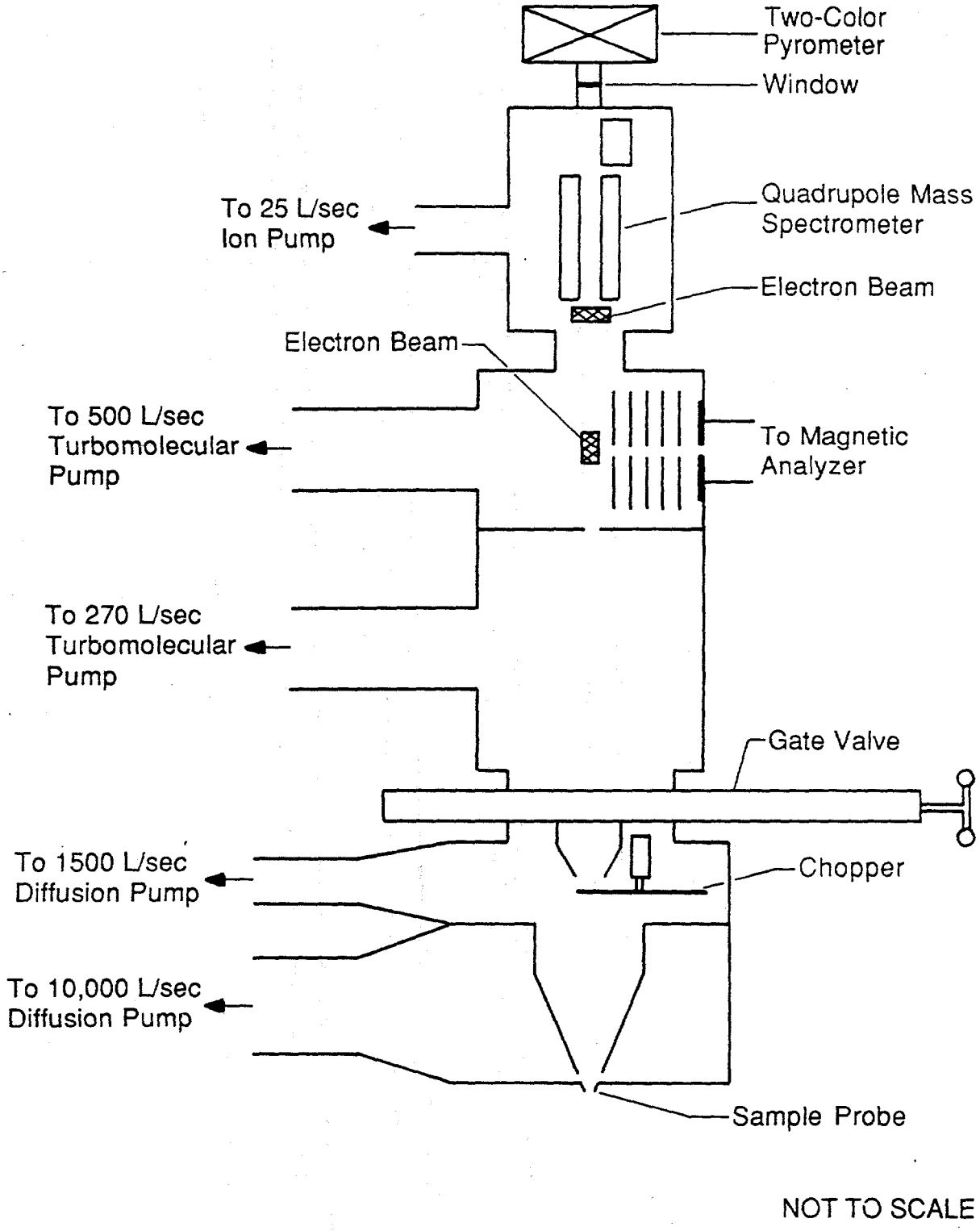

Figure 1. Schematic of the molecular beam sampling system used with the high resolution magnetic and quadrupole spectrometers.

MRI-A\R9316.FR

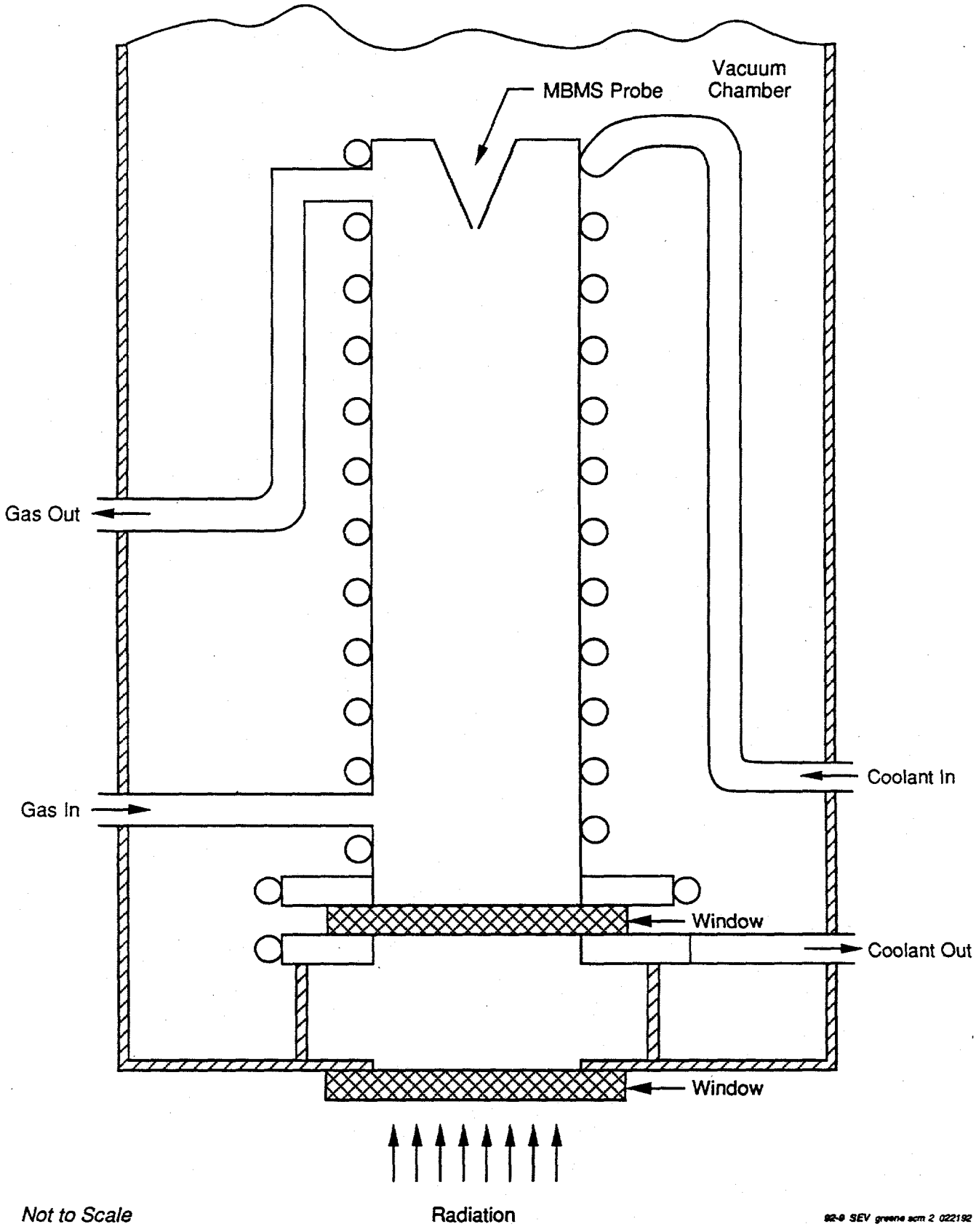

Figure 2. The isothermal photochemical flow reactor.

Molecular Beam, Mass Spectrometric Sampling in Hazardous Waste Destruction

Mark R. Nimlos, Thomas A. Milne, J. Thomas McKinnon*

National Renewable Energy Laboratory
1617 Cole Boulevard
Golden, Colorado 80401

*Department of Chemical Engineering and Petroleum Refining
Colorado School of Mines
Golden, Colorado 80401

Presented at *Specialist Workshop on Applications of Free-Jet Molecular Beam, Mass Spectrometric Sampling*, October 12, 1994

Abstract
This paper describes the study of the destruction of hazardous waste in which compounds and conditions are screened and byproducts are detected with a molecular beam, mass spectrometer (MBMS). Three destruction techniques were investigated as potential solar-driven processes: catalytic steam reforming, photothermal oxidation, and photocatalytic oxidation. These processes were investigated using an MBMS-equipped with a triple quadrupole mass spectrometer. The MS/MS capabilities of this instrument were used to characterize products using daughter and parent ion scanning modes.

With catalytic steam reforming, a number of chlorinated and nonchlorinated compounds were screened for their susceptibility to destruction using a rhodium catalyst. The destruction efficiencies were high at modest temperatures (700 - 900°C) and few byproducts were measured.

Choloronaphthalene was studied as a model compound for the photothermal oxidation processes. An enhancement in the destruction rate in air was measured by adding near UV light (300-340 nm). Byproducts were measured and the identities of these products were determined using daughter ion MS/MS spectrometry.

The gas-phase photocatalytic oxidation of trichloroethylene (TCE) was measured at ambient temperatures using the MBMS. The identity of these byproducts was determined using parent ion MS/MS spectrometry.

Introduction

Hazardous waste destruction is an important national issue, and the discovery of new destruction techniques is needed to help lessen the economic impact of compliance with increasingly stringent environmental

requirements. New destruction techniques are needed to help clean soil and water that has been contaminated through past excesses, but they are also needed to control the emissions of organic wastes in existing and future processes. The new processes that are developed must be economically viable and must not produce dangerous byproducts.

NREL and Sandia National Laboratories have been investigating the use of solar energy to destroy hazardous waste. Three gas phase processes have been considered:

1) Catalytic steam reforming, where the catalyst is radiantly heated by a high-flux solar furnace.

2) Photothermal oxidation, where the visible and infrared portions of the solar spectrum heat the gas and the ultraviolet portion causes the organic compounds to breakdown photochemically.

3) Photocatalytic oxidation, where the ultraviolet portion of the solar spectrum excites a semiconductor catalyst which breaks down organic compounds in the air. We have used the MBMS to investigate these three process for their effectiveness in destroying organic wastes in air.

The MBMS has some unique features that make it useful for studying hazardous waste destruction. Direct sampling from hot, corrosive environments is possible as is real-time measurements of the starting material and products. These attributes allow for rapid screening of reaction conditions for processes being investigated. Furthermore, the triple quadrupole mass spectrometer used in this study enhances the ability to identify byproducts.

Experimental

Figure 1 presents a schematic diagram of the MBMS used in this study. More detailed descriptions are available elsewhere [1-2] and only a brief description will be provided here. Gases are sampled through a small orifice into a vacuum chamber, where a molecular beam is formed and sent into a quadrupole mass spectrometer. The mass spectrometer is controlled by a personal computer program (Teknivent), which also collects the data. Collisionally induced dissociation (CID) mass spectra are obtained by bleeding a collision gas into the second quadrupole.

The reactor for the catalytic steam reforming experiments is shown in detail in reference 1. Liquid organic is injected with a syringe pump into a flow of 80% steam and 20% helium. This mixture is passed through a heated tube reactor containing the catalyst, rhodium, on a alumina monolith. The reactant and product gases were monitored using the MBMS.

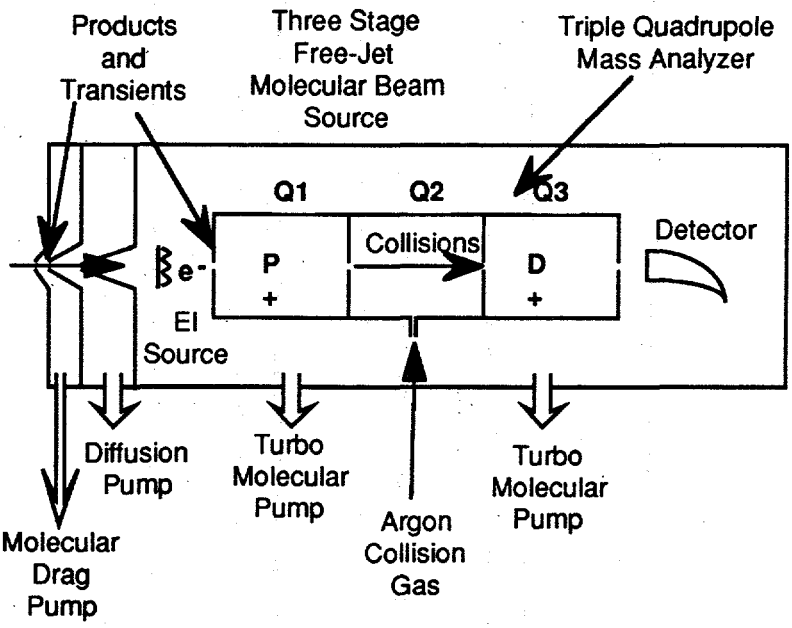

Figure 1. Schematic Diagram of MBMS.

Photothermal experiments were also conducted in a heated tube reactor, with windows on either end to allow transmission of ultraviolet light from a laser[3]. This arrangement allowed independent variation of the heat and the ultraviolet flux. A mixture of 20% oxygen and 80% helium was spiked with chloronaphthalene and passed through the reactor. Products were measured with and without the ultraviolet light using the MBMS, and were identified by comparing the measured daughter ions CID spectra to those of standards.

For photocatalytic oxidation experiments, the gas passed through a monolith support that was illuminated with an ultraviolet laser [2]. The support was a reticulated alumina frit (Hi-Tech), coated with titanium dioxide. The gas was a mixture of oxygen (20%) and helium (80%) that was spiked with TCE. Destruction levels and the formation of products were measured using the MBMS. The products were identified using CID spectrometry.

Results and Discussion

Catalytic Steam Reforming

Twelve chlorinated and nonchlorinated compounds were screened to determine if the rhodium catalyst was effective in destroying these compounds [1]. We found that in all cases the starting compound was destroyed and that there were no detectable byproducts. The only products measured were carbon monoxide. Because of the large dynamic range of the instrument, we measured destruction levels grater than 99.9999% for some compounds.

Photothermal Oxidation of Chloronaphthalene

Chloronaphthalene was used as a model compound in this study because its absorption spectrum [4] overlaps with the terrestrial spectrum of solar emission [5]. Experiments were conducted at a variety of temperatures and residence times to measure the effect of intense ultraviolet light upon the thermal oxidation. We found that the ultraviolet light significantly enhanced the destruction rate of chloronaphthalene and that this effect was increased with increasing temperatures. By comparing the destruction in synthetic air (80% helium/20% oxygen) and in pure helium, we determined that the enhancement resulted from a chain reaction mechanism.

Table II. Reaction intermediates observed in the photothermal and thermal destruction of chloronaphthalene.

Mass	Identification*	
78	Benzene	C_6H_6
94	Phenol	C_6H_5OH
102	Ethynylbenzene	C_8H_6
104	Styrene	C_8H_8
105,106	Benzaldehydde	C_7H_6O
112	Chlorobenzene	C_6H_5Cl
116	Indene	C_9H_8
118	Ethynylphenol	C_8H_5OH
128	Naphthalene	$C_{10}H_8$
130	Indenone	C_9H_6O
136	Chloroethynylbenzene	C_8H_7Cl
139,140	Chlorobenzaldehyde	C_7H_5OCl
144	Naphthol	$C_{10}H_7OH$
146	Indenedione	$C_9H_2O_2$
152	Chloroethynylphenol	C_8H_4ClOH
158	Naphthaquinone	$C_{10}H_6O_2$
152	Chloroindenone	C_9H_5ClO

*Product identifications are based upon CID results.

Using the MBMS, we also measured and identified products from the thermal and photothermal oxidation of chloronaphthalene. We found that there was no significant difference in the products from these two processes. Table II lists the products that were identified by their CID fragmentation patterns. When possible, the fragmentation spectra were compared to the spectra of standards.

Heterogeneous Photocatalytic Oxidation of Trichloroethylene

Trichloroethylene (TCE) is a common contaminant of groundwater [6]. Gas-phase photocatalytic oxidation (PCO) could be used to control the emissions from an air stripper, which are commonly used to remove TCE from contaminated aquifers. Cost studies have shown that this may be a viable alternative to conventional control technologies [7].

The gas-phase photocatalytic oxidation of TCE was originally studied by Dibble and Raupp [8], who showed that PCO could be effective for destroying this compound. They measured the kinetics of this destruction process using a packed bed [9] and detected no intermediates.

In our experiments, we confirmed Dibble and Raupp's high rate of conversion of TCE, but we also measured a number of byproducts [2]. Using the MBMS, we detected dichloroacetyl chloride (DCAC), phosgene and molecular chlorine, in addition to the desired products, hydrogen chloride and carbon dioxide. The identity of DCAC and phosgene were confirmed using CID mass spectrometry.

Table III Comparison of Products from Homogeneous Cl-Atom Initiated Oxidation and Photocatalytic Oxidation

	Results from Homogeneous Reaction [10]		Results From Photocatalytic Oxidation	
Compound	Products (percent)	Quantum Yield	Products	Quantum Yield
Cl_2CCCl_2	CCl_3CClO(75), $COCl_2$(25)	300	CCl_3CClO, $COCl_2$	0.08
$ClHCCCl_2$	CCl_2HCClO(90), $COCl_2$	200	CCl_2HCClO, $COCl_2$	0.22
Cl_2CCH_2	$CH_2ClCClO$(98), $COCl_2$	172	$CH_2ClCClO$, $COCl_2$	0.14
c-ClHCCClH	CHClO(71), $COCl_2$(3)	21.5	CCl_2HCClO, $COCl_2$	0.06
t-ClHCCClH	CHClO(71), $COCl_2$(3)	21.5	CCl_2HCClO, $COCl_2$	0.05

In addition to TCE, the products from the photocatalytic oxidation of 1,2-dichloroethylene, 1,1-dichloroethylene and percholoroethylene were measured. Like TCE, these compounds produced phosgene and acetyl chlorides. These products are similar to what is found in homogeneous reactions initiated by chlorine atoms [10]. In these homogeneous studies, a

chain reaction mechanism was invoked. Table III compares the results of the homogeneous experiments with heterogeneous PCO. This strongly suggests that the PCO reaction is driven by a chlorine atom chain reaction mechanism, which accounts for the high rates of conversion measured.

Conclusions

The MBMS has been demonstrated to be very effective to study new waste destruction techniques. Its direct sampling capabilities allow the measurement of destruction levels in reactive environments and detection of byproducts that are often difficult to detect using other analytical techniques. When the MBMS is combined with MS/MS capabilities, it is indeed a very powerful technique for these studies.

References

1. Nimlos, M. R. ; Milne, T. A. *Environ. Sci. and Technol.* **1992,** *26,* 545-552.

2. Nimlos, M. R.; Jacoby, W. A.; Blake, D. M.; Milne, T. A. *Environ. Sci. and Technol.* **1993,** *27,* 732-740.

3. Nimlos, M. R.; Milne, T. A.; McKinnon, J. T. *Environ. Sci. and Technol.* **1994,** *28,* 816-822.

4. Mackey, M. M.S. Thesis, University of Colorado at Boulder, 1992.

5. Hulstrom, R; Bird. R; Riordan, L. *Solar Cells* **1985,** *15,* 365-391.

6. Dyksen, J. E.; Hess, A. F. *J.-Am. Water Works Assoc.* **1983,** 394-403.

7. Turchi, C. S.; Wolfrum, E. J.; Nimlos, M. R. presented at *Fith Annual; Symposium on Emerging Technologies in Hazardous Waste Management,* I&EC Special Symposium, American Chemical Society, Atlanta, GA, September 27-29, 1993.

8. Dibble, L. A.; Raupp, G. B., *Proc. of Arizona Hydrological Society,* First Annual Symposium, Sept. 16-17, Pheonix AZ. **1988,** 221-229

9. Dibble, L. A.; Raupp, G. B., *Catalysis Lett.* **1990,** *4,* 345-354.

10. Sanhueza, E.; Hisatsune, I. C.; Heiklen, J. *Chem. Rev.* **1976,** *76,* 801-826

CONTINUOUS DIESEL EMISSIONS SPECIATION WITH A TRANSPORTABLE MBMS SYSTEM

Matthew A. Ratcliff, David A. Gratson and Thomas A. Milne
National Renewable Energy Laboratory

Michael S. Graboski
Colorado Institute for Fuels and
High Altitude Engine Research

Scott W. Cowley
Colorado School of Mines

INTRODUCTION

A unique transportable molecular beam mass spectrometer (TMBMS) has been developed at the National Renewable Energy Laboratory (NREL) to extend the virtues of MBMS analysis to new applications beyond the traditional laboratory scope and scale. The TMBMS is based on a three stage vacuum system; the transport capability dictated the minimization of size, weight and required utilities. The instrument has demonstrated a dynamic range of at least 10^6 and a limit of detection of 0.5 ppmv, depending on the species and system being investigated. The instrument has been successfully used as a continuous emissions monitor and a chemical process monitor.

Continuous, near real-time speciation of diesel exhaust demonstrated the potential of MBMS analysis in the field of emissions monitoring. Controlled steady state and transient tests were conducted with conventional diesel and soybean derived methyl-ester biodiesel fuels. The emissions differences between the two fuels were readily apparent, with the diesel fuel producing higher concentrations of hydrocarbon species. It was statistically demonstrated that many unburned diesel fuel hydrocarbons can be reproducibly detected and followed under a variety of steady state conditions. Carbon dioxide, water, nitric oxide and sulfur dioxide were monitored simultaneously with the unburned hydrocarbons. The transient testing demonstrated the instruments ability to follow changes, on the seconds time scale, of multiple combustion products as a function of engine speed, load and throttle position.

EXPERIMENTAL

Instrument Design and Construction

The TMBMS was designed to accommodate two types of mass spectrometers, a quadrupole or a time-of-flight (TOF). However, the TOF was not employed in the research described here. The TMBMS system is shown in the quadrupole configuration in Figure 1. It is comprised of four major components: 1) a mobile cart which carries the vacuum chambers, pumping systems and mass spectrometers. This cart weighs approximately 400 kg and will fit through a 102 cm (40 inch) door. 2) A mobile relay rack for the mass spectrometer electronics, 3) a cart-mounted computer for data acquisition and processing and 4) a mobile recirculating chiller to cool the turbo pumps. The total system weight is approximately 600 kg, the only utility requirement is electrical power: 60 A, 208 V, 3-phase.

A plan view drawing of the TMBMS in the quadrupole configuration is shown in Figure 2. The total distance from the sampling orifice to the ionization region in stage 3 is 27 cm (10.6 inch). Free-jet expansion of gas/vapors through the sampling orifice (typically 0.25 - 0.75 mm diameter) occurs in the first stage (ST1). The gas initially expands to a pressure of approximately 2×10^{-2} torr using an orifice size of 0.5 mm and room temperature air. The entrance to stage 2 is an

electroformed nickel skimmer (typically 1.0-1.2 mm diameter), mounted on a translation stage which allows easy adjustment of the orifice-to-skimmer distance over a range of 7-24 mm. Stage 2 (ST2) pressure is typically 5 x 10^{-5} torr. Stage 3 (ST3) is pumped to approximately 6 x 10^{-7} torr.

Pumps

A key component which allowed the system's relatively compact size, is the Osaka TS440 molecular drag pump (MDP) for the ST1 pumping system. The TS440 weighs 60 kg with a height and diameter of 502 mm (19.76 inch) and 296 mm (11.65 inch), respectively. This pump operates over a wider, and more importantly, higher range of vacuum pressures than conventional diffusion or turbomolecular pumps. The use of this pump makes the system amenable to continuous, direct sampling from sources having pressures as high as 5 atm. The throughput for the MDP is rated at 13 torr-L/s at 50 mtorr and 43 torr-L/s at 750 mtorr (maximum operating pressure). The MDP is backed by a Galileo DO45 two stage rotary vane pump with a rated pumping speed of 17 L/s (36 cfm).

ST2 is pumped by a Balzers TPU 520 turbomolecular pump with a nitrogen pumping speed of 500 L/s. The TPU 520 weighs 13 kg and is backed by a Leybold D16B two stage rotary vane pump. Stage 3 is pumped by a Balzers TPU 240 turbomolecular pump with a nitrogen pumping speed of 230 L/s. This pump weighs 9 kg and is backed by a Welch 8910 two stage rotary vane pump.

Vacuum Chambers

The TMBMS vacuum chambers were fabricated from stainless steel. The cubic design for ST2 was chosen for its versatility in accommodating either a quadrupole or TOF mass spectrometer and for the compactness it gives to the overall system. The separate ST1 chamber added 133 mm (5.25 inch) to the length of the system, but this allows the choice of either mass spectrometer system to be installed onto ST2. When using the quadrupole mass spectrometer, it is mounted axially with respect to the molecular beam, on the back face of the cube (see Figure 2). The stage 2 turbo pump is then mounted orthogonally to the beam path.

The stage 1 vacuum chamber had conflicting design requirements that 1) the molecular beam flight distance to the mass spectrometer be minimized, and 2) the area of the tubing connection to the MDP be kept as large as possible to prevent pumping losses. The best compromise was achieved by specifying that the vertical tubing, connecting ST1 to the MDP, be fabricated with an oval cross section of 7.6 cm x 17.8 cm (3.0 inch x 7.0 inch). The front face of ST1 accommodates a copper or stainless steel sampling orifice plate which seals to ST1 with an o-ring.

The quadrupole ST3 chamber was designed for an Extrel mass spectrometer, in an orientation axial to the molecular beam. Thus it mounts on the rear face of the ST2 cube parallel to the ST1 mounting face. The Extrel mass spectrometer is inserted and sealed to the rotatable flange at the rear of the ST3 chamber. The ST3 isolation valve at the small end of the cone section, is a simple slide valve retaining a captured o-ring. A manual linear actuating rod extends through the interior of ST2 and protrudes through the side ASA 11 blank-off flange via an o-ring sealed feed-through.

Quadrupole Mass Spectrometer

Ions are detected by an Extrel model EXM750 quadrupole mass spectrometer that mounts on the rear flange of stage 3. The mass spectrometer system includes an axial electron impact ionizer, 16.9 mm (5/8 inch) diameter mass filter quadrupole rods, a counting analog electron multiplier,

C50 control electronics, and a 1.2MHz 300W power supply. This equipment gives the TMBMS a mass range of 1-750 atomic mass units (amu), with unit mass resolution. Chemical events can be followed on the 10's of milliseconds to seconds time scale with this system. Data acquisition is accomplished by a Teknivent Vector II system, which is designed for use with the Extrel mass spectrometer. The system has 16-bit A/D and D/A conversion, a GPIB computer interface and an auto-range analog mass spectrometer control board. The system operates with a 486, OS/2 based computer which allows on-line data processing.

Sampling Probe and Interface Design

The sample line/interface (SLI) between the TMBMS and the diesel exhaust system is shown in Figure 3. The raw exhaust sample was taken immediately downstream of the turbocharger. The sample line was constructed from 12.2 m (40 ft) of 6.4 mm (0.25 inch) stainless steel tubing in five equal sections. Each section was wrapped with a 2.4 m (8 ft) length of 13 mm (0.5 inch) wide Samox heat tape. Fiberfrax ceramic insulation was wrapped around the heat traced sections and secured by aluminum foil adhesive tape.

The SLI was divided into four independently temperature controlled, heated zones. The first 2.4 meter section of the sample line (exhaust sample probe end) and the interface were two of these temperature control zones. During initial testing it was determined that a SLI temperature of 300°C was the best trade-off to minimize secondary reactions of the exhaust vapors and to minimize the formation of water clusters. The average calculated velocity was 4.4 m/s, which equates to a SLI residence time of about 3 seconds.

The sampling interface was machined from stainless steel, which was sealed to a copper free-jet sampling orifice plate by a silicone o-ring. The interface was provided with taps for a pressure gauge and thermocouple. The diesel exhaust sample was pulled through the heated SLI, past the sampling orifice, by a 5 L/min Metal Bellows pump (Model MB118) located downstream of the interface. The flow rate was monitored by a rotameter located downstream of the pump on its positive pressure side.

Engine, Dynamometer and Fuels

The engine used for emissions testing was a new 1992 Detroit Diesel 6V92. It was connected to a GE electric dynamometer and controlled by a Digalog system. The engine testing protocol began by changing the engine oil and filter to minimize dissolved fuel contributions to the exhaust emissions. This was especially important when switching fuels to avoid inaccurate results due to fuel carry-over. For the same reasons, the fuel system was drained and refilled with the test fuel and the engine operated for at least one hour to purge the system of old fuel and stabilize the oil composition.

Figure 4 shows the 14 eV mass spectrum of the diesel fuel (D2) obtained with the TMBMS by flashing the fuel in a tube furnace at 400°C in a flow of helium to prevent combustion. The major species observed are the alkylated naphthalenes, for example methylnaphthalene (m/z = 142), C_2- naphthalenes (either dimethyl or ethyl, m/z = 156), and C_3-naphthalenes (m/z = 170). Olefins and paraffins are also represented by compounds such as tetradecene/tetradecane (C_{14} , m/z = 196, 198 respectively), pentadecene/pentadecane (C_{15}, m/z = 210, 212 respectively, and cetene/cetane (C_{16}, m/z = 224, 226 respectively). The relative concentrations between the different classes of compounds can not be inferred from the parent ions in the mass spectrum because of the different stabilities of these ions. The paraffinic ions formed in the mass spectrometer readily fragment giving rise to the classic hydrocarbon fragment ions 57, 71 and 85, whereas the naphthalenic parent ions do not contribute significantly to these fragments.

Figure 5 is the 14 eV mass spectrum of the soybean methyl ester biodiesel (BD) fuel, obtained in the same fashion as the D2 fuel spectrum. The soybean oil from which this fuel is derived is a mixture of C_{18} unsaturated triglycerides. The principal methyl esters that comprise the fuel are methyl-9,12-octadecadienoate ($\geq$50%) and methyl-9-octadecenoate ($\geq$30%) [1]. These compounds have the molecular ions 294 and 296 respectively. Both molecules show signals due to the loss of methanol at 264 and 262 respectively, characteristic for methyl alkenoates. The remaining peaks are due to other fragment ions.

Concurrent with the TMBMS sampling, data from the existing on-line analyzers were collected for NOx, CO_2 , CO and total hydrocarbons (HC's).

RESULTS

Diesel Fuel Emissions from Steady State Tests

The first phase of steady state emissions testing was performed with commercial (not low sulfur) diesel fuel (D2). The test cycle was designed to map the engine operating conditions from idle to peak torque, to maximum speed, with five discrete speed/load steady state steps. The design ensured the statistical significance of the data. The cycle was run in triplicate for each fuel, holding the engine at each load and speed for 4 minutes. In each test, every speed/load point was sampled twice, except the 1200 rpm/400 ftlb point which was sampled three times. These features allowed for statistical analysis of the data to determine the variance within a test cycle as well as between replicate tests. The test design also permitted the observation of any hysteresis in the sampling because the speed/load points were approached from different directions in the speed/load space.

All the following results were obtained with an ionization energy of 22 eV. This parameter was determined to be the optimum trade-off between the need to maximize signal-to-noise and the need to minimize fragmentation of the molecular ions. It should be noted that in all the mass spectra shown, the mass spectrometer was programmed to skip the masses 1-13, 28, 32 and 33, to avoid overloading the detector. Consequently, neither the major air components N_2 (28) and O_2 (32), nor carbon monoxide (also 28) are seen.

Figure 6 shows the mass spectrum of the diesel exhaust sampled at 650 rpm/400 ft-lb of torque, at three different signal intensity scales. This test point is an inefficient lugging condition for the engine and produces a lot of particulates. Many masses that were seen in the mass spectrum of the raw diesel fuel (Figure 4), can be seen in Figure 6C. These signals are assumed to be principally due to unburned fuel molecules, such as the alkylated naphthalenes (eg. m/z = 156) and paraffins (eg. m/z = 226). Although partially oxidized species with the same molecular weights as some of the unburned fuel components, have been found by other researchers in diesel particulate extracts, they were very low in concentration [2]. Other researchers have found unburned fuel molecules to be major constituents of diesel hydrocarbon emissions [3].

The statistically determined detection limit was 622 ion counts (cts; the vertical axis scale in the mass spectra) for the diesel fuel exhaust spectra [4]. Thus, cetane (m/z = 226, intensity = 630 cts) is the lowest concentration species that can be claimed to have been detected in this sample. This claim is with $\geq$95% confidence that the signal is neither due to a random fluctuation of the background, nor that it was mistaken for noise (probability of Types 1 and 2 Errors are both $\leq$5%). Species with signal intensities as low as 480 cts can also claim to have been detected. However, 50% of the time these signals would not be detected due to the normal indeterminate error of the measurement (Type 2 Error). Sulfur dioxide (m/z = 64) is detected as well as nitric oxide (m/z = 30, Figure 6B). At full scale, Figure 6A shows the water (m/z = 18) and carbon

dioxide (m/z = 44) produced by combustion along with argon (m/z = 40) from the combustion air.

For a comparison, Figure 7 shows the mass spectrum from the inlet air that the diesel engine was breathing, at the same signal intensity scales as Figure 6. The argon signal (m/z = 40) can be considered an internal reference in air, and its intensity is comparable in both figures. The most obvious differences are the expected dramatic changes in carbon dioxide and water concentrations. The nitric oxide concentration at m/z = 30 is much lower in the air spectrum and part of this mass intensity is due to the 10 ppmv concentration of $^{15}N^{15}N$ isotope of nitrogen in air. Sulfur dioxide and hydrocarbons are not detected.

As the engine speed and load were increased to 2050 rpm/700 ft-lb, combustion efficiency increased, based on the average intensity of hydrocarbons observed (see Figure 8C). An interesting difference, perhaps unique to this operating condition, is the intensity increase of mass 98. This could be the molecular ion from sulfuric acid and has been observed by MBMS from dilute and concentrated sulfuric acid at 300°C. Part of the intensity of this peak in Figure 8C may be due to hydrocarbon fragment ions that have the same mass. However, the signal intensity ratios of mass 98 to other known hydrocarbon fragment ion signals (such as 57 and 97) was higher for this operating condition than any other investigated. This suggests that mass 98 is due to something other than hydrocarbon fragment ions.

For reasons that are presently uncertain, it appears that some fraction of the SO_2 produced during combustion, is being converted to sulfuric acid at the high speed and load condition. The exhaust gas temperature was highest at this condition, approximately 320°C, and sulfuric acid formation is known to be catalyzed by NO [5]. Although this SO_2 conversion hypothesis has not yet been independently confirmed, sulfuric acid contributes to particulate emissions, consequently, determination of the operating conditions that form it should be of interest to engine manufacturers.

Biodiesel Fuel Emissions from Steady State Tests

Predictably, no SO_2 emissions were detected because the biodiesel is essentially sulfur free. Most noteworthy are the substantially lower emissions of hydrocarbons compared to D2 fuel. The dilution tunnel measurements of hydrocarbons with a conventional flame ionization detector (FID) showed that under all operating conditions investigated, the emissions of hydrocarbons from biodiesel were approximately half the amount from diesel fuel. Thus the TMBMS raw gas and FID diluted gas measurements are qualitatively similar. Examination of the two fuel emissions by comparison of their NO^+/Ar^+ ratios, revealed that the biodiesel produces more nitric oxide than the diesel fuel. These results were confirmed by the dilution tunnel measurements of NOx using a chemiluminescence instrument which indicated 18-33% higher NOx emissions from the biodiesel. These observations are consistent with results reported by other researchers [6].

Figure 9 is the mass spectrum of the biodiesel exhaust emissions at 650 rpm/400 ft-lb torque, complimentary to the diesel fuel exhaust emission data presented in Figure 6. At this test point for biodiesel, the emissions of unburned hydrocarbons are dramatically lower than for diesel fuel. In Figure 9C there is little evidence of the molecular ions corresponding to the major fuel components (m/z = 294 and 296) that were obvious in the BD fuel mass spectrum (Figure 5). The major fuel fragment ion observed is m/z = 55, butylene (C_4H_7+), which is typical from olefinic hydrocarbons. Mass 82 is probably a fuel fragment ion that also appears in Figure 5. The peak at m/z = 78 is above the statistically determined detection limit for the biodiesel fuel tests (586 cts); it is probably benzene. Because the biodiesel fuel was comprised primarily of

two olefinic methyl esters, any aromatic compounds detected in the exhaust, such as benzene, would have to come from a pyro-synthetic process in the engine.

Diesel Fuel Emissions from Transient Tests

We also used the TMBMS to monitor exhaust emissions produced during the standard 20 minute federal driving cycle for heavy-duty diesels (DCS4). The mass scanning frequency was one 14-300 amu spectrum every 5.2 seconds (again skipping masses 28, 32 and 33). This rate could be increased by a factor of ten, however, for the purposes of these tests, maximizing signal-to-noise was deemed more important than scan speed.

Figure 10 is a 10 minute portion of the DCS4 test, tracing the emission of nitric oxide as a function of test time. The actual engine test cycle ran from 4.8 to 24.8 minutes and two different types of backgrounds were acquired before and after the actual test cycle. The TMBMS/SLI was able to follow the various transient events with a response time of approximately 11 s between an engine transient event and detection by the mass spectrometer. The time resolution of the TMBMS/SLI system was quite acceptable, despite the long sample line length and relatively slow scan rate of the mass spectrometer. For example, the four adjacent NO concentration minima shown in Figure 10 (the second point is annotated 1800 rpm, -100 ft-lb, 0% Throttle), each coincides with a momentary coasting (motoring) of the engine. The NO signal traces the engine load very closely, as one would expect, with the highest concentrations of NO correlating to the highest engine loads. The lowest NO concentrations arose under coasting conditions and intermediate loads produced intermediate concentrations. The data acquired were quite reproducible based on the triplicate runs made.

Another example of the time resolving capability of the TMBMS during transient engine events, was its ability to discriminate between cranking and the instant of ignition (see the cranking and ignition points indicated in Figure 10). Figure 11 shows the mass spectrum obtained at 4.8 minutes, during engine cranking at the beginning of the test cycle. At that instant, combustion had not begun, however, the burst of fuel that came through the engine is substantially different than the raw fuel spectrum shown in Figure 4.

The mass spectrum of this event is dominated by the large "hump", centered around mass 200, that masks the region where most of the diesel fuel mass signals would be. This may be particulate induced noise resulting from a diesel soot particle entering the mass spectrometer. Particulate induced noise was an uncommon phenomena during the testing, but what is more interesting are the polynuclear aromatic compounds that accompany the noise. For example, very strong signals for anthracene/phenanthrene (m/z = 178), methyl-anthracene/phenanthrene (m/z = 192) and pyrene (m/z = 202) were observed. These compounds were only minor components in the diesel fuel used, and yet here their signal strength is five to ten times greater than was typically observed during the emissions tests. One explanation for this result is that during cranking, the fuel injected into the engine, while not ignited, was nevertheless subjected to high temperatures (from the highly compressed air) which initiated pyrolytic reactions. Some of these reactions include dealkylation and ring formation. The polynuclear aromatics observed are expected products of the ring forming reactions. Although not clear at the scale of this figure, methane (m/z = 16) was higher in concentration than was otherwise typically observed, presumably the result of dealkylation of the numerous methylnaphthalenes that comprised the diesel fuel.

CONCLUSIONS

A transportable molecular beam mass spectrometer was designed and constructed. This instrument represents a significant improvement in the state-of-the-art of molecular beam systems. It employs molecular drag and turbomolecular pumps to minimize the size, weight and utility requirements of the system. The TMBMS was employed as an on-line, near real-time monitor for speciating the exhaust emissions arising from the combustion of diesel and biodiesel fuels in a Detroit Diesel engine. The emission differences between the two fuels were readily apparent, with the diesel fuel emitting higher concentrations of hydrocarbon species. It was demonstrated that many unburned diesel fuel hydrocarbons can be reproducibly detected and followed under a variety of steady state conditions. Carbon dioxide, water, nitric oxide and sulfur dioxide were monitored simultaneously.

In conventional on-line dilution tunnel measurements of hydrocarbons with a flame ionization detector (FID), the components are not speciated. They also are not fully accounted for, giving an inaccurate integrated measure of the total hydrocarbons; ie. the conventional hydrocarbon measure is operationally defined, as the sum of compounds which are volatile enough to not condense at the dilution tunnel temperature. Many diesel fuel and all lube oil compounds have dew points above typical dilution tunnel temperatures. These condensible species adsorb onto the particulates, and are filtered out before the gas sample reaches the FID.

Conventional off-line analyses for speciating the exhaust hydrocarbons involves double dilution of the exhaust and filtration at 52°C. The collected particulates are then solvent extracted, fractionated and analyzed. Evidently, this method is not efficient for collecting compounds in the diesel fuel vapor pressure range, as demonstrated by Rhead and Trier [3]. Their total exhaust solvent scrubbing apparatus (TESSA) collects significantly more comprehensive hydrocarbon samples than the EPA filtration method. The diesel hydrocarbons detected in the exhaust by the TMBMS, in near real-time, more closely resemble those collected by TESSA.

Biodiesel fuel was found to combust more completely than diesel, however nitric oxide emissions increased. Mass 78 was detected in the biodiesel exhaust under some steady state conditions, this probably is benzene, formed during the combustion process in localized air starved regions.

The detection limit of the TMBMS/SLI system was statistically determined and found to be low enough to be useful for the detection of unburned hydrocarbons from diesel fuel and the inorganic emissions. The transient testing demonstrates the instrument's ability to track engine excursions occurring on the seconds time scale, while acquiring comprehensive emissions data.

ACKNOWLEDGMENTS

The authors gratefully acknowledge the technical assistance of David Dayton, Carolyn Elam, Patrick Fiedler, James Macomber, Bruce Sater and Jeff Ross. The Program Manager was Richard Bain. This work was supported by the U.S. Department of Energy, Office of Energy Efficiency and Renewable Energy, under the Solar Thermal and Biomass Power Program directed by Gary Burch.

REFERENCES

1) Kirk-Othmer *Encyclopedia of Chemical Technology*, J. Wiley & Sons, **1978**, N.Y., 3rd Edition, Vol. 4, p. 836.

2) Bayona, J. M.; Markides, K. E.; Lee, M. L. "Characterization of Polar Polycyclic Aromatic Compounds in a Heavy-Duty Diesel Exhaust Particulate by Capillary Column Gas Chromatography and High Resolution Mass Spectrometry", *Environ. Sci. Technol.* **1988**, Vol. 22, No. 12, pp. 1440-7.

3) Rhead, M. M.; Trier, C. J. "Fuel Residues and Organic Combustion Products in Diesel Exhaust Emissions: Sources, Sampling and Analysis", *Trends in Analytical Chemistry*, **1992**, Vol. 11, No. 7, pp. 255-9.

4) Ratcliff, M. A. "Design and Construction of a Transportable Molecular Beam Mass Spectrometer and its Application to the Analysis of Diesel Exhaust", Masters Thesis, Colorado School of Mines, **1994**, No. T-4606, pp. 45-47.

5) Cotton, F. A. and Wilkinson, G. *Advanced Inorganic Chemistry*, J. Wiley &Sons, **1972**, N.Y., 3rd Edition, p. 180.

6) Schumacher, L. G.; Hires, W. G.; Borgelt, S. C. "Fueling a Diesel Engine with Methyl-Ester Soybean Oil", *Proceedings from the ASAE Liquid Fuels from Renewable Resources Conference*. Nashville, Tennessee, Dec. 14-15, **1992**, pp. 124-31.

Figure 1. Transportable Molecular Beam Mass Spectrometer

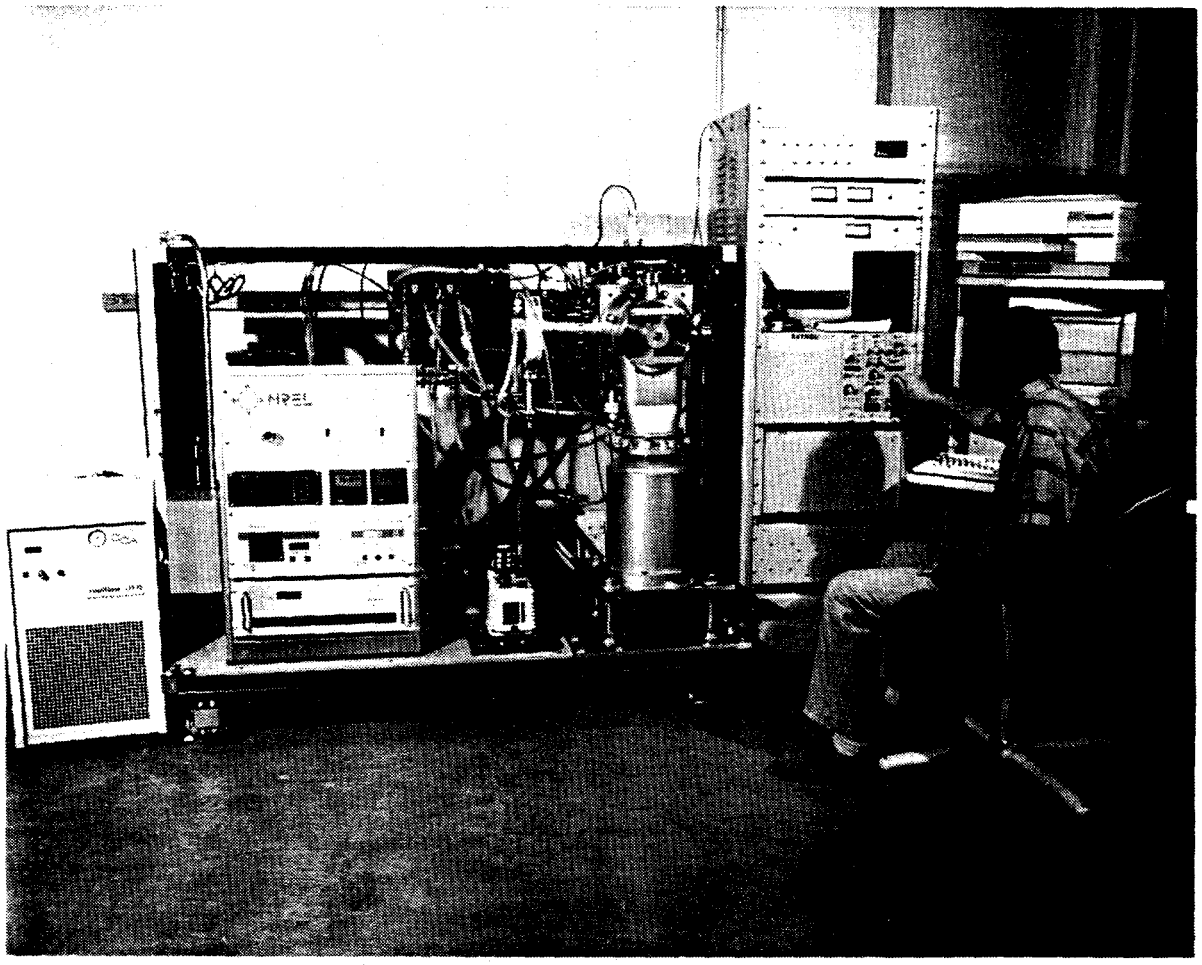

Figure 2. Plan View of the TMBMS in the Quadrupole Configuration

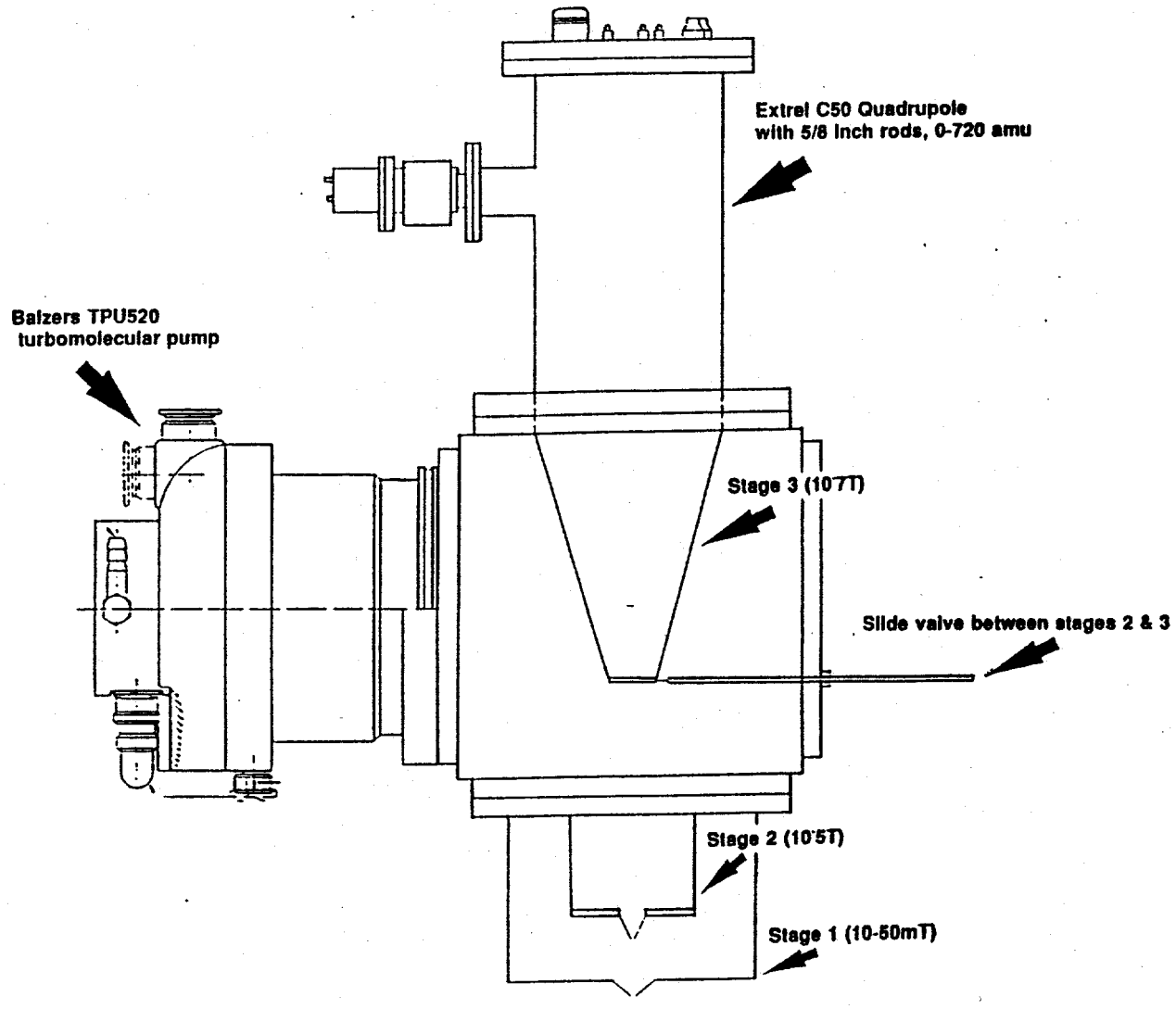

Figure 3. Heated Sample Line and Interface (SLI)

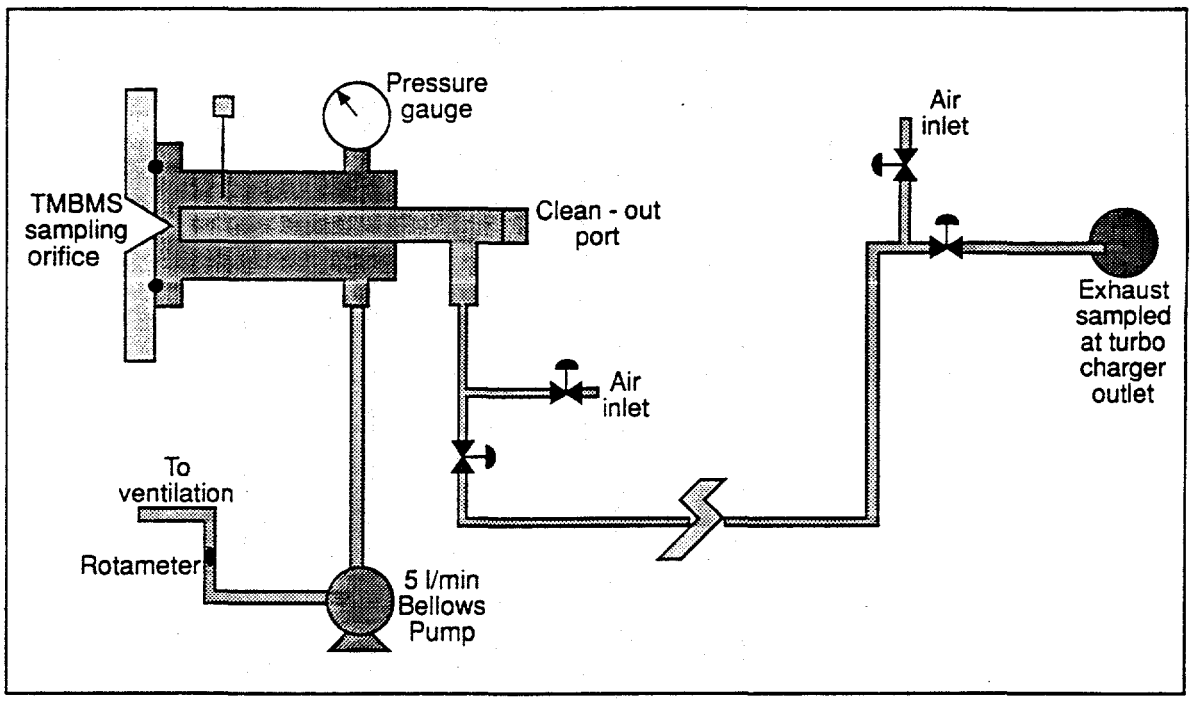

Figure 4. Diesel Fuel

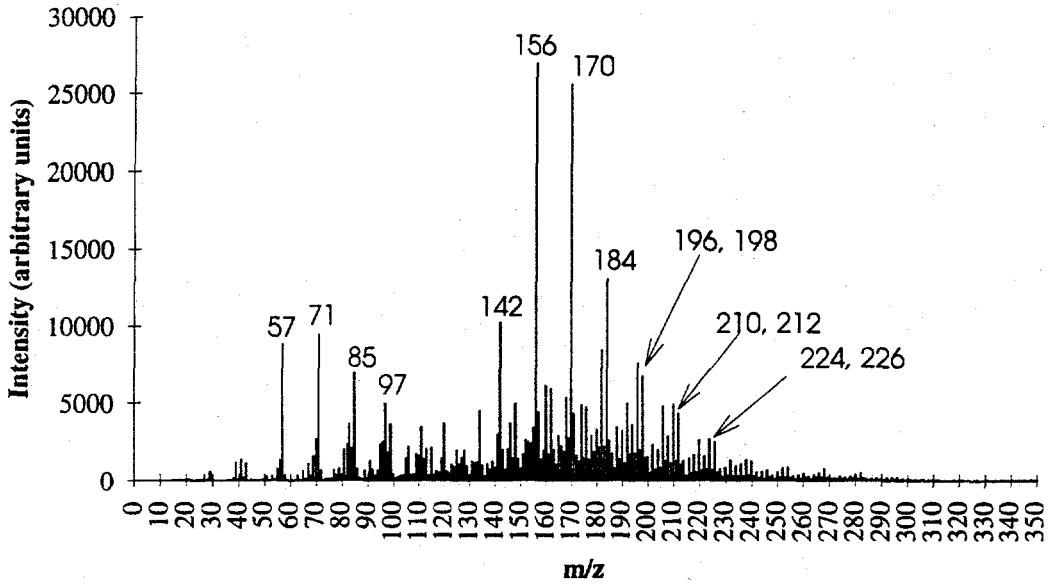

Figure 5. Biodiesel Fuel

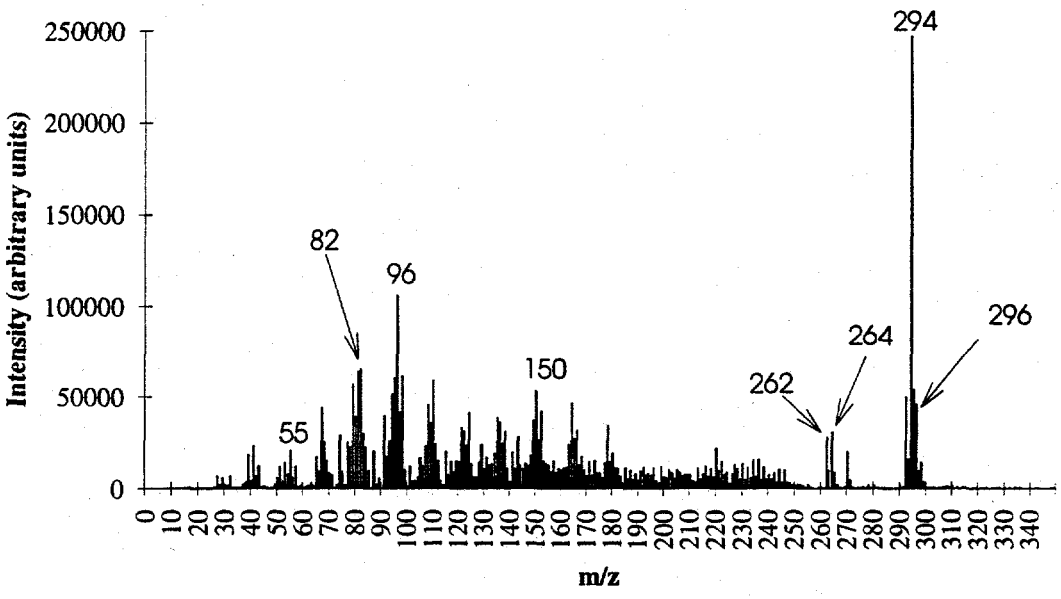

Figure 6. Diesel Fuel Emissions: 650 rpm, 400 ft-lb

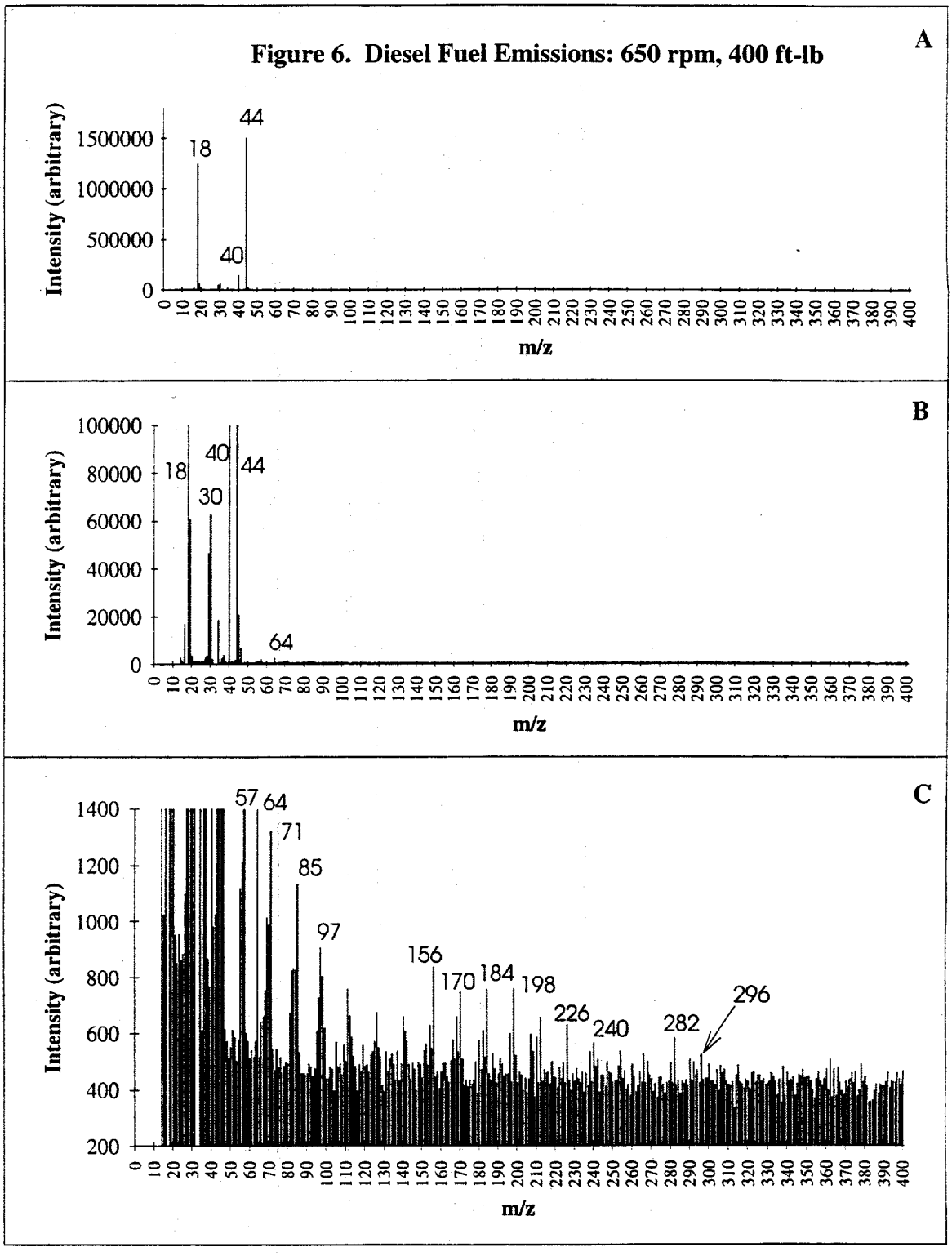

Figure 7. Inlet Air for Diesel Fuel Tests

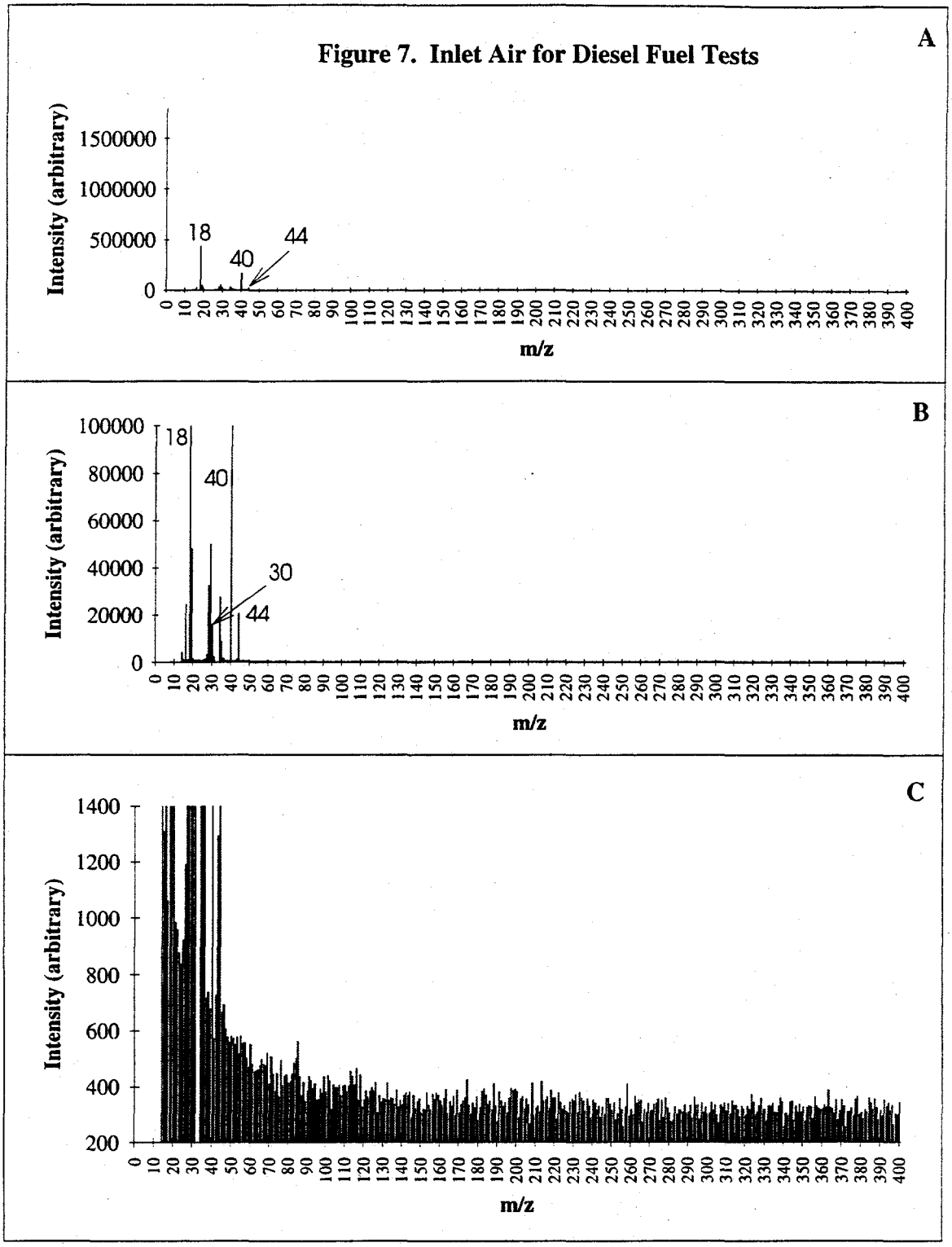

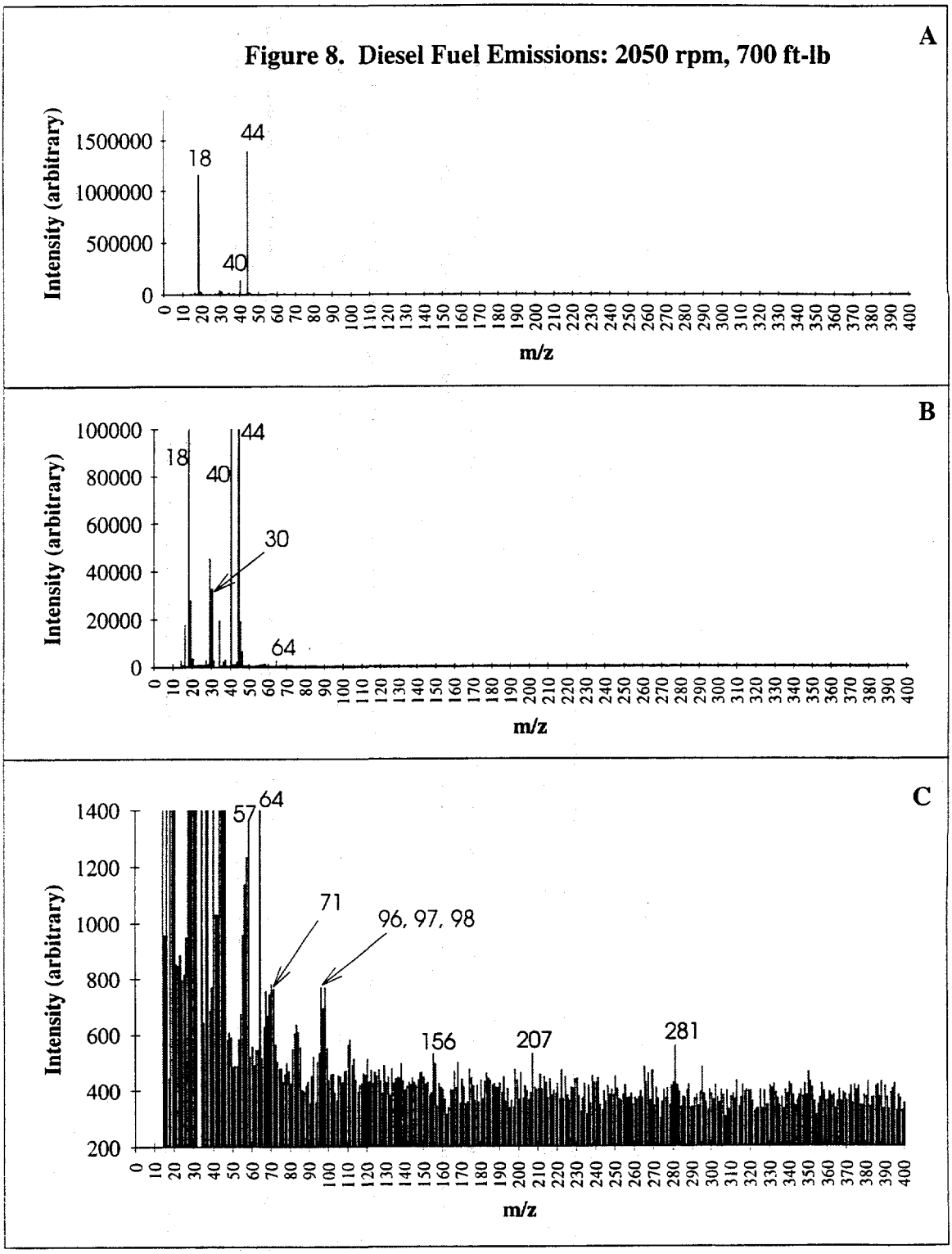
A
Figure 8. Diesel Fuel Emissions: 2050 rpm, 700 ft-lb
Intensity (arbitrary)
1500000
1000000
500000
0
18
44
40
0 10 20 30 40 50 60 70 80 90 100 110 120 130 140 150 160 170 180 190 200 210 220 230 240 250 260 270 280 290 300 310 320 330 340 350 360 370 380 390 400
m/z
B
Intensity (arbitrary)
100000
80000
60000
40000
20000
0
18
40
44
30
64
0 10 20 30 40 50 60 70 80 90 100 110 120 130 140 150 160 170 180 190 200 210 220 230 240 250 260 270 280 290 300 310 320 330 340 350 360 370 380 390 400
m/z
C
Intensity (arbitrary)
1400
1200
1000
800
600
400
200
57
64
71
96, 97, 98
156
207
281
0 10 20 30 40 50 60 70 80 90 100 110 120 130 140 150 160 170 180 190 200 210 220 230 240 250 260 270 280 290 300 310 320 330 340 350 360 370 380 390 400
m/z

Figure 9. Biodiesel Fuel Emissions: 650 rpm, 400 ft-lb

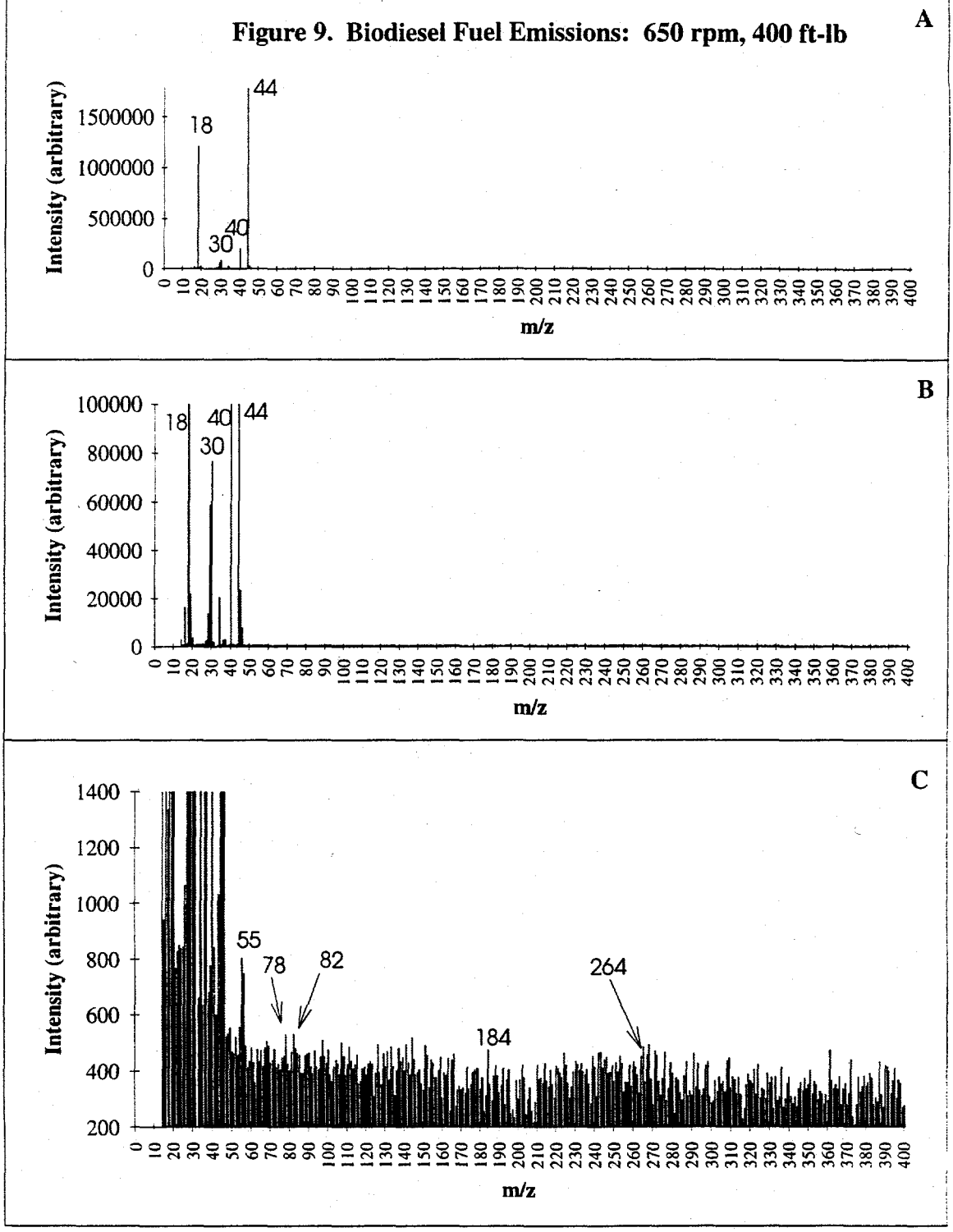

Figure 10. Nitric Oxide During Transient Testing (Diesel)

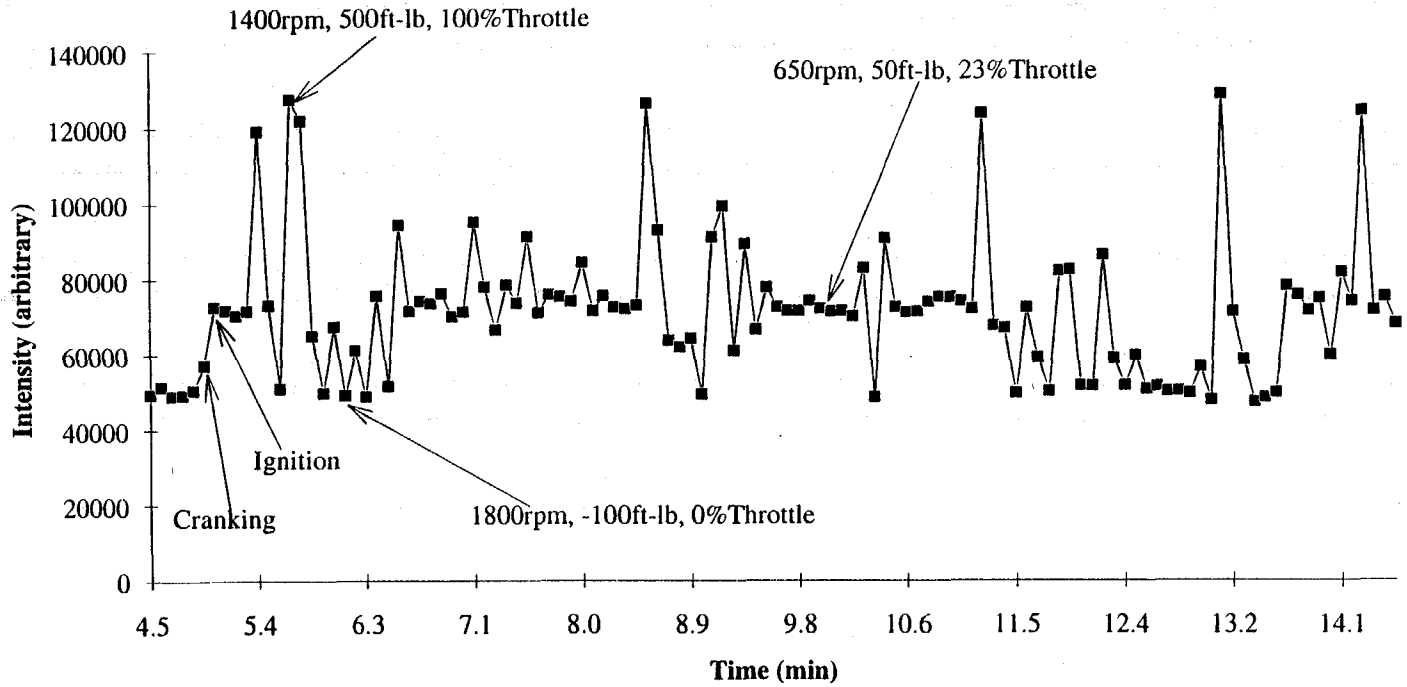

Figure 11. Polynuclear Aromatic Emissions During Engine Cranking

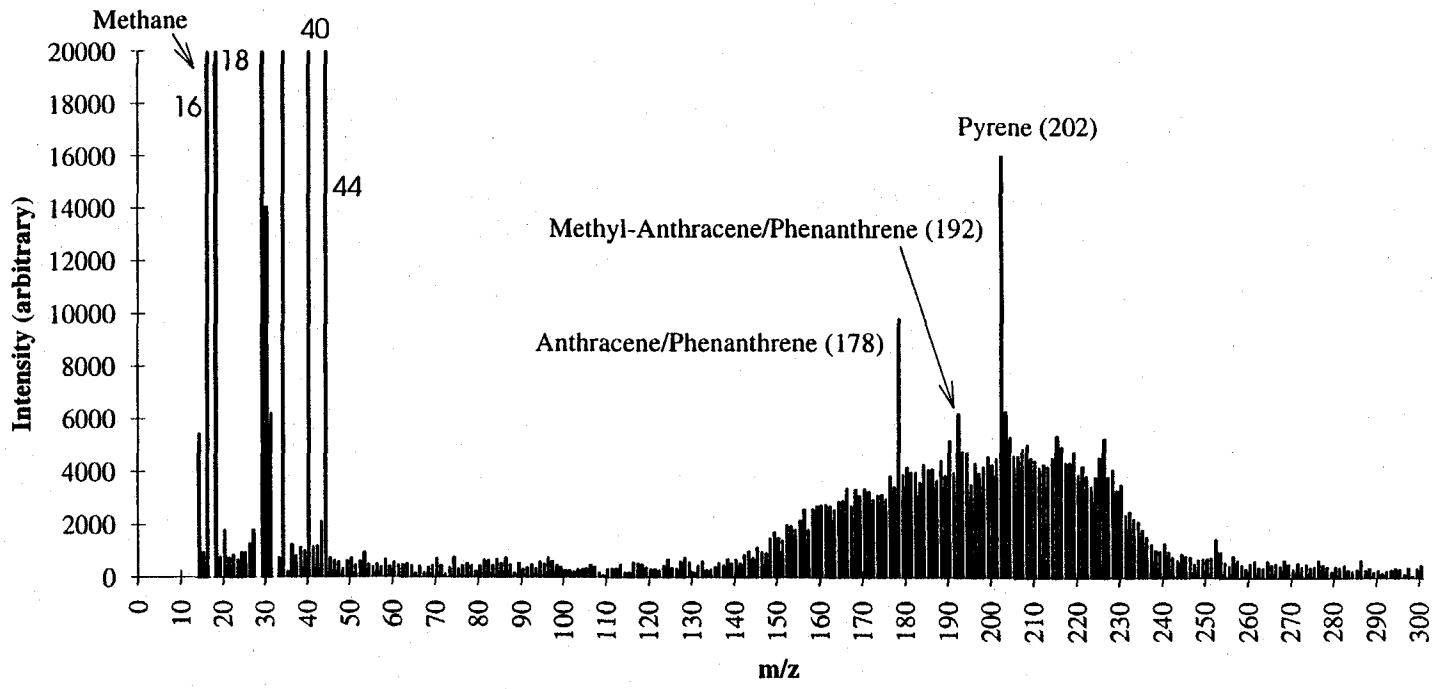

A Study of Sampling Phenomena in a Probe Nozzle for High Temperature MBMS.

Vasilii I. Smirnov
Ivanovo State University
UL Ermaka 39
153377 Ivanovo RUSSIA
e-mail svi@ivgu.ivanovo.su

1. Introduction

One imporatant and difficuilt problem of MBMS is sampling from high temperature systems containing condensable high temperature molecules, for example oxides and hydroxides of d- and f-elements [1]. Condensation in the orifice of a probe nozzle is one of the main difficulties in a practical mass sectrometric analisis of environments which contain highly volatile compounds. Due to condensation the concentrations of compounds in a probe may be changed, therefore the composition in a source may significantly differ from the composition in the mass spectrometric detector. The orifice of a nozzle is pluged in a short time if condensation on the surface of a nozzle is very intensive. Plugging significantly reduces the signal registration time and the sensitivity. There are many classes of important compounds which cannot be analized by MBMS due to these limitations. For example, oxides and hydroxides of d- and f- elements, play the main role in many application systems. To develope a nozzle with a low level of condensation in it, it is essential to understand the quantitative picture of the sampling phenomena - gas dynamic structure, chemical and energetic relaxation, kinetics of homogeneous and heterogeneous condensation etc. To define the state and the composition of a probe in a mass spectrometer ion source it is necessary to build a quantitative model which describes all prehistory of the gas probe from the starting point of acceleration in front of the nozzle to the range of a free molecular flow.

2. Visualization of a gas dynamic structures before a nozzle

The chemical relaxation and condensation are most intensive in front of the nozzle and in the nozzle channel. There is yet a reliable theory of the processes in these ranges although there are precise models which describe the processes in the range after nozzle [2-6]. To develope the models of a pre-nozzle range it is needed to continue the investigation of experimental constants which characterize the properties of a real systems. One important object of investigation is a flow field. If a flow field is known it is possible to describe the composition and temperature in every point of the flow. Therefore it is important to know the size and the form of a probe field tube in front of the nozzle.

2.1 Flow field

In this paper is described a method which allow us to visualize a gas dynamic structure in an atmospheric hydrocarbon flame in front of the nozzle orifice. This method is based on an investigation of the Rayleigh scattering of light in a gas flame. The hot tip of the nozzle was used as the source of light. A conical nozzle with Al-metallic base and Al_2O_3-ceramic covering is convenient for MBMS analisis of a high temperature environment, for example in the flames and transpiration reactors, but they are not appropriate to realize this visualization method. A hot ceramic spot on the tip of a

conical nozzle is too small to radiate intense enougt light. To solve this problem a special diaphragm nozzle was developed (Table 1):

Table 1. Geometric parameters of diaphragm nozzle

Orifice	0.08 - 0.1 mm
Ring central ceramic part	1.0 - 2.0 mm
Aluminium ring base	- 4.0 mm
Copper ring base	- 6.0 mm
Thickness of diaphram	- 0.1 mm

The bottom surface of a the aluminium diaphragm base was join to the copper water cooled cone via intermediate metallic layers.

A copper cone was joined to the vacuum chamber. In the walls of a chamber there were glass windows which allowed us to see an internal surface of the nozzle. External and internal surfaces of a nozzle and a gas dynamic structure in front of the nozzle can be invesigated by optical equipment using color filters and photo registration, optical monochromator, optical pyrometer, laser equipment, thermocouples etc.

The temperature of the hydrocarbon flames was within 2100 - 2800 K.

In the region in front of the diaphragm nozzle a distinctive mushroom structures was observed (figure 1, 2). It was very difficult to visually distinguish this structure from the flame background radiation. The optical spectrum of the flame in the range near the nozzle and far from the nozzle was investigated before the photo registration. Comparative analisis of these spectrums allows us to choose optical filters which suppress background radiation and increase the signal/noise ratio. The photo images were converted into computer form via scanner with a resolution of 300 dpi and 64Kbyte color palette. To increase the signal/noise ratio the computer graphic image was processed by special software.

The most probable cause of this observed phenomenon is the Rayleigh scattering of light radiation from the hot ceramic spot in the gas flame. In the region in front of the nozzle the temperature and density of gas are very different from one point to another, therefore the optical properties of the gas in the probe field tube are very different from the properties of a homogeneous gas in an undisturbed flame.

A special experiment was made to verify this explanation. A ceramic diaphram was changed to a copper diaphragm with same geometric parameters. The mushroom structures was not observed in the flames with a cold copper diaphragm nozzle.

In a high temperature flame this structure is bigger than in a low temperature flame. The axis size is approximately the same in all flames (1 - 1.5 mm), but a transversal size is changed from 3 mm in a low temperature flame to 5 mm in a high temperature flame.

2.2 Boundary layers

A Cu-seeded hydrocarbon flame was used to visualize the boundary layers on the surface of the nozzle used. In this flame there are two zones which are distinguished by colors. Radiation from a hot undisturbed region of the flame is yellow in contrast to cooler regions which are green, for

example from the tail of the flame. This color change is observed on the surface of a cold nozzle. The gas on the boundary layer is colder than inside the flame. To increase the contrast on the photo of the boundary layer structure a green optical filter was used to suppress background radiation. In a figure 3 is shown a typical boundary layer structure. The thickness of the layers was within 0.3 - 0.6 mm in different flames.

3. Surface temperature of nozzle

To mesure the surface temperatue of a ceramic covering on the tip of a nozzle the photopyrometric method was used. The photo sensitivity of the film was calibrated by a photometric standard lamp. Radiation coefficients of the ceramic covering was estimated in a standard oven cell with a standard thermocouple. The accuracy of this photometric method (150-200 K) is not high but sufficient to estimate the temperature field on the surface of the nozzle.

3 . Temperature field in a volume of a composite nozzle

A computer modele was used to define the temperature field in the volume of the nozzle. To calculate a the temperature field in a volume it is nesessary to know the temperature fields on all external surfaces of the nozzle. A conical nozzle has three main surfaces - external cone, internal cone and bottom ring. The temperature field on the external surface was obtained from the pyrometric measurements. The temperature of the bottom surface was equel to the temperature of cool water. In real conditions the density of the gase which contacted with internal surface of the nozzle was very low. Therefore the thermoexchange on this surface was low. This fact may be defined as an adiabatic boundary condition.

Because the nozzle has a symmetric axis it is possible to use a two-dimensional model of thermo-exhcange in a heterogeneous environment.

In figure 4 is shown the temperature field at the edge of the conical Al/Al_2O_3 nozzle with a 0.05 mm thickness covering. The big difference between the temperature gradients in metall and in ceramic is the most interesting results which might be obtained from analisis of this picture. This difference is caused by a big difference in a thermal conductivity of these materials.

4. Computer modeling of a chemical relaxation and condensation in a probe

There are many similar features in the kinetic models of a chemical relaxation and a homogeneous condensation [5-7]. Computer models show that these processes are most intensive in the range in front of the nozzle while the density of the probe gas is high. Moreover, the interval from the start poin of acceleration to a middle point of acceleration is most "critical" because the resident time in this region is much bigger than it is in the next region.

The biggest changes of composition occurs on the periphery of the mushroom region. In this region the path from the start point to the nozzle orifice is longest and the probability of interaction with the surface is high.

5. Discussion

The construction of a composite nozzle must satisfy two contradictory requirements:

1. To reduce the heterogeneous condesation and thermoexchange on the nozzle surface it is nessesary to increase the temperature of the nozzle edge. This requirement can be satisfied by using the nozzle with thick covering and a long edge.
2. The temperature of the edge must be lower than the temperature of ceramic destruction. This requirement can be satisfied by using a nozzle with a thin covering and a short edge.

A suitable geometry of a composite nozzle may be defined by computer modeling for a real gas system.

The condensation temperature of many important compounds is much higher than maximal permissible temperature for a nozzle covering, therefore they can not be analized by a composite nozzle. To overcome this limitation it is nessesary to sharply reduce the flow of the condensable compounds on the surface of the nozzle. In other words, it is nessesary to use a nozzle with active control of the flow field and the boundary layer structure.

One interesting way to solve this problem is to use a nozzle with active changeable geometry, which allows the realization of a poly-layer super sonic jet. Different layers of a jet may have various functions.

In high temperature MBMS an external layer may be used as a gas shield between a probe core and a solid nozzle body.

The influence of the probe nozzle on the analised system may be reduced if external layers are formated independently from the probe core. By varying the composition and the structure of the external layers it is possible to control the flow of the probe core. From this point of view the chanel of the active probe nozzle may be compared with a chanel of a transistor.

An active nozzle has interesting features which may be useful in many applications.

References

[1] Smirnov V.I., Belov P.V. Thermodynamic Analisis of Metalic Compounds in Flames by Mass Spectormetry of Super Sonic Molecular Beams, Ivanovo State Univ. Rept., Ivanovo, 1988.

[2] Rosen P. Potential Flow of Fluid into a Sampling Probe. John Hopkins Univ. Appl. Phys. Lab. Rept. CF - 2248, Silver Spring, Md. 1954.

[3] Knuth E.L. Direct-Sampling Studies of Combustion Processes, In: Engine Emissions: Polutant Formation and Measurement, G.S.Springer and D.J Patterson eds., p.319 - 363 (Plenum Publishing Co., 1973).

[4] Stern C.A., Kohl F.J., Fryburg T.C., Miller R.A. High Pressure Molecular Beam Mass Spectrometric Sampling of High Temperature Molecules. - In: Characterization of High Temperature Vapors and Gases, U.S.N.B.S, v.1, p.303 - 356.d

[5] Dulov V.G., Lukyanov G.A. Gas Dynamics of Flow Processes, Novosybirs, Nauka, 1984.

[6] Pirumov U.G, Roslakov G.S. Gas Dynamis of Nozzles, Moscow, Nauka, 1990.

[7] Avduyevsky V.S., Ashratov E.A., Ivanov A.V., Pirumov U.G. Gas Dynamics of Super Sonic Non Isobaric Jets, Moscow, Mashinostroyenie, 1989.

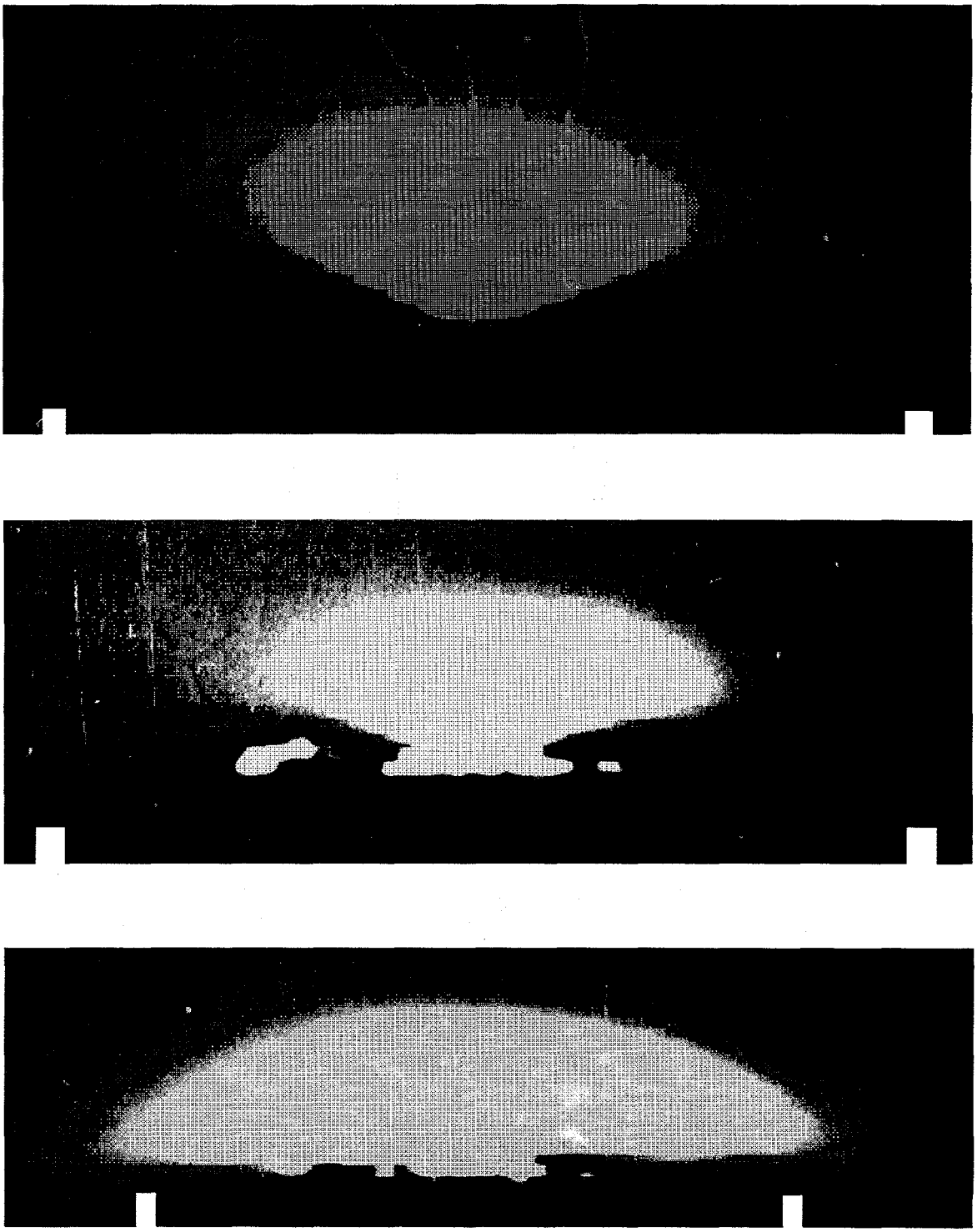

Figure 1. Visualization of a flow field in front of a nozzle.
Computer graphic images before processing by special software
The temperature of the flame: a) T = 2140 K b) T = 2302 K c) T = 2852 K .
Distance between lables 6 mm.

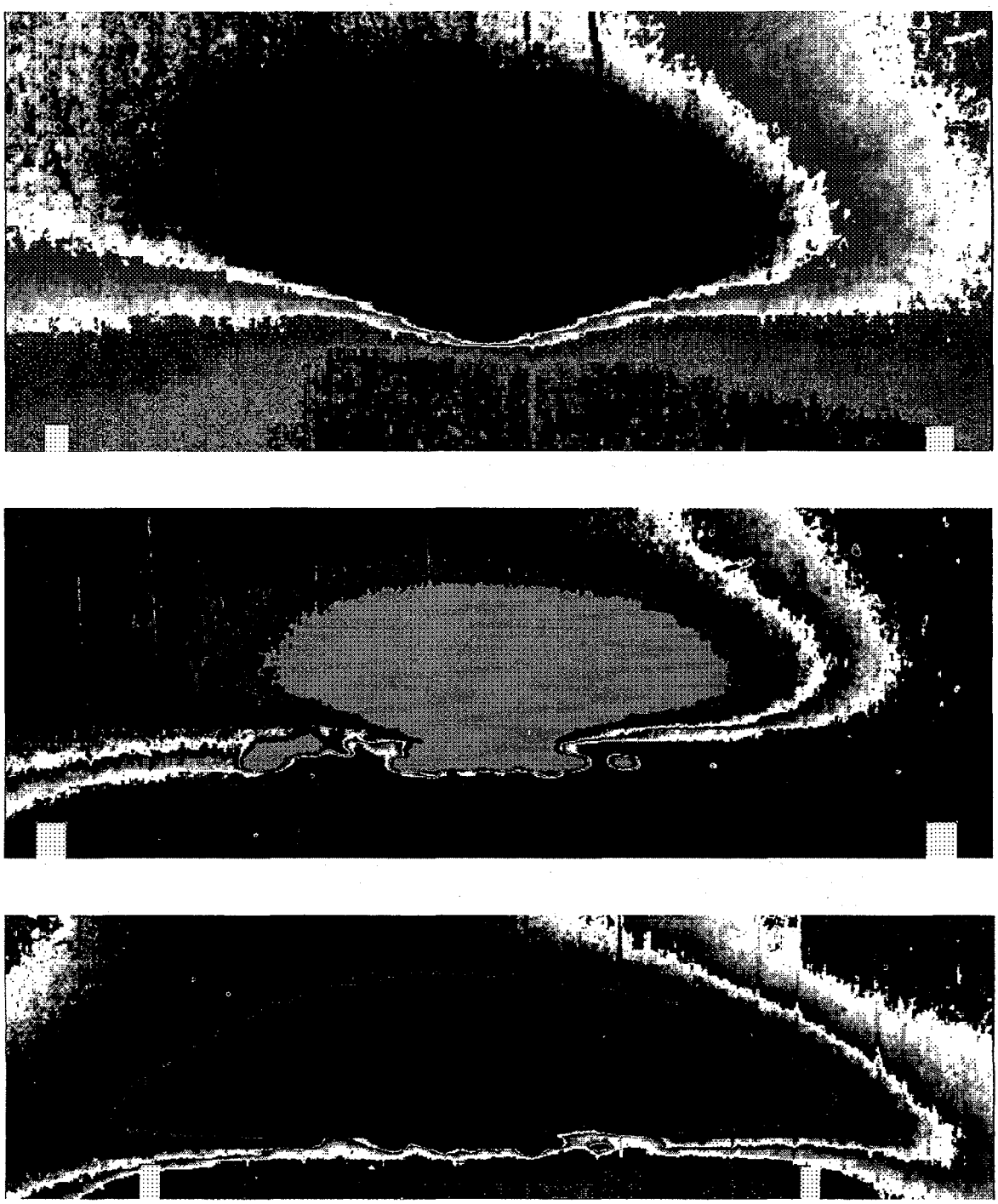

Figure 2. Visualization of a flow field in front of a nozzle.
Computer graphic images after processing by special software
The temperature of the flame: a) T = 2140 K b) T = 2302 K c) T = 2852 K .
Distance between lables 6 mm.

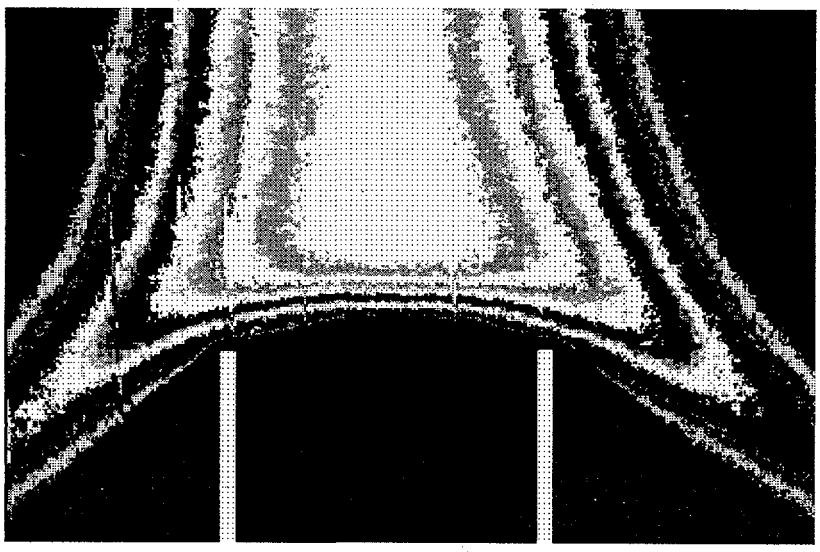

Figure 3. Visualization of a boundary layers in flame : T = 2302 K .

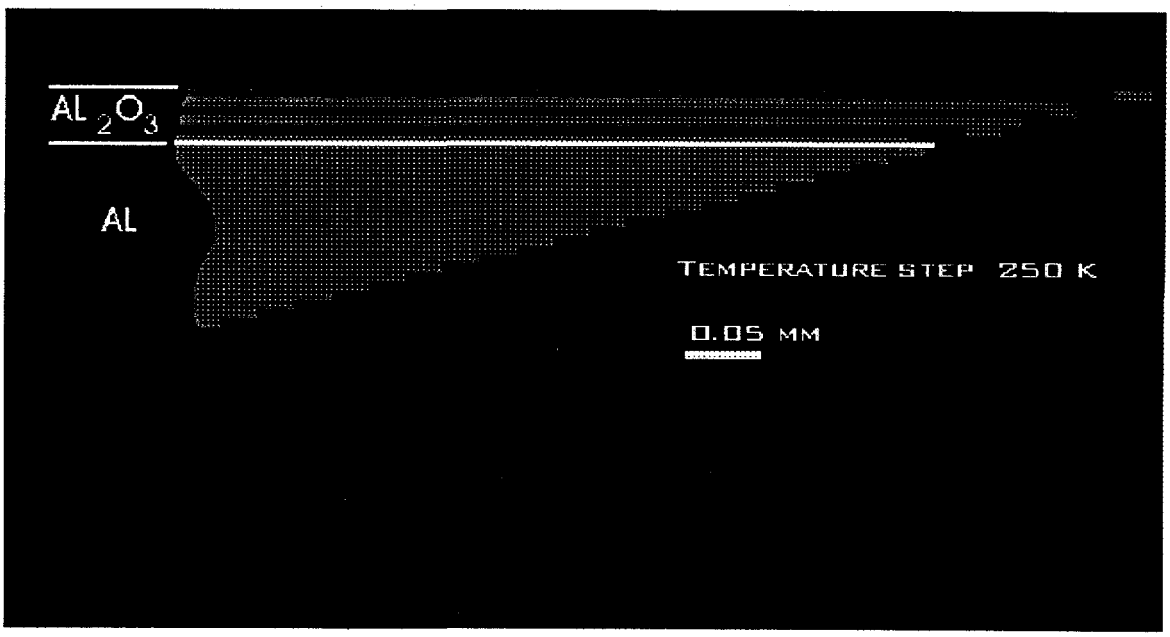

Figure 4. Temperature field in a volume of a composite nozzle.
Temperature step 250 K.

Quantitative Sampling with Free-Jet, Molecular Beam Mass Spectrometry

Dingneng Wang, Robert Meglen and Robert J. Evans
Process Research Branch
National Renewable Energy Laboratory
Golden, CO 80401

Introduction

The MBMS technique is used in our laboratory as a rapid screening tool to provide qualitative information about complex mixtures from high temperature processes. It has been widely applied to the various research projects to develop new technologies for energy conservation and renewable energy. They include thermochemical conversion of biomass, municipal solid waste, and other waste materials to fuels and high value chemicals, plastics recycling, solar destruction of hazardous wastes, employing pyrolysis, catalysis, and sometimes sunlight. It often becomes desirable to know product yields in order to assess the economics of the process under study. Unfortunately, when it comes to quantitative analysis, MBMS has not matched the performance of conventional methods such as GC or GC/MS. The main problem is the interference of peaks from overlapping fragment ions in multicomponent mixtures. In addition, when the MBMS is interfaced with a pyrolysis/catalysis reactor system, it becomes much more difficult to control the whole system well enough to achieve identical performance from one day to the other, or even within the same day.

In this paper we will review several approaches that we have used, with some degree of success, to estimate yields of individual products in a mixture from MBMS data. They are based on calibration methods using a single ion, multiple ions, or the whole mass spectrum. Among the approaches examined are linear least square regression, multiple linear regression (MLR) and principle component regression (PCR). We will discuss a few of the major problems encountered in using these methods. They have resulted in less accurate or sometimes erroneous measurements. Our most recent approach to obtaining quantitative analysis with MBMS at NREL is based on partial least squares (projections to latent structures, PLS). We will present some preliminary results and discuss future plans to realize this approach in practical applications and to generalize it to other environments where MBMS has advantages over conventional techniques.

Experimental

The molecular beam mass spectrometer (MBMS) used in this study was a home-built instrument equipped with an Extrel C-50 triple quadrupole mass analyzer. A schematic diagram is shown in Figure 1. Detailed descriptions of the instrument under current configuration and its predecessor single quadrupole mass spectrometric detector have been published in previous reports from this laboratory.[1] Some of the important features are mentioned here. Gases are extracted from a reactor at ambient to high temperatures and pressures through an orifice (90° conical, 0.27-0.75mm diameter) into a vacuum chamber (0.02 to 0.05 torr). The gases undergo a free-jet, supersonic expansion to form a molecular beam. This beam is further collimated through a skimmer (60° conical, 1-1.4 mm diameter), which has been made movable so that the orifice-to-skimmer distance can be adjusted between 2 to 40 mm. In this stage the pressure is maintained at low 10^{-5} torr range. It last passes through a third oricice into the third stage where gaseous molecules are ionized with an electron impact ionization source. Positive ions generated this way are detected by the triple quadrupole mass analyzer, which is kept at high vacuum (10^{-7} torr). The pumping hardware is listed

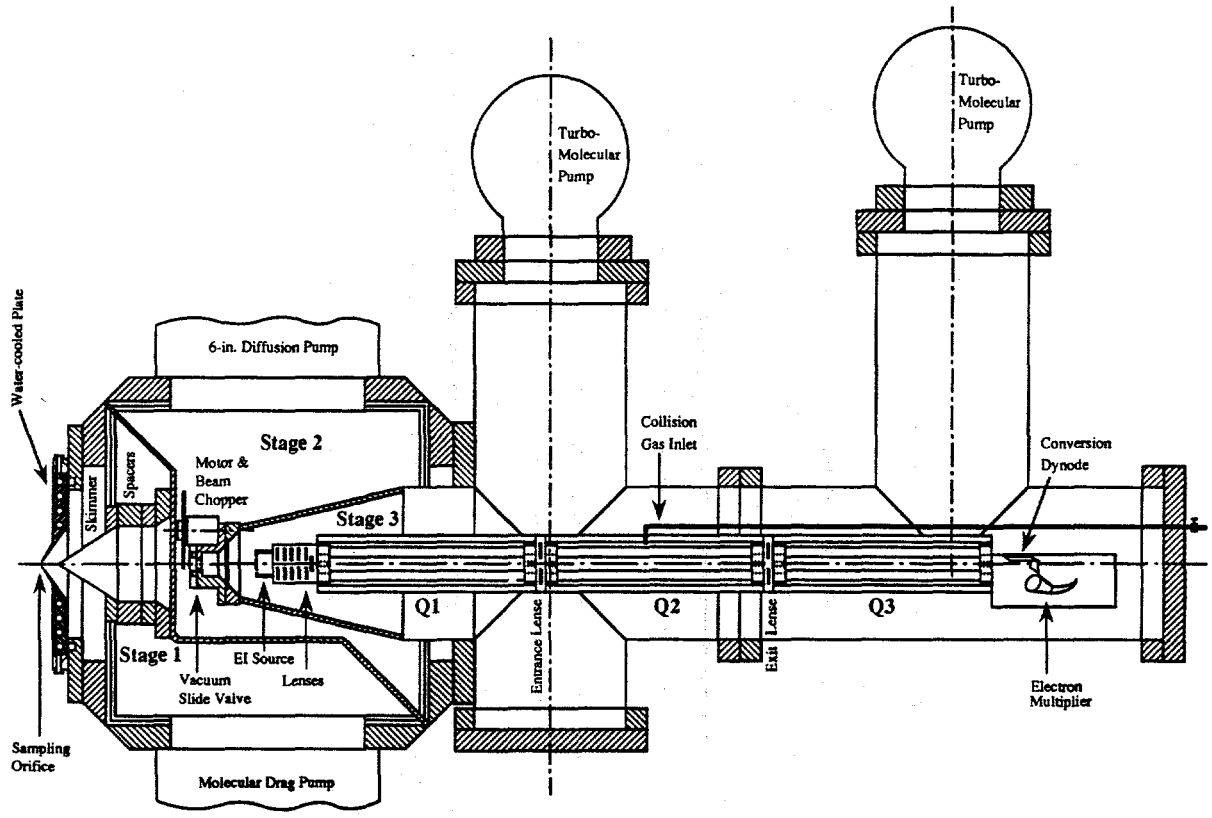

Figure 1. A cross-section view of the molecular beam triple quadrupole mass spectrometer.

Table 1. Pumping Hardware for the MBMS Instrument

Stage	Pressure	Turbo Pump	Backing Pump
1 Free-jet expansion	20-50 mT	Osaka TS440[a] 440 l/s	Galileo DO45 36 cfm
2 Collimation	10^{-5} T	Balzers TPU520[b] 500 l/s	Lebold D16B 11.7 cfm
3 MS Detector	10^{-7} T	Balzers TPU240 2×230 l/s	Welch 8910 3.1 cfm

a Replacing a 12" booster diffusion pump. b Replacing a 6" diffusion pump.

in Table 1. The mass analyzer has three quadrupoles with 5/8" rods and 1.2 MHz, 300 W RF power supplies. It has a mass range from 1 to 720 amu with scan rates up to 1000 amu·s^{-1}. It is operated in the analog mode with a conversion dynode and a Galileo Channeltron electron multiplier. The instrument is computer-controlled with an IBM-PC and a Teknivent Vector Two data system. Mass spectral data are acquired using a 16 bit A/D and D/A board with a GPIB computer interface and AutoRange analog MS control board. The Teknivent data system has a sampling rate of 30,000 s^{-1}.

MBMS is a universal, direct, real-time, rapid extractive sampling and detection system. It preserves reactive and condensible species by isolating these molecules at very low temperatures through free-jet expansion. The added MS/MS capability of the triple quadrupole mass analyzer in our instrument provides a tool to obtain more structural information on the products being formed.

The experimental setup varies with the process under study. Most reactors are made of quartz and used from ambient to high temperatures, sometimes with a catalyst bed or photon source. We use helium (3-5 SLM) to dilute product vapors to obtain a better molecular beam and to minimize cluster formation. Calibration gases are either metered into the reactor via mass flow controllers or

injected into a buffering flask with pressure-lock syringes. Liquid standards are injected into a vaporization zone of the reactor through syringe pump systems. Liquid samples are analyzed in a similar manner and solid samples are pyrolyzed in quartz boats. Argon is added as a standard to correct for fluctuations in instrument response and the molecular beam. The calibration experiments are performed at short residence times and below the temperature threshold for thermal decomposition.

Results and Discussion

We view quantitative analysis with MBMS as an expansion of the rapid screening role it has played in our study of new technologies. Our initial approach is to push, as far as we can, the limit of quantitative analysis potential of the MBMS. It became sometime desirable to know the composition of samples, not just fingerprints and also to obtain product yield and mass balance of a process to judge its feasibility. This information is usually required for an economic assessment of the process. However, we often deal with starting materials and products that are complex mixtures of many components, which makes it more difficult to quantify the individual component by MBMS due to interference of peaks from overlapping fragment ions. Furthermore, there are instrument fluctuations resulting from drifts in baseline or background, electronics, and the molecular beam is variable due to changes in its alignment, temperature and composition of gases (especially during the evolution of pyrolysis vapors), etc.

In order to obtain reliable quantitative results from MBMS data, we have to first investigate the influence of all the above factors on the final accuracy. Therefore, the question is not only how can we obtain quantitative information with MBMS, but also how reliable is it or how big are the errors. An accuracy of ±20% was satisfactory in the earlier days when we could obtain the results in a very short time on the micro-scale reactor and did not have the resources to scale up the process and perform conventional analysis on isolated products. These results are more useful when compared with each other on a relative scale. In the last few years, however, we needed to improve on the MBMS quantitative analysis for process optimization on the microscale to save time and expenses that are required for the scale up. The latest challenge for MBMS is to provide more accurate quantification of the desired products, even as accurate as conventional techniques. Our most recent results indicate that it has a good potential to produce accurate quantitative results from MBMS data.

Historic Approaches. We have employed the following methods of data analysis to extract quantitative or semi-quantitative information. The first is to normalize all mass spectra with respect to the total ion current (TIC). The TIC-normalized data that contain several hundred mass peaks are then reduced with principle component analysis, or factor analysis, to a few major components (or factors).[2] These new variables represent concentrations of groups of compounds and are used to separate the samples into categories. With some calibration, one can obtain concentrations of individual components by linear least square regression or principle component regression (PCR).

Another method is to normalize the averaged mass spectral data with respect to an internal standard such as argon and then to convert them into integrated areas and divide by the sample weight. Abundances of grouped peaks are summed as an indicator of yields for a particular class of products. However, one needs to be cautious about using these results, since they are not directly proportional to the total amount of the class of products. It is known that, molecules, even those of the same category, can have significantly different response factors (e.g., the relative response factors, for propylene, benzene, toluene, and naphthalene could be 1:2.5:5:20).

Single-Ion Approach. The simplest approach is to use one or more unique mass peaks as

a surrogate for the compound to be quantified, namely the single ion approach. It is best suited for systems with no or constant interference in calibration and prediction. For instance, water can be monitored at *m/z* 17 and 18, while hydrogen has its unique molecular ion at *m/z* 2. There is hardly any interference at these *m/z* values, especially at low ionization energies. The instrument response is calibrated by injecting the pure target compound or standards containing known amounts of it. One example of the this approach is shown in Figure 2. A single ion H_2^+ (*m/z 2*) was used for measuring the amount of hydrogen formed from catalytic steam reforming reactions of oxygenated model compounds. The two calibration lines for low and high flow rates of hydrogen were obtained by linear least square regression using the 'inverse' model (response on concentration), with excellent correlation coefficients of 0.99998 and 0.99976 for straight line fits through the origin. The results predicted for hydrogen produced from complete conversions of methanol and hydroxyacetaldehyde (eq. 1 and 2) were in good agreement (100±3%) with the stoichiometric value calculated according to equation 1 and 2. Alternatively, if there is no interference, the standard addition method may also be used. This method requires sequential additions of known amounts of a target compound to the sample being analyzed. The abundance of surrogate ions is plotted against amount added to obtain a straight line fit, which intersects with the amount axis at a value that corresponds to the negative of the amount present in the sample.

$$CH_3OH \xrightarrow[excess\ H_2O]{catalyst,\ \Delta} 3H_2 + CO_2 \qquad (1)$$

$$HOCH_2CHO \xrightarrow[excess\ H_2O]{catalyst,\ \Delta} 4H_2 + 2CO_2 \qquad (2)$$

Multiple Linear Regression. Applications of the single ion approach is limited to only a few special cases. In addition to water and hydrogen, stable aromatic compounds that do not undergo much fragmentation upon ionization with low energy electrons can also be measured this way. In one NREL project, we needed to measure the yield of olefins produced from catalytic upgrading of pyrolysis vapors from biomass and MSW.[3,4] There are significant overlaps in the mass spectra of aliphatic hydrocarbons. Most alkenes larger than butene produce abundant smaller alkene ions as fragments, formed by losing another neutral alkene molecule. Shown in Table 2 are partial mass spectra of aliphatic hydrocarbons from methane to hexene as well as CO and CO_2. The intense peak at m/z 42 (butene ion) in the mass spectra of both pentene and hexene clouds any quantitative results for mixtures that contain butene, pentene and hexene. In order to correct for these fragmentation interferences, we tried multiple linear regression (MLR) which is based on a multivariate additive mixture model. Two linear regressions are involved in this approach. First mass spectra are deconvoluted by MLR to obtain contributions of all constituents present in a mixture (eq. 3). Secondly contribution coefficients are regressed on concentrations in known mixtures to get response factors for each constituent (eq. 4).

$$\boldsymbol{y} = \boldsymbol{X}\boldsymbol{c} + \boldsymbol{e} \qquad (3)$$

$$\boldsymbol{c}_i = k_i \cdot \boldsymbol{f}_i + b_i \qquad (4a)$$

$$\log(\boldsymbol{c}_i) = k_i \cdot \log(\boldsymbol{f}_i) + b_i \qquad (4b)$$

where $\boldsymbol{y}$ = MS of a mixture; $\boldsymbol{X}$ = pure MS matrix, $\boldsymbol{c}$ = coefficients, $\boldsymbol{k}$ = response factors, $\boldsymbol{f}$ = flow

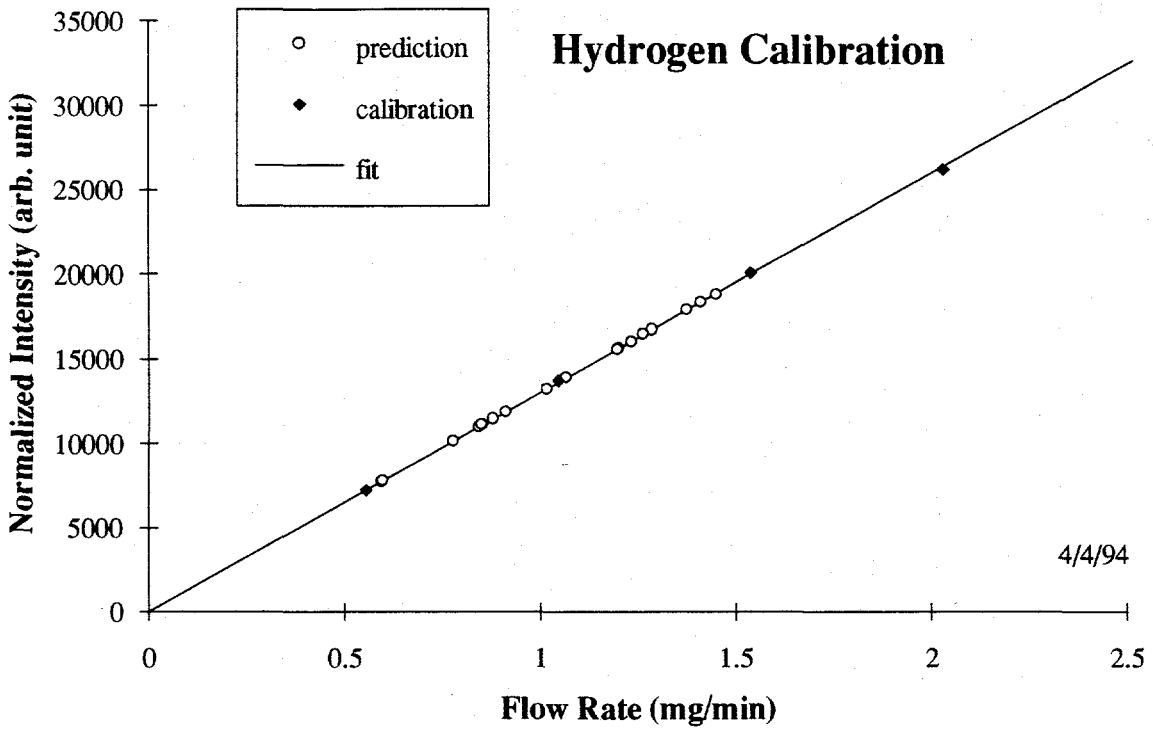

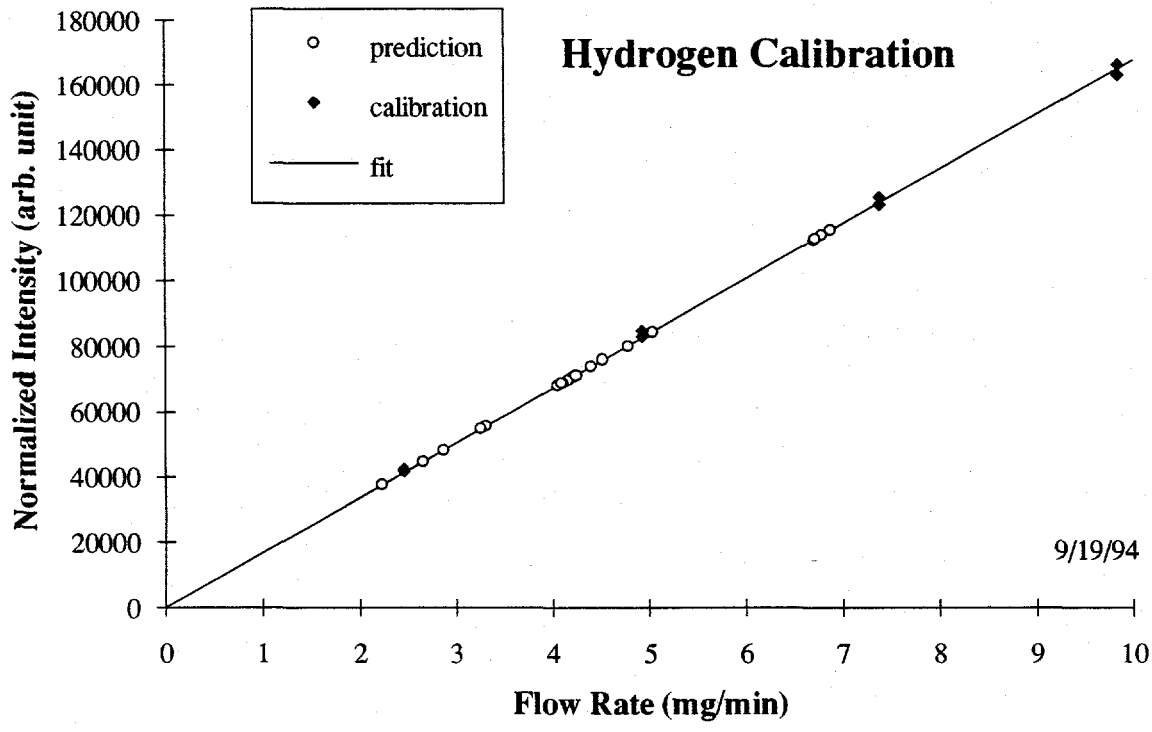

Figure 2. Typical hydrogen calibration data for low and high flow rate ranges.

rates, $\boldsymbol{e}$ and $\boldsymbol{b}$ = errors. In practice, there are several assumptions to be met for MLR of MBMS data to work. (a) Pure component mass spectra are precise and reproducible; (b) Variations in relatively abundances of high and low masses (caused by adjustments of tuning parameters or electronics) can be mathematically corrected with known standard compounds or mixtures of known concentrations; (c) Pure component mass spectra independent on their concentration and the presence of other constituents. (d) All components in the mixture identified. e) Pure component mass spectra are orthogonal to each other.

Procedures for carrying out an experiment using MLR modelling are as follows. (1) Validate that the mass spectrometer tuning can be normalized so that the same behavior is realized from the mass spectrometer from day to day. (2) The protocol used for correcting mass spectrometer tuning is based on the mass spectra of two standards. For mass range above *m/z* 69, the 50 eV EI intensities of peaks at *m/z* 69, 131, 219, 264, 414, 502 and 614 from PFTBA are used. For mass range below *m/z* 69, either 2,2-dimethylbutane (DMB, 50 e EI) or a calibration gas mixture (misch gas, 25 e EI), or both are used: *m/z* 15, 27, 43, 55 and 71 from DMB and *m/z* 15, 27, 43, 56, and 70 from misch gas. Correction values are calculated at these points and linear interpolation is used for masses in between them. All mass spectral data were normalized with respect to *m/z* 69 (for PFTBA), 70 (for misch gas) or 71 (for DMB), for which the correction factors are set to be unity. This correction function is applied to all mass spectra obtained. (3) Collect mass spectra of all pure components identified in product mixtures to be analyzed. (4) Calibration gases are either metered into reactor via mass flow controllers or injected into a buffering flask with pressure-lock syringes. Liquid standards are injected into a vaporization zone of the reactor through syringe pump systems. (5) Samples are analyzed in similar manners (solid samples pyrolyzed in quartz boats).

The actual, fitted and difference mass spectra of products from basswood pyrolysis/upgrading over zeolite are displayed in Figure 3. The fit is reasonably good with underfitted peaks in the negative part, mainly from unidentified components. Shown in Table 3 are some results obtained using this approach for zeolite upgrading of pyrolysis vapors from various biomass samples and related materials.[5] The amount of coke formed on the catalyst is assumed to be 5% and the overall mass balances range from 90% to 104%. The discrepancy in the overall mass balance may have resulted from the product species not accounted for, such as higher molecular weight hydrocarbons shown as an insert in Figure 3 (top).

There are several factors that cause the MLR model to fail. If any of the assumptions are not met, the results obtained from MLR model will be inaccurate or even erroneous. Events that may lead to this include: (i) A shift of the electron ionization energy from the set value due to a decay in filament performance. (ii) Drifts in peak shape and peak center. (iii) Change in process results in unidentified products. (iv) Formation of clusters due to a high concentration of polar components. We have not pursued these issues further since PLS has been shown to be a better tool for multivariate calibration than MLR.

Multivariate Calibration with Partial Least Squares. The latest approach in our pursuit for better models to be used for quantitative analysis of MBMS data is based on partial least squares (projections to latent structures, PLS).[6] PLS is a powerful, flexible approach to multivariate calibration. It relates the systematic information in a matrix $\boldsymbol{X}$ (mass spectra) to the information in a matrix $\boldsymbol{Y}$ (concentrations) with the purpose to predicting $\boldsymbol{Y}$ from $\boldsymbol{X}$. PLS simultaneously calculates multivariate projections of the predictor variables ($\boldsymbol{X}$) and the dependent variables ($\boldsymbol{Y}$) so that the projection scores of the two data blocks are maximally correlated. In this way a quantitative expression (model) of the relationship between the two matrices is obtained and the impact of large, but irrelevant $\boldsymbol{X}$-variations in the calibration modeling is reduced. For calibration, the spectra of

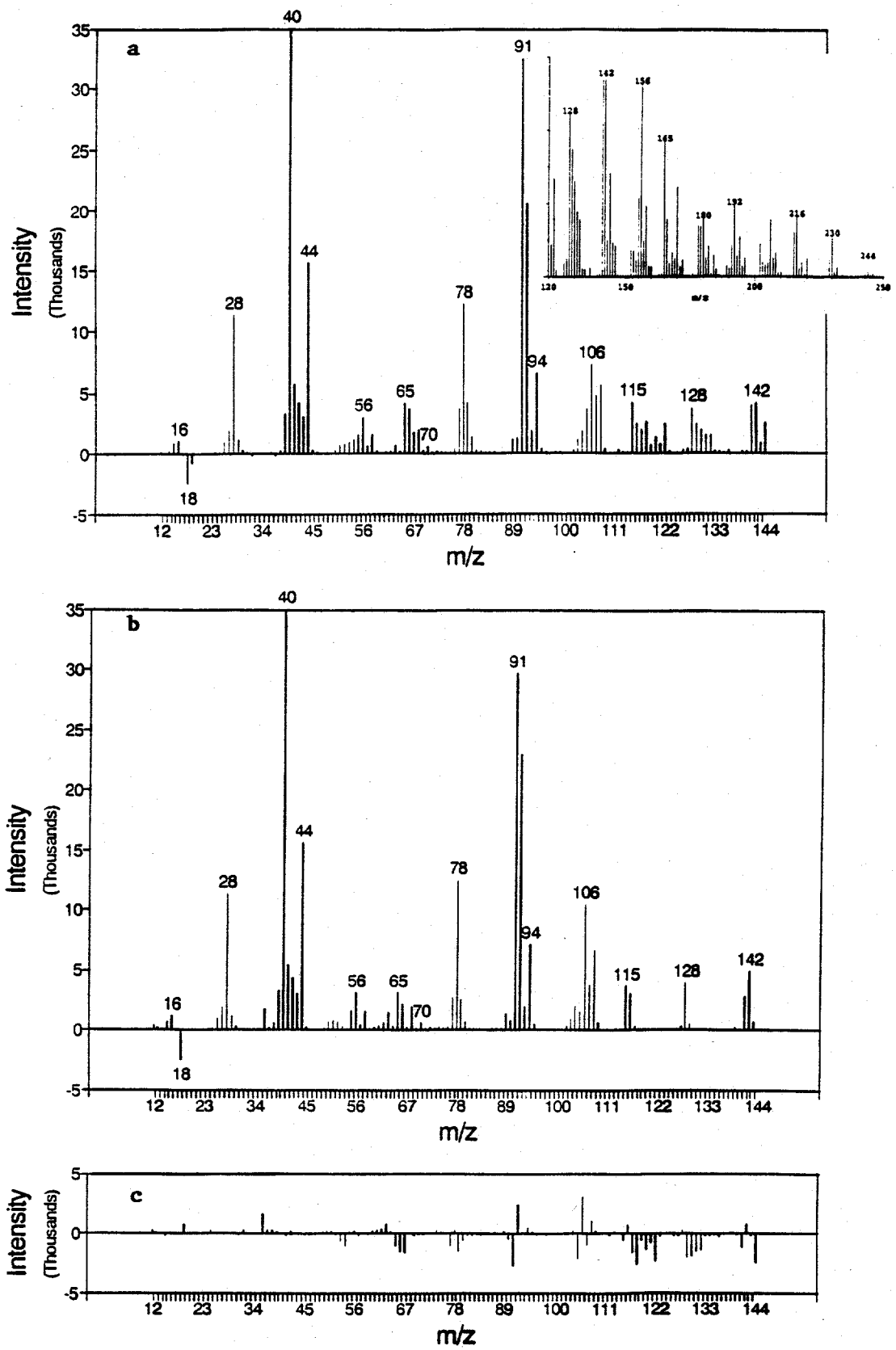

Figure 3. The mass spectra of products from basswood pyrolysis/upgrading over zoelite: (a) actual, (b) fitted and (c) difference. The insert in (a) shows the unfitted spectrum of high masses.

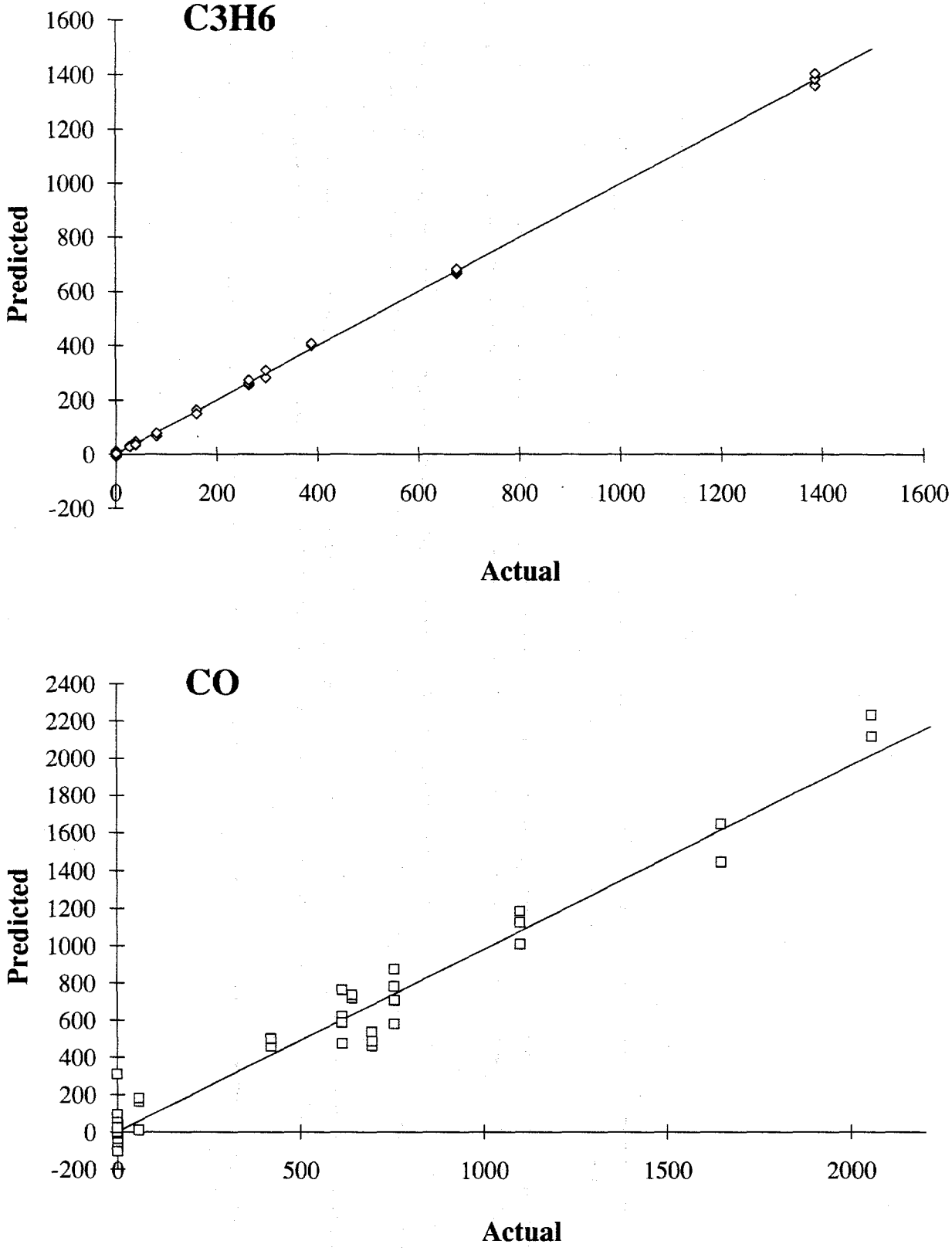

Figure 4. Plots of predicted vs. actual amounts for propylene and CO.

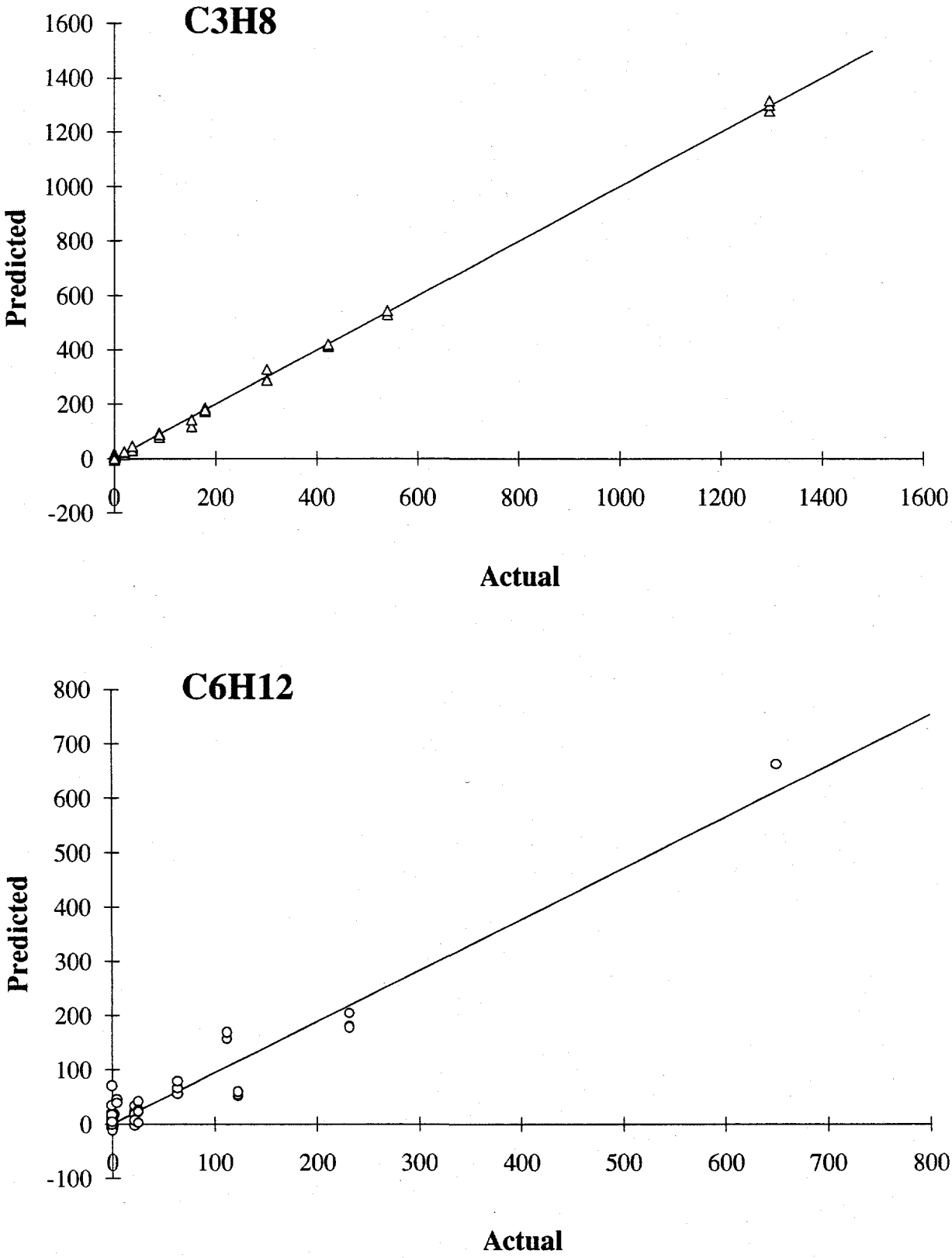

Figure 5. Plots of predicted vs. actual amounts for propane and 1-hexene.

known mixtures are obtained. A PLS model is constructed and applied to spectra of unknown mixtures to obtain their component concentrations.

A series of simulations was performed to confirm the expected efficacy of using PLS modeling to calibrate the MBMS for quantitative analysis of mixtures of selected plastics (by pyrolysis-MBMS) and hydrocarbons. PLS calibration and prediction were applied on MBMS data for real mixtures of nylon-6, nylon-66, styrene, and polypropylene with known composition and the root-mean-square prediction errors were less than 10%. It was also shown that quantitative analysis of the four-constituent system was reproducible over several weeks.

In the latest set of experiments, mixtures of 12 components (10 C_1-C_6 hydrocarbons, CO and CO_2) plus residual air were first analyzed by GC prior to analysis by MBMS with the results shown in Table 4. The experiment was repeated twice on one day then once three days later. The data from the third experiment were used to construct a calibration model from which the runs of the previous two experiments were predicted. Excellent linear calibrations were obtained from which detection limits (10-100 ppm) and ranges (2-3 orders of magnitude) were computed. Shown in Figure 4 and 5 are plots of predicted amount (unit: µl of gas sample at 22°C and 0.82 atm, as an one minute pulse in a 4 $L \cdot min^{-1}$ helium flow) vs. the true value based on the total injection volume multiplied by the concentration. Depending on the sample concentration range in the calibration mixtures, the detection limit may be as low as tens of ppb. The results of the experiment predicting unknowns run on one day from the calibration performed on a different day indicate that it should be possible to calibrate on one day and analyze on a different day by using updating calibration checks or an empirical instrument bias parameter.

Conclusions

We have been able to obtain good to excellent quantitative analysis results for simple systems with no, or constant, interferences, or slightly complex mixtures with all components identified and valid pure mass spectra for each of them. The accuracy of quantitative analysis results from MLR modelling on MBMS data is estimated to about ±20%. The sources of errors are deviations from assumptions, calibration standards, fluctuations in reactor temperatures, gas compositions, mass flow controllers and syringe pumps, etc. For every other experiment, we may need to collect the pure MS again and ensure that most of the assumptions are still valid for the MLR approach. We do not know how often is necessary to validate the assumptions used in MLR modelling, especially how well the correction of MS tuning works in a long period (months).

Multivariate PLS modelling has been successfully applied to MBMS data to produce *quantitative analysis* of complex organic mixtures. Excellent linear calibration models have been obtained for 13 components over four orders of magnitude. Preliminary results suggest that instrumental "drift" and day-to-day variability may be modelled so that the diurnal bias may be corrected empirically. The method described here will be extended to additional species and its generality will be explored. Additional work on empirical bias correction will be undertaken so that re-calibration demands are reduced.

References

1. Evans, R. J. and Milne, T. A. *Energy & Fuels* **1987**, *1*, 123-137 and 311-319.
2. Windig, W.; McClennen, W.H. and Meuzelaar, H.L.C. *Chemometrics and Intelligent Laboratory Systems* **1987**, *1*, 151-165.

3. Rejai, B.; Evans, R. J.; Milne, T. A.; Diebold, J. P. and Scahill, J. W. *Energy from Biomass and Wastes XV* (March 1991, Washingto DC), Klass, D. L. (ed), Elsevier Applied Sc. Pub., London and IGT, Chicago. p.855.

4. Agblevor, F. A.; Rejai, B.; Wang, D.; Wiselogel, A.; Chum, H. L. and Keany, F. proceedings of *the Alternative Energy - Liquid Fuels from Renewable Sources* , Nashville, TN, December 14-15, 1992. *pp.* 201-214.

5. (a) Rejai, B.; Agblevor, F. A.; Evans, R. J. and Wang, D. proceedings of the *Solar '92 Congress*, Cocoa Beach, Florida, June 13-18, 1992. *pp.* 259-263. (b) Wang, D. and Rejai, B. *unpublished results* (c) Milne, T.A.; Evans, R.J. and Filley, J. *Research in Thermochemical Biomass Conversion*, 1988, pp. 910-926.

6. Harald Martens and Tormod Næs *Multivariate Calibration*, John Wiley & Sons Ltd. New York, 1989, 116-165.

Table 2. Partial Mass Spectral Data for Aliphatic Hydrocarbons, CO and CO_2

M	CH_4	C_2H_4	CO	C_2H_6	C_3H_6	C_3H_8	CO_2	1-C_4H_8	1-C_4H_{10}	1-C_5H_{10}	1-C_5H_{12}	1-C_6H_{12}
m/z (M^+)	16	28	28	30	42	44	44	56	58	70	72	84
m/z (base peak)	16	28	28	28	42	29	44	56	43	55	43	56
rel. abun. of M^+	100%	100%	100%	25%	100%	55%	100%	100%	17%	84%	29%	26%
surrogate ion	16	27	28	30	42	43	44	56	58	70	72	84
16	100	0	1.01	0	0	0	1.47	0	0	0	0	0
27	0	27	0	**40**	11.2	**31.3**	0	3.69	**31.5**	8.16	16.7	**21.4**
28	0	**100**	100	**407**	1.85	**117**	6.09	12.8	**73.6**	3.15	4.15	9.88
30	0	0	0	100	0	5	0	0.11	2.17	0.36	0.57	0.38
41	0	0	0	0	**79.7**	**26.2**	0	**76.4**	**121**	**30.3**	**114**	**139**
42	0	0	0	0	100	15.3	0	3.49	**83.7**	**110**	**198**	**146**
43	0	0	0	0	4.45	98.1	0	0	**586**	5.28	**343**	**108**
44	0	0	0	0	0	**100**	100	0	**24.3**	0	13.0	5.42
56	0	0	0	0	0	0	0	100	10.4	7.09	**19.9**	**382**
58	0	0	0	0	0	0	0	0	100	0	4.87	0
70	0	0	0	0	0	0	0	0	0	100	3.43	11.1
72	0	0	0	0	0	0	0	0	0	0	100	0
84	0	0	0	0	0	0	0	0	0	0	0	100

Values in bold face indicate significant interferences.

Table 3. Product Yields for Pyrolysis/Catalytic Upgrading of Biomass

Product	product yield (wt %)[a]									
	aspen	BGS	BSWD	MP	ECWD	SL	WS	AX	ALSEA	willow
CO	17.1	13.7	13.5	18.0	14.3	7.9	8.4	16.8	9.1	10.1
CO_2	14.5	12.3	14.3	11.3	12.9	13.7	13.2	14.4	5.7	13.4
methane	1.7	1.2	1.6	1.4	1.5	1.3	1.1	1.0	3.1	1.4
ethylene	3.5	3.2	3.9	3.1	2.8	2.5	2.1	3.5	2.5	2.8
ethane	0.6	0.5	0.6	0.5	0.4	0.5	0.6	0.5	0.5	0.5
propylene	3.3	3.2	3.7	3.0	2.8	3.0	2.3	3.4	1.2	3.1
propane	0.1	0.2	0.2	0.1	0.1	0.2	0.2	0.0	0.0	0.2
butene	1.3	1.1	1.4	1.0	1.0	1.5	0.9	1.4	0.8	1.2
pentene	0.2	0.1	0.2	0.1	0.1	0.2	0.1	0.2	0.2	0.2
benzene	0.6	0.6	0.7	0.7	0.6	0.6	0.5	0.6	0.7	0.6
toluene	1.2	0.9	1.2	1.0	0.9	0.9	0.7	1.3	1.0	1.0
styrene	0.1	0.1	0.1	0.1	0.1	0.1	0.1	0.1	0.1	0.1
xylene	0.5	0.4	0.5	0.4	0.4	0.4	0.3	0.7	0.5	0.4
indene	0.1	0.1	0.1	0.1	0.1	0.1	0.1	0.1	0.1	0.1
$C_{10}H_8$	0.1	0.1	0.1	0.1	0.1	0.1	0.1	0.1	0.2	0.1
Me-$C_{10}H_7$	0.2	0.2	0.2	0.2	0.2	0.1	0.1	0.1	0.3	0.2
acetone	0.9	0.9	1.0	0.8	0.8	0.7	0.7	1.2	0.2	0.8
furan	0.1	0.1	0.2	0.1	0.1	0.1	0.1	0.3	0.0	0.1
phenol	0.7	0.7	0.5	0.6	0.9	0.6	0.5	0.3	1.7	0.7
cresol	0.6	0.5	0.5	0.5	0.7	0.5	0.4	0.3	1.5	0.5
coke[b]	5.0	5.0	5.0	5.0	5.0	5.0	5.0	5.0	5.0	5.0
char/ash	12.6	14.7	15.4	12.7	13.7	19.1	27.7	11.6	28.5	13.7
water[c]	23.6	32.2	30.2	31.6	32.6	31.6	33.7	24.9	26.0	34.9
total	88.6	92.0	95.1	92.4	92.1	90.7	98.9	87.8	88.9	91.1
subtotals:										
olefins	8.3	7.6	9.2	7.2	6.7	7.2	5.4	8.5	4.7	7.3
aromatics	4.1	3.6	3.9	3.7	4.0	3.4	2.8	3.6	6.1	3.7
oxygenates	2.3	2.2	2.2	2.0	2.5	1.9	1.7	2.1	3.4	2.1

a Results obtained with Mobil HZSM-5 catalyst at 550°C; S/B≈2.5; WHSV≈3.6; $\tau \approx 0.1$s.[5a,b] BGS=bagasse, BSWD=basswood, MP=monterey pine, ECWD= eastern cotton wood, SL=sericea lespediza, WS=wheat straw, AX=acetylated xylan, ALSEA=acetylated lignin (steam explosion aspen). $C_{10}H_8$ = naphthalene, Me-$C_{10}H_7$ = methylnaphthalene; Yields of butane, pentane and hexene: < 0.05%.

b Assumed, based on previous experimental results.[5c]

c By oxygen balance, assuming no oxygen in coke and char/ash.

Table 4. Composition of Gas Mixtures Used in PLS Modeling (Analysis by GC)

No.	1[a]	2	3	4	5	6	7	8	9	10	11	12	13
Air	0.41	10.14	7.40	16.30	*23.02*	13.08	14.09	17.66	11.34	6.04	6.43	8.29	21.16
Methane	14.85	0.82	1.15	2.59	4.16	6.54	11.91	17.55	55.07	0.40	0.43	1.09	11.66
Ethylene	9.77	0.48	2.38	5.28	0.01	13.48	17.98	49.57	0.04	0.10	0.04	0.00	12.60
CO	20.10	12.32	20.99	17.33	30.69	60.07	45.23	0.01	0.00	0.01	0.03	1.64	17.40
Ethane[b]	*2.43*	0.11	0.17	0.40	0.00	0.01	0.03	0.04	0.03	0.07	0.02	0.00	0.02
Propene	7.40	8.69	12.65	19.38	38.76	0.02	0.03	0.01	0.03	0.71	1.08	2.48	3.99
Propane[b]	5.05	12.14	17.23	36.87	0.55	0.02	0.03	0.01	1.03	7.52	2.43	0.08	3.82
CO2	29.86	17.69	37.70	0.07	0.08	0.04	0.11	0.50	1.94	16.27	49.18	53.98	12.14
1-Butene	7.61	37.35	0.00	0.24	0.00	0.03	0.47	0.98	4.16	30.67	9.90	14.89	3.84
n-Butane	0.98	0.12	0.07	0.33	0.01	0.30	0.01	2.22	4.89	9.36	13.09	*17.42*	3.67
1-Pentene	0.51	0.04	0.01	0.12	0.13	0.93	1.97	4.04	8.80	12.71	*17.34*	0.03	3.37
n-Pentane	0.50	0.07	0.03	0.28	0.72	1.93	3.40	7.40	12.65	*16.12*	0.02	0.09	3.25
1-Hexene	0.51	0.02	0.21	0.82	1.86	3.55	*4.75*	0.00	0.02	0.02	0.03	0.01	3.09
Total	100.0	100.0	100.0	100.0	100.0	100.0	100.0	100.0	100.0	100.0	100.0	100.0	100.0

a Gas mixture was obtained from Matheson Gas Products, and was used as a calibration standard for the GC analysis. All other mixtures were made in our lab by mixing approximate amounts of pure gases (and liquids for 1-pentene, n-pentane and 1-hexene). Some mixtures contained small amounts of hexane, measured by GC to be up to 0.004%.

b Ethane was not available. The propane gas used for making the 12 mixtures contained some ethane and propene.

Quantitative Measurement of Radical Intermediates by Molecular-Beam-Sampling-Mass-Spectrometry

Albert Y. Chang Anthony M. Dean and Mark D. Weisel
Corporate Research Labs, Exxon Research and Engineering Company,
Annandale, NJ 08801

Complementary advances in theory and experiment have provided significant new insights into the complex chemistry occurring during high temperature pyrolysis and combustion. Detailed models have been developed for reactions in flames and engines as well as hydrocarbon pyrolysis. Such detailed models are generally considered to be more reliable if they can successfully describe the behavior of reactive intermediates, since these are usually much more sensitive to subtle details of the chemistry than either the reactants or products. In particular, accurate knowledge of the concentration-time profiles of these intermediates provide a rigorous test of the accuracy of the proposed kinetic model.

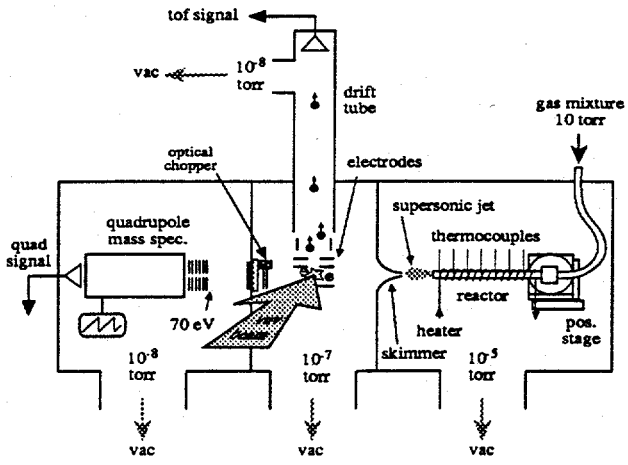

Figure 1 Experimental Apparatus

We use a molecular-beam-sampling apparatus which utilizes both a vacuum ultraviolet (VUV) photoionization time-of-flight (TOF) spectrometer and an electron-impact (EI) quadrupole spectrometer to measure reactive intermediates as well as stable products of flow tube experiments. The apparatus is as shown in Fig. 1. The instrument consists of three independently pumped vacuum chambers. The source chamber can accommodate different reactor designs and is pumped by a 5000 L/sec diffusion pump. A 1 mm diameter skimmer separates this from a photoionization chamber which has attached a TOF drift tube and detection apparatus (RM Jordan Co.). The third chamber, separated from the photoionization chamber by a 0.080" aperature houses a quadrupole mass spectrometer (Extrel). Presently in the source chamber we are using a straight-nozzle alumina reactor which is run over a temperature range of 300-1400K. Typical pressures in the reaction zone are ~5-10 torr, residence time in the hot zone is ~2 ms. The

flow forms a supersonic jet at exit which raises the pressure in the source chamber to ~7 x 10^{-5} torr. This rapid expansion effectively quenches the chemistry on the order of a few microseconds, much shorter than the millisecond time in the hot zone of the reactor. Mounted thermocouples are used to measure the reactor wall temperature profiles and were included in a model using 1-D compressible flow code coupled to detailed chemical kinetic modeling.

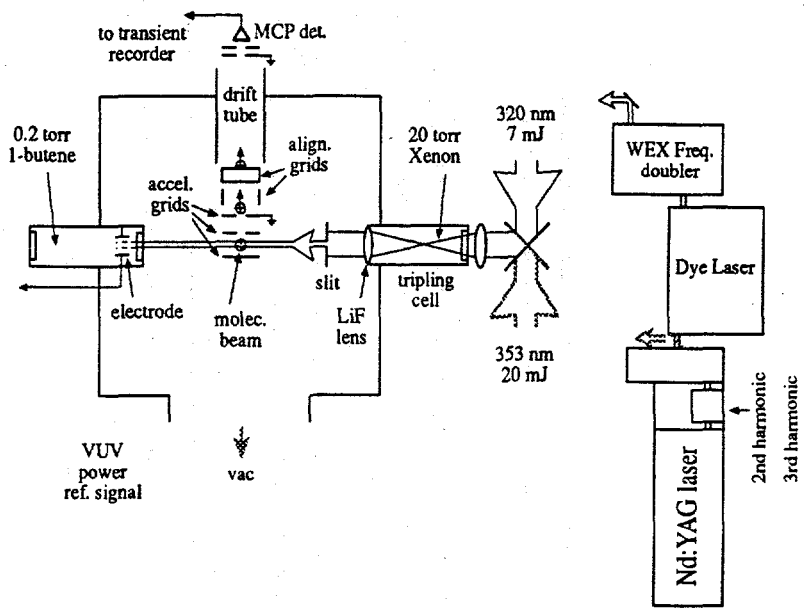

Figure 2 Photoionization Generation System

Fig. 2 describes the photoionization system used for ionizing species for the TOF spectrometer. We use two different methods to generate photoionization energies at 118 nm (10.5 eV) and 106.5 nm (11.65 eV). The 106.5 nm was the shortest wavelength we could use without going to exotic windowless designs. The VUV radiation at 10.5 eV. (118 nm) is generated by frequency-tripling the third harmonic of a Nd-YAG laser. The VUV radiation at 11.7 eV. (106.5 nm) is generated by taking the second harmonic of a Nd-YAG laser and pumping a dye laser. The dye laser output is frequency doubled and then frequency-tripled. Each spectra recorded is averaged over 200 laser shots and normalized to the per shot laser energy. A second tool, complementary to the TOF, is the electron impact (EI) mass spectrometer. The EI Mass spectrometer is typically run at 70 eV to check for all present species and as a comparison measurement to the TOF. These spectra are taken using analog techniques and each data point averaged over 500 samples. Waveforms are obtained by scanning over the desired mass range at 15 pts/amu resolution, giving an effective scan rate of ~2 S/amu. Detailed comparisons of quadrupole and TOF data have shown very good agreement between the two techniques, both for stable species and reactive intermediates. Fragmentation of the species using the higher energy EI source of the quadrupole makes it difficult to determine radical intermediates from chemistry or fragmentation of parent. Fig. 3 provides comparison spectra of butene

at 1350K using TOF (@10.5eV) and EI quadrupole analysis. From this figure it is clear that using the TOF technique make species interpretation less complicated than that of the EI technique. The minimal fragmentation obtained with a selectable VUV source

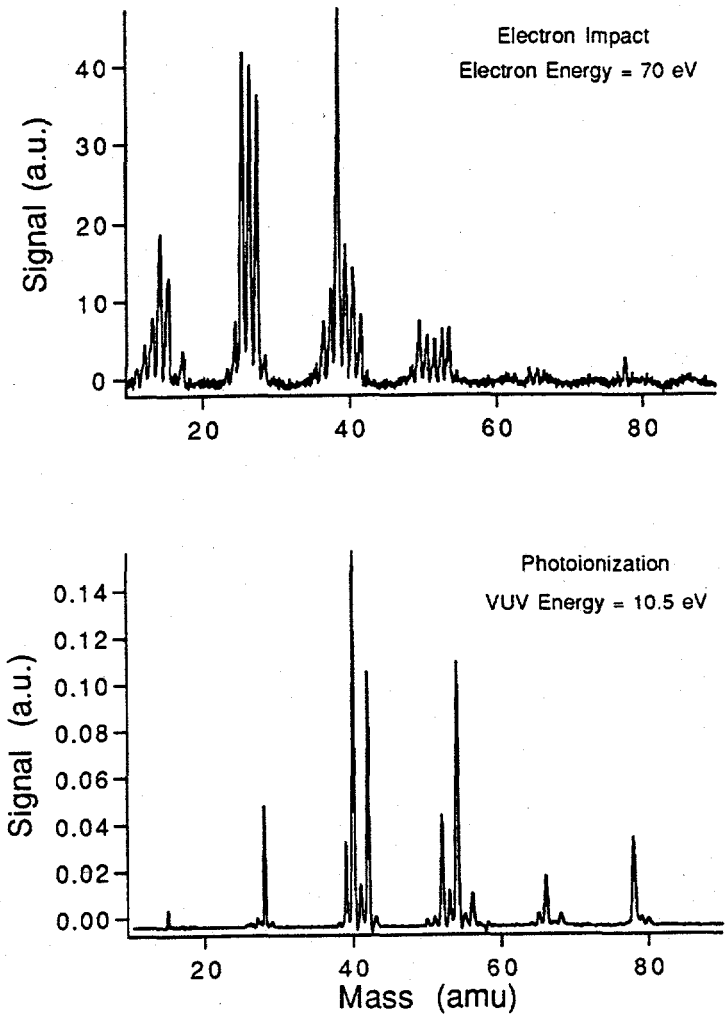

Figure 3 Mass Spectra Comparison of VUV vs. EI Ionization

makes this the preferred technique for obtaining detailed concentration information of both stable molecules and radical intermediates. Fig. 4 is a TOF spectra of a 1:1:1 test mixture of n-butane, 1,3 butadiene and acetylene acquired using VUV radiation at 11.65 eV and at 300K. We show in this figure that although the photionization techniques reduces fragmentation, there is still fragmentation as seen with n-butane.

Our initial experiments were performed to validate the reactor apparatus. A simple well-understood reaction was the pyrolysis of cyclohexene, where the main reaction is a reverse Diels-Alder reaction producing 1,3 butadiene and ethylene. The reaction mixture was 10 sccm of 50% cyclohexene, 25% neon (a quadrupole reference) and 25% nitric oxide (a TOF reference). Although the VUV radiation employed was 10.5 eV, ethylene (I.P. =10.5 eV) is detectable at the higher temperatures where it is formed as a

decomposition product. One result of ethylene's relatively low I.P. is a small cross section. The results of our cyclohexene pyrolysis experiments were compared to our

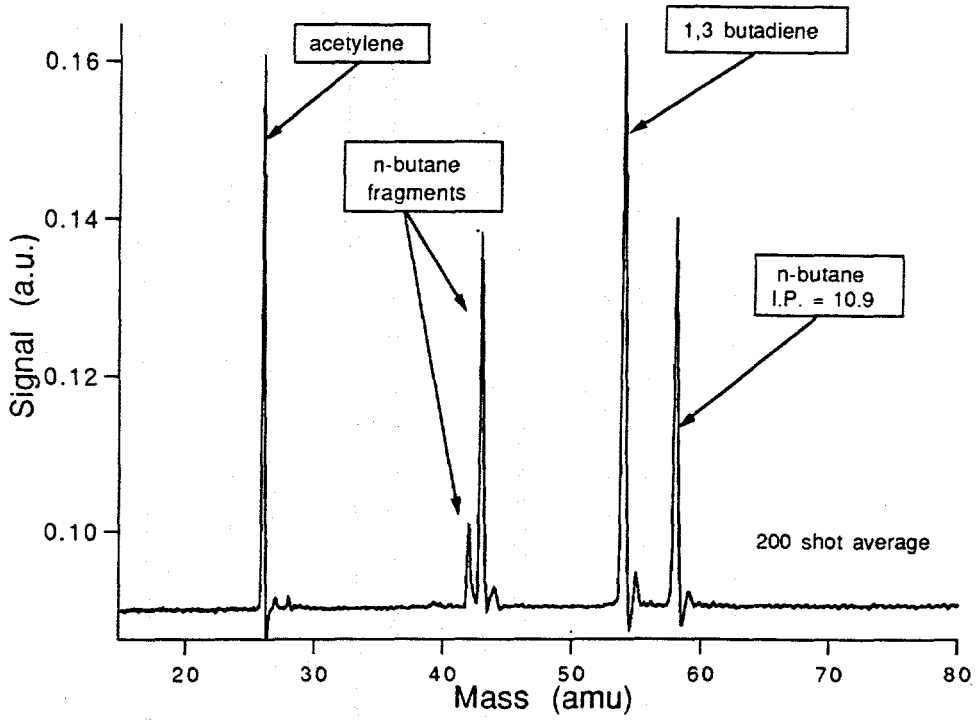

Figure 4 VUV Fragmentation of N-Butane

detailed kinetic model (43 channel reaction mechanism, mostly to account for the free radical induced dissociation) and are partially shown in part in Fig. 5. With unadjusted

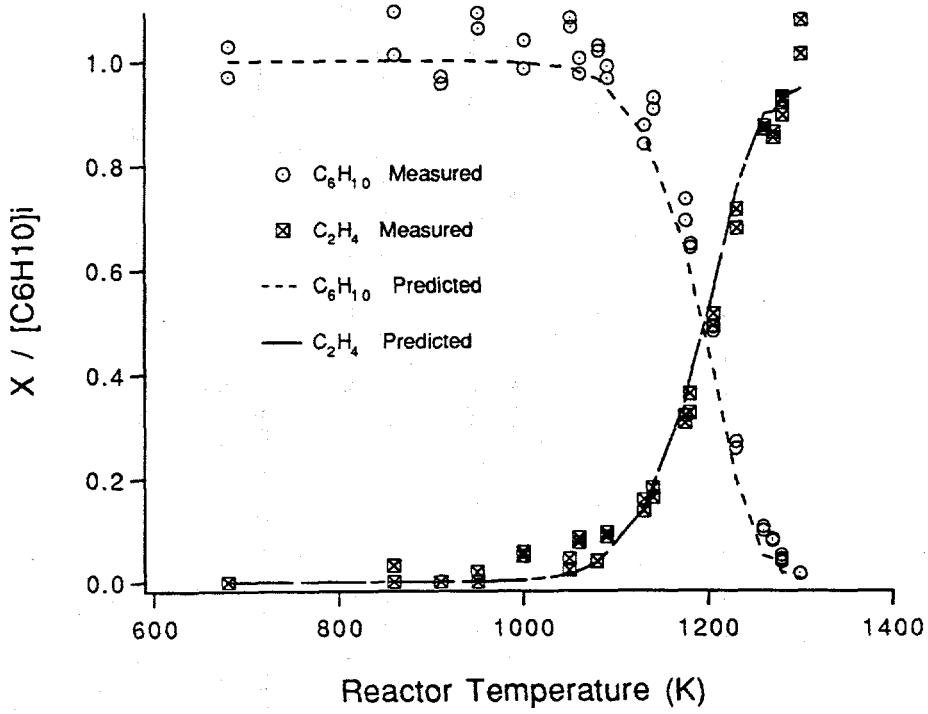

Figure 5 Cyclohexene Mechanism Validation

rate constants from the literature, this comparison showed good agreement between model and experiment. More recently, experiments using 11.65 eV VUV radiation have been performed to develop models of n-butane and iso-butane pyrolysis. Fig. 6, TOF spectra of n-butane, show the fragmentation products formed at low temperatures and the mixture of reaction and fragmentation products at high temperature. Fig. 7 illustrates a

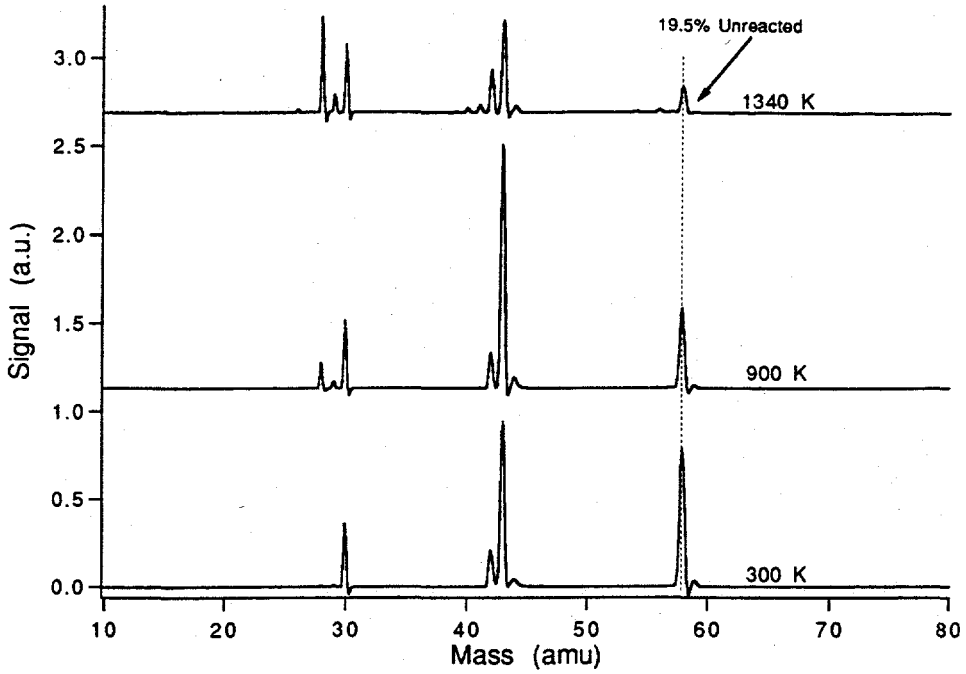

Figure 6 TOF Spectra of n-butane Pyrolysis

simplified mechanism for the early stages of reaction for the pyrolysis of n-butane and isobutane. From these mechanisms we would expect to see C_1, C_2, and C_3 species formed from n-butane and C_1, C_3, and C_4 species from isobutane. Fig. 8 plots normalized signal intensities of two radicals as a function of reaction temperature for n-butane and isobutane. The n-butane data indicate that pyrolysis of the parent molecule begins at ~600K as seen by growth of the ethyl radical, the allyl radical appears at 1150K. . For isobutane, the allyl appears at 1150K as well with relatively no evidence of ethyl radicals until 1225K. These data agree with the initial steps proposed earlier.

The experiments presented permit us the possibility of extending our growing understanding of the quantitative details of free-radical chemistry to more complex systems, with potential impact in a variety of areas. We demonstrate methods of measurement of these (free radical) intermediates, as well as the stable species. Experimental data combined with newly developed reaction mechanisms will provide us with key insights to reaction pathways. Such validation is a critical component for developing the knowledge base in free radical chemistry that, in turn, will allow more confident application of the "rules" to complex systems.

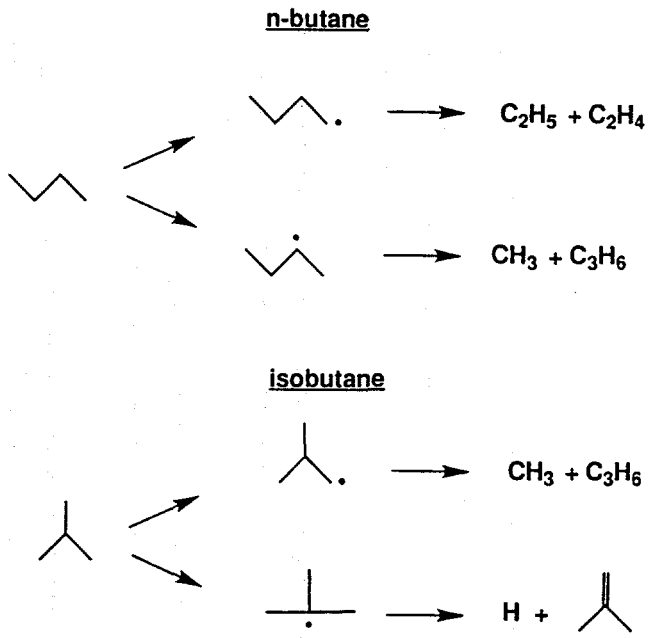

Figure 7 Simple Reaction Mechanisms

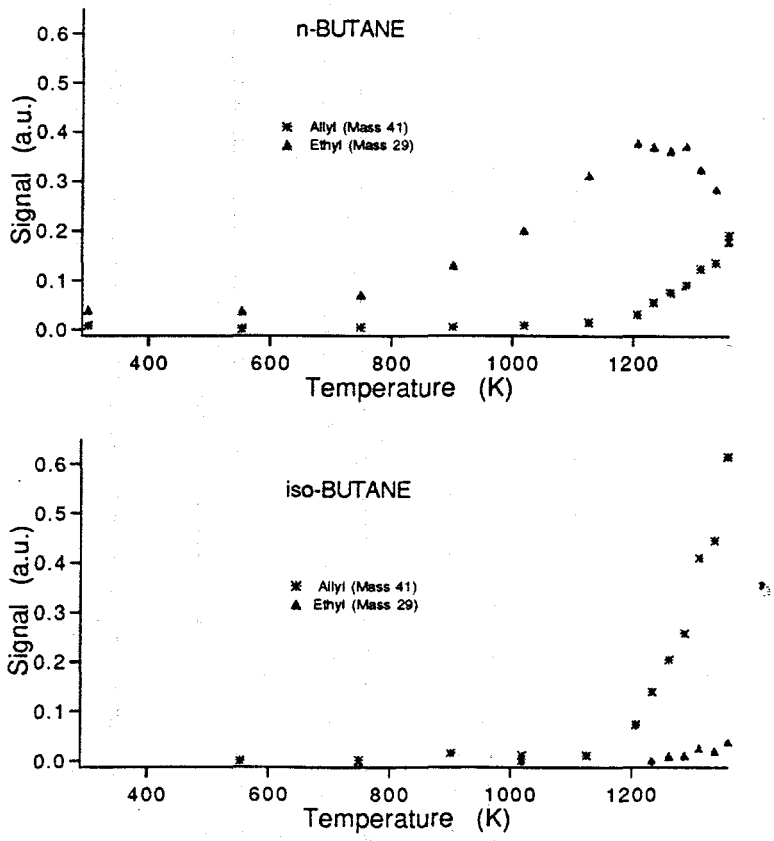

Figure 8 Radical Temperature Profiles

A New MBMS Flame Chamber for the Study of Molecular Weight Growth Reactions

L. I. Yeh and K. M. Creegan
Exxon Research and Engineering
Route 22 East, Clinton Township
Annandale, NJ 08801

A description of the new molecular beam/mass spectrometer flame chamber just constructed is given. The purpose of this system is to study molecular weight growth reactions leading to soot precursors as a function of flame conditions including fuel composition. Formation of the first aromatic rings is believed to be the bottleneck to soot formation and will be the focus of our initial studies. Because radicals are crucial to molecular weight growth reactions, this chamber has been designed to optimize radical detection from premixed flames.

A schematic of the flame MBMS chamber is shown in Fig. 1. The chosen fuel, oxidant, and inert gases flow through MKS mass flow controllers to a sintered bronze McKenna burner. The diameter of the burner is 2.5 inches and the diameter of the concentric shroud ring is 2.9 inches. The pressure in this region is maintained at 30 torr using a Roots blower with choked flow as well as a feedback loop controlling a valve to an argon line. The burner is mounted on a movable bellows assembly with a travel of over 6 inches in the Z direction. This allows different positions in the flame to be sampled by a quartz cone custom made by Finkenbeiner. The cone is of the "hybrid" shape with an angle of 40° near the tip and 90° at the base. The tip of the cone has a 115 μm hole and a wall thickness of 50-100μm. This serves as the nozzle for a supersonic expansion into the first differential pumping region.

At this point, collisions cease allowing the very reactive radicals to survive in the molecular beam. The pressure in this first differential region is typically low 10^{-4} to high 10^{-5} torr when the main chamber is at 30 torr. An Edwards Diffstak 160/700 is used to pump this region. The beam path in this region is defined on one end by the quartz cone and on the other by a movable skimmer. The skimmer is mounted on a bellows assembly allowing the nozzle-skimmer distance to vary from less than 1 inch to 2.7 inches. A schematic of the skimmer assembly is shown in Fig. 2. Effects of translating the skimmer are shown in Fig. 3.

The skimmer is an electroformed nickel skimmer manufactured by Beam Dynamics. Two skimmers are used, one with a hole diameter of 1.0 mm and the other with a diameter of 1.5 mm. The skimmers are easily interchanged as they are welded

Flame Chamber for Combustion Chemistry Study

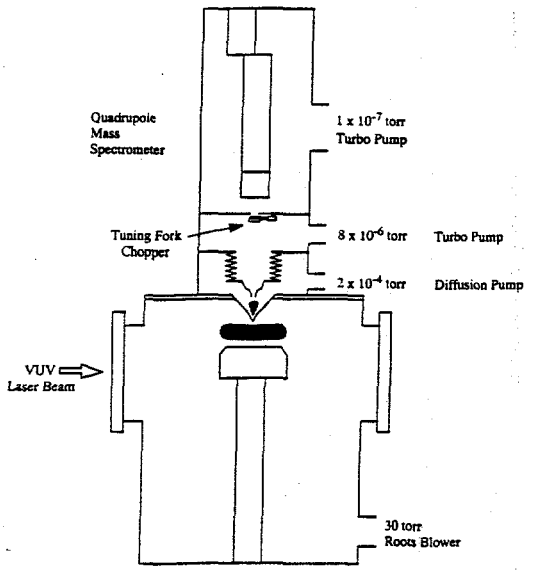

Fig. 1

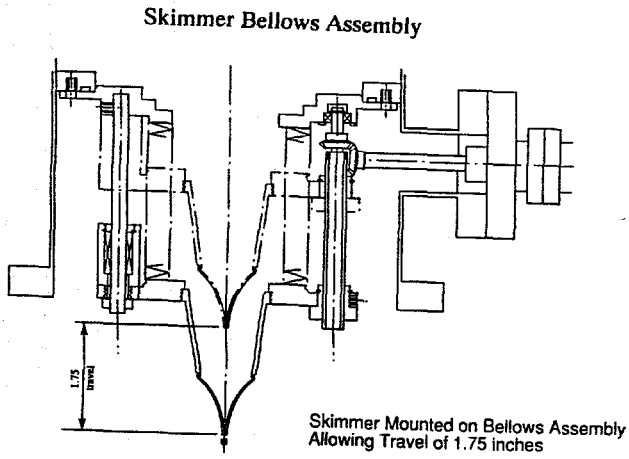

Fig. 2

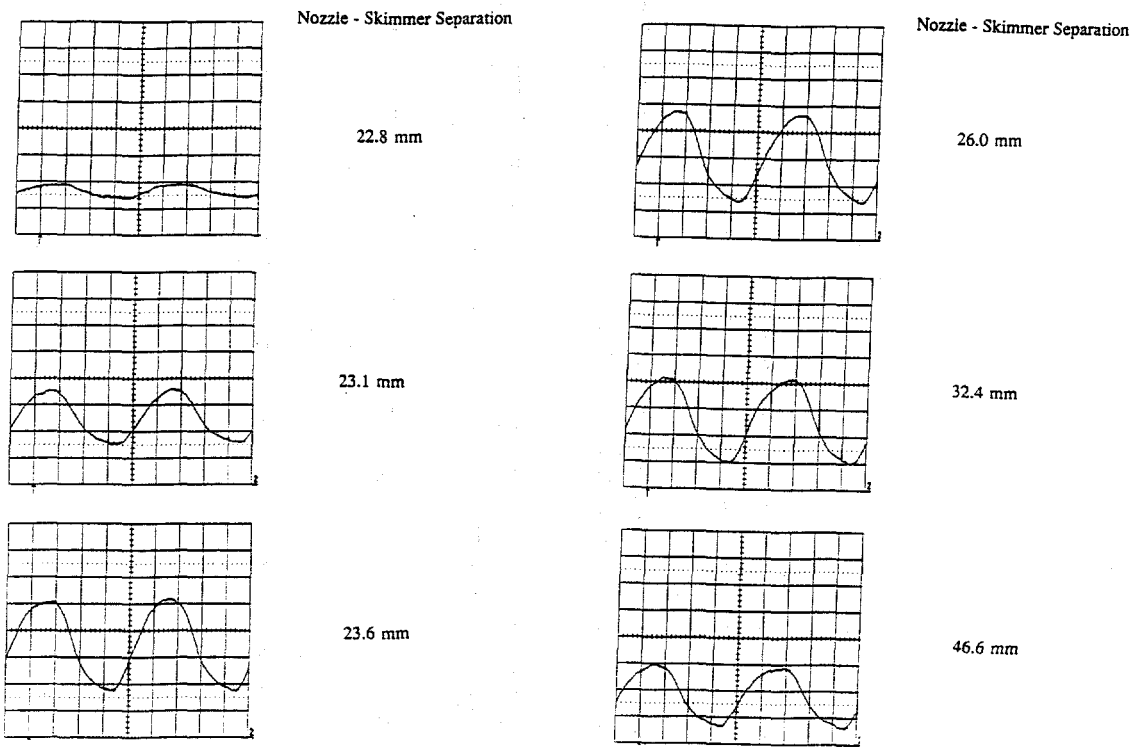

Fig. 3

to bases that are threaded and they simply screw into the bellows assembly bottom plate. Both skimmers have tapered walls that angle from 30° at the tip to 70° at the base. Once through the skimmer, the molecular beam is in a chamber pumped by a Leybold TMP50 turbo pump which maintains a pressure in the mid 10^{-6} torr range.

The third differential pumping region is separated by a 0.25 inch aperture in a stainless steel plate. On the upstream side of this plate is mounted a 400 Hz tuning fork chopper. This third pumping region is generally in the low 10^{-7} to high 10^{-8} torr range with the flame on. Pumping is done using a Leybold TMP361 turbo pump. The quadrupole mass spectrometer resides in this chamber. The MS is an Extrel system with an axial ionizer, Model 041-11 and 3/4 inch rods. This gives a mass range of 0-500 amu. The quadrupole was chosen as the primary detection technique because of its capability of detecting many stable and radical species. By making use of the relatively low ionization potentials of radicals, they can be detected readily by varying the electron energy used. An example of this for CH_3 and OH is shown in Fig. 4.

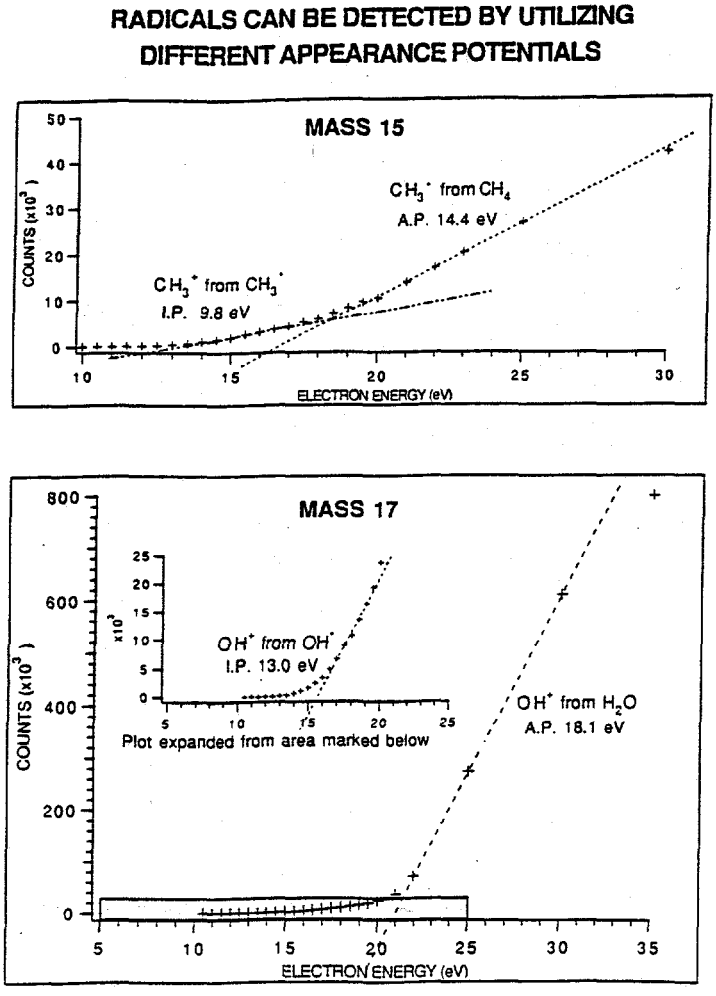

Fig. 4

A second approach to studying flame intermediates is laser induced fluorescence. LIF has been used quite extensively for detecting OH radical. Although laser based techniques are usually more cumbersome than mass spectrometric techniques, they have the advantage of minimal perturbation to the flame. A concern when inserting the quartz cone directly into the flame to form the molecular beam is that the presence of the quartz cone will change the flame temperature and gas flows. Therefore, LIF is used as a complementary technique.

Gas-chromatography/ mass spectrometry is a third technique that will be useful. Because the goal is to study molecular weight growth reactions leading to soot precursors, it would be useful to detect a variety of polycyclic aromatic hydrocarbons. PAH's are difficult to detect using electron impact ionization due to the extensive fragmentation that occurs in the ionizer. GC/MS is better suited to the detection of larger PAH's.

In order to calibrate this system, a fuel rich laminar methane flame will be studied first under conditions similar to Langley and Burgess. Their flame conditions are 27% CH_4, 33% O_2, 40% Ar for Φ=1.60, pressure =31 torr, and cold gas velocity of 80 cm/s. Species profiles using the quadrupole mass spectrometer are obtained by translating the burner vertically closer and farther from the quartz cone. Some preliminary data obtained with our new system has recently been obtained. In Fig. 5 is shown the profiles for the major reactants and products. Profiles for acetylene, methyl radical, and hydroxyl radical are shown in Fig. 6. Species profiles such as these will later be compared with profiles predicted from chemical models in order to better understand the chemistry occurring in fuel rich flames.

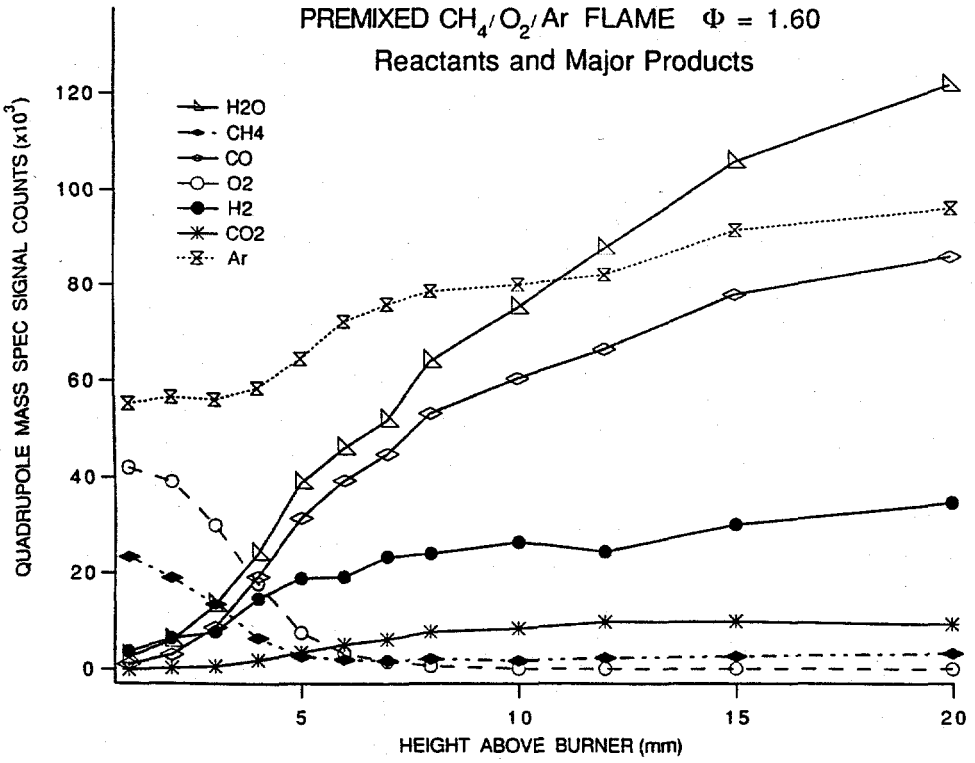
PREMIXED $CH_4/O_2/Ar$ FLAME Φ = 1.60
Reactants and Major Products
H2O
CH4
CO
O2
H2
CO2
Ar
QUADRUPOLE MASS SPEC SIGNAL COUNTS (x10^3)
120
100
80
60
40
20
0
5
10
15
20
HEIGHT ABOVE BURNER (mm)

Fig. 5

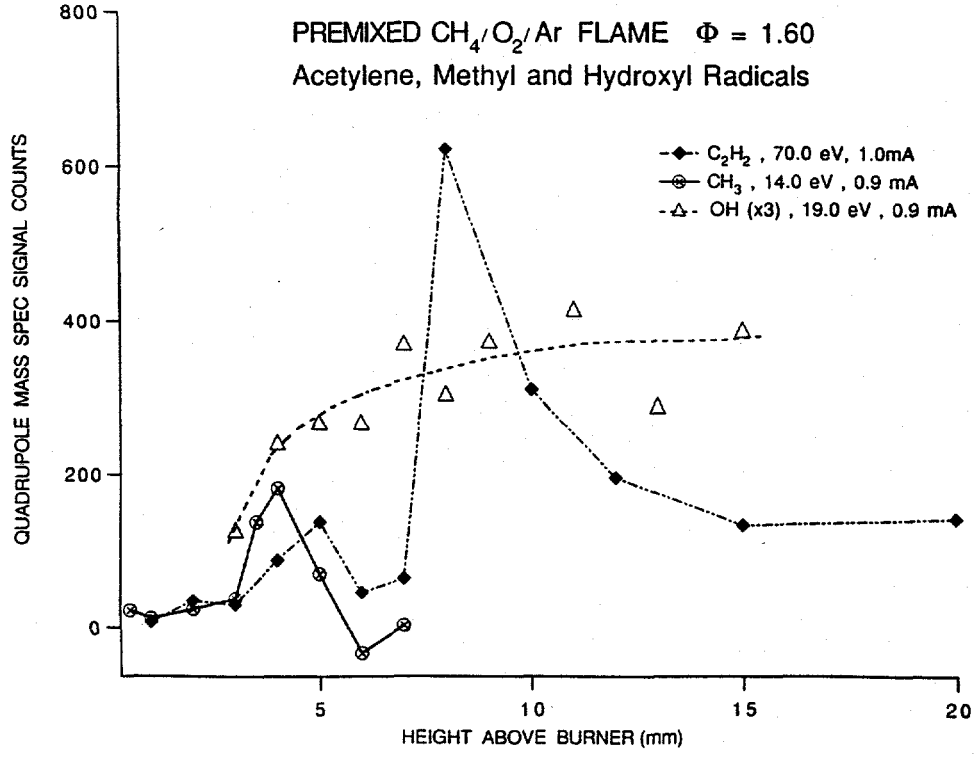
PREMIXED $CH_4/O_2/Ar$ FLAME Φ = 1.60
Acetylene, Methyl and Hydroxyl Radicals
C_2H_2 , 70.0 eV, 1.0mA
CH_3 , 14.0 eV , 0.9 mA
OH (x3) , 19.0 eV , 0.9 mA
QUADRUPOLE MASS SPEC SIGNAL COUNTS
800
600
400
200
0
5
10
15
20
HEIGHT ABOVE BURNER (mm)

Fig. 6

ATTENDEE LIST

A Specialists Workshop on Applications of Free-Jet, Molecular Beam, Mass Spectrometric Sampling

---

Foster Agblevor
National Renewable Energy Lab.
1617 Cole Boulevard
FTLB/168-22
Golden, CO 80401
Phone: (303)-384-6244
Fax : (303)-384-6103

Carmela Amata-Wierda
NIST
Building 221, Rm B-316
Gaithersburg, MD 20899
Phone: (301)-975-2607
Fax : (301)-869-5924

Aviv Amirav
Tel Aviv University
School of Chemistry
Ramat Aviv
Tel Aviv,69978
Israel
Phone: 972-3-6408253
Fax : 972-3-6409293

William Anderson
U.S. Army Research Laboratory
AMSRL-WT-PC, Aberdeen Proving Ground,
Aberdeen Proving Gr, MD 21005-5066
Phone: (410)-278-9992
Fax : (410)-278-7333

Deon Anex
Sandia National Laboratories
M.S. 9055
Livermore, CA 94551-0969
Phone: (510)-294-3294
Fax : (510)-294-1004

Richard Behrens
Sandia National Lab
Combustion Research Facility
MS 9055
Livermore, CA 94551-0969
Phone: (510)-294-2170
Fax : (510)-294-2276

Melvyn Branch
Center for Combustion Research
Mechanical Engineering Dept
University of Colorado
Boulder, CO 80309-0427
Phone: (303)-492-6318
Fax : (303)-492-2863

Roger Campargue
CEA - CE/SACLAY
Laboratoire des Jets
Moleculaires SCM/DRECAM/DSM
Gif-SUR-YVETTE DP 91,91191CEDEX
FRANCE
Phone: 33-1-6908-4319
Fax : 33-1-6908-7963

David Dayton
National Renewable Energy Lab
1617 Cole Boulevard
Golden, CO 80401
Phone: (303)-384-6216
Fax : (303)-384-6103

Christine Doute
CNRS
LCSR 1F Avenue de la Rechesche Scientifique
Orleans,45071
FRANCE
Phone: 33 38 51 5494
Fax : 33 38 51 76 70

Carolyn Elam
National Renewable Energy Lab
1617 Cole Boulevard
Golden, CO 80401
Phone: (303)-275-3780
Fax : (303)-384-6103

Robert Evans
National Renewable Energy Lab
1617 Cole Boulevard
FTLB/150
Golden, CO 80401
Phone: (303)-384-6284
Fax : (303)-384-6103

John Fenn
Virginia Commonwealth Univ.
Dept. of Chemistry
Box 2006, 1001 West Main St.
Richmond, VA 23226
Phone: (804)-828-7511
Fax : (804)-828-8599

Ciaran Fox
Sandia National Laboratory
Rains 29 G, 704 Campus Dr.
Stanford, CA 94305
Phone: (510)-294-3069
Fax : (510)-294-3231

Richard French
National Renewable Energy Lab
1617 Cole Boulevard
Golden, CO 80401
Phone: (303)-384-6135
Fax : (303)-384-6103

Steve Gebhard
National Renewable Energy Lab
1617 Cole Boulevard
FTLB/250-03
Golden, CO 80401
Phone: (303)-384-6249
Fax : (303) 394-6103

David Gratson
National Renewable Energy Lab
1617 Cole Boulevard
FTLB/168-28
Golden, CO 80401
Phone: (303)-384-6274
Fax : (303)-384-6103

Frank Greene
Midwest Research Institute
425 Volker Boulevard
Kansas City, MO 64110-2299
Phone: (816)-753-7600 1273
Fax : (816)-753-8420

J.W. Hastie
NIST
Materials Building 223/A215
Gaithersburg, MD 20899
Phone: (301)-975-5754
Fax :

Klaus Homann
Tech. Hochschule Darmstadt
Inst. fur Physikalische Chemie
Petersenstr .20
Darmstadt,64287
Phone: 49-6151-162172
Fax : 49-6151-164298

Nathan Jacobson
NASA Lewis Research Center
Mail Stop 106-1
21000 Brookpark Road
Cleveland, OH 44135
Phone: (216)-433-5498
Fax : (216)-433-5544

Don Kern
University of New Orleans
Department of Chemistry
Lake Front
New Orleans, LA 70148
Phone: (504)-286-6847
Fax : (504)-286-6860

Eldon Knuth
UCLA
Chemical Engineering Dept.
5531 Boelter Hall
Los Angeles, CA 90024
Phone: (310)-825-8485
Fax : (310)-206-4107

Oleg Korobeinichev
Inst. of Chem. Kinetic Combust
Institutes Kay Street 3 UL
Pirogova 2, Academgorodok
Novosibirsk,
RUSSIA
Phone: +73 38 235 7082
Fax : +73 83 235 2366

Thomas Litzinger
Penn State
Dept of Mechanical Engineering
201 D Reber Bldg
University Park, PA 16802
Phone: (814)-865-4015
Fax : (814)-865-4021

Mike Looker
National Renewable Energy Lab
1617 Cole Boulevard
Golden, CO 80401
Phone: (303)-384-6233
Fax : (303)-384-6103

Marion Maniet
Extrel Corporation
575 Epsilon Drive
Pittsburgh, PA 15238-2838
Phone: (412)-963-7530
Fax : (412)-963-6578

Henk Meuzelaar
University of Utah
Center for Micro Analysis
EMRL, Bldg. 16, Rm 214
Salt Lake City, UT 84112
Phone: (801)-581-4200
Fax : (801)-581-4526

David Miller
Univ of California/San Diego
Dept. AMES - D310
LaJolla, CA 92093-0310
Phone: (619)-534-3182
Fax : (619)-534-5354

Thomas Milne
National Renewable Energy Lab
1617 Cole Boulevard
Golden, CO 80401
Phone: (303)-384-6245
Fax : (303)-384-6103

Mark Nimlos
National Renewable Energy Lab
1617 Cole Boulevard
Golden, CO 80401
Phone: (303)-384-6271
Fax : (303)-384-6103

Joseph Patrick
National Renewable Energy Lab
1617 Cole Boulevard
Golden, CO 80401
Phone: (303)-384-6243
Fax : (303)-384-6103

Randy Pedder
Extrel Corporation
575 Epsilon Drive
Pittsburgh, PA 15238-2838
Phone: (412)-963-7530
Fax : (412)-963-6578

Gerald Pellett
NASA Langley Research Center
Mail Stop 198
Hampton, VA 23681-0001
Phone: (804)-864-6241
Fax : (804)-864-7923

David Rakestraw
Sandia National Laboratories
M.S. 9055
Livermore, CA 94551-0969
Phone: (510)-294-3297
Fax : (510)-294-1004

Matthew Ratcliff
National Renewable Energy Lab
1617 Cole Boulevard
Golden, CO 80401
Phone: (303)-384-6129
Fax : (303) 384-6103

Rosario Sausa
U.S. Army Research Laboratory
AMSRL-WT-PC
Aberdeen Prov. Grnd., MD 21005
Phone: (410)-278-7070
Fax : (410)-278-7333

Rick Schaeffer
Extrel Corporation
575 Epsilon Drive
Pittsburgh, PA 15238-2838
Phone: (412)-963-7530
Fax : (412)-963-6578

Kuni Tatsumoto
National Renewable Energy Lab
1617 Cole Boulevard
Golden, CO 80401
Phone: (303)-384-6138
Fax : (303)-384-6103

Jacques Vandooren
Univ Catholique De Lovvain
Lab de Physico/chimie-Combust
1, pl. L. Pasteur
Louvain-La-Neuve,B-1348
BELGIUM
Phone: 32 10 472727
Fax : 32 10 472468

Christian Vovelle
CNRS
LCSR 1C Avenue de la Rechercha
Scientifique
Orleans,45071
FRANCE
Phone: 33 38 51 54 82
Fax : 33 38 51 76 70

Dingneng Wang
National Renewable Energy Lab
1617 Cole Boulevard
Golden, CO 80401
Phone: (303)-384-6127
Fax : (303)-384-6103

Mark Weisel
Exxon
79 Route 22 East
Room LF 362
Annandale, NJ 08801
Phone: (908)-730-2816
Fax : (908)-730-3344

Phillip Westmorland
Univ of Massachusetts
Chemical Engineering
159 Goessmann Lab, Box 33110
Amherst, MA 01003-3110
Phone: (413)-545-1750
Fax : (413)-545-1647

Lisa Yeh
Exxon Research & Engineering
Route 22 East
Annandale, NJ 08801
Phone: (908)-730-2686
Fax : (908)-730-3344

Paul Ziemann
University of Minnesota
125 Mechanical Engineering
111 Church St. SE
Minneapolis, MN 55455
Phone: (612)-626-0285
Fax : (612)-625-6069

EXTREL Quadrupole Mass Spectrometry

Presents

Building Blocks For Your Molecular Beam System

Complete Modulated Molecular Beam System
Extrel Corporation
575 Epsilon Drive
Pittsburgh, PA 15238
(800) 445-7090
(412) 963-6578 Fax

Quadrupole Mass Spectrometers - Components
Extrel Corporation
575 Epsilon Drive
Pittsburgh, PA 15238
(800) 445-7090
(412) 963-6578 Fax

Lock-In Amplifiers
Ithaco
735 West Clinton Street
Ithaca, NY 14851-6437
(607) 272-7640
(607) 272-4550 Fax

Stanford Research Systems (SRS)
1290 D Reamwood Avenue
Sunnyvale, CA 94089
(408) 744-9040
(408) 744-9049 Fax

EG&G PARC (Princeton Applied Research)
PO Box 2565
Princeton, NJ 08543-2565
(609) 530-1000
(609) 883-7259 Fax

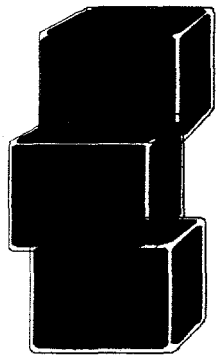

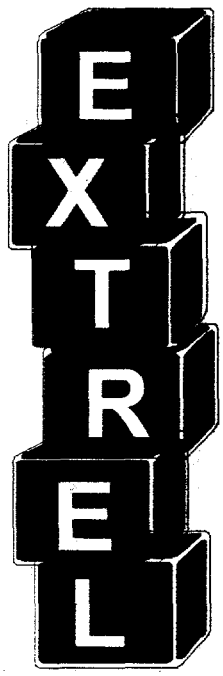

Tuning Fork Choppers
Electro-Optical Products Corp.
P.O. Box 650441
Fresh Meadow, NY 11365
(718) 776-4960
(718) 776-4978 Fax

Molecular Beam Skimmers - Metal
Beam Dynamics, Inc.
708 East 56th Street
Minneapolis, MN 55417
(612) 823-8151
(612) 371-0181 Fax

Molecular Beam Skimmers - Quartz
G. Finkenbeiner, Inc.
33 Rumford Avenue
Waltham, MA 02154
(617) 899-3138
(617) 647-4044 Fax

Precision Apertures
Buckbee-Mears
245 East 6th Street
6th Floor
St. Paul, MN 55101
(612) 228-6400
(612) 228-6572 Fax

REPORT DOCUMENTATION PAGE

Form Approved
OMB NO. 0704-0188

1. AGENCY USE ONLY (Leave blank)	2. REPORT DATE	3. REPORT TYPE AND DATES COVERED
	March 1995	Conference proceedings

4. TITLE AND SUBTITLE
Application of Free-Jet, Molecular Beam, Mass Spectrometric Sampling: Proceedings

5. FUNDING NUMBERS
(C)
(TA) 4300.4000

6. AUTHOR(S)
Thomas Milne, editor

7. PERFORMING ORGANIZATION NAME(S) AND ADDRESS(ES)

8. PERFORMING ORGANIZATION REPORT NUMBER
DE95004052

9. SPONSORING/MONITORING AGENCY NAME(S) AND ADDRESS(ES)

National Renewable Energy Laboratory
1617 Cole Boulevard
Golden, CO 80401-3393

10. SPONSORING/MONITORING AGENCY REPORT NUMBER
NREL/CP-433-7748

11. SUPPLEMENTARY NOTES

12a. DISTRIBUTION/AVAILABILITY STATEMENT

National Technical Information Service
U.S. Department of Commerce
5285 Port Royal Road
Springfield, VA 22161

12b. DISTRIBUTION CODE
UC-1400

13. ABSTRACT *(Maximum 200 words)*

A collection of papers following a conference in Colorado on applications of free-jet, molecular beam, mass spectrometric sampling, to assess the current state of the art and to forge a community that develop this novel analytical approach.

14. SUBJECT TERMS
chemical reactions, biomass, pyrolysis oils, mass spectrometry

15. NUMBER OF PAGES
305

16. PRICE CODE
A13

17. SECURITY CLASSIFICATION OF REPORT	18. SECURITY CLASSIFICATION OF THIS PAGE	19. SECURITY CLASSIFICATION OF ABSTRACT	20. LIMITATION OF ABSTRACT
Unclassified			